Journal of Geophysics
Zeitschrift für Geophysik

Volume 59 1986

Springer International

Journal of Geophysics – Zeitschrift für Geophysik

This journal was founded by the Deutsche Geophysikalische Gesellschaft on the initiative of L. Mintrop in 1924 as the Zeitschrift für Geophysik and edited by G. Angenheister from Vol. 1–18 (1944). It reappeared in 1954 edited by B. Brockamp from Vol. 19–26 (1960), and edited by W. Dieminger from Vol. 27–33 (1961), and from Vol. 34 (1968) edited by W. Dieminger and J. Untiedt. After Vol. 40 (1970) the title was changed to Journal of Geophysics – Zeitschrift für Geophysik.

Published: Vols. 19–39 by Physica-Verlag, Würzburg, from Vol. 40 by Springer Berlin, Heidelberg, New York, Tokyo.

Copyright

Submission of a manuscript implies that the work described has not been published before (except in the form of an abstract or as part of a published lecture, review or thesis), that it is not under consideration for publication elsewhere, that its publication has been approved by all the authors and by the responsible authorities – tacitly or explicitly – in the laboratories where the work was carried out and that, if accepted, it will not be published elsewhere in the same form, in either the same or another language, without the consent of the copyright holders. By submitting a manuscript, the authors agree that the copyright for their article is transferred to the publisher if and when the article is accepted for publication. The copyright covers the exclusive rights to reproduce and distribute the article, including reprints, photographic reproductions, microform, electronic data-base, video-disks, or any other reproductions of similar nature, and translations.

Photographic reproduction, microform, electronic data-base, video-disks, or any other reproduction of text, figures, or tables from this journal is prohibited without permission obtained from the publisher.

The use of general descriptive names, trade names, trade marks, etc., in this publication, even if the former are not specifically identified, is not to be interpreted as exempt from the relevant protective laws and regulations and may accordingly be used freely by anyone.

Special Regulations for the USA

The Article Fee Code on the first page of an article in this journal indicates the copyright owner's consent that in the USA copies may be made for personal or internal use, provided the stated fee for copying beyond that permitted by Section 107 or 108 of the United States Copyright Law is paid through the Copyright Clearance Center, Inc., 21 Congress Street, Salem, Mass. 01970, USA.

If a code does not appear, copies of the article may be made without charge, provided permission is obtained from the publisher.

The copyright owner's consent does not extend to copying for general distribution, for promotion, for creating new works, or for resale. Specific written permission must be obtained from the publisher for such copying.

Other Regulations

Authors of this journal can benefit from library and photocopy fees collected by VG WORT if certain conditions are met. Authors of German nationality and those resident in the Federal Republic of Germany or Berlin (West), as well as citizens of Austria, Switzerland and member countries of the European Community, may apply to Verwertungsgesellschaft WORT, Abteilung Wissenschaft, Goethestraße 49, D-8000 München 2, for detailed information.

Springer-Verlag Berlin Heidelberg New York Tokyo

Printed in Germany by Universitätsdruckerei H. Stürtz AG Würzburg

Volume 59 1986
No. 1 1-88 issued in February 1986
No. 2 89-148 issued in May 1986
No. 3 149-208 issued in August 1986

Author Index

Subject Index

Journal of Geophysics
Zeitschrift für Geophysik

Volume 59 Number 1 1986

Indexed in Current Contents

Evaluated for Physics Briefs and INKA-PHYS data base

Springer International

252 J. Geophys.—ISSN 0340-062X—JGEOD4 59(1) 1–88 (1986)—February 1986

Journal of Geophysics – Zeitschrift für Geoph

Edited for the **Deutsche Geophysikalische Gesellschaft** by **W. Dieminger, G. Müller, and J**

This journal was founded by the Deutsche Geophysikalische Gesellschaft on the initiative of L. Mintrop in 1924 as the *Zeitschrift für Geophysik* and edited by G. Angenheister from Vols. 1–18 (1944). It reappeared in 1954, edited by B. Brockamp from Vols. 19–26 (1960), by W. Dieminger from Vols. 27–33 (1961), by W. Dieminger and J. Untiedt from Vols. 34 (1968), and edited by W. Dieminger, J. Untiedt and G. Müller from Vol. 45 (1979). After Vol. 40 (1970) the title was changed to *Journal of Geophysics – Zeitschrift für Geophysik.*

Published: Vols. 19–39 by Physica-Verlag, Würzburg, from Vol. 40 by Springer-Verlag GmbH & Co. KG Berlin, Heidelberg, New York, Tokyo.

Manuscripts may be addressed to any of the Editors. For addresses see last cover page. Manuscripts should conform with the journal's accepted practice as described in the Instructions to Authors.

The Journal accepts

- Review articles (invited by the editors)
- Original papers
- Short communications
- Letters to the editors
- Book reviews

in the field of Geophysics and Space Physics.

Copyright

Submission of a manuscript implies: that the work described has not been published before (except in the form of an abstract or as part of a published lecture, review, or thesis); that it is not under consideration for publication elsewhere; that its publication has been approved by all coauthors, if any, as well as by the responsible authorities at the institute where the work has been carried out; that, if and when the manuscript is accepted for publication, the authors agree to automatic transfer of the copyright to the society; and that the manuscript will not be published elsewhere in any language without the consent of the copyright holders. All articles published in this journal are protected by copyright, which covers the exclusive rights to reproduce and distribute the article (e.g., as offprints), as well as all translation rights. No material published in this journal may be reproduced photographically or stored on microfilm, in electronic data bases, video disks, etc., without first obtaining written permission from the publisher.

The use of general descriptive names, trade names, trademarks, etc., in this publication, even if not specifically identified, does not imply that these names are not protected by the relevant laws and regulations.

While the advice and information in this journal is believed to be true and accurate at the date of its going to press, neither the authors, the editors, nor the publisher can accept any legal responsibility for any errors or omissions that may be made. The publisher makes no warranty, express or implied, with respect to the material contained herein.

Special regulations for photocopies in the USA: Photocopies may be made for personal or in-house use beyond the limitations stipulated under Section 107 or 108 of U.S. Copyright Law, provided a fee is paid. This fee is US $ 0.20 per page, or a minimum of US $ 1.00 if an article contains fewer than five pages. All fees should be paid to the Copyright Clearance Center, Inc., 21 Congress Street, Salem, MA 01970, USA, stating the ISSN 0340-062X, the volume, and the first and last page numbers of each article copied. The copyright owner's consent does not include copying for general distribution, promotion, new works, or resale. In these case, specific written permission must first be obtained from the publisher.

Other regulations: Authors publishing in this journal can, under certain conditions, benefit from library and photocopy fees collected by VG WORT. Authors of German nationality and those resident in the Federal Republic of Germany or Berlin (West), as well as citizens of Austria, Switzerland and member countries of the European Community, may apply to Verwertungsgesellschaft WORT, Abteilung Wissenschaft, Goethestraße 49, D-8000 München 2, for detailed information.

Subscription information

Volumes 59–60 (3 issues each) will appear in 1986.

Members. Members of the Deutsche Geophysikalische Gesellschaft are entitled to purchase the Journal for their own use at a privilege price of DM 98.00 payable with the Membership dues. Orders should be sent to the Society's office at the following address: Postfach 230, D-3392 Clausthal-Zellerfeld.

North America. Annual subscript
Approx. US $ 166.00 (single issu
Approx. US $ 32.00), including c
charges. Subscriptions are enter
prepayment only. Orders should
to:
Springer-Verlag New York Inc.
Service Center Secaucus
44 Hartz Way
Secaucus, NJ 07094, USA
Tel. (2 01) 3 48-40 33, Telex 0 23-

All other countries. Annual subsc
DM 432.00 plus carriage charge
delivery on request only. Volume
DM 216.00, single issue price: D
carriage charges. Carriage charg
(Surface Airmail Lifted) to Japan,
Australia and New Zealand are a
request. Orders can either be pla
bookdealer or sent directly to:
Springer-Verlag
Heidelberger Platz 3
D-1000 Berlin 33
Tel. (0)30/82 07-1, Telex 1-83 319,

Changes of address: Allow six w
changes to become effective. All
tions should include both old and
addresses (with Postal Codes) a
accompanied by a mailing label f
issue.

Back volumes: Prices are availa

Microform: Microform editions a
from:
University Microfilms Internation
300 N. Zeeb Road
Ann Arbor, MI 48106, USA

Production

Springer-Verlag
Journal Production Department
Postfach 10 52 80
D-6900 Heidelberg 1
Federal Republic of Germany
Tel. (0)62 21/4 87-3 42, Telex 4-61

Responsible for advertisemen

Springer-Verlag
E. Lückermann
Heidelberger Platz 3
D-1000 Berlin 33
Tel. (0)30/8 20 71, Telex 1-85 411.

Printers

Universitätsdruckerei H. Stürtz A

Printed in Germany

Springer International

J Geophys (1986) 59:1–10

Journal of
Geophysics

The detailed velocity structure of the Urach geothermal anomaly

Ch. Walther, H. Trappe, and R. Meissner
Institut für Geophysik der Christian-Albrechts-Universität zu Kiel, D-2300 Kiel, Federal Republic of Germany

Abstract. Two combined reflection-refraction profiles across the geothermal anomaly of Urach were observed in 1978. The reflection records overlap about 16-fold for a distance of 23 km. The first (refracted) arrivals provide detailed information on the structure and P-wave velocities of the sediments and the crystalline basement to a depth of 4 km. A basin-like depression in the basement at the centre of the anomaly coincides with the near-surface features of the Urach volcano. A P-wave anisotropy of about 1 to 5% has been obtained for the upper part of the basement, while the correlation between horizontal P-wave velocities and the temperature remains vague to a depth of 4 km.

Reflection data from the near-vertical and wide-angle ranges are interpreted through model calculations of the shape and lateral dimensions of the low-velocity body detected by previous studies. The models are based on the travel times of wide-angle events recorded by laterally emplaced portable refraction stations in a fan-like configuration. The shape of the low-velocity body shows a remarkable correlation with that of the geothermal anomaly. The southwestern boundary of the body seems to coincide with the Hohenzollern Graben, one of the most seismically active lineaments in Central Europe.

Key words: Low-velocity body – Urach geothermal anomaly – Multiple-coverage refraction seismics – Wide-angle observations– Fan shooting

Introduction

The Urach geothermal anomaly in Southwest Germany has been intensively studied by a large geoscientific community. The deep structure of the anomaly was examined by geophysical, geological and petrological methods, and a borehole was drilled down to 3334 m. The first results were published by Haenel (1982). One of the experiments, the combined reflection-refraction investigation, revealed a large body of low velocity below the centre of the anomaly. While the main results of the reflection-refraction survey were published by Meissner et al. (1980), Bartelsen et al. (1982) and Meissner et al. (1982a, b), two additional lines of interpretation were directed towards:

1. An optimum evaluation of the first (refracted) arrivals from the long reflection spread, to make use of their multifold coverage; and

2. An interpretation of the laterally emplaced portable geophone stations to determine the shape and the lateral extension of the low-velocity body.

The first topic was discussed by Walther (1983) and the second by Trappe (1983). This paper combines their results with previous results obtained along the Urach geothermal anomaly, in order to find a relationship between seismic parameters and temperature.

Geological and geophysical framework

The Urach geothermal anomaly, as shown in Fig. 1, lies in the southwestern part of the Federal Republic of Germany. In this area, north-south outcropping Jurassic rocks form the western part of the Swabian Alb. Together with Triassic layers in the north, these rocks form part of the southern German massif and present an example of a practically undisturbed cuesta landscape (Schädel, 1982). The crystalline basement consists of granitic and gneissic rocks of Variscan age, overlain by Permo-Carboniferous and Upper Permian strata, generally thickening in Variscan-striking (SW-NE) troughs, e.g. the Schramberger Trough, which reaches its greatest thickness in the Urach volcanic area. These strata are overlain by Triassic and Jurassic rocks. Approximately 350 Miocene volcanic pipes (Geyer and Gwinner, 1968) are generally filled with tuffs with rare ultrabasic material.

Important tectonic lineaments are the Variscan-striking Bebenhäuser fault zone, lying northwest of the Urach anomaly, and the WNW-ESE-striking Hohenzollern Graben in the southwest with a length of about 30 km and a width of 1.5–2.0 km. The graben lies in one of the most active seismic zones in Central Europe (Schneider, 1971). For a long time the Urach geothermal anomaly was thought to originate from a shallow magma chamber at the boundary between the sediments and the basement (Cloos, 1941). Geomagnetic measurements by Mäussnest (1956, 1982), however, showed no continuous strong anomalies and suggested magnetic sources of at least 3–4 km in depth. More recent petrographical and petrological interpretations by Wimmenauer (1982) are compatible with a magma chamber deeper in the crust. Groundwater circulation to great depths has also been proposed as an explanation for the origin of the thermal anomaly (Carlé, 1974; Dietrich, 1982).

At an early stage of the seismic investigation of the Urach anomaly, it was proposed that thermal anomalies might be detected by means of anomalies in the seismic velocity field (Meissner et al., 1980). The velocity change

---

Offprint requests to: H. Trappe

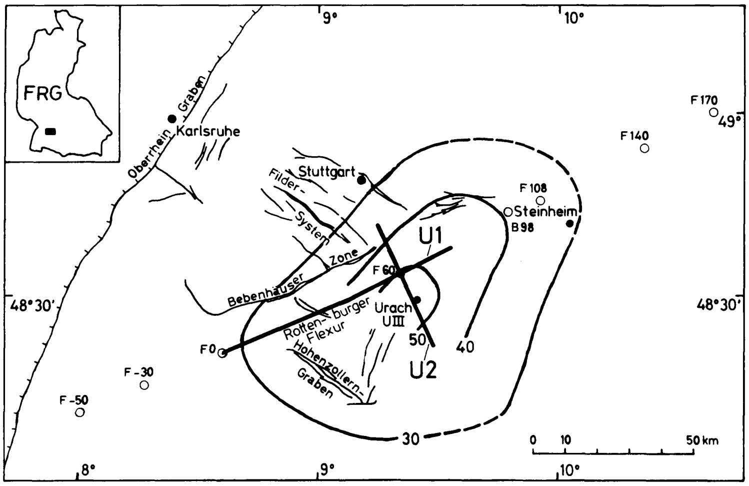

Fig. 1. Location map of the Urach geothermal anomaly, showing the two seismic profiles U 1 and U 2, wide-angle stations F 50 to F 170 and some tectonic features. Contour lines are temperature isotherms in °C at 500 m after Haenel (1976)

for a temperature anomaly is quite small. Laboratory experiments by Kern (1978) showed that the expected decrease in P-wave velocity is only about 1% for a temperature increase of 100° C. Velocity changes caused by anisotropy may be much larger, although possibly restricted to small-scale features. In either case, the most precise determinations of velocity are required. Obviously, unusually long spread-lengths had to be introduced in order to obtain reliable move out times for linear control of the velocities.

The seismic experiment

Figure 1 shows the location of the two profiles, termed U 1 and U 2. The field recordings were carried out in the summer of 1978. Profile U 1 was measured by a 23-km geophone spread, consisting of three independent reflection units, which made it possible to record a moveout of 1 s for the Moho reflection. Some modifications were made in recording profile U 2. Seismic energy was generated by 51 borehole shots along profile U 1 and 12 along U 2. An eightfold reflection coverage and a 16-fold refraction coverage was obtained for profile U 1. On average a sixfold coverage was achieved for profile U 2.

Portable refraction stations of the MARS 66 type (Berckhemer, 1970) were employed along U 1 and its lateral extension, as seen in Fig. 1, operated by observers from universities and other institutions. Seventeen semi-permanent stations, at distances of 20–40 km, provided additional information for the first arrivals, while some permanent stations recorded wide-angle reflections of the deep crustal layers.

First arrivals of the reflection spreads

The first arrivals were the refracted arrivals of the seismic reflection measurements, comprising 63 shots correlated along 144 traces. As discussed, new techniques had to be developed to allow for the high redundancy of the 16-fold overlapping refraction branches and make an optimum interpretation. Figure 2 (profile U 1) shows the first arrivals as a time-distance diagram. They have been reduced to a reference plane of 300 m above sea level. In addition, a meander correction (for shot points with a lateral offset from the profile) and a weathering correction were applied, using velocities characteristic of refractions from the Dogger, Keuper and Muschelkalk layers and the crystalline basement. No refraction arrivals were recorded from the Rotliegend layer (Upper Permian) because the velocities are lower there than in the overlying Triassic layers. Instead, a pronounced time delay was observed, separating the refracted waves of the overburden from those of the basement. To determine the horizontal velocities in the basement a further correction was required, the reduction of the travel-times to a datum level within the crystalline layer.

In modelling the sedimentary layers and their velocities, borehole data on the near-surface geology in the area around the profiles and the approximate thickness of the Rotliegend layer (as obtained from the time delays) were incorporated. The final model was determined by varying the model parameters in ray-tracing calculations to provide the best fit between the calculated travel-times and those of the observed arrivals from the overburden and the upper crystalline region. All velocity values are listed in Walther (1983). The structure of the sediments is shown on Fig. 3 and 4. Travel-time differences between the observations and the model were determined with an accuracy of ±11 ms, i.e. the deviations were in the range of the assumed digitization error of ±10 ms. The velocities vary by about ±0.08 km/s. The scatter of the travel-times may be related to the variable depth to crystalline basement, which was about ±40 m assuming constant velocity.

To model profile U 1, the western part at 0–58 km was used, and the subcrystalline datum plane was fixed at 630 m below sea level. Residual travel-times were calculated by applying static corrections, and the reciprocal travel-times were finally determined. The residual travel-times were smoothed by the Wiechert-Herglotz method (Wiechert and Herglotz, 1931), whereby small irregularities along the travel-time curve are smoothed by second degree polynomials. An initial evaluation using this method showed extremely strong horizontal variations, most of them caused by dipping layers or small inhomogeneities in velocity. In order to apply the Wiechert-Herglotz method, these effects had to be eliminated and the method restricted to discrete parts of the profile. As a first step, the apparent velocities from forward and reverse shots in the form of normal and reciprocal residual travel-time branches were determined, and "true" velocities were calculated by an averaging process.

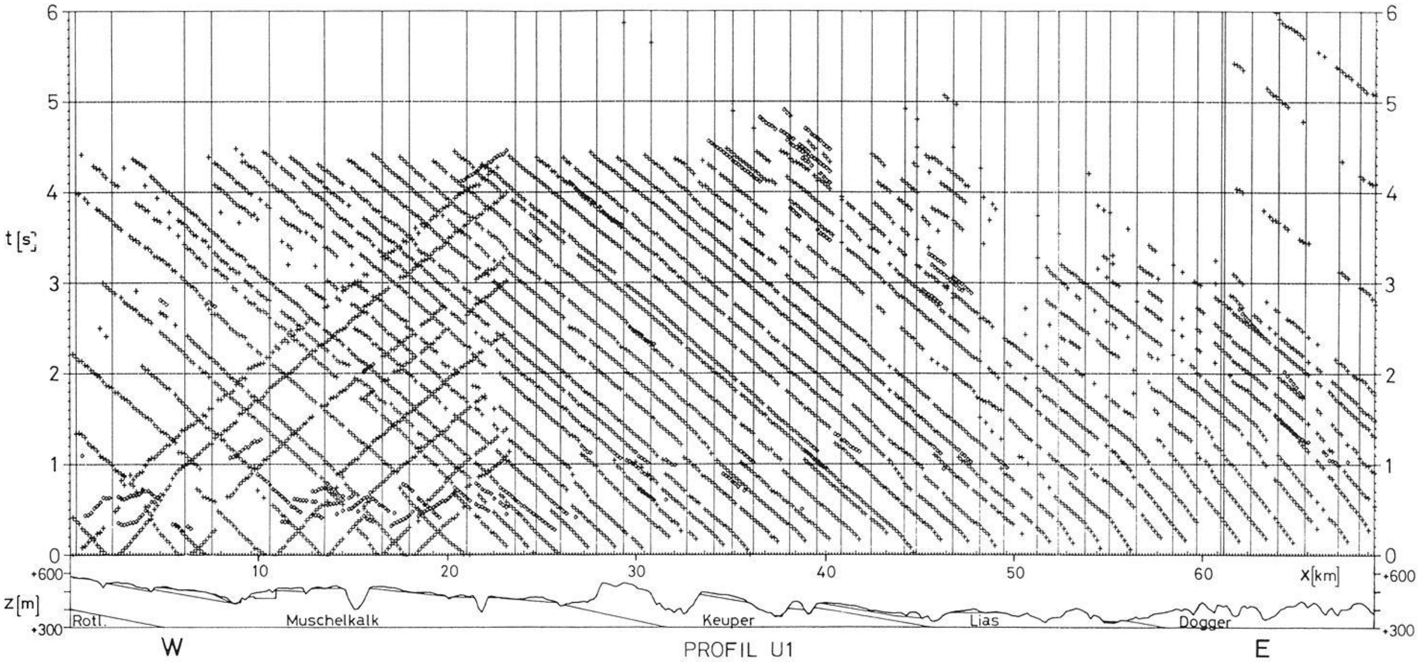

Fig. 2. Travel-time diagram of the first (+) and second arrivals (◇) of profile U1 after correction to a reference level of 300 m above sea level; near-surface geology is included

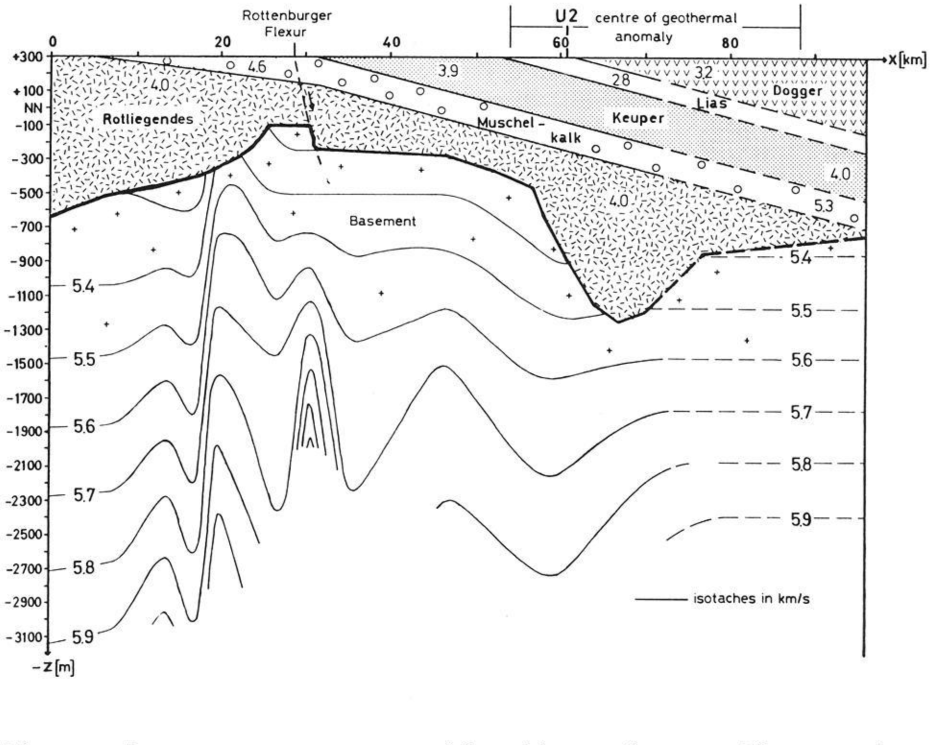

Fig. 3. Model of sedimentary layers and velocity isotachs (km/s) in the crystalline basement along profile U1. Vertical exaggeration: 20

The second step was to construct a tight grid over the "time-distance field". Form, size and weighting of the area around the intersections of the travel-time branches were determined by the use of a theory developed by Matheron (1965) concerning regionalized variables and the related variogram function (David, 1977). The Wiechert-Herglotz method was then applied to the velocities and distance values of the intersections at the vertical grid lines, thus converting the "time-distance field" to a "depth-distance field".

The ray-tracing program was applied to this new model of velocities in the overburden and basement. After many iterations, the final model of profile U1 was obtained (Fig. 3). The error between the calculated and observed travel-times was determined for two time zones (relating to different depth zones). The scatter for the 2.5-s zone was ±12 ms, and for the 3.5-s zone, ±17 ms.

The short-wavelength velocity variations on the left side of Fig. 3 certainly look surprising. They may indicate a horst-like structure, possibly associated with steep fault

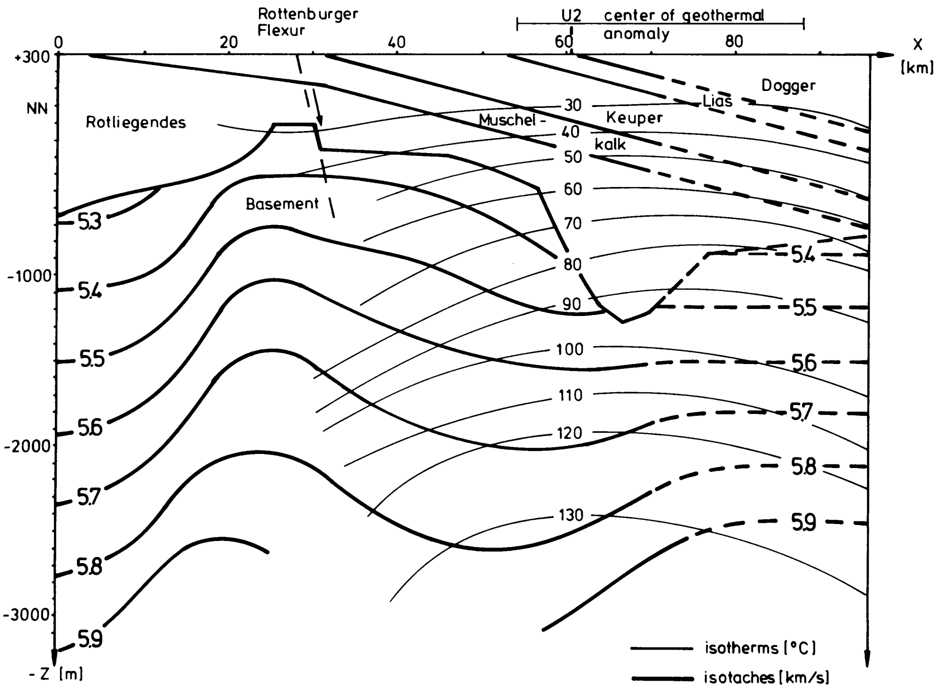

Fig. 4. Low-pass filtered variations of the velocity (km/s) in the crystalline basement along profile U 1; isotherms (°C) after Carlé (1974), Haenel (1976) and Zoth (1982). Vertical exaggeration: 20

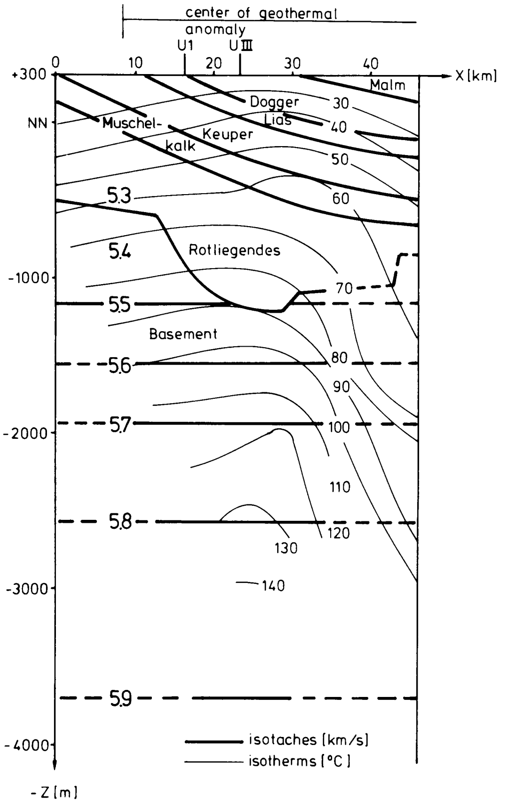

Fig. 5. Model of sedimentary layers and velocity structure (km/s) along profile U 2; isotherms (°C) after Carlé (1974), Haenel (1976) and Zoth (1982). Vertical exaggeration: 20

zones. In order to check the reliability of the model, a low-pass filter was used to smooth the velocity values and the error analysis was repeated. This "low-pass" model is presented in Fig. 4. However, the travel-time errors in the soothed section were larger than in the original model, indicating that the short-wavelength anomalies shown on Fig. 3 are real.

Profile U 2 (Fig. 5) was interpreted only by the ray-tracing method. The poor quality data and two large gaps in the spreads did not warrant a more refined interpretation. The differences between calculated and observed travel-times, though, are small, being ±15 ms for the 3-s zone and ±12 ms for the 5-s zone.

Discussion of results obtained from the first-arrival studies

From the 20-fold exaggeration of the sections in Figs. 3, 4 and 5, the top of the crystalline basement appears as a rough, strongly undulating boundary. The flanks on both sides of the Rotliegend trough at the centre of the geothermal anomaly have a dip of about 6°. In this trough the deep borehole U III was drilled, and both profiles, U 1 (Figs. 3 and 4) and U 2 (Fig. 5), cross this area. While the velocities of the overlying sediments vary between 2.8 and 5.3 km/s, as shown on Fig. 3, values of about 5.3–5.5 km/s are found at the top of the basement, increasing to about 5.9 km/s at about 3 km depth. No similar gradients were found in the vertically determined velocities, V_z, of borehole U III, nor in sonic logs or well shooting (Haenel, 1982; Wohlenberg, 1982). At the top of the basement, at about 1.6 km depth, both velocities agree: $V_Z = 5.5 \pm 0.1$ km/s and $V_H = 5.6 \pm 0.1$ km/s (this study). At 2 km $V_Z = 5.5 \pm 0.1$ km/s and $V_H = 5.7 \pm 0.1$ km/s. At the bottom of the borehole, at about 3 km, $V_Z = 5.6 \pm 0.1$ km/s and $V_H = 5.9 \pm 0.15$ km/s. The tendency for higher V_H values, i.e. a velocity anisotropy, was often found in the sediments as well as in the crystalline basement, where nearly always $V_H > V_Z$ (Meissner, 1967). With average values of V_Z and V_H, the anisotropy increases from 1% at the top of the basement to about 5% at 3 km depth. The V_H values in this study also agree with those of Jentsch et al. (1982), who found an average value of 5.66 km/s to a depth of 4–5 km for refraction profiles. However, this average is a rough one, considering the limited resolution in distance and depth of such low-coverage measurements.

Figures 3, 4 and 5 suggest a correlation between the velocity and the temperature field. Many laboratory studies have shown that the sensitivity of P-waves to temperature T increases with increasing T and that their sensitivity may be low for the low-temperature along the top of the crystalline basement. Nevertheless, some correlation between V_P and T is indicated for the geothermal anomaly. This is best seen in the long-wavelength interpretation of Fig. 4. The upturned isotherms as calculated by various authors and summarized by Walther (1983) correspond to downturned isotachs.

Another interesting correlation was found between the area of the Rotliegend trough, below the centre of the geothermal anomaly, and that of the vocanic pipes. This correlation clearly has a genetic relationship. Post-Variscan extensional stress patterns dominated the upper Permian and formed a number of basins and troughs like that in the Urach area. These zones of weakness, probably associated with extensional faults, might have allowed the ascent of basaltic lava, which may well have been stored at medium crustal levels (Wimmenauer, 1982). Further, the low-velocity area in the western-most part of profile U1 coincides with CO_2 exhalations near Sulz.

Near-vertical reflection studies

As mentioned in the introduction, interpretations of the near-vertical reflection data have been published by Bartelsen et al. (1982) and Meissner et al. (1982a, b). The most exciting discovery of these studies was a huge low-velocity body in the crust below the Urach geothermal anomaly, as seen from variations of the stacking velocity along profile U1. Transformation from stacking velocities to interval velocities was performed by a method of Krey (1978, 1980). Up to 10% variation was found in the vertical-interval velocities compared with the surrounding "normal" values.

As a basis for discussion of the wide-angle observations, Fig. 6 indicates the quality of the data and Fig. 7 shows the U1 profile of the low-velocity body.

Figure 6 shows an eightfold stacked record section of profile U1. In general, the reflection density increases towards the base of the crust, where the reflections terminate abruptly. Quality is generally good, especially in the left-hand side of the section, where phase correlations of over 30 km are possible for reflections near the Moho boundary. Only those reflections that are relevant for the wide-angle studies are marked.

Figure 7 shows the low-velocity body along profile U1 as detected by the previous near-vertical reflection studies. It is interesting that the presence of this body leads to a remarkable change of Moho dips. Neither COCORP- nor BIRPS-type reflection surveys with their short spread lengths, nor refraction observations, would have been able to gather such detailed velocity information.

Linear wide-angle reflection studies

Two of the 17 record sections along profile U1 are presented in Fig. 8. The stations (FO and F 108) (located on Fig. 1) that recorded these sections covered the centre of the anomaly, and recorded all the U1 shots. Amplitudes were normalized to the maximum amplitude in each trace. The P_g-wave, penetrating the upper part of the basement, the P_MP-wave, a wide-angle event from the Moho, and some intracrustal reflections are shown on these sections.

Initially the depths to the reflecting boundaries in all sections were estimated by conventional t^2-x^2 calculations and plotted below the centre of the shot-geophone distance. These uncorrected depth values, which were taken to be boundaries with a positive reflection polarity, i.e. marking a jump to a higher-velocity layer, were compared with the uncorrected reflection elements from the near-vertical reflections. Figure 9 shows the two sets of data, the reflecting elements from a composition of single-coverage records and the boundaries from the wide-angle studies (shaded grey lines). The latter appear more continuous, but show a much lower depth resolution than the individual reflections. In general, there is some correlation between both kinds of boundaries: the near-vertical reflection density generally increases near the wide-angle boundaries. In particular, the lowermost reflector, the Moho is clearly visible on both

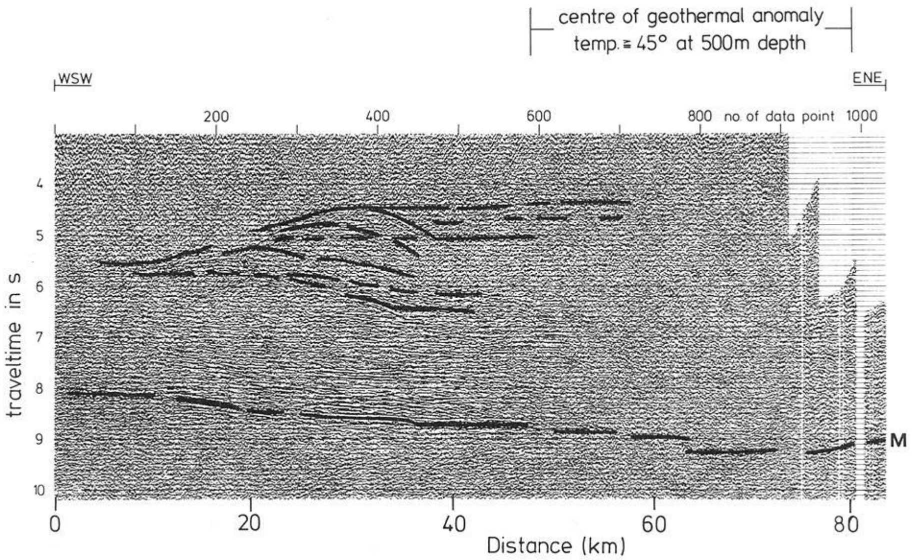

Fig. 6. Eight-fold stacked seismogram section of profile U1. Some reflections relevant to the low-velocity body are indicated (Meissner et al., 1982a)

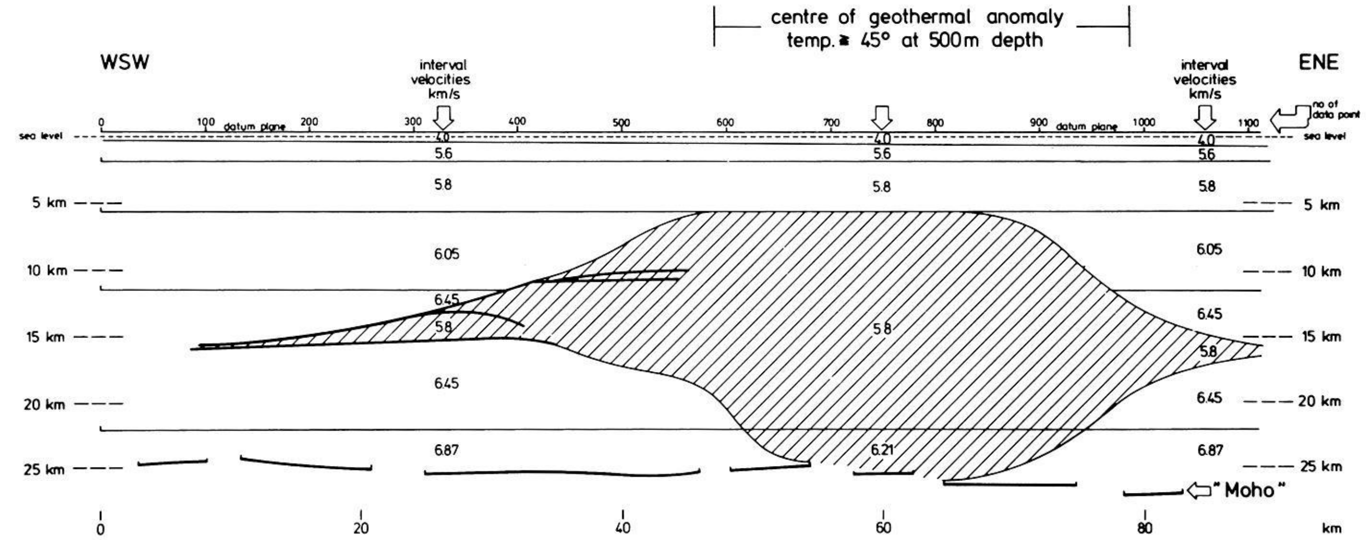

Fig. 7. The Urach low-velocity body along profile U1 (*hatched area*), as obtained by Bartelsen et al. (1982) from variations in stacking velocities (after Krey, 1980)

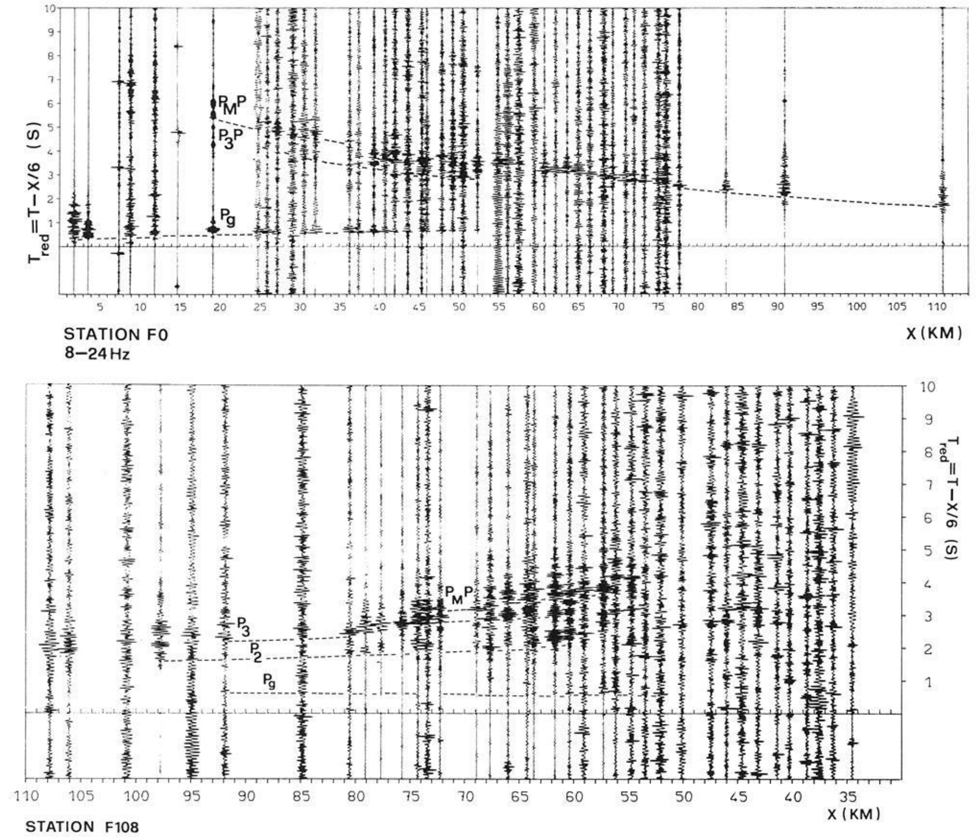

Fig. 8. Two examples of wide-angle record sections, stations F0 top and F108 bottom, reduced with 6 km/s. P_MP is the wide-engle event from the Moho; P_g is the steep wave in the crystalline basement. Other correlations refer to intracrustal boundaries

data sets. A remarkable deviation, however, occurs below the centre of the anomaly at the intersection with profile U2. The fictious trough in the Moho is much more pronounced in the wide-angle data, perhaps indicating that the oblique rays of the wide-angle events take a longer travel time in the low-velocity body.

Another interesting feature is the concentration of reflections at 10–13 km depth, which is especially strong in the left side of Figs. 6, 7 and 9. These reflections were not matched by any wide-angle arrivals, and hence may indicate the upper boundary of the low-velocity body and may have a negative polarity. Wide-angle reflections would be too weak to reveal such a boundary. This suggestion is compatible with the depth-penetration of the steep P_g-wave, which reached about 10 km all along profile U1, showing a positive velocity gradient down to this depth. The uppermost reflections of Fig. 6 at about a 4.4-s two-way travel-time also correspond to a depth of 10–11 km. Both observations

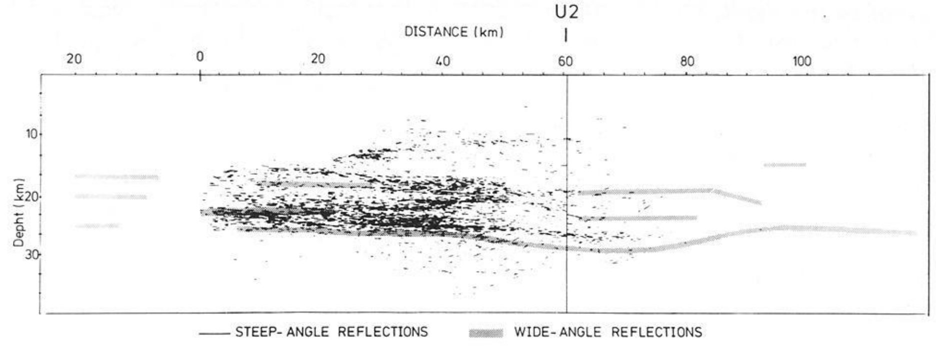

Fig. 9. Comparison between a composition of single-coverage near-vertical reflections and wide-angle bondaries along profile U 1

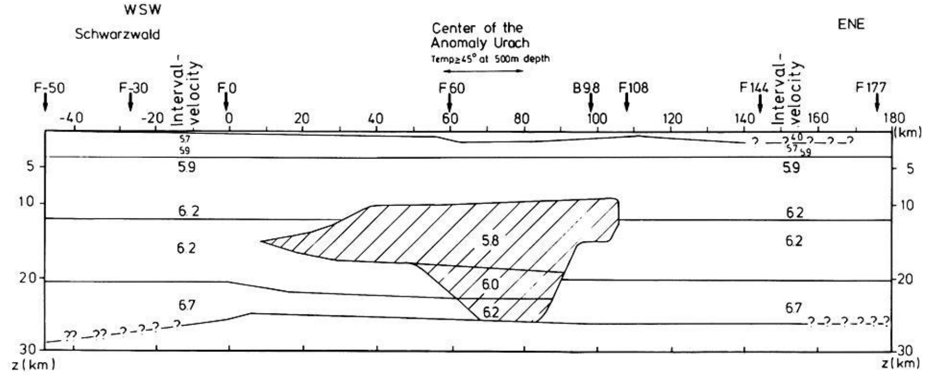

Fig. 10. The Urach low-velocity body as obtained by wide-angle model calculations

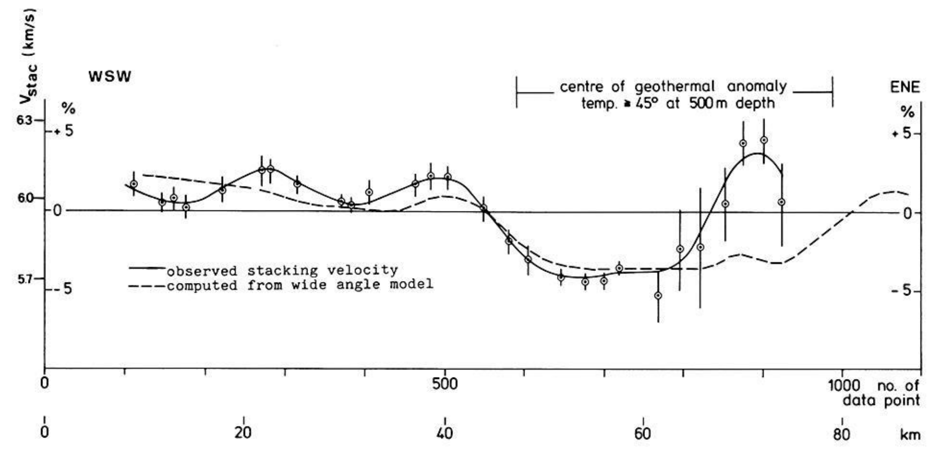

Fig. 11. Moho stacking velocities (——) with error bars (Bartelsen et al., 1982) and stacking velocities as calculated (––––) for the wide-angle low-velocity body of Fig. 10

indicate that the upper boundary of the low-velocity body is at about 10 km, and not at 6 km depth as shown in the model of Fig. 7.

The following interpretation assumes that the upper boundary of the low-velocity body is fixed at 10 km at the centre and at 10–15 km at the left-hand part (Fig. 7), based on the reflection pattern. It is further assumed that the lower boundary coincides with the Moho and that the interval velocities in the central part remain unchanged. With these assumptions, Trappe (1983) applied a trial and error ray-tracing procedure with the objective of obtaining the best fit between observed and calculated wide-angle events by modifying the shape of the boundaries, i.e. the flanks, of the low-velocity body. The outcome of these calculations is shown on Fig. 10. Compared with the low-velocity body in Fig. 7 the shape looks slightly different, but its lateral extension and its velocity structure are very similar. By calculating synthetic seismograms using the reflectivity method (Fuchs and Müller, 1971), Trappe (1983) also showed that the boundaries inside the low-velocity body that correspond to P_2 and P_3 events in Fig. 8 may originate at thin layers of higher velocities. This model could explain the surprisingly large amplitudes of P_2 and P_3 at the centre of the low-velocity body. It is also compatible with the assumption of a laminated structure for the lower crust (Meissner, 1967, 1973).

It has still to be shown that the shape of the "wide-angle low-velocity body" agrees with the velocity data from the near-vertical reflection studies, especially with the stacking velocities along profile U 1. Figure 11 compares the observed variations of the Moho stacking velocity and its error bars after Bartelsen et al. (1982) with the calculated stacking velocity from the new model of the low-velocity body. Both lines show the same trends and agree within the error bars over most parts of the section. However, there are large deviations at the right side of the low-velocity body and here the largest differences occur in the shapes of the two models. It might be argued that here, also, the quality of near-vertical reflections was poor and the error bars show a maximum. In general, though, this discrepancy cannot be solved with the available data. Since the stacking velocities generally coincide along the profile, both models are compatible with the velocity data from the western flank up to the centre of the anomaly.

Wide-angle reflection studies from laterally emplaced stations

This part of the interpretation deals with the signals from shot points along profile U2, recorded by the permanent stations along profile U1. Station FO (Fig. 1) was one of the most reliable. Figure 12 gives a record section from this station, showing P_g- and P_MP arrivals from distances of 61.4–67.3 km (lower scale) and the offset from the U1-U2 intersection (upper scale). While there is agreement between observed and calculated travel times in the northern part (left side), there is a pronounced deviation between these data in the southern sector. Even the P_g arrivals show a slight deviation. The figure indicates a strong delay in P_MP, which can be explained by a low-velocity body along its ray paths, the low-velocity body being mainly situated south of the intersection U1-U2.

Travel-time delays for P_MP at three stations are plotted in Fig. 13 showing Δt up to 0.3 s. For comparison, the deviation of stacking velocities along profile U2 is also presented (upper part), showing a velocity minimum in the area of the largest travel-time delay of the wide-angle signals. The lowermost part of Fig. 13 shows the travel-time variations caused by a southward dipping Moho boundary. Clearly, they provide only minor corrections to the delays caused by the low-velocity body.

In modelling the lateral extension of the LVB, two assumptions were made. First, the general shape of the low-velocity body was assumed to be similar to that of the cross section of profile U1, as suggested by a similar variation in stacking velocities. Second, the upper boundary at about 10 km and the lower boundary at the Moho were assumed to be unchanged, since the P_g and P_MP waves behaved similarly along both profiles. With these assumptions, the lateral dimensions of the low-velocity body were systematically changed until the ray-tracing process achieved the best fit for the calculated and observed travel times.

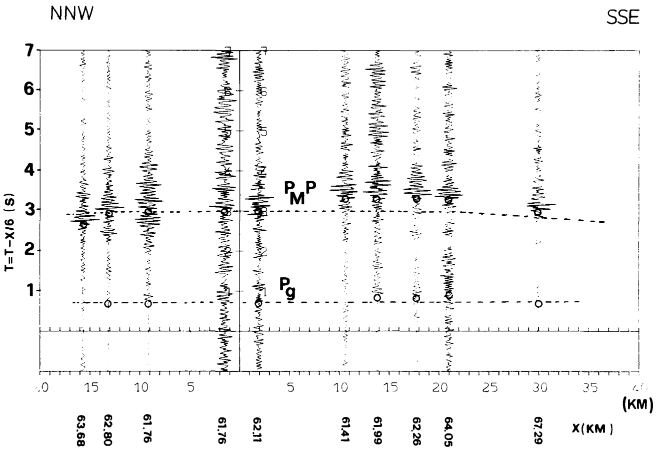

Fig. 12. Record section from station F0, showing arrivals from the fan-like arrangement of shots along profile U2. Total distance is indicated by the lower scale; distance along profile U2, north and south of the U1-U2 intersection, is shown by the upper scale. The *dashed lines* show calculated travel times based on a standard velocity-depth function (for the western part of profile U1) outside the low-velocity body. *Open circles* mark P_MP and P_g arrivals

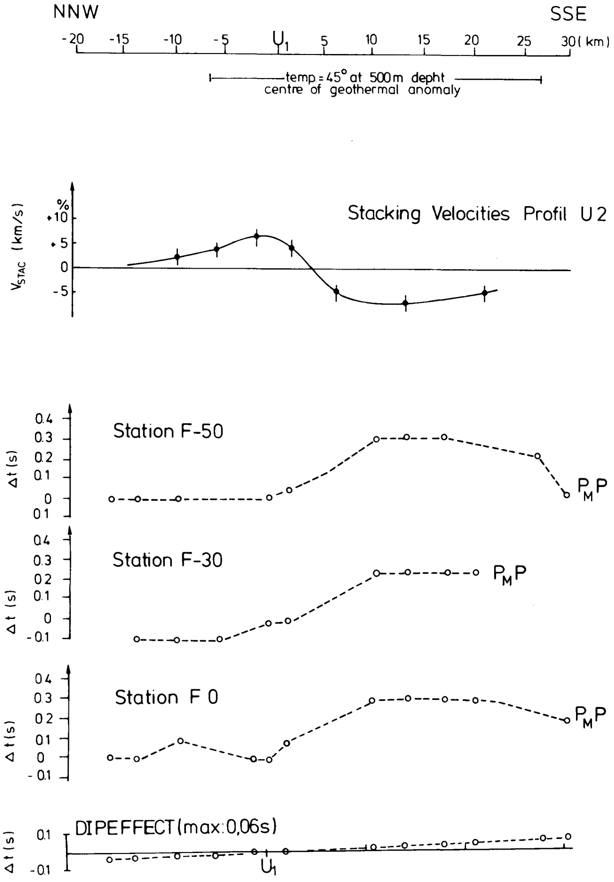

Fig. 13. Travel-time delays (Δt) in observed P_MP arrivals compared with calculated travel-times based on a standard velocity-depth function valid outside the low-velocity body, for stations F-50, F-30 and F0. Also shown are stacking velocities along profile U2 (upper part) and travel-time delays in P_MP-waves caused by a southward dip in the Moho

Figure 14 shows the extension of the lower part of the low-velocity body as obtained from the match of the P_MP arrivals. Not only does its centre coincide with that of the geothermal anomaly, but its general shape matches those of the temperature isotherms at 500 m depth. The southwestern boundary of the low-velocity body just touches the Hohenzollern Graben, one of the most seismically active lineaments in Central Europe. The upper boundary of the body and its general shape are similar to the model of Gajewski and Prodehl (1985) which was based on wide-angle refraction studies.

Conclusions

Geophone spreads with lengths of up to 23 km were able to reveal the velocity structure below the Urach geothermal anomaly: the large moveout times and the multiple coverage of first arrivals permitted calculation of the near-surface

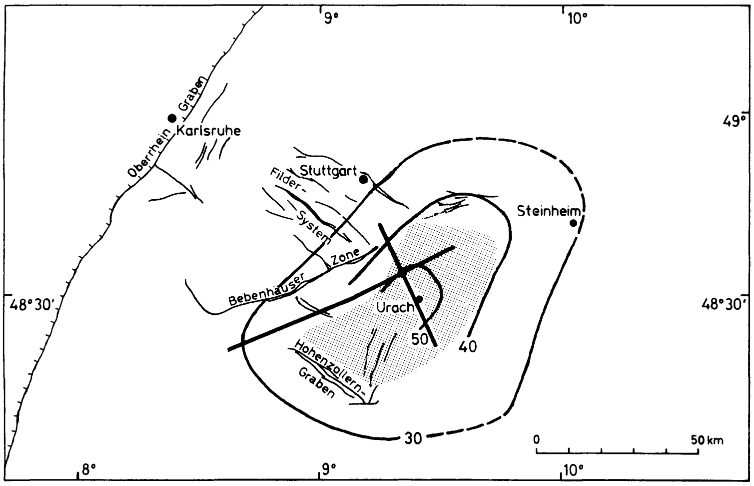

Fig. 14. The lateral extension of the Urach low-velocity body (shaded area) compared with temperature isotherms at 500 m depth (Haenel, 1976)

velocity structure with unusual accuracy. In the upper part of the crystalline basement a seismic anisotropy of 1–5% and a weak, inverse correlation between temperature and seismic velocity were observed. Additional geophone stations in the wide-angle area, both linear and off-set, allowed assessment of the shape of the low-velocity body by means of oblique or horizontal wide-angle signals. The large low-velocity body in the middle and lower crust seems to have its upper boundary at about 10 km depth, as indicated by the first continuous reflections and the maximum penetration of P_g waves.

The shape and the velocity structure of the "wide-angle low-velocity body" is similar to that of the "steep-angle low-velocity body" of Meissner et al. (1982a, b). Differences appear in the upper boundary (10 versus 6 km depth) and in the lateral extension to the NNE, as shown on Figs. 7 and 10.

Comparison of the results for the low-velocity body with those from a refraction network (Gajewski and Prodehl, 1985) in the southern part of the geothermal anomaly produced a strong similarity for the upper 10–18 km depth. No anomalies in velocity, however, were detected in the lower crust. This discrepancy may have been caused by the limited resolution of refraction work in general or by the different location of the profiles.

Velocity anomalies up to 10% are not uncommon in the centres of geothermal anomalies, e.g. in the Geysers and in the Yellowstone area (Iyer and Hitchcock, 1975; Smith et al. 1978); Meissner et al. (1982a, b) and Bartelsen et al. (1982) have argued that a velocity reduction of up to 10% cannot be explained by a purely thermal effect, which would result in an unreasonably large temperature anomaly of + 500–600° C compared with surrounding temperatures. Hydrothermal alterations or cracks by cooling processes of a former large intrusion might contribute substantially to the existence of the strong low-velocity body. There is at least some relation to temperature, as indicated by the observation that the maximum depth of hypocentres is definitely shallower in the area of the geothermal anomaly than in its vicinity (Trappe et al., 1984). A similar correlation between temperature and maximum earthquake depth was established by Smith et al. (1977) and Meissner and Strehlau (1982).

Extensional stresses in the Upper Permian, with the formation of the central trough and the Tertiary mafic to ultramafic volcanism, might be related to intermediate magma lenses or to chambers which might have cooled and concentrated by now, but might still be responsible for the low velocities, the heat flow anomaly and the extremely strong concentration of near-vertical reflectors in the middle and lower crust.

Acknowledgements. The field work and part of the interpretation were supported by the Bundesministerium für Forschung und Technologie (Federal Ministry for Research and Technology; grant No. T82-160). Reflection measurements were carried out by PRAKLA-SEISMOS, while portable refraction stations were operated by scientists and students from 10 different geophysical institutes. Thanks are due to all participants.

References

Bartelsen, H., Lüschen, E., Krey, Th., Meissner, R., Schmoll, H., Walther, Ch.: The combined seismic reflection-refraction investigation of the Urach Geothermal Project. In: The Urach Geothermal Project, Haenel, R., ed., pp 231–245. Stuttgart: Schweizerbart, 1982

Berckhemer, M.: MARS-66, eine Magnetbandapparatur für seismische Tiefensondierung. Z. Geophys. **36**, 501–518, 1970

Carlé, W.: Die Wärme-Anomalie der mittleren Schwäbischen Alb (Baden-Württemberg). In: Approaches to Taphrogenesis. Illies, N.J., Fuchs, K., eds., pp 207–212. Stuttgart: Schweizerbart, 1974

Cloos, H.: Bau und Tätigkeit von Tuffschloten. Untersuchungen an dem Schwäbischen Vulkan. Geol. Rdsch. **32**, 705–800, 1941

David, M.: Geostatistical ore reserve estimation. Developments in Geomathematics 2. Amsterdam: Elsevier Scientific Publishing Co., 1977

Dietrich, H.-G.: Hydrogeological Results from the Urach 3 Research Borehole. In: The Urach Geothermal Project, Haenel, R., ed., pp 59–79. Stuttgart: Schweizerbart, 1982

Fuchs, K., Müller, G.: Computation of synthetic seismograms with the reflectivity method and comparison with observations. Geophys. J. R. Astron. Soc. **23**, 417–433, 1971

Gajewski, P., Prodehl, C.: Crustal structure beneath the Swabian Jura, SW Germany, from seismic refraction investigation. J. Geophys. **56**, 69–80, 1985

Geyer, O.F., Gwinner, M.P.: Einführung in die Geologie von Baden-Württemberg. Stuttgart: Schweizerbart, 1968

Haenel, R.: Möglichkeiten der Nutzung geothermischer Energie in der Bundesrepublik Deutschland. Report N28B, NLfB, Hannover, 1976

Haenel, R. (ed.): The Urach Geothermal Project. Stuttgart: Schweizerbart 1982

Iyer, H.M., Hitchcock, T.: Teleseismic residuals at the geysers geothermal area. Eos **56**, 1020, 1975

Jentsch, M., Bamford, D., Emter, D., Prodehl, C.: A seismic refraction investigation of the basement structure in the Urach geothermal anomaly, Southern Germany. In: The Urach Geothermal Project. Haenel, R., ed., pp 231–245. Schweizer'bartsche Verlagsbuchhandlung, Stuttgart: 231–245, 1982

Kern, H.: The effect of high temperature and high confinig pressure on compressional wave velocities in quartz-bearing and quartz-free igneous and metamorphic rocks. Tectonophysics **44**, 185–203, 1978

Krey, Th.: Seismic stripping helps unravel deep reflections. Geophysics **43**, 91–111, 1978

Krey, Th.: Mapping non-reflecting velocity interfaces by normal moveout velocities of underlying horizons. Geophys. Prospect. **28**, 359–371, 1980

Mäussnest, O.: Erdmagnetische Untersuchungen im Kirchheim-Uracher Vulkangebiet. Ober. Mitt. oberrhein. geol. Ver., Stuttgart, **38**, 23–54, 1956

Mäussnest, O.: The volcanic phenomena in the Urach region. In: The Urach Geothermal Project, Haenel, R., ed., pp 157–160. Stuttgart: Schweizerbart 1982

Matheron, G.: Les variables régionalisées et leur estimation. Paris: Edition Masson, 1965

Meissner, R.: Zum Aufbau der Erdkruste. Ergebnisse der Weitwinkelmessungen im bayerischen Molassebecken. Teil I und II. Gerland Beitr. z. Geophys. **76**, , 295–314, 1967

Meissner, R.: The Moho as a transition zone. Geophys. Surv. **1**, 195–216, 1973

Meissner, R., Strehlau, J.: Limits of stresses in continental crusts and their relation to the depth-frequency distribution of shallow earthquakes. Tectonics **1**, 73–89, 1982

Meissner, R., Bartelsen, H., Krey, Th., Lüschen, E., Schmoll, J.: Combined reflection and refraction measurements for investigating the geothermal anomaly of Urach. Detailed Summary. In: Advances in European Geothermal Research. Strub, A.S., Ungemach, P., eds. Dordrecht-Boston-London: D. Reidel Publ. Co., 1980

Meissner, R., Bartelsen, H., Krey, Th.: reflexionsseismische Untersuchungen struktureller und lithologischer Parameter in geothermisch anomalem Gebiet am Beispiel Urach. BMFT-Forschungsbericht, T82–160, 1982a

Meissner, R., Bartelsen, H., Krey, Th., Schmoll, J.: Detecting Velocity Anomalies in the Region of the Urach Geothermal Anomaly by means of new Seismic Field Arrangements. In: Geothermics and Geothermal Energy, Cermak, V., Haenel, R., ed. pp 285–292. Stuttgart: Schweizerbart 1982b

Schädel, K.: The geology of the heat anomaly of Urach. In: The Urach Geothermal Project, Haenel, R., ed., pp 147–156. Stuttgart: Schweizerbart 1982

Schneider, G.: Seismizität und Tektonik der Schwäbischen Alb. Stuttgart: Enke, 1971

Smith,R.B., Shuey, R.T., Pelton, J.R., Bailey, J.P.: Yellowstone hot spot: contemporary tectonics and crustal properties from earthquake and aeromagnetic data. J. Geophys. Res. **82**, 3665–3676, 1977

Smith, R.B., Schilly, M.M., Braile, L.W., Ansorge,J., Lehmann, J., Baker, M.R., Prodehl, C., Healy, J.H., Mueller, S., Greensfelder, R.W.: The 1978 Yellowstone-Eastern Snake River Plain Seismic Profiling Experiment: Crustal structure of the Yellowstone Region and experiment design. J. Geophys. Res. **87**, 2583–2596, 1978

Trappe, H.: Auswertung von Weitwinkelreflexionen des Projektes Urach und eine Korrelation zu den Ergebnissen der Steilwinkelseismik. Diplomarbeit, Institut für Geophysik, Kiel, 1983

Trappe,H., Strehlau, J., Walther, Ch.: The low velocity body below the Urach geothermal anomaly: An important tectonic element of the Swabian Alb (abstract). Terra cognita, **4**, 120, 1984

Walther, Ch.: Auswertung der Ersteinsätze reflexions-seismischer Messungen im Bereich der geothermischen Anomalie Urach-Südwestdeutschland. Diplomarbeit, Institut für Geophysik, Kiel, 1983

Wiechert, E., Herglotz, G.: Handbuch der Experimentalphysik. Geophysik, **2**, 555, 1931

Wimmenauer, W.: Remarks on the depth of the Urach magma chamber. In: The Urach Geothermal Project. Haenel, R., ed., pp 161–163. Stuttgart: Schweizerbart 1982

Wohlenberg, J.: Seismo-Acoustic and Geoelectric Experiments within the Urach 3 Borehole. In: Haenel, R., ed., pp 97–100. Stuttgart: Schweizerbart 1982

Zoth, G.: The temperature field of the Urach area. In: The Urach Geothermal Project. Haenel, R., ed., pp 97–100. Stuttgart: Schweizerbart 1982

Received August 10, 1984; Revised version February 22, 1985
Accepted July 26, 1985

J Geophys (1986) 59:11–15

Journal of Geophysics

The effect of *SKS* scattering on models of the shear velocity-structure of the D" region

T. Lay and C.J. Young
Department of Geological Sciences, University of Michigan, Ann Arbor, Michigan 48109-1063, USA

Abstract. Several recent seismological models for the *P*- and *S*-wave velocity structure of the lowermost 300 km of the mantle (D" region) have proposed the existence of first-order discontinuities several hundred kilometers above the core-mantle boundary. Long-period transverse-component *S*-waves in the distance range 72°–95° provide the clearest evidence for a lower-mantle discontinuity. Arrivals between *SH* and *ScSH* in the range 72°–82°, and a double *S* arrival in the range 90°–95°, have been interpreted as effects of a lower-mantle triplication produced by a 2.75% velocity increase 280 km above the core. However, it is well established that the D" layer has significant lateral heterogeneity and caution must be exercised when interpreting lower-mantle signals with radially symmetric structures. This paper explores the possibility that the tangential component complexity, which has previously been interpreted by a discontinuity model, is actually produced by *SKS* contamination. It is shown that *SKS* has the wrong timing and ray parameter to possibly account for the *SH* observations in all but a small portion (77°–80°) of the triplication range (72°–95°). Even when strong *SKS* arrivals are apparent on the radial *SV* components, *SKS* contamination of the transverse components is usually very minor in the previously modeled long-period data. The fact that *SKS* is typically nodal in that data set further supports the lower-mantle discontinuity model interpretations. These results do not preclude the existence of lateral variations in the discontinuity or within the D" layer beneath it, and do not eliminate the need for caution to avoid possible *SKS* contamination in future data analysis.

Key words: Lower-mantle velocity structure – S-wave triplication – *SKS* signals – D" region – Velocity heterogeneity

Introduction

It is well established that the *P*- and *S*-wave velocity gradients at the base of the mantle are anomalous, being lower than gradients in the mid-mantle, and also that the lowermost 300 km of the mantle (D" region) has significant lateral heterogeneity. However, despite numerous studies of *P*- and *S*-wave signals, there is no agreement on the detailed characteristics of the velocity structure in D" (Cormier, 1985). Several recent studies, typically utilizing synthetic waveform modeling and careful analysis of large, high-quality data sets, are providing significant advances in our understanding of D" velocity structure. This is an exciting field of research, because accurate seismic models are critical for resolving the questions of compositional stratification of D" and the existence of any thermal boundary layer above the core-mantle boundary. These are important issues for models of the dynamic, petrological, and thermal evolution of the Earth.

Most seismological studies of the D" region have attempted to determine radially symmetric velocity models that satisfy either global travel time or diffracted *P*- and *S*-wave data sets (e.g. Doornbos and Mondt, 1979; Mula and Müller, 1980; Dziewonski and Anderson, 1981). These usually have resulted in velocity models with smooth negative or slightly positive velocity gradients throughout D". Generally, such studies incorporate significant horizontal averaging, reducing their sensitivity to fine details of the velocity structure. Also, given the abundant evidence for lateral heterogeneity of D", it is not clear whether the resulting models are even adequate "average" structures on which to base interpretations of the thermal structure of the region. Body-wave modeling studies that selectively sample separate regions of the D" layer promise to provide more detailed local velocity structures and hence better control on lateral variations. In most cases, it appears that the scale lengths of predominant lateral variations in D" are comparable to those in the upper mantle (Ruff and Lettvin, 1984; Lay and Helmberger, 1983a). By this we mean that when analyzing long-period bodywaves, regions with 1,000-km dimensions in D" have sufficiently stable behavior to allow determination of reliable local structures, as has also proved true in the more variable upper mantle (e.g. Grand and Helmberger, 1984; Walck, 1985).

Several recent detailed studies of *P* waveforms that sample isolated areas in the D" layer have indicated substantial fine velocity structure within D", as well as lateral variations in that fine structure (e.g. Ruff and Helmberger, 1982; Ruff and Lettvin, 1984; Wright and Lyons, 1981). In a recent *P* slowness study using a temporary network in Australia that recorded *P*-waves bottoming beneath southeast Asia, Wright et al. (1985) argue for the presence of a sharp increase in *P* velocity of 2.5%–3.0% about 160 km above the core-mantle boundary. It must be emphasized that all studies of short-period *P*-waves traversing the D" region are complicated by the scattering of the signals that occurs all along their paths, as well as by the intrinsically high *P* velocities in the lower mantle which inhibit isolation of discrete triplication branches, even in short-period data.

Offprint requests to: Thorne Lay

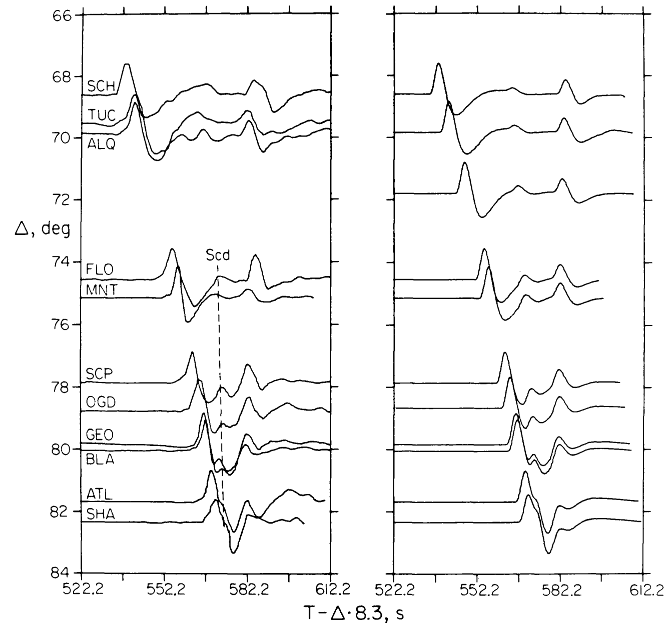

Fig. 1. Profiles of long-period tangential component data (*left*) and synthetics (*right*) for a deep-focus (583 km) earthquake in the Sea of Okhotsk. The stations are WWSSN and Canadian stations in North America. The first arrival in each trace is direct *S* and the arrival around 580 s is *ScS*. Note the arrival ahead of *ScS* which interferes with the downswing of *S*. This arrival, S_{cd}, is produced in the synthetics by the triplication resulting from the lower-mantle discontinuity in model SLHO (Fig. 2)

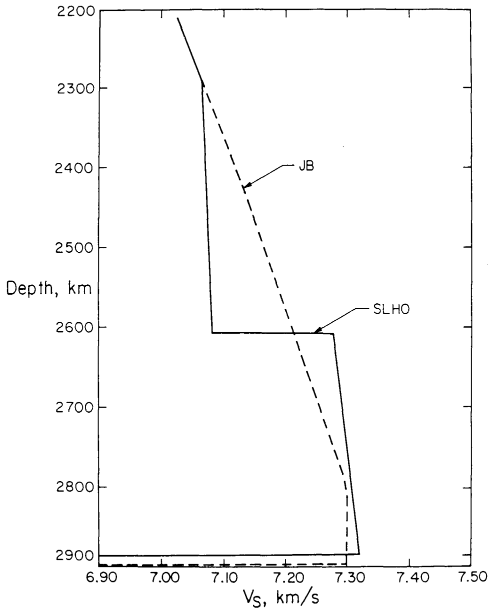

Fig. 2. Shear-velocity profiles in the D" region for the JB model and model SLHO of Lay and Helmberger (1983a), which was derived for paths bottoming beneath Alaska. SLHO has a 2.75% velocity increase 270 km above the core. Both models are identical above 2,200 km depth

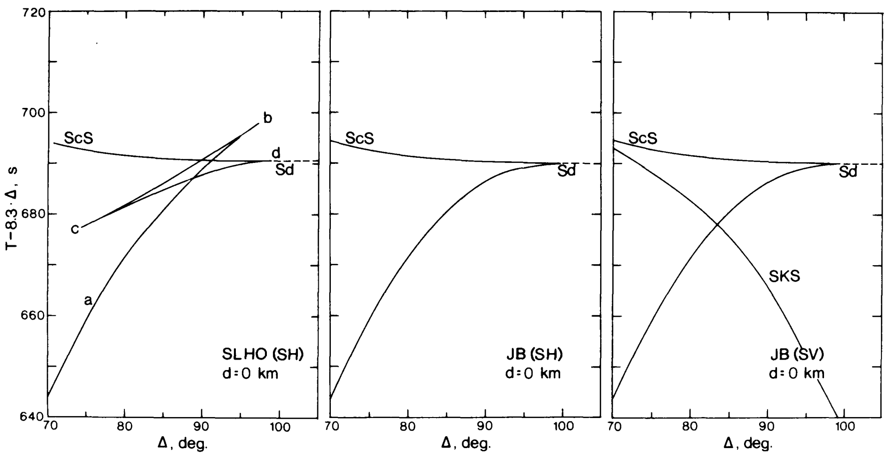

Fig. 3. Surface-focus travel-time curves for lower-mantle *S*-wave arrivals. The SLHO curve shows the triplication expected for a lower-mantle *S*-wave discontinuity compared with the *SH* travel-time curve for the JB model. The *SV* travel-time curve is for the JB model, and illustrates that *SKS* does arrive between *SV* and *ScSV* in the range 75°–85°, but with a much different $dT/d\Delta$ than the triplication arrivals in SLHO. *SKS* clearly cannot produce the interference seen near 95° where S_{ab} and S_{cd} spread apart beyond the crossover distance

Lay and Helmberger (1983a) utilized the fact that the *S*-wave velocities in D" are significantly lower than the *P* velocities in detecting a precursor to *ScSH* that reflects from a lower-mantle velocity discontinuity. Figure 1 shows an example of this arrival, which can be directly observed in rotated *SH* data profiles. This profile is for a 583-km-deep Sea of Okhotsk event recorded at North American stations spanning a narrow azimuth range from the source. The *S* and *ScS* arrivals are clear, as is the systematic arrival labelled *Scd*, which precedes *ScS* by about 10 s. This arrival produces a distinctive distance-varying interference pattern in the range 74°–80°. Observations of this arrival for numerous events with different source depths and distances led to the interpretation that the arrival results from a triplication produced by an abrupt 2.5%–3% shear-velocity increase above the core-mantle boundary. The model obtained for this particular path, SLHO, is shown in Fig. 2, along with a reference JB model, and synthetics for model SLHO are compared with the data in Fig. 1. The timing, amplitude, and interference effects of *Scd* are accurately predicted over the entire range.

Figure 3 shows an *SH* travel-time curve for the SLHO model indicating the timing of the *Scd* branch. As one would expect, the observed long-period *SH* signals in the distance range 82°–88° are generally quite simple, since all the triplication and *ScS* phases arrive within the instrument upswing. However, beyond 89° the triplication opens up again and two arrivals should be apparent. Lay and Helmberger (1983a) showed that this is in fact observed in the data, with the waveforms being modeled-well by SLHO.

However, as demonstrated by Schlittenhardt et al. (1985), synthetics for model SLHO do not closely match all observations in the range 95°–110°.

By analyzing numerous events in a given source region recorded by the same receiver array it is possible to empirically establish receiver structure effects, to determine the stability of the *Scd* arrival, and to develop an appropriate local D" structure for that particular path. Lay and Helmberger (1983a) did this for three D" samples (beneath Alaska, northern Eurasia, and the Caribbean) and in all cases, data throughout the range 70°–95° show waveform complexity that is well predicted by a discontinuity model. Variations of 50 km in the depth of the discontinuity were detected between the three regions sampled. However, the size of the velocity increase did not vary. The general consistency of the models for such different patches of D" suggests the possibility that the discontinuity is a global feature, embedded within the laterally varying D" structure, but much further data analysis is needed to test this hypothesis.

The proposal that there is a deep mantle velocity discontinuity has stimulated several additional studies of D". Cormier (1985) suggested that in some cases the *Scd* arrivals in Fig. 1 are the result of *SKS* contamination of the transverse components. This presumably would be the result of off-great-circle rotation of the *S*-polarization angle produced by near-receiver heterogeneity or by some complex distribution of heterogeneity in D". Schlittenhardt et al. (1985) argue that diffracted *S* and *P* profiles do not clearly show the expected post-critical refraction along the discontinuity and feel that the *ScS* precursor is due to some other phenomenon. Schlittenhardt (1983) calculated short-period *P*-wave synthetics for a D" model, with a 2.7% *P*-wave velocity discontinuity, and concluded that such a structure is not consistent with some *P*-wave observations. In this paper we explore the question of whether *SKS* contamination affects the data set initially utilized to detect the *Scd* arrival.

Analysis of *SKS* contamination

Figure 3 shows *SH* travel-time curves for the SLHO and JB models along with an *SV* travel-time curve for the JB model. *SKS* arrives between *SV* and *ScSV* in the distance range 80°–85°, which makes it difficult to use *SV* signals to model the D" region (Lay and Helmberger, 1983a, b). There is clearly a several degree range in which *SKS* arrives at the same time as the *Scd* branch. Figure 4 shows the longperiod waveform effects produced by *SKS* in the precrossover triplication range, for the two events analyzed by Lay and Helmberger (1983a, b) that have the strongest *SV* arrivals. In the range 78°–80° the *SKS* arrival peaks close in time to the arrival between *S* and *ScS* on the transverse components. It is plausible that given the relatively strong *SKS* arrivals, some contamination of the transverse components could occur, as suggested by Cormier (1985). Note, however, that this contamination must be systematic to produce the apparent moveout of the *Scd* arrival, and it must change in nature from station to station.

This possibility was explored further by computing *SV* and *SH* synthetic wavetrains for the smooth PREM model (Dziewonski and Anderson, 1981), which were then rotated onto incorrect back azimuths, allowing *SKS* to 'leak over' onto the '*SH*' in a procedure similar to that in Cormier (1985). Figure 5 shows a few results of this simulation, with observed waveforms from a Sea of Okhotsk event in the triplication range being compared with SLHO and PREM synthetics. For station FLO (74.6°), the small arrival between *S* and *ScS* apparent in the data and in the SLHO synthetics is never reproduced by the PREM models, regardless of the amount of *SKS* contamination. This is because *SKS* arrives only a few seconds ahead of *ScS*, well after the small arrival of the *SH* component, at this distance (see Fig. 3). For SCP (77.9°), it does prove possible to pro-

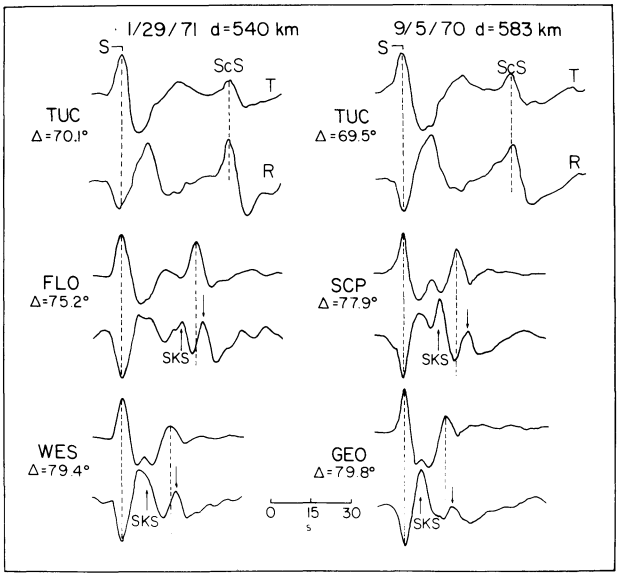

Fig. 4. Comparison of tangential (*T*) and radial (*R*) components of two deep-focus Sea of Okhotsk events recorded in North America. The *SH* and *SV* peak amplitudes arrive at the same time at all distances. The peak of the *SKS* arrivals on the radial components (arrows) are shown

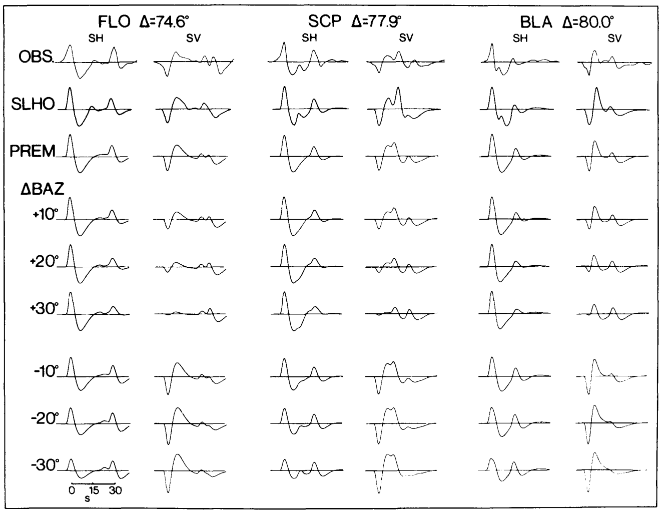

Fig. 5. Comparison of observed *SH* and *SV* waveforms for the Sea of Okhotsk event of 9/05/70 with synthetics for PREM and SLHO. Each *SH* and *SV* pair has true relative amplitude. The PREM synthetics are shown with incorrect back azimuth rotations in 10° increments to simulate *SKS* contamination of the *SH* component as advocated by Cormier (1985). Such contamination fails to reproduce the observed arrival between *S* and *ScS* at FLO and BLA, and mimics the SCP observation only with at least a 25° off-azimuth contamination that ruins the agreement with the *SV* waveform and the *SV*/*SH* amplitude ratio

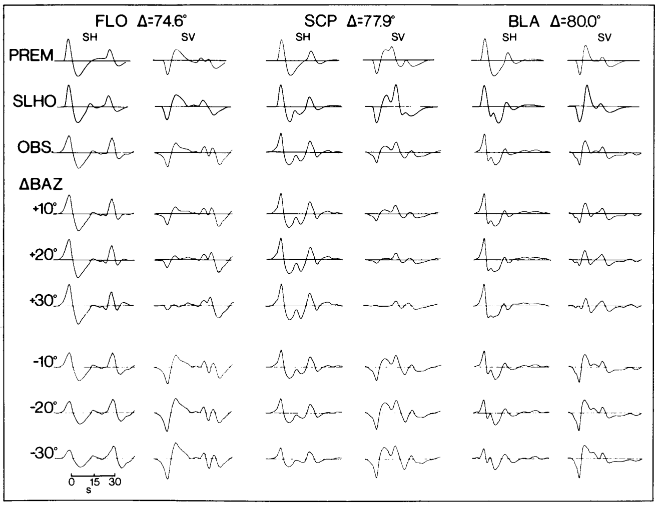

Fig. 6. A similar comparison to that in Fig. 5, but the data are shown with back azimuth rotations that deviate from the great circle by 10° increments. Note the stability of the arrival between *S* and *ScS* on the *SH* observations, even for back azimuth errors of 30°. This illustrates the predominantly *SH* character of this arrival, consistent with the model SLHO calculations

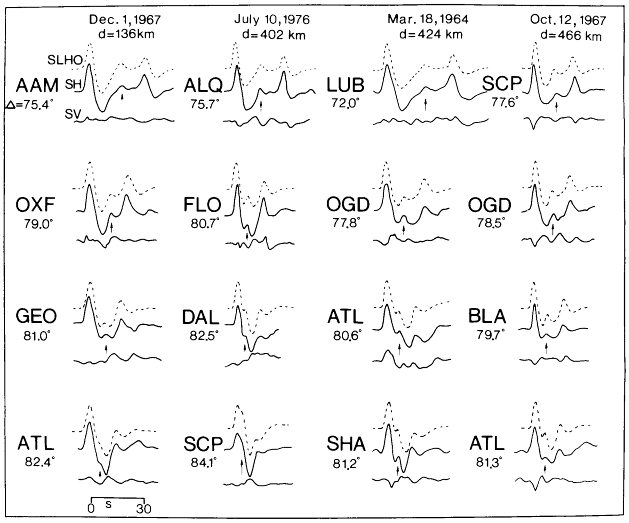

Fig. 7. Examples of *SH* and *SV* (radial) recordings with true relative amplitudes for Sea of Okhotsk events analyzed by Lay and Helmberger (1983a). The *dashed curves* show *SH* synthetics for model SLHO, which was constructed to produce the triplication arrival between *S* and *ScS* indicated by the *arrows*. Note that the very low amplitude radial components do not have strong *SKS* arrivals at these times.

duce an arrival between *S* and *ScS* at about the right time if a 25° off-azimuth *SKS* contamination is allowed. Note, however, that this results in a very clear degradation of the fit between the *SV* synthetic and the data, as well as an incorrect *SV*/*SH* amplitude ratio. For BLA (80°), the timing of *SKS* is again such that no back azimuth error in the PREM synthetics can produce the observed arrival between *S* and *ScS*, which is well matched by the SLHO discontinuity model. Similar calculations for stations at nearby ranges corroborate these findings.

Lay and Helmberger (1983a) show that in the range 72°–76° there are numerous picks of the *Scd* branch which cannot be attributed to *SKS*, which arrives much to late. Thus, in this distance range the *Scd* observations clearly require a different explanation than *SKS* contamination. The possibility of receiver reverberations was ruled out in their study by individual station analysis.

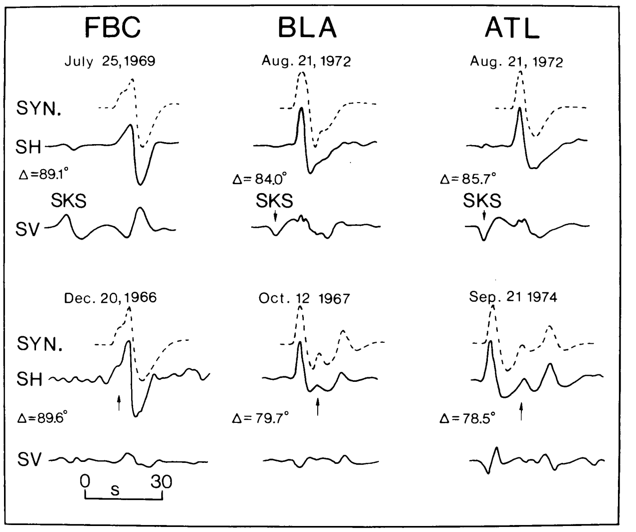

Fig. 8. Examples of stations recording *SH* and *SV* signals at distances where *SKS* is well ahead of the *S* arrival (see the travel-time curves in Fig. 3) along with closer observations at the same stations. Note that the typical *SKS* contamination apparent on the *SH* components is a very small fraction of the actual *SKS* amplitudes (the *SH* and *SV* components are on true relative scales). The *dashed curves* show *SH* synthetics for model SLHO. Note the agreement between the SLHO calculations and the observed data at these stations at all distances, including distances within the triplication range. This illustrates that receiver complexity is not responsible for the arrival between *S* and *ScS*, as well as showing that *SKS* cannot produce the waveform complexity beyond crossover distance (near 90°)

Figure 6 is similar to Fig. 5 except that the *data* are shown rotated with back azimuths departing from the great circle. The arrival between *ScS* and *S* on the *SH* component does not vary significantly, even for large off-great-circle rotations. This stability testifies to the predominantly *SH* character of the arrival. The tests in Figs. 5 and 6 were conducted for the event with the strongest *SV* and *SKS* arrivals of all the events used by Lay and Helmberger (1983a). Figure 7 presents much more typical examples of *SH* and *SV* waveforms in the triplication range for several of their events. Each *SH* and *SV* pair is plotted with true relative amplitude. There are no strong *SKS* arrivals on the radial components at the time of the *Scd* arrivals (arrows), and the *SH* waveforms are modeled well by the SLHO synthetics. The observed *SV*/*SH* amplitude ratios are very consistent with the known *P*-wave first motion mechanisms of these events (Lay and Helmberger, 1983a). There is no reason to believe that the *S*-waves are so strongly contaminated by near-receiver structure that *all* of the *SV* signal ends up on the transverse components when the great-circle back azimuth is assumed in the rotation.

By examining observations beyond 84°, where *SKS* is an isolated first arrival (see Fig. 3), one can obtain a better estimate of how much *SKS* contamination actually does occur. Figure 8 shows examples of recordings at this distance as well as recordings at closer distances for the same stations. For these stations, rotation assuming the great-circle back azimuth leads to less than 10% contamination of the *SKS* signal on the *SH* component. These same stations show strong *Scd* arrivals within the triplication range, but these are not accompanied by *SKS* signals at least ten times as strong on the radial component. Indeed, the *SKS* arrivals are observed to be nodal, as predicted by the known focal mechanisms. It is also clear in Fig. 8 that the *SKS* signals cannot possibly account for the double *S* arrivals observed near 90° (see Figs. 16, 34, and 37 of Lay and Helmberger, 1983a), because *SKS* is well ahead of the *S* arrival at this distance. These arguments refute the possibility that the discontinuity models are invalid because of *SKS*. It is important to note that this conclusion is based on the long-period waveforms. Short-period waveforms (and occasionally long-period records from notorious stations like OXF) in our data set often show appreciable *SKS* contamination on the transverse component, partially due to the greater difficulties in accurately digitizing and rotating the short-period records. Thus, analysis of short-period or broadband *S*-waves must be performed very carefully, and optimally for events with nodal *SV* arrivals. Zhang and Lay (1984) analyzed data from an array of broadband stations for such events and still found tremendous receiver complexity effects that must also be accounted for.

Discussion

In this paper we have concentrated on establishing whether *SKS* contamination has led to a misinterpretation of lower-mantle shear-velocity structure by Lay and Helmberger (1983a). There appears to be very little evidence to support this possibility, as it could require a tremendous number of special circumstances to account for the consistency of the *SH* data and to explain away the lack of *SKS* signals on the radial components. Clearly the D" layer has lateral heterogeneity, and any radial model (even for a localized portion of the D" region) may be in error to some degree because it attributes scattered effects to a deterministic radial structure. However, the consistency of the observations for nearby stations and from event to event strongly indicates that such errors in the discontinuity models are minor. It has proved possible to determine reliable upper-mantle velocity structures for different tectonic regions despite 10% velocity heterogeneity, which probably greatly exceeds variations in D". There is no question that modeling the D" region is difficult, and data-intensive studies are the best way to reliably account for upper-mantle, source, and receiver effects. While all earth models are undoubtedly simplifications of the actual structure, if they are able to predict the detailed behavior of many observations it seems reasonable to believe they are valid, at least to first order.

Much additional analysis of lower-mantle *P*- and *S*-waves is certainly needed, particularly with regard to possible anisotropy and variations in fine scale features. This modeling must be performed with an open mind toward both possible stratification, general heterogeneity, and apparent or intrinsic anisotropy, as advocated by Cormier (1985), given the proximity of D" to the largest compositional and density discontinuity within the Earth.

Conclusions

A detailed analysis of *SV* and *SH* waveforms in the distance range 72°–95° has been performed with the intent of appraising the possibility that *SKS* contaminates the transverse components leading to incorrect D" velocity models. For the data which has previously been interpreted as evidence of a lower-mantle shear-velocity discontinuity, it is very unlikely that *SKS* has caused any systematic problem. The strongest argument for this is that in the majority of the data the *SKS* arrival is much smaller than the arrivals on the transverse component, consistent with the known radiation patterns. Furthermore, the timing of *SKS* is not the same as that of the triplication arrivals on the *SH* components except over a narrow in distance. Well-controlled experiments show that typically less than 10% of the *SKS* waveform contaminates long-period *SH* signals rotated assuming the great-circle back azimuth.

Acknowledgements. We thank V.F. Cormier and D. Helmberger for discussions on this analysis. Comments on the manuscript by the two reviewers and G. Müller are appreciated. C.J.Y. was partially supported by a University of Michigan Regent's Fellowship. This research was supported by the National Science Foundation under Grant NSF EAR 8407792.

References

Cormier, V.F.: Some problems with S, SKS, and ScS observations and implications for the structure of the base of the mantle and the outercore. J. Geophys. **57**, 14–22, 1985

Doornbos, D.J., Mondt, J.C.: P- and S-waves diffracted around the core and the velocity structure at the base of the mantle. Geophys. J. R. Astron. Soc. **57**, 381–395, 1979

Dziewonski, A.M., Anderson, D.L.: Preliminary reference earth model. Phys. Earth Planet. Int. **25**, 297–356, 1981

Grand, S., Helmberger, D.V.: Upper mantle shear structure of North America. Geophys. J. R. Astron. Soc. **76**, 399–438, 1984

Lay, T., Helmberger, D.V.: A lower mantle S-wave triplication and the shear velocity structure of D". Geophys. J. R. Astron. Soc. **75**, 799–838, 1983a

Lay, T., Helmberger, D.V.: The shear-wave velocity gradient at the base of the mantle. J. Geophys. Res. **88**, 8160–8170, 1983b

Mula, A.H., Müller, G.: Ray parameters of diffracted long period P- and S-waves and the velocities at the base of the mantle. Pageoph. **18**, 1272–1292, 1980

Ruff, L., Helmberger, D.V.: The structure of the lowermost mantle determined by short period P-wave amplitudes. Geophys. J. Astron. Soc. **68**, 91–119, 1982

Ruff, L., Lettvin, E.: Short period P-wave amplitudes and variability of the core shadow zone boundary. EOS **65**, 999, 1984

Schlittenhardt, J.: Investigation of the velocity structure of the lowermost mantle with short period PcP/P amplitude ratios (abstract). IASPEI Program and abstracts, XVIII General Assembly, IUGG, 259, 1983

Schlittenhardt, J., Schweitzer, J., Müller, G.: Evidence against a discontinuity at the top of D". Geophys. J. R. Astron. Soc. **81**, 295–306, 1985

Walck, M.: The upper mantle beneath the northeast Pacific rim: a comparison with the Gulf of California. Geophys. J. R. Astron. Soc. **81**, 243–275, 1985

Wright, C., Lyons, J.A.: Further evidence for radial velocity anomalies in the lower mantle. Pageoph. **119**, 137–162, 1981

Wright, C., Muirhead, K.J., Dixon, A.E.: The P-wave velocity structure near the base of the mantle. J. Geophys. Res. **90**, 623–634, 1985

Zhang, J., Lay, T.: Investigation of a lower mantle shear wave triplication using a broadband array. Geophys. Res. Lett. **6**, 620–623, 1984

Received July 16, 1985; Revised version October 4, 1985
Accepted October 15, 1985

J Geophys (1986) 59:16–22

Journal of Geophysics

Spheroidal and torsional global response functions

H. Wilhelm

Geophysikalisches Institut, Hertzstrasse 16, D-7500 Karlsruhe 21,
Federal Republic of Germany

Abstract. The response of a spherically symmetric non-rotating elastic isotropic (SNREI) model earth to spheroidal forcing is described by six coefficients, five of which, h_n, k_n, l_n, h'_n and l'_n, are related to earth tide measurements. The sixth parameter, l_n^-, a spheroidal stress coefficient, is completely independent, whereas all other coefficients used to describe the response to spheroidal forcing are linearly dependent on the five coefficients above. The corresponding relations are compiled in this paper.

The response of the SNREI model earth to torsional forcing is completely described by the torsional stress coefficient, l_n^*, which is resonant at the corresponding eigenperiods of the torsional free oscillations of the earth. For $n=1$, the zero frequency mode, ${}_0T_1$, corresponding to a rigid rotation, is established, and can only be excited by external forcing. After attenuation is introduced eigenperiods and quality factors of the fundamental torsional modes, ${}_0T_2$–${}_0T_{10}$, are calculated for the isotropic preliminary reference earth model (PREM). A comparison with the corresponding values originally determined for the PREM yields a small bias. As a probable cause of the bias, differences in the procedures of numerical integration are discussed.

Key words: Earth tides – Torsional free oscillations – Love-numbers – Response functions – Numerical integration – Q determination

Introduction

At spherical coordinates r, ϑ, λ, every physical vector field can be decomposed in spheroidal and torsional fields (Morse and Feshbach, 1953). These constituents in spherical harmonics can be developed for surfaces where r is constant to produce a component representation of the spherical coordinate system. For example, the r, ϑ, λ components of the surface traction, $\tau(r, \vartheta, \lambda)$, acting on spherical surfaces where r is constant can be shown as

$$\tau(r,\vartheta,\lambda)=\sum_{n=0}^{\infty}\sum_{m=0}^{n}\sum_{q}\left\{\begin{array}{l} U_n^{mq}(r)\,Y_n^{mq}(\vartheta,\lambda)\\ V_n^{mq}(r)\dfrac{\partial Y_n^{mq}}{\partial\vartheta}\\ V_n^{mq}(r)\dfrac{1}{\sin\vartheta}\dfrac{\partial Y_n^{mq}}{\partial\lambda}\end{array}\right. +\sum_{n=1}^{\infty}\sum_{m=0}^{n}\sum_{q}\left\{\begin{array}{l} 0\\ W_n^{mq}(r)\dfrac{1}{\sin\vartheta}\dfrac{\partial Y_n^{mq}}{\partial\lambda},\\ -W_n^{mq}(r)\dfrac{\partial Y_n^{mq}}{\partial\vartheta}\end{array}\right. \tag{1}$$

where

$$Y_n^{mq}(\vartheta,\lambda)=P_n^m(\cos\vartheta)\left\{\begin{array}{ll}\cos m\lambda & \text{for } q=c\\ \sin m\lambda & \text{for } q=s\end{array}\right.$$

are spherical harmonics. The first term on the right hand side of Eq. (1) represents the spheroidal and the second term the torsional part of the surface traction, τ.

A corresponding decomposition can be given for the displacement field, $\mathbf{s}(r, \vartheta, \lambda)$:

$$\mathbf{s}(r,\vartheta,\lambda)=\sum_{n=0}^{\infty}\sum_{m=0}^{n}\sum_{q}\left\{\begin{array}{l} u_n^{mq}(r)\,Y_n^{mq}(\vartheta,\lambda)\\ v_n^{mq}(r)\dfrac{\partial Y_n^{mq}}{\partial\vartheta}\\ v_n^{mq}(r)\dfrac{1}{\sin\vartheta}\dfrac{\partial Y_n^{mq}}{\partial\lambda}\end{array}\right. +\sum_{n=1}^{\infty}\sum_{m=0}^{n}\sum_{q}\left\{\begin{array}{l} 0\\ w_n^{mq}(r)\dfrac{1}{\sin\vartheta}\dfrac{\partial Y_n^{mq}}{\partial\lambda}\\ -w_n^{mq}(r)\dfrac{\partial Y_n^{mq}}{\partial\vartheta}.\end{array}\right. \tag{2}$$

Corresponding to the spheroidal and torsional types of vector fields, forced motions and free oscillations of a spherically symmetric non-rotating elastic isotropic (SNREI) earth are described by two separate systems of differential equations with adequate boundary conditions (Alterman et al., 1959; Aki and Richards, 1980; Lapwood and Usami, 1981). Both types of motion, spheroidal and torsional, are forced by corresponding stress fields and are completely decoupled. Any deviation from the SNREI properties will act to couple these fields (Masters et al., 1983).

Forced motions can be induced by volume or surface forces. For example, tidal forces exerted by the moon and the sun, or loading forces at the earth's surface such as the tidally varying ocean load, are volume forces. Their gravitational potential is only involved in the spheroidal system of equations, and therefore earth tides are spheroidal in character. In loading tides, both volume forces (gravitational attraction) and surface forces (pressure) are active. The load pressure squeezing the earth's surface, $r=a$, is a vectorial field, $\tau(r, \vartheta, \lambda)$, of spheroidal character, since it has only a radial component at $r=a$.

Torsional motions are restricted to movements on spherical surfaces and therefore do not change the mass distribution within a spherically symmetric earth. For an SNREI model earth they can only be induced by horizontal traction, e.g. friction caused by winds or ocean currents. In this context two questions arise:

1. Is it possible that both spheroidal and torsional motions are induced by purely horizontal traction at $r=a$?

2. What kind of structure of applied horizontal traction will induce torsional motions alone?

Boundary conditions for stress

These questions can be answered quite generally if the surface traction, $\tau(r, \vartheta, \lambda)$, is decomposed according to Eq. (1) and if the continuity of the stress at $r=a$ is taken into account. With applied traction of $\mathring{\tau}(\vartheta, \lambda)$, the continuity of stress yields

$$\tau(a, \vartheta, \lambda)=\mathring{\tau}(\vartheta, \lambda). \qquad (3)$$

The radial component of $\mathring{\tau}(\vartheta, \lambda)$, developed in spherical harmonics, is

$$\mathring{\tau}_r(\vartheta, \lambda)=\sum_{n=0}^{\infty} \sum_{m=0}^{n} \sum_q a_n^{mq} Y_n^{mq}(\vartheta, \lambda), \qquad (4)$$

where

$$a_n^{mq}=U_n^{mq}(a) \qquad (5)$$

follows from Eqs. (1) and (3). For reasons which will immediately become evident, the horizontal components of $\mathring{\tau}(\vartheta, \lambda)$ are developed in spherical harmonics according to Eq. (1), but are also decomposed in the following way:

$$\frac{1}{\sin\vartheta}\left[\frac{\partial}{\partial\vartheta}(\sin\vartheta\,\mathring{\tau}_\vartheta)+\frac{\partial\mathring{\tau}_\lambda}{\partial\lambda}\right]$$
$$=\sum_{n=0}^{\infty} \sum_{m=0}^{n} \sum_q b_n^{mq} Y_n^{mq}(\vartheta, \lambda), \qquad (6)$$

$$\frac{1}{\sin\vartheta}\left[\frac{\partial\mathring{\tau}_\vartheta}{\partial\lambda}-\frac{\partial}{\partial\vartheta}(\sin\vartheta\,\mathring{\tau}_\lambda)\right]$$
$$=\sum_{n=0}^{\infty} \sum_{m=0}^{n} \sum_q c_n^{mq} Y_n^{mq}(\vartheta, \lambda). \qquad (7)$$

From Eq. (1), for the stresses σ_{rr}, $\sigma_{r\vartheta}$, $\sigma_{r\lambda}$ at $r=a$, it follows that

$$\frac{1}{\sin\vartheta}\left[\frac{\partial}{\partial\vartheta}(\sin\vartheta\,\sigma_{r\vartheta})+\frac{\partial\sigma_{r\lambda}}{\partial\lambda}\right]_n^{mq}$$
$$=-n(n+1)\,V_n^{mq}(a)\,Y_n^{mq}(\vartheta, \lambda), \qquad (8)$$

$$\frac{1}{\sin\vartheta}\left[\frac{\partial\sigma_{r\vartheta}}{\partial\lambda}-\frac{\partial}{\partial\vartheta}(\sin\vartheta\,\sigma_{r\lambda})\right]_n^{mq}$$
$$=-n(n+1)\,W_n^{mq}(a)\,Y_n^{mq}(\vartheta, \lambda), \qquad (9)$$

with

$$\frac{1}{\sin\vartheta}\frac{\partial}{\partial\vartheta}\left(\sin\vartheta\frac{\partial Y_n^{mq}}{\partial\vartheta}\right)+\frac{1}{\sin^2\vartheta}\frac{\partial^2 Y_n^{mq}}{\partial\lambda^2}$$
$$=-n(n+1)\,Y_n^{mq}(\vartheta, \lambda).$$

From Eqs. (1) and (3), which are valid for each harmonic component specified by a given combination of n, m, q,

$$[\sigma_{r\vartheta}]_n^{mq}=[\mathring{\tau}_\vartheta]_n^{mq},$$
$$[\sigma_{r\lambda}]_n^{mq}=[\mathring{\tau}_\lambda]_n^{mq}.$$

at $r=a$. The following relations are deduced from Eqs. (6)-(9):

$$b_n^{mq}=-n(n+1)\,V_n^{mq}(a), \qquad (10)$$
$$c_n^{mq}=-n(n+1)\,W_n^{mq}(a), \qquad (11)$$

yielding vanishing coefficients for $n=0$. With the relations of Eqs. (5), (10) and (11), it is obvious that question (1) of the introduction has to be answered with *yes*. Clearly, question (2) is answered by simply stating that the horizontal traction must be torsional in order to induce only torsional motion. A sufficient condition for this is that the applied horizontal traction, $\mathring{\tau}(\vartheta, \lambda)$, is zonal, i.e. $\mathring{\tau}_\vartheta=0$ and $\mathring{\tau}_\lambda$ is independent of λ. In this case

$$\mathring{\tau}_r(\vartheta)=0=\sigma_{rr}(a, \vartheta, \lambda),$$
$$\mathring{\tau}_\vartheta(\vartheta)=0=\sigma_{r\vartheta}(a, \vartheta, \lambda),$$
$$\mathring{\tau}_\lambda(\vartheta)=\sigma_{r\lambda}(a, \vartheta)=-\sum_{n=1}^{\infty} W_n^0(a)\frac{dP_n}{d\vartheta};$$

hence

$$a_n^{mq}=0=b_n^{mq}$$

and

$$U_n^{mq}(a)=0=V_n^{mq}(a).$$

The boundary conditions for the stress field at $r=a$ can be specified according to the character of the forcing field. In the spheroidal case four types of boundary conditions can be formulated (Molodenskiy, 1977; Saito, 1978; Okubo and Saito, 1983; Varga, 1983). For

(a) a forcing external potential (e.g. tidal potential),

$$S_n^{mq}(r, \vartheta, \lambda)=G_n^{mq}\left(\frac{r}{a}\right)^n Y_n^{mq}(\vartheta, \lambda), \qquad 0<r<\infty$$

and then $U_n^{mq}(a)=0=V_n^{mq}(a)$;

(b) a forcing mass-load potential,

$$S_n'^{mq}(r,\vartheta,\lambda)$$

$$=G_n'^{mq}\,Y_n^{mq}(\vartheta,\lambda)\begin{cases}\left(\dfrac{r}{a}\right)^n & \text{for } 0<r<a\\[2ex] \left(\dfrac{a}{r}\right)^{n+1} & \text{for } a<r<\infty\end{cases},$$

with $G_n'^{mq}=\dfrac{4\pi G a}{2n+1}\,\rho_L\,\xi_n^{mq}$,

where G is the gravitational constant, ρ_L the mass-load density and ξ_n^{mq} the corresponding coefficient of the mass-load height development in spherical harmonics, so that $\rho_L\,\xi_n^{mq}\,Y_n^{mq}(\vartheta,\lambda)$ is the surface-load density (e.g. Zürn and Wilhelm, 1984), and then

$$U_n^{mq}(a)=-\frac{(2n+1)\,g_0}{4\pi G a}\,G_n'^{mq}$$

$$V_n^{mq}(a)=0;$$

(c) a forcing pressure $\mathring{p}_n^{mq}\,Y_n^{mq}(\vartheta,\lambda)$ at $r=a$, then

$$U_n^{mq}(a)=-\mathring{p}_n^{mq}=-\frac{(2n+1)\,g_0}{4\pi G a}\,G_n^{+mq} \tag{12}$$

$$V_n^{m}(a)=0,$$

where G_n^{+mq} is defined by Eq. (12), and g_0 is the gravitational force per unit mass at the surface $r=a$;

(d) a forcing horizontal surface traction at $r=a$,

$$\mathring{\tau}_n^{mq}(\vartheta,\lambda)=\begin{cases}0\\[1ex] \mathring{\tau}_n^{mq}\dfrac{\partial Y_n^{mq}}{\partial\vartheta}\\[2ex] \mathring{\tau}_n^{mq}\dfrac{1}{\sin\vartheta}\dfrac{\partial Y_n^{mq}}{\partial\lambda}\end{cases}$$

and then

$$U_n^{mq}(a)=0,$$

$$V_n^{mq}(a)=\mathring{\tau}_n^{mq}=\frac{2n+1}{n(n+1)}\,\frac{g_0}{4\pi G a}\,G_n^{-mq}, \tag{13}$$

with G_n^{-mq} defined by Eq. (13).

The boundary conditions of (b) evolve from superposing the conditions of (a) and (c).

In the torsional case the forcing traction is given by

$$\mathring{\tau}_n^{mq}(\vartheta,\lambda)=\begin{cases}0\\[1ex] \mathring{\tau}_n^{mq}\dfrac{1}{\sin\vartheta}\dfrac{\partial Y_n^{mq}}{\partial\lambda}\\[2ex] -\mathring{\tau}_n^{mq}\dfrac{\partial Y_n^{mq}}{\partial\vartheta}\end{cases} \tag{14}$$

and the boundary condition for the stress yields

$$W_n^{mq}(a)=\mathring{\tau}_n^{mq}=\frac{g_0}{4\pi G a}\,G_n^{*mq}, \tag{15}$$

with G_n^{*mq} defined by Eq. (15).

Additional boundary conditions

The continuity of the potential at $r=a$ can be achieved by defining a response potential in case (a) by

$$\tilde{S}_n^{mq}(r,\vartheta,\lambda)$$

$$=G_n^{mq}\,Y_n^{mq}(\vartheta,\lambda)\begin{cases}k_n(r)\left(\dfrac{r}{a}\right)^n & \text{for } 0<r<a\\[2ex] k_n(a)\left(\dfrac{a}{r}\right)^{n+1} & \text{for } a<r<\infty\end{cases}$$

and a corresponding response potential in cases (b), (c) and (d) by replacing k_n by k_n', k_n^+, k_n^- and G_n^{mq} by $G_n'^{mq}$, G_n^{+mq}, G_n^{-mq}, respectively.

A further boundary condition is a result of the continuity of the expression (Farrell, 1972)

$$(\nabla\tilde{S}_n^{mq}-4\pi G\,\rho(r)\,\mathbf{s}_n^{mq})\cdot\hat{\mathbf{r}},$$

where $\hat{\mathbf{r}}$ is the unit vector in the radial direction. From Eq. (2), it follows for case (a) that

$$\left[\left(\frac{dk_n}{dr}+\frac{2n+1}{r}\,k_n(r)\right)G_n^{mq}-4\pi G\,\rho(r)\,u_n^{mq}(r)\right]_{r=a}=0, \tag{16}$$

and there is a corresponding relation for the other cases.

Relations between spheroidal coefficients

In the spheroidal state a system of six first-order linear differential equations can be used to describe the forced and free motions of the spherical earth. Alterman et al. (1959) introduced the five variables:

$$y_1(r)=u_n^{mq}(r),\qquad y_2(r)=U_n^{mq}(r),$$

$$y_3(r)=v_n^{mq}(r),\qquad y_4(r)=V_n^{mq}(r),$$

$$y_5(r)=G_n^{mq}\left(\frac{r}{a}\right)^n(\delta+k_n(r)),$$

and a variable, y_6, which is not used here in its original form but as defined by Saito (1974):

$$y_6=\frac{dy_5}{dr}+\frac{n+1}{r}\,y_5-4\pi G\,\rho\,y_1,$$

which is

$$y_6(r)=\left[\frac{dk_n}{dr}+\frac{2n+1}{r}(\delta+k_n(r))\right]G_n^{mq}\left(\frac{r}{a}\right)^n-4\pi G\,\rho\,y_1,$$

with $\delta=1$ in cases (a) and (b) and $\delta=0$ in cases (c) and (d). In addition, Saito showed that between two solutions $(y_{11},\dots,y_{61})$ and $(y_{12},\dots,y_{62})$, for two different sets of boundary conditions, the relation

$$\begin{aligned}&y_{11}\,y_{22}+n(n+1)\,y_{31}\,y_{42}+(4\pi G)^{-1}\,y_{51}\,y_{62}\\ &=y_{12}\,y_{21}+n(n+1)\,y_{32}\,y_{41}+(4\pi G)^{-1}\,y_{52}\,y_{61}\end{aligned} \tag{17}$$

holds at $r=a$. While y_2, y_4 and y_6 are determined by boundary conditions, y_1, y_3 and y_5 are linearly related to the forcing function by coefficients and factors according to Table 1 (Okubo and Saito, 1983).

Table 1. Factors and coefficients used to describe the earth's response to spheroidal forcing

	G_n^m	$G_n^{\prime m}$	G_n^{+m}	G_n^{-m}
y_1	h_n/g_0	h'_n/g_0	h_n^+/g_0	h_n^-/g_0
y_3	l_n/g_0	l'_n/g_0	l_n^+/g_0	l_n^-/g_0
y_5	$(1+k_n)$	$(1+k'_n)$	k_n^+	k_n^-
y_2	0	$-\dfrac{(2n+1)\,g_0}{4\pi G a}$	$-\dfrac{(2n+1)\,g_0}{4\pi G a}$	0
y_4	0	0	0	$\dfrac{(2n+1)\,g_0}{n(n+1)\,4\pi G a}$
y_6	$(2n+1)/a$	$(2n+1)/a$	0	0

By combining the solutions for two different sets of boundary conditions, six relations between the coefficients are derived (Saito, 1978; Okubo and Saito, 1983; Varga, 1983):

$$\begin{aligned}
&\text{(a), (b):} && k'_n = k_n - h_n\\
&\text{(a), (c):} && k_n^+ = -h_n\\
&\text{(a), (d):} && k_n^- = l_n\\
&\text{(b), (c):} && h_n^+ = h'_n + k_n^+ = h'_n - h_n\\
&\text{(b), (d):} && h_n^- = k_n^- - l'_n = l_n - l'_n\\
&\text{(c), (d):} && l_n^+ = -h_n^- = l'_n - l_n,
\end{aligned} \tag{18}$$

and trivially, because of the linearity of the boundary conditions and the differential equations,

$$\begin{aligned}
h'_n &= h_n + h_n^+\\
k'_n &= k_n + k_n^+\\
l'_n &= l_n + l_n^+.
\end{aligned}$$

From the twelve coefficients introduced in Table 1 six coefficients can be expressed as linear combinations of h_n, k_n, l_n, h'_n and l'_n, which can therefore be regarded as independent coefficients. However, the stress coefficient l_n^- does not appear in the relations [Eq. (18)], being completely independent. From earth tide measurements and model calculations the first five coefficients are fairly well known, but l_n^- has not yet been investigated. However, a complete knowledge of the reaction of the spherical non-rotating earth to spheroidal forcing fields requires the determination of l_n^-. From the definition in Table 1, it is clear that l_n^- appears in spheroidal motions of the earth that are induced by horizontal frictional forces exerted on the earth's surface, e.g. by winds and ocean currents. It is, however, expected that local disturbances will inhibit the identification of this effect.

Torsional forced motions

In the torsional case there is no disturbing potential and the displacements are purely horizontal everywhere. For a spherical earth with a fluid outer core, only two boundary conditions, at the earth's surface and at the core-mantle boundary, need be taken into account. There are only two differential equations, of first order, for the two variables (Alterman et al., 1959):

$$\begin{aligned}
y_1(r) &= w_n^{mq}(r)\\
y_2(r) &= W_n^{mq}(r),
\end{aligned} \tag{19}$$

viz.:

$$\begin{aligned}
\frac{dy_1}{dr} &= y_1/r + y_2/\mu\\
\frac{dy_2}{dr} &= ((n^2+n-2)\,\mu/r^2 - \omega^2\,\rho)\,y_1 - 3y_2/r,
\end{aligned} \tag{20}$$

where μ is the shear modulus and ρ the density, both depending on the radial distance, r.

The boundary condition at $r=a$ for a given torsional traction field, $\mathring{\boldsymbol{\tau}}_n^{mq}(\vartheta,\lambda)$ according to Eq. (14), is given by Eqs. (15) and (19), yielding

$$y_2(a) = \mathring{\tau}_n^{mq},$$

whereas the displacement is linearly related to the torsional stress by

$$y_1(a) = l_n^*\,G_n^{*mq}/g_0$$

where G_n^{*mq} is given by Eq. (15). Numerical integration of the system [Eq. (20)] yields the torsional stress coefficient, l_n^*.

For torsional motions it is particularly easy to describe an attenuating medium, achieved by introducing a complex shear modulus:

$$\hat{\mu} = \mu(1 + i/Q_\mu),$$

where μ, but not the dissipation parameter Q_μ, is assumed to be frequency-dependent (Kanamori and Anderson, 1977), so that

$$\mu(\omega) = \mu(\omega_r)\,(1 + 2/(\pi\,Q_\mu)\ln(\omega/\omega_r)),$$

and ω_r is a reference frequency.

Consequently, the stress and the displacement also become complex quantities:

$$\begin{aligned}
\hat{w}_n^{mq} &= w_n^{mq} + i\,\bar{w}_n^{mq} = y_1 + i\,\bar{y}_1\\
\hat{W}_n^{mq} &= W_n^{mq} + i\,\bar{W}_n^{mq} = y_2 + i\,\bar{y}_2.
\end{aligned}$$

Correspondingly, there are now four differential equations instead of two:

$$\begin{aligned}
\frac{dy_1}{dr} &= y_1/r + y_2/(\mu(\omega)\,(1+Q_\mu^{-2})) + \bar{y}_2/(Q_\mu\,\mu(\omega)\,(1+Q_\mu^{-2}))\\
\frac{d\bar{y}_1}{dr} &= \bar{y}_1/r + \bar{y}_2/(\mu(\omega)\,(1+Q_\mu^{-2})) - y_2/(Q_\mu\,\mu(\omega)\,(1+Q_\mu^{-2}))\\
\frac{dy_2}{dr} &= y_1((n^2+n-2)\,\mu(\omega)/r^2 - \omega^2\,\rho)\\
&\quad - 3y_2/r - \bar{y}_1(n^2+n-2)\,\mu(\omega)/(r^2\,Q_\mu)\\
\frac{d\bar{y}_2}{dr} &= \bar{y}_1((n^2+n-2)\,\mu(\omega)/r^2 - \omega^2\,\rho)\\
&\quad - 3\bar{y}_2/r + y_1(n^2+n-2)\,\mu(\omega)/(r^2\,Q_\mu),
\end{aligned} \tag{21}$$

and the resulting stress coefficient is also complex:

$$\hat{l}_n^* = l_n^* + i\,\bar{l}_n^*.$$

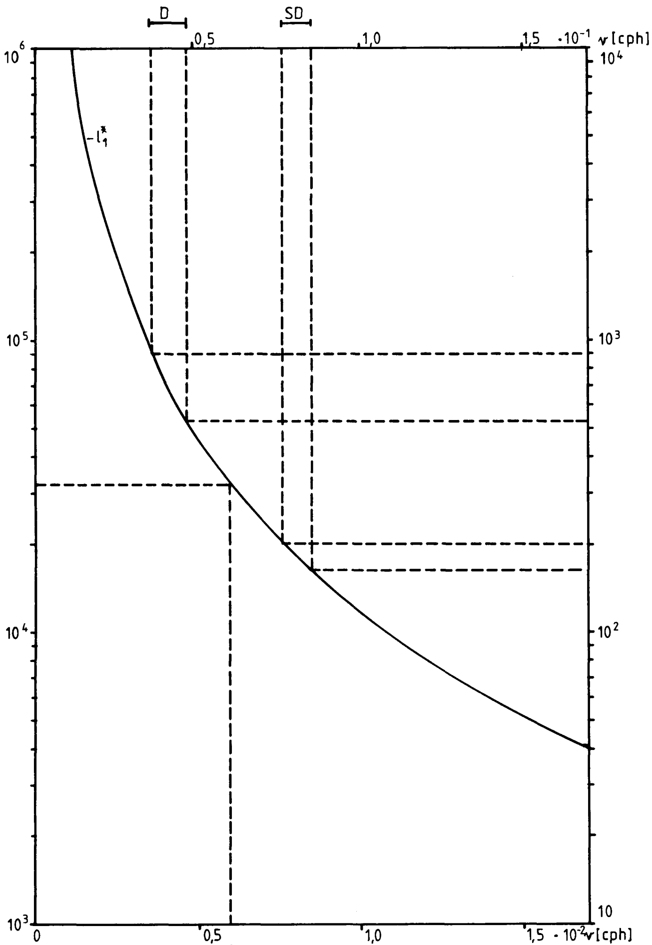

Fig. 1. Negative real part l_1^* of complex torsional stress coefficient $\hat{l}_1^*$ for small frequencies using the preliminary earth reference model (PREM). Two frequency and ordinate scales are used. Long period (*LP*), diurnal (*D*), and semi-diurnal (*SD*) tidal frequency bands are indicated

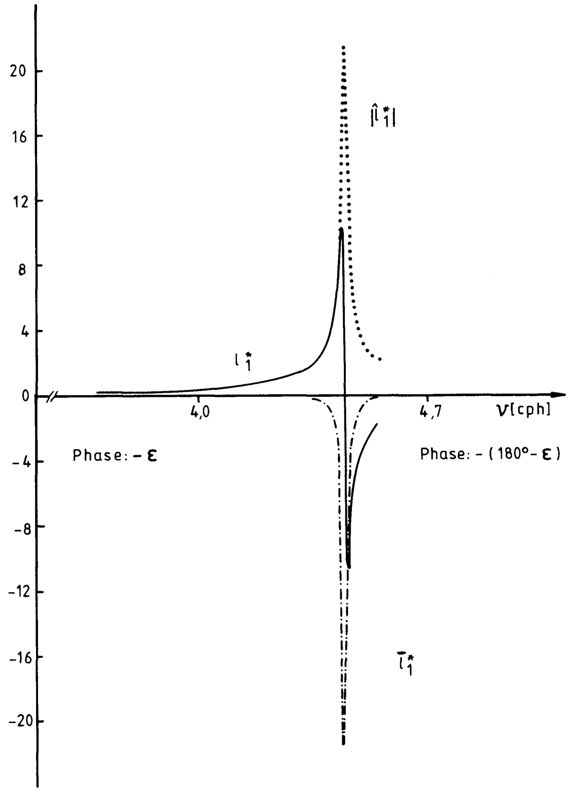

Fig. 2. Frequency dependence of the complex stress coefficient, $\hat{l}_1^*$, in the vicinity of the mode ${}_1T_1$ using the preliminary earth reference model (PREM). The real part, l_1^*, the imaginary part, $\bar{l}_1^*$, and the magnitude, $|\hat{l}_1^*|$, were determined

If the forcing field is assumed to be a real quantity, i.e. $\bar{y}_2(a)=0$, and if $y_2(a)$ is given, the response of the earth, i.e. the displacement and the stress within the earth, can be calculated by numerical integration of the system [Eq. (21)]. At the earth's surface, $r=a$, the coefficient $\hat{l}_n^*$ completely describes the response, since according to

$$\hat{y}_1=\hat{l}_n^*\,G_n^{*mq}/g_0 \tag{22}$$

the amplitude and phase of $\hat{l}_n^*$ relates the displacement linearly to the forcing field.

The torsional stress coefficient, $\hat{l}_n^*$, has been calculated for the anelastic isotropic preliminary reference earth model (PREM) (Dziewonski and Anderson, 1981) and a varying circular frequency ω. For $n=1$ and small frequencies, $\hat{l}_n^*$ has an extremely small imaginary part compared to the real part, which is resonant for $\omega \to 0$, whereas the imaginary part becomes zero. This resonance at zero frequency corresponds to the torsional free mode, ${}_0T_1$, which can only be excited by static external forces exerting a torque on the earth. The earth's response to the torque is a rotation which leads to infinite displacements with respect to a non-rotating coordinate system. Figure 1 shows the negative real part of $\hat{l}_1^*$ for the two frequency bands 0–0.017 c/h and 0–0.17 c/h. For small frequencies the phase difference between the displacement and the applied stress is almost 180°, since the imaginary part of $\hat{l}_1^*$ is positive. This corresponds to the behaviour of a damped harmonic oscillator for frequencies greater than the resonance frequency. For $n=2, 3, \ldots, \hat{l}_n^*$ has definite real limits for $\omega \to 0$. In a rotating coordinate system the zero frequency mode is transformed into a free mode, with a period corresponding to the rotation of the inertial frame (Dahlen and Smith, 1975).

At the appropriate frequencies of the applied traction, the torsional vibrations of the earth lead to a resonant behaviour. Figure 2 shows this behaviour for $\hat{l}_1^*$ in the neighbourhood of the eigenfrequency of the ${}_1T_1$ mode. The zero crossing of l_1^* determines the resonance frequency.

By calculating $\hat{l}_n^*$ in the vicinity of the resonances, the eigenperiod ${}_kT_n$ and the quality factor ${}_kQ_n$ of the corresponding torsional oscillation can be determined. For a damped harmonic oscillator with resonance frequency ${}_k\omega_n$ and quality ${}_kQ_n$ the frequency response is given (Ben Menahem and Singh, 1981) by

$$M(\omega)=({}_k\omega_n^2-\omega^2+i\,\omega_n\,\omega_k/{}_kQ_n)^{-1}.$$

The ratio of the real to the imaginary part of $M(\omega)$ is

$$G(\omega)=(\omega/{}_k\omega_n-{}_k\omega_n/\omega)\,{}_kQ_n. \tag{23}$$

Fourier transformation of Eq. (22) yields the corresponding frequency response, $\hat{l}_n^*(\omega)$; the ratio of the real

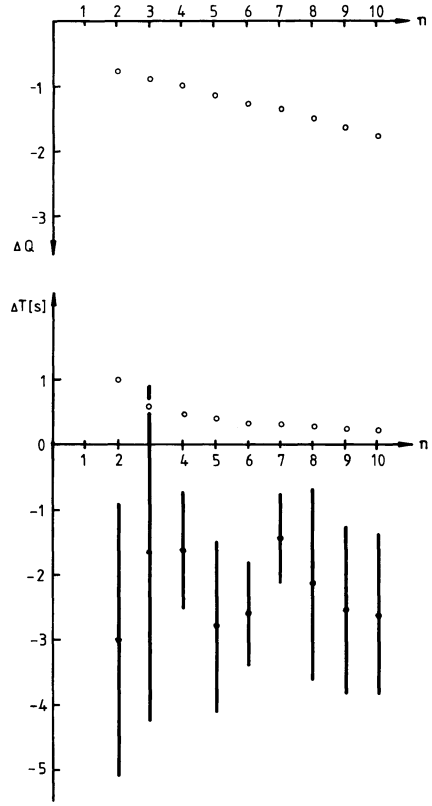

Fig. 3. Differences, $\Delta Q = Q_{nC} - Q_{nDA}$ and $\Delta T = T_{nC} - T_{nDA}$, between the calculated values, Q_{nC} and T_{nC}, from the resonances of $\hat{l}_n^*$ and the values Q_{nDA} and T_{nDA}, given by Dziewonski and Anderson (1981) for ${}_0T_n$ and the preliminary earth reference model (PREM), $n = 2 \dots 10$. Differences of the observed values are given with *error bars*

to the imaginary part of $\hat{l}_n^*$ is well represented by a function like Eq. (23), with ${}_k\omega_n$ and ${}_kQ_n$ as parameters whose values are determined by least squares fitting of the calculated ratio $l_n^* : \bar{l}_n^*$ to the response ratio [Eq. (23)] for different values of ω. The frequencies used for the least squares fit have to be chosen sufficiently close to and symmetrically distributed around the zero crossing value. It happens that the least squares fit is also a robust fit in the calculated numerical examples. In this way eigenperiods and quality factors of torsional oscillations have been determined for the PREM. For the lowest fundamental modes, the differences between ${}_0T_n = 2\pi/{}_0\omega_n$ and ${}_0Q_n$ obtained by this method and the corresponding values given by Dziewonski and Anderson (1981) are shown in Fig. 3. In addition the differences of the observed eigenperiods are shown with error bars. There is a bias of about 0.1% between the corresponding eigenperiods and about 1% between the Q values.

Though this bias is rather small it looks systematic. Since it might have arisen through neglecting the influence of neighbouring eigenperiods on the determination of ${}_k\omega_n$, in the response function up to 12 eigenfrequencies were taken into account instead of one. The effect of the additional resonances is to give a deviation of about 0.01 s for the resonance required, at low degrees of n. For $n = 8$ the deviation is 0.02 s for the period ${}_0T_8$, and 0.03 for ${}_0Q_8$. This difference is reached after taking the next four additional resonances into account, and the use of additional eigenfrequencies does not change the result further at the five-digit level. Therefore, saturation is reached with a limited number of neighbouring resonances. For growing values of n the number of resonances that have to be respected also increases. This effect, however, cannot be responsible for the bias shown in Fig. 3 because the corresponding differences are much lower than the bias. Only those eigenfrequencies with the same degree n but different node number k are involved in this problem.

Table 2. Numerical methods used to integrate the linear system $y'(r) = A(r)\,y(r)$ (Stiefel, 1976) and corresponding results for the fundamental mode ${}_0T_2$: 1. Heun method, with predictor for unequal integration intervals; 2. Runge-Kutta method, with predictor for unequal integration intervals; 3. modified Runge-Kutta method with inversion for unequal integration intervals; 4. Runge-Kutta first method with predictor and linear interpolation for equal integration intervals; 5. Runge-Kutta second method with predictor and linear interpolation for equal integration intervals; 6. calculated values of Dziewonski and Anderson (1981); 7. observed values according to Dziewonski and Anderson (1981)

Procedure	${}_0T_2$ [s]	${}_0Q_2$
1	2640.8	249.61
2	2629.5	250.33
3	2640.4	249.63
4	2640.0	249.63
5	2640.0	249.63
6	2639.4	250.40
7	2636.38 ±2.11	?

Another proposal was that different methods of numerical integration may yield differences in the results. Hence, as a computational example, different methods of integration were applied for the determination of the period and quality of ${}_0T_2$. The result is shown in Table 2 for five different procedures. Lines 6 and 7 show the values calculated by Dziewonski and Anderson (1981) compared with the observed values. Except for method 2, the least squares fitted values agree to within ±0.01 for ${}_0Q_2$ and to within ±0.04 s for ${}_0T_2$. The differences between the results are comparable with the differences shown in Fig. 3. Therefore it can be concluded that a possible cause of the bias may be found in different integration procedures. In particular, two inherently different methods (4 and 5; Table 2) yield the same results within five digits, yet differ from the results of the Dziewonski and Anderson method (1981).

Dziewonski and Anderson (1981) calculated the Q of a normal mode with index j according to a procedure described by Sailor and Dziewonski (1978):

$$Q_j^{-1} = \frac{1}{a^3} \int_0^a \left(\mu(r)\,\tilde{M}_j(r)\,Q_\mu^{-1}(r) + K(r)\,\tilde{K}_j(r)\,Q_k^{-1}(r)\right) r^2\,dr,$$

where $\tilde{M}_j(r)$ and $\tilde{K}_j(r)$ are defined by Backus and Gilbert (1967, eqs. 30, 31), and $\mu(r)$ and $K(r)$ are the shear and the bulk modulus and $Q_\mu^{-1}(r)$ and $Q_k^{-1}(r)$ the radially dependent imaginary parts of the corresponding complex moduli (Ben Menahem and Singh, 1981, eqs.

10.130, 10.198). The method finally used in this paper is a combined determination of the eigenfrequency and the quality factor of a normal mode, using the response of a linear oscillator to an external forcing function. If there are $N+1$ resonances the response is given by

$$\begin{aligned} M(\omega)= \sum_{j=0}^{N} \{&(\omega_j^2-\omega^2)/[(\omega_j^2-\omega^2)^2+(\omega\,\omega_j/Q_j)^2] \\ &-i(\omega\,\omega_j/Q_j)/[(\omega_j^2-\omega^2)^2+(\omega\,\omega_j/Q_j)^2]\}, \end{aligned} \tag{24}$$

where $j=0$ is the resonance in which ω_0 and Q_0 are to be determined and $j=1,2,\ldots N$ are the resonances which have to be taken into account for the determination of ω_0 and Q_0, and for which preliminary values of sufficient accuracy are inserted in Eq. (24) in order to determine the influence of the other N resonances on ω_0 and Q_0. The ratio of the real to the imaginary part of $M(\omega)$ is $G(\omega;\ \omega_0, Q_0;\ \omega_j, Q_j)$, $j=1 \ldots N$, which is calculated from Eq. (24). By fitting the ratio $l_n^*:\bar{l}_n^*$ to the ratio of the real to the imaginary part of $M(\omega)$ in a linearized least squares procedure, the unknown values of ω_0 and Q_0 are determined.

Conclusions

The response of an SNREI model earth to a forcing spheroidal field is completely described by six coefficients, five of which (h_n, k_n, l_n, h_n' and l_n') can, in principle, be calculated by numerical integration of the corresponding set of linear differential equations, and are related to earth tide measurements. Except one, all other coefficients used to describe the response are linearly composed of these five coefficients. The exception is l_n^-, which is completely independent and difficult to determine by measurements. Until now, it has not received any attention, but it is fundamental. Model calculations should reveal its numerical value as a function of frequency.

The response of an SNREI model earth to a forcing torsional stress field acting at the earth's surface can be completely described by only one coefficient, l_n^*. After introducing attenuation to the earth model, the eigenperiods and quality factors of the torsional free oscillations can be determined by a least squares fit procedure to the response function of a linear oscillator model. For the isotropic PREM (Dziewonski and Anderson, 1981), the calculated values yield differences of 0.1% for the period ${}_0T_n$ and 1% for ${}_0Q_n$ with respect to the values given by Dziewonski and Anderson (1981). Using different integration procedures, differences of the same order can be obtained.

Acknowledgements. This work was continuously stimulated and supported by discussions with Walter Zürn, which I highly appreciate. Critical comments of a referee are gratefully acknowledged. The calculations were performed on the UNIVAC 1100/61 of the Karlsruhe University Computing Centre.

References

Aki, K., Richards, P.G.: Quantitative Seismology, Theory and Methods, Vol. I, San Francisco: Freeman and Co., 1980

Alterman, Z., Jarosch, H., Pekeris, C.L.: Oscillation of the earth. Proc. R. Soc. London, Ser. A, **525**, 80–95, 1959

Backus, G.E., Gilbert, J.F.: Numerical applications of a formalism for geophysical inverse problems. Geophys. J. R. Astron. Soc. **13**, 247–276, 1967

Ben Menahem, A., Singh, S.J.: Seismic Waves and Sources. New York: Springer 1981

Dahlen, F.A., Smith, M.L.: The influence of rotation on the free oscillations of the earth. Philos. Trans. R. Soc. London, Ser. A, **279**, 583–629, 1975

Dziewonski, A., Anderson, D.L.: Preliminary reference earth model. Phys. Earth Planet. Int. **25**, 297–356, 1981

Farrell, W.E.: Deformation of the earth by surface loads. Rev. Geophys. Space Phys. **10**, 761–797, 1972

Kanamori, H., Anderson, D.L.: Importance of physical dispersion in surface waves and free oscillation problems. Rev. Geophys. Space Phys. **15**, 105–112, 1977

Lapwood, E.R., Usami, T.: Free Oscillations of the Earth. Cambridge: Cambridge University Press, 1981

Masters, G., Park, J., Gilbert, F.: Observation of coupled spheroidal and toroidal modes. J. Geophys. Res. **88**, 10285–10298, 1983

Molodenskiy, S.M.: Relation between Love numbers and load factors. Izv. Earth Phys. **13**, 147–149, 1977

Morse, P.M., Feshbach, H.: Methods of Theoretical Physics. New York: McGraw Hill, 1953

Okubo, S., Saito, M.: Partial derivative of Love numbers. Bull. Géod. **57**, 167–179, 1983

Sailor, R.V., Dziewonski, A.M.: Measurements and interpretation of normal mode attenuation. Geophys. J. R. Astron. Soc. **53**, 559–581, 1978

Saito, M.: Some problems of static deformation of the earth. J. Phys. Earth **22**, 123–140, 1974

Saito, M.: Relationship between tidal and load Love numbers. J. Phys. Earth **26**, 13–16, 1978

Stiefel, E.: Einführung in die numerische Mathematik. Stuttgart: Teubner, 1976

Varga, P.: Potential free Love numbers. Manuscripta Geodaetica, **8**, 85–91, 1983

Zürn, W., Wilhelm, H.: Tides of the Solid Earth. In: Landolt-Börnstein, New Series, Vol. 2a, pp 280–299, 1984

Received October 23, 1984; Revised version August 6, 1985

Accepted August 12, 1985

J Geophys (1986) 59:23–31

Journal of Geophysics

Magnetometer array studies in southeastern Finland on the Baltic shield

Kari Pajunpää
Department of Geophysics, University of Oulu, SF-90570 Oulu 57, Finland

Abstract. Results of two magnetometer array studies on the Baltic shield in southeastern Finland are presented. The first array consisted of 29 Gough-Reitzel type magnetometers recording for about 2 months during autumn 1982. The results indicated two nearly perpendicular anomalous current concentrations crossing the array. The other operation, in 1983, with denser magnetometer spacing, revealed more detailed information about these anomalies.

Magnetograms, induction vectors, hypothetical event maps and profile data are presented to show the spatial behavior of the magnetic field variations, and to locate the anomalies. The east-west striking Mikkeli anomaly is thought to be continuous across the whole array. Two-dimensional modelling of one profile found this anomaly at a depth of 12 km. The Outokumpu anomaly is interpreted to lie at a greater depth than the Mikkeli anomaly, separating the very resistive Archaean eastern Finland from the less resistive Svecofennian central Finland.

The results are compared with electromagnetic deep soundings around Lake Ladoga in the Soviet Union and with deep seismic soundings in Finland. The Outokumpu anomaly and a discontinuity in the Moho depth appear to be related. The continuation of the Ladoga electric anomaly to Finland is not fully understood on the basis of the present results.

Key words: Magnetometer arrays – Conductivity anomalies – Crustal structures – Baltic shield

Introduction

The electrical structure of the earth's crust in central and southern Finland was studied with six magnetometer arrays during 1981–1984. These studies, together with magnetotelluric soundings and some controlled source measurements, formed part of an electromagnetic deep structure research project organized by the University of Oulu (Hjelt et al. 1985). Two of the six magnetometer arrays covered south-eastern Finland. This paper describes the results of these two operations, presenting anomalous zones and relating them to deep electromagnetic sounding data around Lake Ladoga, deep seismic results, and to some tectonic features, are presented.

The first of the two arrays in south-eastern Finland was operated in the autumn of 1982. Twenty-nine modified Gough-Reitzel magnetometers, on loan from the University of Münster (Küppers and Post, 1981), formed three lines 50 km apart, running northeast from the coast of the Gulf of Finland for about 300 km. This array was numbered IV and the three lines, shown on Fig. 1, were labelled G, H and I. Nearly parallel to these lines, in the same region, is the Baltic deep seismic sounding profile measured in August 1982 (Luosto et al. 1984a). Southeast of this array, in the Soviet Union, Rokityansky et al. (1979) have traced an electric anomaly under Lake Ladoga to the Finnish-Soviet border.

The preliminary results of array IV were available in early 1983, and were published together with data from three previous arrays by Pajunpää (1983, 1984). Two zones of intense concentration of induced currents were observed; the first, running north-south across the array, was named the Outokumpu anomaly and the other, running nearly east-west, was named the Mikkeli anomaly.

The other array in this region, numbered V, was designed to cover some interesting regions with a denser spacing. It was divided into two parts, with 15 magnetometers on the western end of the east-west striking anomaly (lines O, P and Q in Fig. 1) and 14 on the I line along the Finnish-Soviet border. The interesting central part of the array IV had to be excluded because it has many lakes and few roads. The station spacing on the lines was 10–30 km, and the array was operated during summer 1983.

The arrays operated for about 2 months, the data being stored on analogue films with a recording interval of 10 s. The amplitude resolution for the field variations is 2–3 nT. Over 90% of all recordings were useful.

Events and data processing

Three events of 2–4 h length from both arrays were digitized and analysed for the intervals listed in Table 1. The arrays were located between latitudes 56° and 58° geomagnetic north. The events were chosen with special care to avoid source field effects on transfer functions, as discussed in a previous paper by Pajunpää (1984). Only the wavenumber estimates for each event are presented in Table 1. The estimates are the average of the mean wavenumbers for 100–500-s periods and the values correspond to spatial wavelengths of 1000–3000 km.

After magnetograms had been drawn, the data for each station and event were processed with a method described

---

Present address: Hollming Ltd, PL 14, SF-26101 Rauma, Finland

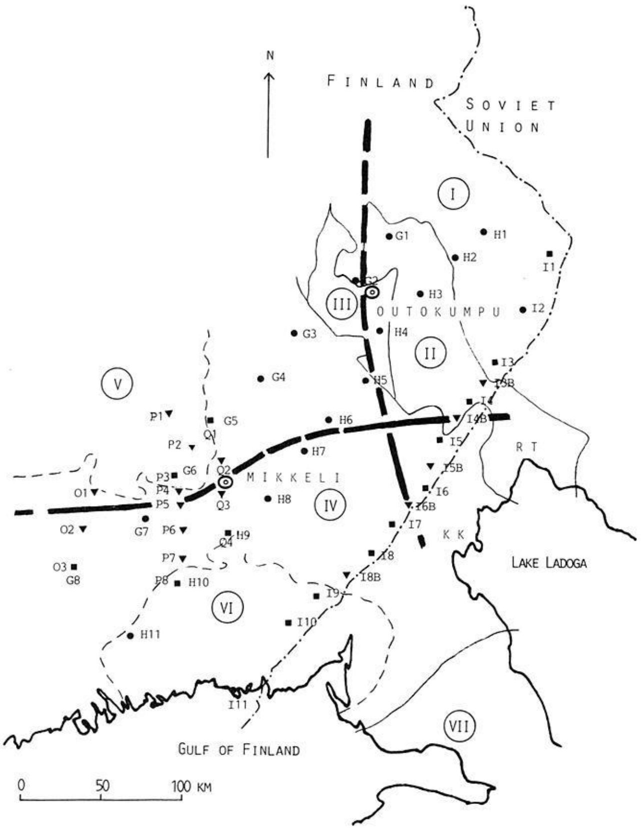

Fig. 1 a. Measured arrays on a map showing the anomalous zones and the main geological units according to Laajoki (1983). *Circles* are stations measured in 1982, *triangles* those measured in 1983 and *squares* are those measured in both operations; *I* Archean basement; *II* karelian schist belt; *III* Outokumpu allochton; *IV* Svecokarelidic supracrustal and plutonic rocks; *V* Central Finland granite area; *VI* Rapakivi rocks; *VII* Paleozoic and younger rocks. **b** Location of the research area on a tectonic map of the Baltic shield (Laajoki, 1983). *3* the Ladoga – Bothnian Bay zone; *5* the Outukumpu allochthon

Table 1. Events

Event number	Date	Time (UT)	Length (h)	Array	Lines	Wavenumber (km^{-1})
5	1982–10–26	1000–1300	3	IV	G,H,I	0.03
6	1982–11–25	0500–0700	2	IV	G,H,I	0.06
13	1982–11–24	1000–1300	3	IV	G,H,I	0.06
15	1983–05–25	0100–0400	3	V	I,O,P,Q	0.02
16	1983–06–18	0400–0800	4	V	I,O,P,Q	0.03
22	1983–07–23	0800–1200	4	V	I,O,P,Q	0.03

by Jones (1981) to obtain smoothed auto- and cross-spectral estimates. Thereafter, all data at each station were combined for the final transfer function estimates. As acceptance criteria and weighting functions firstly, the bias-reduced multiple coherence function (>0.8) between the vertical and the horizontal components (Jones et al. 1983) and, secondly, the product of the spatial wavenumber k and the inductive scale-length C ($kC<0.3$) (Pajunpää, 1984) were used.

Magnetograms

Since the magnetograms of event 5 have been presented by Pajunpää (1984), only those stations showing the maximum amplitudes of the horizontal components are repeated here. The northward component, X, has high amplitudes at stations G7, G4, H6–H7 and I4, while the eastward component, Y, has a maximum at stations G7–G8, H5 and I6.

The magnetograms from line P of event 22 are presented in Fig. 2. Line P crosses and is nearly perpendicular to the Mikkeli anomaly, as shown by the strong increase in the X component at station P4 and the rather flat Y component. The vertical component Z has a clear phase-reversal between P4 and P6, for which data are modelled below.

Induction vectors

Figure 3 shows the reversed real induction vectors at periods of 100, 215, 464 and 1000 s. The corresponding unreversed imaginary induction vectors, with 68% confidence intervals for the transfer function estimates, are shown in Fig. 4. The confidence intervals, which do not necessarily include the possible source-field error, are greatest at 100 and 1000 s and smallest at the mid-periods. This is mainly due to the number of data that were accepted for the different periods. At 100 s the low coherence between vertical and horizontal components and at 1000 s the large inductive scale length, C, with regard to the horizontal scale length, k, reduced the number of accepted data.

The following observations were made about the real induction vectors:

1. There is a clear reversal in the southwest between stations O1–O2, P4–P6 and Q2–Q3.

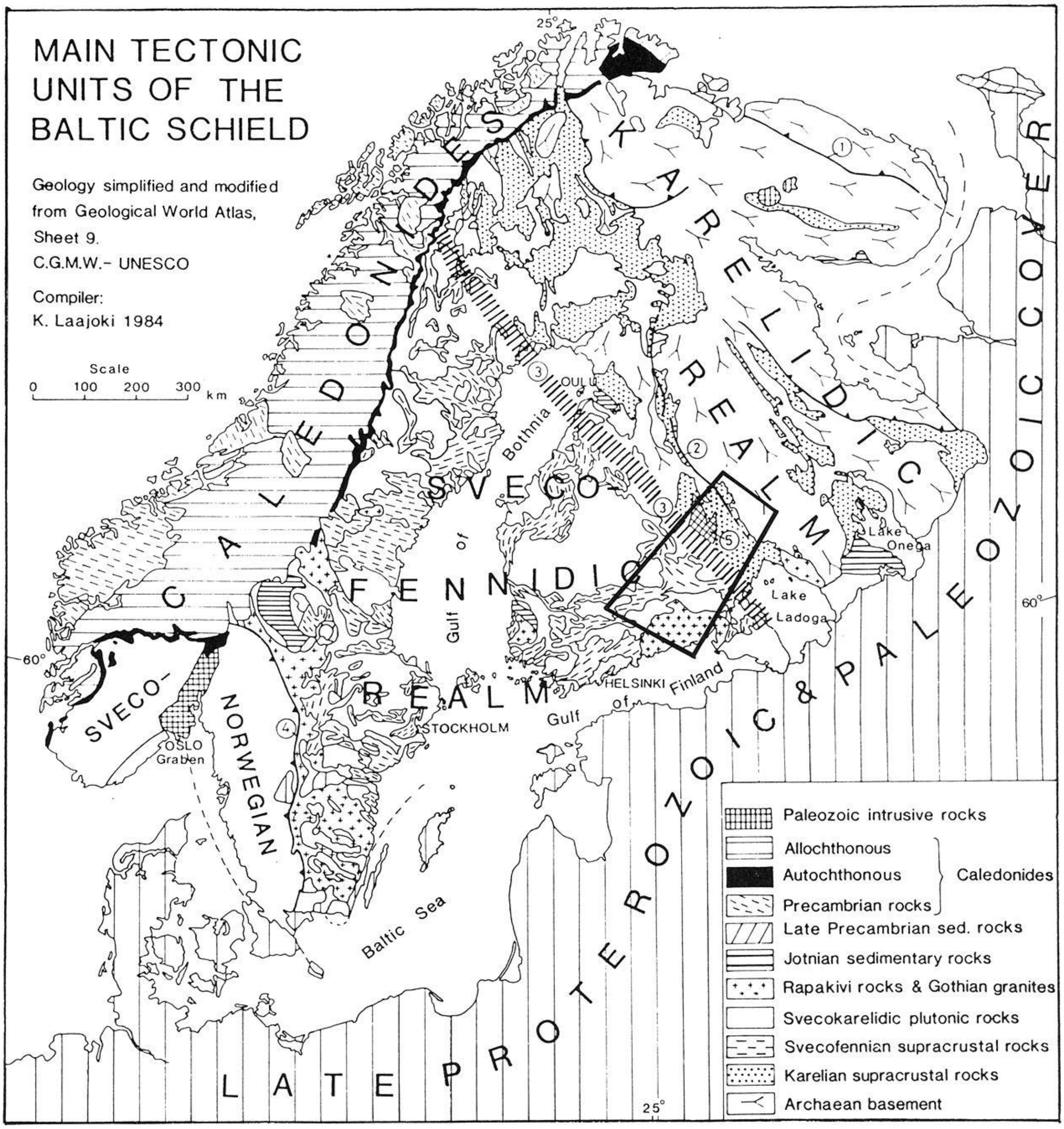

Fig. 1b

2. The vectors decrease in length towards the coast in the south.

3. There are very large vectors in the northeast.

4. There is a reversal between stations I6–I7 and H4–H6.

5. There is a reduction in the magnitude from I3 to I5 at 100 s and to I6B at 1000 s.

These vectors clearly represent the east-west directed current concentration in the west. The southern and northeastern parts seem to be electrically homogeneous whereas the central part is extremely complex. The shallow Gulf of Finland appears to have no effect at these periods.

The real induction vectors are more reliable than the imaginary ones. However, some observations about the imaginary vectors included:

1. the reversal between P4–P6, both vectors pointing away from the anomaly;

2. the reversal between G1–G2 at 100 s; and

3. the rather short length of all the imaginary vectors compared to the real ones.

The last point may indicate that the currents are mainly not shallow and that the conductivity contrasts are very high.

Hypothetical event maps

Following the method of Bailey et al. (1974) of presenting transfer function data for specific polarizations, hypothetical event maps were computed for two periods, 100 and 1000 s, and for two polarizations. Figure 5 shows the real part and Fig. 6 the imaginary part of the hypothetical vertical field for the polarizations shown on the figures.

The most striking feature in the real-part maps is the strong gradient in the west for the southward inducing field.

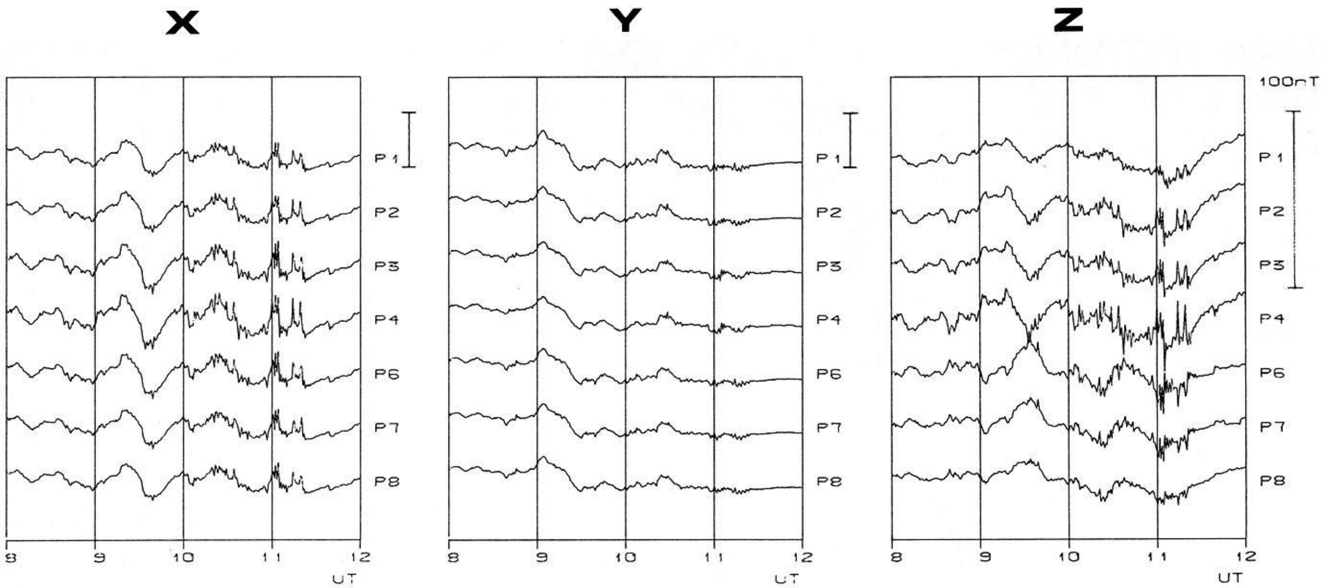

Fig. 2. Magnetograms of a substorm at 0800–1200 UT on July 23, 1983, for the P line

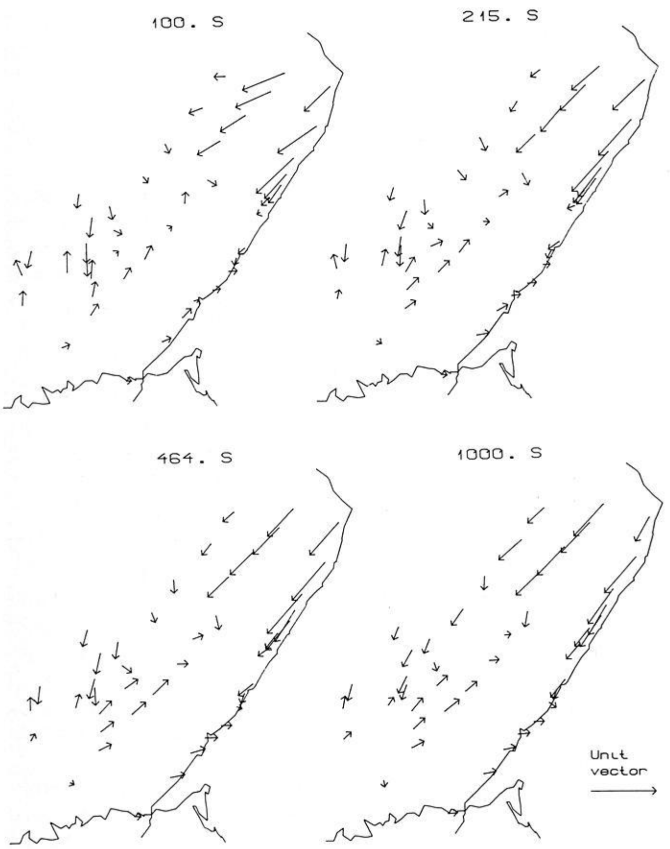

Fig. 3. Reversed real induction vectors

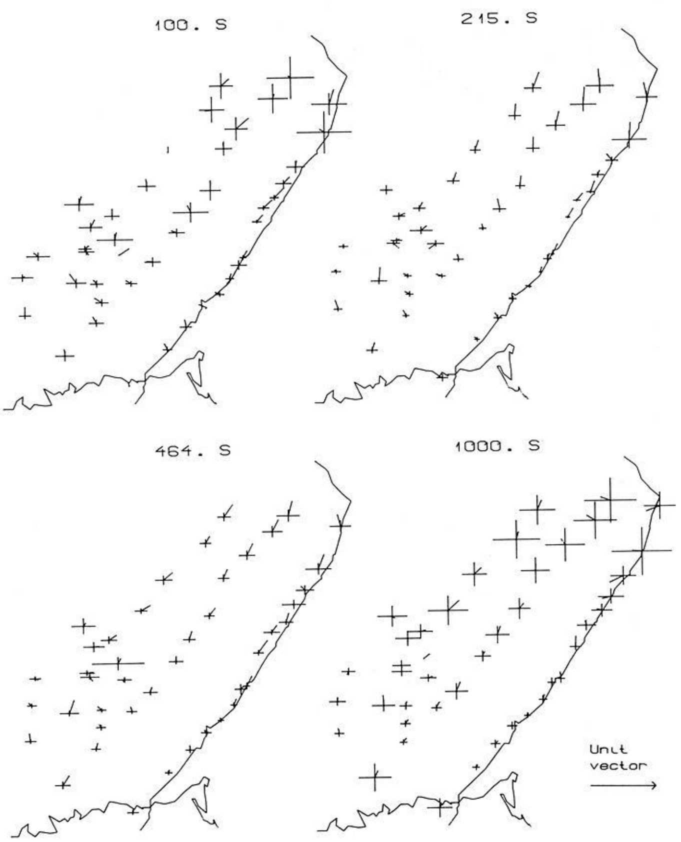

Fig. 4. Unreversed imaginary induction vectors with 68% confidence intervals

The anomaly seems to be very narrow and continues in the west of the array, but in the east it seems to turn northeast and diverge somewhat. Between H5 and H6 a strong gradient can be observed again, and then the two periods behave differently on line I; at 100 s, the stronger gradient is between I3 and I5 and at 1000 s between I6 and I7. For the westward inducing field, the western anomaly is observed only at 1000 s. A large gradient is observed in the northeast at 100 s, while at 1000 s, again, the gradient seems stronger around I6.

The imaginary maps for the southward polarization give only a weak indication of the anomaly in the southwest.

At 1000 s there is some anomalous behavior around I3–I4 and at 100 s between G2 and H3. The westward polarization indicates the anomaly between G2 and H3 more clearly at 100 s but it cannot be seen at 1000 s. Obviously this mainly north-south current concentration, which has a clear out-of-phase response, is very shallow.

Profile data on the I line

The I line appears to have a very complex magnetic field response. To give a more precise idea of the induced currents on this line, Figs. 7 and 8 show the behaviour of the transfer functions and of the horizontal field amplitude as north-south and east-west projections of this line. The horizontal field has been normalized by the mean value of the corresponding component at stations I1, I3 and I10 for the X-component and at I3 and I10 for the Y component.

Although neither of the directions agrees with the I-line direction, these projections show some interesting features. There is a very high transfer function amplitude in the north-east. The X-component in the north-south projection has a very high amplitude at the station I4B, with a rather broad maximum, its half-width being some 50 km. Almost nothing is seen of the Y component, showing that the current flows in the east-west direction. The large half-width of the anomaly is probably not directly related to the depth of the current; rather, it implies that the current flow itself is wide. This explanation is preferable because the field decreases sharply towards longer periods. The maximum response is at about 200 s.

The maximum anomaly in the Y component is at station I6B, some 50 km southwest of I4B. Here, also, the X component has a low anomaly, with about the same frequency response as the Y component, revealing that the mainly north-south directed current also has an east-west component. The maximum response of this anomaly is at about 500 s and clearly lasts for longer periods than the other anomaly.

Two-dimensional modelling on the P line

The hypothetical event maps in Fig. 5 show that the Mikkeli anomaly is a narrow zone striking west from the P line. In the east it turns northeast and obviously diverges, indicating that on the P line, where the best data are available, the current flow is not purely two-dimensional. Obviously, the anomalous field is increased in the north and decreased in the south due to the geometry. However, a two-dimensional model was constructed to estimate the depth of the anomaly. The model is shown on Fig. 9 together with measured and calculated transfer function data. The finite difference method was used, with a program written by Brewitt-Taylor and Weaver (Brewitt-Taylor and Weaver, 1976; Weaver and Brewitt-Taylor, 1978).

The model consists of a good conducting (0.5 ohm m) body at a depth of 12 km, with an area of 5×5 km^2 and total areal conductivity of 5×10^7 Sm. At the surface there is another good conducting (2 ohm m) body, representing the schists and especially affecting the imaginary part of the field. The resistivity of the host rock is 10000 ohm m down to 50 km and 200 ohm m below that. This one-dimensional structure is rather arbitrary and the data cannot resolve it. To the south of the anomaly a low-resistive layer (80 ohm m) is used to explain the asymmetry of the anomaly, although this layer may not be obvious because the asymmetry of the anomaly can be explained also by the three-dimensionality of the anomaly. However, it coincides with a low-velocity layer under the Rapakivi area observed in the deep seismic sounding on the Baltic profile (Luosto et al. 1984a). It was very difficult to find a model that would explain the asymmetric behavior satisfactorily at all periods from 100 to 1000 s. However, it was always necessary to have the good conducting body at a depth of 10 or 12 km. That depth and the total conductivity of the body are the main and most reliable results of this modelling.

Results and discussion

The two main anomalous zones in the research area are (Fig. 1):

1. the east-west striking Mikkeli anomaly and
2. the north-south striking Outokumpu anomaly.

The Mikkeli anomaly lay below about 10 km on the P line, with a maximum response on both the P and I lines at about 200 s. The total longitudinal conductivity of the two-dimensional model is 5×10^7 Sm. In the western part the Mikkeli anomaly is rather narrow, but in the east it is probably wider – some 10–20 km. Although the anomaly cannot be located as sharply on the H line as on the I and P lines, it seems to be continuous across the whole region.

On the geological map the Mikkeli anomaly is located mainly below the Svecofennian schist area. However, close to the Finnish-Soviet border it is clearly overlain by plutonic granites, while in the east it seems to lie below the Karelian schist belt. This anomaly cannot be explained by surface formations such as schist zones. Golod et al. (1983) have presented a map of the electrical conductance of the crust in Soviet Karelia, which shows, among other anomalies, a southeast-northwest striking zone of anomalous conductance exceeding 200 S. This zone meets the Finnish-Soviet border close to the same place as the Mikkeli anomaly, although its direction is rather different. Recent magnetometer array studies in southwestern Finland show that the Mikkeli anomaly continues far to the west along the schist belt, following the southern edge of the central Finland granite area.

The main tectonic outlines do not agree with the Mikkeli anomaly. The Ladoga-Bothnian Bay zone cuts the Mikkeli anomaly and the other tectonic lines are mainly north-south. However, some features coming from the northwest e.g. the Suvasvesi fault, end at a front close to the anomaly (T. Koistinen, 1985 personal communication).

The Outokumpu anomaly gives a maximum response at 500 s, and using the empirical data collected by Rokityansky (1982, fig. 106, p. 296), a total conductivity of about 10^8 Sm is obtained. Application of Biot-Sawart law and a line-current assumption for the Outokumpu anomaly to the data at 500 s on Fig. 8 gives depth estimates for the line current of 15–23 km, using seven stations from I5 to I9. Moreover, the currents are located between 16B and I7, with a horizontal scatter of less than 8 km. This means that the currents are very concentrated but, as the chosen east-west direction is not necessarily strictly perpendicular to the anomaly, the depth estimates can be regarded only as approximations. However, this result together with the frequency dependence indicates that the Outokumpu anom-

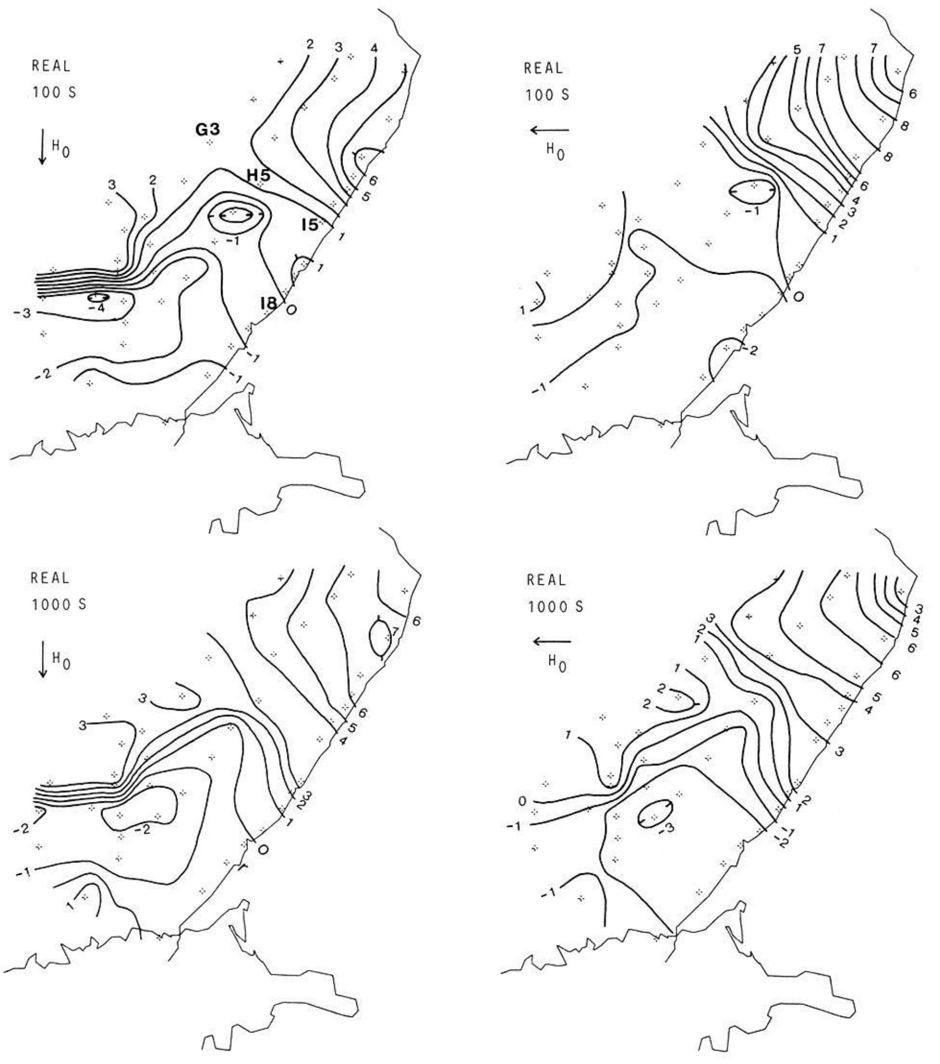

Fig. 5. Hypothetical event contour maps of the in-phase vertical field (× 10) generated by a unified, linearly polarized, horizontal field directed southward (left column) and westward (right column)

aly has a deeper origin than the Mikkeli anomaly. On the H line the Outokumpu anomaly can be located quite accurately close to station H6. North of this the currents seem to diverge to the northwest and the anomaly becomes a conductivity boundary. A new, shallow current concentration is observed in the Kainuu schist belt (Pajunpää, 1984). Under the Outokumpu allochthon the anomaly is shaded by a large number of shallow graphitic schist dykes that respond only to short-period variations and to the imaginary part of the Z-field as seen on Fig. 6.

Pajunpää (1984) showed that the Outokumpu anomaly continues as a conductivity boundary for about 200 km north of the Outokumpu allochthon. The Archaean basement and also the Karelian schist belt east of the anomaly are very highly resistive. West of this conductivity boundary the average resistivity of the crust is lower, and there are probably conductive layers, at least locally, as presented by Jones et al. (1983). In the north the conductivity boundary seems to fit with the Archaean Kuhmo schist belt. If the Outokumpu anomaly has the same origin in the south as in the north, the tectonic line of the Kuhmo schist belt must continue southward under the younger Karelian schists and Svecofennian formations. Nevertheless, there are large faults in the Ladoga-Bothnian Bay zone which clearly cut the Outokumpu anomaly but cannot be found in the available current data, although the anomaly (if it is connected with the Kuhmo schist belt) should be older than the faults.

Deep seismic soundings along the Baltic profile give interesting material for comparison. Preliminary results for this profile published by Luosto et al. (1984a) show that in the central part of the profile the Moho is more than 50 km deep. In the southwest and the northeast the crust is clearly thinner. The deepening of the Moho takes place slightly north or northeast of station G1 (see Fig. 1) and the Moho is clearly less than 50 km in the northeast. Some 200 km north of this station, Yliniemi (1985 personal communication) has reported an increase in crustal thickness of more than 10 km from east to west, near the Kuhmo schist belt and the northern part of the Outokumpu anomaly. Seismic results from the Sveka profile in central Finland (Luosto et al. 1984b) give a Moho depth of more than 50 km for the central and northern part of the profile. If the electrical conductivity boundary of the Outokumpu anomaly and the thickening of the crust are related to each other at the two places, the seismic boundary may coincide with the conductivity boundary.

Rokityansky (1983) has reviewed results of the electromagnetic soundings on the Baltic shield, including magnetic variation (MV) and magnetotelluric (MT) studies of the

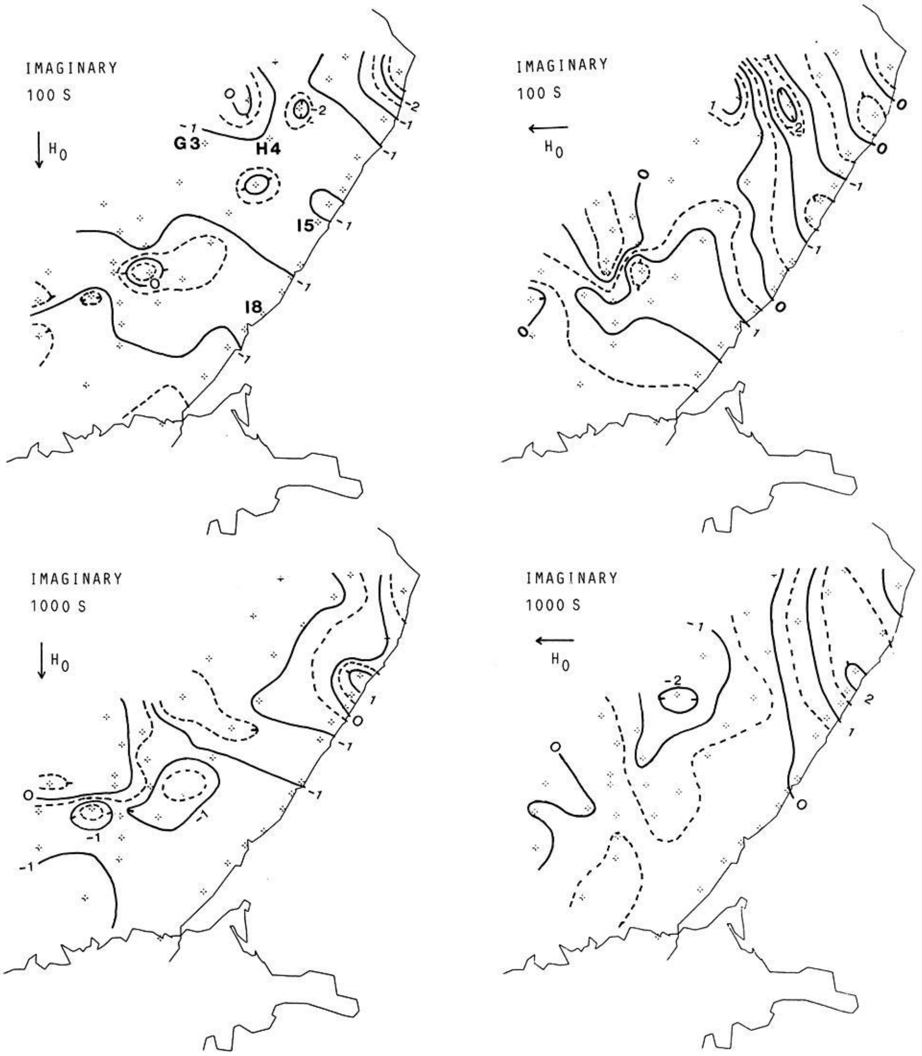

Fig. 6. Hypothetical event contour maps of the out-of-phase vertical field (×10)

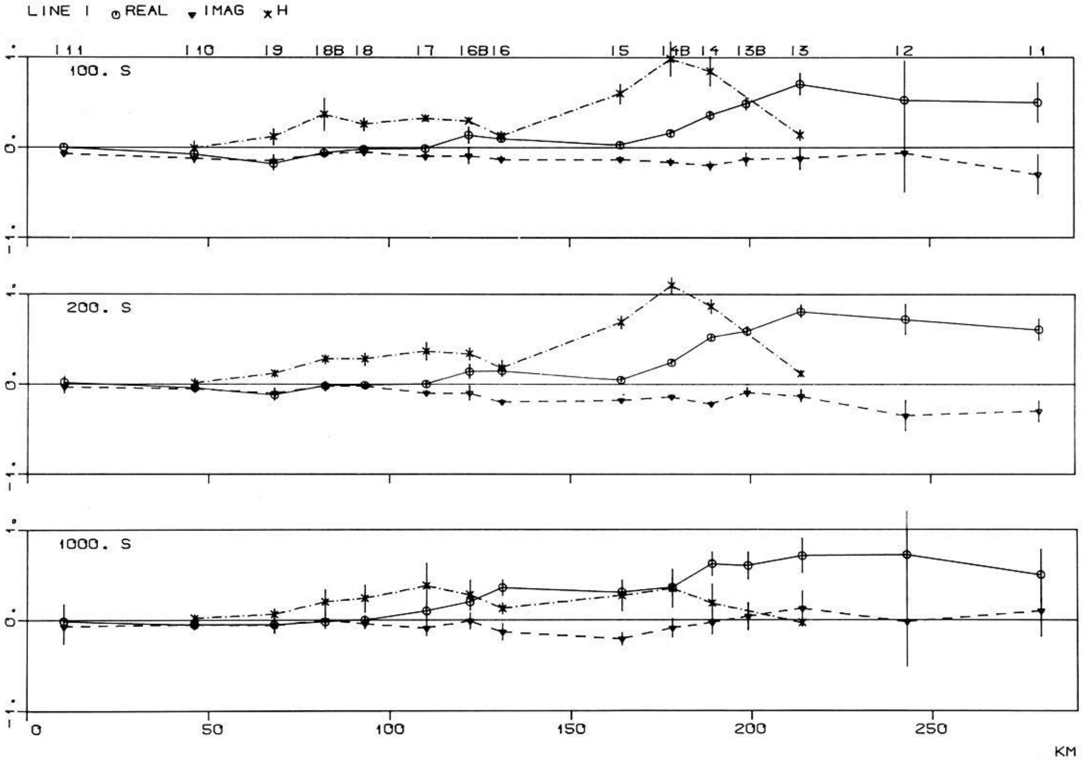

Fig. 7. North-south projection of the data on the I line. The *solid curve* with *circles* is the real part and the *dashed curve* with *triangles* the imaginary part of the transfer function with 68% confidence intervals. The *dashed-dotted curve* with *crosses* is the normalized amplitude of the horizontal north-south component with standard deviation

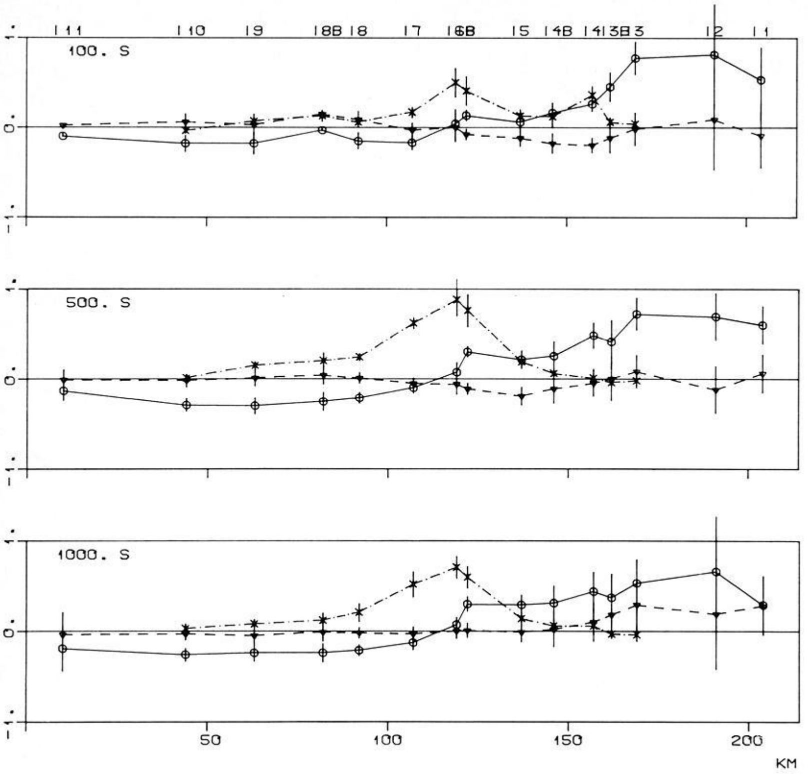

Fig. 8. East-west projection of the data on the I line. The curves are as shown in Fig. 7 except that east-west components are shown

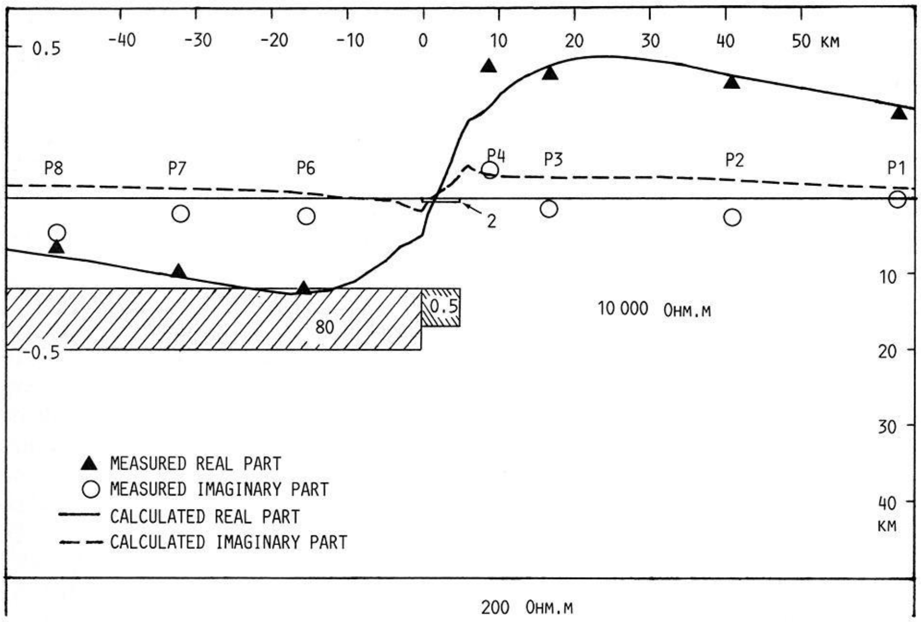

Fig. 9. Geoelectric two-dimensional model for the P line

Ladoga anomaly observed by Rokityansky et al. (1979). This anomaly runs under Lake Ladoga in a northeast-southwest direction to reach the Finnish-Soviet border. Its depth has been determined from MT studies at about 10 km and total conductivity from MV studies is 2×10^8 Sm. The depth is therefore very close to that observed for the Mikkeli anomaly. However, it is rather difficult to connect the Ladoga anomaly with either the Mikkeli or the Outokumpu anomaly.

Rokityansky (1983) also reported a high normalized north-south component (1.8–1.9) at periods of 5–90 minutes at station KK, near the area where the Outokumpu anomaly meets the Finnish-Soviet border (see Fig. 1). However, the normalized east-west component at the station KK is also as high as 1.5. This result is in agreement with the Outokumpu anomaly, if it is assumed that the Outokumpu anomaly turns to the southeast and joins the Ladoga anomaly. At station RT in the northernmost corner of Lake Ladoga the normalized X component is 1.4 at periods of 5–30 minutes and the Y component is only 1.1–1.05. This result agrees with the east-west directed Mikkeli anomaly.

Rokityansky (1983) assumed that the Ladoga anomaly and the Storavan anomaly (Jones 1981) in northern Sweden are parts of a unified Transscandinavian anomaly. The results presented here and by Pajunpää (1984) do not support this thesis.

The data produced by the two magnetometer arrays do not allow a detailed study of the depth, width and uniformity of the observed anomalies. Therefore, magnetotelluric or some other deep electrical soundings are needed across and over the anomalous zones, particularly to determine the depth and accurate location of the Outokumpu anomaly and the related conductivity boundary. Moreover, the proposed crossing structure of the two anomalies should be studied.

Acknowledgements. This work was financed by the Academy of Finland, the Ministry of Commerce and Trade and the University of Oulu. The magnetometers were on loan from the University of Münster. The author wishes to thank Prof. S.E. Hjelt, the leader of this project, for organizing it and for much advice, Prof. J. Untiedt for the use of the magnetometers and Dr. A.G. Jones for the analysis programs. The author also thanks T. Korja, H. Juntti and K. Koivukoski for help with the field work, E. Trast for numerous computer runs, T. Valtanen for digitizing and P. Pöntiö for drawing and typing. Further the author acknowledges useful discussions with Dr. T. Koistinen and T. Pernu.

References

Bailey, R.C., Edwards, R.N., Garland, G.D., Kurtz, R., Pitcher, D.: Electrical conductivity studies over a tectonically active area in eastern Canada. J. Geomagn. Geoelectr. **26**, 125–146, 1974

Brewitt-Taylor, C.R., Weaver, J.T.: On the finite difference solution of two-dimensional induction problems. Geophys. J.R. Astron. Soc. **47**, 375–396, 1976

Golod, M.I., Klabukov, B.N., Grishin, A.S. Vasin, N.D.: The geoelectric model of central Karelia. In: The development of the deep geoelectric model of the Baltic shield, Part 2, Hjelt, S.E., ed., pp 180–204. Proc. 1st Project Symp., Oulu, 15–18.11.1983, Dept. of Geophysics, Univ. of Oulu, Report No. **8**, 1983

Hjelt, S.E., Kaikkonen, P., Pajunpää, K., Korja, T., Heikka, J.: Electromagnetic studies of the Baltic shield in Finland. Ann. Geophys. in print 1985

Jones, A.G.: Geomagnetic induction studies in Scandinavia – II Geomagnetic depth sounding, induction vectors and coast effects. J. Geophys. **50**, 23–36, 1981

Jones, A.G., Olafsdottir, B., Tiikkainen, J.: Geomagnetic induction studies in Scandinavia – III. Magnetotelluric observations. J. Geophys **54**, 35–50, 1983

Küppers, F., Post, H.: A second generation Gough-Reitzel magnetometer. J. Geomagn. Geoelectr. **33**, 225–237, 1981

Laajoki, K.: The main tectonic features of the Baltic shield in Finland. In: The development of the deep geoelectric model of the Baltic shield, Part 2, Hjelt, S.E., ed., pp 233–244. Proc. 1st Project Symp., Oulu, 15–18.11.1983, Dept. of Geophysics, Univ. of Oulu, Report No. 8, 1983

Luosto, U., Ilmola, V.-M., Zverev, S.M., Kosminskaya, I.P., Sharov, N.V., Korhonen, H.: Results from the DSS study on the Baltic profile in SE Finland. Paper read at the XIX General Assembly of the European Seismological commission, Moscow, 1.–6. Oct. 1984a

Luosto, U., Lanne, E., Korhonen, H., Guterch, A., Grad, M., Materzok, R., Perchuc E.: Deep structure of the Earth's crust on the SVEKA profile in central Finland. Ann. Geophys. **2**, 559–570, 1984b

Pajunpää, K.: Magnetometer array studies in central and southeastern Finland. In: The development of the deep geoelectric model of the Baltic shield, Part 2, Hjelt, S.E., ed. pp 245–262. Proc. 1st Project Symp., Oulu, 15–18.11.1983. Dept. of Geophysics. Univ. of Oulu, Report No. 8, 1983

Pajunpää, K.: Magnetometer array studies in Finland – determination of single station transfer functions. J. Geophys. **55**, 153–160, 1984

Rokityansky, I.I., Vasin, N.D., Golod, M.I., Novitsky, G.P., Rokityanskaya, D.A., Sokolov, S.Ja.: Electric conductivity anomalies in the south of Karelia (in Russian). Geophys. Commun. Kiev **89**, 36–39, 1979

Rokityansky, I.I.: Geoelectromagnetic investigation of the Earth's crust and mantle. Springer: Berlin-Heidelberg-New York, pp 381, 1982

Rokityansky, I.I.: Geoelectromagnetic studies of the Baltic and Ukrainian shield: Review of some results. In: The development of the deep geoelectric model of the Baltic shield, Part 2, Hjelt, S.E., ed., pp 110–150. Proc. 1st Project Symp. Oulu, 15–18.11.1983, Dept. of Geophysics, Univ. of Oulu, Report No. 8, 1983

Weaver, J.T., Brewitt-Taylor, C.R.: Improved boundary conditions for the numerical solution of E-polarization problems in geomagnetic induction. Geophys. J.R. Astron. Soc **54**, 309–317, 1978

Received March 18, 1985; Revised version July 15, 1985
Accepted July 31, 1985

J Geophys (1986) 59:32–41

Journal of Geophysics

Magnetovariational and magnetotelluric studies of the Oulu anomaly on the Baltic Shield in Finland

T. Korja[1], P. Zhang[2], and K. Pajunpää[1]

[1] Department of Geophysics; University of Oulu, SF-90570 Oulu 57, Finland
[2] Department of Solid Earth Physics; University of Uppsala, S-751 22 Uppsala 1, Sweden

Abstract. The electrical conductivity structure of the Baltic Shield in Finland has been studied by magnetovariational (MV) and magnetotelluric (MT) work. First magnetometer arrays revealed the crustal Oulu conductivity anomaly which consists of a crustal conductive zone and a conductivity boundary. Since 1983 the magnetotelluric technique has been used to study the Oulu anomaly in more detail.

The information obtained from the induction vectors of the MV and MT data are compared. 1D and 2D models of the Oulu anomaly were constructed from MT data using induction vectors as additional information. In the centre of the research area the anomalous body (with a resistivity of 0.5 ohm m) lies below a depth of 4–7 km. Its width is about 25 km and its length is more than 100 km. To the south-west of this anomaly a low-resistive crustal layer exists at a depth of 14 km, whereas to the north-east no crustal layer was identified in the very resistive Karelidic realm.

Key words: Baltic Shield – Crustal conductivity structure – Oulu conductivity anomaly – Magnetotellurics – Magnetovariational studies

Introduction

Since 1980 the deep geoelectric structure of the Baltic Shield has been investigated under a research project in Finland (Hjelt et al. 1985). In order to get information about the electrical conductivity distribution within the Earth's crust, and even within the upper mantle, magnetovariational (MV) and magnetotelluric (MT) measurements have been carried out.

With magnetometer arrays one can map lateral variations in the electrical conductivity of the Earth's crust by measuring time variations of the Earth's magnetic field simultaneously at several sites. Once some conductivity anomaly has been revealed with MV, one can investigate with the magnetotelluric method and try to obtain more knowledge about the depths and conductivity values of the formations which caused the anomaly.

Following the above procedure, several magnetometer arrays have been operated in Finland since 1981. The first arrays were located in central Finland (Pajunpää et al. 1983). These arrays revealed, among others, the conductivity anomaly near Oulu – called the Oulu anomaly [first indicated in the results of Lange (1979) and Küppers et al. (1979)]. After the array studies, magnetotelluric soundings were undertaken in 1983 and 1984 to study this anomaly in more detail. MT measurements were accomplished as a joint project between the universities of Oulu and Uppsala.

The research area of interest (Fig. 1) is situated on the boundary of two of the three main Precambrian tectonolithological units of the Baltic Shield (Laajoki, 1984). The northeastern part belongs to the Karelidic realm where the Archean basement is exposed in many places. Berthelsen (1984) calls this realm the Archean nucleus or age province. It consists of 3,100-2,500-Ma-old Archean and Early Proterozoic rocks; mainly granodioritic gneisses, different kinds of schists (quartz-feldspar and mica) and greenstones. The southwestern part of the research area lies on the 1,900-Ma-old Svecofennidic realm, the rocks of which are granites, granodiorites and migmatic gneisses with granite veins. Between these two units is a geological border. According to Berthelsen (1984), this border is a 2,000-Ma-old fossil plate boundary. However, the existence and the character of this boundary is to some extent unresolved and, according to Berthelsen, it may be impossible to identify this boundary at present. In the middle of the research area above these old Precambrian rocks lies the well-known Muhos formation which consists of unfolded Jotnian silt and shale sediments (1,300 Ma). According to geophysical and borehole data these sediments reach a depth of 1,000 m.

Measurements

Magnetovariational (MV) measurements (or geomagnetic deep soundings) were performed with 31 magnetometers of Gough-Reitzel type (Küppers and Post 1981) which were on loan from the University of Münster. The MV data used in this study were collected with three arrays. The stations with letters A, B, C and II belong to array number II, the stations with letters M and N to array number III and with R to array number VI (see Fig. 2). Based on the results of the array II, the profiles M, N and R were planned to cross the anomaly to locate it better.

When starting with MT one could follow the proposal of Rokityansky (1982) and group the measurements above the anomaly to find out the depth and the conductivity of the anomalous body. This provides very fast results about the character of the anomaly. In our case, however, the location of the anomaly was not very well determined

---

Offprint requests to: T. Korja

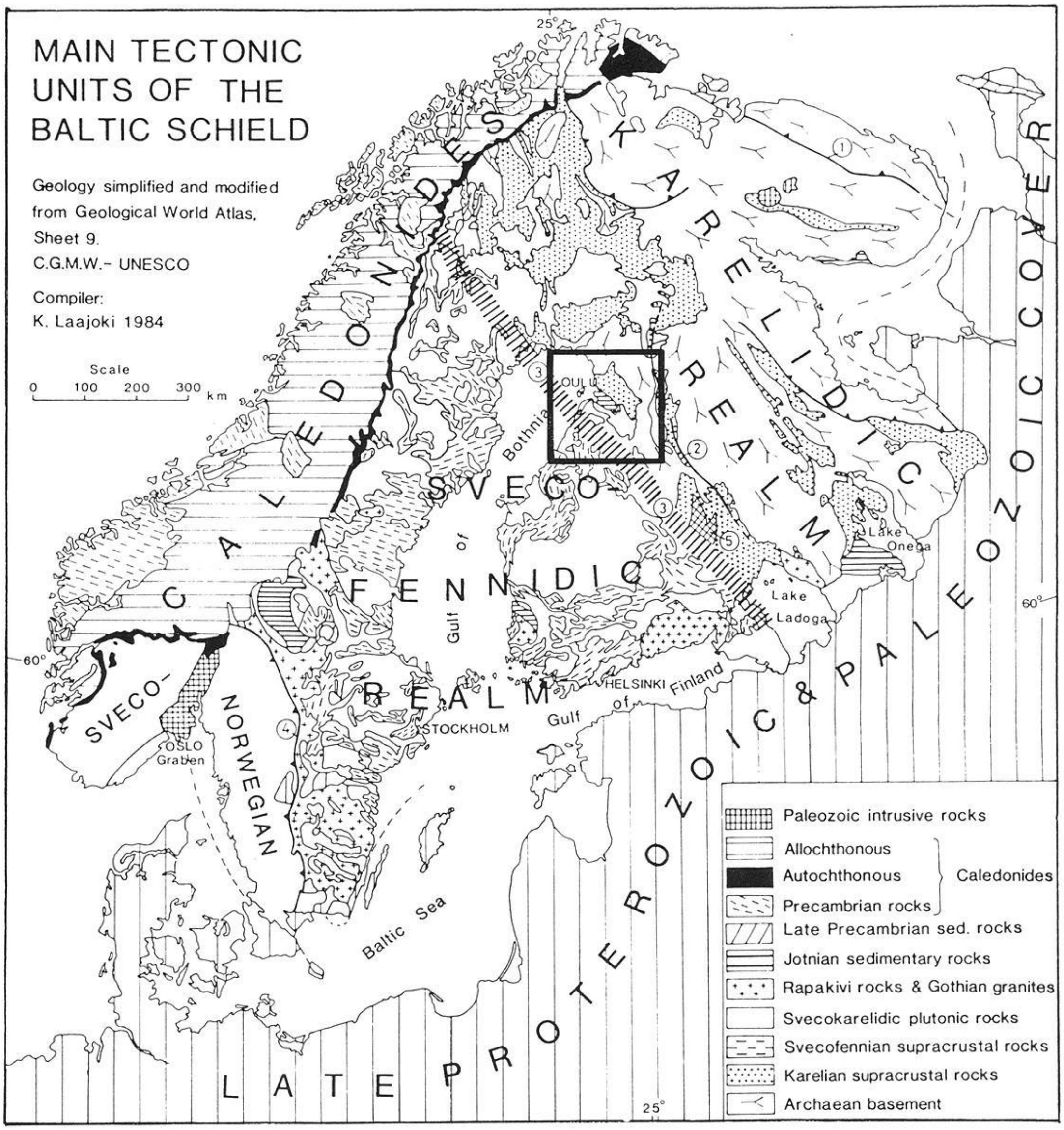

Fig. 1. Main tectonic outlines of the Baltic Shield and the location of the research area. Tectonic zones: *2* Koillismaa-Kainuu-North-Karelia, *3* Raahe-Ladoga. (Map of Laajoki, 1984)

and in addition to the anomalous zone there is also the above-mentioned conductivity boundary. We therefore decided to make profiles across the anomaly. This also give a chance to perfom 2D modelling when constructing a geoelectric model.

The first profile (OULU I) parallels magnetometer profile N, and thus enables a direct comparison of induction vectors. In the northeastern part it enters the Archean basement. The second profile (OULU II), which runs from east to west and crosses the anomaly perpendicularly, is mostly on the younger Svecokarelidic realm. This profile also traverses the Muhos formation, thus making it possible to sound the electrical structure under the sediments.

MT measurements were made with two five-component MT stations on loan from the University of Uppsala. On profile OULU II, mainly horizontal components were recorded. Recordings were usually made simultaneously with both equipments to enable the "remote reference" processing (Gamble et al. 1979) of the data. However, due to timing errors when starting recordings, especially on profile OULU II, it has frequently proved impossible to identify the time shift between two data sets and so far it has proved impossible to apply the RR technique. The data were collected with a digital acquisition system constructed in Uppsala. Signals were divided into two period bands: 2–3,600 s and 0.1–10 s. The sampling intervals and recording times were, correspondingly, 2 Hz and 16 h for long periods and 64 Hz and $^1/_2$ h for short periods.

A total of 24 MT soundings were carried out. The data from seven sites were useless (due to tape record errors, instrumentation errors, very poor signal to noise ratio etc.) but the data from ten sites on OULU I and seven sites on OULU II were of high enough quality to be analysed.

Induction vectors

Some induction vectors are presented here to show the location of the anomaly and to examine the vectors determined from the MT data. Two main data sets were used to calculate the estimates of the single-station induction vectors:

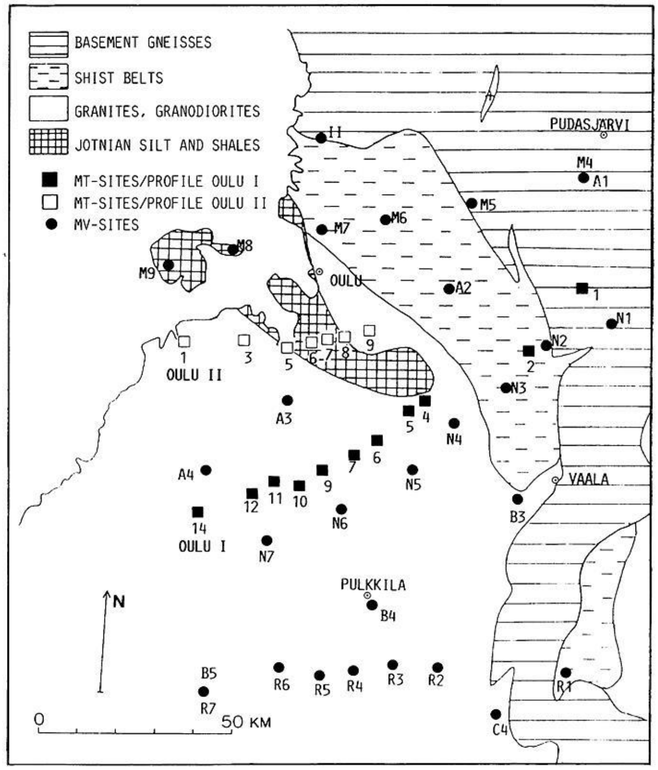

Fig. 2. The simplified geology of the research area and locations of the MV sites (*circles*) and MT sites (*squares*). The geological map is simplified from Simonen (1980)

firstly, the data compiled from the three magnetometer arrays and secondly, the data recorded during the MT measurements on the southern MT profile (OULU I). On the northern profile (OULU II) we measured only horizontal EM-field components.

The two data sets differ from each other in three points. The available period range in the array measurements is from about 60 s up to 1 or even 24 h, whereas in the MT measurements it is from 0.1 s up to 1 h. The recording period in the array operations was about 2 months and in the MT 16 h. This strongly restricts the selection of MT records for analysis. The magnetometer array data allow a control on the source field characteristics, whereas the MT data do not.

The analysis method for the magnetometer array data was described by Jones (1981) and Pajunpää (1984). The transfer functions were calculated from three events of 2–4 h except at stations R1–R6 where only one event of 4 h has been used. The acceptance level of the bias-reduced multiple coherence functions between vertical and horizontal components (see Jones et al., 1983) was 0.8 for the N and M lines and 0.6 for the A and B lines. The acceptance level of the product of the horizontal field spatial wavelength and the inductive scale length (see Pajunpää, 1984) was 0.3. At stations R1-R6, no acceptance criteria were used.

The induction vectors from the MT data were determined using the MT-analysis program of Jepsen and Pedersen (1981). Data sets were averaged using 0.8 as a threshold value of predicted coherencies when accepting data sets for further analysis. From these averaged power spectra, the induction vectors (**A**, **B**) were calculated.

Figure 3a shows the reversed real and unreversed imaginary induction vectors for a period of 100 s around the Oulu anomaly. The imaginary part of the vectors determined from the MT data are not displayed here. If we compare the real vectors of the two data sets we can see that they both reveal the presence of an anomaly, but the vectors from MT data have obviously some large errors (stations 4 and 5). The lack of the source field control may cause heterogenous errors on different days so that every MT station has its own source error. Figure 3c shows the vectors from the MT instruments at 10 s period. They indicate an anomaly between stations 2 and 4. This is in good agreement with the array data, which indicates shallow currents around station N3. Obviously the MT vectors are more reliable at this shorter period than at 100 s due to a larger number of periods (degrees of freedom) in the record and due to a smaller skin-depth of the field. As a conclusion we can say that a group of induction vectors determined from MT records, as here, can be used qualitatively, whereas a single vector should not be used.

Figure 3b shows the induction vectors determined from the arry data at 500 s period. Figure 3a and b give somewhat different pictures of the anomaly. At 500 s there is a clear reversal of the vectors between stations M6 and M7, N5 and N6. Thus the main current at this period flows along that axis striking slightly west of north.

At 100 s the anomaly seems to be much broader on the N line. The vectors are short at stations N3, N4 and N5. The imaginary vectors at 100 s reverse between N2 and N3 and are large at N4 and also at M6. At 10 s the vectors from the MT instruments reverse between stations 2 and 4. This can be explained by a shallow current flowing from about N3 to the northwest. The geological explanation of this shallow current is the schist belt in the same region. The conductive dykes, which are mainly graphite, have concentrated in the southwestern border of this schist belt (Pernu, 1979). Also, the Muhos sediment formation may carry shallow currents affecting station N4 especially. Moreover, the main anomaly has a different frequency response along its eastern and western borders.

The deeper north-south-striking or "main" anomaly and the shallow current in the schist belt meet around station M7, causing very large real induction vectors at stations M6 and I1. The width of the "main" anomaly is not well determined. Its length is more than 100 km beginning from about station B4 and continuing north-northwest from station M7. On the R line the anomaly is more like a boundary.

MT data analysis

As mentioned previously, the MT data were collected in two period bands; 2–3,600 s and 0.1–10 s. The data processing was carried out at Uppsala University using a slightly modified version of the program of Jepsen and Pedersen (1981), which estimates several parameters including:

a) The polarization parameters of the horizontal magnetic and electric fields (Fowler et al., 1967).

b) The ordinary and predicted coherencies between the magnetic and electric fields.

c) The magnetotelluric (MT) impedance both in the measuring and rotated directions. By rotating the MT-impedance tensor, a direction is found in which the sum of

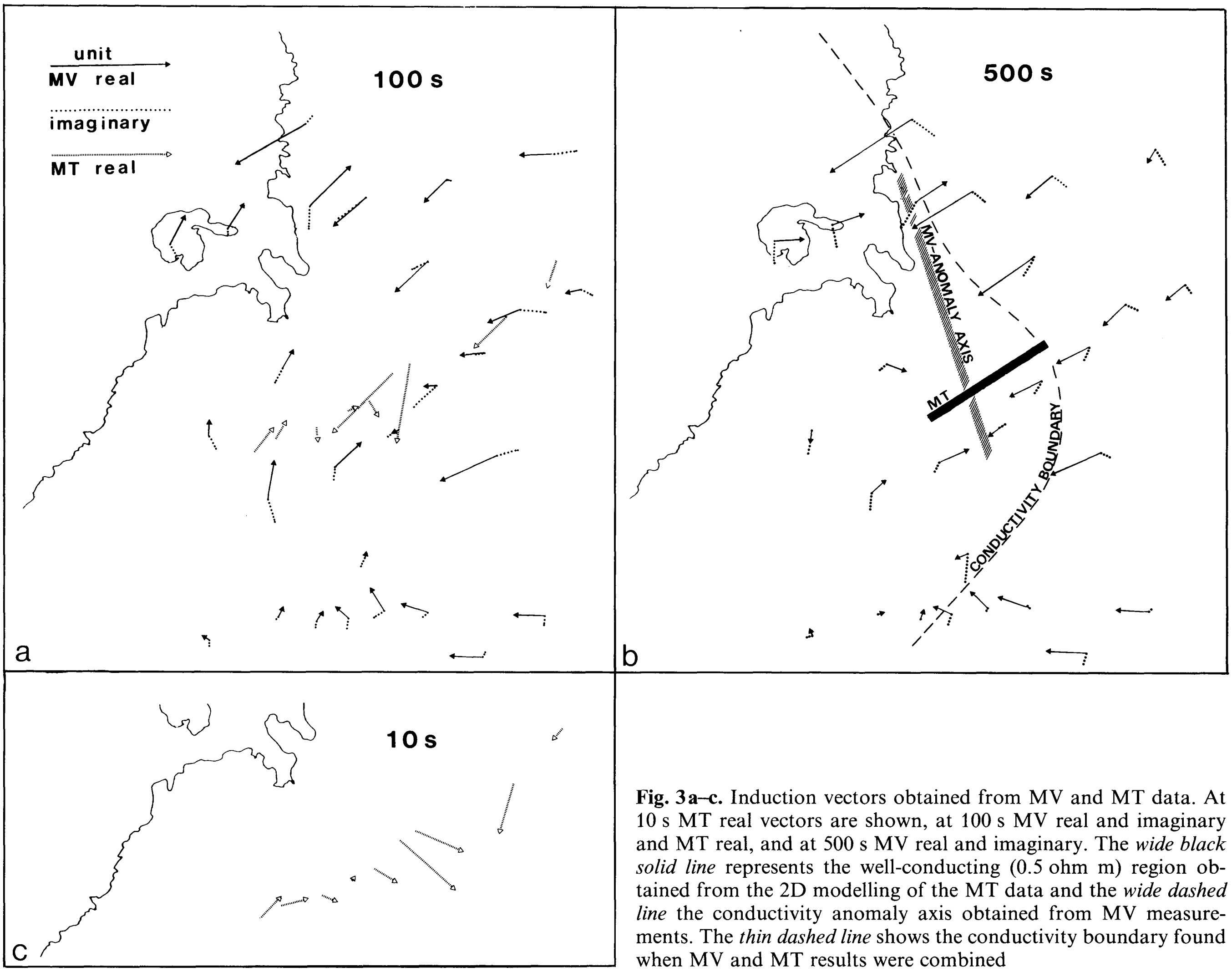

Fig. 3a–c. Induction vectors obtained from MV and MT data. At 10 s MT real vectors are shown, at 100 s MV real and imaginary and MT real, and at 500 s MV real and imaginary. The *wide black solid line* represents the well-conducting (0.5 ohm m) region obtained from the 2D modelling of the MT data and the *wide dashed line* the conductivity anomaly axis obtained from MV measurements. The *thin dashed line* shows the conductivity boundary found when MV and MT results were combined

the diagonal elements of the impedance tensor is a minimum.

d) Apparent resistivity and phase in the unrotated and rotated directions.

As stated above, due to timing problems, only a few of the stations could be processed using the "remote reference" technique. Fortunately, the data was usually of high quality, with the predicted coherence usually 0.8 or higher (a value of 0.8 was used as an acceptance threshold when rejecting poor data segments). This, and the lack of severe polarization in the horizontal magnetic field at most sites, means that the problems sometimes associated with "single-station" data (see e.g. Pedersen and Svennekjär, 1984; Roberts et al., 1984) can be expected to be of small significance for this data set. All data have been processed using the single-station technique.

It is a common practise in MT data analysis to present the estimated apparent resistivities in the rotated directions (see above) on the assumption that these directions are determined by the predominant strike of the Earth structure in the vicinity. In our case the data does not produce a stable "strike" direction. The magnetometer array study of Pajunpää (1984) indicates that the electrical structure in the Oulu area is dominated by a conducting zone which strikes about 340° (N 20° W). Comparison of results of one-dimensional inversion of the unrotated data from the two profiles (Fig. 5) also suggests that the predominant strike is roughly in this direction. Thus, we can conclude that the predominant strike is north-south, the lack of a consistent strike direction in the data presumably being due to the influence of three-dimensionality within the Earth. The two-dimensional modelling of profile OULU I (see below) was carried out assuming this strike Analysis of the data in the measuring coordinate system has an additional advantage; because of complex near-surface structure and the consequent strong polarization of the electric field, it is found that the data quality in the two measuring directions (north-south and east-west) can be very different, and thus the rotation would combine low- and high-quality data leading to a degradation of the "best" data.

Figure 4 shows examples of unrotated apparent resistivities and phases with the associated 68% confidence limits from the profile OULU I (stations 3, 8, 13 and 15 produced no useful data). Examination of the data shows that the profile can be split into three distinct sections. Stations 1 and 2 in the northeastern part have an apparent resistivity about two orders of magnitude greater than those of the central stations. The apparent resistivity at these stations

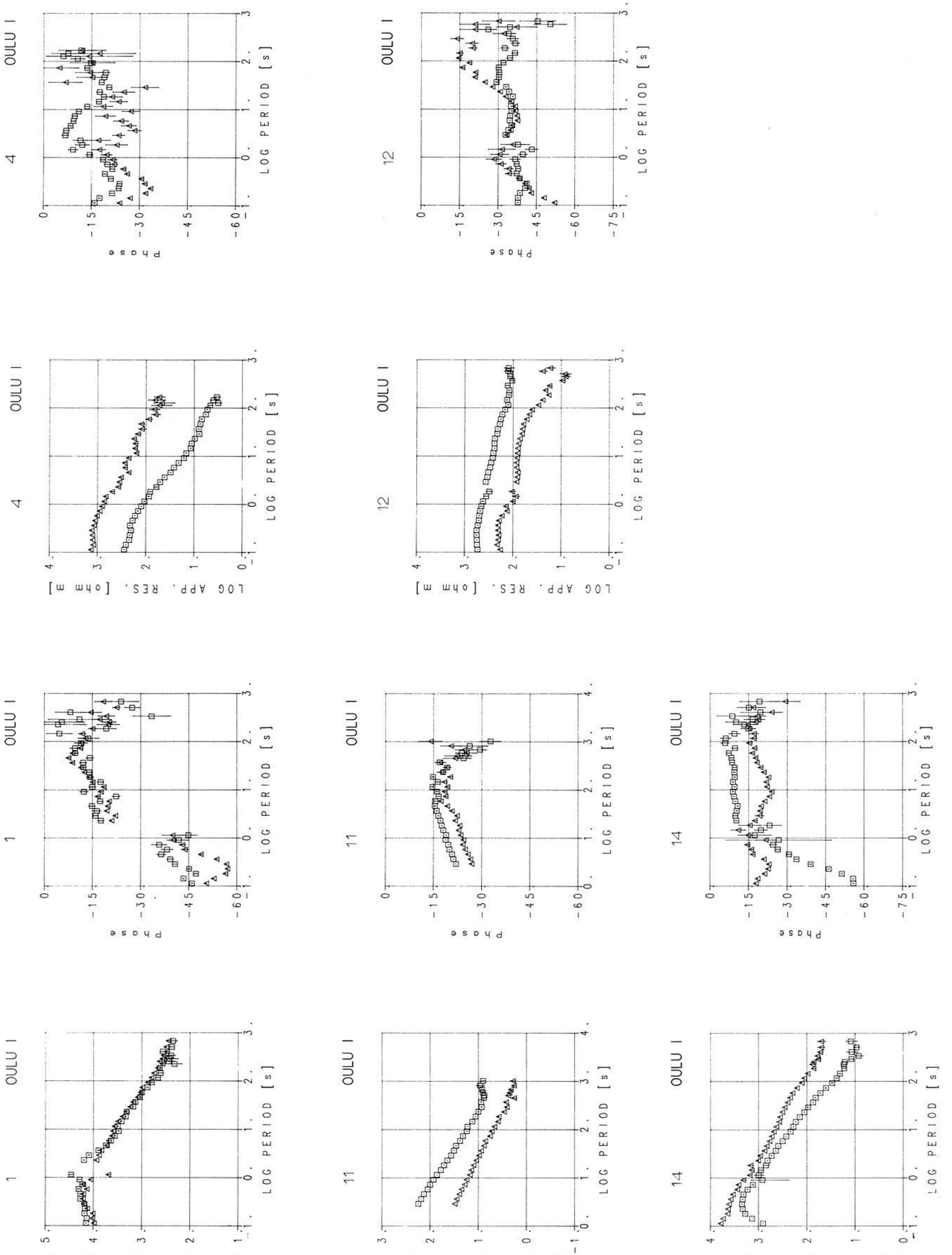

Fig. 4. Apparent resistivity and phase curves from profiles OULU I and OULU II. *Squares* represent measured data curves in NS direction (telluric line direction – *E*-polarization) and *triangles* in EW direction (*H*-polarization). *Vertical bars* show the 68% confidence limits. Apparent resistivity values and periods are presented in logarithmic scale

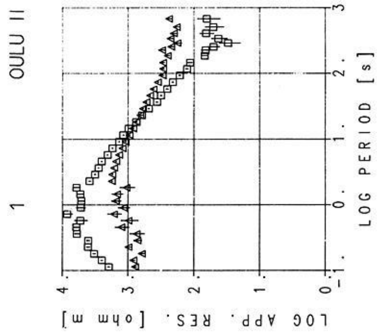
1
OULU II
LOG APP. RES. [ohm m]
4
3
2
1
0
LOG PERIOD [s]
-1
0
1
2
3

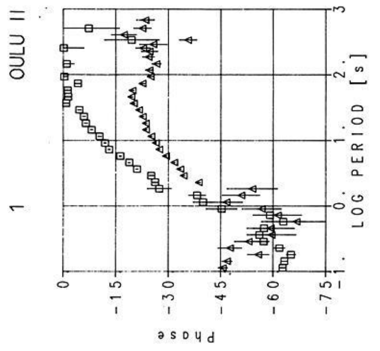
1
OULU II
Phase
0
-15
-30
-45
-60
-75
LOG PERIOD [s]
-1
0
1
2
3

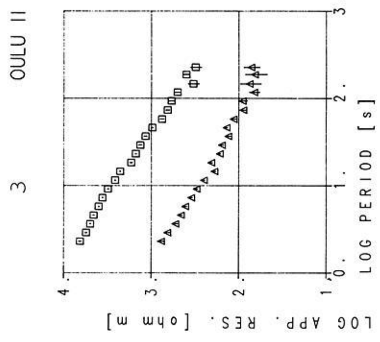
3
OULU II
LOG APP. RES. [ohm m]
4
3
2
1
LOG PERIOD [s]
0
1
2
3

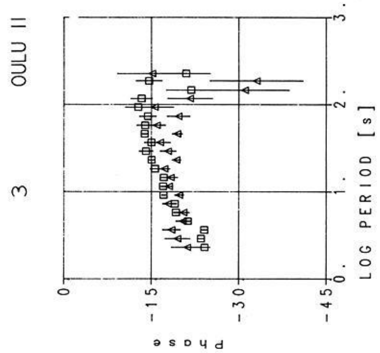
3
OULU II
Phase
0
-15
-30
-45
LOG PERIOD [s]
0
1
2
3

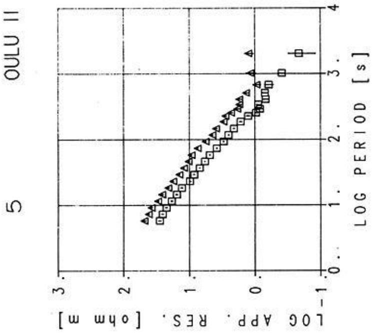
5
OULU II
LOG APP. RES. [ohm m]
3
2
1
0
-1
LOG PERIOD [s]
0
1
2
3
4

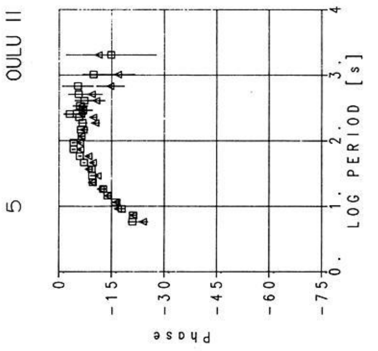
5
OULU II
Phase
0
-15
-30
-45
-60
-75
LOG PERIOD [s]
0
1
2
3
4

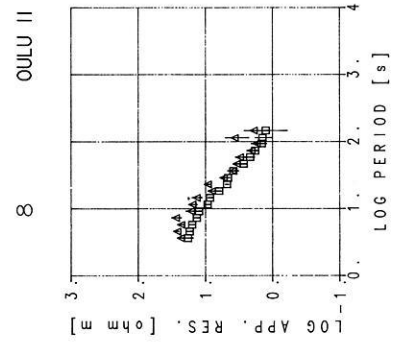
8
OULU II
LOG APP. RES. [ohm m]
3
2
1
0
-1
LOG PERIOD [s]
0
1
2
3
4

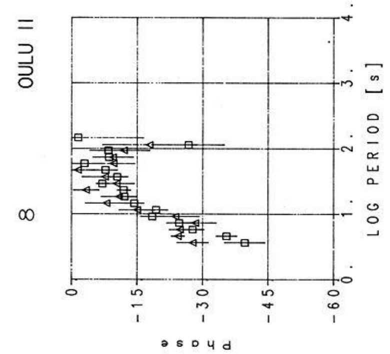
8
OULU II
Phase
0
-15
-30
-45
-60
LOG PERIOD [s]
0
1
2
3
4

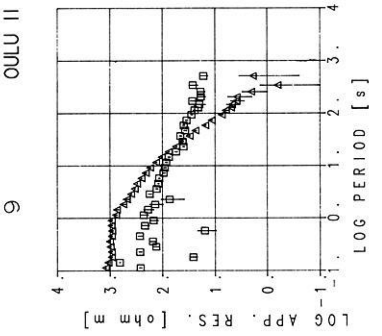
9
OULU II
LOG APP. RES. [ohm m]
4
3
2
1
0
-1
LOG PERIOD [s]
-1
0
1
2
3
4

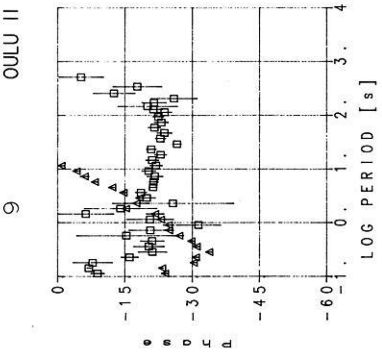
9
OULU II
Phase
0
-15
-30
-45
-60
LOG PERIOD [s]
-1
0
1
2
3
4

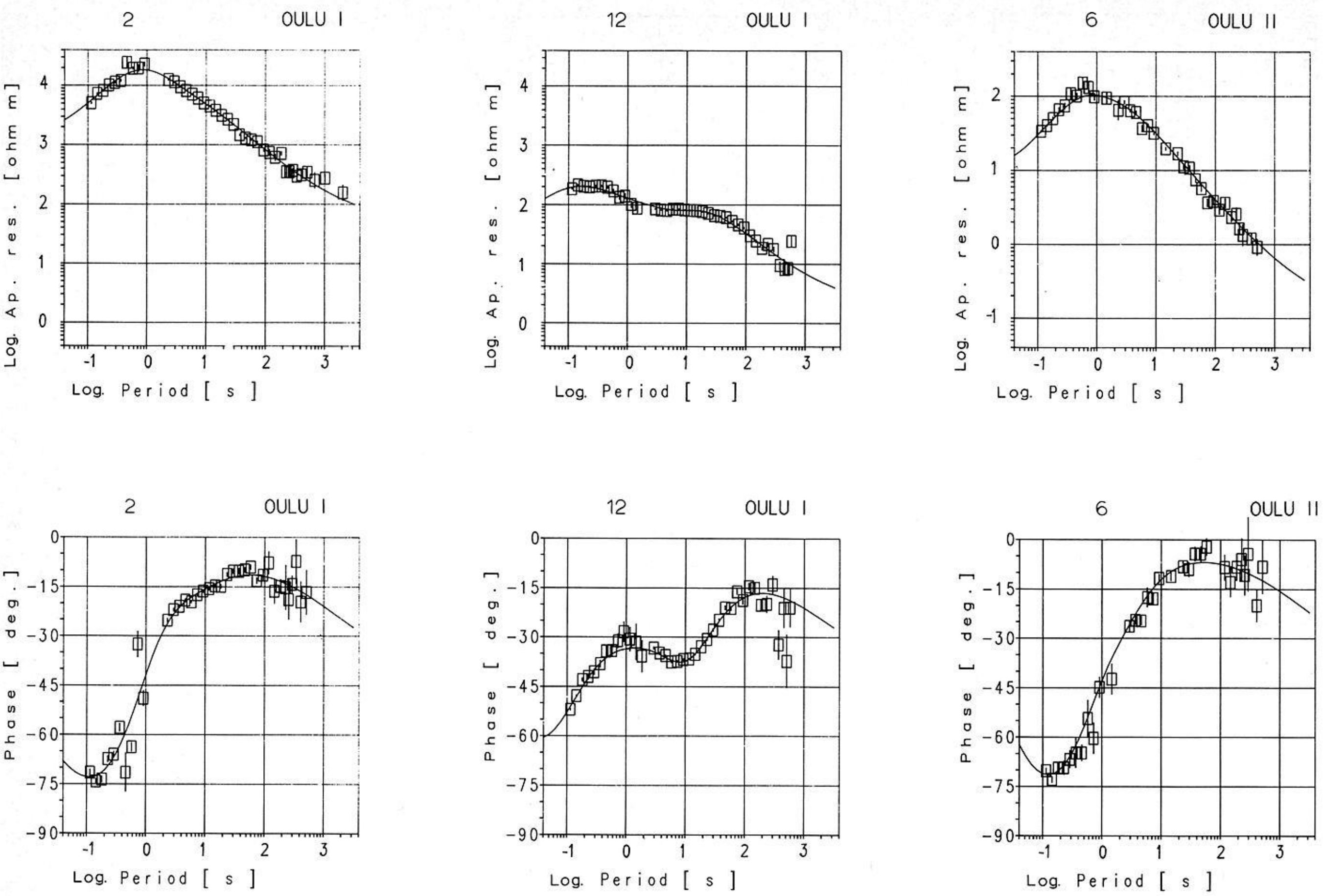

Fig. 5. Apparent resistivity and phase curves and corresponding 1D-fitting curves from MT sites 2/OULU I, 12/OULU I and 6/OULU II. *Squares* represent measured EW data (telluric line direction = EW, *H*-polarization) and *solid line* best fitting the data. Corresponding models are shown in Fig. 6. *Vertical bars* show the 68% confidence limits. Apparent resistivity values and periods are presented in logarithmic scale

(from 4 to 12) is similar, both in magnitude and frequency dependence. The phase shows some differences from site to site. The apparent resistivity at station 14, at the south-western end of the profile, is one order of magnitude greater than at the central stations.

The data along profile OULU II shows similar behaviour to that along profile OULU I. Stations 1 and 3 and station 9, at either end of the profile, were resistive compared to the central stations (5–8) (stations 2 and 4 produced no useful data). The east-west component at station 9 is anomalous in both amplitude and phase especially at periods 1 s and longer. The apparent resistivity changes too rapidly with frequency to be consistent with induction in a "one-dimensional" Earth by a uniform inducing field. The phase (over 90°) is also inconsistent with "one-dimensional" induction. As the data is of high quality, this is presumably a manifestation of two- or three-dimensionality within the Earth. In some sites on both profiles the so-called static shift or parallel shift phenomena in apparent resistivity curves due to the horizontal and vertical current gathering in three-dimensional resistivity heterogenities (Park, 1985) can be seen. For instance, the shape of the apparent resistivity curve of site 8 on profile OULU II is similar to those of sites 5, 6 and 7 but the curve is sifted downwards, which means that site 8 is closer to an edge of the conductive body. Also, when comparing the EW apparent resistivity curve of 1/OULU II and 3/OULU II, it can be seen that at the longer periods (over 1 s) 3/OULU II is shifted downwards due to the fact that it is closer to the conductive zone under sites 5, 6, 7 and 8/OULU II.

One-dimensional modelling of the MT data

One-dimensional inversion, by using the program of Johanssen (1977), was undertaken for all stations on both measuring directions (north-south and east-west). Figure 5 shows some examples of the data fit in EW direction, i.e. in *H*-polarization. In most cases a one-dimensional model can give us quite a reasonable fit to the data. It indicates that to some extent the measuring area can be approximated by a one-dimensional model; at least it can give us some general ideas about the geoelectric structure in the area. Figure 6 shows the results of 1D inversion of the east-west apparent resistivity and phase (*H*-polarization) for all sites along both profiles. The *H*-polarization was chosen, instead of *E*-polarization, on a conductive zone mainly because at some sites we had rather poor data in *E*-polarization (not shown on Fig. 4).

From these one-dimensional "cross-sections" we can clearly see that on both profiles there exists a highly conducting layer in the middle part of the profiles. The depth to the conducting layer is about 7 km for profile OULU I

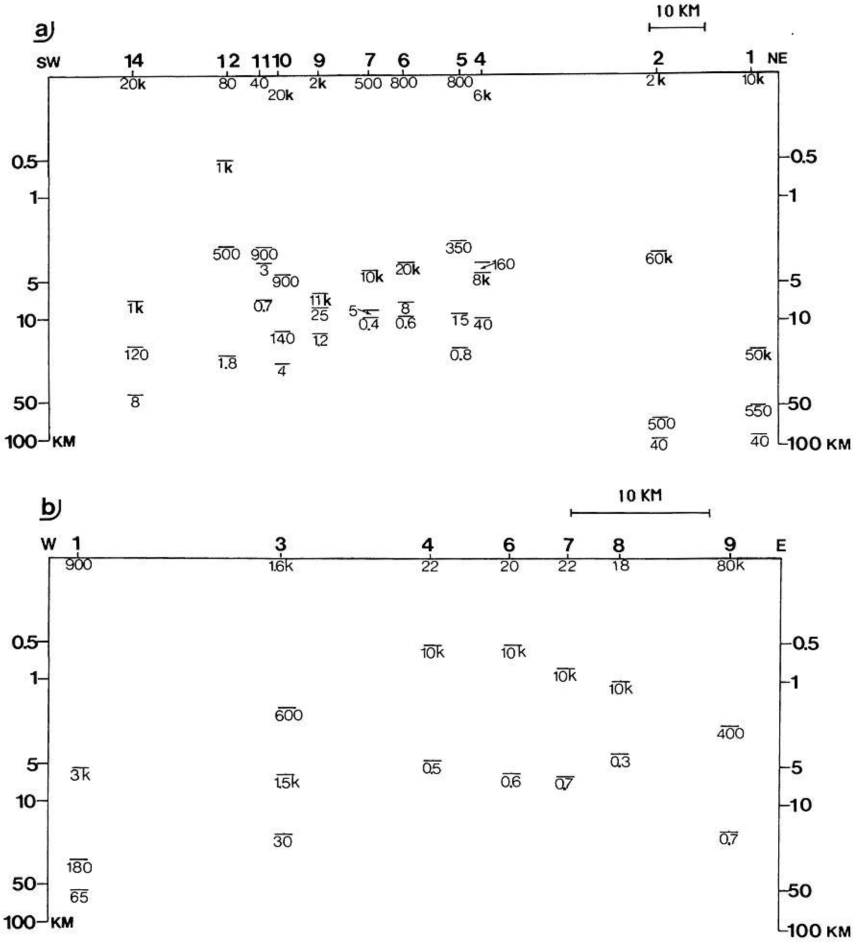

Fig. 6a and b. Geoelectrical cross-section obtained from the 1D modelling of the data measured in EW direction (H-polarization). **a** the cross-section from OULU I and **b** from OULU II. *Numbers* denote the resistivity value of the corresponding layer in ohm m ($k=10^3$)

and about 4 km for profile OULU II. The difference in depths is quite clear and, according to the SVD analysis, h_2 is really the best resolved parameter (A.G. Jones, personal communication). The different structure features, when comparing central parts with SW part of both profiles, indicate that there is a geoelectric boundary between the central and the SW parts. However, due to insufficient data we cannot locate the exact position of this boundary. On the contrary, a very clear geoelectric boundary was found on profile OULU I between sites 2 and 4. The SW part of the profile OULU I is generally more conductive than the NE part where no crustal conducting layer was identified, at least down to 100 km. On profile OULU II (at sites 5–8) the Muhos formation can be clearly identified. The resistivity value (20 ohm m) is of the same order as was found from borehole measurements, but the thickness of sediments ($\sim$400 m) is less than that from the borehole (950 m). This contradiction could be due to the lack of resolution of the parameters of the surface layer. According to the SVD analysis, h_1 is not well-resolvable (A.G. Jones, personal communication).

Two dimensional modelling of the MT data

On the basis of the one-dimensional inversion, a two-dimensional model was constructed for profile OULU I with north-south as a geoelectric structure direction. Modelling was performed using the program of Brewitt-Taylor and Weaver (1976). Figure 7 shows the data and response from profile 1 at two selected periods, 100 s and 10 s, for both E- and H-polarization. The final two-dimensional model is shown in Figure 8. At some stations it was impossible to obtain a good fit to the data (especially to the phase). This may be due to the presence of three-dimensional structure within the Earth. While such three-dimensional effects clearly have some significance to the inversion and modelling procedures, we believe that the models presented here are a valid first approximation. This two-dimensional model also presents a conducting zone at a depth of 7 km to the east and 14 km to the west with a conductivity less than 5 ohm m (even 0.5 ohm m at its central part). Both depths, i.e. depths to the upper surface of the conductive zone, appear well resolved. It is not possible to decide how far southwest this layer extends but by the data from station 14 (OULU I) we can suppose that this site is beyond the conductive zone (or the most conductive zone) or close to its edge. The northeast part of profile 1 is on a very resistive area; down to about 100 km we are still unable to find any conducting layer. Towards the southwest the lower crust becomes quite conductive but, due to the "skin-depth effect", we cannot get more detailed information about the deeper structure. In this case the two-dimensional model in the southwest part below 30 km is very uncertain.

As seen in Fig. 3b the MV anomaly axis agrees with the MT model, although the MT model is very wide. As discussed above, the anomaly determined from MV is strongly frequency dependent. At 500 s the strongest current concentration is clearly in the western part of the MT

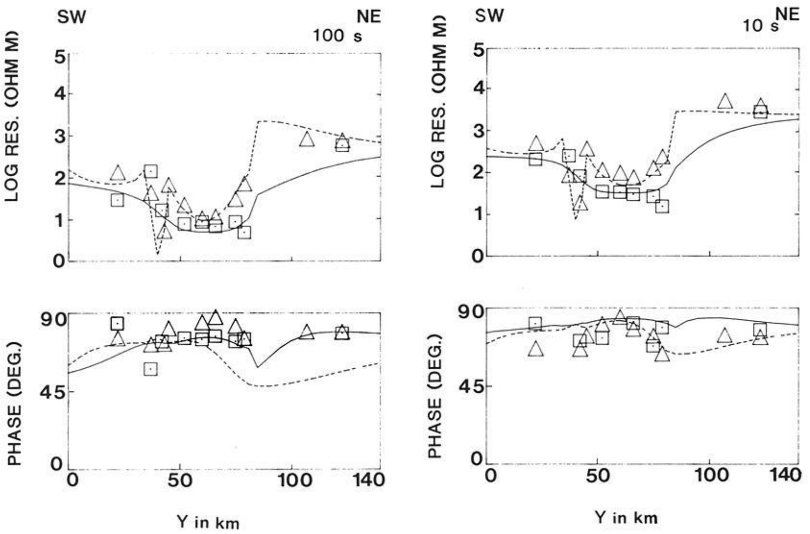

Fig. 7. The 2D model data fitted to measured data along profile OULU I. *Squares* represent the data measured in NS direction, *triangles* in EW direction, the *solid line* represents the model response in NS direction (*E*-polarization) and *dashed line* in EW direction (*H*-polarization). Both apparent resistivity and phase curves are shown at two periods, 10 s and 100 s

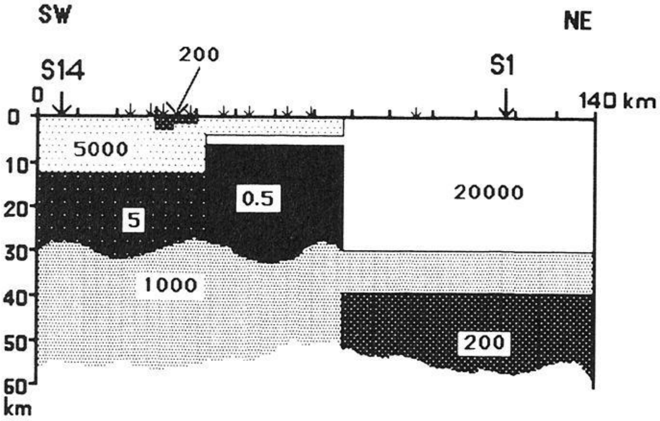

Fig. 8. The final 2D model from OULU I. The model corresponds to the data fit shown in Fig. 6. *Numbers* are the resistivities in ohm m

model. However, at 100 s both methods give about the same northeastern border for the anomaly. The MT method does not give any variations inside the conductive block.

Discussion

In this paper we have presented results from an electromagnetic study over the Oulu conductivity anomaly. The anomaly was located by MV measurements and thereafter studied by MT to obtain depths and conductivities. The anomalous body, with a very low resistivity of 0.5 ohm m, was found at a depth of 4–7 km. The thickness of the body proved to be unresolvable. To the west of the anomaly there was found to be a low-resistive crustal layer from a depth of 14 km probably down to 25–30 km. In the eastern part, no conductive crustal layer seems to exist.

A heat flow measurement from the borehole of Liminka (Järvimäki and Puranen, 1979) gave a heat flow value of 43.8 m W/m^2. No glacial corrections have been performed for these values. According to Parasnis (1975), a glacial correction increased a heat flow value by 10%–20% in Sweden, which would also apply in Finland. The borehole lies 5 km north of MT sites 5 and 6 on the Muhos formation. Using this heat flow value, the 2D model of profile OULU I and the procedure described by Shankland and Ander (1983), data were transformed into log (conductivity) versus 1/temperature scale. Data from low-conductivity layers are in good agreement with the data from LCLs (low conductivity layers) of stable zones (Shankland and Ander, 1983, Fig. 6), while logσ versus 1/T values from those very conductive layers (0.5 and 5 ohm m) are anomalous – they stand even above the limit of "wet" granite with 1%–2% water. If the 10%–20% glacial correction is taken into account, it increases temperature and decreases 1/T which means that logσ versus 1/T values from 0.5 and 5 ohm m layers come closer to the limit of "wet" granite.

The liquids in the porous rocks have been mentioned as possible highly conducting material in the upper crust, for example on the Skellefte field in northern Sweden (Pedersen et al., 1985). In the Oulu anomaly the liquids could originate from the mantle during tectonic movements when the Svecofennian crust overthrusted the Archean realm. On the other hand, the superdeep well at Kola in the Soviet Union has revealed a zone of hydraulic disaggregation of metamorphic rock accompanied by microfracturing at a depth of 4,500–9,000 m (Kozlovsky, 1984). In that zone, numerous flows of highly mineralized water, "water of crystallization", were found. This kind of thick Archean brine zone could also help in explaining the origin of the Oulu anomaly, although, at least in the western part, the thickness of the conductive body seems to be much larger than the "water zone" in Kola. Also, as stated above, to explain this anomaly by free water in rocks (assuming rocks to be granites) the water content must be very large. If the same situation, that free water increases conductivity, is also valid for other rocks, the anomaly could be explained by more conductive rocks than granite added to the effect of fluids in rocks. The lack of the conducting material in the uppermost few kilometres could be explained by the younger igneous rocks above the thrust zone.

Acknowledgements. This work was performed under the research projects "Deep EM research in Finland" (055), "The deep geoelectric model of the Baltic Shield" (111) and "Geoelectrical studies of the crust and upper mantle in the Baltic Shield" (04/111) all financed by the Academy of Finland with additional support from the University of Oulu and the University of Uppsala. The authors wish to return many thanks to Prof. S.E. Hjelt, the leader of the project, for the support and advice along the course of this work as well as to Prof. L.B. Pedersen for much advice and for the loan of the MT stations. The magnetometers were on loan from the University of Münster with the kind help of Prof. Untiedt. Dr. Alan Jones gave us useful comments and very kind help in SVD analysis. Our best thanks to him. The authors are also very grateful to Dr. R.G. Roberts, T. Rasmussen, K. Koivukoski, P. Kääntee, J. Heikka and H. Juntti for help during the field work and for useful discussions. Thanks to Prof. K. Laajoki and Lic. T. Pernu are also deserved for their useful comments and discussions.

References

Berthelsen, A.: The tectonic division of the Baltic Shield. Proceedings of the First Workshop on the European Geotraverse (EGT), the Northern Segment. European Science Foundation, 13–22, 1984

Brewitt-Taylor, C.R., Weaver, T.J.: On the finite difference solution of two dimensional induction problems. Geophys. J.R. Astron. Soc. **47**, 375–396, 1976

Fowler, D.F., Kotick, B.J., Elliott, R.D.: Polarization analysis of natural and artifically induced geomagnetic micropulsations. J. Geophys. Res. **12**, 2871–2883, 1967

Gamble, T.D., Goubau, W.M., Clarke, J.: Magnetotellurics with a remote magnetic reference. Geophysics **44**, 53–68, 1979

Hjelt, S.E., Kaikkonen, P., Pajunpää, K., Korja, T., Heikka, J.: Electromagnetic studies of the Baltic Shield in Finland. Ann. Geophys. 1985 (in press)

Jepsen, J.B., Pedersen, L.B.: Evaluation of tensor AMT measurement system. Laboratory of Geophysics, Aarhus Univ. Geoskrifter **15**, 1981

Johanssen, H.K.: A man/computer interpretation system for resistivity soundings over a horizontally stratified Earth. Geophys. Prosp. **25**, 667–691, 1977

Jones, A.G.: Geomagnetic induction studies in Scandinavia II. Geomagnetic depth sounding, induction vectors and coast-effect. J. Geophys. **50**, 23–36, 1981

Jones, A.G., Olafsdottir, B., Tiikkainen, J.: Geomagnetic induction studies in Scandinavia III. Magnetotelluric observations. J. Geophys. **54**, 35–50, 1983

Järvimäki, P., Puranen, M.: Heat flow measurements in Finland. In: Terrestial heat flow in Europe, V. Cermak and L. Rybach, eds.: pp , Berlin Heidelberg New York, Springer-Verlag 1979

Kozlovsky, Ye.A.: The world's deepest well. Scientific American, December 1984, 106–112, 1984

Küppers, F., Post, H.: A second generation Gough-Reitzel magnetometer. J. Geomagn. Geoelectr. **33**, 225–237, 1981

Küppers, F., Untiedt, J., Baumjohann, W., Lange, K., Jones, A.G.: A two-dimensional magnetometer array for ground-based observations of auroral zone electric currents during the International Magnetospheric Study (IMS). J. Geophys. **46**, 429–450, 1979

Laajoki, K.: The main tectonic features of the Baltic Shield in Finland. In: The development of the deep geoelectric model of the Baltic Shield, Part 2. Proceedings of the 1st project symposium, Oulu 15–18 November 1983, S.E. Hjelt, ed.: pp. 233–244. Dept. of Geophysics, Univ. of Oulu, Report No. 8., 1984

Lange, K.: Inductionseffekte in Nordskandinavien – untersucht am Beispiel zweier ostwärts fliessender polarer Elektrojets. Dipl. thesis, Universität zu Münster, 160 pp, 1979

Pajunpää, K.: Magnetometer array studies in Finland – determination of single station transfer functions. J. Geophys. **55**, 153–160, 1984

Pajunpää, K., Heikka, J., Korja, T.: Magnetometer array studies in Finland. J. Geomagn. Geoelectr. **35**, 543–553, 1983

Parasnis, D.S.: Temperature phenomena and heat flow estimates in two Precambrian ore-bearing areas in North Sweden. Geophys. J.R. Astron. Soc. **43**, 531–554, 1975

Park, S.K.: Distortion of magnetotelluric sounding curves by three dimensional structures. Geophysics **50**, 785–797, 1985

Pedersen, L.B., Svennekjär, M.: Extremal bias coupling in magnetotellurics. Geophysics **49**, 1984

Pedersen, L.B., Rasmussen, T., Roberts, R.G., Zhang, P.: Remote reference magnetotellurics at Uppsala University. Paper presented at the XV Scandinavian Geophysicist Meeting (NOFTIG), Espoo, Finland, 15–17 January 1985

Pernu, T.: Studying of soil and bedrock structures with DC-resistivity measurements especially in Finnish conditions (in Finnish). Lis. thesis, Univ. of Oulu, 99 pp. 1979

Roberts, R., Zhang, P., Pedersen, L.B.: Remote reference magnetotelluric measurements (0.1–10 s) across the mylonite shear zone in southern Sweden. In: The development of the deep geoelectric model of the Baltic shield, Part 2. Proceedings of the 1st symposium of project no. 13 between the Academy of Finland and the Soviet Academy of Sciences, Oulu, 15–18 November 1983, S.E. Hjelt, ed.: pp. 328–339, Dept. of Geophysics, Univ. of Oulu, Report no. 8, 1984

Rokityansky, I.I.: Geoelectromagnetic investigation of the Earth's crust and mantle. New York: Springer-Verlag 1982

Shankland, T.J., Ander, M.E.: Electrical inductivity, temperatures and fluids in the lower crust. J. Geophys. Res. **88**, 9475–9484, 1983

Simonen, A.: Precambrian in Finland. Geological Survey of Finland, Bull. **304**, 1980

Received April 22, 1985; Revised version September 9, 1985
Accepted September 9, 1985

J Geophys (1986) 59:42–48

Journal of Geophysics

Glacio-isostatic adjustment in Fennoscandia revisited

Detlef Wolf*
Department of Physics, University of Toronto, Toronto, Ontario, Canada, M5S 1A7

Abstract. The theory of load-induced relaxation of the layered Maxwell half-space is applied to the study of glacio-isostatic adjustment in Fennoscandia. The interpretation uses emergence data from Ångermanland (Sweden) and uplift-rate data from the Gulf of Bothnia. With mantle viscosity fixed at 10^{21} Pa s, the data can be explained by an earth model characterized by (a) an elastic surface layer of conventional thickness (about 100 km) superimposed on a low-viscosity layer or (b) an elastic surface layer of enhanced thickness (about 200 km) and no low-viscosity layer. Reasons for this ambiguity and possible ways to resolve it in future studies are suggested. The investigation also attempts to interpret the negative free-air gravity anomaly observed over the deglaciated region of Fennoscandia. Either (i) enhanced mantle viscosity below 670 km depth or (ii) a transition zone in viscosity between an elastic surface layer and a viscous mantle is required to predict negative anomalies substantially larger than 3 mgal.

Key words: Fennoscandia – Isostasy – Maxwell continuum

Introduction

More than 50 years ago, Reginald Daly drew attention to post-glacial uplift and discussed two rheological earth models, which he designated "bulge hypothesis" and "punching hypothesis" (Daly, 1934, pp. 120–126).

The bulge hypothesis assumes that flow is restricted to a near-surface layer (channel model). Mass conservation then requires the existence of a substantial peripheral bulge during glaciation. During and after deglaciation, the central depression is elevated to equilibrium while the bulge collapses.

Daly believed that geological evidence in support of a peripheral bulge is missing in Fennoscandia and North America. He therefore suggested that the glacial load had been punched through the elastic crust, forcing flow to great depths (deep-flow model). A distinctive feature of this model is that, with deglaciation, both central and peripheral regions are initially uplifted sympathetically. The later stages of readjustment include crustal failure and a reversal of the upward movement in the periphery (Daly, 1934, Fig. 70).

The following year, Haskell (1935) demonstrated quantitatively that the main features of Daly's punching hypothesis are also produced by a uniform, Newtonian viscous half-space. Haskell also interpreted the Fennoscandian uplift with this model. His estimate of the dynamic mantle viscosity was about 10^{21} Pa s. An essential ingredient of Haskell's analysis was the assumption of a residual depression of 20 m near the glaciation centre, corresponding to a free-air gravity anomaly of approximately -3 mgal.

The question of the causal relation between the observed gravity anomaly and the Pleistocene glaciation in Fennoscandia has been discussed since Haskell's pioneer study (summarized by Cathles, 1975, pp. 151–154; Balling, 1980). The difficulties in interpreting the gravity field are related to the fact that, although negative anomalies predominate in Fennoscandia, the gravity pattern is irregular. In particular, there is no pronounced correlation with the topography of the Pleistocene ice-sheet. Therefore, differing values for the remaining uplift can be inferred from the free-air gravity data.

Niskanen (1939), for example, suggested that the deglaciation-induced portion has a peak value of about -30 mgal, giving a residual depression of about 200 m. This led several investigators to dismiss Haskell's deep-flow model and use various kinds of channel model, which produce enhanced residual depressions. The quantitative development of channel models was initiated by van Bemmelen and Berlage (1935) and subsequently extended by many other investigators (summarized by Cathles, 1980; Walcott, 1980). Since there is now evidence for an almost uniformly viscous mantle (Cathles, 1975; Peltier and Andrews, 1976; Wu and Peltier, 1983), channel models have fallen into disrepute.

Recently, Balling (1980) attempted to substantiate previous claims of more moderate deglaciation-induced anomalies (e.g. Walcott, 1973). After filtering out a non-glacial component believed to be related to the structure of the earth's crust and upper mantle, Balling inferred a glacial component of about -17 mgal for central Fennoscandia (Fig. 1). This value implies that the positive anomalies in the peripheral region reflect a superimposed long-wavelength geoid high. However, deglaciation-induced anomalies of this order are still substantial and, as Haskell's (1935) and Cathles' (1975) work shows, incompatible with simple deep-flow models.

A possible way out of this impasse was proposed by Anderson (1984). Using statistical analysis, he suggested

---

* *Present address:* Division of Gravity, Geothermics and Geodynamics, Earth Physics Branch, Energy, Mines and Resources Canada, Ottawa, Ontario, Canada, K1A 0Y3

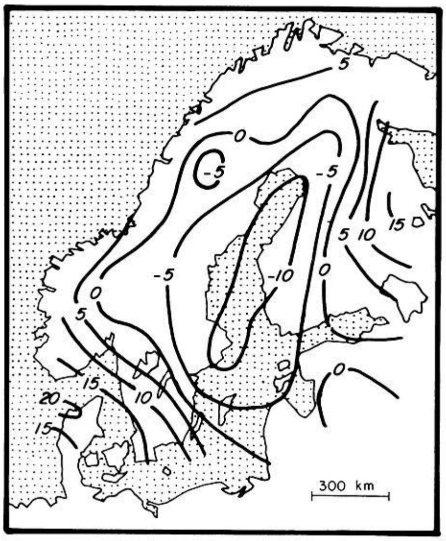

Fig. 1. Glacial component of free-air gravity anomaly in Fennoscandia (in units of mgal; after Balling, 1980)

that the observed geoid low over Fennoscandia is caused predominantly by an approximately twofold increase in crustal thickness from the Norwegian Sea and northern Germany toward central Fennoscandia. Anderson therefore concluded that contributions to the geoid anomaly associated with crustal structure are much more substantial than generally assumed. If this is true, the glacial component of the gravity anomaly must be quite small and can be easily explained with simple deep-flow models.

An alternative way to reconcile gravity observations with gravity predictions was discussed by Peltier and Wu (1982). Using Maxwell earth models, of essentially uniform viscosity and with the same density and elastic structure as seismic earth model 1066B (Gilbert and Dziewonski, 1975), Peltier and Wu predicted free-air gravity anomalies of about −20 mgal for Fennoscandia. The increase in magnitude was largely a consequence of treating the entire density structure of model 1066B as non-adiabatic.

It has also been suggested that an elastic surface layer (lithosphere) is actively involved in the isostatic adjustment process in Fennoscandia. One of the modern investigators who devoted explicit attention to the lithosphere was McConnell (1968), who interpreted relaxation-time estimates from a spectral decomposition of strandline data from Fennoscandia. He used a layered, Newtonian viscous half-space model and proposed a lithospheric thickness of 120 km.

Cathles' study of glacio-isostatic adjustment was biased by his idea that the Fennoscandian uplift is insensitive to the presence of the lithosphere (Cathles, 1975, p. 153). In his flat-earth analysis, he arbitarily adopted a lithosphere of about 70 km thickness (Cathles, 1975, pp. 184–191). Recent results (Wolf, 1984, 1985a) showed that this is probably a misconception.

In the light of these inconsistencies, the present study re-interprets glacio-isostatic adjustment in Fennoscandia, based on the theory of the layered, incompressible Maxwell halfspace. The complex Fennoscandian deglaciation history is simulated by several simplified models. Particular attention is paid to the question of lithospheric thickness. The results will show that, although the adjustment data used are compatible with a lithosphere of about 200 km thickness below Fennoscandia, the data *cannot* be construed to require this value.

Further, the seismic discontinuity at 670 km depth is discussed in relation to the free-air gravity anomaly over Fennoscandia. According to the preliminary reference earth model (PREM; Dziewonski and Anderson, 1981), this discontinuity is characterized by a density increase of 390 kg m^{-3}, which is treated as non-adiabatic in the present study. Although the gravity predictions are largely insensitive to this density contrast, results will show that they are very sensitive to the value adopted for the viscosity below 670 km depth. The study also proposes an alternative explanation of the gravity anomaly, suggesting that it is related to the relaxation of a transition zone in viscosity between the elastic surface layer and the mantle.

Theoretical model

The rheological model basic to this interpretation is the layered, incompressible Maxwell half-space. Each of its

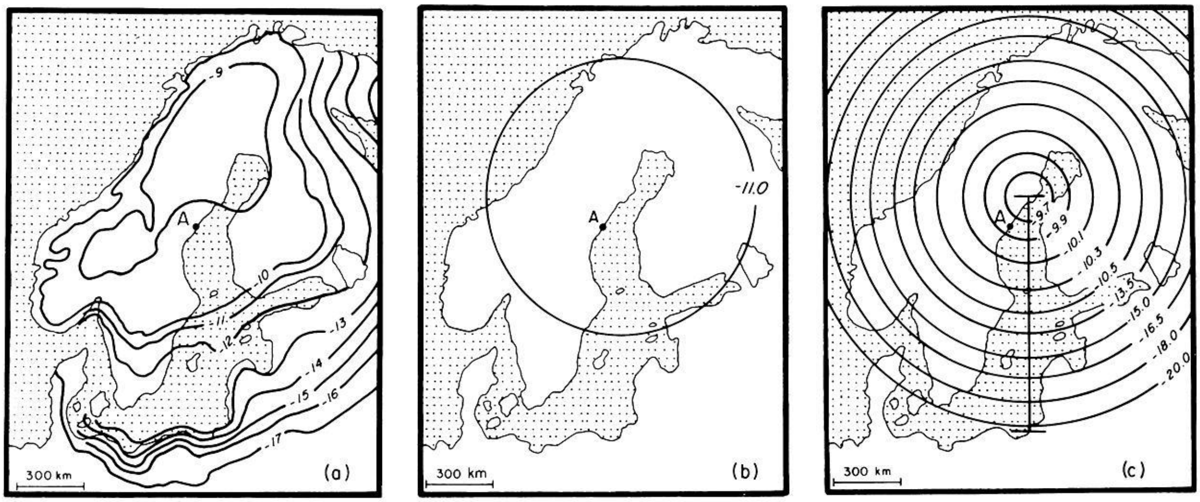

Fig. 2a–c. a Fennoscandian deglaciation isochrons (after De Geer, 1954), **b** load model 1 and **c** load model 2; *A* denotes Ångermanland, *the bar* in **c** illustrates uplift-rate profile, times (in units of ka) are with respect to present time

Table 1. Parameters of load models

Cycle N	t (ka)	R (km)
Load model	1	
	$-\infty$ to -11.0	600
	-11.0 to 0.0	0
Load model	2	
1	-2000.0 to -1900.0	R
2	-1900.0 to -1800.0	R
.	. .	.
.	. .	.
.	. .	.
19	-200.0 to -100.0	R
20	-100.0 to -80.0	200
	-80.0 to -60.0	400
	-60.0 to -40.0	600
	-40.0 to -20.0	800
	-20.0 to -18.0	1000
	-18.0 to -16.5	900
	-16.5 to -15.0	800
	-15.0 to -13.5	700
	-13.5 to -10.5	600
	-10.5 to -10.3	500
	-10.3 to -10.1	400
	-10.1 to -9.9	300
	-9.9 to -9.7	200
	-9.7 to -9.5	100
	-9.5 to 0.0	0

Table 2. Parameters of earth models

Layer l	h_l (km)	ρ_l (kg m^{-3})	μ_l (N m^{-2})	η_l(Pa s)
Earth model A.1				
1	100.0	3380	0.67×10^{11}	∞
2	100.0	3380	1.45×10^{11}	η_2
3	∞	3380	1.45×10^{11}	1.0×10^{21}
Earth model L.1				
1	h_1	3380	0.67×10^{11}	∞
2	∞	3380	1.45×10^{11}	1.0×10^{21}
Earth model L.4				
1	142.0	3380	0.67×10^{11}	∞
2	19.5	3380	0.67×10^{11}	1.0×10^{25}
3	24.1	3380	0.67×10^{11}	1.0×10^{23}
4	∞	3380	1.45×10^{11}	1.0×10^{21}
Earth model L.5				
1	93.7	3380	0.67×10^{11}	∞
2	28.7	3380	0.67×10^{11}	1.0×10^{25}
3	44.6	3380	0.67×10^{11}	1.0×10^{23}
4	∞	3380	1.45×10^{11}	1.0×10^{21}
Earth model M.4				
1	h_1	3380	0.67×10^{11}	∞
2	670.0-h_1	3380	1.45×10^{11}	1.0×10^{21}
3	∞	ρ_3	1.45×10^{11}	η_3

layers is characterized by four parameters: thickness h, density ρ, rigidity μ and viscosity η. The response of this model to surface loads was analysed and discussed previously (Wolf, 1985a).

The glaciation of Fennoscandia (Fig. 2a) is modelled as a Heaviside unloading event at 11 ka B.P. (Fig. 2b, Table 1, load model 1) and as a stepwise-discontinuous loading history (Fig. 2c, Table 1, load model 2). Load model 1 is the first approximation. It simulates the fast decay of the Fennoscandian ice-sheet following a period of stagnation between 12 and 10 ka B.P. Load model 2 is more realistic, although several important features of the Fennoscandian glaciation are unknown, for example, the extent of the ice-sheet in the shelf regions of the Norwegian and Barents Seas. However, the location of the uplift site employed in this study in Ångermanland (Sweden) (Fig. 2) is very close to the Pleistocene glaciation centre and therefore largely insensitive to complications near the ice margin.

Load model 1 can only be used with earth models that have short relaxation times (Table 2, earth models A.1 and L.1). For simplicity, the cross-section of load model 1 is assumed to be rectangular and the load thickness to be a free parameter. For the same earth models, load cycle 20 of load model 2 may also be used. This cycle uses a parabolic cross-section and a fixed ratio h_0^2/R between the square of axial load thickness h_0 and load radius R (details in Paterson, 1981, pp. 154–155; Wolf, 1985b). However, with earth models that support modes of long relaxation times (Table 2, earth models L.4, L.5 and M.4), the long-term glaciation history can no longer be neglected [see Imbrie and Imbrie (1979, pp. 153–173) on the time sequence of glaciations during the Pleistocene]. This is taken into account by load model 2, where load cycle 20 is preceded by 19 similar load cycles. For computational ease, the cross-section of the load is assumed to be rectangular and the load radius to be fixed during load cycles 1–19. During each of these cycles the load thickness increases according to $h_0(t-t_N)/(t_{N+1}-t_N)$, where t_N is the beginning of the N-th load cycle and $t_N<t<t_{N+1}$. The maximum thickness h_0 reached at the end of each cycle is determined by the ratio h_0^2/R adopted for load cycle 20. The load density is always assumed to be 1000 kg m^{-3}.

Data analysis and discussion

The emergence data from Ångermanland are of prime importance to this interpretation. The data set is based on a series of raised beaches, whose ages are constrained by varve sequences. The data were originally published by Lidén (1938), but can also be found elsewhere (e.g. Lliboutry, 1971; Cathles, 1975, p. 196). Since the dating of the strandlines is based on varve chronology, the relative ages of the Ångermanland strandline series are very accurate.

The observed emergence of a strandline is controlled by uplift of the earth's surface *and* by changes in sea level. Sea-level changes are related to (a) influx of melted ice and (b) geoid perturbations produced by redistribution of water and by simultaneous redistribution of mantle material. Contribution (a) has been named eustatic change. This has a clear meaning only if it is defined as the ocean-wide average change in mean sea level (Walcott, 1972). Contribution (b) depends on location but can become as large as contribution (a) (Farrell and Clark, 1976; Clark et al., 1978; Peltier et al., 1978).

Near major glaciation centres, sea-level changes have been small compared with surface uplift after about 10 ka B.P. Before that, the lowering of eustatic sea level was partially counterbalanced by the rise of the geoid below the melting ice mass (Wu and Peltier, 1983, Fig. 4a). The portion of the emergence of old strandlines caused by uplift of the earth's surface may therefore be approximately bracketed by the observed emergence and this emergence corrected for eustatic sea-level rise.

The following uplift diagrams symbolize this range by vertical bars, where corrections for eustatic sea-level change according to Fairbridge (1961, Fig. 8) have been applied. The observed uplift during the time interval $[t,0]$ can now be compared with the predicted uplift $H(t)=w(t)-w(0)$, where w is the (downward) surface displacement for the model under consideration and $t=0$ is present time.

The study of the Fennoscandian uplift begins by using load model 1. The observed uplift in Ångermanland is compared with the theoretical uplift for two distinct earth models, both of which use a mantle viscosity of 10^{21} Pa s.

Figure 3a shows an interpretation similar to that proposed by Cathles (1975, pp. 184–191), with a load thickness of 1.50 km. The earth model uses a lithosphere of *conventional* thickness (100 km) underlain by a low-viscosity layer (asthenosphere) (Table 2, earth model A.1). If the viscosity of the asthenosphere is selected properly, a satisfactory fit of the data is achieved.

Figure 3b proposes an alternative interpretation of the same data set. The load thickness has been increased to 1.90 km, and the Earth model has a lithosphere but no asthenosphere (Table 2, earth model L.1). This time the data are bracketed by the curves for *enhanced* lithospheric thicknesses of 170 km and 230 km.

If the load thickness is further increased, the observations are compatible with even larger lithospheric thicknesses. Conversely, the fit produced in Fig. 3a is a consequence of the reduced load thickness that is used. This behaviour is consistent with results by Wolf (1985a, Figs. 10a and 11a). The ambiguous interpretation is therefore partly a consequence of a trade-off between lithospheric thickness and load thickness.

The next step is to use earth model L.1 with load model 2. For lithospheric thicknesses of about 200 km, this requires $h_0^2/R=4.0\times10^{-3}$ km. As Fig. 4a shows, the fit of the uplift data is similar to that in Fig. 3b. Closer inspection of Fig. 4a reveals, however, that younger beaches are consistent with a lithosphere slightly thinner than 200 km, whereas older beaches are better explained if the lithosphere is somewhat thicker.

Figure 4b shows the observed uplift rates (e.g. Balling, 1980) on a north-south profile in the Gulf of Bothnia (Fig. 2c) as stippled band and the theoretical uplift rates for the same model parameters. The uplift rates are obviously very sensitive to lithospheric thickness. Similarly to Fig. 4a, a thickness of approximately 170 km produces the best fit.

As expected, the theoretical models discussed so far have small free-air gravity anomalies. For the 200 km thick lithosphere, the peak value is approximately -4 mgal, giving a residual depression of about 28 m. If Balling's (1980) filtered anomaly (Fig. 1) represents the deglaciation-induced portion of the gravity field in Fennoscandia, this interpretation appears untenable.

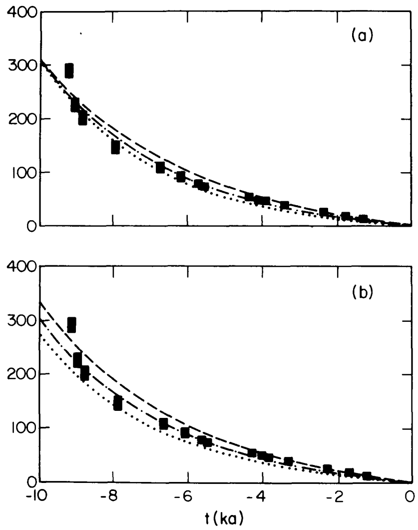

Fig. 3a and b. Ångermanland uplift data (Lidén, 1938) and uplift prediction H as functions of time t; **a** applies to load model 1 with $h_0=1.50$ km and earth model A.1 with $\eta_2=5.0\times10^{19}$ Pa s (*dashed*), $\eta_2=1.5\times10^{19}$ Pa s (*dot-dashed*) or $\eta_2=1.0\times10^{19}$ Pa s (*dotted*); associated free-air gravity prediction at $r=0$, $t=0$ is $\Delta g=-6.1$ mgal (*dashed*), $\Delta g=-3.4$ mgal (*dot-dashed*) or $\Delta g=-2.4$ mgal (*dotted*); **b** applies to load model 1 with $h_0=1.90$ km and earth model L.1 with $h_1=170$ km (*dashed*), $h_1=200$ km (*dot-dashed*) or $h_1=230$ km (*dotted*); associated free-air gravity prediction at $r=0$, $t=0$ is $\Delta g=-5.7$ mgal (*dashed*), $\Delta g=-3.9$ mgal (*dot-dashed*) or $\Delta g=-2.7$ mgal (*dotted*)

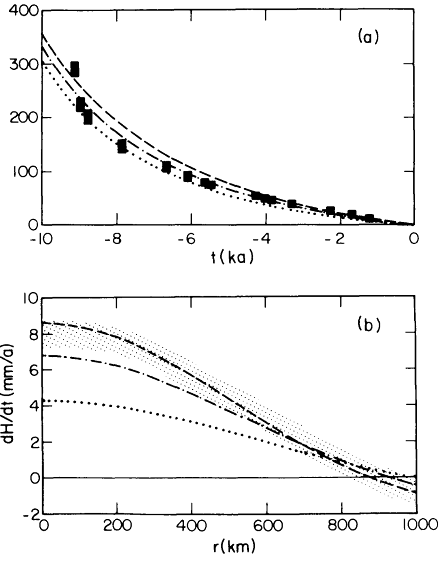

Fig. 4a and b. a Ångermanland uplift data (Lidén, 1938) and uplift prediction H as functions of time t and **b** Gulf of Bothnia uplift-rate data (Balling, 1980) and uplift-rate prediction dH/dt as functions of axial distance r; predictions apply to load model 2 with $h_0^2/R=4.0\times10^{-3}$ km and earth model L.1 with $h_1=170$ km (*dashed*), $h_1=200$ km (*dot-dashed*) or $h_1=230$ km (*dotted*); associated free-air gravity prediction at $r=0$, $t=0$ is $\Delta g=-5.6$ mgal (*dashed*), $\Delta g=-4.0$ mgal (*dot-dashed*) or $\Delta g=-2.8$ mgal (*dotted*)

The study therefore investigates the effects of a contrast in viscosity or density at 670 km depth (Table 2, earth model M.4). The modifications apply to a saw-tooth loading history (Fig. 5) and are shown in Fig. 6. The radius of 1000 km for the rectangular load is selected to represent conditions during the last glacial maximum at about 18 ka B.P. The sensitivity of the response to lower-mantle viscosity is obvious. At time $t=12$ ka, the residual surface depression is increased threefold for a twofold increase in lower-mantle viscosity. The modifications produced by the internal density contrast are much smaller in comparison.

Figure 7 interprets the Ångermanland uplift data using

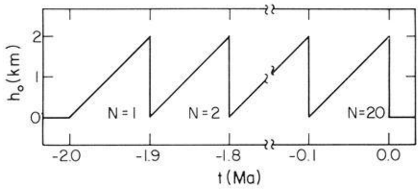

Fig. 5

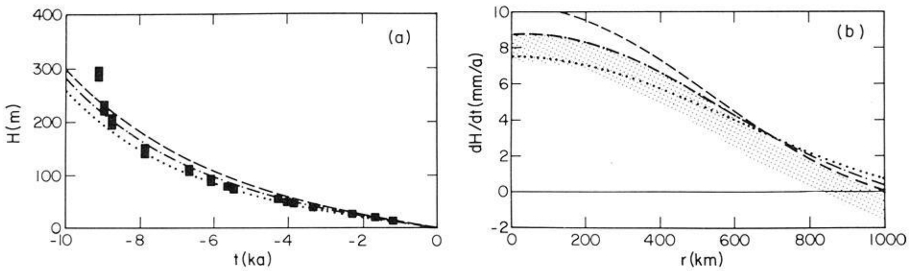

Fig. 7a

b

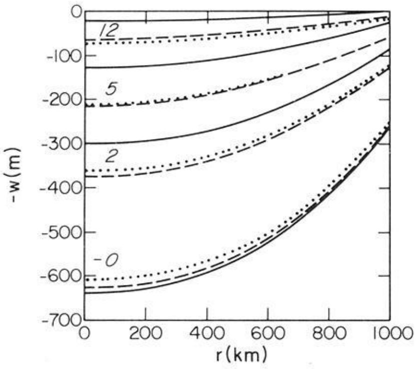

Fig. 6

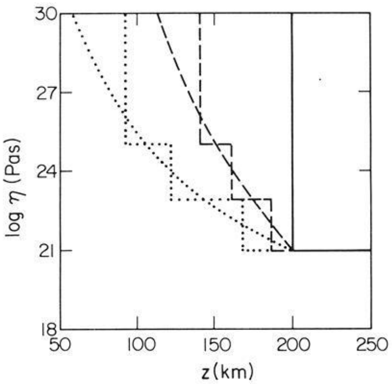

Fig. 8

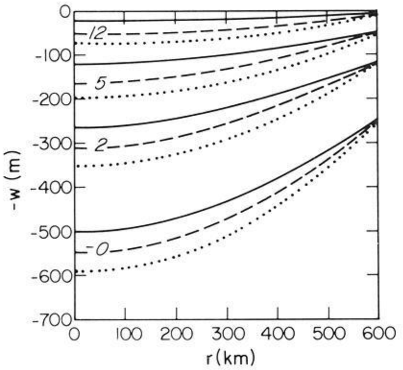

Fig. 9

Fig. 5. Saw-tooth loading history applicable to Figs. 6, 9 and 11

Fig. 6. Vertical surface displacement w as function of axial distance r for several times (in units of ka) after load removal; predictions apply to saw-tooth loading history (Fig. 5) with R = 1000 km and earth model M.4 with $h_1 = 200$ km and $\rho_3 - \rho_2 = 0$, $\eta_3 = 1.0 \times 10^{21}$ Pa s (*solid*), $\rho_3 - \rho_2 = 0$, $\eta_3 = 2.0 \times 10^{21}$ Pa s (*dashed*) or $\rho_3 - \rho_2 = 390$ kg m^{-3}, $\eta_3 = 2.0 \times 10^{21}$ Pa s (*dotted*)

Fig. 7a and b. As for Fig. 4 except that predictions apply to load model 2 with $h_0^2/R = 3.0 \times 10^{-3}$ km and earth model M.4 with $\rho_3 - \rho_2 = 390$ kg m^{-3}, $\eta_3 = 2.0 \times 10^{21}$ Pa s and $h_1 = 170$ km (*dashed*), $h_1 = 200$ km (*dot-dashed*) or $h_1 = 230$ km (*dotted*); associated free-air gravity prediction at $r = 0$, $t = 0$ is $\Delta g = -9.4$ mgal (*dashed*), $\Delta g = -7.7$ mgal (*dot-dashed*) or $\Delta g = -6.4$ mgal (*dotted*)

Fig. 8. Viscosity η as function of depth z for $Q \rightarrow \infty$ (*solid*), $Q = 500$ kJ mol^{-1} (*dashed*) or $Q = 200$ kJ mol^{-1} (*dotted*); continuous functions are approximated by three uniform layers

Fig. 9. As for Fig. 6 except that predictions apply to saw-tooth loading history (Fig. 5) with R = 600 km and earth model L.1 with $h_1 = 200$ km (*solid*), earth model L.4 (*dashed*) or earth model L.5 (*dotted*)

this earth model. Compared with the model used for Fig. 4, the viscosity below 670 km is higher by a factor of two and the density is increased by 390 kg m^{-3} in this depth range. As before, results apply to load model 2. During load cycles 1–19, $R = 1000$ km; during load cycle 20, $h_0^2/R = 3.0 \times 10^{-3}$ km. The reduction in load thickness, compared with Fig. 4, is required to predict the correct present-day uplift rates. The fit of the uplift and uplift-rate data is comparable to Fig. 4, but the theoretical free-air gravity anomaly is enhanced significantly ($\Delta g = -7.7$ mgal for $h_1 = 200$ km).

In order to predict a value near -17 mgal, either additional internal buoyancy or a further increase in lower-mantle viscosity is required. Neither alternative appears practicable, however. Whereas the former hinges on the assumption that each additional density discontinuity is modelled as a non-adiabatic increase, the latter renders a satisfactory fit of the uplift and uplift-rate data increasingly difficult.

An alternative mechanism for enhancing gravity predictions is provided by the introduction of a transition zone in viscosity between the elastic surface layer and the viscous mantle. For example, assuming a linear geotherm which passes through points $T = 0°$ C, $z = 0$ km and $T = 1400°$ C, $z = 200$ km (Jordan, 1981), the temperature distribution can be converted into a viscosity distribution, provided that the viscosity η at depth $z = 200$ km and the activation energy Q in the depth range $0 \leqq z \leqq 200$ km are known (details in Wolf, 1985a).

Figure 8 uses a mantle viscosity of 10^{21} Pa s and shows viscosity-depth distributions for three activation energies. For computational ease, the continuous distributions are approximated by three uniform layers, which constitute the *thermal* lithosphere (Table 2, earth models L.4 and L.5). The portion which responds elastically is called the *mechanical* lithosphere. If the loading time is sufficiently short or if the activation energy is sufficiently high, the "mechanical thickness" approaches the "thermal thickness".

The modifications of the response produced by a transition zone in viscosity are shown in Fig. 9 for earth models L.1, L.4 and L.5. As for Fig. 6, results apply to a saw-tooth loading history (Fig. 5). However, the radius of the rectan-

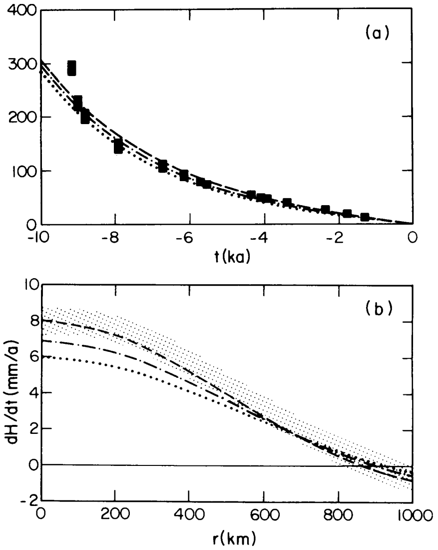

Fig. 10a and b. As for Fig. 4 except that predictions apply to load model 2 with $h_0^2/R = 3.0 \times 10^{-3}$ km and earth model L.5 (*dashed*), earth model L.4 (*dot-dashed*) or earth model L.1 with $h_1 = 200$ km (*dotted*); associated free-air gravity prediction at $r = 0$, $t = 0$ is $\Delta g = -10.9$ mgal (*dashed*), $\Delta g = -7.5$ mgal (*dot-dashed*) or $\Delta g = -3.5$ mgal (*dotted*)

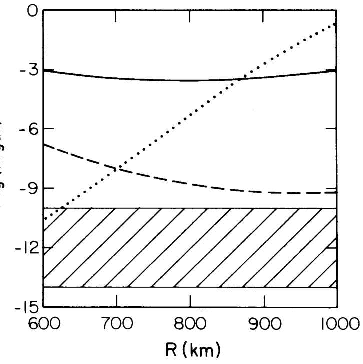

Fig. 11. Free-air gravity prediction Δg at $r = 0$, $t = 12$ ka as function of load radius R; predictions apply to saw-tooth loading history (Fig. 5) and earth model L.1 with $h_1 = 200$ km (*solid*), earth model M.4 with $h_1 = 200$ km, $\rho_3 - \rho_2 = 390$ kg m^{-3} and $\eta_3 = 2.0 \times 10^{21}$ Pa s (*dashed*) or earth model L.5 (*dotted*); *cross-hatched* band indicates glacial component of gravity anomaly (Fig. 1)

gular load is reduced to 600 km. Because of the long relaxation times of the modes supported by the transition zone (Wolf, 1985a, Fig. 7), the initial decay of the excess deformation produced by the cyclic loading is not appreciable. Therefore, predictions of *relative* uplift are nearly unaffected. The *absolute* value of the surface depression at time $t = 12$ ka, and thus the theoretical free-air gravity anomaly, is, however, two- to threefold larger compared with the model without transition zone.

This is substantiated by Fig. 10, which shows uplift and uplift-rate predictions for the same earth models. The theoretical curves apply to load model 2. During load cycles 1–19, $R = 600$ km; during load cycle 20, $h_0^2/R = 3.0 \times 10^{-3}$ km. The fit is optimized for earth model L.5, but, as expected, theoretical uplift proves essentially insensitive to the viscosity stratification of the lithosphere. The opposite holds for free-air gravity. For earth model L.5, peak values of -11 mgal are predicted.

By intuitive reasoning, the importance of lithospheric relaxation is expected to depend on the ratio between load radius and lithospheric thickness. If this ratio is large, the lithosphere is virtually "transparent"; conditions close to local compensation apply, and the response should be insensitive to lithospheric relaxation.

This is illustrated in Fig. 11, which, for the saw-tooth loading history (Fig. 5), shows gravity predictions for rectangular loads of different radii. Comparison of the anomalies for earth models L.1 and L.5 shows that lithospheric relaxation becomes insignificant if the load radius exceeds about 700–800 km [see Wolf (1985a, Fig. 13) for a different example]. Loads of larger radii are, however, sensitive to lower-mantle viscosity and to internal buoyancy associated with the density contrast at 670 km depth, as shown for earth model M.4. For comparison, Fig. 11 also shows filtered peak gravity values according to Balling (1980) (without corrections for the long-wavelength geoid high).

Conclusion

The main conclusion of this study is that uplift data from Ångermanland and uplift-rate data from a profile in the Gulf of Bothnia are insufficient to constrain lithospheric thickness in Fennoscandia. The study has placed special emphasis on earth models with a lithosphere of about 200 km thickness and shown that these models are compatible with the two data sets. In a previous investigation, a lithosphere of about 70 km thickness was adopted, and a comparable fit of the data sets used here was achieved (Cathles, 1975, pp. 184–191).

A characteristic feature of interpretations that use earth models with a thin lithosphere appears to be that an asthenosphere is required below the lithosphere. Various model calculations have shown that the presence of an asthenosphere controls the movement of the zero-crossings separating the downwarped central region from the upwarped peripheral region. If mantle viscosity is uniform, the zero-crossings move inward after deglaciation. The presence of an asthenosphere leads, however, to stationary zero-crossings or even reverses the direction (e.g. Cathles, 1975, Figs. IV-28 and IV-29). At present, opinions differ on the movement of the zero-crossings in Fennoscandia (e.g. Cathles, 1980; Mörner, 1980). This feature therefore cannot be employed yet as circumstantial evidence for the thickness of the lithosphere.

More promising for this purpose are the delevelled strandlines associated with pro- or post-glacial lakes or seas. If the strandlines are sufficiently old, their tilts are sensitive to lithospheric thickness. Pro-glacial-lake tilts were used to constrain lithospheric thickness in North America (Walcott, 1970; Wolf, 1985b, 1986). The interpretations favoured a thickness of less than 100 km, which is lower than Peltier's (1984) estimate of about 200 km based on relative sea-level data from the North American east coast. In Fennoscandia, a complete sequence of strandlines has been mapped and dated (e.g. Donner, 1980; Eronen, 1983). The oldest of these strandlines was formed at approximately 10 ka B.P. It is therefore pro-glacial, and its tilt is expected to be sensitive to lithospheric thickness. A careful analysis of strandline tilt may therefore help resolve the ambiguity in the interpretation.

The second aspect of this study has been the investigation of mechanisms which are capable of enhancing the gravity predictions without sacrificing the fit of the uplift data. Peltier and Wu (1982) achieved this largely by allowing sufficient internal buoyancy. The present study has restricted internal buoyancy to the density contrast at 670 km depth, in order to display more clearly the effect of lower-mantle viscosity on the gravity predictions. Alternatively, a transition zone in viscosity has been invoked to enhance the gravity anomaly. Either modification allows the prediction of negative anomalies of up to 11 mgal. This is rather small compared with the value proposed by Balling (1980) for the glacial component of the Fennoscandian gravity anomaly. Conversely, it is large in view of Anderson's (1984) study, which implies that the glacial component is minor.

Whether the Fennoscandian gravity data can constrain the earth's viscosity structure therefore depends on accurate determination of the size of the non-glacial component of the anomaly. Until this problem has been solved, studies of the kind discussed here mainly serve to demonstrate that interpretations using deep-flow models do not fail automatically if the glacial component turns out to be large.

Acknowledgements. This research was financially supported by a Postgraduate Scholarship and Postdoctoral Fellowship granted by the Natural Sciences and Engineering Research Council of Canada.

References

Anderson, A.J.: Geophysical interpretation of features in the marine geoid of Fennoscandia. Mar. Geophys. Res. **7**, 191–203, 1984

Balling, N.: The land uplift in Fennoscandia, gravity field anomalies and isostasy. In: Earth rheology, isostasy, and eustasy, N.-A. Mörner, ed.: pp. 297–321, New York: Wiley 1980

Bemmelen, R.W. van, Berlage, H.P. jr.: Versuch einer mathematischen Behandlung geotektonischer Bewegungen unter besonderer Berücksichtigung der Undationstheorie. Gerlands Beitr. Geophys. **43**, 19–55, 1935

Cathles, L.M.: The viscosity of the earth's mantle. Princeton: Princeton University Press 1975

Cathles, L.M.: Interpretation of postglacial isostatic adjustment phenomena in terms of mantle rheology. In: Earth rheology, isostasy, and eustasy, N.-A. Mörner, ed.: pp. 11–43. New York: Wiley 1980

Clark, J.A., Farrell, W.E., Peltier, W.R.: Global changes in postglacial sea level: a numerical calculation. Quat. Res. **9**, 265–287, 1978

Daly, R.A.: The changing world of the ice age. New Haven: Yale University Press 1934

De Geer, E.H.: Skandinaviens geokronologi. Geol. Fören. Stockholm Förh. **76**, 299–329, 1954

Donner, J.: The determination and dating of synchronous Late Quaternary shorelines in Fennoscandia. In: Earth rheology, isostasy, and eustasy, N.-A. Mörner, ed.: pp. 285–293. New York: Wiley 1980

Dziewonski, A.M., Anderson, D.L.: Preliminary reference earth model. Phys. Earth Planet. Inter. **25**, 297–356, 1981

Eronen, M.: Late Weichselian and Holocene shore displacement in Finland. In: Shorelines and isostasy, D.E. Smith, A.G. Dawson, eds.: pp. 183–207. New York: Academic Press 1983

Fairbridge, R.W.: Eustatic changes in sea level. In: Physics and chemistry of the earth, Vol. 4, L.H. Ahrens, F. Press, K. Rankama, S.K. Runcorn, eds.: pp. 99–185. London: Pergamon Press 1961

Farrell, W.E., Clark, J.A.: On postglacial sea level. Geophys. J.R. Astron. Soc. **46**, 647–667, 1976

Gilbert, F., Dziewonski, A.M.: An application of normal mode theory to the retrieval of structural parameters and source mechanisms from seismic spectra. Philos. Trans. R. Soc. London Ser. A **278**, 187–269, 1975

Haskell, N.A.: The motion of a viscous fluid under a surface load. Physics **6**, 265–269, 1935

Imbrie, J., Imbrie, K.P.: Ice ages, solving the mystery. Hillside: Enslow 1979

Jordan, T.H.: Continents as a chemical boundary layer. Philos. Trans. R. Soc. London Ser. A **301**, 359–373, 1981

Lidén, R.: Den senkvartära strandförskjutningens förlopp och kronologi i Ångermanland. Geol. Fören. Stockholm Förh. **60**, 397–404, 1938

Lliboutry, L.A.: Rheological properties of the asthenosphere from Fennoscandian data. J. Geophys. Res. **76**, 1433–1446, 1971

McConnell, R.K. jr.: Viscosity of the mantle from relaxation time spectra of isostatic adjustment. J. Geophys. Res. **73**, 7089–7105, 1968

Mörner, N.-A.: The Fennoscandian uplift: geological data and their geodynamical implication. In: Earth rheology, isostasy, and eustasy, N.-A. Mörner, ed.: pp. 251–284. New York: Wiley 1980

Niskanen, E.: On the upheaval of land in Fennoscandia. Ann. Acad. Sci. Fenn. Ser. A **53**, 1–30, 1939

Paterson, W.S.B.: The physics of glaciers, 2nd edn. Oxford: Pergamon Press 1981

Peltier, W.R.: The thickness of the continental lithosphere. J. Geophys. Res. **89**, 11303–11316, 1984

Peltier, W.R., Andrews, J.T.: Glacial-isostatic adjustment, 1, the forward problem. Geophys. J.R. Astron. Soc. **46**, 605–646, 1976

Peltier, W.R., Farrell, W.E., Clark, J.A.: Glacial isostasy and relative sea level: a global finite element model. Tectonophysics **50**, 81–110, 1978

Peltier, W.R., Wu, P.: Mantle phase transitions and the free air gravity anomalies over Fennoscandia and Laurentia. Geophys. Res. Lett. **9**, 731–734, 1982

Walcott, R.I.: Isostatic response to loading of the crust in Canada. Can. J. Earth Sci. **7**, 716–727, 1970

Walcott, R.I.: Past sea levels, eustasy and deformation of the earth. Quat. Res. **2**, 1–14, 1972

Walcott, R.I.: Structure of the earth from glacio-isostatic rebound. Annu. Rev. Earth Sci. **1**, 15–37, 1973

Walcott, R.I.: Rheological models and observational data of glacio-isostatic rebound. In: Earth rheology, isostasy, and eustasy, N.-A. Mörner, ed.: pp. 3–10. New York: Wiley 1980

Wolf, D.: The relaxation of spherical and flat Maxwell earth models and effects due to the presence of the lithosphere. J. Geophys. **56**, 24–33, 1984

Wolf, D.: The normal modes of a layered, incompressible Maxwell half-space. J. Geophys. **57**, 106–117, 1985a

Wolf, D.: An improved estimate of lithospheric thickness based on a reinterpretation of tilt data from Pleistocene Lake Algonquin. Can. J. Earth Sci. **22**, 768–773, 1985b

Wolf, D.: On deglaciation-induced perturbations of the geoid. Can. J. Earth Sci. 1986 (in press)

Wu, P., Peltier, W.R.: Glacial isostatic adjustment and the free air gravity anomaly as a constraint on deep mantle viscosity. Geophys. J.R. Astron. Soc. **74**, 377–449, 1983

Received February 22, 1985; Revised version August 19, 1985
Accepted August 27, 1985

J Geophys (1986) 59:49–55

Journal of Geophysics

Modelling active audio-magnetotelluric data

G. Fischer and P.-A. Schnegg
Observatoire Cantonal, CH-2000 Neuchâtel, Switzerland

Abstract. A major improvement in the new pulsed AMT method recently proposed by the authors has been achieved by modelling the field data with the analytic response of layered structures to point-source excitations. The pulsed field data can be modelled quickly to yield the best-fitting one-dimensional model. Small departures from one-dimensionality often seem to manifest themselves as a rotation of the transmitted fields through a vertical axis. This rotation can also be modelled and leads to a significant improvement of the fit. A trade-off analysis of the model parameters shows that these are well constrained in the practical example considered. The correct number of layers with which to model the data can also be derived with confidence.

Key words: Active audiomagnetotellurics – Modelling active magnetotelluric data

Introduction

Electromagnetic sounding methods using artificial or controlled signal sources are gaining in popularity, perhaps as a consequence of the ever-increasing level of perturbations caused by human activity. Ward (1983) has reviewed some of these methods and their application to deep exploration. Recent examples of the use of controlled sources in magnetotellurics (MT) or audiomagnetotellurics (AMT) have been described by Sandberg and Hohmann (1982), Otten and Musmann (1983), Adam et al. (1983), Szarka (1983) and Heikka et al. (1984).

Schnegg and Fischer (1984) have recently set up a method with which it is possible to perform a natural-source and a controlled-source AMT sounding in quick succession with the same equipment. The implementation of their method to one-dimensional (1D) or layered structures was based on the following observation. If, at constant period T, the logarithm of the apparent resistivity, $\log \rho_a(r, T)$, and the phase, $\varphi(r, T)$, are plotted against the inverse distance, $1/r$, to a grounded dipole source (cf. Fig. 1), a linear behaviour is usually observed over a broad range of large source-receiver separations r. As the distance r is allowed to become larger still, the signal strength becomes weaker and the data scatter increases. It was tempting, therefore, to assume that the $1/r$ trend was the limiting asymptotic behaviour of $\log \rho_a$ and φ when r becomes very large. This was questioned (Musmann, personal communication), however, and indeed a number of analytical computations of the response of 1D structures to grounded dipole excitation (Sunde, 1949; Goldstein and Strangway, 1975; Kauahikaua, 1978) show that the behaviour of $\log \rho_a(r, T)$ and $\varphi(r, T)$ is in fact more complicated than Schnegg and Fischer (1984) had assumed. Figure 2, which illustrates this point, was computed with an analytical program kindly supplied by Dr. Weidelt (personal communication). This figure confirms both the more complicated behaviour at large distances and the apparently linear trend observed experimentally over a wide range of inverse distances. It also shows, however, that extrapolating the linear portion toward the $1/r = 0$ limit does not yield the correct far-field or MT values.

Because of limitations in the signal power available, the far-field condition between source and receiver can often not be achieved. We have thus asked ourselves whether it was possible, under the assumption of one-dimensionality, to model the near-field data with Weidelt's forward analytical program.

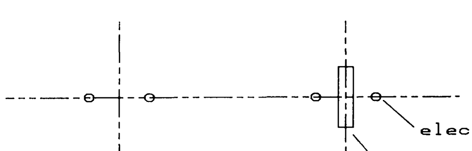

BROADSIDE GEOMETRY

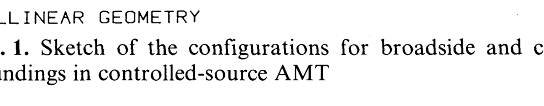

COLLINEAR GEOMETRY

Fig. 1. Sketch of the configurations for broadside and collinear soundings in controlled-source AMT

Offprint requests to: Gaston Fischer

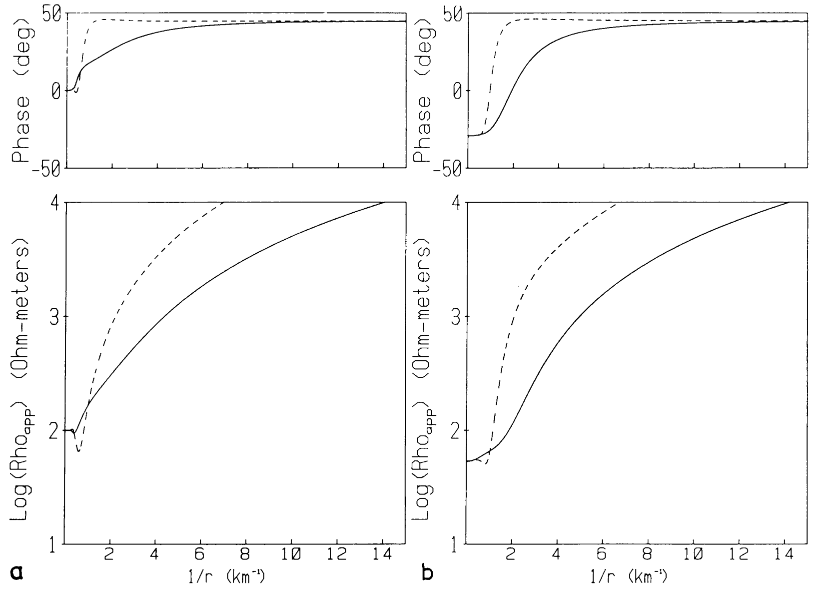

Fig. 2. a Logarithm of apparent resistivity and phase versus the inverse distance from a 100-Hz ac grounded dipole source at the surface of a uniform half-space of 100-Ωm resistivity. The phase plotted is 45° minus the lag of the electric versus the magnetic fields (cf. Fischer et al., 1981). The *full curve* refers to broadside excitation, the *dashed curve* belongs to the collinear geometry (cf. Fig. 1). **b** Plot similar to Fig. 2*a*, but for a half-space with 1-Ωm resistivity, covered with a 250-m overburden of 100 Ωm

Modelling near-field MT data

The past few years have witnessed great improvements in the methods of modelling natural (i.e. far-field) one-dimensional MT and AMT data. Among these many new schemes, Fischer and Le Quang (1981, 1982) have proposed an efficient search routine to find the layered model which gives the best fit, in the least squares sense, to a given field data set. This search routine has also been used successfully to model other kinds of data, like Schlumberger or Wenner apparent resistivities. It also proved very well suited to model near-field MT or AMT data, as can be seen in Fig. 3. The data in this figure were obtained over a dried-up marsh in the Swiss Molasse Basin. The site is level with near perfect horizontal layering. The top layers consist of a few metres of peat and a succession of recent Quaternary sediments, the total thickness of which is not known exactly at the BELE sounding site but probably does not exceed 50–100 m. This is followed by a series of sandstones typical of the Swiss Molasse Basin, down to a depth of the order of 500–1000 m (Axelrod, 1978; Schlanke et al., 1978) where the transition to the much more resistive Jura limestones takes place, with resistivities in the range 180–1000 Ωm.

At the site of Fig. 3, data have been gathered with the source placed at 14 different distances from 200 to 1659 m. At the greatest separation the data scatter is somewhat larger than that visible in Fig. 3. As the distance of injection is reduced the scatter decreases, but plots of log ρ_a and φ versus the period T also become more and more featureless. It seems preferable, therefore, to model intermediate distances in the range 500–1000 m for our AMT periods and the rather low resistivities of the BELE site.

A rather striking feature in Fig. 3 is the greater variation with distance of the measured data when compared to the computed data. This feature is not peculiar to the BELE site, but has been observed repeatedly at other sites, all of which could be considered, from independent geological evidence, to be fairly 1D. It is worth stressing, as Fig. 3 clearly shows, that this is a systematic effect, much larger than – and obviously distinct from – the intrinsic data scatter, and it therefore contributes significantly to the rather large standard deviation E.

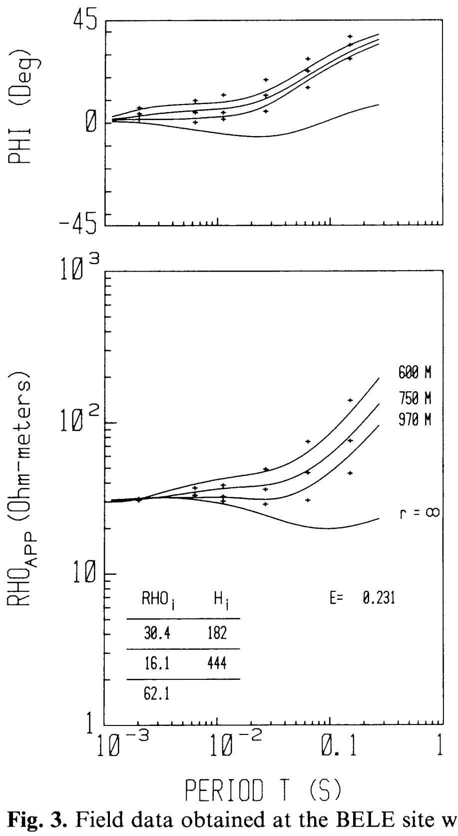

Fig. 3. Field data obtained at the BELE site with pulsed excitation at distances of 970, 750 and 600 m in the broadside configuration (cf. Fig. 1). These data have been modelled with a three-layer structure whose best-fitting parameters are shown in the inset, together with the standard deviation E between computed curve and measured data. Also shown is the computed AMT curve ($r = \infty$) for the model found. The standard deviation E is computed according to Fischer et al. (1981), without weighting the data. To reduce computing time, the data from six periods only have been modelled

In attempting to identify the cause of this stronger dependence of the field data on the distance separating current source and receiver station our first idea was to check whether it could be due to the presence of a highly conduct-

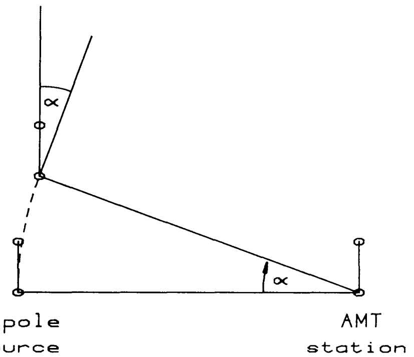

Fig. 4. Geometrical configuration for broadside injection: the source and receiver electrode pairs are placed at right angles to the line joining the two sites (cf. Fig. 1). If the field at the receiving station appears to have been rotated around a vertical axis by an angle α, this is equivalent to assuming that the transmitter has been moved without rotation and is seen under an azimuth α with respect to the original direction

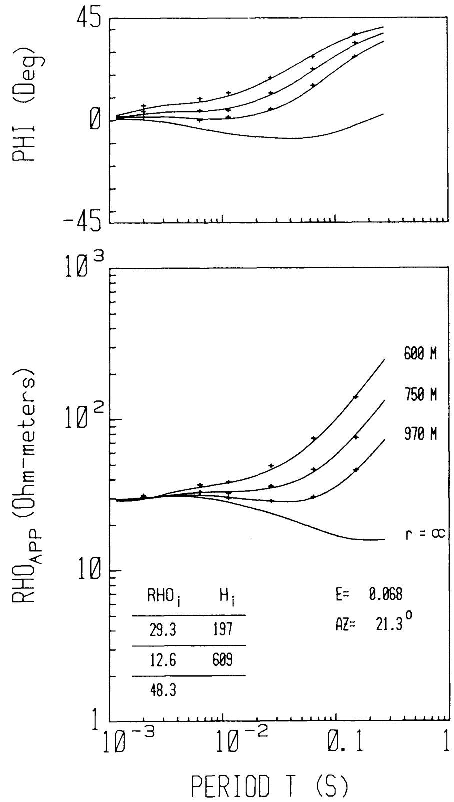

Fig. 5. Plot similar to Fig. 3, but assuming that the fields at the receiving station have been rotated through an angle $\alpha = 21.3°$. This angle corresponds to the most suitable combination of broadside ($\cos \alpha$) and collinear ($\sin \alpha$) geometries

ing thin overburden, but this proved fruitless. We then remembered, as Fig. 2 shows, that the collinear geometry yields data which vary more rapidly with distance than broadside data. Although the data of Fig. 3 refer to the broadside geometry (cf. Fig. 1), with current injection and receiving electrodes both perpendicular to the line joining the two sites, we decided to treat the received signal as if it were a combination of broadside and collinear fields. In other words, we considered the fields recorded at the receiving site as having been rotated through an angle α around a vertical axis. Looking at Fig. 4, this is equivalent to the assumption that the point-source has been moved without rotation and is now seen from the receiving station under an azimuth α with respect to the original source-receiver direction. Our minimizing routine is therefore instructed to select not only the best-fitting model, but also the most appropriate azimuth. We see in Fig. 5 that this procedure is very effective: it brings the standard deviation back to a value well below $E = 0.1$, while requiring only a modest rotation of $\alpha = 21.3°$. The structural model found remains fairly close to the one achieving the best possible fit without the rotation.

We should also like to stress that phase and apparent resistivity appear to contribute equally to the model determination. Our graphs, as for example Fig. 5, are constructed with ordinate scales which give $\log \rho_a$ and φ the same sensitivity (cf. Fischer et al., 1981). With such representations one generally observes a larger scatter of the MT or AMT phase than of the corresponding $\log \rho_a$. With our pulsed technique we are able to secure phase data which seem much less scattered, and it is gratifying to see that our modelling scheme makes full use of these improved phase data.

Justification of a non-vanishing azimuth

As we said above, the respective configurations of the grounded dipole source and of the receiving electrodes and magnetic sensing coil refer to the broadside geometry as defined in Fig. 1. If the structure were perfectly one-dimensional, the data could be expected to yield a strictly broadside response. Several factors, however, are likely to distort the transmitted field which, at the receiving station, would then appear as a mixture of broadside and collinear components: (1) small misalignment errors at the transmitting and receiving stations are unavoidable, amounting to perhaps a degree or two; (2) naturally occurring structures are never ideally 1D and both lateral variations of geometry as well as of resistivity, even in the same formation, must be expected to lead to rotations of the field; (3) another frequent departure from ideal 1D conditions lies in the topography which is seldom perfectly level; (4) the field may also suffer distortions and will therefore appear as having been rotated, because of artificial sub-surface metal structures like drainage pipes and other conduits.

As was said before, the data displayed in Fig. 5 were obtained at the surface of a dried-up marsh. This site is therefore quite level, but the sounding area is crossed by a number of drainage channels and the sediments at depth cannot be taken as forming a perfect horizontal layering (Axelrod, 1978). After modelling the entire data set with a single model structure and a single azimuth α, the fit cannot be improved much if a different azimuth is allowed for each distance r. A different azimuth $\alpha(r)$ for different injection distances r must be expected, however, as the four factors listed above will contribute differently when the injection site is moved. As an example of this we give, in Table 1, the azimuths obtained when we model data sets arising from groups of three injection distances, where these distances are systematically decreased. We note in this table that the azimuth appears to become smaller when the sources move closer. This is what one would expect from

Table 1. Model parameters and azimuths obtained at the BELE site when the signal sources are moved closer to the receiving station

Injection distances [m]	ρ_1 [Ωm]	h_1 [m]	ρ_2 [Ωm]	h_2 [m]	ρ_3 [Ωm]	E	Azimuth
970 750 600	29.3	197	12.6	609	48.3	0.0681	21.3°
750 600 500	29.6	201	13.2	654	58.3	0.0772	18.5°
600 500 429	29.6	199	14.0	835	35.9	0.0787	17.2°
500 429 375	30.4	188	14.9	844	39.7	0.0883	16.0°
429 375 333	30.8	177	16.2	882	35.9	0.0995	16.5°

the major causes of field rotation we have envisaged. Table 1 also shows that the five model parameters are quite stable with respect to the varying distance of the source. As we have said before, however, the response curves are less well featured when the sources move closer to the receiver, and modelling then loses resolution.

The results displayed in Table 1 also suggest that it will generally suffice to acquire data with the dipole source placed at two or three different locations, with distances approximately in the range of one half to one skin-depth for the longer periods recorded. For the BELE site the MT apparent resistivity is about 20 Ωm (cf. Fig. 5) and, with long periods of around 0.1 s, we have an apparent skin-depth of about 700 m in agreement with our observation that injection distances in the range from 500 to 1000 m seemed most appropriate for this site. Distances larger than these would of course also be suitable, but they would require a more powerful signal source than ours.

Parameter trade-off

When geophysical data are modelled it is crucial to ask whether a given sounding method leads to models which are well constrained or whether the model parameters one derives are susceptible of large variations, i.e. are poorly resolved. Because the new pulsed AMT technique leads to data which are far less scattered than those of traditional AMT, it is of interest to determine the range of definition of the derived model parameters. As we have shown elsewhere (Fischer and Le Quang, 1982), this can best be done by way of a parameter trade-off analysis in which one looks for the family of models whose standard deviation E remains within 10% of the minimum value E_0. Taking the data of Fig. 5 as an example, with $E_0 = 0.068$, each of the model parameters in turn is varied systematically to larger or smaller values. Under the constraint of the imposed variation *all the other parameters are adjusted to minimize E.* The set of limiting parameters are obtained when $E = 1.1\ E_0$. These limiting parameters can be expressed in terms of those of the best-fitting model and are represented in the form of a parameter trade-off diagram as shown in Fig. 6. In this diagram the trade-off limits are given by the full lines. The dashed lines define the narrower ranges where E reaches 1.1 E_0 when a given model parameter is varied *without adjusting* the other parameters to minimize E.

What Fig. 6 shows is that, with the exception of the basement resistivity ρ_3, all the model parameters are extremely well constrained: ρ_1, h_1, and ρ_2 have variation ranges of less than 10% around their best-fitting values; for h_2 the limits are -17% and $+28\%$; and while there is a very large upper bound at 3000 Ωm for ρ_3, its lower bound at 23 Ωm is only a factor of two below the best-fitting value of 48.3 Ωm. The trade-off analysis also yields a range of permitted azimuths α. This range, from $\alpha = 17.2°$

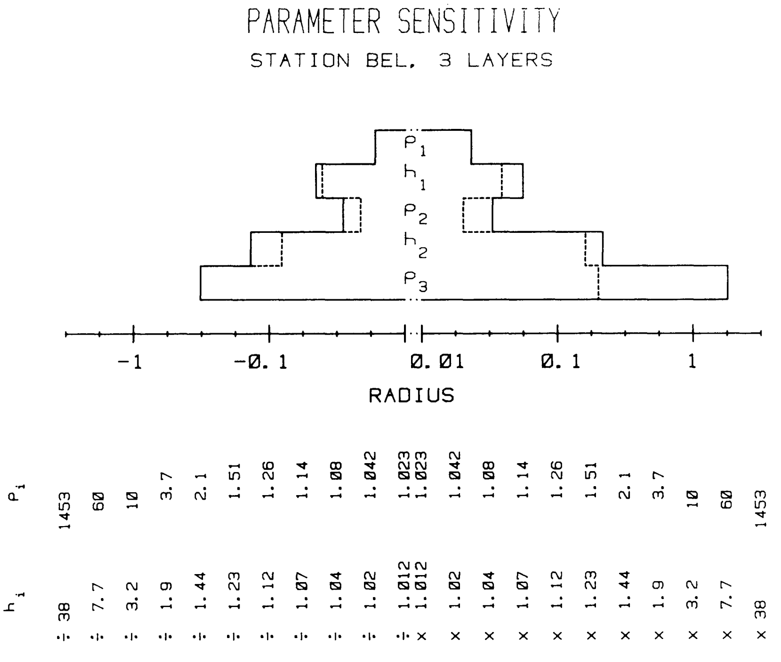

Fig. 6. Trade-off diagram for the data and model of Fig. 5 (cf. Fischer and Le Quang, 1982). The radii refer to distances in the space of model parameters. The scales are logarithmic and normalized to the parameters of the best-fitting model. The diagram gives the parameter range within which the standard deviation E exceeds the minimum E_0 of the best model by less than 10%. Note the different scales for ρ_i/ρ_{i0} and for h_i/h_{i0}. As an example, h_2 can be varied between $h_{20}/1.10$ and 1.20 h_{20} without changing the other parameters (*dashed limits*), and between $h_{20}/1.17$ and 1.28 h_{20} if the other parameters are adjusted to keep E minimal under the imposed variation of h_2 (*solid limits*). The solid limits thus give the extreme excursions of the parameters within which it is possible to achieve $E \leq 1.10\ E_0$. This same procedure yields a maximum range of 17.2°–24.0° for the azimuth α

to $\alpha = 24.0°$, is very narrow and therefore rather supports the assumption that the fields at the receiving station have undergone a small rotation around a vertical axis.

It is of interest to compare the trade-off diagram of Fig. 6 with similar diagrams for typical MT data (cf. Fig. 4 of Fischer and Le Quang, 1982). Quite clearly the new pulsed AMT method leads to model parameters which are far more precisely defined. In part this is of course a consequence of the much smaller scatter of the data, possible with a controlled-source technique, but it is probably also an inherent property of this particular method based on a grounded dipole source.

How many layers are resolved?

The trade-off diagram of Fig. 6 makes it clear that the resistivity ρ_3 of the lowermost layer is poorly resolved. It may therefore seem questionable whether the data support a structure with three layers, or whether a model with only two layers would not explain them equally well. There is more reason to ask such a question with the controlled-source method than with natural MT or AMT, because the shape of the response curves does not immediately suggest a minimum number of necessary layers. This is true equally for the shape of the responses as function of distance (cf. Fig. 2a and b) and for their shape when plotted versus the period (cf. Fig. 5). The natural AMT curves in Fig. 5, labelled $r = \infty$, are quite clearly three-layer curves. That this is not self-evident for the controlled-source curves can be seen in Fig. 7, where the analytical response has been plotted for a two-layer model which turns gradually into a three-layer model. Again the far-field curves ($r = \infty$) at once suggest the correct number of layers, whereas nothing similar can be deduced from the near-field curves.

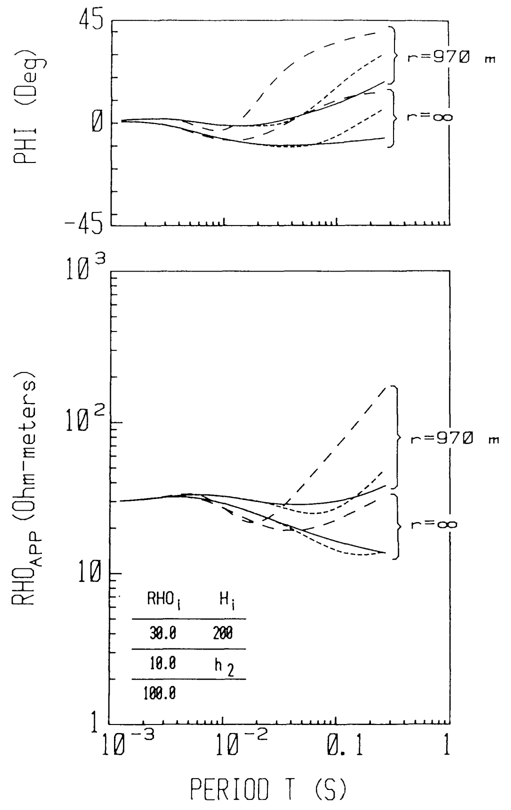

Fig. 7. Model responses for the structure given in the inset. The *full lines* correspond to $h_2 = \infty$, i.e. a structure with only two layers. The *dotted curves* refer to $h_2 = 500$ m and the *dashed curves* to $h_2 = 150$ m. The sets of three curves each correspond to source-receiver distances of 970 m and infinity. This graph illustrates the difficulty of deciding visually whether a given response is caused by structures with two or three layers

Table 2. Modelling the field data with a varying number of layers. These data demonstrate that three layers are appropriate. With four layers the standard deviation E decreases by 0.5%; with only two layers it increases by 42%

n	ρ_1 [Ωm]	h_1 [m]	ρ_2 [Ωm]	h_2 [m]	ρ_3 [Ωm]	h_3 [m]	ρ_4 [Ωm]	Azimuth [degrees]	E
1	19.8	∞						1.8	0.5238
2	29.7	187	13.9	∞				20.6	0.0964
3	29.3	197	12.6	609	48.3	∞		21.3	0.0681
4	29.4	195	12.9	487	18.4	345	57.5	21.4	0.0677

In spite of the impossibility of establishing a realistic estimation of the correct number of layers merely by looking at the observed response curves, other arguments can be called upon to derive this number with confidence. We propose to show with the example of Fig. 5 that these data indeed give evidence in favour of a three-layer structure.

While the trade-off diagram of Fig. 6 does show ρ_3 to be poorly determined, it gives all the other model parameters as very well resolved; in particular h_2 and $h_1 + h_2$, i.e. the depth to the basement layer. An even more powerful argument is obtained when we attempt to model the field data with different numbers of layers, as seen in Table 2. The standard deviation E between field and model data can be reduced to $E = 0.0681$ if a three-layer model is postulated. This value can almost not be reduced further with a four-layer model, but it jumps by 42% to $E = 0.0964$ when modelling with only two layers. Obviously three layers is the correct number to postulate.

Comparison of natural and controlled source AMT

In Fig. 8 we have plotted the results of a natural AMT sounding at the BELE site, together with the response curve from the best-fitting model yielded by the controlled-source sounding. Also plotted in Fig. 8 are the data resulting from the linear extrapolation against the inverse distance described previously (Schnegg and Fischer, 1984). As already noted, the latter data are systematically too low, both as regards the apparent resistivity and the phase. The comparison of the natural- and controlled-source responses is of more interest. There is strong disagreement between the two responses at the longer periods. This is not surprising since it is precisely at the long periods that artificial perturbations propagate furthest. At periods shorter than about 0.1 s, the skin-depth and thus the extent of the perturbations have decreased and the two sounding methods yield concordant results. At the very shortest periods there is a hint that the natural sounding data again deviate from the controlled-source response. We believe that this is of instrumental origin: at periods below 2 ms the signal to noise ratio of our system begins to deteriorate and generally the amplitude of the natural signals becomes weaker toward 1 or 2 kHz.

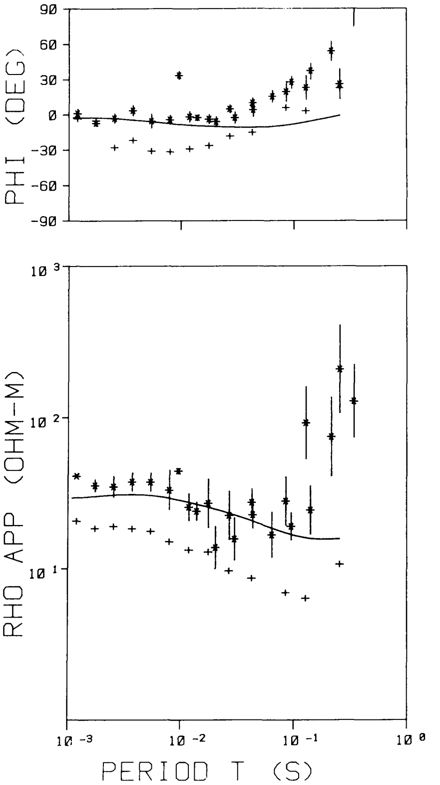

Fig. 8. Comparison of natural source AMT data (*stars*) with the response of the model derived from the active-source AMT (*smooth curve*) at the BELE site. The diagram also shows the results obtained by the linear extrapolation of log ρ_a and φ against $1/r$ (*crosses*) originally proposed by the authors (Schnegg and Fischer, 1984)

We return now to the family of models required by the controlled-source sounding and specified jointly by the best-fitting model given in Fig. 5 and the extremal model parameters according to the trade-off diagram of Fig. 6. It is of course meaningless to attribute great significance to the parameters of the top layer. With a shortest period of about 1.5 ms and a 30-Ωm resistivity, the skin-depth is about 106 m; variation within the thin and highly conducting Quaternary formations can, therefore, not be resolved. All that can be said is that the upper 100–200 m behave as if they had a conductance of about $h_1/\rho_1 = 6.7$ S, but these top formations certainly comprise several separate layers of different resistivities. Note that the trade-off diagram gives ρ_1 and h_1 with uncertainties of less than $\pm 10\%$. The second layer is the only one which is well resolved: $11.8 \le \rho_2 \le 13.6$ Ωm and $520 \le h_2 \le 780$ m. It follows, therefore, that the depth to the limestones, i.e. $h_1 + h_2$, is comprised between about 610 and 990 m, in perfect accord with the other geophysical and geological knowledge available for this site (Axelrod, 1978; Schlanke et al., 1978). As was said before, with a range of 23–3000 Ωm, the limestone resistivity is the least well resolved. Its true value in this area is in the range 180–1000 Ωm.

Conclusion

The new pulsed AMT method proposed by Schnegg and Fischer (1984) is somewhat more complicated than these authors had assumed on the basis of their experimental observations. However, the field data which are obtained with the new technique are clearly far more reproducible and less scattered than natural AMT data. It was therefore worth investigating whether the data obtained by this new method could be modelled with a one-dimensional algorithm. We were able to achieve this with the same search routine used previously to model natural MT or AMT data (Fischer and Le Quang, 1981). Our artificial AMT technique thus remains an efficient new electromagnetic sounding tool.

The detailed study of a set of field data suggested that the various departures from ideal one-dimensionality, like lateral changes of the structure or topographical accidents, seem to lead to small rotations of the polarization plane of the field. This can easily be taken care of by determining not only the model that fits the field data best, but also the most appropriate azimuth.

The MT or AMT responses of layered structures to natural, or far-field, excitations give very explicit visual indications about the minimum number of layers necessary to model measured data. With our artificial near-field data this information is less direct, but it can be derived with equal confidence by way of a trade-off analysis and by modelling with fewer or more layers. The trade-off analysis indicates that the model parameters derived are generally well resolved.

The new method was applied to the determination of the depth to the limestones at a site in the Swiss Molasse Basin. It gave this depth as 800 ± 190 m at that particular site, in perfect accord with independent Schlumberger soundings (Axelrood, 1978).

Acknowledgements. Quite obviously we are particularly indebted to Dr. P. Weidelt for the very efficient computer programs he kindly made available to us. Without these programs this paper could never have been written. Financial assistance was gratefully received from the Swiss National Science Foundation and from the Geophysical Commission of the Academy of Natural Sciences.

References

Adam, A., Szarka, L., Varga, M.: Physical and mathematical modelling of crustal conductivity anomalies in the Pannonian Basin. Acta Geodaet., Geophys. et Montanist. Hung. **18**, 467–488, 1983

Axelrod, A.: Contribution à l'étude géophysique de la région des Lacs de Neuchâtel, Bienne et Morat. Thèse de doctorat présentée à la Faculté des Sciences (Institut de Géophysique) de l'Université de Lausanne, 1978

Fischer, G., Le Quang, B.V.: Topography and minimization of the standard deviation in one-dimensional magnetotelluric modelling. Geophys. J.R. Astron. Soc. **67**, 279–292, 1981

Fischer, G., Le Quang, B.V.: Parameter trade-off in one-dimensional magnetotelluric modelling. J. Geophys. **51**, 206–215, 1982

Fischer, G., Schnegg, P.-A., Peguiron, M., Le Quang, B.V.: An analytic one-dimensional magnetotelluric inversion scheme. Geophys. J.R. Astron. Soc. **67**, 257–278, 1981

Goldstein, M.A., Strangway, D.W.: Audio-frequency magnetotellurics with a grounded electric dipole source. Geophysics **40**, 669–683, 1975

Heikka, J., Zhamaletdinov, A.A., Hjelt, S.E., Demidova, T.A., Velikhov, Ye. P.: Preliminary results of MDH test registrations in northern Finland. J. Geophys. **55**, 199–202, 1984

Kauahikaua, J.: Electromagnetic fields about a horizontal electric wire source of arbitrary length. Geophysics **43**, 1019–1022, 1978

Otten, J., Musmann, G.: Aktive Audiomagnetotellurik bei Travale. Protokoll Elektromagnetische Tiefenforschung, Neustadt a.W., pp. 183–188, 1982. See also Musmann, G., Otten, J.: Active audiomagnetotelluric application in geothermal areas. Abstract I3.18/IAGA XVIII General Assembly, Hamburg, August 15–27, 1983

Sandberg, S.K., Hohmann, G.W.: Controlled-source audiomagnetotellurics in geothermal exploration. Geophysics **47**, 100–116, 1982

Schlanke, S., Hauber, L., Büchi, U.: Lithographie und Sedimentpetrographie der Molasse in den Bohrungen Tschugg 1 und Ruppoldsried 1 (Berner Seeland). Eclogae Geologicae Helvetiae **71**, 409–425, 1978

Schnegg, P.-A., Fischer, G.: A new pulsed audiomagnetotelluric technique. J. Geophys. **55**, 191–198, 1984

Sunde, E.D.: Earth conduction effects in transmission systems. London: D. Van Nostrand Co. Inc. 1949

Szarka, L.: Exploration of high resistivity basement using electrical and magnetic fields of quasi-static point sources. Geophys. Prosp. **31**, 829–839, 1983

Ward, S.H.: Controlled source electrical methods for deep exploration. Geophys. Surv. **6**, 137–152, 1983

Received May 10, 1985; Revised version September 2, 1985
Accepted September 6, 1985

J Geophys (1986) 59:56–61

Journal of Geophysics

A comparison of upper mantle subcontinental electrical conductivity for North America, Europe, and Asia

Wallace H. Campbell[1] **and Edward R. Schiffmacher**[2]

[1] U.S. Geological Survey, MS 964, Box 25046, Denver Federal Center, Denver, CO 80225, USA
[2] 2155 Emerald Road, Boulder, CO 80303, USA

Abstract. Spherical harmonic analysis coefficients of the external and internal parts of the quiet-day geomagnetic field variations (Sq), separated for the North American, European, Central Asian and East Asian regions, were used to determine conductivity profiles to depths of about 600 km by the Schmucker equivalent-substitute conductor method. All three regions showed a roughly exponential increase of conductivity with depth. Distinct discontinuities seemed to be evident near 255–300 km and near 450–600 km. Regional differences in the conductivity profiles were shown by the functional fittings to the data. For depths less than about 275 km, the North American conductivities seemed to be significantly higher than the other regions. For depths greater than about 300 km, the East Asian conductivities were largest.

Key words: Upper mantle – Electrical conductivity – Electromagnetic induction

Introduction

In an earlier paper (Campbell and Schiffmacher, 1985) a Gauss spherical harmonic analysis (SHA) technique was applied to quiet-day geomagnetic variation (Sq) data to separate the external and internal contributions of the observed magnetic field at the Earth's surface. A hypothetical sphere was used to determine the separation for restricted regions of the Earth, so that equivalent ionosphere source currents were found individually for North America, Europe, Central Asia and East Asia. The field at any geomagnetic colatitude, θ, and longitude, ϕ, within the continental study region, was represented by ordered sets of spherical harmonic analysis (SHA) external cosine, $(\mathrm{aex})_n^m$, and sine, $(\mathrm{bex})_n^m$, coefficients and internal cosine, $(\mathrm{ain})_n^m$, and sine, $(\mathrm{bin})_n^m$, coefficients. The order index, m, was equal to 1, 2, 3, or 4 for the 24-, 12-, 8- and 6-h components of the quiet daily variation, Sq, and the analysis was computed with degree indices, n, equal to m to 12. The three orthogonal field components in the geomagnetic northward, X, eastward, Y, and downward, Z, directions were represented by the expressions:

$$X(\theta,\phi)=\sum_{m=1}^{4}\sum_{n=m}^{12}\{[(\mathrm{aex})_n^m+(\mathrm{ain})_n^m]\cos(m\phi)+[(\mathrm{bex})_n^m+(\mathrm{bin})_n^m]\sin(m\phi)\}\frac{dP_n^m}{d\theta},\tag{1}$$

$$Y(\theta,\phi)=\sum_{m=1}^{4}\left(\frac{-m}{\sin\theta}\right)\sum_{n=m}^{12}\{[(\mathrm{bex})_n^m+(\mathrm{bin})_n^m]\cos(m\phi)-[(\mathrm{aex})_n^m+(\mathrm{ain})_n^m]\sin(m\phi)\}P_n^m,\tag{2}$$

$$Z(\theta,\phi)=\sum_{m=1}^{4}\sum_{n=m}^{12}\{[n(\mathrm{aex})_n^m-(n+1)(\mathrm{ain})_n^m]\cos(m\phi)+[n(\mathrm{bex})_n^m-(m+1)(\mathrm{bin})_n^m]\sin(m\phi)\}P_n^m,\tag{3}$$

where P_n^m is the Schmidt Normalized Associated Legendre function (Chapman and Bartels, 1940).

In the application of SHA coefficients to earth conductivity determinations, Schmucker (1970, 1979) showed that for any specified n and m the ratio of the vertical, $(Z)n,m$, to one of the horizontal field components, $(X)n,m$ or $(Y)n,m$, determines a complex transfer function, C_n^m, in kilometres such that

$$C_n^m=\left[\frac{R(dP_n^m/d\theta)}{n(n+1)P_n^m}\right]\frac{(Z)n,m}{(X)n,m}\tag{4}$$

and

$$C_n^m=i\left[\frac{-mR}{n(n+1)\sin\theta}\right]\frac{(Z)n,m}{(Y)n,m},\tag{5}$$

where R is the earth's radius in kilometres. Writing this function in the complex real (z) and imaginary ($-p$) form

$$C_n^m=z-ip\tag{6}$$

he was able to determine the earth's electrical response to the penetrating fields using uniform substitute conducting layers at depths determined by the transfer function.

Offprint requests to: W.H. Campbell

Campbell and Anderssen (1983) showed that the real and imaginary parts of this transfer function may be written directly in terms of the SHA coefficients:

$$z=\frac{R}{n(n+1)}\left\{\frac{A_n^m[n(\mathrm{aex})_n^m-(n+1)(\mathrm{ain})_n^m]+B_n^m[n(\mathrm{bex})_n^m-(n+1)(\mathrm{bin})_n^m]}{(A_n^m)^2+(B_n^m)^2}\right\} \tag{7}$$

and

$$p=\frac{R}{n(n+1)}\left\{\frac{A_n^m[n(\mathrm{bex})_n^m-(n+1)(\mathrm{bin})_n^m]-B_n^m[n(\mathrm{aex})_n^m-(n+1)(\mathrm{ain})_n^m]}{(A_n^m)^2+(B_n^m)^2}\right\}, \tag{8}$$

where z and p are given in kilometres and the coefficient sums are given by

$$A_n^m=[(\mathrm{aex})_n^m+(\mathrm{ain})_n^m] \quad \text{and} \quad B_n^m=[(\mathrm{bex})_n^m+(\mathrm{bin})_n^m]. \tag{9}$$

For each m, n set of coefficients the depth to the uniform substitute layer is given by

$$d_{n,m}=z-p(\mathrm{km}) \tag{10}$$

with a substitute-layer conductivity of

$$\sigma_{n,m}=5.4\times 10^4/m(\pi p)^2 \quad \text{(siemens/meter)}. \tag{11}$$

The ratio, S_n^m, of the internal to external components of the geomagnetic surface field is then

$$S_n^m=u+i\,v \tag{12}$$

where

$$u=\frac{(\mathrm{aex})_n^m(\mathrm{ain})_n^m+(\mathrm{bex})_n^m(\mathrm{bin})_n^m}{[(\mathrm{aex})_n^m]^2+[(\mathrm{bex})_n^m]^2} \tag{13}$$

and

$$v=\frac{(\mathrm{bex})_n^m(\mathrm{ain})_n^m-(\mathrm{aex})_n^m(\mathrm{bin})_n^m}{[(\mathrm{aex})_n^m]^2+[(\mathrm{bex})_n^m]^2}. \tag{14}$$

The validity of Eqs. (10) and (11) is limited by three conditions. The first of these is:

$$0°\geqq \arg(C_n^m)\geqq -45°, \tag{15}$$

a condition described by Schmucker (1979). The second is

$$\arg(S_n^m)\geqq 9°, \tag{16}$$

a requirement that the angle between the internal and external components be neither small nor negative. The third condition is that the SHA amplitudes (Eq. 9) are not small:

$$[(A_n^m)^2+(B_n^m)^2]^{0.5}\geqq G_m. \tag{17}$$

A study of the data samples showed that sufficient sizes of the low-amplitude exclusion factors, in gamma, are $G_1=1.5$, $G_2=1.0$, $G_3=0.5$ and $G_4=0.25$, in a ratio of 1 : 2/3 : 1/3 : 1/6. The shorter wavelength, higher m, components of the field are typically smaller in amplitude. This ratio is approximately the same as that of the averaged amplitudes of the 24-, 12-, 8- and 6-h Fourier components of the Sq field at each 2.5-degree latitude increment weighted by the cosine of latitude.

This paper uses the coefficients from the earlier spherical harmonic analysis of Sq fields in North America, Europe, Central Asia and East Asia to determine the equivalent conductivity profiles beneath these three continental regions, by applying the Schmucker (1970, 1979) technique with the above equations.

Analysis

The original data set for this determination comprised the Sq variations on exceptionally quiet days of the quiet-sun year, 1965. Figure 1 shows the locations of the thirty observations used for the study. Spherical harmonic representations of the field variations for the 7th and 21st day of each month were obtained with the analysis sequence outlined in the earlier paper (Campbell and Schiffmacher, 1985). This sequence was used to form a regional station representation of the three orthogonal field components of Sq from the 24-, 12-, 8- and 6-h Fourier coefficients together with their seasonal (annual and semiannual) changes. The Fourier coefficients were appropriately smoothed with respect to geomagnetic latitude, and then the SHA technique was used on 2.5°-latitude samples to obtain the Gauss coefficients $(\mathrm{aex})_n^m$, $(\mathrm{bex})_n^m$, $(\mathrm{ain})_n^m$, and $(\mathrm{bin})_n^m$ for order 4 and degree 12. The analysis procedure was applied to each region separately with the local time change of field made equivalent to longitude position and the southern hemisphere field modelled appropriately from that of the northern observatory region. This analytical method was roughly equivalent to the creation of a sphere surrounded by a unique-source current pattern and having an internal, spherically symmetrical, conductivity-depth profile that was representative of the grouped stations of the study region. Figure 2 shows the internal induced currents obtained by the SHA. The corresponding external-source current representations were given in the earlier paper (Campbell and Schiffmacher, 1985).

The 24 sets of internal and external SHA coefficients (two for each month) calculated for each region of the model provided the input to the above equations. Conductivity-depth values were determined and plotted as separate regional data sets (Fig. 3). A trial exponential curve was fitted (by least squares) separately for each data set, after excluding a few obvious outliers, and a histogram was drawn for the distribution of data points about each trial curve. Often, the distribution was bimodal and a further separation of the data could be made for a depth of about 250–300 km. In these cases, a second exponential curve was

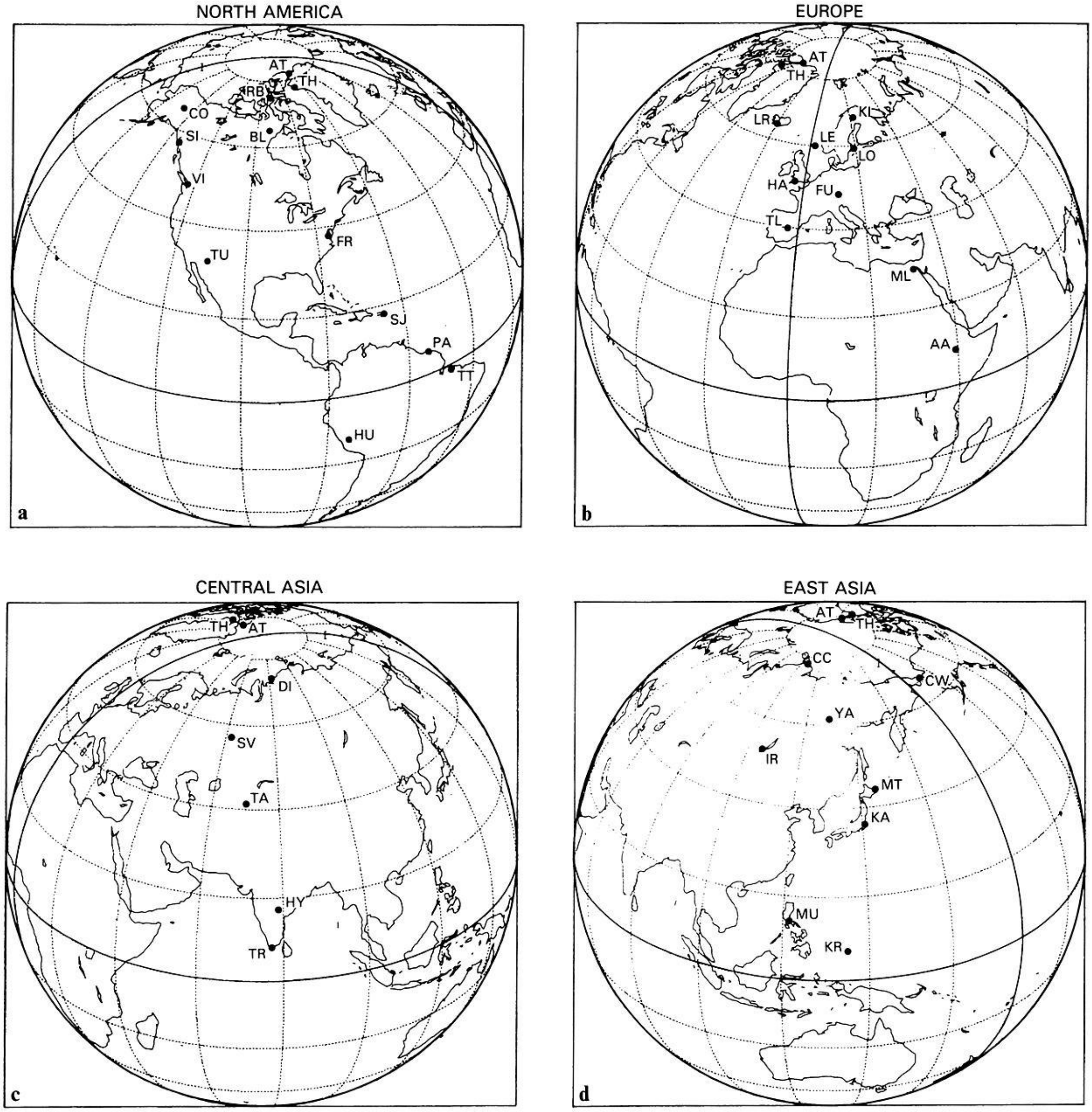

Fig. 1 a–d. Map of four analysis regions showing location of geomagnetic observatories used in the spherical harmonic analysis of the quiet-day records for **a** North America, **b** Europe, **c** Central Asia, **d** East Asia. (Station names and coordinates are given in Campbell and Schiffmacher, 1985.)

fitted to each of the new, more limited data sets, and further histograms were drawn to determine the distribution of the points about these curves. Values at the tails of the histograms were excluded and final determinations made of the best exponential representations of the data sets. Table 1 and Fig. 4 give the exponential depth-conductivity functions for the four regions after the exclusion of points at the distribution tails. Figure 5 shows the data points remaining after exclusion of distribution tails about the exponentials of Fig. 4.

Discussion

Although the results all indicated a general exponential increase of conductivity with depth from about 30–650 km, slightly different distributions of the values were obtained for the separate regions. In addition, there seemed to be some evidence for discontinuities near 225–300 km and near 450–600 km. These locations are near phase change depths identified on seismic records (Dziewonski and Anderson, 1981). At depths less than about 275 km the North American conductivity seemed to be significantly higher than that of the other three regions. At depths greater than about 275 km there seemed to be a bifurcation of the East Asian values, a main branch providing slightly greater conductivities than the other two regions and a minor branch with lower conductivities.

Most previous determinations of deep earth conductivity (c.f. Banks, 1969; Lahiri and Price, 1939) used the global data in such a way that an average, spheri-

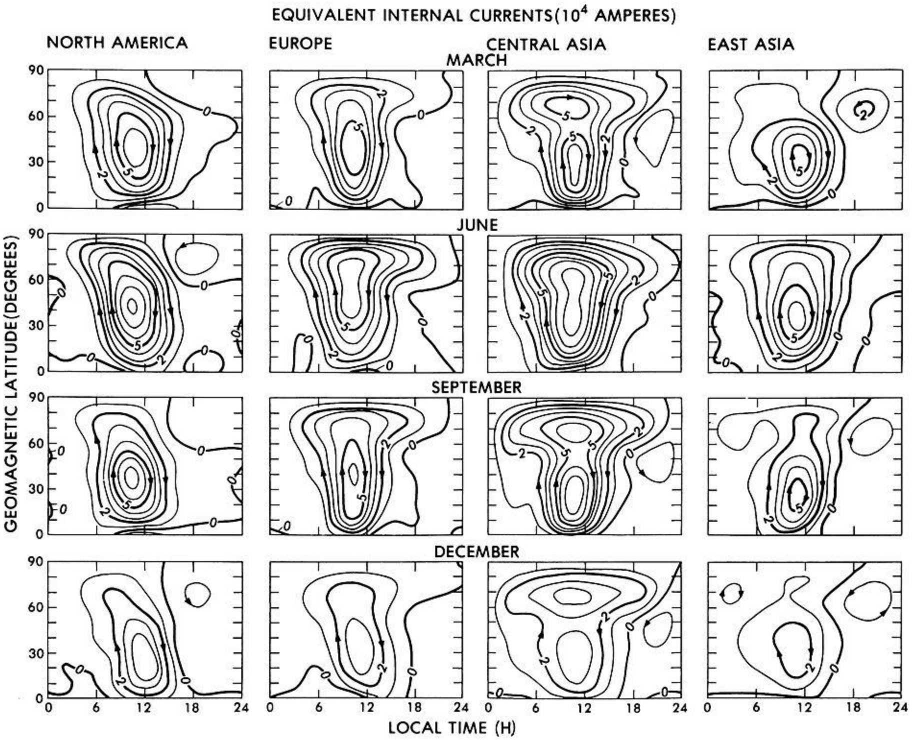

Fig. 2. Equivalent internal induced current for Sq daily variations of field in continental regions of North America (*first column*), Europe (*second column*), Central Asia (*third column*) and East Asia (*fourth column*). Examples for the four selected months of March, June, September and December are given in the top to bottom rows respectively. Each pattern in local-time versus latitude coordinates shows the equivalent current contours in 10^4-A steps with *arrows* for the required flow direction. A midnight zero current level was assumed

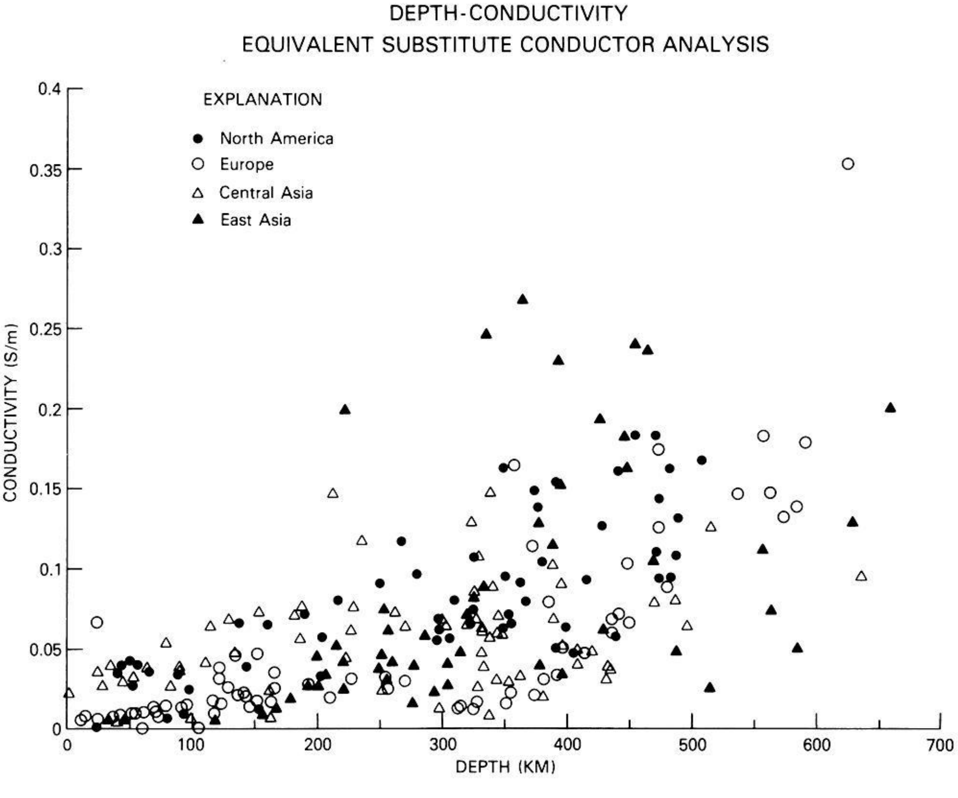

Fig. 3. Depth-conductivity values from Eqs. (10) and (11) obtained by application of the spherical harmonic analysis coefficients to Eqs. (7) and (8). The evaluations are separated for the North American, European, Central Asian and East Asian regions

cally symmetric profile was obtained. The method presented here shows some separation of regions, with slightly differing distributions of conductivity beneath the three continental regions. The large differences in the source and induced currents of the three regions justify the regional separation in the analysis. If the observatory data of all three regions had been included in a single analysis a conductivity profile close to the mean distribution of all the points in Fig. 5 would have been obtained.

We would like to assume that the differences in the exponential curves of Fig. 4 represent the differences in

Table 1. Exponential representations of conductivity

Region	Approx. depth d (km)	Conductivity σ(s/m)
North America	30–275	0.031 exp(0.0045d)
	275–500	0.027 exp(0.0032d)
Europe	10–275	0.0097 exp(0.0052d)
	275–620	0.0012 exp(0.0089d)
Central Asia	20–300	0.033 exp(0.0032d)
	300–640	0.041 exp(0.0011d)
East Asia	30 475	0.0049 exp(0.0085d)
	275–650	0.0049 exp(0.0053d)

conductivity beneath the three regions. The problem, of course, is that the stations used to sample each region are located over a variety of upper mantle conditions. Certainly, because the analysis excluded low amplitude values and removed distribution outliers, those parts of a region beneath the more intense source currents and those stations above similar conductivity profiles are emphasized in the results.

The electrical conductivity, σ, of the multiphase silicates expected to exist in the upper mantle is thought to vary with the temperature, T, roughly as

$$\sigma = C e^{-D/T}, \tag{18}$$

where C and D are constants for the average characteristics at a given depth (Shankland and Waff, 1977). Thus, for a given composition and principal phase of the silicates in the upper mantle, as the temperature increases with depth the conductivity also increases. In regions of thin crust, where upper mantle magma is closest to the surface, measurements of the heat flow have larger values. Pollack and Chapman (1977) published global heat-flow contours and related this information to the thickness of the earth's lithosphere. The conductivity profiles of the first few hundred kilometres should show lower values for thicker lithospheres (or lower heat-flow values). Taking those several stations not too far from the Sq current focus as the significant ones, it seems to us that Pollack and Chapman's (1977) lithosphere is thinner beneath the North American group than the other three groups, justifying the differences in conductivity profiles that we found down to about 275 km. However, the lithospheric differences are not very clear.

Anderson and Dziewonski (1984) used a seismic tomography technique to map the earth's mantle in three dimensions. They identified large-scale convective heat-flow patterns beneath the continental regions, which would produce regional electrical conductivity differences of the type shown in Fig. 5.

It is also possible that the two branches of the East Asia profile below 275 km show the effect of the subducting oceanic slab on the important stations of that region, but certainly this cannot be confirmed at present.

In summary, Schmucker's (1970, 1979) method of determining effective depth and conductivity was applied to data from four separated continental regions. In all cases the conductivity increased exponentially with depth. There appeared to be distinct discontinuities near 225–300 km and near 450–600 km, and there were significant differences in conductivity profiles for the four regions. Although the differences seemed real, they could not be simply explained because

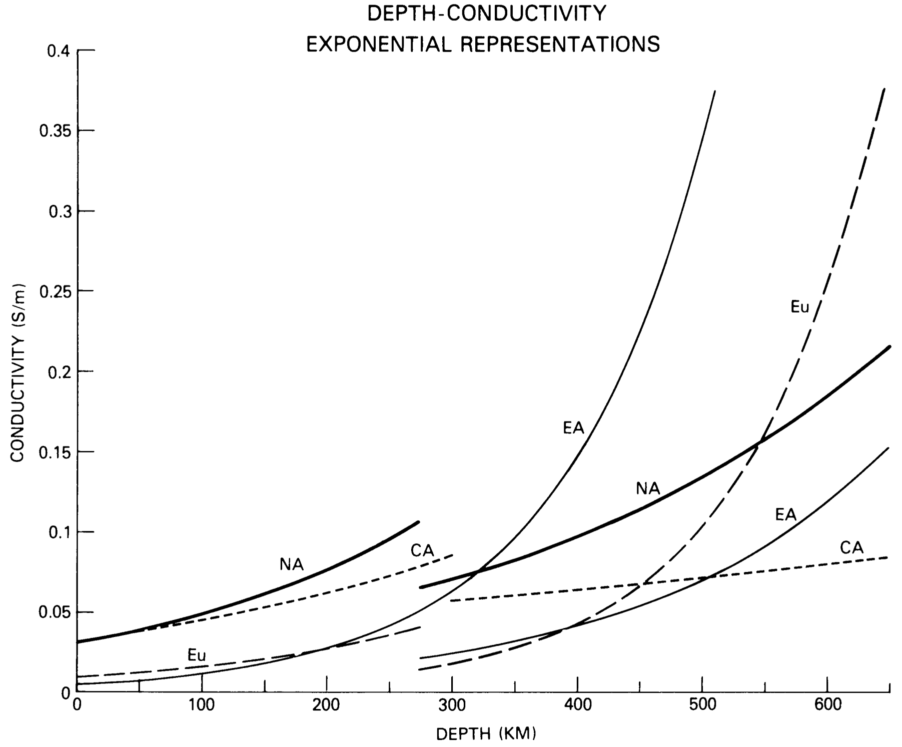

Fig. 4. Best exponential representations of depth-conductivity data given in Fig. 3. Separate curves are shown for North America (*NA*), Europe (*Eu*), Central Asia (*CA*) and East Asia (*EA*). The functions are listed in Table 1

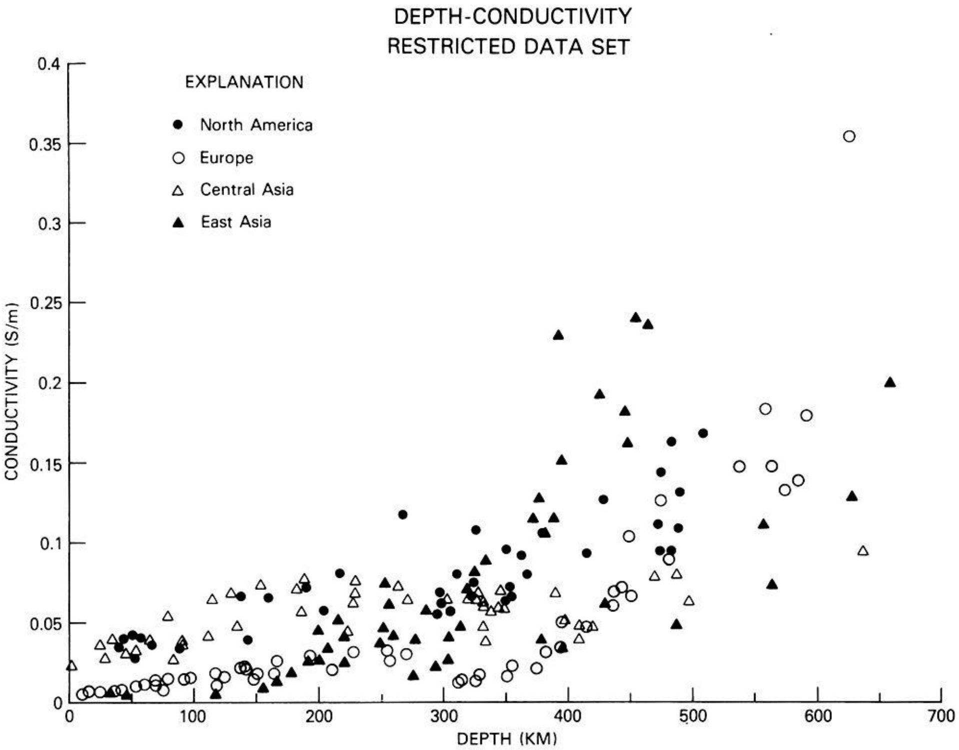

Fig. 5. Depth-conductivity values of Fig. 3, restricted by removal of the normal distribution tails about exponential curves given in Fig. 4. Separate groups represent North America, Europe, Central Asia and East Asia

there was an unknown mixture of contributions to the computations by the selected regional observatories.

Acknowledgements. We wish to thank Professor Schmucker of the University of Göttingen for his assistance in interpreting his effective-conductivity analysis method. We also thank the staff of World Data Center A for Solar Terrestrial Physics for providing magnetograms and for their stimulating scientific discussions.

References

Anderson, D.L., Dziewonski, A.M.: Seismic tomography. Sci. Am., **251**, 58–66, Oct. 1984

Banks, R.J.: Geomagnetic variations and the electrical conductivity of the upper mantle. Geophys. J. R. Astron. Soc., **17**, 457–487, 1969

Campbell, W.H., Anderssen, R.S.: Conductivity of the subcontinental upper mantel: An analysis using quiet-day geomagnetic records of North America, J. Geomagn. Geoelectr., **35**, 367–382, 1983

Campbell, W.H., Schiffmacher, E.R.: Quiet ionospheric currents of the Northern Hemisphere derived from geomagnetic field records. J. Geophys. Res., **90**, 6475–6486, 1985

Chapman, S., Bartels, J.: Geomagnetism. Oxford: Clarendon Press, 1940

Dziewonski, A.M., Anderson, D.L.: Preliminary reference earth model. Phys. Earth Planet. Inter., **20**, 297–356, 1981

Lahiri, B.N., Price, A.T.: Electromagnetic induction in nonuniform conductors and the conductivity of the earth from terrestrial magnetic variations. Phil. Trans. R. Soc. London, A**237**, 509–540, 1939

Pollack, H.N., Chapman, D.S.: The flow of heat from the Earth's interior. Seis. Am. **237**, 60–76, 1977

Schmucker, V.: An introduction to induction anomalies. J. Geomagn. Geoelectr., **22**, 9–33, 1970

Schmucker, V.: Erdmagnetische Variationen und die elektrische Leitfähigkeit in tieferen Schichten der Erde. Sitzungsber. Mitt. Braunschw. Wiss. Ges., **4**, 45–102, 1979

Shankland, T.J., Waff, H.S.: Partial melting and electrical conductivity anomalies in the upper mantle. J. Geophys. Res., **82**, 5409–5417, 1977

Received March 8, 1985/Revised version July 17, 1985
Accepted July 31, 1985

J Geophys (1986) 59:62–66

Journal of Geophysics

Paleomagnetism of the tertiary intrusives from Chalkidiki (northern Greece)

D. Kondopoulou[1] **and M. Westphal**[2]

[1] Geophysical laboratory, University of Thessaloniki, Thessaloniki, Greece
[2] Institut de Physique du Globe, Strasbourg, France

Abstract. Paleomagnetic measurements made on Eocene-Oligocene intrusives of Chalkidiki (northern Greece) have given normal and reversed directions. The mean direction is $D=37°$, $I=30°$, $\alpha_{95}=9°$ and the pole is 50°N, 140°E. This direction indicates a clockwise rotation of about 25° for Chalkidiki, similar to the rotations observed in western Greece but different from Bulgarian results.

Key words: Paleomagnetism – Northern Greece – Chalkidiki – Oligocene – Rotation

Introduction

Paleomagnetic results from western Greece (Epirus, Ionian islands), in the external zones of the Hellenides, have shown major clockwise rotations of 50°–60° (Laj et al., 1982; Horner and Freeman, 1983; Kissel et al., 1985). It was interesting to check if the core of the Dinaric-Hellenic chain had also suffered any rotations. We studied paleomagnetically the widespread Tertiary intrusives of Chalkidiki.

Geological setting

The Chalkidiki peninsula is part of the innermost zones of the Dinaric-Hellenic fold system. From east to west these "internal Hellenides" are constituted by:

a) The Rhodope massif. It is formed of old Proterozoic and Paleozoic rocks, mainly metamorphosed into amphibolites in Paleozoic times. This massif was the backbone of the Serbomacedonian and Vardar zones (Fig. 1).

b) The Serbomacedonian massif represents a crystalline complex, mainly constituted of Paleozoic and Precambrian rocks, as well as Hercynian and Alpine intrusives. During the Mesozoic it is considered to have acted as a continental margin (Mercier, 1966).

c) The Vardar zone has been separated into three subzones by Mercier (1966) which are, from east to west: the Peonias trough, the Paikon ridge and the Almopias trough; constituted by Jurassic limestones, a metamorphic Trias-Jurassic basement, an ophiolitic sequence, upper Paleocene flysch and Miocene volcanism. Recent geological studies have distinguished a circum-Rhodopian zone between the Serbomacedonian massif and the Vardar zone (Kauffman et al. 1976). This zone extends towards Sithonia and near Mt. Athos gulf. It turns to the E–NE and appears again in the SE Rhodope.

The Serbomacedonian zone is cut by several granitic and granodioritic bodies whose ages were poorly known until recently. The Sithonia peninsula is mainly formed by several plutons of granodiorites and monzonites (Soldatos et al., 1976). In the main Chalkidiki body we find the Arnea and the Gomati intrusives. The Arnea body is a schistosed, medium-grained granite similar to the Sithonia plutonites. The Gomati complex is a hornblende diorite. More to the east, two other granitic complexes are found; one near Ouranopolis, at the beginning of Mount Athos, intruded in metasediments. The other one is the Stratoni-Olymbias complex with a granodioritic to calcalkaline granite.

There is only little stratigraphic evidence for the age of these intrusives. But two age determinations by the K-Ar method on biotites have been obtained. One by Montigny (personal communication) on Sithonia peninsula (paleomagnetic sampling site SA) with an age of 40.5±1.5 Ma and the second one near sites STR and MDL by Papadakis (1971) with an age of 30.5±1.5 Ma. We can thus estimate that these intrusives are Upper Eocene to Lower Oligocene in age.

Sampling and measurements

Oriented hand-samples were collected at several sites in Sithonia eight sites), Arnea (one site), Ouranopolis (one site) and Stratoni-Olymbias (two sites). At each site, three–seven samples separated by several metres were taken. The samples were then drilled in standard 25-mm cores and measured with a Digico spinner magnetometer. The samples were stepwise demagnetized, either by alternating field or thermally.

Results

For most of the formation sampled, the intensity of natural remanent magnetization is between 1 and 100 mA/m. Some sites, for instance BO, CR, SA, LIN had very stable monocomponent magnetizations with high blocking temperatures and high coercive forces. Other sites (ZIB, MDL) had much softer magnetizations with a strong secondary component eliminated at 25 mT and with a median destructive field

---

Offprint requests to: M. Westphal, Institut de Physique du Globe, 5 rue Desartes, F–67084 Strasbourg Cedex, France

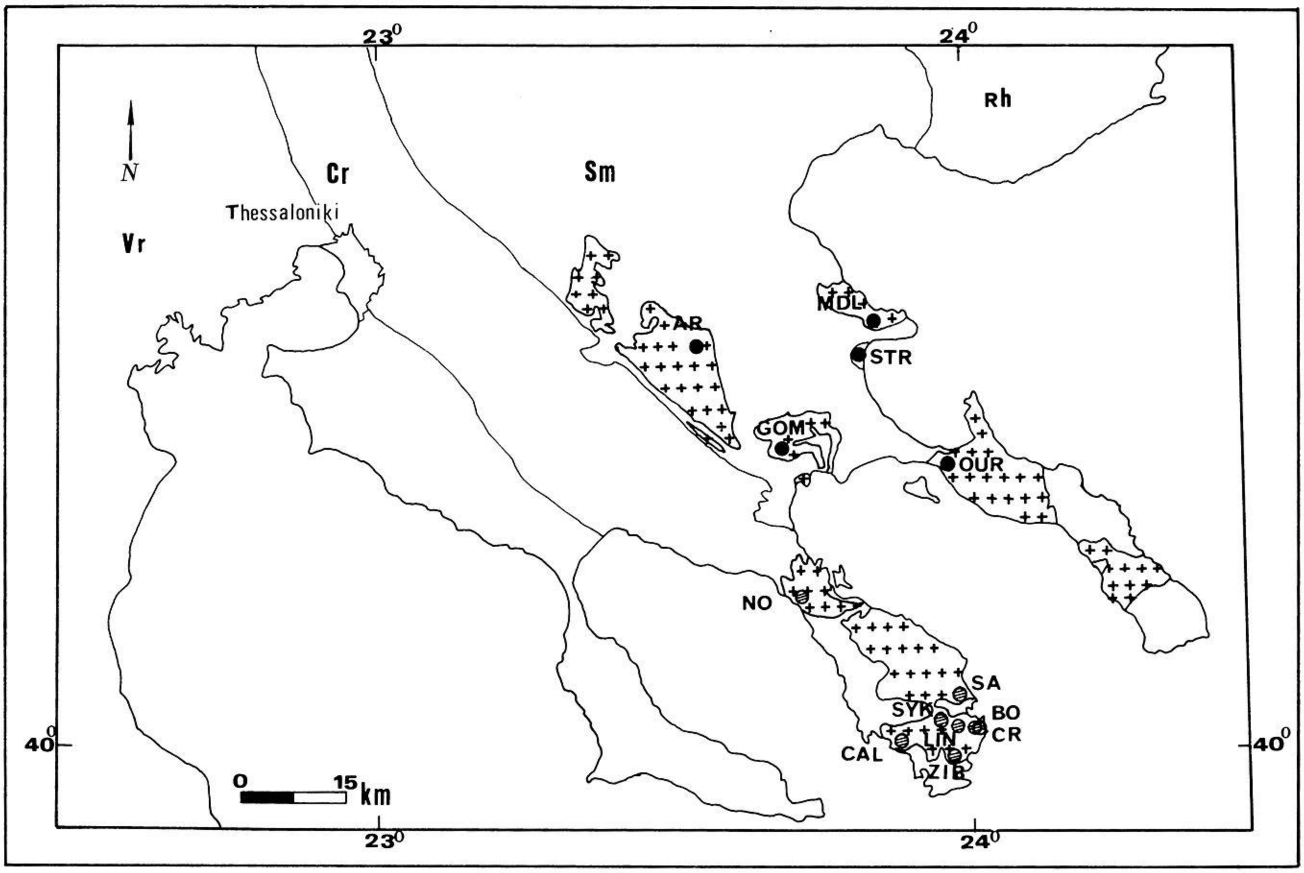

Fig. 1. Outline of Chalkidiki with sampling sites (and sites names) and granitic and granodioritic intrusives. *Rh* Rhodope massif, *Sm* Serbomacedonian zone, *Cr* Circum Rhodope zone, *Vr* Vardar zone

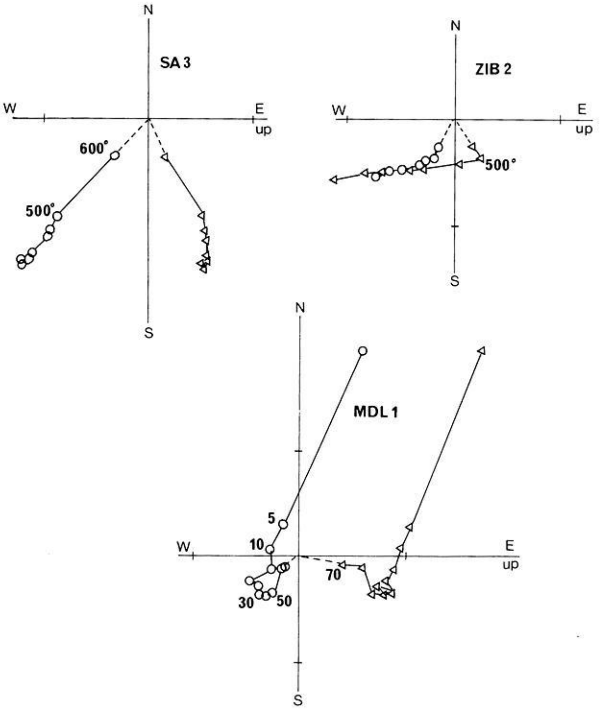

Fig. 2. Examples of demagnetization; thermal and by alternating fields. *Circles*: projection of the vector in the horizontal plane. *Triangles*: projection in the vertical, north-south plane. Numbers indicate temperatures (° C) or field (in mT)

for the main component of about 50 mT (Fig. 2). After demagnetization three groups of characteristic remanent magnetization directions were found:

- reversed directions with $D=216°$, $I=-32°$ corresponding to sites NO, CAL, ZIB, SA, MDL and OUR
- normal directions nearly antiparallel to the first group: $D=38°$, $I=29°$ corresponding to sites LIN, SYK, BO and CR
- normal directions close to the present dipole field: sites GOM and AR.

At site STR the scatter of directions was too large even after demagnetization and no characteristic remanent magnetization could be defined. We could only observe that a few samples had normal or reversed components close the characteristic directions of the first two groups.

Differences in behaviour between different sites were also found in IRM acquisition curves. Two extreme cases are shown in Fig. 3. MLD 4 shows a very quick increase in magnetization, and saturation is reached at about 0.1 T. This is probably due to multidomain magnetite grains and may explain the strong and soft secondary components (see Fig. 2). The other extreme is shown by OUR 6. It is a metasediment intruded and reheated by granitic sills. The IRM aquisition curve grows slowly and saturation is reached only above 0.5 T. Most of the NRM is destroyed only at high temperature above 600° C showing that a great part of the magnetization is carried by fine-grained haematite. Other sites show intermediate curves. The characteristic magnetization is probably carried by fine-grained haematite

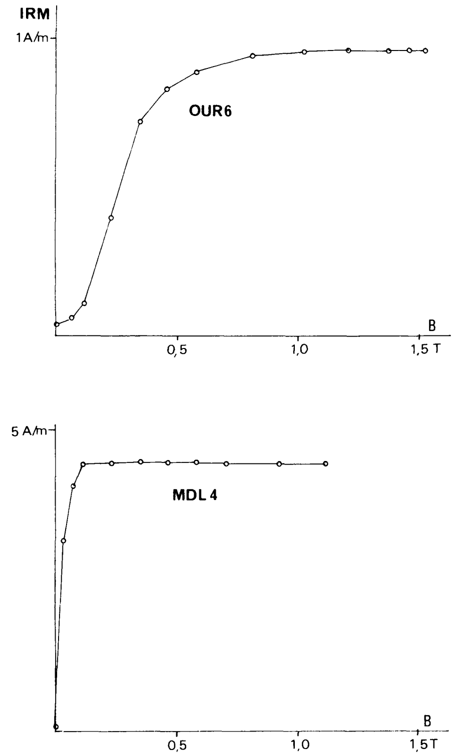

Fig. 3. Isothermal remanent magnetization acquisition curves for two samples. B: field in Tesla. Magnetization is in A/m

and secondary components, when present, by multidomain magnetite.

At site OUR only metasediments gave reliable results. A bedding plane can be seen there and if we use it as a paleohorizontal marker we see that the tectonic-corrected direction (Table 1) is in better agreement with other sites than the uncorrected direction. We have thus retained this corrected direction. Unfortunately, no paleohorizontal evidence could be seen at other sites.

Discussion

Except for sites AR and GOM, normal and reversed directions are nearly antiparallel. Thus, we can assume that almost all common secondary magnetizations have been eliminated. We feel also that the two sites AR and GOM are significantly different from other site means, although the number of sites is too low to apply statistical tests. We see at least in Table 1 that the scatter is strongly reduced when we eliminate these two sites: k increases from 15–28 for normal and reversed sites, from 13 to 152 with normal sites only. Therefore, we decided to use the mean direction calculated with ten sites: $D=37°$, $I=31°$, $k=28$, $\alpha_{95}=9°$.

This mean CARM direction is significantly different from the axial dipole field of $D=0°$, $I=50°$ in the sampling area. The mean pole position for stable Europe and for about 35 Ma is 83° N and 136° E (Westphal et al., 1985). The corresponding field direction is $D=8°$ and $I=57°$. The direction obtained in Chalkidiki is also significantly differ-

Table 1. Characteristic remanent magnetization of Chalkidiki intrusions. Site: site name, N: number of samples used in the statistics; N_O: number of samples collected in the field; D: declination; I: inclination; k, α_{95}: Fisher statistical parameters; polarity: N-normal, R-reversed

Site	N/N_O	D(°)	I(°)	k	α_{95}	Polarity	
NO	3/3	240	−32	8000	1	R	
CAL	6/7	193	−19	23	14	R	
ZIB	4/4	220	−36	51	13	R	
LIN	4/4	35	20	37	17	N	
SYK	6/6	37	28	103	7	N	
BO	4/4	38	32	108	9	N	
CR	3/3	41	34	43	19	N	
SA	7/4	215	−20	30	11	R	
STR	0/6	scattered					
MDL	6/6	224	−58	176	5	R	
OUR	3/6	219	7				uncorrected
		213	−24	83	13	R	corrected
AR	3/4	1	62	142	10	N	
GOM	3/4	354	62	44	19	N	
Means							
Overall mean							
	12	33	36	15	11		
Normal sites							
	6	29	41	13	19		all sites
	4	38	29	152	7		without AR+GOM
Reversed sites							
	6	216	−32	17	16		
Retained mean							
	10	37	31	28	9		

Pole: 50° N 139° E dp=6° dm=10°
(mean sites coordinates: 40.2° N 23.8° E)

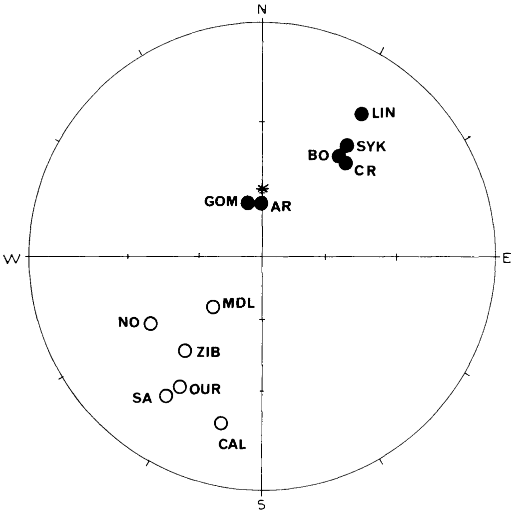

Fig. 4. Stereogram showing the mean characteristic directions for Chalkidiki. *Solid circles*: positive inclination; *open circles*: negative inclination; *star* is present-day dipole field direction

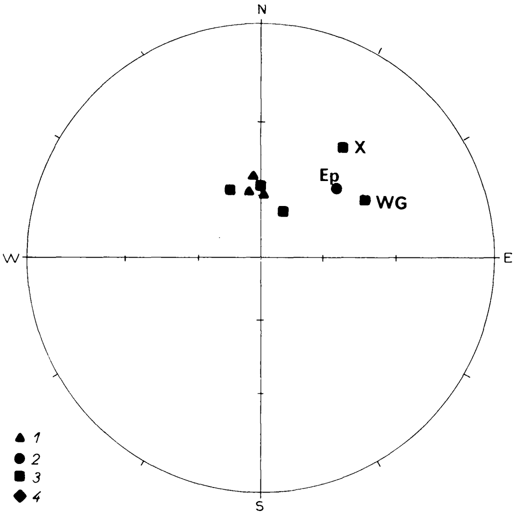

Fig. 5. Stereogram showing the magnetic directions obtained in continental Greece and in Bulgaria. *1* Cretaceous; *2* Paleocene; *3* Oligocene; *4* Lower Miocene. *X* Chalkidiki (this paper); *Ep* Epirus (Horner and Freeman); *WG* Western Greece (Kissel et al.). Other results are Bulgarian ones

ent from this one. There is a strong difference in declination, but also in inclination. The inclination obtained is too low. An average tilt toward the north may explain a part of the inclination difference of about 30°, but not all of it. Even site OUR, where a tectonic correction could be made, has too low an inclination (−24°).

Paleomagnetic results for similar periods have been obtained in western Greece (Horner and Freeman, 1983; Kissel et al., 1985), in the Rhodope massif and in the Stara Planina chain (Nozharov and Petkov, 1976a, 1976b, 1977; Nozharov et al., 1977a, 1977b). Figure 5 and Table 2 show a clear difference of directions between continental Greece and more northern parts. The Rhodope and other Bulgarian results are more or less close to a north-south declination and have an inclination of about 50°–70°. Inland Greece, mainly the external zones of the Hellenides, have an easterly declination of about 30°–50° and shallower inclinations.

Table 2. Paleomagnetic results from the Dinaric-Hellenic chain. *D*, *I*: declination, inclination, α_{95} and pole position. Ref.: 1 Nozharov et al. (1977a); 2 Nozharov et al. (1977b); 3 Nozharov and Petkov. (1976a); 4 Nozharov and Petkov. (1976b); 5 Nozharov and Petkov. (1977); 6 Horner and Freeman (1983); 7 Kissel et al. (1985); 8 This paper

	D (°)	*I* (°)	α_{95} (°)	Pole (° N)	(° E)	Ref.
Bulgaria						
Upper Cretaceous						
Sredna Gora	357	52	19	83	224	2
Srednogoriye	353	59	14	85	254	1
Maritsa	2	59	12	88	151	4
Oligocene						
Madjarovo	337	55	25	73	294	3
	27	66	9	70	85	3
Sredna Gora	high scatter					2
Lozen	355	56	24	84	245	5
Greece						
External Hellenides						
Paleocene						
Epirus	47	44	4	48	116	6
Oligocene						
Nortwestern Greece	58	39	5	38	112	7
Internal Hellenides						
Eocene-Oligocene						
Chalkidiki	37	31	9	50	141	8

The Chalkidiki results are closer to the western Greece results than those of the Rhodope and Stara Planina. But sites GOM and AR are similar to the latter. Upper Cretaceous results from Bulgaria are similar to Oligocene results and show that no rotation occurred during this period for this region. This means that, although the different tectonic zones from the Hellenides look more or less rectilinear, important rotations occurred in them. The external zones have been rotated clockwise through 60° since the Oligocene. This rotation is clearly shown by Kissel et al. (1985) and Laj et al. (1982) as a rotation in two phases: the first at about 13 Ma and the second since 5 Ma. The more internal zone in Chalkidiki has also rotated in the same direction. At the present time wo do not yet know if the different results from sites GOM and AR are due to a younger age of these intrusions or a later remagnetization. Thus, we cannot yet conclude about the location of the limit between the unrotated parts seen in Bulgaria and the rotated part of Chalkidiki. We have also to explain the discrepancy in inclination.

Acknowledgements. We would like to thank Dr. Ph. Voidomatis and Dr. S. Dimitriadis for help given in the field work. One of us acknowledges the French Ministry of External Relations for a travel grant.

References

Horner, F., Freeman, R.: Paleomagnetic evidence from pelagic limestones for clockwise rotation of the ionian zone, Western Greece. Tectonophysics **98**, 11–27, 1983

Kauffman, J., Kockel, F., Mollat, H.: Notes on the stratigraphic and paleogeographic position of the Svoula formation in the innermost of the Hellenides (Northern Greece). Bull. Soc. Geol. F. **18**, 225–230, 1976

Kissel, C., Laj, V., Muller, C.: Tertiary geodynamical evolution of northwestern Greece: paleomagnetic results. Earth Planet. Sci. Lett. *72*, 190–204, 1985

Laj, C., Jamet, M., Sorel, D., Valente J.P.: First paleomagnetic results from Mio-Pliocene series of the Hellenic sedimentary arc. Tectonophysics **86**, 45–67, 1982

Mercier, J.: Mouvements orogéniques, épirogéniques et magmatisme d'âge jurassique supérieur-éocrétacé dans les zones internes des Hellenides (Macédoine, Grèce). Rev. Géogr. Phys. et Géol. Dyn. **8**, 265–278, 1966

Nozharov, P., Petkov, N.: Palaeomagnetism and palaeomagnetic stability of certain magmatic rocks in the Madjavoro ore field (in russian). Bulgarian Geophys. J. **11** (4), 90–104, 1976a

Nozharov, P., Petkov, N.: Paleomagnetism of some rocks of upper Cretaceous plutonian in the Maritsa neointrusive zone. C.R. Acad. Bulg. Sc. **29** (9), 1285–1288, 1976b

Nozharov, P., Petkov, N.: Paleomagnetism of some rocks forming the Lozen paleovulcan (East Rhodopes). C.R. Acad, Bulg. Sc. **30** (3), 359–361, 1977

Nozharov, P., Veljovic, D., Petkov, N.: Results of paleomagnetic studies of some magmatic rocks in Srednogoriyé and Strandja. C.R. Acad. Bulg. Sc. **30** (4), 531–533, 1977a

Nozharov, P., Veljovic, D. Petkov, N.: Paleomagnetism of some Upper Cretaceous and Tertiary vulcanites in Sredna Gora and Eastern Rhodopes. C.R. Acad. Bulg. Sc. **30** (6), 843–845, 1977b

Papadakis, A.: On the age of the granitic-intrusion near Straton-ion, Chalkidiki (Greece). Ann. Geol. Pays Helléniques **23**, 297–300, 1971

Soldatos, K., Sapountzis, E., Eleftheriades, G., Christofides, G.: Contribution to the study of the Sithonia plutonic complex. Ann. Geol. Pays Helléniques **28**, 62–134, 1976

Westphal, M., Bazhenov, M., Lauer, J.P., Pechersky, D., Sibuet, J.C.: Paleomagnetic implications on the evolution of the Tethys belt from the Atlantic ocean to Pamir since Trias. Tectonophysics 1985 (in press)

Received March 11, 1985; Revised version September 4, 1985
Accepted September 6, 1985

J Geophys (1986) 59:67–72

Journal of Geophysics

Absolute intensity of daytime whistlers at low and middle latitudes and its latitudinal variation

M. Hayakawa[1], **Y. Tanaka**[1], **K. Ohta**[2], **and T. Okada**[1]

[1] Research Institute of Atmospherics, Nagoya University, Toyokawa, Aichi, 442, Japan
[2] Department of Electronic Engineering, College of Engineering, Chubu University, Kasugai, Aichi, 487, Japan

Abstract. The statistical study on the field intensity of daytime whistlers at low (geomag. lat. 25°) and middle (35°) latitudes has been made, based on a lot of data obtained by the field-analysis direction finding system based on the simultaneous measurement of two horizontal magnetic field components and one vertical electric field component. At low latitude, the maximum absolute intensity is estimated to be 250 μV/m, while the corresponding maximum intensity at middle latitude amounts to 600 μV/m, being about 2.4 times that at low latitude. This latitudinal variation of daytime intensity is interpreted in terms of the joint influence of (a) source activity, (b) magnetospheric propagation effect and (c) ionospheric transmission loss. As the result, it is found that whistlers at each station are attributed to ducted propagation in the magnetosphere and have exited the ionosphere close to each observing station, as determined by the direction finding results. Furthermore, the cloud distributions observed by meteorological satellites have yielded that the duct entrance point of whistlers at each station fall within the active thunderstorm region. Hence, we can conclude that daytime whistlers are originated in the active thunderstorms in each conjugate region, are trapped in field-aligned ducts and followed by nearly the vertical exit from the ionosphere at each station. Finally the latitudinal difference of the intensity is satisfactorily interpreted in terms of the difference in the ionospheric transmission loss on the assumption of the same source intensity at each conjugate point and of no amplification in the magnetosphere.

Key words: Whistler – Magnetosphere – Absolute intensity – Direction Finding – Ducted propgation – Thunderstorm Activity – Ionospheric transmission loos

1. Introduction

The measurement of absolute intensities of VLF waves including whistlers and VLF/ELF emissions having propagated through the magnetosphere provides useful information not only on their propagation characteristics such as the ionospheric absorption and magnetospheric propagation (Helliwell, 1965; Hayakawa and Tanaka, 1978), but also on the wave amplification as a consequence of wave-particle interactions (Helliwell et al. 1973; Lohrey and Kaiser, 1979; Carpenter and LaBelle, 1982).

The present paper is concerned with the measurement of field intensity of whistlers. The apparent field strength of a whistler can be measured in a few ways. If the whistler is very strong, it is sufficient simply to record the amplitude as a function of time. From this record, the maximum, minimum and average values are readily be obtained (Helliwell, 1965). Another method, less quantitative, is to match an artificially generated whistler of known amplitude aurally with the natural whistler in question (Iwai and Outsu, 1958). The absolute intensities of whistlers cannot be accurately estimated unless both the wave normal direction and wave polarization are specified, and the measurement of them essentially requires the adoption of the direction finding. During the last decade, several kinds of VLF direction finding methods have been proposed (Tanaka, 1972; Cousins, 1972; Bullough and Sagredo, 1973; Tsuruda and Hayashi, 1975; Tanaka et al., 1976; Okada et al., 1977, 1981; Leavitt et al., 1978; Ohta et al., 1984). The results on the ionospheric exit regions have been extensively utilized to study the whistler propagation mechanism and duct properties (Matthews et al., 1979; Lester and Smith, 1980; Hayakawa et al., 1981 a, b; Strangeways et al., 1983) and also the magnetospheric plasma dynamics (Sagredo and Bullough, 1973; Carpenter, 1980). However, reports are as yet very lacking on the absolute intensity of whistlers, because most of the direction finding systems except those by Okada et al. (1977, 1981) and Ohta et al., (1984) are only intended to find the wave normal directions without any interest in wave polarization.

The present paper deals with the measurement of the absolute intensity of whistlers as estimated by our field-analysis direction finding method based on the simultaneous measurement of two horizontal magnetic field components and a vertical electric field component (Okada and Iwai, 1980; Okada et al., 1981; Ohta et al., 1984), which determines not only the wave normal direction, but also the wave polarization. The measurements have been made at two different geomagnetic latitudes; a low-latitude station of Yamaoka (geomag. lat. 25° N) and a middle-latitude station of Moshiri (35° N), and we restrict ourselves to daytime whistlers because there exist many unsolved factors in the propagation of nighttime whistlers (Hayakawa and Tanaka, 1978). The intensity at each station has been presented in Sect. 2 and 3, respectively. Section 4 describes the latitudinal variation of the whistler intensity and the

---

Offprint requests to: M. Hayakawa

physical implications are discussed in terms of the joint influence of the source activity and the ionospheric and magnetospheric propagation characteristics.

2. Whistler intensity at Yamaoka (geomag. lat. 25° N)

The direction finding measurement at Yamaoka is intended to be fully automatic at a specific frequency of 5 kHz (Ohta et al., 1984) and the measurement has been continued since December, 1981. We have selected only events of high whistler activity (and, in turn, high intensity) and the summarized results are presented in Fig. 1. The data for these daytime events are based on nine events (the total number of whistlers used in deriving Fig. 1 is about 180.) and the local time (L.T.) of those events falls in the L.T. interval from ~15 h–~19 h (Hayakawa et al., 1985). The duration of all of the events is not larger than 2 h (Ohta et al., 1984; Hayakawa et al., 1985), those kind of occurrence burst being considered to be attributed to the life of a single duct as found by Hayakawa et al. (1983). The daytime intensity exhibits a relatively flat distribution in a range from 50–150 μV/m with a maximum occurrence at 100–125 μV/m. Then, the occurrence distribution of the intensity shows a decrease above 150 μV/m, and the peak intensity we have recorded is 225–250 μV/m.

Previously, Okada et al. (1977) carried out the field-analysis direction finding at Takayama (25°) very close to Yamaoka, but the observation period was too short to have a statistical study such as done in the present paper. They have succeeded in measuring the absolute intensity for a few whistlers during the most active period over a few days' observation interval. Their peak measured intensity at day was about 200 μV/m, which is found to be in good agreement with the present result.

As the measure of intensity, we use two quantities; one is the maximum intensity we have recorded and the other the intensity with maximum occurrence, which are 250 μV/m and 100–125 μV/m, respectively, at Yamaoka.

3. Whistler intensity at Moshiri (geomag. lat. 35°)

Although the direction finding at Moshiri was not automatic, the timing for the direction finding was made by monitoring the auxilliary real-time whistler analyzer (Okada et al., 1981; Hayakawa et al., 1983) in order to acquire as much useful direction finding data as possible. The observation was carried out for two months; January and February, 1978. The percentage occurrence of the field intensity of the most active daytime event; 22 January, 1978 (15:10–18:07 h L.T.) among the two months' observation period, is presented in Fig. 2. The total number of whistlers for this event amounted to more than two hundred, enabling us to have a statistical significance. The observing frequency is 5.6 kHz.

The figure indicates that a majority of whistlers have the field intensity in a range from 100 to 300 μV/m, and the most probable intensity is 250–300 μV/m. Furthermore, the number of whistlers become depleted sharply above the intensity of 300 μV/m, and the maximum intensity recorded at Moshiri is 600 μV/m.

Now we compare the maximum intensity (600 μV/m) and the intensity with maximum occurrence (250–300 μV/m) at Moshiri with the corresponding quantities at Yamaoka in Section 2. The maximum intensity at Moshiri is found to be 2.4 times that at Yamaoka, and the most probable intensity at Moshiri is again about 2.4 times that at Yamaoka. No matter whether we adopt the maximum recorded intensity or the most probable intensity, the intensity at Moshiri is always about 2.4 times larger than that at Yamaoka.

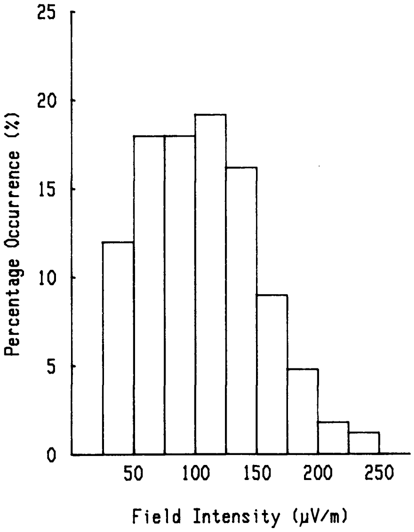

Fig. 1. Percentage occurrence of field intensity of daytime whistlers at Yamaoka (geomag. lat. 25°). The observing frequency is 5.0 kHz

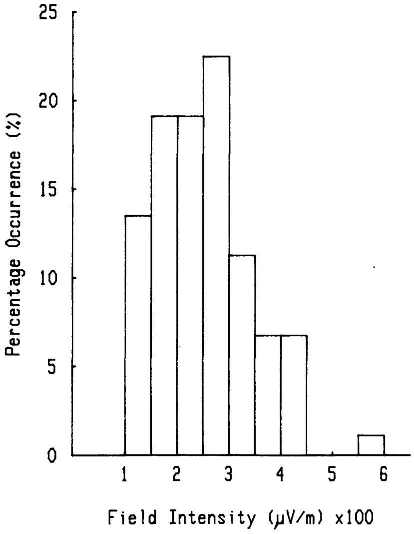

Fig. 2. Percentage occurrence of field intensity of daytime whistlers at Moshiri (geomag. lat. 35°). The observing frequency is 5.6 kHz

4. Latitudinal variation of the daytime whistlers intensity

The important factors determining the observed whistler intensity include, (a) the source activity of source intensity, (b) the ionospheric transmission loss passing through the ionosphere and (c) the propagation loss and/or amplification in the magnetosphere.

First we are concerned with the characteristics of daytime whistlers at Yamaoka in Sect. 2. The third point (c) on the propagation in the magnetosphere is studied first. The results of direction finding studies for all of those events have yielded that the ionospheric exit points are located

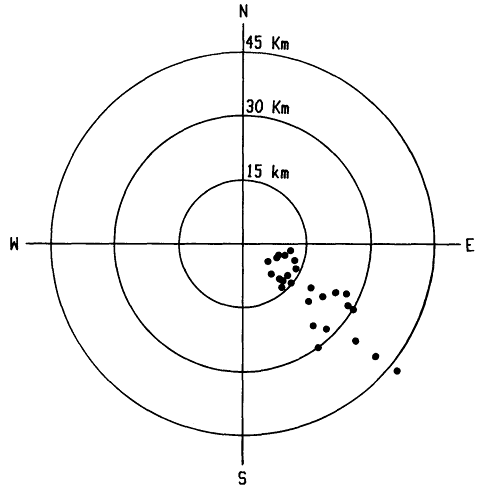

Fig. 3. An example of ionospheric exit points of daytime whistlers observed at Yamaoka at 16:00–16:50 h L.T. on 16th January, 1982

close to the observing station and also that those whistlers are identified as being attributed to the propagation entrapped in field-aligned ducts (Ohta et al., 1984; Hayakawa et al., 1985), so that we have negligibly small propagation loss in the magnetosphere. An example of the direction finding result on the ionospheric exit points of whistlers is illustrated in Fig. 3 for the event of ~16 h L.T. on 16th January, 1978. We now mention the amplification in the magnetosphere. Taking into account the results by Carpenter and LaBelle (1982) and Lohrey and Kaiser (1979), the whistler amplification seems to be possible even at $L < 2$, but only during major magnetic disturbances and for a number of days following those disturbances. However, the whistler data in the present study are not obtained during the severe magnetic disturbances, which enables us to consider that the amplification did not take place, at least, for our events analyzed. This supposion seems to be furthermore supported by the success of our interpretation of the latitudinal dependence of whistler intensity in terms of the ionospheric absorption loss alone, to be discussed below. Then, the source activity (a) at the duct entrance point in the opposite hemisphere is examined by means of the cloud distribution observed by the Japanese meteorological satellite, GMS 2. The cloud distribution for the event at the time close to the event in Fig. 3, is illustrated in Fig. 4 as an example, from which we understand that the duct entrance point falls within the active thunderstorm region. These kinds of case studies have given strong support to the similar conclusion based on the statistical map of atmospheric intensity (Tanaka and Hayakawa, 1980). Furthermore, we have examined the cloud distributions during more than 6 h including the relevant whistler active period, and it is found that the duct entrance point is always located in the active thunderstorm region during the relevant time, and hence we can conclude that the duration of whistler activity of the order of a few hours (1–2 h) is not controlled

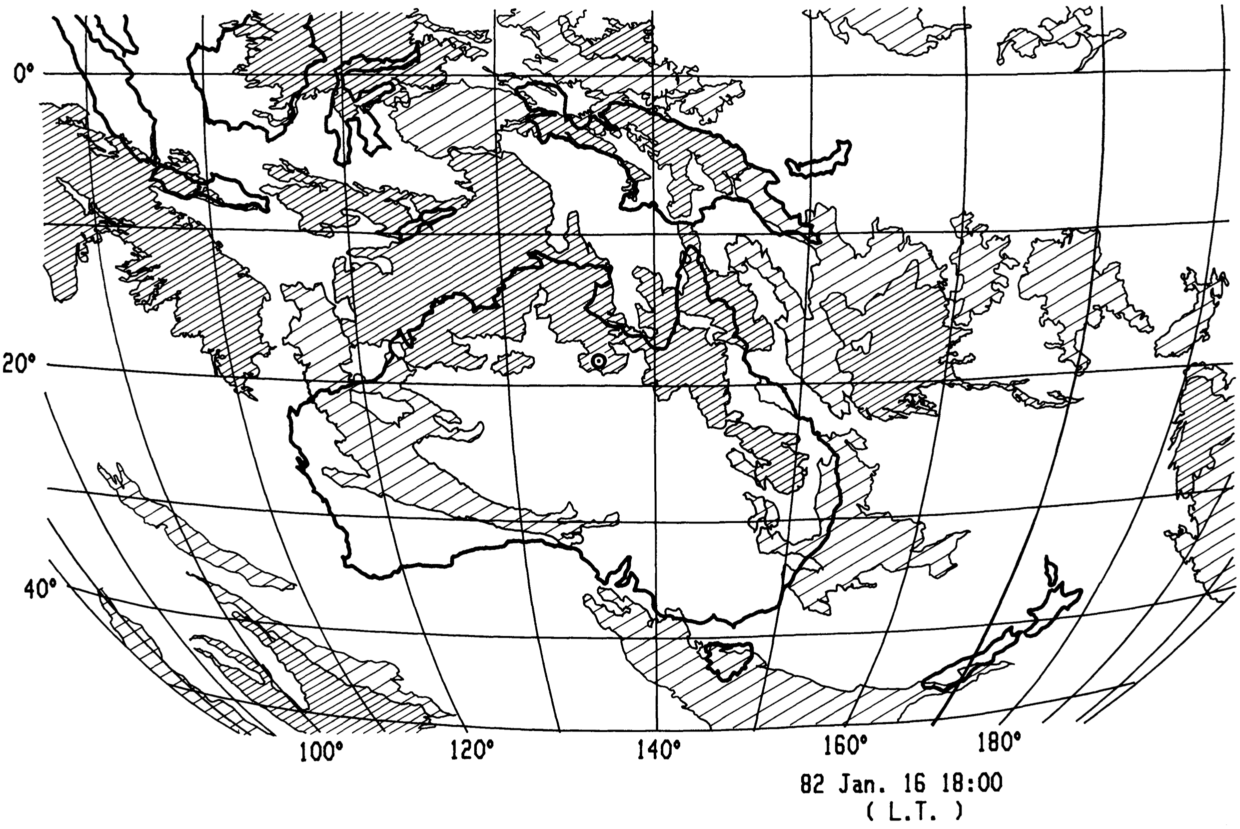

Fig. 4. The cloud distribution around the conjugate region of Yamaoka at 18:00 h L.T. on 16th January, 1982, being closest to the whistler active period in Fig. 3. *Densely-hatched region* indicates the active thunderstorm region, while *hatched region* the less active region. *The dot with a circle* indicates the conjugate point of Yamaoka, calculated by using the IGRF (1975) model

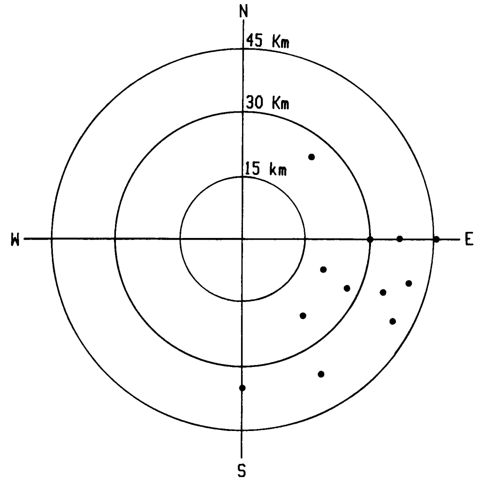

Fig. 5. Distribution of the ionospheric exit points of daytime whistlers observed at Moshiri during the most active period (16:00–16:05 h L.T.) on 22nd January, 1978

by the source activity, but by the duct lifetime itself, lending further support to the previous finding (Hayakawa et al., 1983; Ohta et al., 1984; Hayakawa et al., 1985). These facts have been extensively confirmed to be valid for all other events.

Next we pay attention to the characteristics of daytime whistlers at Moshiri in Section 3. The direction finding study by Hayakawa et al. (1981a) has indicated that whistlers for the event studied in the present paper have exited the ionosphere very close to the observing station of Moshiri, as shown in Fig. 5, where the ionospheric exit points are located at the time of maximum whistler activity (16:00–16:05 h L.T., 22 January, 1978). Consideration of those results suggests ducted propagation of whistlers in the magnetosphere (Hayakawa et al., 1985), as in the case of Yamaoka. Hence, we are able to assume no propagation loss in the magnetosphere. Furthermore, the magnetospheric amplification is not considered on the same reason mentioned in the previous paragraph of the observation at Yamaoka. Then, the corresponding source activity at the duct entrance region for this event has been examined by using the cloud distribution in Fig. 6, observed by the NOAA 5 satellite at the time (19:30 h L.T.) closest to the whistler peak (~16 h L.T.), though a few hours apart from the whistler peak. At 19:30 h L.T. the whistler activity was still not small, as seen in Hayakawa et al. (1981a). The duct entrance point is found to be located at the edge of the active thunderstorm region extending to the west. Although we have examined the NOAA cloud pictures before and after 19:30 h L.T., no maps have been available, on the cloud distributions around the conjugate point of Moshiri. Hence, we cannot say definitely that the duration of whistler occurrence of a few hours in this event is again attributed to the formation and decay of a duct, but it would be reasonable to accept it, from the considerations for the case of Yamaoka. We should add that the difference in observing frequency does not make any significant difference in the ducted propagation in the magnetosphere.

From the above considerations, daytime whistlers observed at Yamaoka and Moshiri are identified to originate in the active thunderstorm region at the conjugate point of each station, followed by vertical incidence into the ionosphere and ducted propagation in the magnetosphere and to be exited the ionosphere nearly from the zenith at each station.

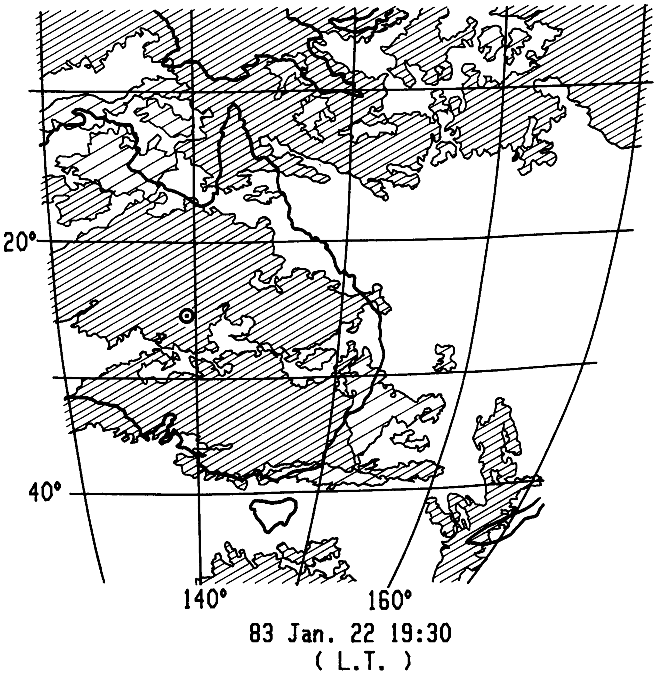

Fig. 6. Cloud distribution at 19:30 h L.T. on 22nd January, 1978, closest to the most active whistler period in Fig. 5

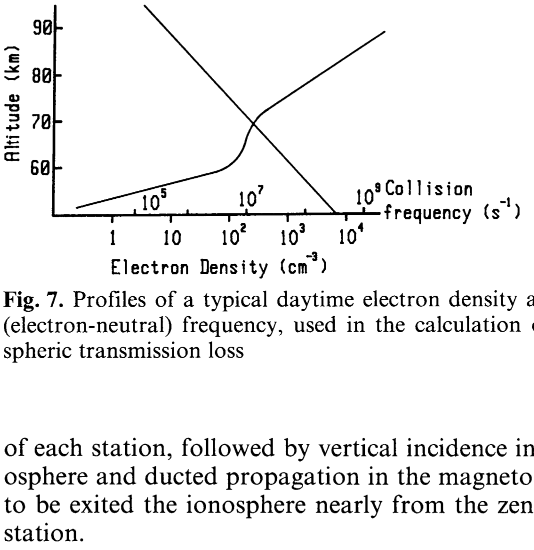

Fig. 7. Profiles of a typical daytime electron density and collision (electron-neutral) frequency, used in the calculation of the ionospheric transmission loss

The second factor (b) of the ionospheric transmission loss has been theoretically calculated by means of the full-wave computation by Pitteway and Jespersen (1966). Figure 7 gives a typical daytime electron density profile and the typical collision frequency profile. These profiles are assumed to be independent of geomagnetic latitude, but the gyrofrequency is varied with latitude according to the dipole model. Figure 8 illustrates the latitudinal dependence of the ionospheric transmission loss on the assumption of vertical incidence just for one transit through the ionosphere. One can find that this vertical incidence is validated at the duct entrance and at the wave emergence, as mentioned above. The figure indicates that the difference in the ionospheric transmission loss at Moshiri (35°) and Yamaoka (25°) is 4 dB, taking into account the difference in observing frequency, and the total difference is 2 × 4 dB = 8 dB, implying that the intensity at Moshiri is about 2.5

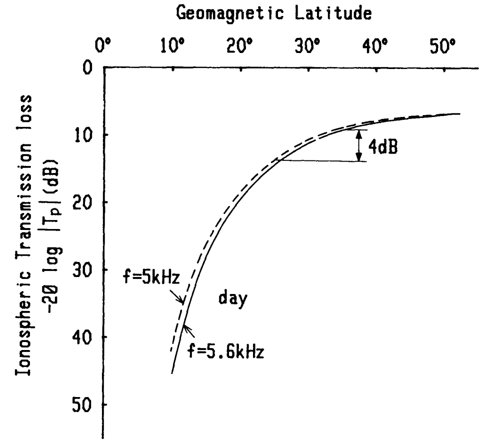

Fig. 8. Latitudinal dependence of the ionospheric transmission loss for vertical incidence (one transit through the ionosphere). T_p is the transmission coefficient of the penetrating mode defined in Pitteway and Jespersen (1966)

times that at Yamaoka, on the assumption that the source intensity is the same at the conjugate point of each station. This theoretical prediction seems to be in excellent agreement with the experimental findings summarized at the end of Sect. 3, and this enables us to suppose that the source intensity is not different at the conjugate points of two stations, Moshiri and Yamaoka. Furthermore, it is known that the source spectrum exhibits a negligibly small difference between 5.0 and 5.6 kHz (Taylor, 1963) and so the difference in observing frequency is considered to have no influential effect.

Finally, we briefly comment on the possibility of whistler amplification at middle and low latitudes. Our previous whistler studies (Hayakawa et al., 1969; Tanaka and Hayakawa, 1973a, b; Hayakawa and Tanaka, 1978) have yielded that the occurrence rate of whistlers increases abruptly from the onset of a magnetic storm and exhibits a maximum a few days after the storm. This experimental fact seems to be consistent with the property of whistler amplification reported by Carpenter and LaBelle (1982), which may lead us to suppose that those delayed enhanced occurrence (in turn, the intensity) of whistlers is indicative of such an amplification in the magnetosphere at $L<2.0$. In order to study these in a quantitative wave, we plan to make an application of the simultaneous measurement of absolute intensity of a causative atmospheric and the resultant whistler, simultaneous to the measurement of the corresponding particle precipitation based on the measurement of the phase variation of subionospheric VLF waves such as done by Lohrey and Kaiser (1979) and Carpenter and LaBelle (1982).

Acknowledgement. The authors wish te express their sincere thanks to Prof. J. Ohtsu of Nagoya University and Prof. H. Eguchi of Chubu University for their useful discussion. Thanks are also due to Japanese meteorological Agency for supplying the cloud maps by the GMS 2 satellite and we are indebted to Dr. D. Thiel of Griffith University, Australia who has obtained the NOAA cloud maps from Australian Meteorological Agency. The present work is partly supported by Japan Society of Promotion of Science and also partly by Takeda Science Foundation, to which we are grateful. Finally, we appreciate the continual encouragement of Prof. A. Kimpara, Emeritus Professor of Nagoya University.

References

Bullough, K., Sagredo, J.L.: VLF goniometer observations at Halley Bay, Antarctica, I. The equipment and measurement of signal bearing. Planet. Space Sci. **21**, 899–912, 1973

Carpenter, D.L. (1980): Fast fluctuations in the arrival bearing of magnetospherically propagating signals from the Siple, Antarctica. J. Geophys. Res. **85**, 4157–4166, 1980

Carpenter, D.L., LaBelle, J.W.: A study of whistlers correlated with bursts of electron precipitation near L = 2. J. Geophys. Res. **87**, 4427–4434, 1982

Cousins, M.: Direction finding on whistlers and related VLF signals. Tech. Rep. SEL-72-013, Radioscience Lab., Stanford Univ., 1972

Hayakawa, M., Ohtsu, J., Iwai, A.: Occurrence rate and dispersion of whistlers during magnetically disturbed periods at lower latitudes. Rep. Ionosph. Space Res. Japan **23**, 9–20, 1969

Hayakawa, M., Tanaka, Y.: On the propagation of low latitude whistlers. Rev. Geophys. Space Phys. **16**, 111–123, 1978

Hayakawa, M., Okada, T., Iwai, A.: Direction findings of medium-latitude whistlers and their propagation mechanism. J. Geophys. Res. **86**, 6939–6946, 1981 a

Hayakawa, M., Tanaka, Y., Okada, T., Iwai, A.: Goniometric direction finding for low-latitude whistlers and their propagation characteristics. J. Geophys. Res. **86**, 6781–6793, 1981 b

Hayakawa, M., Tanaka, Y., Okada, T., Ohtsu, J.: Time scales of formation, lifetime and decay of whistler ducts at low latitudes. Ann. Geophysicae **1**, 515–518, 1983

Hayakawa, M., Ohta, K., Tanaka, Y.: Further direction finding evidence on ducted propagation of low-latitude daytime whistlers and the duct structure To be published in Res. Lett. Atmosph. Electr., 1985

Helliwell, R.A.: Whistlers and Related Ionospheric Phenomena, p. 124. Stanford CA: Stanford University Press, 1965

Helliwell, R.A., Katsufrakis, J.P., Trimpi, M.L.: Whistler induced amplitude perturbation in VLF propagation. J. Geophys. Res. **78**, 4679–4688, 1973

Iwai, A., Outsu, J.: On an investigation of the field intensity of whistling atmospherics. Proc. Res. Inst. Atmos., Nagoya Univ. **5**, 50–52, 1958

Leavitt, M.K., Carpenter, D.L., Seely, N.T., Padden, R.R., Doolittle, J.H.: Initial results from a tracking direction finding receiver for whistler mode signals. J. Geophys. Res. **83**, 1601–1610, 1978

Lester, M., Smith, A.J.: Whistler duct structure and formation. Planet. Space Sci. **28**, 645–654, 1980

Lohrey, B., Kaiser, A.B.: Whistler induced anomalies in VLF propagation. J. Geophys. Res. **84**, 5121–5130, 1979

Matthews, J.P., Smith, A.J., Smith, I.D.: A remote unmanned ELF/VLF goniometer receiver in Antarctica. Planet. Space Sci. **27**, 1391–1401, 1979

Ohta, K., Hayakawa, M., Tanaka, Y.: Ducted propagation of daytime whistlers at low latitudes as deduced from the ground-based direction finding. J. Geophys. Res. **89**, 7557–7564, 1984

Okada, T., Iwai, A., Hayakawa, M.: The measurement of incident and azimuthal angles and the polarization of whistlers at low latitudes. Planet. Space Sci. **25**, 233–241, 1977

Okada, T., Iwai, A.: A new device for measuring polarization and field intensity of low-latitude whistlers. Trans. Inst. Electr. Engrs. Japan **100**, 21–28, 1980

Okada, T., Iwai, A., Hayakawa, M.: A new whistler direction finder. J. Atmos. Terr. Phys. **43**, 679–691, 1981

Pitteway, M.L.V., Jespersen, J.L.: A numerical study of the excitation, internal reflection and limiting polarization of whistler waves in the ionosphere. J. Atmos. Terr. Phys. **28**, 17–43, 1966

Sagredo, J.L., Bullough, K.: VLF goniometer observations at Halley Bay, Antarctica, II. Magnetospheric structure deduced from whistler observation. Plant. Space. Sci. **21**, 913–923, 1973

Strangeways, H.J., Madden, R.A., Rycroft, M.J.: High latitude observation of whistlers using three spaced goniometer receivers. J. Atmos. Terr. Phys. **45**, 387–399, 1983

Tanaka, Y.: VLF hiss observed at Syowa Station, Antarctica, I. Observation of VLF hiss. Proc. Res. Inst. Atmos. Nagoya Univ. **19**, 33–61, 1972

Tanaka, Y., Hayakawa, M.: The effect of geomagnetic disturbances on duct propagation of low-latitude whistlers. J. Atmos. Terr. Phys. **35**, 1699–1703, 1973a

Tanaka, Y., Hayakawa, M.: Storm-time characteristics of low-latitude whistlers. Planet. Space Sci. **21**, 1997, 1973b

Tanaka, Y., Nishino, M., Hayakawa, M.: A study of VLF auroral hiss observed at Syowa, Antarctica. Mem. Natl Inst. Polar Res., Tokyo, Series A13 (Aeronomy), pp. 58. 1976

Tanaka, Y., Hayakawa, M.: Longitudinal effect in the enhancement of daytime whistler activity at low latitudes. Ann. Geophys. **36**, 577–585, 1980

Taylor, W.L.: Radiation field characteristics of lightning discharges in the band 1 kc/s to 100 kc/s. J. Res. NBS, D. Radio Propagation **67D**, 539–550, 1963

Tsuruda, K., Hayashi, K.: Direction finding technique for ellipitically polarized VLF electromagnetic waves and its application to the low latitude whistlers. J. Atmos. Terr. Phys. **37**, 1193–1202, 1975

Received July 31, 1985; Revised version September 6, 1985;
Accepted October 1, 1985

J Geophys (1986) 59:73–86

Journal of Geophysics

Electric fields and currents at the Harang discontinuity: a case study

T. Kunkel[1]*, W. Baumjohann[1,2], J. Untiedt[1], and R.A. Greenwald[3]

[1] Institut für Geophysik der Universität Münster, Correnssstr. 24, D-4400 Münster, Federal Republic of Germany
[2] Max-Planck-Institut für Physik und Astrophysik, Institut für extraterrestrische Physik, D-8046 Garching, Federal Republic of Germany (Present affiliation)
[3] Applied Physics Laboratory, The Johns Hopkins University, Laurel, MD 20707, USA

Abstract. On 2 December 1977, 1600–1700 UT (around 19 MLT) a section of the Harang discontinuity moved westward over northern Scandinavia with a velocity of about 1 km/s, during a disturbed time interval. The westward movement was clearly identified in the IMS Scandinavian Magnetometer Array observations and is consistent with simultaneous STARE electric field measurements. The magnetic measurements showed a marked increase of the overhead current density during the westward movement while the electric field amplitudes stayed at the same level, thus indicating a temporal enhancement of the ionospheric conductivity. The westward movement gave the opportunity to combine subsequently observed two-dimensional distributions of equivalent current vectors (after correction for the magnetic field intensity increase) and electric field vectors into two corresponding patterns fairly extended in the east-west direction and covering the total extent of the most interesting part of the Harang discontinuity region. The electrically defined Harang discontinuity was located 200–300 km to the north of the magnetically defined discontinuity. The combined observational data were used to determine, as far as possible, the ionospheric distributions of height-integrated conductivities, of horizontal height-integrated current density vectors and of field-aligned currents. The results show a reduction of the Hall conductivities and upward Birkeland currents at and around the electrically defined Harang discontinuity. Some horizontal ionospheric current crosses the discontinuity, being diverged northward from the eastward electrojet and joining the westward electrojet, after further counterclockwise rotation.

Key words: Polar ionosphere – Harang discontinuity – Ionospheric electric field – Ionospheric conductivity – Ionospheric and field-aligned currents

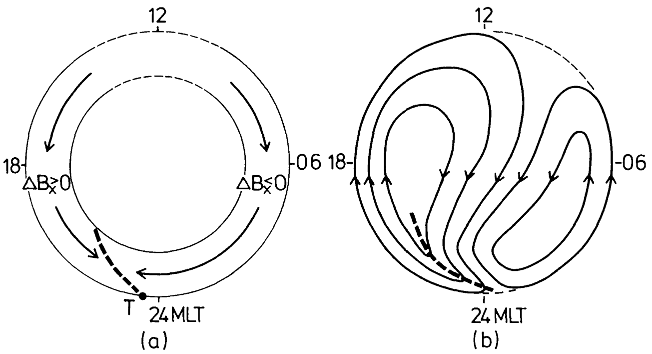

Fig. 1a and b. Schematic representation of **a** equivalent current flow within the auroral oval (cf. Hughes and Rostoker, 1979) and **b** plasma convection flow within the auroral oval and the polar cap (cf. Heppner, 1977, for example). In each diagram, the *heavy broken line* represents the respectively defined Harang discontinuity. ΔB_x denotes the northward component of the magnetic disturbance field

Introduction

Today there are two main definitions of the Harang discontinuity in use. In the first case, it is defined as the evening sector separatrix between the two parts of the auroral oval which are dominated by the eastward and westward electrojet, respectively (Fig. 1a). Because it is very difficult to measure true ionospheric currents, equivalent currents (i.e. horizontal magnetic disturbance vectors observed at the earth's surface and rotated clockwise by 90°) are used in this definition. This corresponds to the work of Harang (1946) who first detected that in the disturbed auroral zone there exists a line which is moderately inclined with respect to circles of magnetic latitude and separates positive disturbances in the magnetic north component B_x to the south and west from negative disturbances to the north and east. This line was named the Harang discontinuity by Heppner (1972). It is not fixed even in a magnetic latitude – magnetic local time coordinate system but may change position rapidly especially in connection with strong magnetic activity. For example, the penetration of the westward electrojet into the evening and afternoon sector during substorms (Rostoker and Kisabeth, 1973; Wiens and Rostoker, 1975) may shift the discontinuity by several hours of local time towards the west. Sometimes such a shift may occur during a fraction of an hour as noted by Heppner (1967) who spoke of discrete jumps of the discontinuity within this context. Note, that the magnetical Harang discontinuity can be defined only if magnetic disturbances are present. If magnetic activity is small it usually terminates at the southern bound-

---

* *Present address:* Siemens AG, München, Federal Republic of Germany

Offprint requests to: J. Untiedt

ary of the auroral oval near magnetic midnight (cf. point T in Fig. 1a).

In the second case, the Harang discontinuity is defined from the two-cell configuration of the ionospheric electric field **E** at high latitudes (e.g. Heppner, 1977) and denotes the line which separates westward from eastward convection ($\mathbf{E} \times \mathbf{B}/\mathbf{B}^2$) flow in the evening-midnight sector within and near to the auroral oval (Fig. 1b). Usually the flow shows an additional southward component at and near to the discontinuity. The electrical Harang discontinuity has been studied particularly by advanced techniques such as satellite instruments (e.g. Maynard, 1974), incoherent scatter radars (e.g. Banks et al., 1973; Wedde et al., 1977; Horwitz et al., 1978a, b) and coherent twin auroral radar systems like STARE and SABRE (e.g. Nielsen and Greenwald, 1979; Zi and Nielsen, 1982; Waldock et al., 1985). Usually it is situated 1°–2° to the north of the magnetic Harang discontinuity (Kamide and Vickrey, 1983). Like the latter, it is highly dynamic in nature. As magnetic activity increases, the region of predominantly westward electric field which includes the discontinuity narrows and moves to lower latitudes, on average (Maynard, 1974). The velocity of this movement increases with increasing Kp (Nielsen and Greenwald, 1979). The discontinuity generally appears earlier when magnetic activity is higher (Heppner, 1972; Nielsen and Greenwald, 1979; Zi and Nielsen, 1982; Waldock et al., 1985). Most of these features may be understood if the following view suggested by Zi and Nielsen (1982) on the basis of STARE observations is adopted (see also Burrage et al. 1985; Waldock et al., 1985). As magnetic activity increases: (1) the convection flow speeds increase; (2) the polar two-cell flow pattern expands; (3) the morning cell is enlarged with respect to the evening cell; and (4) the whole convection pattern rotates clockwise towards earlier local times.

As pointed out by Kamide (1982), there still exists much ambiguity about how such features like ionospheric horizontal and field-aligned currents, or ionospheric conductivities, change across the discontinuity. For example, three sheets of alternatively directed Birkeland currents have been deduced from the Triad satellite magnetic field observations for the 20–24 MLT sector of the auroral oval, under most conditions, with upward flow in the middle sheet (Iijima and Potemra, 1978; see also Rostoker et al., 1975). During periods when the westward auroral electrojet had intruded deeply into the evening sector, the Triad observations indicated the presence of even more complex field-aligned currents in this sector. On the other hand, Kamide (1978) discussed the possibility, which is also supported by observations, that there is no field-aligned current flow at the Harang discontinuity. He presented a model (cf. also Kamide et al. 1976a, b) in which poleward ionospheric current across the discontinuity region connects the eastward electrojet and the westward electrojet in the pre-midnight sector. Baumjohann et al. (1980) supported such a model by giving qualitative observational evidence for it, but at the same time described in detail a case where the eastward electrojet terminated exclusively by feeding strong and localized upward field-aligned current. Probably these are two extreme opposite possibilities which in most cases will be mixed in some way.

Very little is known about the behaviour of the height-integrated Hall and Pedersen conductivities, Σ_H and Σ_P, respectively. Recently, Kamide and Vickrey (1983), combining observations of the Chatanika incoherent scatter radar and the IMS Alaska meridian chain of magnetometers, found conductivity enhancements only on the poleward side of the electric Harang discontinuity during relatively quiet times and the early stage of a substorm. However, the enhancement surged equatorward extending beyond the discontinuity when the substorm reached the maximum to recovery phase. On the other hand, Baumjohann et al. (1981), after studying a multiple onset substorm over Scandinavia around magnetic midnight, reported that each auroral break-up occurred slightly south of the Harang discontinuity in the region of northwestward-directed electric field vectors. Observation of energetic particle precipitation into the region of the Harang discontinuity (Wedde et al., 1977) suggests a local increase of the ratio Σ_H/Σ_P, whereas Vickrey et al. (1981) found a decrease. Kamide and Vickrey (1983) also deduced a comparatively small conductivity ratio of 1.3 from the Harang discontinuity which they observed.

In view of these ambiguities it seems worthwile to study single cases of occurrences of the discontinuity in greater detail and by different methods of observation. A unique opportunity for such studies is offered by the data set simultaneously acquired over Scandinavia during the years 1977–1979 from the two-dimensional IMS Scandinavian Magnetometer Array (SMA) (Küppers et al., 1979; Maurer and Theile, 1978) and the Scandinavian Twin Auroral Radar Experiment (STARE) (Greenwald et al., 1978). The SMA consisted of more than 30 magnetometer stations, separated by about 100–150 km in northern Scandinavia where the network was most dense. It was mainly operated by the University of Münster and partly by the Technical University of Braunschweig.

The STARE system which is operated by the Max-Planck-Institut für Aeronomie at Katlenburg-Lindau consists of two radars at Malvik in Norway and Hankasalmi in Finland with a common area of observation above the northernmost part of Scandinavia and the neighbouring ocean. The radars are sensitive to electrostatic plasma waves in the auroral E region. These waves, often called irregularities, are produced by the combined effects of the two-stream and gradient drift plasma instabilities (see Greenwald, 1974). Greenwald (1979) has summarized evidence that, in the auroral E layer, the net drift velocity of the irregularities is nearly a pure $\mathbf{E} \times \mathbf{B}$ drift. Hence, the transverse ionospheric electric field vector is orthogonal and proportional to the measured drift velocity vector. Experimental evidence for this relationship has been found by Ecklund et al. (1977), Cahill et al. (1978) and Zanetti et al. (1980). Recently, Nielsen and Schlegel (1983, 1985) compared data of ionospheric electron drift velocities estimated by STARE with data of simultaneous velocity measurements made with the European Incoherent Scatter Facility (EISCAT). The magnitudes of the estimated drift velocities were in agreement with the EISCAT measurements for small velocities ($\lesssim 700$ m/s, corresponding to electric fields $\lesssim 35$ mV/m), but the authors found the estimates to be increasingly too low as the velocities become larger. The directions of the estimated vectors were in agreement with the EISCAT measurements for all drift magnitudes.

The drift velocities which may be converted to electric field vectors are observed with a temporal resolution of 20 s and a spatial resolution of about 20 km. The area viewed by STARE is located between about 68° and 73° northern geographic latitude and between about 14° and

24° eastern geographic longitude, corresponding to an extent between about 65° and 70° revised corrected geomagnetic latitude Φ_c (Gustafsson, 1970). Because the SMA reaches about $\Phi_c = 67.5°$ at the northernmost coast of Scandinavia, there is only partial overlap between the STARE and the SMA areas of observation. In many cases, there are quite extended gaps in the STARE data which may further diminish the overlap. These gaps result from regions in which the electric field does not exceed the threshold value of about 15–20 mV/m (Cahill et al., 1978) required to excite the plasma instabilities observable by STARE.

It is the purpose of the present paper to describe, for the first time, a single-event study of the Harang discontinuity using two-dimensionally distributed simultaneous data from the SMA and STARE. Our main intention was to estimate the spatial distribution of the height-integrated ionospheric conductivities, of height-integrated horizontal ionospheric currents and of field-aligned currents in the particular case considered. We do not intend to generalize the results from this investigation. As indicated above, the Harang discontinuity is a very dynamic and variable phenomenon so that many and perhaps improved studies of the kind which we are presenting will probably be necessary before general conclusions can be drawn.

In the course of our investigation we detected that the section of the discontinuity which we were able to observe by means of the SMA was a fast travelling phenomenon, moving in the same manner in which a westward travelling surge or in which eastward drifting omega bands will move. In previous studies, this motion was used to superimpose magnetic field distributions consecutively observed by the SMA in order to get snapshots of the westward travelling surge (Inhester et al., 1981; Opgenoorth et al., 1983b) or of eastward travelling omega bands (Gustafsson et al., 1981; André and Baumjohann, 1982; Opgenoorth et al., 1983a) within a field of view much extended in the direction of motion, as compared to the field of view of the SMA. In the present case, the motion was uniquely determinable only from the SMA observations, whereas the STARE data were at least consistent with the hypothesis that the electric field around the Harang discontinuity studied was moving together with the magnetic field. By accepting this obvious hypothesis we were able to reproduce not only a probably realistic extended snapshot of the magnetic field, but also a corresponding snapshot of the electric field distribution around the investigated Harang discontinuity with an east-west extent of about 2000 km equivalent to about 3 h in local time. We consider these extended field distributions to constitute a first interesting result of our study.

The event

In selecting a suitable event for our investigation we required it not to be an exceptional case according to previous experience with SMA and STARE data. Several cases of former observations of the Harang discontinuity by STARE were presented by Nielsen and Greenwald (1979), and the result of a corresponding statistical study based on STARE observations during 18 disturbed days was given by Zi and Nielsen (1982). As concerns SMA data, papers by Baumjohann et al. [1978, their Fig. 4b; cf. also Richmond and Baumjohann (1983) and Murison et al. (1985)], Küppers et al. (1979, their Fig. 9b) and Baumjohann et al. (1980, their Fig. 15) show examples of temporary appearance of the Harang discontinuity at different magnetic local times (which is about UT + 2.5 h in northern Scandinavia) within the evening sector, in connection with enhanced magnetic activity. In most of these examples and other cases not published hitherto, the equivalent current pattern shows a rotational transition from eastward currents in the south over northward currents to northwestward currents in the north. Furthermore, we required that the discontinuity appeared in the region of overlap of the STARE and SMA fields of view and, finally, that the STARE data did not show too many extended gaps (due to the threshold effect mentioned).

The event selected occurred on 2 December 1977 between 1600 and 1700 UT (about 1900 MLT). This is rather early in magnetic local time but, in view of the strong magnetic activity (Kp = 6+ for the time interval 1500–1800 UT and ΣKp = 44 for the UT day), not really exceptional. Note that Zi and Nielsen (1982; cf. also Nielsen and Greenwald, 1979) got an average shift of the discontinuity by about 3 h to earlier local time for ΣKp = 40–50, and that Waldock et al. (1985) gave an average appearance of the discontinuity at 2030 MLT for Kp = 6 and for the SABRE field of view which is located several degrees to the south as compared to northern Scandinavia and therefore may be expected to see the Harang discontinuity later.

To give a first impression on how the Harang discontinuity occurred on 2 December 1977, and what kind of magnetic activity followed, Fig. 2 shows the horizontal magnetic disturbances observed in the Scandinavian region on that day between 1500 and 2300 UT (about 1730 and 0130 MLT) along one of the meridian magnetometer lines of the SMA. The eight stations of this line stretch from $\Phi_c = 67.4°$ (SOY) at the northernmost coast of Norway to $\Phi_c = 58.8°$ (SAU) in southern Finland. The disturbances are defined as deviations from the quiet night level and are given in a system of coordinates and field components which has been particularly designed for the analysis of SMA data and has been named the Kiruna system (Küppers et al., 1979).

As regards coordinates, the Kiruna system is obtained by projecting the Scandinavian part of the curved earth's surface onto a tangential plane centred at the town of Kiruna (67.8° N, 20.4° E in geographic coordinates) which is located at the centre of the most important northern part of the SMA. Then, a Cartesian system of coordinates x_{KI} and y_{KI} is introduced with its origin at Kiruna. The orientation of this system has been chosen in such a way that at Kiruna the y_{KI} axis is tangent to the projection of the line of constant revised corrected geomagnetic latitude running through this place. x_{KI} increases roughly towards the north and y_{KI} increases towards the east. At Kiruna, the x_{KI} axis points 12° west of geographic north. If the third dimension is needed, height is used as the corresponding coordinate. Finally, horizontal components of a magnetic or electric field are transformed in the same way as described by Küppers et al. (1979). For the sake of brevity the magnetic disturbance field component parallel to the x_{KI} axis is usually denoted by A, and the corresponding component parallel to the y_{KI} axis is denoted by B. The Kiruna system will be used exclusively within the present paper. When we mention northerly and westerly directions this will imply that directions parallel to the x_{KI} axis and the y_{KI} axis are being indicated, respectively. Correspond-

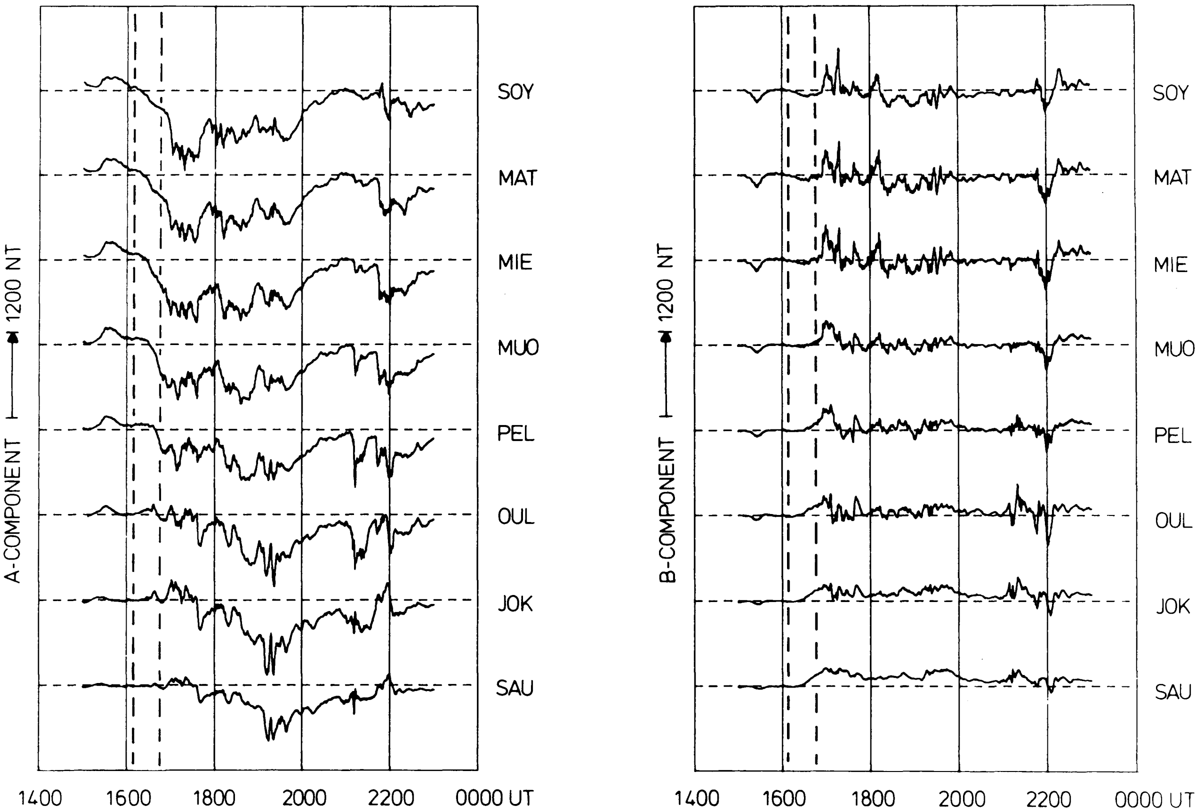

Fig. 2. Geomagnetic disturbances as recorded along one of the meridian magnetometer lines of the IMS Scandinavian Magnetometer Array on 2 December 1977. The *A* and *B* components are effectively directed towards corrected geomagnetic north and east, respectively (cf. Küppers et al., 1979). The revised corrected geomagnetic latitudes (Gustafsson, 1970) of the stations vary from 67.4° (SOY, northernmost Norway) to 58.8° (SAU, southern Finland). The disturbances are defined as deviations from the quiet night level

ingly, *A* and *B* components may be called north and east components, respectively.

As Fig. 2 shows, the event which we studied (cf. vertical broken lines) occurred at the transition from northerly to southerly magnetic disturbances over northern Scandinavia, with mostly moderate intensities of about 100–200 nT. Additionally, the northern stations showed small westerly disturbances, whereas easterly disturbances in middle and southern Finland became relatively strong towards 1700 UT after having been negligible during the first half of the event.

The temporal development of the spatial structure of the magnetic disturbance field throughout the transitional interval is illustrated by a series of four subsequent instantaneous distributions of equivalent current vectors over Scandinavia (Fig. 3). In each case, the simultaneous distribution of electric field vectors as observed by STARE is added. Note that the STARE data have been averaged over 50×50 km^2 areas.

At 1615 UT (Fig. 3, upper left) the whole of northern Scandinavia is still under the eastward electrojet, as indicated by essentially eastward equivalent current vectors and northward electric fields. However, the northernmost coastal magnetometer stations show small but clearly northward-pointing current arrows corresponding to $A \approx 0$. Therefore, it may be anticipated that the magnetic signature of the Harang discontinuity has already reached the northernmost coast of Scandinavia. This is in accord with the predominantly westward current observed by the Norwegian observatory on Bear Island to the north.

At 1628 UT (Fig. 3, upper right) the magnetic signature of the Harang discontinuity (i.e. northward equivalent current vectors) has moved to the south and is now well observed by magnetic stations, stretching in a northwest-southeasterly direction over northern Scandinavia. In the same area, STARE still shows north- to northwestward-directed electric field vectors, whereas at some distance to the north a westward field, i.e. the electric signature of the Harang discontinuity, has appeared. As mentioned above, such a meridional separation between the magnetic and electric signatures of the Harang discontinuity has recently been pointed out by Kamide and Vickrey (1983). Note that there are quite extended gaps in the STARE data. As mentioned above, they result from regions in which the electric field does not exceed the threshold value of about 15–20 mV/m (Cahill et al., 1978). In fact, the northward or northwestward electric fields detected at 1615 UT and 1628 UT have just this intensity, whereas the westward fields at 1628 UT show a somewhat larger magnitude of 25–30 mV/m.

About 10 min later (Fig. 3, lower left) both signatures of the Harang discontinuity are located even further south. In the equivalent current pattern the eastward electrojet in the south and the westward electrojet in the north are well separated with almost no current crossing the Harang discontinuity. The electrical signature of the discontinuity is again displaced to the north, by about 200 km as compared to the magnetic signature, and is indicated by a data gap between northwestward field vectors to the south and southwestward field vectors to the north. It may safely be

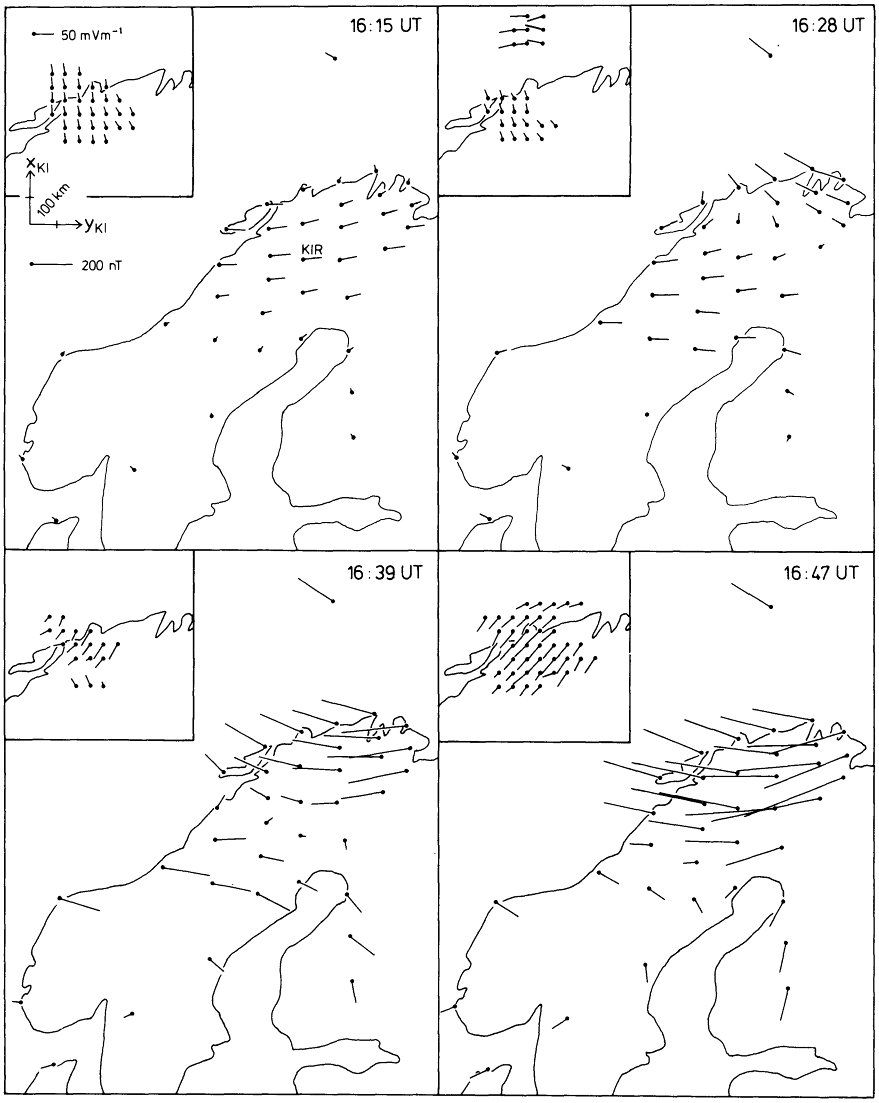

Fig. 3. Distributions of horizontal magnetic disturbance vectors rotated clockwise by 90° (equivalent current vectors) and of ionospheric electric field vectors observed on 2 December 1977. Note that the STARE area of observation is displaced (cf. coast line). Also displaced is the x_{KI}–y_{KI} system of coordinates (for details, see text) shown in the *upper left main panel*. In reality, its origin is located at the magnetic station Kiruna (*KIR* indicated). The directions of its axes coincide with the directions of the *A* and *B* components displayed in Fig. 1. The single magnetic station to the north is the Norwegian permanent observatory on Bear Island

assumed that within this gap the field is mainly westward, with an intensity below threshold. Note that obviously the width of the electrically defined Harang discontinuity has decreased much between 1628 UT and 1639 UT, and that equivalent currents have intensified whereas such an effect can barely be recognized in the STARE data. Probably the southeastward orientation of equivalent current vectors south of the auroral zone indicates an at least partial divergence of the eastward polar electrojet as upward net field-aligned current (cf. Baumjohann et al., 1980, particularly their Fig. 11).

Finally, at 1647 UT (Fig. 3, lower right) an intense westward electrojet is flowing above northern Scandinavia and STARE observes southwestward-directed fields at 35–45 mV/m intensity which in reality may be somewhat larger according to Nielsen and Schlegel (1983).

In summary we may state that between about 1615 UT and 1650 UT the Harang discontinuity, with the electrical and magnetic signatures separated as reported by Kamide and Vickrey (1983), moved from north to south over Scandinavia. At the same time, the character of the equivalent current pattern changed significantly. Whereas early within the time interval eastward electrojet current diverged northward and then joined the northwestward currents to the north after crossing the Harang discontinuity, later the eastward jet turned southward away from the discontinuity.

Generation of extended snapshots of the magnetic and electric fields

These very different characters of the equivalent current patterns (i.e. of the magnetic fields) observed early and late within the time interval mentioned can be reconciled if the subsequent patterns are shifted with respect to each other as shown by Fig. 4. Within this figure, and in the remainder of our paper, only the six equivalent current distributions observed at 5-min distances from 1620 to 1645 UT are used because it turned out that the rest of the magnetic data from this time interval contained effectively redundant information. The shift between any two subsequent current patterns has been adjusted in such a way that current flow within the overlapping parts of the patterns was parallel. Note that generally a similar fitting of equivalent current configurations observed subsequently throughout the course of magnetic substorms will not be possible, with the exception of westward travelling surges etc. (see above). The obvious possibilitiy of such a fitting was an early unexpected result of our study.

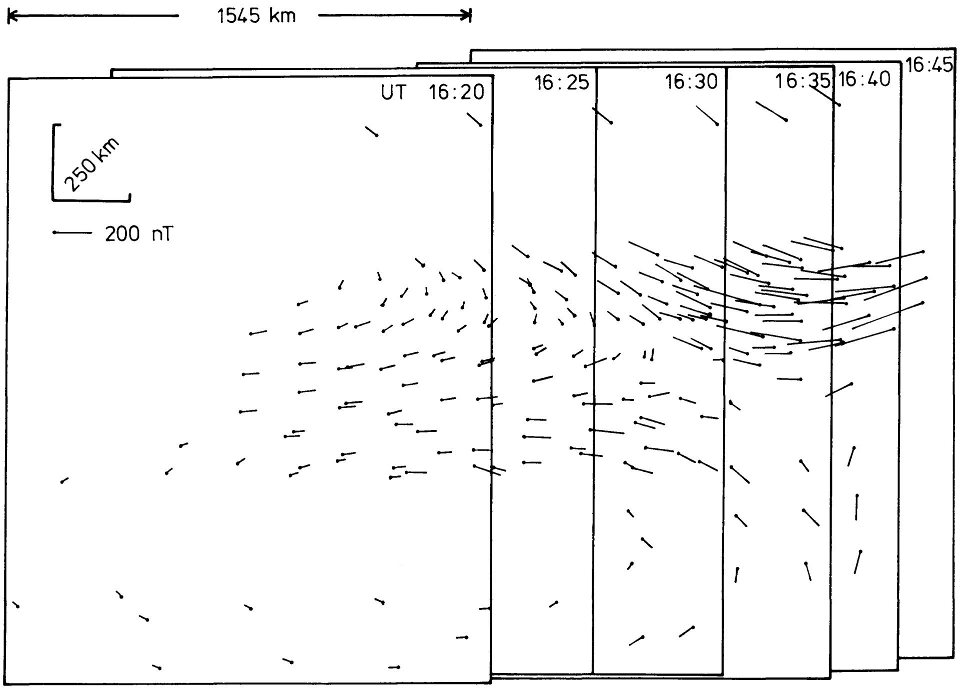

Fig. 4. Extended equivalent current vector distribution generated by properly combining the six corresponding distributions that were observed from 1620 UT to 1645 UT at 5-min intervals. The fit of the different observed patterns was done under the condition that current directions agree in overlapping areas. Frames are identical to those used within Fig. 3 for presentation of the magnetic (equivalent current) data

Figure 4 demonstrates that each one of the equivalent current patterns, observed at 1620 UT, 1625 UT and so on, may be considered to be a different and more and more easterly shifted section from a single extended pattern which becomes obvious in the figure. Conversely, we may state that on 2 December 1977 between 1620 and 1645 UT an extended equivalent current distribution as shown by Fig. 4 moved almost exactly westward over Scandinavia with a speed that varied slightly, as readable from the different values of shift per 5 min, around an average speed of 1.0 km s^{-1} (1,545 km as indicated within the figure divided by 25 min).

The final goal in our magnetic data analysis was the generation of a consistent and uniform version of the current vector field indicated by Fig. 4. However, before accomplishing this we had to undertake one additional step. By shifting the subsequently observed current patterns as described above it was possible to match current directions but not current intensities, within overlapping sections. Obviously, current intensity increased with time, as is also suggested by the sequence of equivalent current patterns shown in Fig. 3. Figure 5 gives the result of a crude determination of this increase which apparently was not constant over the event. For subsequent 5-min intervals, i.e. 1620–1625 UT, 1625–1630 UT, etc., intensification factors were measured for as many station pairs that were nearly coincident after translation as possible. The ratios were calculated from the equivalent current intensities separated by 5-min intervals. As Fig. 5 shows, there is much scatter in the results, possibly indicating that the stations were sensing regimes of eastward, northward and/or westward equivalent currents. From Fig. 5 we have derived average intensification factors 1.14, 1.39, 1.23, 1.03 and 1.20 for the five subsequent 5-min time intervals of the event, respectively.

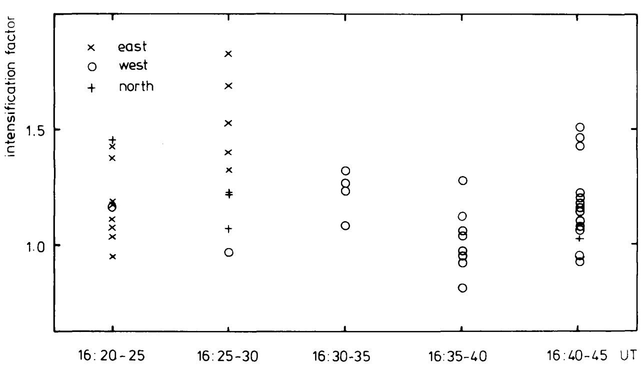

Fig. 5. Intensification factors which describe the increase of intensity of the observed travelling equivalent current system (cf. Fig. 4) over the five consecutive 5-min intervals between 1620 UT and 1645 UT. The factors were estimated by comparing the lengths of equivalent current vectors situated at almost the same location within Fig. 4 but observed 5 min apart

With these factors, we reduced all the equivalent current (i.e. ground magnetic field) data observed at 1620 UT, 1625 UT and so on, to the epoch 1630 UT before finally superposing them. At the same time, we transferred all the superposed data to an equally spaced 100 km × 100 km station grid, by averaging data falling into the same grid cell if necessary. The final result is given by Fig. 6 which is considered to represent the equivalent current distribution which would have been observed over Scandinavia and its western and eastern vicinity on 2 December 1977 at 1630 UT if a corresponding array consisting of about 130 magnetometers extending from $y_{KI} = -1{,}100$ km to $y_{KI} = +1{,}000$ km and $x_{KI} = -1{,}000$ km to $x_{KI} = +700$ km had been available.

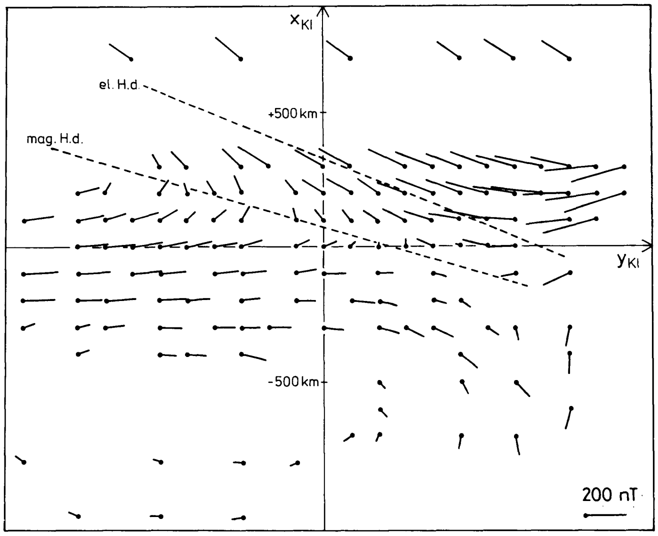

Fig. 6. Distribution of equivalent current vectors at 1630 UT as derived from Fig. 5 by reduction to an equidistant grid of fictitious stations separated by 100 km in both directions and after normalization of current strength to the time 1630 UT (see text). The lines denoted by 'mag. H. d.' and 'el. H. d.' give the locations of the magnetically and electrically defined Harang discontinuities, respectively. The latter discontinuity is transferred from Fig. 7

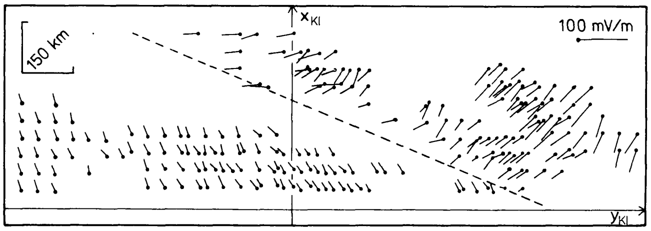

Fig. 7. Extended ionospheric electric field distribution at 1630 UT generated by combining 12 corresponding distributions that were observed consecutively by STARE from 1620 UT to 1645 UT. The composition was done in a similar way to Fig. 4 but under the assumption that the electric field had travelled with the same velocity vector as that deduced from the magnetic observations and applied in Fig. 4. The *dashed line* denotes the estimated locus of the electric signature of the Harang discontinuity (i.e. westward electric field)

This extended snapshot of the equivalent current distribution shows an eastward electrojet intruding into the area along the y_{KI} axis with its centre at about $x_{KI} = -100$ km. It diverges partly towards the north and afterwards northwest joining the continuation of the westward electrojet that intrudes with its centre at about $x_{KI} = +200$ km. The remaining part of the eastward electrojet turns southward within the southeastern section of the area shown. To the southwest, there is equivalent return current to the eastward jet. The locus of the magnetic signature of the Harang discontinuity, i.e. of northward equivalent current, is indicated by a broken line. Whereas it may be anticipated to be continued towards the northwest, it clearly terminates in the southeastern part of the figure at a location probably corresponding to the point T shown within Fig. 1a.

The next objective was to generate a corresponding snapshot of the ionospheric electric field, if possible. However, the area covered by STARE observations is relatively small and often diminished by the presence of data gaps where the electric field is below threshold. Therefore, we were not able to deduce translation vectors from the subsequently observed electric field distributions. On the other hand, it seemed reasonable to assume that the electric field motion was identical to that shown so clearly by the equivalent current (i.e. magnetic field) patterns. Under this assumption, Fig. 7 has been produced by the translation and superposition of twelve 20-s and 50×50 km^2 averages of the electric field distributions observed by STARE between 1620 UT and 1645 UT. We omitted STARE data patterns that showed too much scatter or too extended data gaps. Because we did not find any evidence of a temporal increase of the overall electric field intensity during this period, as we did in the case of the magnetic field, the field intensities are shown as observed.

Again, we consider Fig. 7 to represent the electric field vectors which an earth-based observer would have measured at 1630 UT if he had had a STARE type system with an area of view much extended in the east-west direction. In other words, Fig. 7 shows a snapshot of the moving ionospheric electric field pattern as seen from the earth. Note that it does not give the field in a moving frame of reference.

The electric field vectors shown in Fig. 7 exhibit more scatter than do the equivalent current vectors in Fig. 4. This difference is typically observed if one compares STARE data with ground-based magnetic measurements. Most likely it is due to the fact that the magnetic measurements are made 100 km below the ionosphere and so are subject to spatial filtering of the smaller-scale structures (cf. Ziesolleck et al., 1983).

It may be noted in Fig. 7 that the absence of electric field data in the westward region of the figure makes it difficult to localize the Harang discontinuity, defined by $E_{x_{KI}} = 0$. However, the discontinuity is easily discernible in the eastern part of the figure and we have indicated it by a dashed line. This line has been extended toward the west where it is at least consistent with the existing data. Note that the electrically defined Harang discontinuity is situated 200–300 km to the north of the magnetically defined discontinuity (cf. Fig. 6 above). This result is consistent with previous observations (e.g. Kamide and Vickrey, 1983).

For a later joint interpretation (cf. next section) of the magnetic and electric observations we will need the electric field with sufficient uniformity and with an extension over a larger area so that it is comparable to the equivalent current distribution as given by Fig. 6. Therefore, we fitted the existing data shown in Fig. 7 and did an interpolation and extrapolation where there were no data by using as simple as possible analytic functions $E_{x_{KI}}$ and $E_{y_{KI}}$ depending on x_{KI} and y_{KI} and imposing the additional condition that the determined smooth electric field be curl-free. Furthermore, we assumed that the southward electric field component far north of the STARE field of view is approximately constant, and that the locus of the electric signature of the Harang discontinuity continues as a straight line towards the southeast. We feel the assumption of a more complicated structure for the model electric field pattern – such as an increase of the southward component to the north, or a changing slant of the Harang discontinuity south of the STARE field of view – to be unwarranted for the present purposes.

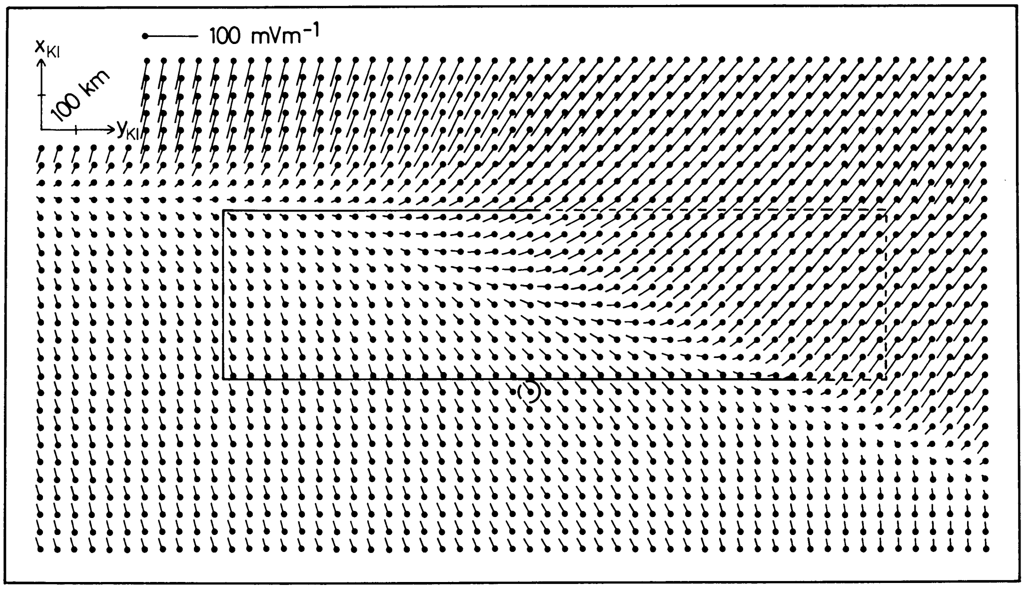

Fig. 8. Similar to Fig. 6 but for the electric field distribution. In this case, the grid spacing is only 50 km, and much smoothing, interpolation and extrapolation has been applied imposing certain conditions (cf. text). The location of the extended STARE area of view (area largely covered by data in Fig. 7) has been marked by a *rectangle*. For clarity, only the origin of the x_{KI}–y_{KI} system (displayed, for example, in Figs. 6 and 7) is indicated by a *circle* (station KIR, cf. Figure 3)

The result is shown on a $50 \times 50\ \mathrm{km}^2$ grid by Fig. 8, with the extended STARE field of view indicated by a rectangle. We think that this is a particularly plausible smoothed representation of the electric field that existed in the region of the Harang discontinuity on 2 December 1977 at 1630 UT. It is both consistent with the STARE observations and also in accord with current knowledge of convection flow at high latitudes (see above). We do not think that much change to the distribution shown in Fig. 8 would be justifiable under these respects, with the exception of the field vectors in the northeastern part of the area where STARE possibly underestimated field intensities (cf. Nielsen and Schlegel, 1983, 1985).

Trial and error determination of ionospheric conductivities and currents

Finally, we tried to find a reasonable ionospheric conductivity distribution which is able to generate Fig. 6 from Fig. 8. As far as the result is unique, it may be considered to represent the conductivity distribution that existed over Scandinavia on 2 December 1977 at 1630 UT. Simultaneously, this conductivity distribution together with the electric field gives true horizontal ionospheric currents, in contrast to equivalent currents, and also the field-aligned currents that are of particular interest in the region of the Harang discontinuity, as discussed above.

We proceeded as described by Baumjohann et al. (1981) who interpreted simultaneously observed SMA and STARE data for three cases of local auroral break-ups, by applying a trial and error method. We assumed a two-dimensional distribution for Σ_H and Σ_P (height-integrated Hall and Pedersen conductivities, respectively) and calculated the ionospheric surface current density $\mathbf{J} = \mathbf{J}_{\mathrm{Hall}} + \mathbf{J}_{\mathrm{Ped}}$, using the electric field shown by Fig. 8. The divergence of $\mathbf{J}$ gave the field-aligned current density $j_{\|}$. Currents induced within the earth were neglected, in view of the low conductivities found in the crust and upper mantle under northern Scandinavia (Küppers et al., 1979; Jones, 1983). By applying Biot-Savart's law we computed the magnetic field at the ground and finally, by a 90° rotation, equivalent currents. The latter were compared to the observed equivalent current configuration (Fig. 6), and the conductivity distribution was changed until there was adequate agreement between the computed and observed equivalent currents [for more details, see Baumjohann et al. (1981)].

To illustrate and to justify the way in which we proceeded, we present four different models of height-integrated conductivity distributions which, when combined with the electric field distribution given in Fig. 8, yielded model equivalent current patterns on the earth's surface. The conductivity models (Fig. 9) are a selection from a large number of models which gave increasingly better conformity with the observed equivalent current pattern.

In all of the models, we set $\Sigma_H = \Sigma_P = 0$ to the north and to the south of the area covered by electric field vectors in Fig. 8, assuming that it represented the Scandinavian section of the auroral oval and that conductivities outside the oval were negligible. The location of the southern boundary of the adopted auroral oval was suggested by Fig. 6, where the transition from the eastward electrojet to equivalent return currents occurred at about $x_{KI} = -500$ km. If these currents were assumed to be generated by overhead ionospheric currents in a northward electric field this would require negative conductivities which is impossible. The adopted northern boundary of the oval is somewhat arbitrary. However, the exact location of it is of minor influence on the computed equivalent current distribution within the area of interest.

In model 1 (not shown within Fig. 9) we started with uniform oval conductivities and a conductivity ratio $\Sigma_H / \Sigma_P = 2.0$ which is a value typically observed at auroral zone latitudes at nighttime under moderately disturbed conditions (e.g. Banks and Doupnik, 1975; Horwitz et al., 1978a). The values $\Sigma_H = 12$ S and $\Sigma_P = 6$ S were adopted in order to get agreement, as far as possible, between com-

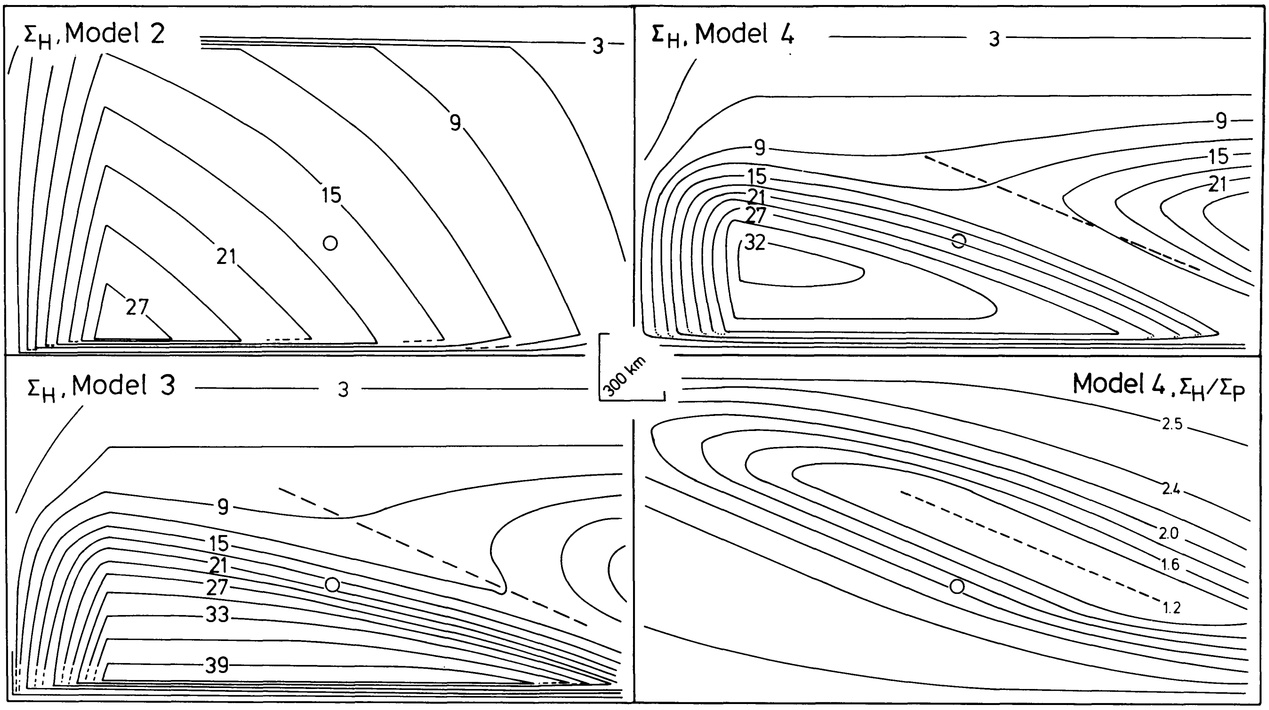

Fig. 9. Different distributions of ionospheric height-integrated conductivities used for modelling the three-dimensional current flow in the Harang discontinuity region by fitting equivalent current distributions calculated for the respective models (cf. Fig. 10) to the observed normalized equivalent current vectors (Fig. 6). For the starting model (model 1; not shown) a uniform conductivity distribution ($\Sigma_H = 12$ S, $\Sigma_P = 6$ S) was used. The Hall conductivity distributions given by isocontours in the *left row* represent intermediate stages (models 2 and 3, $\Sigma_H/\Sigma_P = 2$) while the *upper right panel* gives the Hall conductivity distribution for the final model (model 4). The *lower right panel* gives the spatial distribution of the Hall-to-Pedersen conductivity ratio Σ_H/Σ_P used in model 4. The *dashed lines* denote the electric Harang discontinuity. The centre of the x_{KI}–y_{KI} coordinate system is indicated by a *circle* (as in Fig. 8)

puted equivalent currents (Fig. 10, upper left) and observed equivalent currents within the westward electrojet region. On comparing these currents, one sees that this model is inadequate in that it yields overly small values for the eastward electrojet flow and the equivalent current closure in the southwest.

In order to improve the agreement, the Hall conductivity distribution of model 2 (upper left panel of Fig. 9) has positive Σ_H gradients towards the southwest over most of the model area except for the far west where the gradients are towards the east. These gradients are needed to generate the downward field-aligned currents which provide better equivalent current closure in the southwest. A value of 2 has been retained for the ratio Σ_H/Σ_P. The equivalent current pattern of model 2 is given in the lower left panel of Fig. 10. It shows that the calculated magnetic signature of the Harang discontinuity (dashed line) is located too far to the northeast of the observed one (solid line) and that more westward equivalent current is needed in the central and southern portion of the current pattern. This may be accomplished either by an upward field-aligned current in the east or by more downward field-aligned current in the west. However, since the latter possibility would lead to negative Σ_H values in the far west, Σ_H must increase in the region to the east of the electric signature of the Harang discontinuity.

The conductivity distribution of model 3 includes the above-mentioned modification (Fig. 9, lower left panel, and again $\Sigma_H/\Sigma_P = 2$) and the corresponding calculated equivalent current configuration shown in Fig. 10 (upper right panel) indicates that this indeed leads to the desired results.

The finally adopted Σ_H distribution (model 4), i.e. the final result of our trial and error modelling, is also given in Fig. 9 (upper right). This distribution shows large values around 20–30 S near the eastward end of the eastward electrojet, indicates similar values for the westward jet and gives only 10–15 S in the southern vicinity of the electrically defined Harang discontinuity. Northward of $x_{KI} = 400$ km, Σ_H is below 10 S and decreases steadily towards the north.

In the final conductivity model (model 4) we used a Σ_H/Σ_P distribution with a minimum value of 1.2 at the electrical Harang discontinuity and values increasing above 2.0 away from it (Fig. 9, lower right). We tried such a distribution in view of the above-mentioned observations of Vickrey et al. (1981) and Kamide and Vickrey (1983) and found that it gave slightly better results than a constant ratio and much better results than an assumed increase of Σ_H/Σ_P at the discontinuity. Note that the equivalent current pattern computed from the final conductivity model (Fig. 10, lower right) agrees fairly well with the observed pattern (Fig. 6), and that, in particular, the locations of the magnetically defined Harang discontinuities agree.

The height-integrated ionospheric currents **J** and the field-aligned currents $j_{\parallel}$ computed for the final conductivity model (model 4) are represented in Fig. 11. Apparently, the northeastward-directed ionospheric currents in the region of the eastward electrojet are fed by downward field-aligned current in the west and at the southern border of the auroral oval, as indicated by crosses in the lower panel of Fig. 11. The currents then partially turn northward and join the westward electrojet and partially flow up magnetic field lines. Most of the westward electrojet current termi-

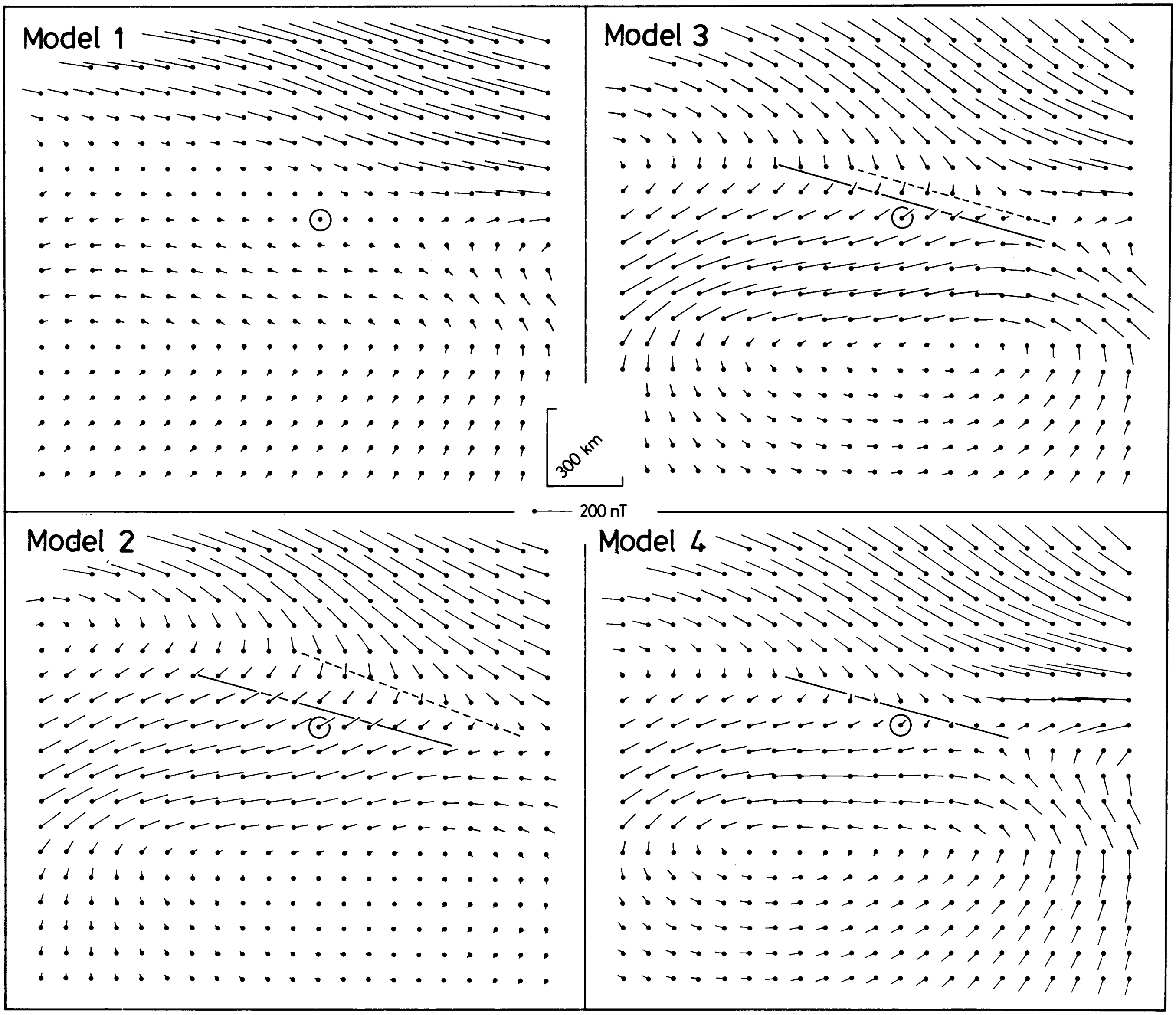

Fig. 10. Model equivalent current vectors on the Earth's surface calculated from the four different conductivity models (cf. Fig. 9 and text) and from the electric field distribution given in Fig. 8. The patterns have to be compared to the observed normalized pattern shown in Fig. 6. Note, that the frames used in Fig. 6 and in this figure are identical. The *circles* bear the same meaning as in Figs. 8 and 9. The *solid lines* denote the observed magnetic Harang discontinuity, whereas the *dashed lines* give the same discontinuity as calculated from the different models. Note, that both lines coincide in the final model (*lower right panel*)

nates in the Harang discontinuity region, particularly near its southeastern part. Altogether, an area of about 600 km × 2,000 km around the electrically defined Harang discontinuity is occupied by upward-flowing Birkeland current of about 1–4 $\mu\mathrm{Am}^{-2}$ intensity.

Because it may be of interest, Fig. 12 shows the field-aligned current distributions estimated separately, by computing the horizontal divergence, from the Hall and from the Pedersen height-integrated currents. It indicates that, in the vicinity of the Harang discontinuity, the Birkeland currents generated by the termination of the eastward electrojet are predominantly from upward-diverging Hall currents; whereas north of the Harang discontinuity, in the region of the westward electrojet, the Birkeland currents are fed mainly by the divergence of Pedersen currents. Note that there are other areas where the field-aligned currents computed separately from the Hall and Pedersen currents partly cancel each other (e.g. to the east of the Harang discontinuity).

Discussion

The first result of our study was the SMA observation of the rapid westward motion of a magnetic field distribution characteristic for the vicinity of the Harang discontinuity. Note that the value of speed determined (about 1.0 kms^{-1}) was large compared to the westward speed corresponding to the earth's rotation (0.16 kms^{-1} at 70° latitude). We feel that this rapid motion corresponds to an early observation by Heppner (1967) (see also Heppner, 1972, p. 115) who studied the local time pattern of geomagnetic disturbance in detail as a function of universal time using data

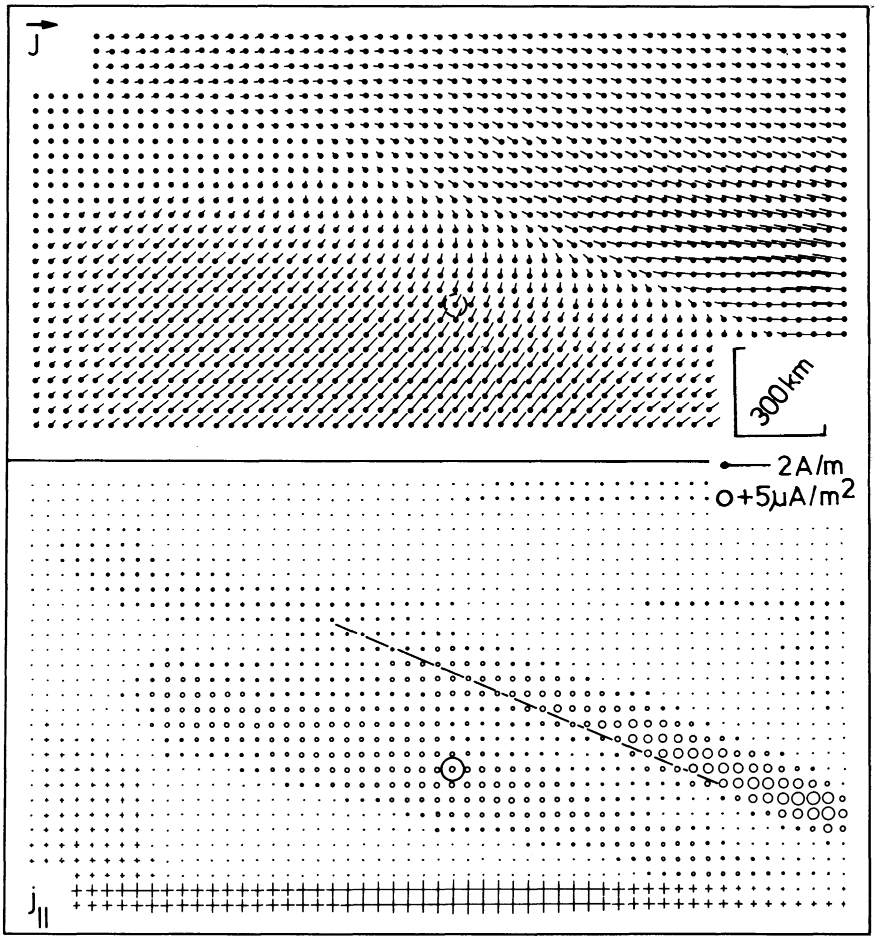

Fig. 11. Ionospheric and field-aligned currents for the final model (model 4, cf. Fig. 9). The *upper panel* gives the height-integrated ionospheric current density. The *lower panel* shows the field-aligned current density (*circles and crosses* denote upward- and downward-directed current flow, respectively). The *two large circles* bear the same meaning as in previous figures. The *straight line* denotes the electric Harang discontinuity

from 25 northern high-latitude observatories for 16 consecutive days in October 1957. Heppner (1967, 1972) found that the transition from + to $-\Delta H$ disturbance (i.e. the magnetic signature of the Harang discontinuity) progressed rather smoothly for most of the time, moving successively from one auroral belt observatory to the next as the earth rotated. However, intermittently superimposed on this general behaviour, discrete jumps occurred in which the discontinuity shifted suddenly (e.g. within 10–20 min) between observatories to an earlier geomagnetic local time. We feel that the magnetic disturbance fields which we observed may have been due to such a jump.

It should be stressed that our conclusions about westward motion have been drawn primarily from the magnetic data. On the basis of the STARE data alone, it was impossible to deduce a westward drift velocity. This is probably due to the limited longitudinal extent of the STARE viewing area, the presence of data gaps and the afore-mentioned greater variability of the STARE data. We have assumed that the STARE observations had been produced by a fixed electric field pattern which moved westward with the velocity of the disturbed magnetic field pattern. Using this assumption, we obtained an extended east-west pattern of the electric field (Fig. 7) in which the locus of the signature of the Harang discontinuity is rotated slightly clockwise from the magnetic (Kiruna system) east-west direction. This inclination leads to a southward motion of the discontinuity as observed between the consecutive STARE plots throughout the event (cf. Fig. 3).

At first glance there appears to be a disagreement between these results and the results of Nielsen and Greenwald (1979) who found that the Harang discontinuity was essentially east-west aligned in the STARE plots that they studied. However, it should be noted that the geographic system of coordinates which they used is rotated by 12° with respect to the magnetically oriented Kiruna system in which we present our results. Therefore, a Harang discontinuity which is exactly east-west aligned in the system used by Nielsen and Greenwald (1979) (an example of such a case is displayed in their Fig. 2) will be rotated 12° clockwise from the y_{KI} axis if it is transferred to our present system of coordinates. This is in essential agreement with our observations and it is only through our ability to overlap numerous magnetic field patterns that we are led to our conclusion of a westward movement of the discontinuity.

The final major results of our study are the distributions of Σ_H, **J** and $j_\parallel$ given by Fig. 9 (upper right panel) and by Fig. 11, respectively. It is important to ask how well-determined or unique these distributions are. This question may be split into three questions. How reliable is the finally adopted electric field shown by Fig. 8 as compared to Fig. 7, and how much would corresponding possible changes within Fig. 8 influence our final results? How far does the trial and error method that was applied give a unique solution?

Regarding the first two questions, the immediate vicinity of the electrically defined Harang discontinuity is most im-

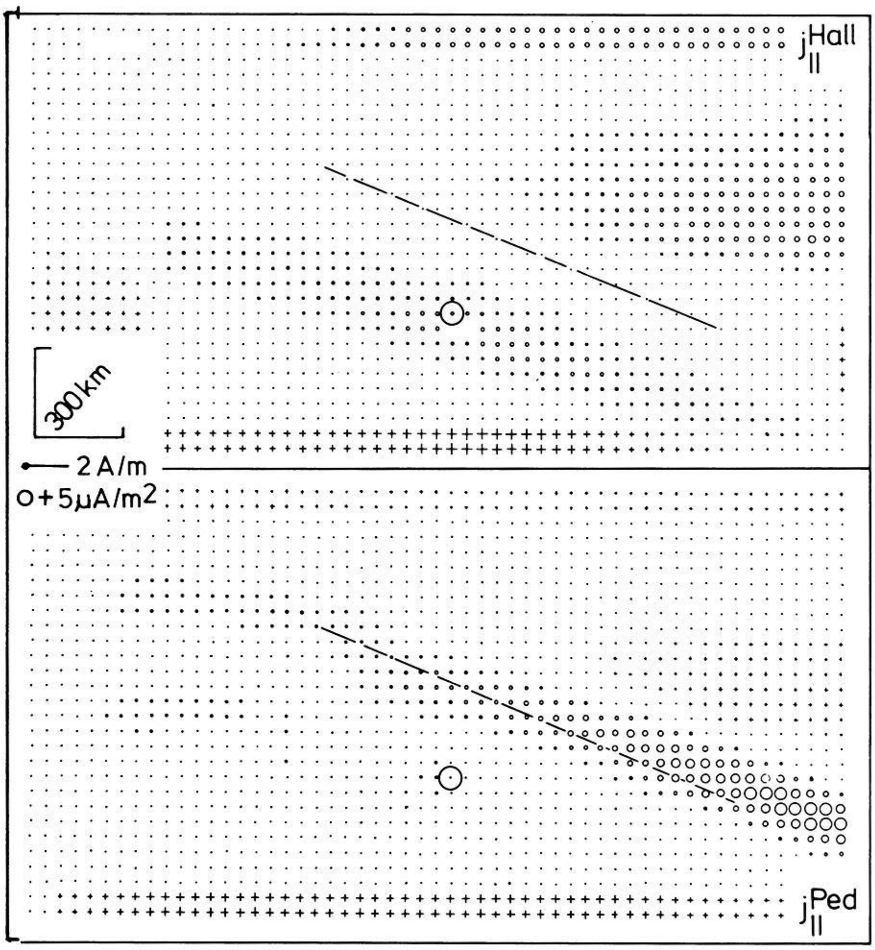

Fig. 12. Field-aligned currents as in Fig. 11, but separately computed from the divergence of the Hall and Pedersen currents, respectively. Otherwise as Fig. 11. Note that the total field-aligned currents shown in Fig. 11 (*lower panel*) are equal to the sum of $j_{\|}^{\mathrm{Hall}}$ and $j_{\|}^{\mathrm{Ped}}$

portant. Here, the extended STARE data set (Fig. 7) shows large gaps. In our interpolation and regression analysis, we filled these gaps with an electric field that had a constant component parallel to the discontinuity, directed approximately northwestward, and a smooth zero transition in the perpendicular component, with the latter component being constant at constant distance from the discontinuity, in a first approximation. This is in accord with the condition that the electric field be curl-free or, with the equivalent condition, that the convection field be source-free. After a first glance at Fig. 7 it may be asked why it should not be possible, for example, to assume $\mathbf{E}=0$ at the Harang discontinuity. However, consideration of the two equivalent conditions mentioned shows that this would lead to improbable small-scale electric field structure and to an improbable convection flow not consistent with the generally accepted pattern indicated in Fig. 1b, because convection would not be allowed to cross the Harang discontinuity. In the northeastern part of Fig. 8 the electric field vectors reach a magnitude of almost 50 mVm^{-1}. Such large electric fields observed by STARE may have been underestimated as shown by Nielsen and Schlegel (1983, 1985), whereas the field directions remain reliable. If we increase the field strengths correspondingly and simultaneously keep or $\Sigma_{\mathrm{H}}/\Sigma_{\mathrm{P}}$ ratios, all Σ_{H} values in the northeastern part of Fig. 9 (upper right panel) should be reduced by the same factors. On the other hand, $\mathbf{J}$ and $j_{\|}$ as shown by Fig. 11 would remain unchanged. Of course, second-order changes of the electric field distribution shown in Fig. 8 would everywhere be possible. However, such minor changes would not give results markedly different from those shown within Fig. 9 (upper right panel) and Fig. 11.

Addressing the third question, we found that the height-integrated Hall conductivities may be changed by up to about 10% as compared to our final model conductivity values without leading to noticeable effects on the equivalent current pattern on the ground. On the other hand, the computed equivalent currents are rather insensitive to the height-integrated Pedersen conductivities. As indicated above, constant ratios $\Sigma_{\mathrm{H}}/\Sigma_{\mathrm{P}}$ with values between about 1.5 and 2.5 give almost the same results, and the results are only slightly better for the distribution of $\Sigma_{\mathrm{H}}/\Sigma_{\mathrm{P}}$ shown in Fig. 9 (lower right panel). Those results shown in Fig. 11 that we consider to be the most important – namely currents crossing the Harang discontinuity towards the north and upward Birkeland currents in its vicinity – will remain untouched by all such changes of conductivity.

It should be mentioned that some noticeable differences remained between the calculated equivalent current vectors of our final conductivity model and the observed vectors in the far west and in the northeast. They could not be eliminated since the east-west extension of the model ionosphere was limited to about 3000 km. Presumably the region of downward field-aligned current feeding the eastward electrojet in the west – due to the conductivity increase towards the east – was, in reality, extended several hundreds of kilometres more to the west than indicated by our model. Similarly, the region of increasing conductivity east of the Harang discontinuity may actually be located even further to the east.

Very recently, M. Segatz from the University of Münster developed quite another method for the determination of the Σ_H distribution from jointly observed SMA and STARE data, under the assumption of a given Σ_H/Σ_P distribution (personal communication). The method is based on the solution of a first-order differential equation for Σ_H. Segatz applied this method to the present data set and found essentially the same results as given above, namely high Σ_H values in the termination region of the eastward electrojet and the coexistence of northward and upward diverging ionospheric currents at the location of the electrically defined Harang discontinuity (personal communication). We feel that this also gives further support to the particular trial and error method which was applied in the present case as well as in previous studies (e.g. Baumjohann et al., 1981; Inhester et al., 1981; Opgenoorth et al., 1983b).

Some readers may ask why we did not make use of magnetic vertical component data that also existed. Such data can be reconstructed almost perfectly from the distribution of the two horizontal components (i.e. of equivalent current vectors) if the latter are observed over a densely spaced and extended two-dimensional array, and if the effects of currents induced within the earth may be neglected. Both conditions were fulfilled in our case [as regards the second condition, cf. Küppers et al. (1979)]. Therefore, inclusion of the vertical component would almost not have given additional information and, accordingly, we omitted such data.

Since the magnetic measurements showed a marked increase of the overhead current density during the westward movement while the electric field amplitudes remained essentially at the same level, we conclude that the current increase was due to a temporal enhancement of the total overhead conductivity distribution. We modelled the three-dimensional current flow in the vicinity of the Harang discontinuity by fitting an equivalent current configuration which had been generated by the superposition of subsequently observed and suitably normalized data. Since the total overhead conductivity distribution presumably increased with time and led to the equivalent current increase given by the intensification factors shown in Fig. 5, the isocontour values of the ionospheric conductivity distribution of the final model (Fig. 9, upper right panel) have to be considered to be representative of the time interval around 1630 UT. For other time intervals the conductivities have to be multiplied with normalization factors as indicated by Fig. 5.

Basically, the three-dimensional current flow pattern in and near to the Harang discontinuity on 2 December 1977 which we finally obtained in our study (Fig. 11) corresponds to the concept given by, for example, Baumjohann (1983). Towards the eastern end of the Harang discontinuity, the eastward and the westward electrojet partially terminate by feeding upward field-aligned currents slightly to the south and north of the Harang discontinuity, respectively. The remainder of the eastward electrojet turns northward in this region and joins the westward electrojet.

The model which we obtained may also shed some light upon the Pedersen current circuit in the Harang discontinuity region. This current, which is fed by downward field-aligned current in the south and northeast, diverges upward in a narrow zone which is only a few hundreds of kilometres wide. The zone is colocated with the electric, not with the magnetic, Harang discontinuity (cf. Fig. 6 and Fig. 12, lower panel). This may be considered as additional evidence for the view that the electric Harang discontinuity is the more fundamental demarcation line compared to the magnetic Harang discontinuity.

The existence and intensity of upward field-aligned current in the Harang discontinuity region may depend on how abruptly the horizontal ionospheric electric fields turn counterclockwise from north to south and on how much the conductivity is reduced in the Harang discontinuity. We feel that such different viewpoints as those given by Kamide (1978) – possibility of a non-existence of field-aligned currents in the Harang discontinuity in certain cases – and by Rostoker et al. (1975) or Iijima and Potemra (1978) – importance of field-aligned current in this region – may easily be reconciled under such aspects.

Acknowledgements. The magnetic observations were performed in cooperation with the Aarhus University, the Royal Institute of Technology at Stockholm, the Finnish Meteorological Institute at Helsinki, the University of Bergen, the Geophysical Observatory at Sodankylä, the Kiruna Geophysical Institute, the University of Oulu and the University at Tromsö. The STARE radars are operated with ELAB and the Norwegian Technical University at Trondheim and the Finnish Meteorological Institute at Helsinki. We thank these institutions and all members of the former magnetometer group at the University of Münster and the STARE group at the MPAE for their support. We would also like to thank St. Berger from the University at Tromsö and H. Maurer from the Technical University of Braunschweig for supplying us with magnetic data from the permanent observatory on Bear Island and from the Braunschweig IMS magnetometer chain, respectively. The magnetometer array observations and part of the work by W. Baumjohann were supported by grants from the Deutsche Forschungsgemeinschaft. The effort of R.A. Greenwald was supported by an NSF grant of the Division of Atmospheric Sciences.

Our sincere thanks go also to three unknown referees who sent us extended and well-founded critical but very helpful comments on the first version of this paper.

References

André, D., Baumjohann, W.: Joint two-dimensional observations of ground magnetic and ionospheric electric fields associated with auroral currents. 5. Current system associated with eastward drifting omega bands. J. Geophys. **50**, 194–201, 1982

Banks, P.M., Doupnik, J.R.: A review of auroral zone electrodynamics deduced from incoherent scatter radar observations. J. Atmos. Terr. Phys. **37**, 951–972, 1975

Banks, P.M., Doupnik, J.R., Akasofu, S.-I.: Electric field observations by incoherent scatter radar in the auroral zone. J. Geophys. Res. **78**, 6607–6622, 1973

Baumjohann, W.: Ionospheric and field-aligned current systems in the auroral zone: A concise review. Adv. Space Res. **2**, No. 10, 55–62, 1983

Baumjohann, W., Greenwald, R.A., Küppers, F.: Joint magnetometer array and radar backscatter observations of auroral currents in northern Scandinavia. J. Geophys. **44**, 373–383, 1978

Baumjohann, W., Untiedt, J., Greenwald, R.A.: Joint two-dimensional observations of ground magnetic and ionospheric electric fields associated with auroral zone currents. 1. Three-dimensional current flows associated with a substorm-intensified eastward electrojet. J. Geophys. Res. **85**, 1963–1978, 1980

Baumjohann, W., Pellinen, R.J., Opgenoorth, H.J., Nielsen, E.: Joint two-dimensional observations of ground magnetic and ionospheric electric fields associated with auroral zone currents: Current systems associated with local auroral break-ups. Planet. Space Sci. **29**, 431–447, 1981

Burrage, M.D., Waldock, J.A., Jones, T.B., Nielsen, E.: Joint STARE and SABRE radar auroral observations of the high-latitude ionospheric convection pattern. Nature **316**, 133–135, 1985

Cahill, Jr., L.J., Greenwald, R.A., Nielsen, E.: Auroral radar and rocket double-probe observations of the electric field across the Harang discontinuity. Geophys. Res. Lett. **5**, 687–690, 1978

Ecklund, W.L., Balsley, B.B., Carter, D.A.: A preliminary comparison of F region plasma drifts and E region irregularity drifts in the auroral zone. J. Geophys. Res. **82**, 195–197, 1977

Greenwald, R.A.: Diffuse radar aurora and the gradient drift instability. J. Geophys. Res. **79**, 4807–4810, 1974

Greenwald, R.A.: Studies of currents and electric fields in the auroral zone ionosphere using radar auroral backscatter. In: Dynamics of the magnetosphere, S.-I. Akasofu, ed.: pp 213–248. Dordrecht: D. Reidel, 1979

Greenwald, R.A., Weiss, W., Nielsen, E., Thomson, N.R.: STARE: A new radar auroral backscatter experiment in northern Scandinavia. Radio Sci. **13**, 1021–1039, 1978

Gustafsson, G.: A revised corrected geomagnetic coordinate system. Ark. Geofys. **5**, 595–617, 1970

Gustafsson, G., Baumjohann, W., Iversen, I.: Multi-method observations and modelling of the three-dimensional currents associated with a very strong Ps6 event. J. Geophys. **49**, 138–145, 1981

Harang, L.: The mean field of disturbance of polar geomagnetic storms. Terr. Mag. Atmos. Electr. **51**, 353–380, 1946

Heppner, J.P.: High latitude magnetic disturbances (A brief review with initial results from motion picture presentation). In: Aurora and airglow, B.M. Mc Cormac, ed.: pp 75–92. New York: Reinhold, 1967

Heppner, J.P.: The Harang discontinuity in auroral belt ionospheric currents. Geofys. Publ. **29**, 105–120, 1972

Heppner, J.P.: Empirical models of high-latitude electric fields. J. Geophys. Res. **82**, 1115–1125, 1977

Horwitz, J.L., Doupnik, J.R., Banks, P.M.: Chatanika radar observations of the latitudinal distributions of auroral zone electric fields, conductivities, and currents. J. Geophys. Res. **83**, 1463–1481, 1978a

Horwitz, J.L., Doupnik, J.R., Banks, P.M., Kamide, Y., Akasofu, S.-I.: The latitudinal distributions of auroral zone electric fields and ground magnetic perturbations and their response to variations in the interplanetary magnetic field. J. Geophys. Res. **83**, 2071–2084, 1978b

Hughes, T.J., Rostoker, G.: A comprehensive model current system for high-latitude magnetic activity – I. The steady state system. Geophys. J.R. Astron. Soc. **58**, 525–569, 1979

Iijima, T., Potemra, T.A.: Large-scale characteristics of field-aligned currents associated with substorms. J. Geophys. Res. **83**, 599–615, 1978

Inhester, B., Baumjohann, W., Greenwald, R.A., Nielsen, E.: Joint two-dimensional observations of ground magnetic and ionospheric electric fields associated with auroral zone currents. 3. Auroral zone currents during the passage of a westward travelling surge. J. Geophys. **49**, 155–162, 1981

Jones, A.G.: The electrical structure of the lithosphere and asthenosphere beneath the Fennoscandian shield. J. Geomagn. Geoelectr. **35**, 811–827, 1983

Kamide, Y.: On current continuity at the Harang discontinuity. Planet. Space Sci. **26**, 237–244, 1978

Kamide, Y.: The relationship between field-aligned currents and the auroral electrojets: A review. Space Sci. Rev. **31**, 127–243, 1982

Kamide, Y., Akasofu, S.-I., Brekke, A.: Ionospheric currents obtained from the Chatanika radar and ground magnetic perturbations at the auroral latitude. Planet. Space Sci. **24**, 193–201, 1976a

Kamide, Y., Vickrey, J.F.: Variability of the Harang discontinuity as observed by the Chatanika radar and the IMS Alaska magnetometer chain. Geophys. Res. Lett. **10**, 159–162, 1983

Kamide, Y., Yasuhara, F., Akasofu, S.-I.: A model current system for the magnetospheric substorm. Planet. Space Sci. **24**, 215–222, 1976b

Küppers, F., Untiedt, J., Baumjohann, W., Lange, K., Jones, A.G.: A two-dimensional magnetometer array for ground-based observations of auroral zone electric currents during the International Magnetospheric Study (IMS). J. Geophys. **46**, 429–450, 1979

Maurer, H., Theile, B.: Parameters of the auroral electrojet from magnetic variations along a meridian. J. Geophys. **44**, 415–426, 1978

Maynard, N.C.: Electric field measurements across the Harang discontinuity. J. Geophys. Res. **79**, 4620–4631, 1974

Murison, M., Richmond, A.D., Matsushita, S.: Estimation of ionospheric electric fields and currents from a regional magnetometer array. J. Geophys. Res. **90**, 3525–3530, 1985

Nielsen, E., Greenwald, R.A.: Electron flow and visual aurora at the Harang discontinuity. J. Geophys. Res. **84**, 4189–4200, 1979

Nielsen, E., Schlegel, K.: A first comparison of STARE and EISCAT electron drift velocity measurements. J. Geophys. Res. **88**, 5745–5750, 1983

Nielsen, E., Schlegel, K.: Coherent radar Doppler measurements and their relationship to the ionospheric electron drift velocity. J. Geophys. Res. **90**, 3498–3504, 1985

Opgenoorth, H.J., Oksman, J., Kaila, K.U., Nielsen, E., Baumjohann, W.: Characteristics of eastward drifting omega bands in the morning sector of the auroral oval. J. Geophys. Res. **88**, 9171–9185, 1983a

Opgenoorth, H.J., Pellinen, R.J., Baumjohann, W., Nielsen, E., Marklund, G., Eliasson, L.: Three-dimensional current flow and particle precipitation in a westward travelling surge (observed during the Barium – GEOS rocket experiment). J. Geophys. Res. **88**, 3138–3152, 1983b

Richmond, A.D., Baumjohann, W.: Three-dimensional analysis of magnetometer array data. J. Geophys. **54**, 138–156, 1983

Rostoker, G., Kisabeth, J.L.: Response of the polar electrojets in the evening sector to polar magnetic substorms. J. Geophys. Res. **78**, 5559–5571, 1973

Rostoker, G., Armstrong, J.C., Zmuda, A.J.: Field-aligned current flow associated with intrusion of the substorm-intensified westward electrojet into the evening sector. J. Geophys. Res. **80**, 3571–3579, 1975

Vickrey, J.F., Vondrak, R.R., Matthews, S.J.: The diurnal and latitudinal variation of auroral zone ionospheric conductivity. J. Geophys. Res. **86**, 65–75, 1981

Waldock, J.A., Jones, T.B., Nielsen, E.: Mean auroral E-region plasma convection patterns measured by SABRE. Nature **313**, 204–206, 1985

Wedde, T., Doupnik, J.R., Banks, P.M.: Chatanika observations of the latitudinal structure of electric fields and particle precipitation on November 21, 1975. J. Geophys. Res. **82**, 2743–2751, 1977

Wiens, R.G., Rostoker, G.: Characteristics of the development of the westward electrojet during the expansive phase of magnetospheric substorms. J. Geophys. Res. **80**, 2109–2128, 1975

Zanetti, Jr., L.J., Arnoldy, R.L., Cahill, Jr., L.J., Behm, D.A., Greenwald, R.A.: Comparative rocket observations of ionospheric electric fields in the auroral oval. Space Sci. Instr. **5**, 183–196, 1980

Zi, M., Nielsen, E.: Spatial variation of electric fields in the high-latitude ionosphere. J. Geophys. Res. **87**, 5202–5206, 1982

Ziesolleck, Ch., Baumjohann, W., Brüning, K., Carlson, C.W., Bush, R.I.: Comparison of height-integrated current densities derived from ground-based magnetometer and rocket-borne observations during the Porcupine F 3 and F 4 flights. J. Geophys. Res. **88**, 8063–8072, 1983

Received August 1, 1984; revised version November 14, 1985
Accepted November 18, 1985

J Geophys (1986) 59:87

Journal of Geophysics

Erratum

In-situ permeability from non-dilatational soil deformation caused by groundwater pumping – a case study

H.-J. Kümpel[1], **G. Lohr**[2]
[1] Dalhousie University, Halifax, Canada; now at University of Kiel, Federal Republic of Germany
[2] University of Kiel, Federal Republic of Germany

J Geophys (1985) 57:184–190

In Vol. 57, p. 188, left column, line 2, in the first paragraph should read:
the dimensionless quantity $K \cdot t/L$ where L is some character-

Book reviews

Robinson, I.S.: Satellite Oceanography – an introduction for oceanographers and remote-sensing scientists. Ellis Horwood Ltd., Chichester/John Wiley & Sons, 455 p., £ 42.50, 1985

The scope of this book, as described by the author, is "to introduce to marine scientists the fundamentals of satellite remote-sensing over the ocean" (p. 22). He himself is an oceanographer who noticed to wide possibilities and advantages of applying space techniques also in the research of the vertical column of the ocean. Compared to the "classical" ship-born measurements (including instrumented moorings and drifting buoys) here a much wider area of the ocean can be covered.

Thus, in the first section (A), the author reviews the fundamentals of satellite remote-sensing, in the oceanographer's viewpoint. Here, the "possibilities in space" are described – satellites and orbits available, different types of sensors and their capabilities, data transmission, and a survey of the "possibilities for oceanography" seeks to place remote-sensing in the broad context of ocean science.

In the second section (B) specific application areas are examined in more detail, e.g. ocean colour scanners and their application, infrared sensors used to measure sea surface temperature, and passive microwave radiometers. Furthermore the microwave altimeter is described as used to measure the absolute height of the sea surface, which provides an exciting possibility to study large-scale ocean dynamics and tidal motions.

The remainder of the book contains four chapters concerned with the measurement of waves and surface roughness by active microwave devices.

Regarding the scope as mentioned above, this book marks a valuable step towards the use of space techniques in ocean sciences. This is well supported by many references, even up to date. One single disadvantage might be seen in the lack of a chapter on satellites for navigation and positioning. The author himself discusses this point and argues, that "the topic is omitted because it does not offer the oceanographer the fundamentally new vantage point in the sky from which to take a fresh look at the ocean which is the essential subject of this text" (p. 23). Of course, this is true; but mentioning navigation and positioning by satellites might be a suitable way to acquaint the "classical" oceanographer to the use of space techniques, and it would increase the value of the book also for marine geophysicists and geologists!

G. Jentzsch

National Research Council, Geophysics Study Committee: Explosive Volcanism: Inception, Evolution, and Hazard. Ser: Studies in Geophysics. National Academy of Sciences, Washington, D.C., 176 pp., 1984 (Nat. Acad. Press, Washington, D.C.)

"The study on Explosive Volcanism was begun soon after the cataclysmic eruptions of Mount St. Helens. It readily became apparent ... that an assessment of the explosive nature of volcanoes must cover all types of volcanic activity; any volcano can be explosive. Consideration of explosive volcanism must start with the generation of magma. Magma-forming processes are intimately connected with tectonics, and there are pronounced differences in the nature of volcanism between regions of compression and subduction and regions of rifting or broader extension. The cyclic and episodic aspects of volcanic activity form a basis for predicting eruptions and can be sources of information on the rates at which magma and energy are introduced to volcanic systems. Improved understanding of the physics of volcanic eruptions is an exciting goal that is vital to progress in hazard evaluation. Finally the study of explosive volcanism must include an appreciation of the severe social problems that are caused by erupting volcanoes. None is of greater urgency than planning for a crisis. This report considers the progress in research on these aspects of explosive volcanism and the need for additional research efforts."

These sentences are quoted from the Preface since they pretty much cover the whole scope of the book.

For someone nursed in the German earth science scene, it is refreshing to see how here the different earth sciences are united under the heading of geophysics: no territoriality of disciplines but cooperation in the study of explosive volcanism. Of the 13 papers, written by experts (some of them quite young) in their fields, two deal with geochemistry and mineralogy, five with geophysics and physical modeling, two with geology and tectonics, three with volcanology in the strict sense and one with aspects of society and science policy.

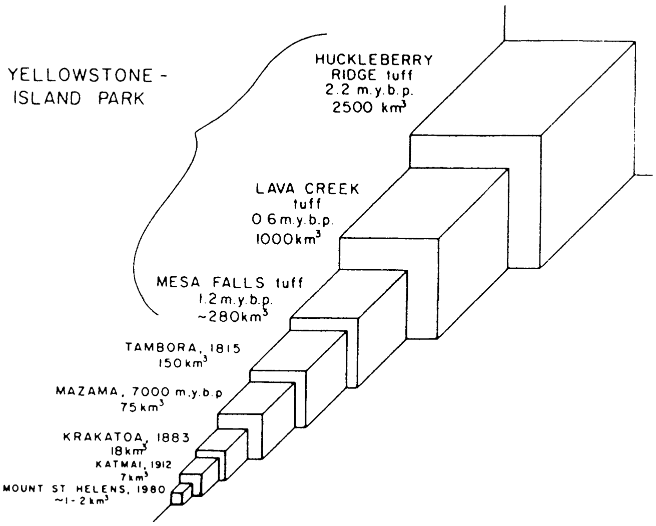

Fig. 7.1. (from Smith and Braile, p. 98) Relative volumes of some wellknown volcanic eruptions (from Williams and McBirney, 1979; Decker and Decker, 1981)

As I would expect from a collection of individual papers, there is considerable heterogeneity, which however will appear different to different readers. Because of the individual nature of the contributions I shall list them here: A.L. Boettcher: The source regions of alkaline volcanoes; R.W. Carlson: Tectonic influence on magma composition of Cenozoic basalts from the Columbia Plateau and northwestern Great Basin, U.S.A.; I.S. Sacks: Subduction geometry and magma genesis; R.L. Smith and R.G. Luedke: Potentially active lineaments and loci in western conterminous United States; B.D. Marsh: Mechanics and energetics of magma formation and ascension; R.L. Christiansen: Yellowstone magmatic evolution: its bearing on understanding large volume explosive volcanism; R.B. Smith and L.W. Braile: Crustal structure and evolution of an explosive silicic volcanic system at Yellowstone National Park; T. Simkin and L. Siebert: Explosive Eruptions in Space and time: durations and intervals, and a comparison of the world's active volcanic belts; R.W. Decker and R.L. Christiansen: Explosive eruptions of Kilauea Volcano; Hawaii; J.G. Moore and C.J. Rice: Chronology and character of the May 18, 1980, explosive eruptions of Mount St. Helens; S.W. Kiefer: Factors governing the structure of volcanic jets; K.H. Wohletz and R.G. McQueen: Experimental studies of hydromagmatic volcanism; R.S. Fiske: Volcanologists, journalists and the concerned local public: a tale of two crisis in the eastern Caribbean.

Evidently there is preponderance on volcanism in the United States, but this is justified by the knowledge and experience of the authors; other parts of the world are taken into consideration.

According to my own inclination, I find the paper on mechanics and energetics of magma formation and ascension particularly enlightening. It is a discussion of the thermodynamic and convection aspects of the problem and gives a number of qualifying order-of-magnitude estimates of processes and effects. Very impressed I am also by the two discussions of the Yellowstone volcanic system. Fig. 7.1 of Smith and Braile, reproduced here, puts perspective to the dimensions and powers explosive volcanism can reach, dwarfing the eruption of Mount St. Helens in May 1980. Human history lacks experience with disasters of the Yellowstone type or e.g. of Lake Taupo, New Zealand (not shown in Fig. 7.1). It is thus somewhat frightening to learn that the geological and geophysical observations of crustal structure and evolution give us no reason to believe that Yellowstone has ceased to live. In view of the geological time scale involved there is also no reason to panic and there is hope that pending big volcanic explosions will become predictable in the future, although predictions will always involve elements of uncertainty and hardship. It is a curious fact of life, that the most dangerous places on earth mostly are also the most attractive ones.

The aim of the book is to focus attention on explosive volcanism and to give recommendations for future work. Not surprisingly these are mainly that more work needs to be done and that all disciplines must cooperate. One of the fruits may be the 1983 symposium "Calderas and Related Volcanic Rocks: The Krakatau Centenial" published in the Journal of Geophysical Research, Vol 89, Issue B10, 30 September 1984.

The book is well produced and well documented. It is a good introduction to the subject of explosive volcanism and will certainly also serve as a good reference book for the specialist.

W. Jacoby

J Geophys (1986) 59:89–97

Journal of Geophysics

Original investigations

A conceptual model of core dynamics and the earth's magnetic field

Charles B. Officer
Earth Sciences Department, Dartmouth College, Hanover, NH 03755, USA

Abstract. A conceptual model of core dynamics and the earth's magnetic field is presented. It differs from previous investigations in the use of an estimated core viscosity of $2 \times 10^7\,\text{cm}^2\,\text{s}^{-1}$. The simplified derivations predict the correct order of magnitude for the external magnetic field and for the westward drift of the nondipole field.

Key words: Earth core – Magnetic field of earth – External magnetic field – Dipole field – Fluid dynamo – Westward drift of nondipole field

Introduction

The theory of magnetic field generation by a fluid dynamo in the core of the earth has received a great deal of attention over the past several years by a number of investigators. The early investigations concentrated on demonstrating that solutions to the magnetic induction equation would lead to an external dipole field, e.g., Elsasser (1941, 1946a, b, 1947, 1950, 1956) and Bullard (1948, 1949a, b). Later investigations concentrated on the core dynamics and the interactions and controls between the hydrodynamic flow and the magnetic field, e.g., Bullard and Gellman (1954), Parker (1955), Hide (1956), Herzenberg (1958), Hide and Roberts (1961), Rikitake (1966), Roberts (1971), Busse (1975, 1976, 1983), Gubbins (1974, 1976), Levy (1976), Braginsky (1976), Watanabe (1977) and Soward (1982). Concurrently, there have been presentations of various possible mechanisms that could lead to the observed polarity reversals, e.g., Parker (1969), Levy (1972a, b) and Robbins (1976, 1977).

There are, indeed, various ways in which an external dipole field can be generated by thermal convection of an electrical conductive fluid in a rotating earth. An important consideration has to be the values of the core parameters which delineate the hydrodynamic flow and the magnetic field, particularly the viscosity.

As discussed in the next section, the kinematic viscosity of the core is one of the least known parameters, with estimated values ranging from $10^{-3}\,\text{cm}^2\,\text{s}^{-1}$ to $10^{11}\,\text{cm}^2\,\text{s}^{-1}$. Most of the previous investigations have used a core viscosity of around $10^{-2}\,\text{cm}^2\,\text{s}^{-1}$, based on theoretical estimates, or have ignored core viscosity effects. This value is not in accord with values determined from various observable geophysical parameters. In particular, a direct interpretation of the damping of seismic waves propagating through the fluid core leads to a value of $2 \times 10^7\,\text{cm}^2\,\text{s}^{-1}$.

The purpose here is to develop a conceptual model of core dynamics and the earth's magnetic field using this value of kinematic viscosity. The derivations are simplified and apply to steady state conditions and the central regime of the convective flow.

The results are encouraging in that they lead to correct order of magnitude estimates for the external field strength and the westward drift, and correctly predict that the nondipole components are related to boundary layer flow effects near the mantle-outer core boundary.

With a viscosity of $2 \times 10^7\,\text{cm}^2\,\text{s}^{-1}$ there is a global circulation including a predominant boundary layer flow; with a viscosity of $10^{-2}\,\text{cm}^2\,\text{s}^{-1}$ the flow breaks up into small scale cyclonic circulations. In essence, the former resembles a worldwide oceanic circulation; and the latter resembles small scale, atmospheric geostrophic circulations.

Outer core parameters

Table 1 lists the parameter values used in the subsequent derivations and calculations. They include d_1, inner core radius; d_2, outer core radius; Ω, angular rotational velocity of the earth; g, gravity for outer core; ρ_0, outer core density; α, thermal coefficient of expansion; c_p, specific heat; k, thermal conductivity; μ, magnetic permeability; σ, electrical conductivity; ν, kinematic viscosity for outer core; ϕ, latitude; H_0, magnetic dipole field at mantle-outer core boundary; and Q, heat conduction at mantle-outer core boundary. The table also includes the dependent parameter values d, outer core thickness; a, Coriolis parameter; D, frictional depth for Ekman-type flow; R, ratio of Lorentz- to Coriolis-forcing terms in the motion equations; λ, horizontal density gradient; and κ, thermal diffusivity.

The values for α, c_p, k, μ and σ are the same as those used by Bullard and Gellman (1954) and are the same or similar to the values used by subsequent investigators. The value for H_0 is taken from the consideration that magnetic field strength was about one-half

Table 1. Core parameter values used in derivations and calculations

$d_1 = 1{,}200\ \text{km}$

$\Omega = 7.3 \times 10^{-5}\ \text{s}^{-1}$

$\alpha = 4.5 \times 10^{-6}\ {}^{\circ}\text{C}^{-1}$

$\mu = 1\ \text{emu}$

$c_p = 0.16\ \text{cal g}^{-1}\ {}^{\circ}\text{C}^{-1}$

$\nu = 2 \times 10^{7}\ \text{cm}^2\ \text{s}^{-1}$

$H_o = 1.9\ \text{gauss}$

$d_2 = 3{,}500\ \text{km}$

$g = 800\ \text{cm s}^{-2}$

$\rho_o = 10.6\ \text{g cm}^{-3}$

$\sigma = 3 \times 10^{-6}\ \text{emu}$

$k = 0.10\ \text{cal cm}^{-1}\ {}^{\circ}\text{C}^{-1}\ \text{s}^{-1}$

$Q = 0.1 \times 10^{-6}\ \text{cal cm}^{-2}\ \text{s}^{-1}$

$\phi = 30^{\circ}$

$$d = d_2 - d_1 = 2{,}300\ \text{km}$$

$$a = \left[\frac{\Omega \sin\phi}{\nu}\right]^{1/2} = 1.35 \times 10^{-6}\ \text{cm}^{-1}$$

$$D = \frac{\pi}{a} = 23.3\ \text{km}$$

$$R = \frac{\sigma \mu^2 H_o^2}{2\Omega \rho_o \sin\phi} = 0.0140$$

$$\lambda = \left[\frac{8\alpha a^3 \rho_o \nu Q}{c_p g d}\right]^{1/2} = 0.253 \times 10^{-15}\ \text{g cm}^{-4}$$

$$\kappa = \frac{k}{\rho_o c_p} = 0.0590\ \text{cm}^2\ \text{s}^{-1}$$

Table 2. Seismological determinations of the kinematic viscosity of the outer core

Source	Q'	P (s)	ν ($\text{cm}^2\ \text{s}^{-1}$)
Sacks (1971)	10,000	1	1×10^7
Buchbinder (1971)	4,000	1	2×10^7
Adams (1972)	$>2{,}200$	1	$<4 \times 10^7$
Qamar and Eisenberg (1974)	5,000–10,000	1	$1\text{–}2 \times 10^7$

its present value throughout the Phanerozoic, e.g., Merrill and McElhinny (1983). The value for Q is taken from the discussion by Verhoogen (1980); this heat flow value per unit area at the mantle-outer core boundary is approximately one-tenth that at the earth's outer surface.

The critical parameter in Table 1 is the viscosity, ν, of the outer core. It is one of the least well known parameters with estimated values differing by several orders of magnitude, ranging from 10^{-3} to $10^{11}\ \text{cm}^2\ \text{s}^{-1}$, e.g., summaries given by Hide (1956), Hide and Roberts (1961) and Jacobs (1975). The lower values have come from theoretical estimates and the higher values from seismological determinations.

The general practice of those who have made theoretical investigations of various aspects of the earth's magnetic field and core dynamics has been to assume a viscosity of around $10^{-2}\ \text{cm}^2\ \text{s}^{-1}$, e.g., Bullard Roberts (1961), Roberts (1967), Gubbins (1974) and Busse (1975, 1976, 1983). In the latter studies this viscosity value was based on the theoretical estimate of Gans (1972). Understandably, the choice of the low viscosity estimate leads to a very different form of core dynamics and delineation of the controlling factors between the hydrodynamic flow and magnetic field than if the assumed viscosity had been several orders of magnitude larger.

The procedure here uses a viscosity based on seismological observations. The assumption is made that the Navier-Stokes equation applies not only to hydrodynamic flow in the outer core but also to seismic wave propagation through the outer core. This method is the same as that used by Jeffreys (1926, 1952), which gives an upper limit estimate for core viscosity. The viscous damping term for seismic wave propagation is of the form, e.g., Lamb (1932),

$$e^{-\frac{2\nu\omega^2}{3c^3}s} \tag{1}$$

where ω is the circular frequency, c the compressional wave velocity and s the ray path distance. The corresponding relation between ν and the seismic dissipation parameter, Q', is, e.g., Stacey (1977),

$$\nu = \frac{3c^2 P}{8\pi Q'} \tag{2}$$

where P is the period of the seismic wave. There have been several determinations of the attenuation of P waves propagating through the core. These results are summarized in Table 2, along with the estimates for ν made from Eq. (2) using a value of $c = 9 \times 10^5\ \text{cm s}^{-1}$. A value of $\nu = 2 \times 10^7\ \text{cm}^2\ \text{s}^{-1}$ was chosen as representative of the outer core viscosity.

There are a number of other observable geophysical parameters from which estimates of core viscosity can be made. Several lead only to an upper limit for the viscosity and, in general, these estimates appear somewhat less definitive than the procedures used in the previous paragraph.

Free oscillations of the earth caused by large earthquakes also undergo damping, and permit estimates for the seismic dissipation factor, Q', to be made as a function of earth radial distance. The damping in the outer core, however, is quite small compared with that in the mantle and precludes more than an approximate estimate of the outer core Q' value. Anderson and Hart (1978a, 1978b) quote a value of $Q' = 10^6$ for the outer core in their earth model. The same relation (2), between ν and Q', applies to free oscillations as well as to seismic wave propagation. Using an appropriate value of $P = 1{,}000$ s, this Q' value converts to $\nu = 14 \times 10^7\ \text{cm}^2\ \text{s}^{-1}$.

Sato and Espinosa (1967) and Suzuki and Sato (1970) have estimated values of the viscosity in the outer core at the mantle-outer core boundary from reflected shear waves. Their results are $\nu = 8 \times 10^{10}\ \text{cm}^2\ \text{s}^{-1}$ and $5 \times 10^9\ \text{cm}^2\ \text{s}^{-1}$, respectively.

Upper limit estimates of core viscosity from a variety of observed geodetic parameters, particularly the damping of the Chandler wobble, have had a long and complex history. Molodenskiy (1981) has recently given upper limit estimates of $10^6\ \text{cm}^2\ \text{s}^{-1}$ from the amplitudes of the forced nutation of the earth, $2 \times 10^9\ \text{cm}^2\ \text{s}^{-1}$ from the damping of the Chandler wobble, and $10^7\ \text{cm}^2\ \text{s}^{-1}$ from tidal variations in the length of day.

Theoretical estimates include those by Bondi and Lyttleton (1948) of $10^7\ \text{cm}^2\ \text{s}^{-1}$, Gans (1972) of $10^{-2}\ \text{cm}^2\ \text{s}^{-1}$, Bukowinski and Knopoff (1976) of $10^0\ \text{cm}^2\ \text{s}^{-1}$, and Watanabe (1977) of $10^3\ \text{cm}^2\ \text{s}^{-1}$.

Derivations and results

The equations defining the magnetohydrodynamics of the outer core are the Navier-Stokes hydrodynamic equation, the heat equation and the magnetic induction equation,

$$\frac{\partial v}{\partial t}+(v\cdot\nabla)\,v=-\frac{1}{\rho_{\mathrm{o}}}\nabla p+\frac{1}{\rho_{\mathrm{o}}}\rho\,g+\nu\,\nabla\cdot\nabla v-2\Omega\times v+\frac{\mu}{4\pi\rho_{\mathrm{o}}}(\nabla\times H)\times H \tag{3}$$

$$\frac{\partial T}{\partial t}+(v\cdot\nabla)\,T=\frac{q}{\rho_{\mathrm{o}}c_{\mathrm{p}}}+\kappa\,\nabla\cdot\nabla T \tag{4}$$

$$\frac{\partial H}{\partial t}+(v\cdot\nabla)\,H=(H\cdot\nabla)\,v+\frac{1}{4\pi\sigma\mu}\nabla\cdot\nabla H \tag{5}$$

where v is the flow velocity, p the pressure, ρ the density, T the temperature, q the internal heat generated per unit volume, H the magnetic field strength and the other parameters are as defined in the previous section. In addition there are the flow and magnetic flux continuity relations and the equation of state relating density and temperature,

$$\nabla\cdot v=0 \tag{6}$$

$$\nabla\cdot H=0 \tag{7}$$

$$\frac{\partial\rho}{\partial T}=-\alpha\,\rho_{\mathrm{o}}. \tag{8}$$

They form a set of coupled, nonlinear partial differential equations. The first two terms on the right hand side of Eq. (3) are the forcing terms, the third the viscous resistance term, the fourth the Coriolis or geostrophic term, and the fifth the Lorentz term. The ultimate driving force for the system is related to the heat flux through the core. The resultant temperature, or density, gradient provides the driving force for the hydrodynamic flow of Eq. (3), and the flow, itself, provides the generating term for the magnetic field of Eq. (5).

The interest, here, is in obtaining solutions to these equations under conditions of an assumed outer core viscosity of $\nu=2\times10^{7}\,\mathrm{cm}^{2}\,\mathrm{s}^{-1}$, in order to delineate the resultant core dynamics as well as to ascertain whether such an outer core viscosity is plausible considering the observed external magnetic field strength and secular changes. Further, it is of interest to retain all three of the terms that may affect the flow, viscous, Coriolis and Lorentz, in the solutions.

We assume steady state conditions. We assume the flows are sufficiently small for the nonlinear term, $(v\cdot\nabla)\,v$, to be neglected in consideration of the other terms in Eq. (3). We assume that the flow is hemispherically symmetrical across the equator and that the first mode of the convection flow is dominant. In the absence of Coriolis and Lorentz effects, the flow pattern would be as shown in Fig. 1. We shall solve the equations in Cartesian coordinates, thus ignoring sphericity effects. For the northern hemisphere we take a coordinate system as shown in Fig. 2.

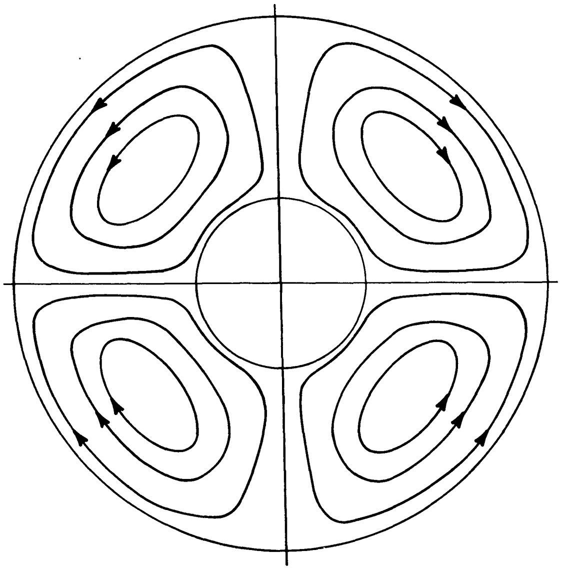

Fig. 1. Thermal circulation in the outer core in the absence of Coriolis and Lorentz forcing terms

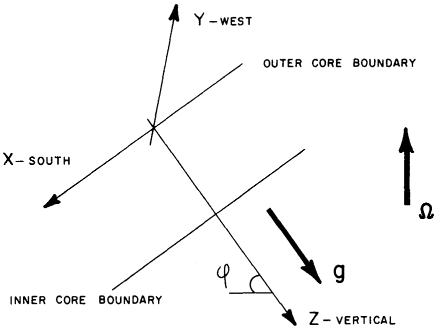

Fig. 2. Coordinate system

We look for solutions applicable to the central, or mid-latitude, region. Under these conditions it is reasonable to assume that the horizontal density gradient, $\partial\rho/\partial x$, is constant. This form of reduction to a description of the flow in its central regime is the same as that applied to gravitational circulation in the upper mantle by Officer and Drake (1983), and in estuaries, by Officer (1976). Since the system is closed in the longitudinal direction, $\partial\rho/\partial y$ is necessarily zero. Under these conditions v and H are functions of z only, and p, ρ and T are the pressure, density and temperature differences from adiabatic, or static, conditions. The flow boundary conditions are $v_x=v_y=v_z=0$ at $z=0$ and $z=d$ which give, from relation (6), $v_z=0$. The magnetic field conditions for a nonconducting mantle and inner core are $H_x=H_y=0$ at $z=0$ and $z=d$ which give, from relation (7), $H_z=H_{\mathrm{o}}=$ constant. The choice of a conducting inner core would change the H_x and H_y fields near the outer core-inner core boundary.

Equations (3) and (5), thus, reduce to

$$\frac{\partial^2 v_x}{\partial z^2}=\frac{1}{\rho_{\mathrm{o}}\nu}\frac{\partial p}{\partial x}+\frac{2\Omega\,v_y\sin\phi}{\nu}-\frac{\mu}{4\pi\rho_{\mathrm{o}}\nu}H_z\frac{\partial H_x}{\partial z} \tag{9}$$

$$\frac{\partial^2 v_y}{\partial z^2}=-\frac{2\Omega\,v_x\sin\phi}{\nu}+\frac{\mu}{4\pi\rho_{\mathrm{o}}\nu}H_z\frac{\partial H_y}{\partial z} \tag{10}$$

$$0=H_z\frac{\partial v_x}{\partial z}+\frac{1}{4\pi\sigma\mu}\frac{\partial^2 H_x}{\partial z^2} \tag{11}$$

$$0=H_z\frac{\partial v_y}{\partial z}+\frac{1}{4\pi\sigma\mu}\frac{\partial^2 H_y}{\partial z^2} \tag{12}$$

and the flow and magnetic flux continuity relations are

$$\int_0^d v_x\,dz=0 \tag{13}$$

$$\int_0^d H_x\,dz=0. \tag{14}$$

It is appropriate to take an isodynamic condition at the mantle-outer core boundary. The pressure will be given by

$$p=\rho g(z-\xi)+p_o \tag{15}$$

where ξ is the dynamic depression of the boundary and p_o a constant. We have, then, for the horizontal pressure gradient,

$$\begin{aligned}\frac{\partial p}{\partial x}&=g\int_0^z\frac{\partial\rho}{\partial x}dz-\rho_o g\frac{\partial\xi}{\partial x}\\&=g\lambda z-\rho_o g i\end{aligned} \tag{16}$$

where we have ignored second order terms and where $i=\partial\xi/\partial x$ is the slope of the mantle-outer core surface and $\lambda=\partial\rho/\partial x$ the horizontal density gradient. Equations (9) through (12) are in the form of four coupled, ordinary differential equations which, with relation (16), may be easily solved. Equation (13) will provide a defining relation between i and λ, and Eq. (14) will provide a defining relation between H_o and the other parameters of the system.

Equations (9) through (12) may be combined to give the following two equations, separable in v_x and v_y,

$$\frac{d^4 v_x}{dz^4}+\left(\frac{4\Omega^2\sin^2\phi}{v^2}-\frac{\sigma^2\mu^4 H_o^4}{\rho_o^2 v^2}\right)v_x=\frac{\sigma\mu^2 H_o^2}{\rho_o^2 v^2}\frac{\partial p}{\partial x} \tag{17}$$

$$\frac{d^4 v_y}{dz^4}+\left(\frac{4\Omega^2\sin^2\phi}{v^2}-\frac{\sigma^2\mu^4 H_o^4}{\rho_o^2 v^2}\right)v_y=-\frac{2\Omega\sin\phi}{\rho_o v^2}\frac{\partial p}{\partial x}. \tag{18}$$

Using the parameter values listed in Table 1 we have for the ratio, R, of the square root of the terms in the parentheses

$$R=\frac{\dfrac{\sigma\mu^2 H_o^2}{\rho_o v}}{\dfrac{2\Omega\sin\phi}{v}}=\frac{\sigma\mu^2 H_o^2}{2\Omega\rho_o\sin\phi}=0.0140. \tag{19}$$

We may neglect the second term in the parentheses with respect to the first term, reducing Eqs. (17) and (18) to

$$\frac{d^4 v_x}{dz^4}+\frac{4\Omega^2\sin^2\phi}{v^2}v_x=\frac{\sigma\mu^2 H_o^2}{\rho_o^2 v^2}\frac{\partial p}{\partial x} \tag{20}$$

$$\frac{d^4 v_y}{dz^4}+\frac{4\Omega^2\sin^2\phi}{v^2}v_y=-\frac{2\Omega\sin\phi}{\rho_o v^2}\frac{\partial p}{\partial x}. \tag{21}$$

Using relation (16), the complementary and particular integral solutions to Eqs. (20) and (21) are

$$\begin{aligned}v_x=&-\frac{Rgi}{2a^2 v}+\frac{Rg\lambda}{2a^2\rho_o v}z+C_1\cosh az\cos az\\&+C_2\sinh az\cos az+C_3\cosh az\sin az\\&+C_4\sinh az\sin az\end{aligned} \tag{22}$$

$$\begin{aligned}v_y=&\frac{gi}{2a^2 v}-\frac{g\lambda}{2a^2\rho_a v}z-(2C_1+RC_4)\sinh az\sin az\\&-(2C_2+RC_3)\cosh az\sin az\\&+(2C_3-RC_2)\sinh az\cos az\\&+(2C_4-RC_1)\cosh az\cos az.\end{aligned} \tag{23}$$

The constants C_1 through C_4 are determined from the boundary conditions that $v_x=v_y=0$ at $z=0$ and $z=d$. Using the condition from Tables 1 and 2 that

$$D=\frac{\pi}{a}\ll d \tag{24}$$

and the continuity condition, Eq. (13), which gives

$$i=\frac{1}{2}\frac{\lambda d}{\rho_o} \tag{25}$$

we obtain

$$\begin{aligned}v_x=\frac{g\lambda d}{4a^2\rho_o v}\Big[&(1-R)e^{-az}\sin az+2Re^{-az}\cos az\\&-2R+\frac{4Rz}{d}-e^{-a(d-z)}\sin a(d-z)\\&-2Re^{-a(d-z)}\cos a(d-z)\Big]\end{aligned} \tag{26}$$

$$\begin{aligned}v_y=\frac{g\lambda d}{4a^2\rho_o v}\Big[&1-\frac{2z}{d}-e^{-az}\cos az+\frac{3R}{2}e^{-az}\sin az\\&+e^{-a(d-z)}\cos a(d-z)+\frac{R}{2}e^{-a(d-z)}\sin a(d-z)\Big].\end{aligned} \tag{27}$$

Let us look for the moment at the type of core dynamics that these solutions delineate. The flow may be considered to consist of three parts, an Ekman-type boundary layer current defined by the frictional depth, $D=\pi/a$, near the mantle-outer core boundary and near the outer core-inner core boundary and a mid-depth drift current. For v_x the upper boundary layer flow is defined by the $\exp(-az)\sin az$ term and the lower boundary layer flow in the opposite direction by the $\exp[-a(d-z)]\sin a(d-z)$ term. In the mid-depth region there is a small drift current related to the Lorentz term in the original equations and given by the expression $[-2R+(4Rz)/d]$. For v_y there are corresponding boundary layer flows and a large mid-depth drift current related to the Coriolis term in the defining equations and given by the expression $[1-(2z)/d]$. In the limit of no Coriolis or Lorentz effects the solutions (26) and (27) reduce to

$$v_x=\frac{g\lambda}{12\rho_o v}[d^2z-3dz^2+z^3] \tag{28}$$

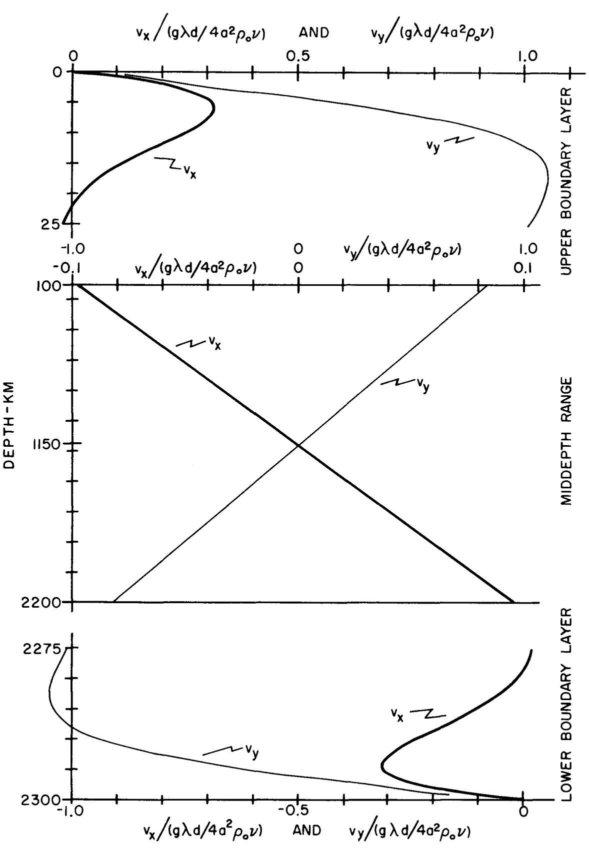

Fig. 3. Graphs of v_x and v_y for boundary layer flows and mid-depth flow. Note changes in ordinate and abscissa scales

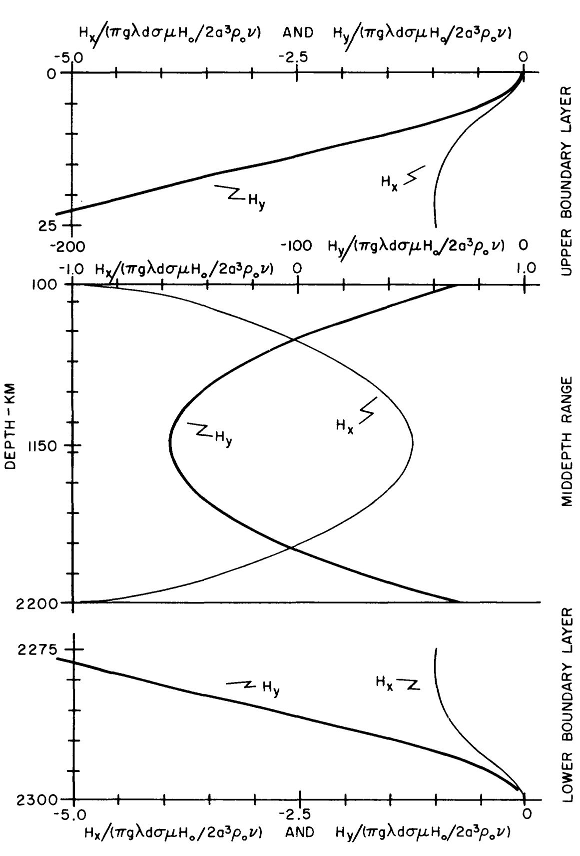

Fig 4. Graphs of H_x and H_y for boundary flows and mid-depth flow. Note changes in ordinate and abscissa scales

$$v_y=0 \tag{29}$$

which are the solutions for gravitational, or horizontal density gradient, circulation of Officer and Drake (1983).

From Eqs. (11) and (12) the corresponding solutions for H_x and H_y may be obtained with the boundary conditions $H_x=H_y=0$ at $z=0$ and $z=d$, giving

$$H_x=-\frac{\pi g\lambda d\sigma\mu H_0}{2a^3\rho_0\nu}\Big[1-e^{-az}(\cos az+\sin az)-4Raz + \frac{4Raz^2}{d}-e^{-a(d-z)}(\cos a(d-z)+\sin a(d-z))\Big] \tag{30}$$

$$H_y=\frac{\pi g\lambda d\sigma\mu H_0}{2a^3\rho_0\nu}\Big[1-e^{-az}(\cos az-\sin az)-2az + \frac{2az^2}{d}-e^{-a(d-z)}(\cos a(d-z)-\sin a(d-z))\Big]. \tag{31}$$

The magnetic flux relation of Eq. (14), then, gives from solution (30) the condition for H_0 in terms of the other parameters of the system that

$$\tfrac{2}{3}Rad=1. \tag{32}$$

From the definition (19) for R, we have

$$H_0=\left[\frac{3\Omega\rho_0\sin\phi}{\sigma\mu^2 ad}\right]^{1/2}=1.1\ \text{gauss} \tag{33}$$

using the parameter values in Table 1. It is, indeed, interesting and encouraging that this simplified exposition does give a value for the external field strength which is the same order of magnitude as the value of 1.9 gauss for the average field strength during the Phanerozoic.

Both the H_x and H_y fields have a depth variation similar to that of the hydrodynamic flow. There is a rapidly varying portion near the mantle-outer core boundary and near the outer core-inner core boundary defined by the frictional depth, D. Within the mid-depth region both components vary slowly. The H_x field lies in a northerly direction in the northern hemisphere near the mantle-outer core boundary. In spherical coordinates, the H_x and H_z components form the poloidal field, and the H_y component determines the toroidal field. The mid-depth portion of the H_x field differs from that of the H_y field by the factor R. In other words, the toroidal field will be about two orders of magnitude greater than the poloidal field. In this formulation a strong toroidal field is predicted for the outer core.

Figures 3 and 4 are graphs of the depth-variable portions of the v_x and v_y flows and the H_x and H_y fields, respectively. The ordinate and abscissa scale changes should be noted in these figures. They illustrate quantitatively the depth variations for each component discussed in the previous paragraphs.

Figures 5 and 6 are schematic representations of the core dynamics assuming a hemispherically symmetrical

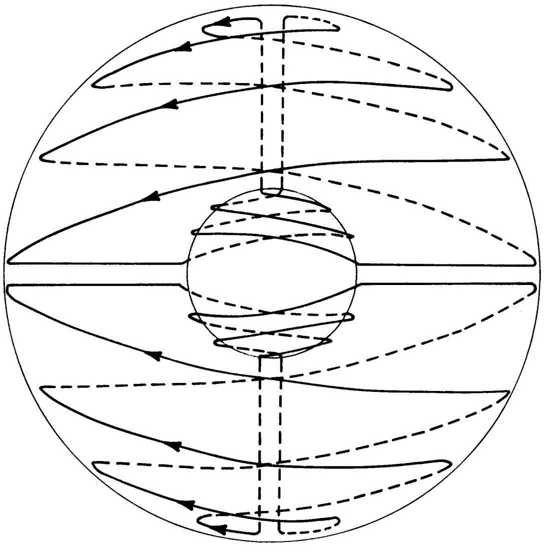

Fig. 5. Schematic representation of global boundary layer circulation in the outer core

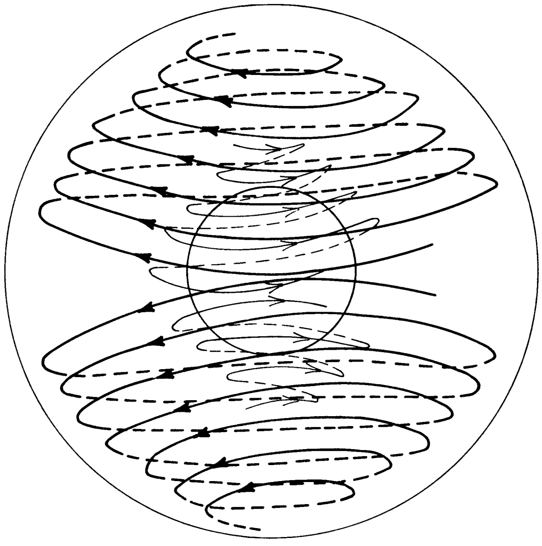

Fig. 6. Schematic representation of global mid-depth circulation in the outer core

circulation. The flows consist of spiral motions in a westerly direction from each pole toward the equator near the mantle-outer core boundary and spiral motions in the opposite direction near the outer core-inner core boundary. For the mid-depth portion the motion is dominantly westerly with a small poleward component in the upper portion, and dominantly easterly with a small equatorward component in the lower portion.

It is necessary, next, to obtain some reasonable estimate for the horizontal density gradient, $\lambda = \partial\rho/\partial x$. The horizontal heat fluxes related to the mid-depth portion of the v_x flow will balance out. For the upper boundary layer flow, the conductive heat flux out at the mantle-outer core boundary per unit distance must be equal to the decrease in the convective heat flux per unit distance and, correspondingly, for the heat flux in at the outer core-inner core boundary, assuming no internal heat generation. We have, then, from Eq. (26)

$$Q = -c_p \rho_0 \frac{\partial T}{\partial x} \int_0^\infty \frac{g\lambda d}{4a^2 \rho_0 \nu} e^{-az} \sin a z\, dz \tag{34}$$

or, using relation (8),

$$\lambda = \left[\frac{8\alpha a^3 \rho_0 \nu Q}{c_p g d}\right]^{1/2} = 0.253 \times 10^{-15}\,\mathrm{g\,cm^{-4}} \tag{35}$$

using the parameter values of Table 1.

The multiplying factors for the v_x and v_y flows of Eqs. (26) and (27) and for the H_x and H_y fields of Eqs. (30) and (31) are, then,

$$A = \frac{g\lambda d}{4a^2 \rho_0 \nu} = 0.0301\,\mathrm{cm\,s^{-1}} \tag{36}$$

and

$$B = \frac{\pi g \lambda d \sigma \mu}{2a^3 \rho_0 \nu} = 0.420. \tag{37}$$

From relations (33) and (35) and the definition for a in Table 1 it is to be noted that the various dependences on the viscosity, ν, are λ proportional to $\nu^{-1/4}$; v_x and v_y proportional to $\nu^{-1/4}$; and H_x, H_y and H_z proportional to $\nu^{1/4}$. All the components show a relatively weak dependence on the viscosity.

Let us look next at the nondipole components of the earth's magnetic field. Elsasser (1941, 1946b) demonstrated that the nondipole components must originate as a skin effect in the outer core adjacent to the mantle-outer core boundary at a depth not in excess of 150 km from the boundary. This is in accord with the core dynamic formulation given here. The nondipole components could originate from spatial variations in the boundary layer flow near the mantle-outer core boundary. Further, the observed secular variations in the nondipole field would originate from temporal variations in the boundary layer flow. Although the simple formulation given here does not include consideration of such effects, spatial and temporal variations are, indeed, an important characteristic of Rayleigh-Benard boundary layer circulation.

It is possible to estimate the drift of these irregularities from the formulation given here. Over the frictional depth of the upper boundary layer flow there is a strong westward drift in both hemispheres, gives by

$$V_w = \frac{1}{D} \int_0^D v_y\, dz = 0.206 \frac{g\lambda d}{a^2 \rho_0 \nu} = 0.025\,\mathrm{cm\,s^{-1}} \tag{38}$$

using the parameter values of Table 1. As with the deduced magnitude of the main field strength, H_0, from relation (33), it is encouraging that the predicted value for the westward drift from this simplified formulation is in accord with the observed westward drift of the main field, e.g., Bullard et al. (1950) as well as others. This formulation also predicts that there should be an additional but much smaller northerly drift in the northern hemisphere and southerly drift in the southern hemisphere given by

$$V_s = \frac{1}{D}\int_0^D v_x\,dz = 0.036\,\frac{g\lambda d}{a^2 \rho_0 \nu} = 0.004\ \mathrm{cm\,s^{-1}}. \qquad (39)$$

Speculations as to the origin of the secular variations and polarity reversals

The principal purpose of this investigation has been do delineate the gross features of core dynamics and the geomagnetic field under conditions of an outer core viscosity of $2 \times 10^7\ \mathrm{cm^2\,s^{-1}}$. The analytic solutions are for steady state and apply only to the central portion of the flow regime. It is of interest to pursue, in a qualitative manner, the implications of this formulation for an understanding of other features of the secular variations and the polarity reversals. The following discussion is admittedly speculative.

Special and temporal instabilities are an inherent characteristic of Rayleigh-Benard circulation, since the defining equations are coupled and nonlinear. Various aspects of these instabilities have been examined by a number of investigators, e.g., Howard (1966), Welander (1967), Krishnamurti (1970a, b), Busse and Whitehead (1971), Moore and Weiss (1973), Nield (1975), Busse and Riahi (1980) and Krishnamurti and Howard (1981). It is possible that both the observed temporal variations in the magnetic moment of the dipole field and the observed movement of the magnetic pole around the geographic pole might be related to such temporal and spatial variations of the global core dynamics about equilibrium. The nondipole field and the temporal variations in its magnitude could be related to smaller scale spatial irregularities and temporal variations in the boundary layer flow near the mantle-outer core boundary.

Of particular interest to a consideration of polarity reversals are the numerical experiments of Welander (1967). His numerical computations are related to a very simple, boundary-layer type flow. It consists of a vertical tube of fluid forming a closed loop that is heated from below and cooled from above. The fluid motion is defined by the usual coupled hydrodynamic and heat continuity equations and there are two equilibrium flow conditions, viz., clockwise or counterclockwise flow. His calculations show that depending on the relative magnitude of the resistive and driving forces, flow instabilities will result, leading in the extreme to flow reversals. The interesting result is that for even this very simple system of heat-driven, boundary-layer type convection flow, reversals are an *inherent* characteristic of the system. Robbins (1977) has extended the calculations for the Welander loop and those for a reversing disc dynamo, defined by similar equations, towards an understanding of the polarity reversals.

Following the results from Robbins (1977), Officer and Lynch (unpublished data, 1985) have continued the numerical calculations for the Welander loop for increasing flow resistance and the ratio of resistive to driving force (Fig. 7). The progression is from (A) steady state, to (B) steady state with oscillatory damping, to (C) nearly neutral oscillations about one of the equilibrium positions, to (D) gradual buildup of the oscillations to a reversal, and then repetition of the sequence about the other equilibrium position, to (E) periodic oscillation sequences, to (F) aperiodic oscil-

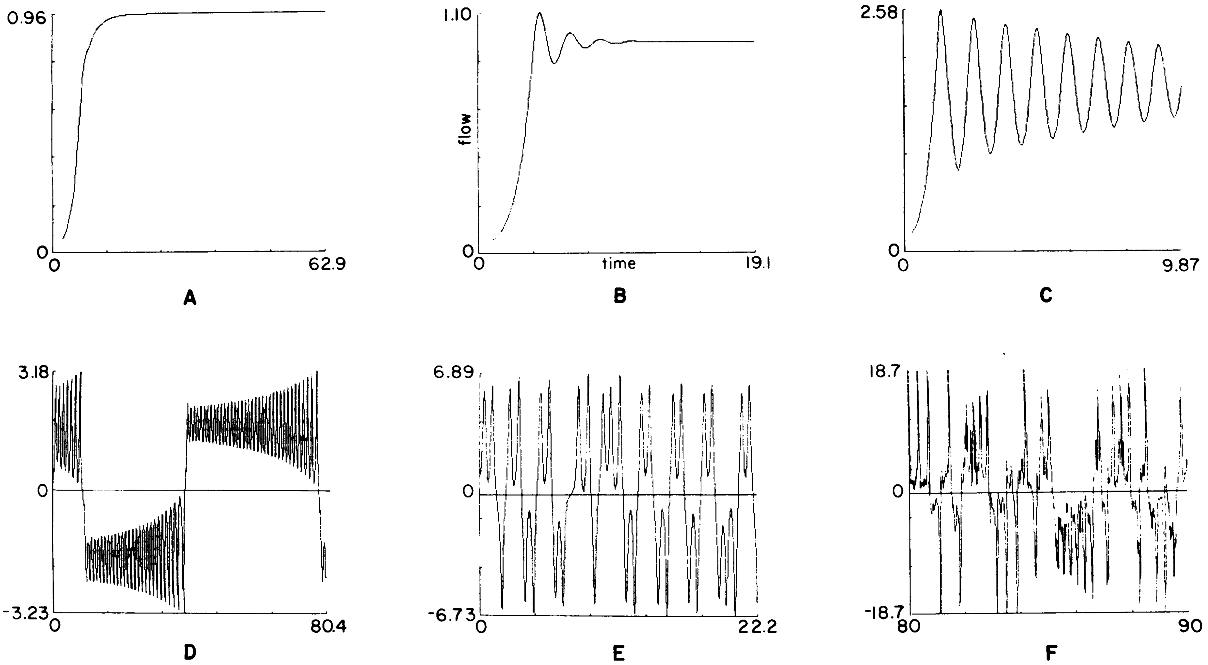

Fig. 7A–F. Plots of fluid flow (nondimensional) versus time (nondimensional) for the Welander loop numerical experiment for various values of the parameters, a and ε. **A** 0.4, 0.2; **B** 2, 1; **C** 20, 3; **D** 40, 6; **E** 102.4, 3.2; **F** 10,240, 96 lations. For the last case the spectral distribution of the reversal time intervals has a peak near the time for one circuit of the loop, dropping off steeply for shorter time intervals and more gradually for longer time intervals. This type of sequential behaviour appears to be characteristic of a number of similar systems, specifically the Lorenz equations, Lorenz (1963) and Sparrow (1982), and the nonlinear oscillator studied by Moore and Spiegel (1966). For the core dynamics formulated herein, the comparison with the Welander loop is that both are heat-driven, boundary-layer type circulations with heat-convective effects dominant over heat-conductive effects. For the core dynamics the mid-depth flow is geostrophically controlled. The boundary layer flow is characterized by a large resistance term and a small driving force, with a time for one complete cycle of about 10000 years.

Assuming that the magnetic polarity reversals are related to reversals in the global circulation in the outer core and that the present core conditions may correspond to Fig. 7F, a number of consequences follow. Throughout the Phanerozoic there would be essentially equal periods of westward and eastward drift of the nondipole field. The circulation, itself, forms a coupled northern and southern hemisphere system. The specifics of the flow reversals may not be exactly the same in each hemisphere, leading to a quadrupole field during the transition. Further, there is an inherent indeterminacy in the determination of the direction of a new dipole field. With flow reversals the new magnetic field may be in the same or the opposite direction to the old field. Thus, we should expect equal episodes of magnetic field excursions toward a zero field strength but return to the original field direction and of episodes of field reversals. Finally, if the core viscosity has increased substantially with geologic time, the flow reversal sequence would progress from Fig. 7D to E to F, leading to a possible explanation for the extended periods of either normal or reversed polarity during the earlier Phanerozoic.

All the above comments are, of course, speculative. The important point is that a more detailed understanding of the Welander loop type of flow instabilities as applied to core dynamics may lead toward an understanding of magnetic polarity reversals, as also concluded by Robbins (1977).

Conclusions

An alternative model of core dynamics and explanation for the origin of the earth's magnetic field has been given. The formulation differs from previous models in the application of an estimated kinematic viscosity for the outer core of $2 \times 10^7\,\mathrm{cm^2\,s^{-1}}$. The simplified derivations assume a hemispherically symmetrical, global circulation in the core. The resulting boundary layer flow is thermally driven, and is controlled in a latitudinal direction by the Coriolis force and in a longitudinal direction by the Lorenz and Coriolis forces. The theory predicts the correct order of magnitude for the dipole field strength, 1.1 gauss, and the correct order of magnitude for the westward drift of the nondipole field, $0.025\,\mathrm{cm\,s^{-1}}$. It is suggested that both the secular variations in the dipole and nondipole fields and the polarity reversals may be related to the instabilities in the Rayleigh-Benard, boundary-layer hydrodynamic flow in the outer core.

References

Adams, R.D.: Multiple inner core reflections from a Novaya Zemlya explosion. Bull. Seismol. Soc. Am. **62**, 1063–1072, 1972

Anderson, D.L., Hart, R.S.: Attenuation models of the earth. Phys. Earth Planet. Inter. **16**, 289–306, 1978a

Anderson, D.L., Hart, R.S.: Q of the earth. J. Geophys. Res. **83**, 5869–5882, 1978b

Bondi, H., Lyttleton, R.A.: On the dynamical theory of the rotation of the earth: I, the secular retardation of the core. Proc. Cambridge Philos. Soc. **44**, 345–359, 1948

Braginsky, S.I.: On the nearly axially symmetrical model of the hydromagnetic dynamo of the earth. Phys. Earth Planet. Inter. **11**, 191–199, 1976

Buchbinder, G.G.R.: A velocity structure of the earth's core. Bull. Seismol. Soc. Am. **61**, 429–456, 1971

Bukowinski, M.S.T., Knopoff, L.: Electronic structure of iron and models of the earth's core. Geophys. Res. Lett. **3**, 45–48, 1976

Bullard, E.C.: The secular change in the earth's magnetic field. Mon. Not. R. Astron. Soc., Geophys. Suppl. **5**, 248–257, 1948

Bullard, E.C.: The magnetic field within the earth. Proc. R. Soc. London, Ser. A, **197**, 433–453, 1949a

Bullard, E.C.: Electromagnetic induction in a rotating sphere. Proc. R. Soc. London, Ser. A, **199**, 413–443, 1949b

Bullard, E., Gellman, H.: Homogeneous dynamos and terrestrial magnetism. Philos. Trans. R. Soc. London, Ser. A, **247**, 213–278, 1954

Bullard, E.C., Freedman, C., Gellman, H., Nixon, J.: The westward drift of the earth's magnetic field. Philos. Trans. R. Soc. London, Ser. A, **243**, 67–92, 1950

Busse, F.H.: A model of the geodynamo. Geophys. J. R. Astron. Soc. **42**, 437–459, 1975

Busse, F.H.: Generation of planetary magnetism by convection. Phys. Earth Planet. Inter. **12**, 350–358, 1976

Busse, F.H.: Recent developments in the dynamo theory of planetary magnetism. Annu. Rev. Earth Planet. Sci. **11**, 241–268, 1983

Busse, F.H., Riahi, N.: Nonlinear convection in a layer with nearly insulating boundaries. J. Fluid Mech. **96**, 243–256, 1980

Busse, F.H., Whiteheed, J.A.: Instabilities of convection rolls in a high Prandtl number fluid. J. Fluid Mech. **47**, 305–320, 1971

Elsasser, W.M.: A statistical analysis of the earth's internal magnetic field. Phys. Rev. **60**, 876–883, 1941

Elsasser, W.M.: Induction effects in terrestrial magnetism: Part I, theory. Phys. Rev. **69**, 106–116, 1946a

Elsasser, W.M.: Induction effects in terrestrial magnetism: Part II, the secular variation. Phys. Rev. **70**, 202–212, 1946b

Elsasser, W.M.: Induction effects in terrestrial magnetism: Part III, electric modes. Phys. Rev. **72**, 821–833, 1947

Elsasser, W.M.: The earth's interior and geomagnetism. Rev. Mod. Phys. **22**, 1–35, 1950

Elsasser, W.M.: Hydromagnetic dynamo theory. Rev. Mod. Phys. **28**, 135–163, 1956

Gans, R.F.: Viscosity of the earth's core. J. Geophys. Res. **77**, 360–366, 1972

Gubbins, D.: Theories of the geomagnetic and solar dynamos. Rev. Geophys. Space Phys. **12**, 137–154, 1974

Gubbins, D.: Observational constraints on the generation process of the earth's magnetic field. Geophys. J. R. Astron. Soc. **47**, 19–39, 1976

Herzenberg, A.: Geomagnetic dynamos. Phil. Trans. R. Soc. London, Ser. A, **250**, 543–583, 1958

Hide, R.: The hydrodynamics of the earth's core. Phys. Chem. Earth **1**, 94-137, 1956

Hide, R., Roberts, P.H.: The origin of the main geomagnetic field. Phys. Chem. Earth **4**, 27-98, 1961

Howard, L.N.: Convection at high Rayleigh number. Proc. Eleventh Int. Cong. Appl. Math., 1109-1115, 1966

Jacobs, J.A.: The earth's core. London: Academic Press 1975

Jeffreys, H.: The viscosity of the earth. Mon. Notices Roy. Astron. Soc., Geophys. Suppl. **1**, 412-424, 1926

Jeffreys, H.: The earth, third edition. London: Cambridge University Press 1952

Krishnamurti, R.: On the transition to turbulent convection: Part 1, the transition from two to three dimensional flow. J. Fluid Mech. **42**, 295–307, 1970a

Krishnamurti, R.: On the transition to turbulent convection: Part 2, the transition to time dependent flow. J. Fluid Mech. **42**, 309–320, 1970b

Krishnamurti, R., Howard, L.N.: Large scale flow generation in turbulent convection. Proc. Natl. Acad. Sci. USA **78**, 1981-1985, 1981

Lamb, H.: Hydrodynamics. London: Cambridge University Press 1932

Levy, E.H.: Kinematic reversal schemes for the geomagnetic dipole. Astrophys. J. **171**, 635–642, 1972a

Levy, E.H.: On the state of the geomagnetic field and its reversals. Astrophys. J. **175**, 573–581, 1972b

Levy, E.H.: Generation of planetary magnetic fields. Annu. Rev. Earth Planet. Sci. **4**, 159–185, 1976

Lorenz, E.N.: Deterministic nonperiodic flow. J. Atmos. Sci. **20**, 130–141, 1963

Merrill, R.T., McElhinny, M.W.: The earth's magnetic field. London: Academic Press 1983

Moore, D.W., Spiegel, E.A.: A thermally excited nonlinear oscillator. Astrophys. J. **143**, 871–887, 1966

Moore, D.R., Weiss, N.O.: Two dimensional Rayleigh-Benard convection. J. Fluid Mech. **58**, 389–312, 1973

Molodenskiy, S.M.: Upper viscosity boundary of the earth's core. Izvestiya Earth Phys. **17**, 903–909, 1981

Neild, D.A.: The onset of convective instability. J. Fluid Mech. **71**, 441–454, 1975

Officer, C.B.: Physical oceanography of estuaries. New York: John Wiley 1976

Officer, C.B., Drake, C.L.: Plate dynamics and isostasy in a dynamic system. J. Geophys. **54**, 1–19, 1983

Parker, E.N.: Hydromagnetic dynamo models. Astrophys. J. **122**, 293–314, 1955

Parker, E.N.: The occasional reversal of the geomagnetic field. Astrophys. J. **158**, 815–827, 1969

Qamar, A., Eisenberg, A.: The damping of core waves. J. Geophys. Res. **79**, 758–765, 1974

Rikitake, T.: Electromagnetism and the earth's interior. Amsterdam: Elsevier 1966

Robbins, K.A.: A moment equation description of magnetic reversals in the earth. Proc. Natl. Acad. Sci. USA **73**, 4297-4301, 1976

Robbins, K.A.: A new approach to subcritical instability and turbulent transitions in a simple dynamo. Math. Proc. Cambridge Philos. Soc. **82**, 309-325, 1977

Roberts, P.H.: An introduction to magnetohydrodynamics. London: Longmans 1967

Roberts, P.H.: Dynamo theory. In: Mathematical problems in the geophysical sciences, II, inverse problems, dynamo theory and tides, Reid, W.H. Ed., pp. 129-206, Providence: American Mathematical Society 1971

Sacks, I.S.: Anelasticity of the outer core. In: Annu. Rep. Dep. Terr. Mag. 1969–1970, Carnegie Inst., Washington, pp. 414–426, 1971

Sato, R., Espinosa, A.F.: Dissipation in the earth's mantle and rigidity and viscosity in the earth's core determined from waves multiply reflected from the mantle-core boundary. Bull. Seismol. Soc. Am. **57**, 829–856, 1967

Soward, A.M., Ed.: Stellar and planetary magnetism. New York: Gordon and Breach 1982

Sparrow, C.: The Lorenz equations: Bifurcations, chaos and strange attractors. Berlin, Heidelberg, New York: Springer 1982

Stacey, F.D.: Physics of the earth. New York: John Wiley 1977

Suzuki, Y., Sato, R.: Viscosity determination in the earth's outer core from ScS and SKS phases. J. Phys. Earth **18**, 157–170, 1970

Verhoogen, J.: Energetics of the earth. Washington: National Academy of Sciences 1980

Watanabe, H.: Bounds on the fluid velocity and magnetic field in the earth's core imposed by hydromagnetic consideration of an $\alpha\omega$-dynamo. J. Geomagn. Geoelectr. **29**, 191–209, 1977

Welander, P.: On the oscillatory instability of a differentially heated fluid loop. J. Fluid Mech. **29**, 17–30, 1967

Received July 30, 1985; revised version December 3, 1985
Accepted December 16, 1985

J Geophys (1986) 59:98–102

Journal of Geophysics

Paleomagnetism of Miocene volcanism from South Syria

P. Roperch[1, 2] **and N. Bonhommet**[2]

[1] ORSTOM département A, 213 rue Lafayette, F-75480 Paris Cedex 10, France
[2] Laboratoire de géophysique interne, Université de Rennes, Institut de Géologie, Campus de Beaulieu, Avenue de Géneral Leclerc, F-35042 Rennes Cedex, France

Abstract. Syrian Miocene alkali basalts have been sampled in the area south of Damascus. Thirty two flows were collected from short vertical sections (one to six flows) at ten sites. The sequence of polarity observed at each site is compatible with a magmatic event taking place during a reversal. Change of polarity and the presence of transitional directions allows: (1) correlation of flows between sites, (2) the assessment of the short duration of this volcanism. Moreover, the mean direction of magnetization ($D=179$, $I=-34$, $K=28$, $\alpha_{95}=6°$) shows clearly that since Miocene times no tectonic rotation occurred in this deformed area close to the east side of the Levant fault and south of the Palmyra chain.

Key words: Paleomagnetism – Arabia – Syria – Miocene – Basalt

Introduction

The opening of the Red Sea which started 20 My ago is responsible for a sinistral movement of 105 km along the Levant transform fault (Freund, 1965). In this area, large deformation occurs on both sides of the main fracture zone with the Lebanon mountain on the western part and the Palmyra Chain on the eastern part (Fig. 1). This tectonic setting has initiated early paleomagnetic studies which have been undertaken in Lebanon and Israel. The first results on Jurassic and Cretaceous formations from Lebanon showed large discrepancies with the apparent polar wander path of Africa and led to the concept of a Lebanese microplate (Van Dongen et al., 1967; Gregor et al., 1974). Further paleomagnetic work in Israel (Freund and Tarling, 1979; Ron et al., 1984) explains the results in terms of block rotation by strike-slip faulting. All these studies have been conducted on the western part of the Levant fault. Although there are fewer structural complexities on the east side of the Levant fault, no paleomagnetic results are available.

We have decided to sample the Miocene volcanic sequence, commonly related to the first stage of volcanic activity along the Levant fault, in Syria in order to provide a Miocene reference pole for this area or, on the contrary, to detect post-Miocene local deformation.

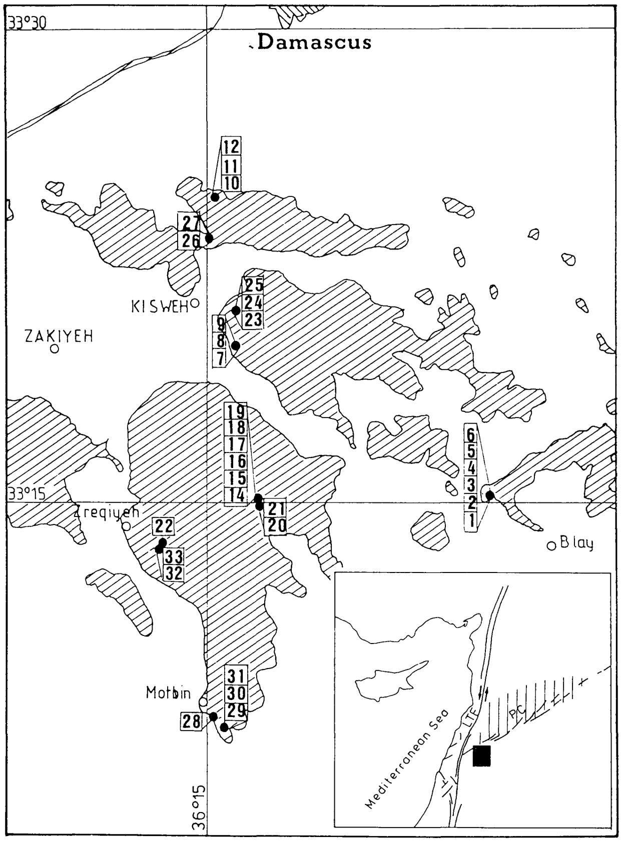

Fig. 1. Sampling map of the Miocene volcanism south of Damascus. For each site, the flow numbers are shown in their stratigraphic position. *The inset* shows the studied area in the major tectonic context. *LTF* Levant Transform Fault: *PC* Palmyra Chain

Sampling, laboratory techniques and measurements

The Miocene volcanism, composed of olivine alkaline basalt, outcrops in the Damascus region. The fact that this volcanism is involved in the Palmyra Chain constrains the age to the Miocene period. Thi interpretation is supported by radiometric Ar^{39}–Ar^{40} dating which gives an age of 19.5 Ma on one flow (No. 24). The volcanic sequence, which appears to be flat-lying, has been highly dissected by erosion. Fresh outcrops were found in quarries, from which all samples were taken. Because the lateral extent

---

Offprint requests to: N. Bonhommet
]

of individual flows is not known, it is difficult to determine the total number of independent flows exposed in this sequence. The paleomagnetic sampling was done in small vertical sections of successive flows at different sites (Fig. 1). Thirty-two flows have been collected with a mean of four cores per flow oriented with both magnetic and sun compasses. The magnetic measurements were done with a computer-assisted Schonstedt spinner magnetometer. Thermal and A.F. demagnetization procedures were also carried out with Schonstedt equipment. The non-magnetic furnace and A.F. demagnetizing apparatus have a very low residual field of about 10 nT.

Results

Magnetic properties

The analysis of the NRM directions shows two types of behaviour. The first group corresponds to flows for which the demagnetization does not change the NRM direction. A very high stability of the remanence is found by alternating field as well as by thermal demagnetization. Some examples are shown on the orthogonal Zijderveld plots (Fig. 2). In some samples, a remarkable feature is the persistence of the NRM directions above the magnetite Curie point, indicating a remanent magnetization obtained by a high-temperature oxidation during the cooling of the flows (Fig. 2). This behaviour is seen on both normal and reversed samples. This is correlated with large median destructive fields and IRM acquisition curves for which saturation was not always obtained at 300 mT, a field high enough to saturate most magnetites (Fig. 3). Therefore, the contribution of hematite to the natural remanence is suggested. For the second group of flows, a random secondary component is generally removed by a low alternating field (20 mT). However, for higher fields, the magnetization direction becomes stable; an example is given in Fig. 2 by sample S0401b.

Table 1 shows the mean direction of magnetization for each flow obtained after stepwise A.F. or thermal cleaning and, for each sample, using the characteristic direction given from the orthogonal diagrams. Characteristic directions were isolated for 30 flows (Table 1).

We have not been able to determine the characteristic mean directions of flows S22 and S30; they were omitted from Table 1. The magnetization of samples from flow S30 consisted of both polarities as illustrated by stepwise thermal demagnetization of sample S3002 (Fig. 4). The orthogonal diagram reveals two anti-parallel directions: a normal component with blocking temperatures up to 490° C and a reverse component with higher blocking temperatures which can be followed above 560° C degrees. As this flow is intercalated between a reverse and a normal magnetized flow, we can interpret this result as a thermal overprint by the overlying flow which has a normal polarity. It is interesting to note that A.F. demagnetization was not successful in isolating the primary remanence component (Fig. 4). A reverse component is determined on two samples ($D=191$, $I=-23$) but, as an accurate determination of the primary component direction was not possible, the result for flow S30 was not included in Table 1. This result was only used for qualitative correlations between flows.

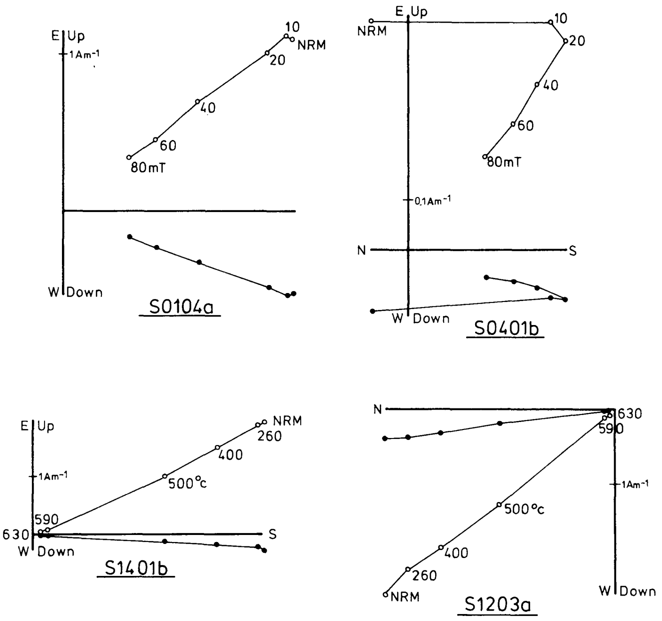

Fig. 2. Examples of thermal and alternating field demagnetization. Intensities of A.F. and thermal treatments vary between 10 and 80 mT and 260° and 630° C, respectively. *Solid circles* represent projections on to the horizontal plane, and *open circles* those on the vertical plane. The plots are in 'in situ' coordinates

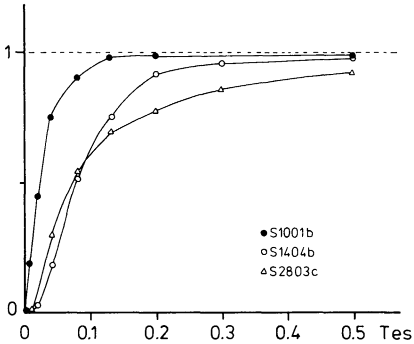

Fig. 3. IRM acquisition curve (normalized by the IRM value acquired in a field of 1.2 T). Saturation is not obtained at 0.5 T for sample S2803C

Paleomagnetic field record

Figure 5 shows the distribution of the mean directions of each flow. Normal and reverse polarities are present at three sites. Normal magnetized flows overlie those with reverse directions: moreover, at two other sites (S1–S6, S26–S27) intermediate directions overlie reversed directions. This magnetostratigraphy is consistent with the sampling of the same reversal of the earth's magnetic field at different sites of a volcanic sequence. In the section S14 to S19, a transitional direction (S18) is intercalated between two normal directions S17 and S19, suggesting that the normal polarity which has been recorded in flow S17 was not completely stable. It is interesting to notice that a similar behaviour (the field reversal occurs in two phases, the first attempt at reversal being unsuccessful) has been recorded in the Steens Mountain transition zone (Prevot et al., 1985) and in a lava sequence from Kauai (Bogue and Coe, 1982).

Table 1. Flow-mean paleomagnetic results

Flow number	N	D	I	K	α_{95}	VGP	
						Latitude	Longitude
S01	5	192.1	−41.0	182	5.7	−75.6	345.5
S02	4	191.9	−43.1	579	3.8	−76.8	341.2
S03	4	188.6	−45.5	561	3.9	−80.3	343.9
S04	5	201.4	−44.5	105	7.5	−70.2	321.3
S05	5	232.4	−30.6	21	17.1	−40.2	312.4
S06	5	233.7	−40.5	176	5.8	−42.1	303.8
S07	6	170.5	−39.8	143	6.0	−76.5	77.0
S08	5	168.3	−43.0	50	11.0	−76.9	90.4
S09,	4	165.7	−34.9	88	9.9	−71.1	82.2
S10	5	169.6	−37.9	139	6.5	−74.9	76.5
S11	4	158.6	−42.1	73	10.8	−69.3	106.3
S12	4	354.5	42.6	126	8.2	80.2	241.1
S14	4	182.6	−22.8	922	3.0	−68.5	29.2
S15	5	183.3	−17.1	934	2.5	−65.4	28.4
S16	4	192.9	−34.9	263	5.7	−71.9	353.5
S17	5	359.2	18.6	250	4.8	66.3	218.2
S18	6	117.5	−14.8	435	3.2	−27.0	117.1
S19	4	17.8	15.6	601	3.8	59.9	179.1
S20	4	162.7	−43.3	150	7.0	−73.0	102.8
S21	4	183.7	−24.4	191	6.7	−69.5	25.6
S23	5	157.4	− 8.4	301	4.4	−54.2	77.1
S24	6	165.4	−40.6	236	4.4	−73.7	92.0
S25	6	182.8	−21.0	196	4.8	−67.5	29.0
S26	6	186.1	−38.4	216	4.6	−77.2	9.7
S27	3	305.2	45.2	109	12.0	42.6	313.6
S28	5	121.4	−13.7	863	2.6	−29.9	114.1
S29	4	170.4	−46.2	963	3.0	−80.0	94.3
S31	5	6.1	25.2	265	4.7	69.3	199.2
S32	5	179.5	21.8	108	7.4	−45.5	36.9
S33	5	7.7	−11.1	38	12.6	50.5	204.1
Mean	30	177.0	−32.2	9	9.3		
(1)	23	179.0	−34.0	28	5.9	−75.0	40.0

N is the number of samples included in the flow mean; D and I are the eastward declination and downward inclination; K is the dispersion parameter (Fisher, 1953); α_{95} is the angular interval of 95% confidence in the mean direction. (1) See text

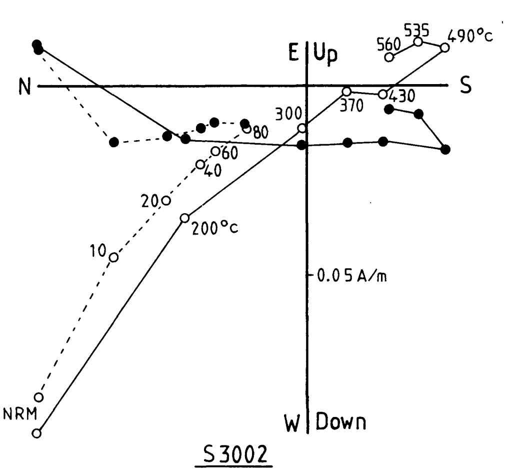

Fig. 4. Comparison of A.F. and thermal demagnetization on two specimens of the core S3002. *Dashed line* for the A.F. demagnetization. *Open and closed circles* used as in Fig. 2

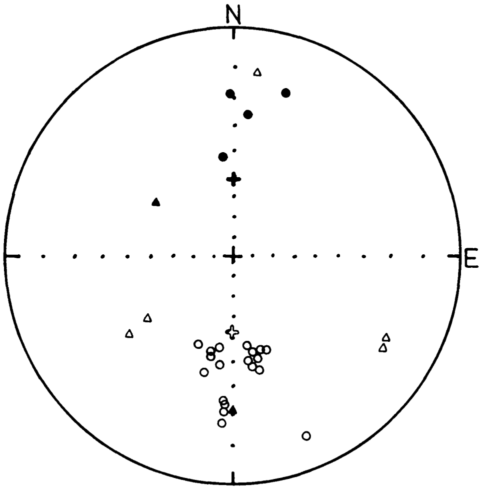

Fig. 5. Stereographic plots of flow-averaged directions. *Solid (open) symbols* indicate downward (upward) directed magnetization vectors. *Triangles* represent the transitional directions rejected from the mean calculation. The *crosses* give the axial dipole direction

Mean paleomagnetic direction and its significance

The stereographic projection of Fig. 5 shows clearly that the 30 directions do not have a Fisherian distribution, making it more difficult to interpret the mean direction and precludes a clear determination of the paleosecular variation. At least two main factors contribute to this situation:

1) Similar paleomagnetic directions of different units may represent repeated sampling of the earth's magnetic field at a particular time, making clusters in the distribution. For example, the most divergent transitional direction ($D=120$, $I=-15$) recorded in two flows S18 and S28, 5 km from one another, has the highest probability of depicting the same event. On the other hand, the reverse directions are distributed principally in three paleomagnetic groups (*a*: south-east declination, *b*: south declination and shallow inclination, *c*: south-west declination) which are found at the different sites. Hence, we propose a time correlation between sites (Fig. 6). The clusters of directions probably indicate a very short time interval between successive flows.

2) The second factor is that some directions are far from the dipole direction and contribute to a large scatter in the distribution. Working with one of the best data sets of more than 2,000 lava flows in Iceland, Kristjansson and McDougall (1982) have shown that it is not easy to separate the transitional from the regular geomagnetic field behaviour to provide the Fisher analysis characteristics of the paleosecular variation. Nevertheless, in recent analyses of worldwide paleosecular variation, a cutoff at colatitude greater than 40 degrees was applied to the VGPS to filter transitional data linked to reversals or excursions (Merrill and McElhinny, 1983; McFadden and McElhinny, 1984). Directions for flow numbers S5, S6, S18, S27, S28, S32 and S33 may be filtered out if we assume they are related to the reversal. The mean direction for all flows after the normal directions have been inverted by 180 degrees is: declination = 177.0; inclination = −32.2; $K=8.9$; $N=30$; $\alpha_{95}=9.3°$; and after the elimination of the seven previous directions: declination = 179.0; inclination = −34.2; $K=27.6$; $N=23$; $\alpha_{95}=5.9°$. Whichever set is selected, we ob-

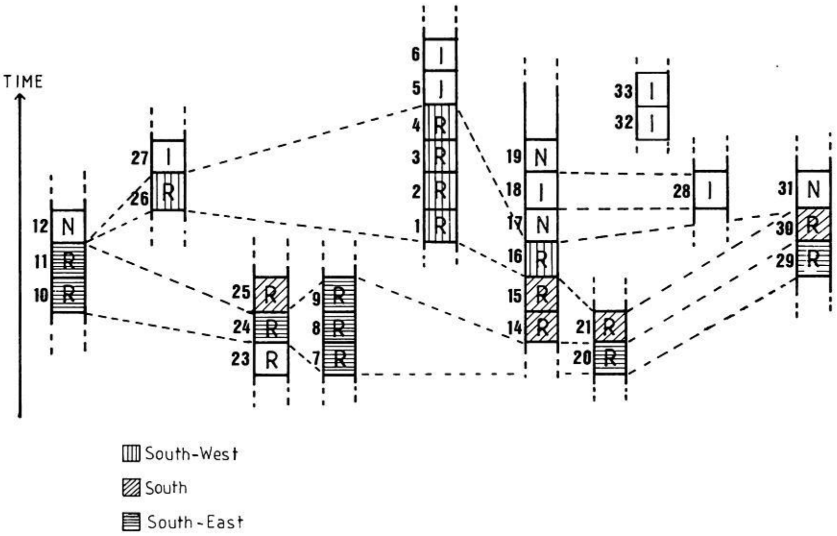

Fig. 6. Attempt at correlation of mean flow directions between sites. Each site shows the stratigraphic position of the flows, and they are diplayed along a north-south trend (see Fig. 1). *R*, *I*, *N* represent, respectively, reverse, intermediate, normal polarities. In the reverse population, three groups have been defined. Only flow No. 23 cannot be correlated with other sites. We are not able to correlate the normal directions, but the diagrams show that they overlay the reverse directions

serve a stability of the mean direction. We consider that a mean direction $D=179$, $I=-34$ is the best estimate of the Miocene mean paleomagnetic field direction in Syria. We think, however, that more data are necessary for a good estimation of the scatter of directions around the mean (i.e. paleosecular variation).

Comparison with data from Africa and Arabia

For the Arabian plate, only very few paleomagnetic studies have been reported and a comparison with the African poles is essential. In order to take into account the opening of the Red Sea, the pole and angle of rotation given by Le Pichon and Francheteau (1978) is used to correct Miocene Arabian data which pre-date the opening.

The selection of reliable African or Arabian data is not easy. The first step for a compilation of data is to ensure that each mean direction corresponds to a good averaging of all the variations of the magnetic field. As nearly all results have been obtained from volcanic rocks, problems arose in the averaging of the paleosecular variation in many cases. A second criterion is the tectonic stability on a regional scale. Some studies which have been undertaken in tectonically active areas, for example the Afar region (Pouchan and Roche, 1971), must be rejected; the results obtained for the Tiberia province in the Lebanon mountains (Nur and Helsley, 1971; Ron et al., 1984) cannot be accepted in a compilation because of the large block rotations which occurred on that side of the Levant fault. The third criterion is a good knowledge of the age of the formations used.

Some compilation of data for Africa has been done recently. In that of Tauxe et al. (1983), the important weight given to the Canary data made it unreliable. The review of Kellog and Reynolds (1983) needs a few modifications. For the Kapiti phonolite (Patel and Gracii, 1972), the semi-angle of confidence ($\alpha_{95}=17°$) is too large to allow its use. The Lybian Garian volcanics have been re-dated as Pliocene (Ade-Hall et al., 1975b). For the Jebel Soda basalts, other data obtained by Ade-Hall et al. (1975a) have been added to those of Schult and Soffel (1973). Finally, we estimate that only six Miocene African poles meet our criteria (Table 2). Nevertheless, the use of the Libyan and Algerian data for the calculation of the mean is questionable. The As-Sarat data (Kellog and Reynolds, 1983) is the unique available data for Arabia.

Table 2. Miocene poles for Africa and Arabia

	VGP		
	Latitude (N)	Longitude (E)	
Turkana lavas	85	163	Reilly et al. (1976)
Rift valley (Kenya)	87	187	Reilly et al. (1976)
Ethiopian lavas	82	200	Musset and Ade-Hall (1975)
Cavallo massif	88	154	Bobier and Robin (1969)
Canary Islands	82	114	Watkins (1973)
Lybia Jebel Soda	73	195	Ade-Hall et al. (1975a)
As Sarat (Arabia)[a]	81	236	Kellog and Reynolds (1983)
Mean ($N=7$)	84	188	$K=138$ $\alpha_{95}=5.2°$
This study	75	220	
This study[a]	76	207	

[a] After rotation of Arabia with the pole and angle of rotation 36.5 N, 18.0 E, 3.25° (Le Pichon and Francheteau, 1978)

The Miocene paleomagnetic pole determined for Arabia and Africa provides an expected paleomagnetic direction for our sampling area of $D=180$, $I=-46$. This calculation takes into account the opening of the Red Sea. A good agreement exists between the observed declination and the expected declination, while there is a discrepancy of 12 degrees between the two inclinations. Shallow inclinations have also been found on Tertiary Egyptian volcanics (Hussain et al., 1979; Schult et al., 1981; Hussain and Aziz, 1983). This problem might be due to an incomplete averaging of the secular variation or to a long-term variation in the dipole field.

Conclusions

The correlations of flows between sites and the single change of polarity from reverse to normal allow us to assess the short duration of this volcanism. Despite the problem of a non-fisherian distribution, we believe that the mean declination is a good marker and so we conclude that no tectonic rotation has occurred in this area south of Damascus since 20 Ma.

Acknowledgements. We thank G. Carlier and J.F. Parrot for their help during the field work and for helpful comments on the geological context. G. Giannerini and G. Feraud from the University of Nice provided us with the radiometric data. This work was supported by O.R.S.T.O.M.

References

Ade-Hall, J.M., Reynolds, P.H., Dagley, P., Musset, A.E., Hubbard, T.P.: Geophysical studies of North African Cenozoic Volcanic Areas: II. Jebel Soda, Libya. Canadian J. Earth Sci. **12**, 1257–1264, 1975a

Ade-Hall, J.M., Gerstein, S., Gerstein, R.E., Reynolds, P.H., Dagley, P., Musset, A.E., Hubbard, T.P.: Geophysical studies of north African cenozoic volcanic ares.: III. Garian, Libya. Canadian J. Earth Sci. **12**, 1264–1272, 1975b

Bobier, C., Robin, C.: Etude paleomagnetique du massif eruptif de Cavallo (nord-Constantinois, Algerie), C.R. hebd. seanc. acad. sci. **269**, ser D, 134–137, 1969

Bogue, S.W., Coe, R.S.: Back to back paleomagnetic reversal records from Kauai. Nature **295**, 399–401, 1982

Fisher, R.A.: Dispersion on a sphere. Proc. R. Soc. London, Ser. A, **217**, 295–305, 1953

Freund, R.: A model of the structural development of Israel and adjacent areas since upper cretaceous times. Geol. Mag. **102**, 189–205, 1965

Freund, R., Tarling, D.H.: Preliminary mesozoic paleomagnetic results from Israel and inferences for a microplate structure in the Lebanon. Tectonophysics **60**, 189–205, 1979

Gregor, C.B., Mertzman, S., Nairn, A.E.M., Negendank, J.: The paleomagnetism of some mesozoic and cenozoic volcanic rocks from the Lebanon. Tectonophysics **21**, 375–395, 1974

Hussain, G.A., Schult, A., Soffel, H.: Paleomagnetism of the basalts of Wadi Abu Tereifiya, Mandisha and dioritic dykes of Wadi Abu Shihat, Egypt. Geophys. J.R. Astron. Soc. **56**, 55–63, 1979

Hussain, G.A., Aziz, Y.: Paleomagnetism of Mesozoic and Tertiary rocks from East El Owenat area, southwest Egypt. J. Geophys. Res. **88**, 3523–3529, 1983

Kellog, K.S., Reynolds, R.L.: Opening of the Red Sea: constraints from a paleomagnetic study of the As Sarat volcanic field, South western Arabia. Geophys. J.R. Astron. Soc. **74**, 649–665, 1983

Kristjansson, L., McDougall, I.: Some aspects of the late tertiary geomagnetic field in Iceland. Geophys. J.R. Astron. Soc. **68**, 273–294, 1982

Le Pichon, X., Francheteau, J.: A plate tectonic analysis of the Red Sea – Gulf of Aden area. Tectonophysics **46**, 369–406, 1978

McFadden, P.L., McElhinny, M.W.: A physical model for paleosecular variation. Geophys. J.R. Astron. Soc. **78**, 809–830, 1984

Merrill, R.T., McElhinny, M.W.: The earth's magnetic field: Its history, origin and planetary perspective. International geophysics series, vol. 32, 1983

Musset, A.E., Ade-Hall, J.M.: Paleomagnetism and potassium argon dating of Ethiopian cenozoic volcanic areas. Eos. Trans. Am. Geophys. Un. **56**, 902, 1975

Nur, A., Helsley, C.E.: Paleomagnetism of tertiary and recent lavas of Israel. Earth Planet. Sci. Lett **10**, 375–379, 1971

Patel, J.P., Gracii, P.: Paleomagnetic studies of the Kapiti Phonolite of Kenya. Earth Planet. Sci. Lett. **16**, 213–218, 1972

Pouchan, P., Roche, A.: Etude paleomagnétique de formations volcanique du territoire des Afars et des Issas. C.R. hebd. seanc. acad. sci. Paris **272**, ser. D, 531–534, 1971

Prevot, M., Mankinen, E.A., Gromme, C.S., Coe, R.S.: How the geomagnetic field vector reverses polarity. Nature **316**, 230–234, 1985

Reilly, T.A., Raja, P.K.S., Musset, A.E., Brock, A.: The paleomagnetism of late cenozoic volcanic rocks from Kenya and Tanzania. Geophys. J.R. Astron. Soc. **45**, 483–494, 1976

Ron, H., Freund, R., Garfunkel, Z., Nur, A.: Block rotation by strikeslip faulting: Structural and paleomagnetic evidence. J. Geophys. Res. **89**, 6256–6270, 1984

Schult, A., Soffel, H.: Paleomagnetism of tertiary basalts from Libya. Geophys. J.R. Astron. Soc. **32**, 373–380, 1973

Scult, A., Hussain, A.G., Soffel, H.C.: Paleomagnetism of Upper Cretaceous volcanics and Nubian sandstones of Wadi Natash. SE Egypt and implications for the polar wander path for Africa in the Mesozoic. J Geophys. **50**, 16–22, 1981

Tauxe, L., Besse, J., Labrecque, J.: Paleolatitude from DSDP leg 73 sediments cores: Implications for the apparent polar wander path for Africa during the late Mesozoic and Cenozoic. Geophys. J.R. Astron. Soc. **73**, 315–325, 1983

Van Dongen, R.G., Van der Voo, R., Raven, Th.: Paleomagnetic research in the Central Lebanon mountains and in the Tartous area (Syria). Tectonophysics **4**, 35–53, 1967

Watkins, N.D.: Paleomagnetism of the Canary Islands and Madeira. Geophys. J.R. Astron. Soc. **32**, 249–267, 1973

Received October 28, 1985; revised February 3, 1986
Accepted February 20, 1986

J Geophys (1986) 59:103–111

Journal of Geophysics

Periadriatic lineament in the Alps studied by magnetotellurics

A. Ádám[1], G. Duma[2], R. Gutdeutsch[3], J. Verő[1], and Á. Wallner[1]

[1] Geodetical and Geophysical Research Institute of the Hungarian Academy of Sciences, Pf. 5, H-9401 Sopron, Hungary
[2] Zentralanstalt für Meteorologie und Geodynamik, Hohe Warte 38, A-1190 Wien, Austria
[3] Universität Wien, Institut für Meteorologie und Geophysik, Währingerstr. 17, A-1090 Wien, Austria

Abstract. The "Periadriatic lineament" (or "Insubric lineament"), as a main tectonic zone, separates the unmetamorphosed southern Alps from the metamorphosed western and eastern Alps. One of its continuations to the east is the Balaton-line. In three parts of it – along the Gail Valley, the Karawanken and Balaton lines – deep magnetotelluric soundings have detected a conducting crustal formation with depths varying between 7 and 17 km. This conducting crustal formation is probably narrow and correlated with the three lineaments. The reason for the increased conductivity in the middle crust may be a deep fracture zone, where cracks and pores are saturated by electrolytes. The basic model of the interpretation and the EM distortions are discussed.

Key words: Magnetotellurics – Periadriatic lineament – MT distortions – Gail Valley – Karawanken – Tectonic effects

Introduction

Within the framework of the topic "Geophysical investigations in the transition between Alps and Pannonicum", joint Austro-Hungarian magnetotelluric (MT) measurements were continued in 1981 and 1983 in two sections of the Periadriatic lineament, along the Gail Valley and the Karawanken, in order to investigate the deep geoelectric structure of this primary tectonic zone.

The Periadriatic lineament

The Periadriatic lineament belongs to the tectonic line system between Lanzo in the western part of the Po-Plane and Pohorje in Yugoslavia. Earlier it was tentatively identified with the Insubric line that divides the western and eastern Alps exposed to Alpine metamorphism from the unmetamorphosed southern Alps. Recent investigations (Ahrendt, 1980) revealed, however, that the Insubric line forks from the Periadriatic lineament near the Tauern window and its continuation lies in the Defferegen-Auterselve-Valles (DAV) line and not in the Pusteria-Gail Valley line. Towards the east the Insubriatic line continues, according to Kovács (1983), in the Rába-line that divides the Penninian, the Lower and Upper eastern Alpine units, from the Transdanubian Central Mountains verging southward The Periadriatic lineament taken in a stricter sense continues in the Balaton line. It is probable that the 3- to 5-km-broad tectonic zone of the Karawanken lineament becomes broader toward the ENE (Fig. 1). Kovács supposes that the 800-km-long chain of Periadriatic magmatites is continued in Hungary in the narrow, elongated, late-Variscan Balaton-Velence granitic zone as well as in the Palaeogene andesites of Hahót-Pusztaszentlászló, Velence and Recsk and thus he speaks about a Gail Valley-Balaton lineament.

Simply the age of the mentioned late-Variscan granite intrusions indicates that the Periadriatic lineament or its precursor had already been active at that time and was rejuvenated during the Alpine tectonogenesis.

Basis of geophysical investigations

The considerable horizontal and vertical movements along the Periadriatic lineament – their scale is being discussed – produced large dragged structures. These have also caused a change of the physical parameters, hence the tectonic zone can be traced by geophysical methods and from their results conclusions can be drawn about the deep structures and the physical processes in the zone.

This assumption has been confirmed by a 70-km-long and about 10-km-broad conductivity anomaly indicated by MT soundings along the Balaton-line at a depth of 7–9 km [see Fig. 2, after Varga (1980)].

Measurement sites and equipment

The magnetotelluric and telluric measuring points along the Gail Valley and the Karawanken lineament are shown in small topographic maps (Fig. 1b and c) and in Tollmann's tectonic map (Fig. 3). Three MT soundings were carried out near the Karawanken lineament (Ebriach, Blasnitzen and Zell Pfarre) and a reference point was measured at Klein St. Paul, about 40 km to the north of it. Two MT soundings (Schlanitzen and Sittmoos) were measured, each together with a telluric satellite point (Schimanberg and Plöckenhaus), in the Gail Valley. The reference point here was Weissensee, about 10 km to the north of the Gail Valley but south of the DAV line.

In the Karawanken the MTS sites Ebriach and Zell Pfarre lie over limestone plateaus covered by only a few metres of loose sediments. In the close environment of Blas-

---

Offprint requests to: A. Ádám

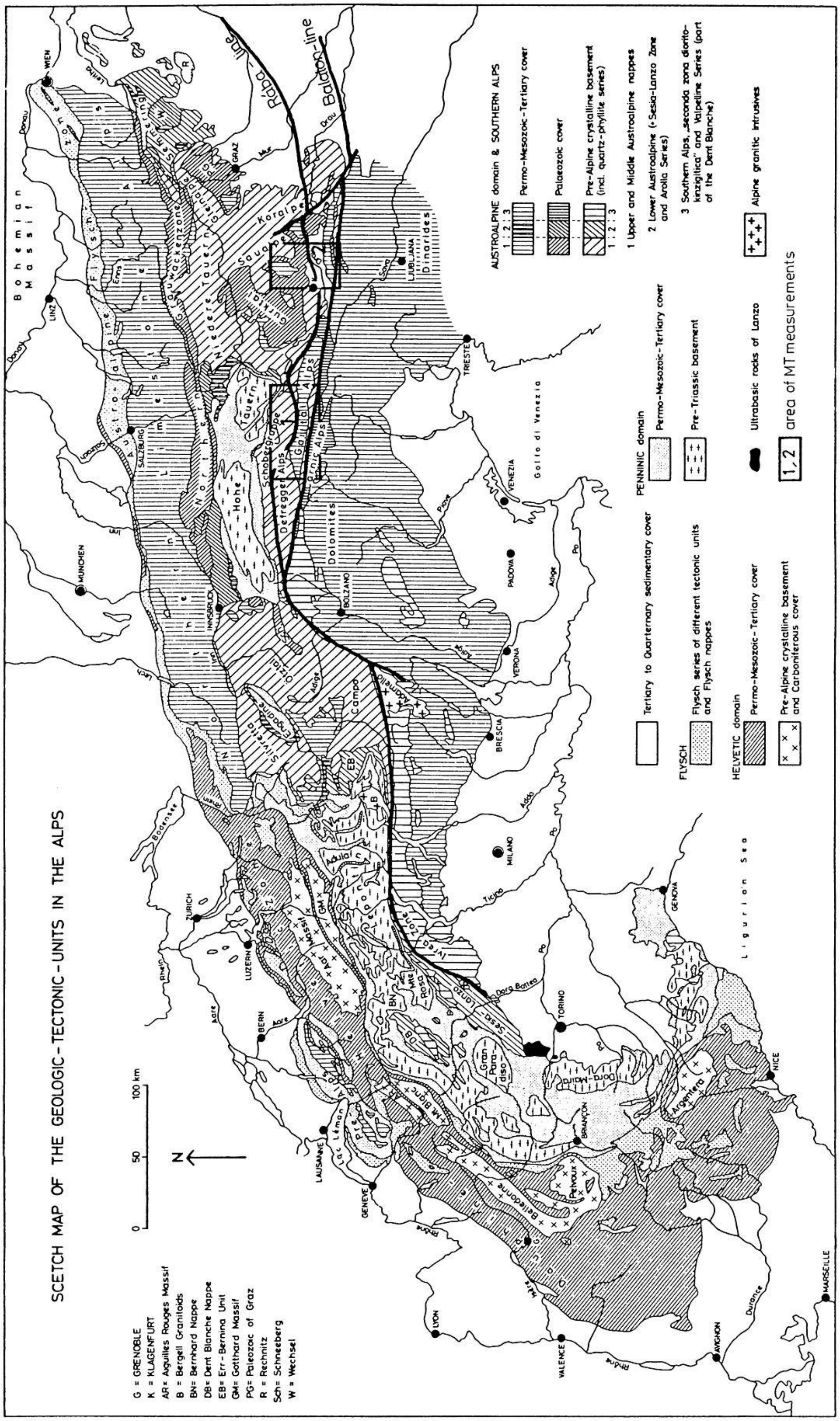
SCETCH MAP OF THE GEOLOGIC-TECTONIC-UNITS IN THE ALPS
G = GRENOBLE
K = KLAGENFURT
AR = Aiguilles Rouges Massif
B = Bergell Granitoids
BN = Bernhard Nappe
DB = Dent Blanche Nappe
EB = Err-Bernina Unit
GM = Gotthard Massif
PG = Paleozoic of Graz
R = Rechnitz
Sch = Schneeberg
W = Wechsel
0
50
100 km
N
Tertiary to Quarternary sedimentary cover
FLYSCH
Flysch series of different tectonic units and Flysch nappes
HELVETIC domain
Permo-Mesozoic-Tertiary cover
Pre-Alpine crystalline basement and Carboniferous cover
PENNINIC domain
Permo-Mesozoic-Tertiary cover
Pre-Triassic basement
Ultrabasic rocks of Lanzo
1,2
area of MT measurements
AUSTROALPINE domain & SOUTHERN ALPS
1 : 2 : 3
Permo-Mesozoic-Tertiary cover
Palaeozoic cover
Pre-Alpine crystalline basement (incl. quartz-phyllite series)
1 : 2 : 3
1 Upper and Middle Austroalpine nappes
2 Lower Austroalpine (+ Sesia-Lanzo Zone and Arolla Series)
3 Southern Alps, „seconda zona diorito-kinzigitica" and Valpelline Series (part of the Dent Blanche)
Alpine granitic intrusives
Bohemian Massif
WIEN
LINZ
SALZBURG
MÜNCHEN
INNSBRUCK
GRAZ
LJUBLJANA
TRIESTE
VENEZIA
PADOVA
VERONA
BOLZANO
BRESCIA
MILANO
GENOVA
TORINO
ZÜRICH
LUZERN
BERN
LAUSANNE
GENEVE
LYON
VALENCE
AVIGNON
MARSEILLE
NICE
BRIANÇON
Golfo di Venezia
Ligurian Sea
Raba-line
Balaton-line
Flysch zone
Austro-alpine
Northern Limestone Alps
Grauwackenzone
Niedere Tauern
Koralpe
Saualpe
Gurktaler
Dinarides
Hohe Tauern
Schobergruppe
Defregger Alps
Gailtal Alps
Carnic Alps
Dolomites
Ötztal
Silvretta
Engadine
Campo
Adamello
Adula
Mte Rosa
Ivrea Zone
Sesia-Lanzo
Gran Paradiso
Dora-Maira
Argentera
Pelvoux
Belledonne
M. Blanc
Préalpes
Lac Léman
Bodensee
Donau
Inn
Lech
Rhein
Aare
Rhône
Isère
Durance
Po
Ticino
Adda
Adige
Piave
Drau
Mur
Sava
Enns
Dora Baltea

Fig. 1a

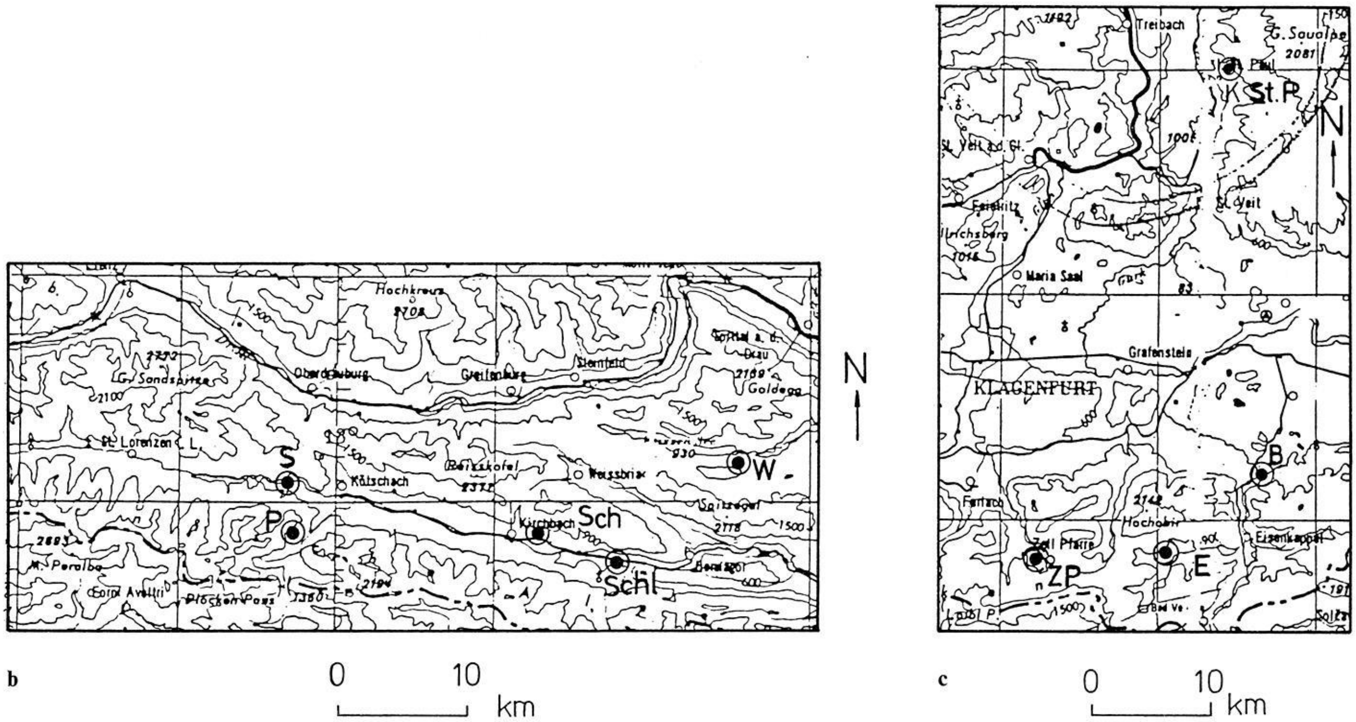

Fig. 1. **a** Geological and tectonic map of the Alps according to Frey et al. (1974). *Thick lines* indicate main tectonic lines (Periadriatic, Insubric, Balaton and Rába-lines). Measuring areas are also given. *1* Gail Valley, *2* Karawanken. **b** Measuring sites ⊙ in the Gail Valley. *P* Plöckenhaus, *S* Sittmoos, *Schl* Schlanitzen, *Sch* Schimanberg, *W* Weissensee. **c** Measuring sites ⊙ in the Karawanken. *ZP* Zell Pfarre, *E* Ebriach, *B* Blasnitzen, *K.St.P* Klein Sankt Paul

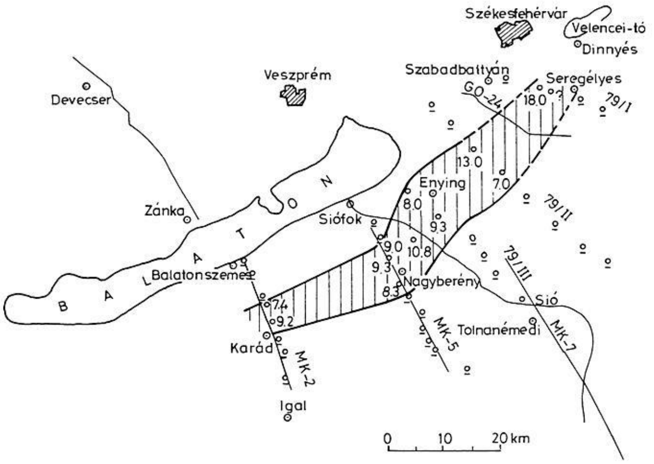

Fig. 2. Depth values of the conductivity anomaly measured along the Balaton line according to Varga (1980)

nitzen no outcrops are visible but limestone rubble lies on the ground.

In the Gail Valley the measuring sites Schlanitzen and Schimanberg lie on slopes at a height of about 150 m above the bottom of the Gail Valley. The thickness of the loose sediments does not exceed some tens of metres at these points. The station Sittmoos is on a terrace at about 200 m above the bottom of the Lesach Valley. In a side valley less than 1 km away from Sittmoos, the limestone is in tectonic contact with the typical schists of the Periadriatic lineament. The station Plöckenhaus is on the bare rocks. Weissensee is at the bottom of a small valley with very few loose sediment.

The MT instrument consisted of telluric and magnetic sensors and a 4-channel analogue recorder. The speed of the record (photo-paper) was 20 mm/min in daytime and 6 mm/min during the night. The minimum scale value of the electrical channels was 10 μV/mm, that of the magnetic variometers (MTV-2) 0.02 nT/mm. From a lower limit of $T = 15$ s upwards, the measuring system ensures linear transfer. Analogue recording enables visual selection of the least disturbed sections of the records for digitizing and data processing (Ádám et al., 1981).

Data processing

The electromagnetic variations to be used for processing are further limited by severe coherence conditions in the MT computer program: Coh $(E_y H_y) \geq 0.9$ and Coh $(E_y H_x) \geq 0.9$. The output of the program run on a HP 2100 computer contained: impedance polar diagrams, weighted extreme values of resistivity (ρ) and their phases (φ) and directions (α). Mean values with their standard deviations were computed as a function of period from the data ρ, φ and α (e.g. see Ádám et al., 1981).

In the Gail Valley synchronous records were taken at two telluric stations in addition to the nearest magnetotelluric stations, the latter being used as the base for the former. Absolute ellipses for both stations were computed from the filtered amplitudes, then the relative ellipses characterizing the connection of the geoelectrical structure of the two points were deduced (see Appendix). With knowledge of the impedance components at the MT base station

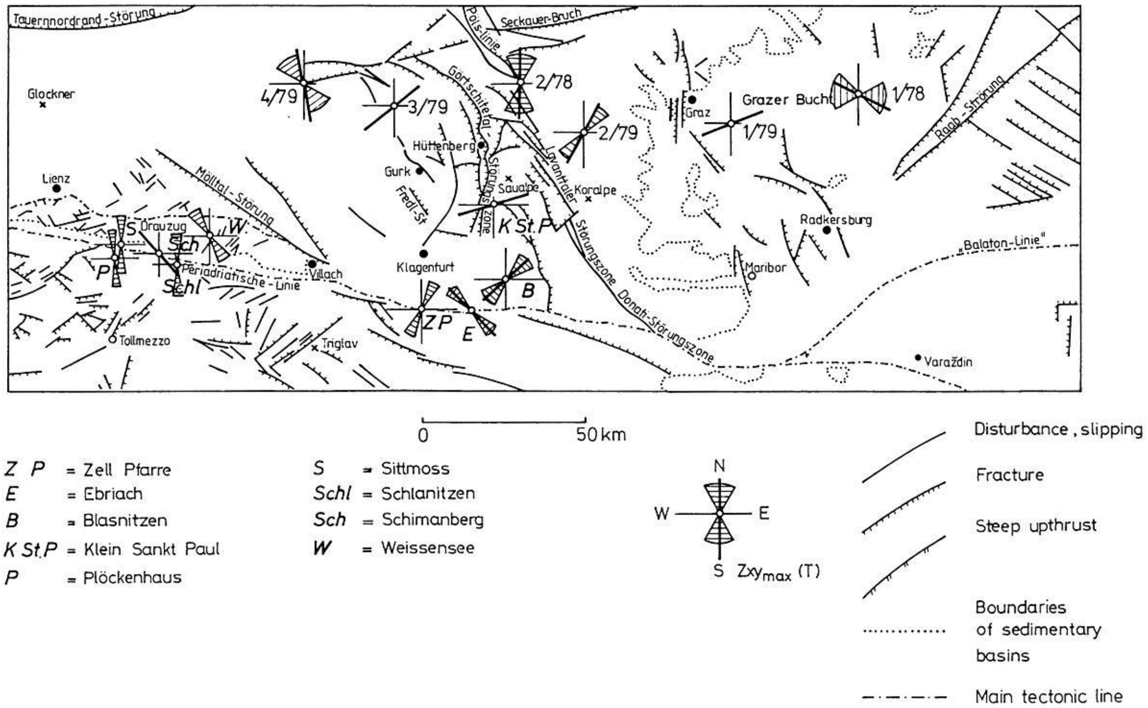

Fig. 3. Tollmann's tectonic map of the eastern Alps and the directions of maxima of the magnetotelluric impedances ($Z_{xy\max}$) together with their change as a function of the period (T)

$[Z^B]$, the MT impedance polar diagrams can be deduced for the telluric satellite station:

$$[Z^{\mathrm{sat}}]=[T]\,[Z^B].$$

Results

The $\rho_{\min}$, $\varphi_{\min}$ and $\alpha_{Z_{xy\min}}$ values at Schlanitzen (in the Gail Valley) with curves representing the best-fitting 1-D models are shown in Fig. 4 as examples. A combined interpretation of the resistivity and phase curves by means of a 1-D inversion method – e.g. Fischer et al. (1981) – did not lead to consistent results. The reason is obvious: in such a strongly tectonized structure the geolelectrical data can be approximated even in an advantageous case at best by a 2-D model. The deviation of the model curve from the measured φ values can be regarded as a certain measure of inhomogeneity, as model curves were primarily fitted to the ρ values.

Hence, only as a first step, the best-fitting models to the values $\rho_{\min}$ and $\rho_{\max}$ (Fig. 5a–g) were determined by the theoretical 1-D model calculation. The model curves corresponding to these models are also illustrated in Fig. 5a–g. The data on depth and conductance of the crustal conductive layer are compiled in Table 1. On Tollmann's tectonic map (Fig. 3), the directions of the maximum impedances ($Z_{xy\max}$) are also plotted.

For the telluric station Plöckenhaus, only strong man-made impulses could be processed as their amplitudes exceeded natural telluric signals several times. An absolute ellipse was computed from these disturbances. The direction of its major axis shows a variation of only a few degrees as a function of period (Fig. 3).

For station Schimanberg, MT data were computed at first by using the magnetic records of its base station Schlanitzen. Then magnetotelluric $\rho_{\min}$ and $\rho_{\max}$ values of Schimanberg were also calculated from the MT impedance values of the Nagycenk observatory, Hungary, via telluric relative ellipse (see Appendix). The magnetotelluric resistivity values resulting from the two bases show a considerable difference (Fig. 6), attributed to differences in the magnetic

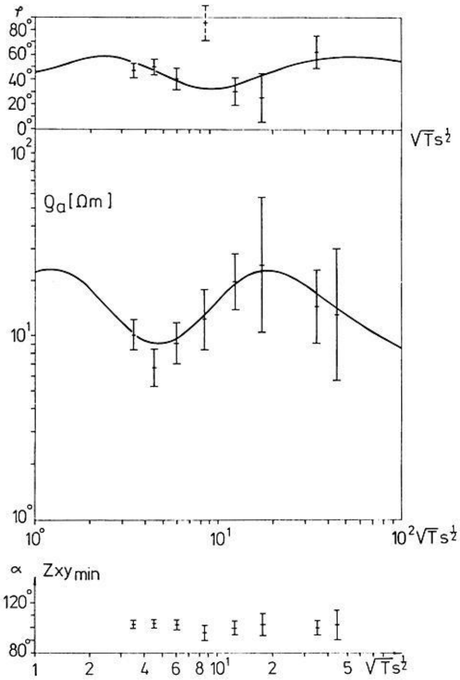

Fig. 4. The measured resistivity (ρ_a) and phase (φ) values as well as impedance directions ($\alpha_{Z_{xy\min}}$) as a function of period with their standard deviations and the curves of 1–D layer models fitted to them for Schlanitzen

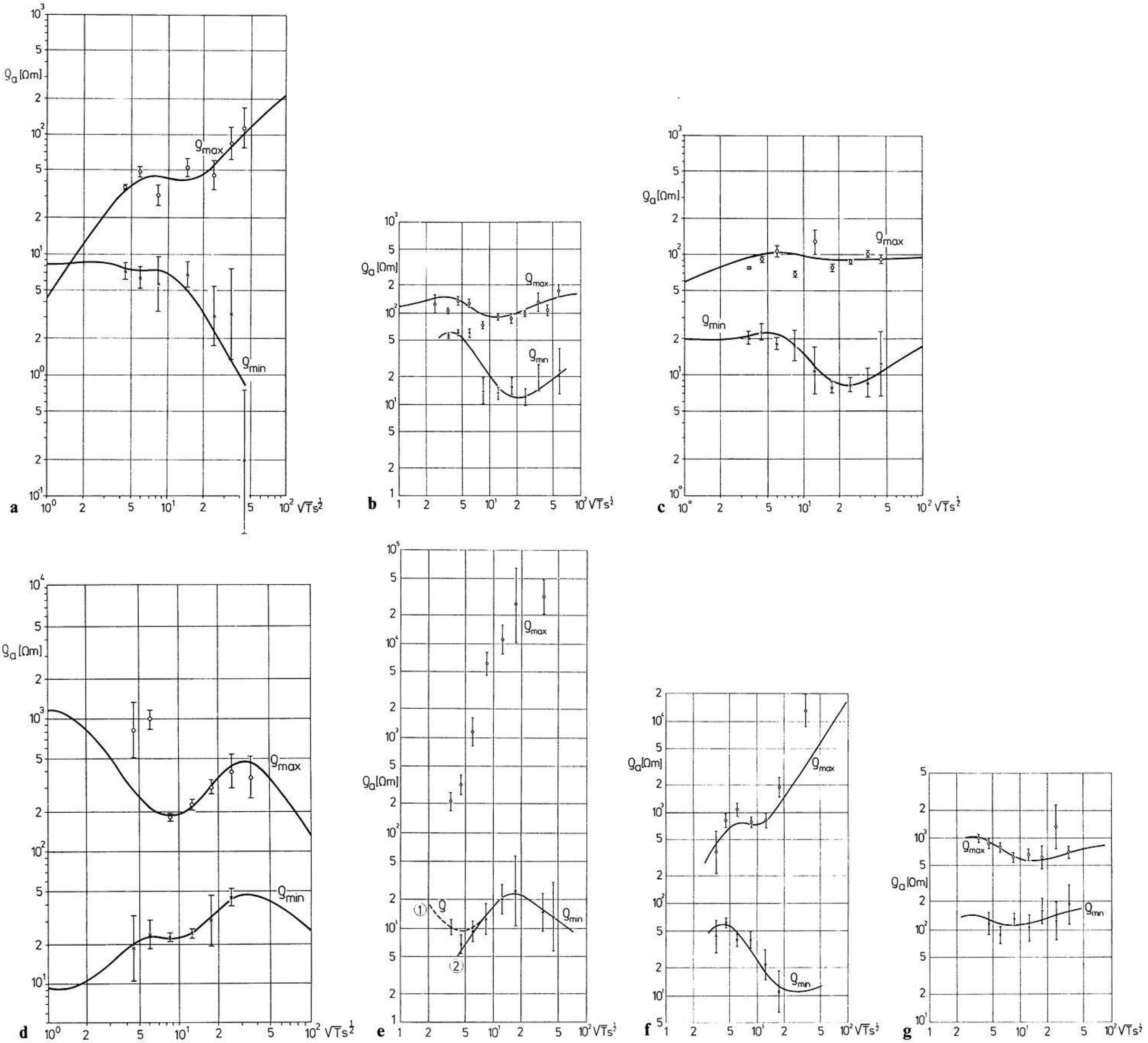

Fig. 5a–g. The average $\rho_{\min}$ and $\rho_{\max}$ values with their error bars and best-fitting 1–D models for:

a Station Ebriach
$\rho_{\min}$ model: $h_1 = 4$, $h_2 = 8.5$, $h_3 = 5$ [km]
$\rho_1 = 8.2$, $\rho_2 = 4$, $\rho_3 = 0.1$, $\rho_4 = 10$ [Ωm]
$\rho_{\max}$ model: $h_1 = 0.5$, $h_2 = 17$, $h_3 = 35$ [km]
$\rho_1 = 3$, $\rho_2 = 120$, $\rho_3 = 40$, $\rho_4 = 500$ [Ωm]

b Station Zell Pfarre
$\rho_{\min}$ model: $h_1 = 1.2$, $h_2 = 14$, $h_3 = 4.5$ [km]
$\rho_1 = 15$, $\rho_2 = 100$, $\rho_3 = 1.8$, $\rho_4 = 50$ [Ωm]
$\rho_{\max}$ model: $h_1 = 1$, $h_2 = 20$, $h_3 = 20$ [km]
$\rho_1 = 80$, $\rho_2 = 150$, $\rho_3 = 50$, $\rho_4 = 200$ [Ωm]

c Station Blasnitzen
$\rho_{\min}$ model: $h_1 = 13$, $h_2 = 8$, $h_3 = 3$ [km]
$\rho_1 = 20$, $\rho_2 = 3$, $\rho_3 = 10$, $\rho_4 = 30$ [Ωm]
$\rho_{\max}$ model: $h_1 = 1.8$, $h_2 = 28$, $h_3 = 30$ [km]
$\rho_1 = 50$, $\rho_2 = 120$, $\rho_3 = 70$, $\rho_4 = 100$ [Ωm]

d Station Klein St. Paul
$\rho_{\min}$ model: $h_1 = 2.2$, $h_2 = 16$, $h_3 = 4.2$, $h_4 = 80$ [km]
$\rho_1 = 10$, $\rho_2 = 45$, $\rho_3 = 8$, $\rho_4 = 170$, $\rho_5 = 10$ [Ωm]
$\rho_{\max}$ model: $h_1 = 20$, $h_2 = 18$, $h_3 = 300$ [km]
$\rho_1 = 1000$, $\rho_2 = 70$, $\rho_3 = 1000$, $\rho_4 = 10$ [Ωm]

e Station Schlanitzen
$\rho_{\min}$ model: $h_1 = 3.5$, $h_2 = 1.1$, $h_3 = 35$ [km]
① $\rho_1 = 20$, $\rho_2 = 2$, $\rho_3 = 60$, $\rho_4 = 5$ [Ωm] or
$h_1 = 1.1$, $h_2 = 35$ [km]
② $\rho_1 = 2$, $\rho_2 = 60$, $\rho_3 = 5$ [Ωm]
$\rho_{\max}$ model cannot be calculated (strongly distorted)

f Station Sittmoos
$\rho_{\min}$ model: $h_1 = 1$, $h_2 = 16$, $h_3 = 4$ [km]
$\rho_1 = 10$, $\rho_2 = 120$, $\rho_3 = 1.5$, $\rho_4 = 20$ [Ωm]
$\rho_{\max}$ model: $h_1 = 2.8$, $h_2 = 100$, $h_3 = 12$ [km]
$\rho_1 = 55$, $\rho_2 = 10{,}000$, $\rho_3 = 100$, $\rho_4 = 100{,}000$ [Ωm]

g Station Weissensee
$\rho_{\min}$ model: $h_1 = 1$, $h_2 = 20$, $h_3 = 10$ [km]
$\rho_1 = 70$, $\rho_2 = 150$, $\rho_3 = 50$, $\rho_4 = 200$ [Ωm]
$\rho_{\max}$ model: $h_1 = 55$, $h_2 = 45$ [km]
$\rho_1 = 1{,}000$, $\rho_2 = 300$, $\rho_3 = 1{,}000$ [Ωm]

Table 1. Depth of the conductive formation (*h*) and *S* value in the Periadriatic lineament

I. Karawanken Site	II. Gail Valley on the basis of			
	ρ_{min}		ρ_{max}	
	h [km]	$S\ [\Omega^{-1}]$	*h* [km]	$S\ [\Omega^{-1}]$
I. Ebriach	12.5	50,000[c]	17	875
Blasnitzen	13.0	2,700–3,000	30	430
Zell Pfarre	15.2	2,500	21	400
Klein St. Paul[a]	18.2	525	20	257
II. Sittmoos	17	2,650[c]	103	120
Schimanberg[b]	16	[c]	40	[c]
Schlanitzen ①	3.5 39.6	550 [c]		
Schlanitzen ②	36.1	[c]	–	–
Weissensee[a]	21	200	55	150

[a] Outside the lineament (side effect)

[b] On the basis of telluric measurements

[c] It appears as conductive basement on the MTS curve

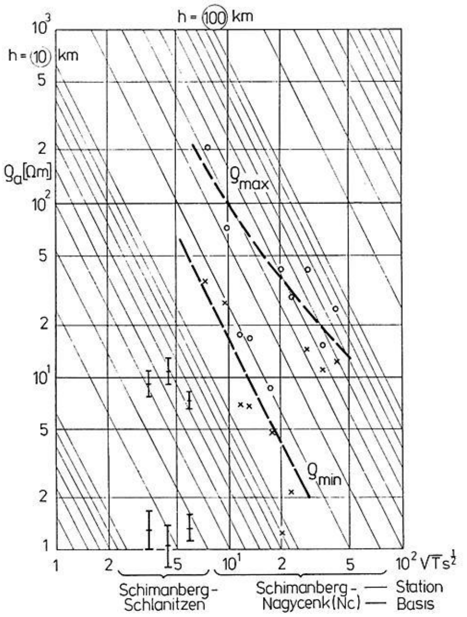

Fig. 6. MT resistivity values of Schimanberg as calculated with the magnetic field variations in Schlanitzen and in Nagycenk. The *h* depth-lines of perfectly conducting layers have been calculated by the formula: $h=\frac{1}{8}\sqrt{10\rho T}$

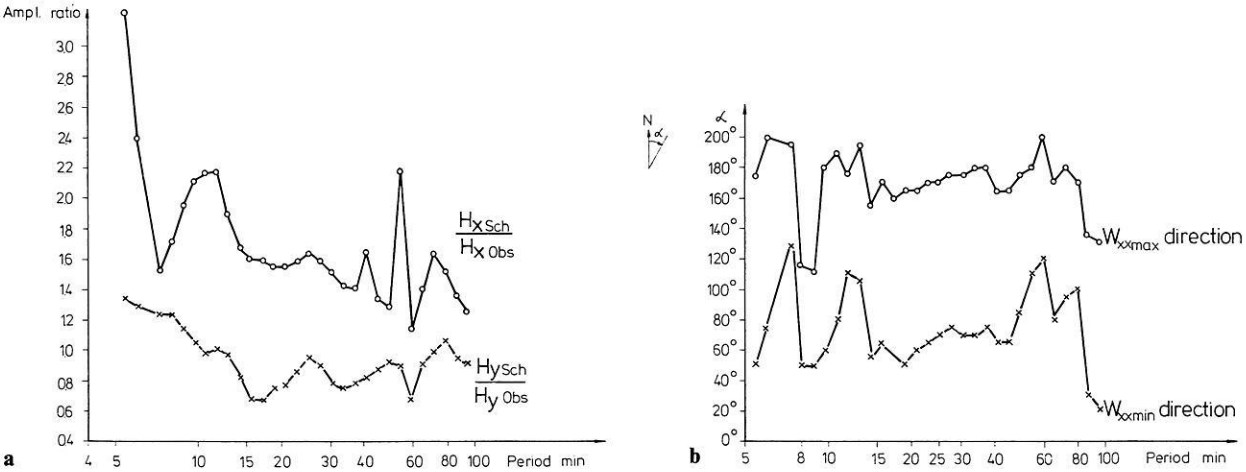

Fig. 7. a Amplitude ratios of the time variations of the horizontal magnetic field components measured at stations Schlanitzen and Nagycenk. **b** Directions of the major ($W_{xx\max}$) and minor ($W_{xx\min}$) axes of the W_{xx} polar diagram

field variations between Nagycenk and Schlanitzen. As there was only so-called "slow recording" of the magnetic field with a film speed of 15 mm per h in the Nagycenk observatory during the field work in Austria, the periods used in the analysis are greater than that measured at station Schlanitzen. In the latter case, the scatter of data is also shown.

As a result of the great electrical inhomogeneity at Schlanitzen, there is a significant increase in the time variations of the magnetic $H_x(H)$ field component and a smaller decrease in the magnetic $H_y(D)$ variations with respect to the data of the Nagycenk observatory in the period range longer than 15 min.

The transfer function between the variations of the horizontal magnetic field components at Schlanitzen (Sch) and Nagycenk (Obs):

$$H_{x\mathrm{Sch}} = W_{xx}\, H_{x\mathrm{Obs}} + W_{xy}\, H_{y\mathrm{Obs}}$$
$$H_{y\mathrm{Sch}} = W_{yx}\, H_{x\mathrm{Obs}} + W_{yy}\, H_{y\mathrm{Obs}}$$

have been calculated by the same computer program as in the case of magnetotelluric soundings (Verő, 1972; Ádám et al., 1981). The filtered amplitude ratios Schlanitzen/Nagycenk vs. period and the direction of the major and minor axes of the W_{xx} polar diagram vs. period are shown in Fig. 7a and b. The $W_{xx\max}$ direction is perpendicular to the Periadriatic lineament except at a few short and long periods strongly influenced by uncertainty in the data. The exceptional character of the point Schlanitzen is also indicated by the steep rise of the $\rho_{\max}$ curve, steeper than the theoretical limit $+63.5^0$, by resistivities higher than $10^5\ \Omega$m and by a great anisotropy increasing with period (Fig. 5e).

Interpretation of the data

A common characteristic feature of the MT sounding curves (Fig. 5a, b, c, e, f) measured in the immediate vicinity of the Periadriatic lineament is a well developed decreasing branch on the $\rho_{\min}$ curves uniformly indicating the conducting body in the crust. This indication is less characteristic on the $\rho_{\max}$ curves and it is combined with a strongly increasing branch at Ebriach, Schlanitzen and Sittmoos.

These results of magnetotelluric measurements are probably caused by a narrow conducting body embedded in resistive host rocks. This interpretation is supported by the following geological and further geophysical data:

a) According to Kovács (1983), the Periadriatic lineament is 3–5 km wide in the Karawanken.

b) The width of the conductivity anomaly along the Balaton line does not exceed 10 km (Fig. 2). As already mentioned, the Balaton line is considered as the continuation in Hungary of the Periadriatic lineament.

c) In Fig. 8 model curves calculated by the finite difference method for a conducting dyke of 10 km width and 7–9 km depth can be seen (Tátrallyay, 1977; Ádám, 1981; Ádám et al., 1981). The measured anisotropy shown by $\rho_{\min}$ and $\rho_{\max}$ curves is similar to that expressed by the ρ_E and ρ_H curves in the case of a narrow dyke.

d) The directions of the $\rho_{\max}$ (or $Z_{xy\max}$) values are perpendicular to the strike of the lineament (Fig. 3) according to the dyke model independent of the position of the measuring sites (see the geological and topographical descriptions of the stations). For example, in Zell Pfarre the direction of the nearby valley is north-south without a corresponding change in the direction of the axes.

e) At increasing distances from the dyke an apparent immersion of the conductive body and a decrease of its conductance are observed. According to this phenomenon the MT sounding curves at Klein St. Paul differ strongly from those in the Karawanken lineament and the MT curves at Weissensee from those in the Gail Valley both in character and in the greater depth and lower conductance of the conducting dyke (Table 1 and Fig. 9). It is very likely that these reference points lie outside the tectonic zone.

f) The very steep rise, the high resistivity values and the anisotropy increasing with depth characterize the $\rho_{\max}$ curves first of all in Schlanitzen and also in Ebriach and Sittmoos. Such characteristics develop immediately besides the boundary of different electrical conductivities (inhomogeneities) on H-polarized sounding curves due to electric charges as proved both by physical model experiments (Ádám et al., 1983) and model calculations (Praus, 1976). This phenomenon also hints at the narrowness of the conductive body.

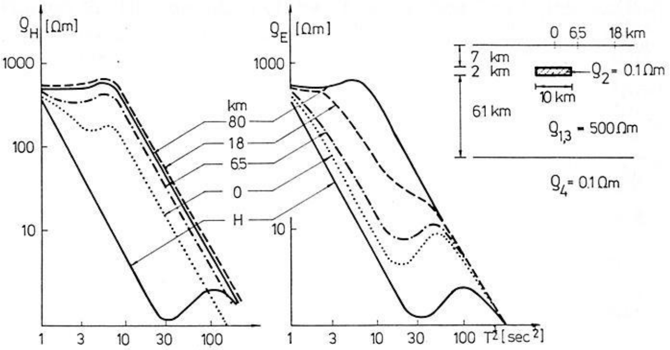

Fig. 8. Synthetic magnetotelluric sounding curves over a model representing a narrow fracture zone with a conducting body at a depth of 7 km. 6.5, 18, 80 km are the distances of the "measuring point" from point 0. The 1–D model shown for comparison has the same conductor depth and thickness (after Tátrallyay, 1977)

g) In addition to the electric field, the magnetic variation field also gets strongly distorted as a result of the conducting body as shown, e.g. for Schlanitzen, in Fig. 7. Similar distortions are seen at all points above the lineament and this distortion also decreases with distance from it. They will be dealt with in a subsequent paper.

As can be seen in Fig. 8, in the case of a narrow conducting dyke, more reliable information is yielded about the depth and the conductance of the dyke by the E-polarized $\rho_{\min}(=\rho_E)$ curves. In addition to this, in the case of E-polarization, the S-effects due to the thickness changes of the near-surfaces sediments are less (Berdichevsky and Dmitriev, 1976). This is why the geoelectric layer sequences calculated on the basis of the best-fitting $\rho_{\min}$ curves only are shown in Fig. 9a and b and are used in the interpretation.

The crustal anomaly in the Periadriatic lineament is considered to be caused by fluids in the increased pores and

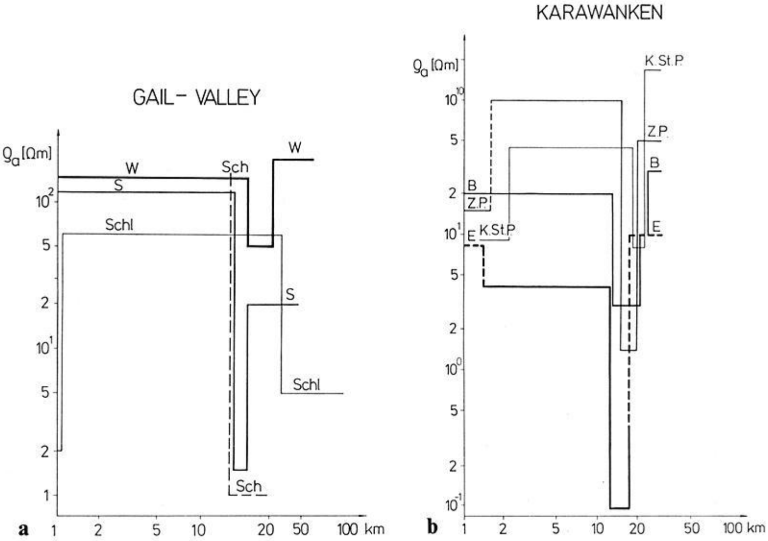

Fig. 9a and b. The geoelectric layer sequences calculated on the basis of the best-fitting $\rho_{\min}$ curves in **a** the Gail Valley and **b** the Karawanken

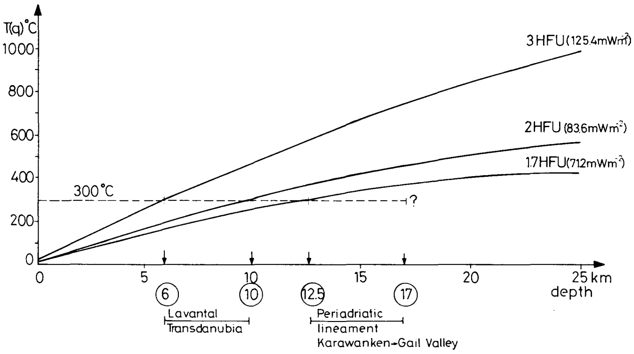

Fig. 10. Temperature-depth curves in the case of different surface heat flow after Haenel (1970) and the depth of the conductive formations (in *circle*) in Transdanubia and the eastern Alps (Ádám, 1985)

cracks of the fractures. The maximum conductivity of the fluids can be expected at the depth of the isotherms of about 300° C according to Quist et al. (1970).

The conductive "layer" lies in the Karawanken lineament at a depth of 12–15 km (Table 1) and its conductance is greatest in Ebriach. The conductive zone is somewhat deeper in the Gail Valley lineament (16–17 km). These depth values can be compared with those of the crustal anomalies in the Lavant Valley and in Transdanubia; in both areas depths of 6–10 km were found (Ádám et al., 1981; Ádám, 1981; Varga, 1980). The differences between the depths measured in these different areas can be of different origin (e.g. different crack and pore porosity, content and salinity of the electrolyte, deep temperature or regional heat flow as its surface indication, etc.). As very different heat flow values were measured in the areas under study, a comparison of heat flow values with the anomaly depth values seems to be reasonable. Both in the Lavant Valley and in Transdanubia heat flow reaches the value 100 mWm^{-2}, while along the Periadriatic lineament the heat flow map of Čermák and Hurtig (1979) gives heat flow values about 30–40 mWm^{-2} less. Since the 300° C isotherms lie deeper in the Periadriatic lineament – as concluded from the surface heat flow – the greater depth of the crustal anomaly seems to be in accordance with geothermics here, as shown in Fig. 10.

The seismic activity is concentrated in the eastern region of the Periadriatic lineament (between Villach and Eisenkappel). The hypocentres lie shallower (Drimmel, 1980) than the crustal conducting zone. On the basis of the heat flow and the conductivity distribution it can be supposed that the Periadriatic lineament represents an older tectonic formation than the fractures in Transdanubia and the Lavant Valley. The greater age of the Periadriatic lineament is supported by a shift of the latter along the Lavant Valley.

Thus, MT measurements along the Periadriatic lineament have also proved to be an effective tool for tracing great tectonic zones and investigating their physical conditions even within the rugged topography of the eastern Alps.

Acknowledgements. The authors wish to thank the Austrian and Hungarian Academies of Sciences for their conceptual and financial support and their colleagues, especially Ms J. Szendrői for her carefulness in the great quantity of computing work.

Appendix

Magnetic or telluric absolute ellipses can be used for the transformation of magnetic or telluric values from one station to another in order to compute MTS curves for the latter (and also for the determination of the distortion of the geomagnetic variations). As a basis, simultaneous filtered complex amplitudes of the geomagnetic or telluric field are used at two (or more) stations. The real and imaginary parts of the square- and product-sums at both stations

$$X^{r^2}+X^{i^2}=X^2; \qquad Y^{r^2}+Y^{i^2}=Y^2$$

$$X^r\,Y^r+X^i\,Y^i=XY \tag{1}$$

enable the determination of the (instantaneous) geomagnetic or telluric absolute ellipse. (The values of X and Y, the north and east components, are sampled roughly in time intervals corresponding to one complete period of the filtered signal.)

The data of the absolute ellipse are as follows (Verő, 1960):

$$\tan 2\alpha=\frac{2XY}{X^2-Y^2} \tag{2}$$

$$A,\,B=\sqrt{\frac{X^2+Y^2\pm\sqrt{(X^2-Y^2)^2+4(XY)^2}}{n}}. \tag{3}$$

Here α is the direction of the major axis of the absolute ellipse, A and B are the lengths of the major and minor axes, n is the number of data points.

The components of the tensor transforming an ideal circularly polarized wave into the observed one are:

$$a=A\cos^2\alpha+B\sin^2\alpha$$

$$d=A\sin^2\alpha+B\cos^2\alpha$$

$$b=c=0.5(A-B)\sin 2\alpha. \tag{4}$$

In these formulas it is supposed that distortions occur only in the direction of the major and minor axes, i.e. the above tensor is a symmetric one. Thus, the instantaneous stationary ellipses of the base (index 0) and secondary (without index) station have the following form, if the components of the circularly polarized field are denoted by x and y:

$$X=ax+by \qquad X_0=a_0x+b_0y$$

$$Y=bx+dy \qquad Y_0=b_0x+d_0y. \tag{5}$$

By eliminating x, y from these equations, the relative ellipse between the base and the secondary station is obtained:

$$X=a_R\,X_0+b_R\,Y_0$$

$$Y=c_R\,X_0+d_R\,Y_0 \tag{6}$$

where the components of the relative ellipse $[T]$ are:

$$a_R=(ad_0-bb_0)\quad 1/t_0$$

$$b_R=(ba_0-ab_0)\quad 1/t_0$$

$$c_R=(bd_0-db_0)\quad 1/t_0$$

$$d_R=(da_0-bb_0)\quad 1/t_0 \tag{7}$$

$$t_0=a_0d_0-b_0^2. \tag{8}$$

With the help of Eq. (6) any geomagnetic or telluric variation can be transformed into variations at the other (secondary) station, or even instantaneous absolute ellipses can be transformed either for MT or for geomagnetic sounding purposes.

With this method the necessity of strictly simultaneous data points is eliminated, and the original MT-processing programme can be used with a subroutine containing Eqs. (1)–(8).

References

Ádám, A.: Statistische Zusammenhänge zwischen elektrischer Leitfähigkeitsverteilung und Bruchtektonik in Transdanubien (Westungarn). Acta Geodaet. Geophys. Mont. Hung. **16**, 97–113, 1981

Ádám, A.: Electric conductivity increases in the earth's crust in Transdanubia (W-Hungary). Acta Geodaet. Geophys. Mont. Hung. **20**, 173–182, 1985

Ádám, A., Märcz, F., Verő, J., Wallner, Á.: Magnetotelluric sounding in the transitional zone between the Eastern Alps and Pannonian Basin. J. Geophys. **50**, 37–44, 1981

Ádám, A., Szarka, L., Varga, M.: Physical and mathematical modelling of crustal conductivity anomalies in the Pannonian Basin. Acta Geodaet Geophys. Mont. Hung. **18**, 467–488, 1983

Ahrendt, H.: Die Bedeutung der Insubrischen Linie für den tektonischen Bau der Alpen. N. Jb. Geol. Paläont. Abh. **160**, 3, 336–362, Stuttgart, 1980

Berdichevsky, M.N., Dmitriev, V.I.: Distortion of magnetic and electric fields by near-surface lateral inhomogeneities. Acta Geodaet. Geophys. Mont. Hung. **11**, 447–483, 1976

Čermák, V., Hurtig, E.: Heat flow map of Europe. Enclosure for terrestrial heat flow in Europe, V. Čermák, L. Rybach, eds. Berlin-Heidelberg New York: Springer-Verlag 1979

Drimmel, J.: 4. Rezente Seismizität und Seismotektonik des Ostalpenraumes. In: Der Geologische Aufbau Österreichs, R. Oberhauser, ed. Wien, New York: Springer 1980

Fischer, G., Schnegg, P.A., Peguiron, M., Le Quang, B.V.: An analytic one-dimensional magnetotelluric inversion scheme. Geophys. J.R. Astron. Soc. **67**, 257–278, 1981

Frey, M., Hunziker, J.C., Frank, W., Bocquet, J., Dal-Piaz, G.V., Jäger, E., Niggli, E.: Alpine Metamorphism of the Alps. A Review. Schweiz. min. petr. Mitt. **54**, 2–3, 247–290, Zürich, 1974

Haenel, R.: Interpretation of the terrestrial heat flow in the Rhinegraben. In: Graben Problems, Illies, J.H., Mueller, S.E., eds., pp 116–120. Stuttgart: E. Schweizerbart'sche Verlagsbuchhandlung 1970

Kovács, S.: A tectonic review of the Alps (in Hungarian). Általános Földtani Szemle **18**, 77–155, Budapest, 1983

Praus, O.: Numerical solutions of the MT field in inhomogeneous structures. In: Geoelectric and geothermal studies, A. Ádám, ed., pp 231–245. KAPG Geophys. Monograph. Budapest: Akadémiai Kiadó 1976

Quist, A.S., Marshal, W.L., Franck, E.U., v. Osten, M.: A reference solution for electrical conductance measurements to 300° C and 12000 bars. Aquaeous 0.01 demal potassium chloride. J. Phys. Chem. **74**, 2241–2243, 1970

Tátrallyay, M.: On the interpretation of EM sounding curves by numerical modelling using the S.O.R. method. Acta Geodaet. Geophys. Mont. Hung. **12**, 279–285, 1977

Varga, G.: Geophysical investigation of geological basic profiles I. Report on telluric and MT measurement (in Hungarian). MÁELGI Manuscript, 1980

Verő, J.: Die Bestimmung der tellurischen Stationsellipsen. Ger. Beitr. z. Geophys. **69** (5), 257–268, 1960

Verő, J.: On the determination of magnetotelluric impedance tensor. Acta Geodaet. Geophys. Mont. Hung. **7**, 333–351, 1972

Received April 22, 1985; revised November 4/December 23, 1985
Accepted December 23, 1985

J Geophys (1986) 59:112–118

Journal of Geophysics

Comparison of fault-plane solutions and moment tensors

Klaus-G. Hinzen

Bundesanstalt für Geowissenschaften und Rohstoffe, Stilleweg 2, D-3000 Hannover 51, Federal Republic of Germany

Abstract. In the last three or four years moment tensors have been obtained for most earthquake sources with seismic moments $M_0 > 10^{24}$ dyne · cm. Fault-plane solutions are published by NEIS for earthquakes with $M_b > 6.0$. In some cases the orientation of the best-fitting double couple of the moment tensor differs from that of the fault-plane solution. Using Euklid's norm of a matrix, the differences of the two source orientations are quantified as a distance parameter D.

120 earthquakes (January 1981–March 1983) are selected for a systematic study comparing the best-fitting double couple from the moment tensor inversion and the ordinary fault-plane solution. The assumption that the differences in source orientation increase with an increase of the non-double-couple contribution to the source is not valid for the 120 events. 11.5% of the events have small deviations from the double couple and large differences between the orientations from fault-plane solutions and moment tensors, while the 2.5% of the events with large deviations from the double couple show small differences in the source orientations derived by the two methods. None of the events has large deviations from the double couple and large differences between the orientations. Results are discussed with respect to source properties.

Key words: Moment tensor – Fault-plane solution – Non-double-couple contribution

Introduction

For more than two decades the fault-plane solution based on first P-wave motions has been the most important technique to derive focal mechanisms of earthquakes. The double-couple model, a principal requirement for this technique, proved to be acceptable for most of the observations. Hundreds of earthquake mechanisms have been studied in this way (e.g. Anderson et al., 1974; Banghar and Sykes, 1969; Forsyth, 1972; Ichikawa, 1971; Isacks et al., 1969, 1981; Johnson and Molnar, 1972; Katsumara and Sykes, 1969; Molnar, 1973; Molnar and Sykes, 1969; Ritsema, 1964, 1965, 1966; Stauder, 1968, 1975; Stauder and Bollinger, 1966; Sykes, 1967). These investigations supplied fundamental arguments for the new global tectonic model.

In the early 1970s more general formulations of seismic source mechanisms were obtained. Gilbert (1970) introduced the concept of the moment tensor, which depends on strength and orientation of the seismic source. It contains all information about the seismic source which can be obtained from far-field observations (Aki and Richards, 1980). Gilbert (1970) demonstrated the linear relation between moment tensors and seismograms. If the transfer function of the elastic medium is known, it is possible to invert source parameters from seismograms. Gilbert and Dziewonski (1975) were the first to calculate moment tensors of two deep South American earthquakes. In the following years the technique of inversion itself became the main point of interest. Mendiguren (1976), McCowman (1976), Aki and Patton (1978) and Kanamori and Given (1981) used surface-wave data: the technique was applied to body waves by Ward (1980), Strelitz (1980) and Langston (1981).

Routine determinations of moment tensors (Sipkin, 1982) and Centroid-Moment Tensors (CMT) (Dziewonski et al., 1981) were the first steps to utilize the advantages of inversion techniques for the study of global tectonics. The work of Dziewonski and Woodhouse (1983), Giardini and Woodhouse (1984) and Giardini (1983) proved the applicability of the CMT concept in order to study seismic sources.

However, the question arises as to what the relations between results of the inversion techniques and fault-plane solutions are and whether the differences between both kinds of source description can be interpreted. An answer to this question may help to elucidate the rupture process of special events and to find out whether the moment tensor concept can fully replace the fault-plane solution technique. The purpose of this study is a systematic comparison between published CMTs and fault-plane solutions for the time interval January 1981–March 1983.

Differences in source orientations

In a number of recent publications, moment tensors and fault-plane solutions of special events have been compared. Dziewonski and Woodhouse (1983) calculated the CMT of 201 earthquakes in 1981. One of the earthquakes discussed in detail was the event of May 25, 1981, off the west coast of the South Island of New Zealand with the seismic moment $M_0 = 2.7 \times 10^{25}$ dyne cm. The fault-plane solution, on the basis of first P-wave motions, is reported by NEIS as a reverse fault. The best-fitting double couple of the CMT is of strike-slip type. If the N31°E-striking and 66°SE-dipping plane of the CMT solution is assumed to be the fault plane, the right-lateral motion agrees well with the expected relative motion between the Pacific and Indian plates.

Choy et al. (1983) analysed teleseismic data of the January 9, 1982, New Brunswick event. The multichannel signal enhancement method and the multichannel vector deconvolution method were applied. The differences for strike and slip are 14° and 21°, respectively. The dip angles of the fault planes are identical. The preferred fault-plane solution has nearly the same dip and slip angles of the fault plane compared to the results of inversion but deviates by 31° and 45° in the direction of strike.

Barker and Langston (1983) compared fault-plane solutions and moment tensors of Mammoth Lake, California, earthquakes. They found first-motion readings of teleseismic recordings to be inconsistent with mechanisms determined from local and regional P-wave first motions. Nevertheless, the inversion of only a few teleseismic body waves gave radiation patterns of moment tensors which are consistent with most of the first P-wave motions in all distances.

The validity of the double-couple model (DC), i.e. the pure shear dislocation with a constant slip direction on a plane discontinuity, is a basic requirement of the fault-plane solution technique. This precondition is not fundamental to the calculation of moment tensors. The only condition in the CMT calculation that is usually assumed is a vanishing isotropic component:

$$tr[\mathbf{M}]=0$$

where $\mathbf{M}$ is the moment tensor. The source is not constrained to be a double couple (Dziewonski et al., 1981). Therefore, the intermediate eigenvalue E_2 of the three eigenvalues E_1, E_2, E_3 does not need to equal zero, as required for the plane shear models.

The ratio of the intermediate eigenvalue E_2 and the largest eigenvalue

$$|\varepsilon|=\frac{E_2}{\mathrm{Max}(|E_1|,|E_2|)}$$

is a quantitative measure for the non-double-couple contribution to the total moment tensor. The absolute value of ε is 0 for plane shear and 0.5 for the largest possible deviation from a double couple. The latter case is interpreted by Knopoff and Randall (1970) as corresponding to a linear vector dipole or equivalently – following Gilbert (1970) – as the special case of equal minor and major double couples into which the tensor is decomposed.

Dziewonski and Woodhouse (1983) found $|\varepsilon|$-values ranging from 0 to 0.35 for shallow sources ($h \leqq 50$ km), $0 \leqq |\varepsilon| \leqq 0.4$ for intermediate depth ($50\text{ km} < h \leqq 300$ km) and $0 \leqq |\varepsilon| \leqq 0.3$ for deep events ($h > 300$ km). The range of $|\varepsilon|$-values reveals that about 20% of the events have significant non-double-couple contributions with $|\varepsilon| > 0.2$. For those earthquakes with large non-double-couple contributions, the validity of the plane shear model has to be questioned and it may be supposed that these deviations from the DC source give different orientations of the fault planes from fault-plane solutions and from the moment tensor calculation, respectively.

Distance parameter

For a systematic comparison of fault-plane solutions and moment tensors, the differences between the two source orientations must be quantified. Therefore, Euklid's norm of a matrix $\mathbf{A}$ is introduced as a measure of distance. The norm is defined as the square root of the trace of the matrix product of $\mathbf{A}^\mathrm{T}$ and $\mathbf{A}$, where $\mathbf{A}^\mathrm{T}$ is the transpose of $\mathbf{A}$:

$$||\mathbf{A}||=(tr[\mathbf{A}^\mathrm{T}\cdot\mathbf{A}])^{1/2}.$$

The normalized matrix $\mathbf{A}_\mathrm{n}$ is defined as:

$$\mathbf{A}_\mathrm{n}=\frac{\mathbf{A}}{||\mathbf{A}||}.$$

The distance parameter for two solutions, which are represented by matrices $\mathbf{A}$ and $\mathbf{B}$, containing the six independent elements of the moment tensor is:

$$D(\mathbf{A},\mathbf{B})=||\mathbf{A}_\mathrm{n}-\mathbf{B}_\mathrm{n}||$$

where

$$0 \leqq D \leqq 2.$$

If two solutions for instance have the same strike and dip angles of the fault plane and differ by 90° in the value of the slip angle, the distance parameter is $D=1$. Reverse sense of motion, which is equivalent to a 180° difference in slip angle, results in the maximum distance parameter $D_{\max}=2$. For the latter case, the directions of the principal axes P and T, corresponding to the smallest and largest eigenvalue, respectively, are exchanged.

Comparison of orientations

The Centroid-Moment Tensors of Dziewonski and Woodhouse (1983) and Dziewonski et al. (1983a, b) represent a large data base of homogeneous inversion results for worldwide seismicity. Nearly 600 CMTs of earthquakes (January 1981–March 1983) have been computed from body- and mantle-wave data of the Global Digital Seismograph Network (GDSN). For comparison, fault-plane solutions are taken from the monthly listings of NEIS. The lower magnitude bound for routine fault-plane solutions is $M_\mathrm{b}=6.0$. Among these data, 120 earthquakes are used in this comparison. Date, origin time (NEIS), depth of the centroid source in kilometres and the scalar seismic moment in dyne · cm are listed in Table 1 together with the quantities D and $|\varepsilon|$.

The distance parameter D has been calculated between the moment tensor corresponding to the douple-couple orientation of the fault-plane solution and the moment tensor of the best-fitting double couple of the Centroid-Moment Tensor. The six independent values of the moment tensor corresponding to the fault-plane solution were determined from the angles of orientation of the source, ϕ, δ, λ (Aki and Richards, 1980), where ϕ, δ and λ are strike, dip and slip angle, respectively. Figure 1 shows the relation between D and $|\varepsilon|$, where $|\varepsilon|$ is calculated from CMT eigenvalues.

Only four events have distance parameters $D > 1.0$. These are indicated by small arrows identified with the event number. The P- and T-axes of events Nos. 3 and 4 (both January 23, 1981) are exchanged with respect to those of the moment tensor: the distance parameters reach nearly the maximum value ($D > 1.9$). By a classification of $|\varepsilon|$ and D values, Fig. 1 is divided into six ranges denoted by *i–vi*. The non-double-couple contribution is divided into three classes:

low $|\varepsilon|$: $0.0 \leqq |\varepsilon| < 0.17$
intermediate $|\varepsilon|$: $0.17 \leqq |\varepsilon| < 0.33$
high $|\varepsilon|$: $0.33 \leqq |\varepsilon|$

and the distance parameter is divided into two classes:

low D: $0.0 \leqq D < 0.5$
high D: $0.5 \geqq D$.

Table 1. Distance parameters D between the fault-plane solution (NEIS) and the best double couple of Centroid Moment Tensors (Dziewonski et al., 1981) are listed for 120 earthquakes from January 1981 to March 1983. In addition, the non-double-couple contribution of the CMT, depth and seismic moment are given

No.	Date	Time (h min s)	h (km)	M_0 (dyne·cm)	exp	D	$\lvert\varepsilon\rvert$	Region
1	18 01 81	18 17 24	20	3.69	26	0.07	0.06	Honshu
2	19 01 81	15 11 01	10	1.17	26	0.48	0.19	Iran
3	23 01 81	21 13 51	15	0.99	26	1.94	0.01	Sichuan
4	23 01 81	21 54 42	10	2.98	26	1.92	0.14	Atl. Indian Ridge
5	24 02 81	20 53 38	20	1.29	26	0.08	0.04	Greece
6	04 03 81	21 58 06	29	3.48	25	0.10	0.24	Greece
7	06 03 81	19 42 59	24	1.18	26	0.62	0.02	Central Am.
8	24 04 81	21 50 06	44	2.25	26	0.13	0.04	Vanuatu Island
9	27 04 81	18 17 34	10	7.53	25	0.08	0.07	Maquarie Island
10	25 05 81	05 25 14	20	2.70	27	0.46	0.10	South Island N.Z.
11	03 06 81	05 42 44	10	8.07	25	0.07	0.06	South Atlantic Ridge
12	06 07 81	03 08 24	58	2.59	27	0.29	0.25	Loyalty Island
13	07 07 81	21 10 57	10	2.46	26	0.29	0.02	Mid Atlantic Ridge
14	15 07 81	07 59 08	30	5.76	26	0.15	0.04	Vanuatu
15	28 07 81	17 22 24	20	6.68	26	0.95	0.21	Iran
16	01 09 81	09 29 31	20	1.94	27	0.64	0.06	Samoa Island
17	03 09 81	05 35 44	36	7.54	25	0.56	0.01	Kuril Island
18	17 09 81	08 23 24	30	1.64	26	0.17	0.14	Loyalty Island
19	16 10 81	03 25 42	40	5.11	26	0.33	0.09	Chile
20	25 10 81	03 22 15	32	7.00	26	0.00	0.07	Mexico
21	03 11 81	13 47 34	10	5.15	25	0.14	0.00	Oregon
22	06 11 81	16 47 49	15	0.91	26	0.52	0.20	Papua
23	07 11 81	03 29 51	66	3.26	26	0.32	0.21	Chile
24	22 11 81	15 05 20	29	5.27	25	0.02	0.03	Cuzon
25	12 12 81	04 52 37	15	4.49	25	0.58	0.03	Ryukyu Island
26	19 12 81	14 10 50	22	2.41	26	0.00	0.06	Aegean Sea
27	24 12 81	04 33 20	19	2.11	26	0.05	0.02	Kermadec
28	26 12 81	17 05 32	30	4.57	26	0.01	0.08	Kermadec
29	27 12 81	17 39 13	22	3.34	25	0.07	0.12	Aegean Sea
30	01 01 82	18 51 01	37	9.00	25	0.17	0.02	Bonin Island
31	03 01 82	14 09 50	10	4.76	26	0.27	0.01	Mid Atlantic Ridge
32	07 01 82	08 42 50	15	7.93	24	0.90	0.25	Gilbert Island
33	09 01 82	12 53 51	10	1.94	24	0.99	0.18	Brunswick
34	11 01 82	06 10 06	17	4.96	26	0.02	0.01	Philippine Island
35	18 01 82	19 27 24	9	9.38	25	0.13	0.10	Aegean Sea
36	24 01 82	06 08 56	19	1.05	26	0.05	0.04	Philippine Island
37	20 02 82	13 26 50	10	1.92	26	1.00	0.20	Santa Cruz
38	20 02 82	19 18 20	30	6.06	25	0.25	0.38	Honshu
39	11 03 82	10 32 27	36	7.43	25	0.47	0.27	Sumbawa Island
40	21 03 82	02 32 07	37	2.64	26	0.58	0.07	Hokaido
41	06 04 82	19 56 53	43	1.44	26	0.13	0.14	Mexico
42	02 05 82	11 19 38	20	4.52	25	0.02	0.00	Kermadec
43	31 05 82	10 21 15	19	7.15	25	0.10	0.06	Komandorsky
44	31 05 82	15 18 55	23	5.86	25	0.03	0.02	W. Caroline Island
45	02 06 82	12 37 34	11	3.95	25	0.95	0.07	Tonga
46	07 06 82	06 52 37	11	2.90	26	0.21	0.01	Mexico
47	07 06 82	10 59 40	19	2.66	26	0.17	0.01	Mexico
48	19 06 82	06 21 58	52	1.05	27	0.47	0.07	El Salvador
49	22 06 82	04 18 40	473	1.77	27	0.05	0.07	Banda Sea
50	30 06 82	01 57 34	21	4.45	26	0.16	0.12	Kuril Island
51	04 07 82	01 20 06	552	1.25	26	0.20	0.17	Ryukyu Island
52	07 07 82	10 43 03	10	4.60	26	0.06	0.25	Maquarie Island
53	23 07 82	14 23 53	27	3.92	26	0.03	0.00	Honshu
54	03 08 82	06 04 39	17	6.15	24	0.11	0.16	Mariana
55	05 08 82	20 32 52	24	3.20	26	0.01	0.02	Santa Cruz
56	07 08 82	20 56 22	18	5.57	25	0.21	0.15	Bali
57	12 08 82	02 13 08	33	6.02	25	0.08	0.06	New Ireland
58	14 08 82	14 27 40	114	1.40	25	0.33	0.08	Papua
59	17 08 82	22 22 24	23	3.98	25	0.17	0.04	Mediterranean Sea
60	19 08 82	15 59 01	25	1.19	26	0.32	0.04	Panama
61	22 08 82	03 42 36	56	3.05	24	0.07	0.02	Vanuatu Island
62	23 08 82	16 40 19	10	2.25	24	0.57	0.16	Honshu
63	26 08 82	05 22 59	92	1.13	25	0.01	0.03	Equador
64	03 09 82	01 32 00	10	1.56	25	0.00	0.05	Kuril Island

Table 1 (continued)

No.	Date	Time (h min s)	h (km)	M_0 (dyne·cm)	exp	D	$\|\varepsilon\|$	Region
65	03 09 82	23 39 39	10	5.50	25	0.07	0.09	Tonga
66	04 09 82	13 31 14	10	1.45	25	0.04	0.09	Fiji Island
67	06 09 82	01 47 02	156	2.02	26	0.54	0.20	Honshu
68	15 09 82	20 22 55	167	3.28	25	0.60	0.24	Peru
69	17 09 82	13 28 24	561	1.73	25	0.09	0.05	Fiji Island
70	28 09 82	15 14 36	42	4.93	25	1.22	0.27	Fiji Island
71	05 10 82	09 14 32	10	8.71	24	0.56	0.12	Vanuatu Island
72	05 10 82	21 39 12	10	2.78	24	0.97	0.06	South Atlantic Ridge
73	07 10 82	07 15 56	521	1.33	26	0.09	0.06	Banda Sea
74	11 11 82	00 43 45	29	2.59	25	0.09	0.30	Sumatera
75	14 11 82	08 29 20	110	2.60	24	0.02	0.00	Kamchatka
76	16 11 82	17 25 53	10	1.45	25	0.34	0.10	Vanuatu Island
77	18 11 82	14 57 52	190	8.19	25	0.25	0.04	Ecuador
78	19 11 82	04 27 13	10	1.06	26	0.28	0.01	Peru
79	03 12 82	22 29 59	229	6.13	25	0.24	0.04	Vanuatu Island
80	05 12 82	05 48 25	65	4.02	24	0.29	0.18	Solomon Island
81	13 12 82	09 12 48	10	2.52	25	0.32	0.10	W. Arab. Penin.
82	16 12 82	00 40 48	33	6.11	25	0.25	0.06	Hindukush
83	17 12 82	02 43 03	94	6.34	25	0.11	0.05	Taiwan
84	19 12 82	17 43 54	29	1.98	27	0.16	0.06	Tonga Island
85	20 12 82	02 58 10	10	3.28	25	0.19	0.12	Tonga Island
86	28 12 82	06 37 42	22	2.09	25	0.01	0.10	Honshu
87	28 12 82	13 49 29	25	1.57	25	0.06	0.03	Philippine Island
88	01 01 83	05 31 56	172	3.16	25	0.08	0.00	Peru
89	08 01 83	11 21 29	53	3.00	25	0.13	0.08	Tonga
90	10 01 83	12 32 21	565	4.78	24	0.13	0.24	Sant. Estero
91	16 01 83	22 10 12	230	8.26	25	0.04	0.04	Papua
92	17 01 83	12 41 29	10	2.35	26	0.06	0.15	Greece
93	18 01 83	15 23 36	28	5.08	25	0.72	0.24	Sandwich Island
94	24 01 83	08 17 39	36	2.06	26	0.52	0.14	Mexico
95	24 01 83	16 34 08	32	8.52	24	0.44	0.24	N. Atlantic Ocean
96	24 01 83	23 09 21	73	1.71	26	0.23	0.42	Andaman Island
97	26 01 83	16 02 21	224	3.66	26	0.14	0.39	Kermadec
98	31 01 83	21 17 31	10	1.89	24	1.16	0.03	Gilbert Island
99	07 02 83	18 23 17	52	1.62	25	0.08	0.05	Kermadec
100	12 02 83	08 47 13	23	3.19	25	0.17	0.12	Philippine Island
101	14 02 83	00 23 19	35	1.30	25	0.03	0.13	Caroline Island
102	14 02 83	03 20 04	19	7.12	25	0.04	0.07	Alaska
103	14 02 83	08 10 04	40	1.00	25	0.11	0.16	Alaska
104	19 02 83	20 14 23	566	1.11	25	0.10	0.30	Philippine Island
105	20 02 83	10 49 54	39	3.71	25	0.12	0.12	Philippine Island
106	25 02 83	22 03 56	217	3.56	24	0.03	0.06	Papua
107	26 02 83	07 10 59	45	3.62	25	0.04	0.01	Kuril Island
108	27 02 83	12 14 21	73	1.52	25	0.04	0.06	Honshu
109	28 02 83	05 44 24	28	1.52	25	0.02	0.14	Kuril Island
110	08 03 83	17 06 37	85	8.38	24	0.01	0.05	Windward Island
111	10 03 83	00 27 48	37	1.23	25	0.02	0.12	Kuril Island
112	11 03 83	03 10 42	58	4.83	24	0.22	0.10	Papua
113	12 03 83	00 53 40	11	1.51	25	0.03	0.23	Banda Sea
114	12 03 83	01 36 36	16	9.25	25	0.32	0.09	Banda Sea
115	15 03 83	19 58 30	21	6.58	25	0.06	0.10	Philippine Island
116	18 03 83	09 05 50	70	4.63	27	0.13	0.11	New Ireland
117	20 03 83	13 45 49	65	4.13	25	0.50	0.08	New Ireland
118	21 03 83	07 44 18	52	1.18	26	0.01	0.05	Tonga
119	23 03 83	06 09 29	49	4.46	25	0.05	0.18	Solomon Island
120	23 03 83	23 51 07	33	2.23	25	0.10	0.14	Greece

The percentages of events in the ranges are:

range *i*	(low D,	low $\|\varepsilon\|$)	66.6%
range *ii*	(low D,	intermediate $\|\varepsilon\|$)	11.5%
range *iii*	(low D,	high $\|\varepsilon\|$)	2.5%
range *iv*	(high D,	low $\|\varepsilon\|$)	11.5%
range *v*	(high D,	intermediate $\|\varepsilon\|$)	7.4%
range *vi*	(high D,	high $\|\varepsilon\|$)	0.0%.

78% of the events (range *i* and *iv*) are well explained by the double-couple model, while 2.5% show large non-double-couple contributions. Intermediate $|\varepsilon|$-values are found for 19% (range *ii* and *v*). 11.5% (range *iv*) of the events show large differences in the source orientations derived by the two methods, though the non-double-couple contributions is small. A striking feature of Fig. 1 is the emptyness

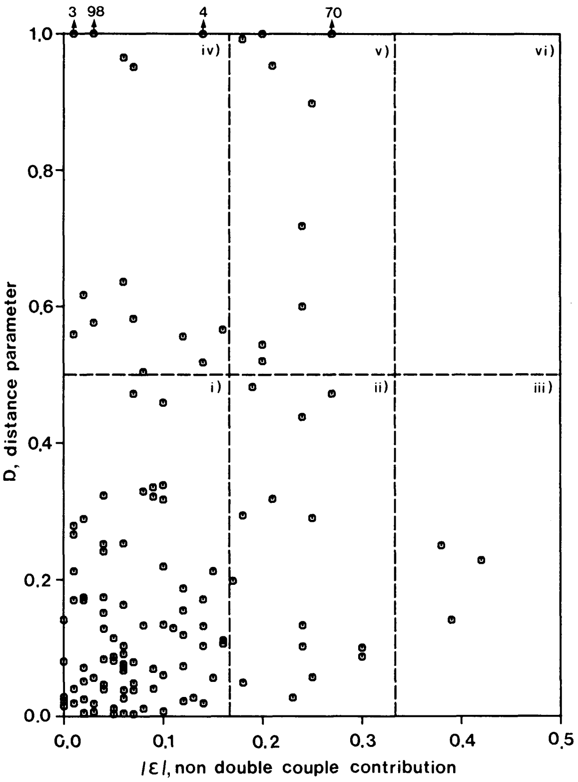

Fig. 1. The distance parameters between fault-plane solutions, FPS (NEIS), and the best-fitting double couple of Centroid Moment Tensors, CMT (Dziewonski et al., 1981), of 120 earthquakes are shown as a function of the non-double-couple contribution of the CMTs. The *arrows at the top* indicate those events with $D > 1.0$. The numbers are those of Table 1

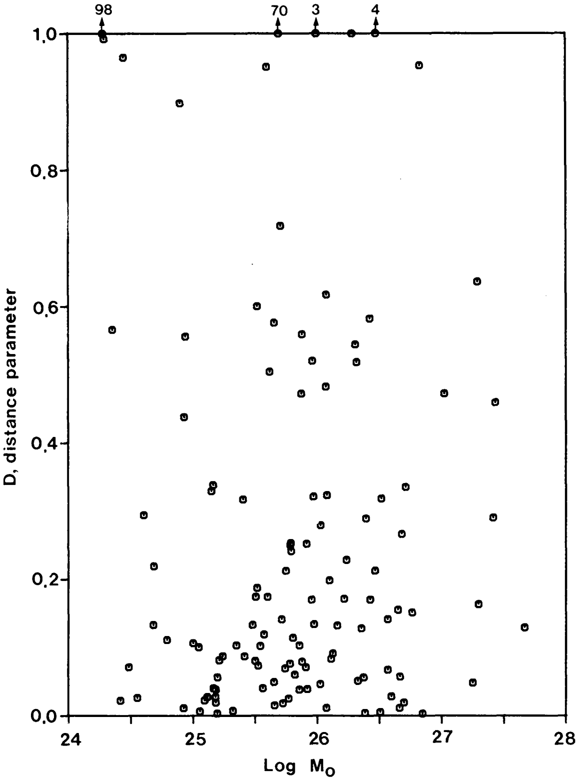

Fig. 2. The distance parameters between fault-plane solutions and the best-fitting double couple of Centroid Moment Tensors are plotted as a function of the logarithm of the scalar seismic moment. M_0 is taken in dyne cm. The notation is the same as in Fig. 1

of range *vi*, i.e. no event with large $|\varepsilon|$ and large D is found among the 120 earthquakes. Nevertheless, 2.5% have small distance parameters and large non-double-couple contributions (range *iii*). In Figs. 2 and 3 the distance parameters are plotted versus the logarithm of the scalar seismic moment, M_0 in dyne · cm, and versus depth of the centroid. The large scatter of distance parameters in the four orders of magnitude of M_0 give no indication for any dependence of D on the strength of the earthquake. From Fig. 3 it may be suggested that the averaged values of D decrease with increasing depth. This speculation can only be verified after more data of intermediate and deep earthquakes are incorporated.

Discussion and conclusions

The fault-plane solution technique and the Centroid-Moment Tensor determination use different spatio-temporal dimensions of the seismic source. The fault-plane solution technique uses the direction of the very first *P*-wave motion from the vertical component. The first-motion readings contain only information about the situation at rupture initiation, whereas the inversion of entire waveform for the optimum point source, like the Centroid-Moment Tensor, is an average over the whole spatio-temporal dimension of the source. If, for example, the earthquake is divided into two or more successive subevents, the ordinary fault-plane solution will only represent the orientation of the first subevent. The moment tensor is a mean solution for all events if the inversion process is not constrained to form two or more events. Therefore, in a seismotectonic interpretation of source orientations, the influence of the method used must be kept in mind.

The 19% of events in ranges *iv* and *v* show that large distance parameters exist in spite of small or intermediate non-double-couple contributions. This may be an indication for a change of fault-plane geometry or slip direction after the initiation of rupture. The 11.5% in range *iv* show that the large distance parameters can not be attributed to the deviation from the plane shear mechanism. The events Nos. 38, 96 and 97 in range *iii* represent the case that the orientation of the fault-plane solution fits quite well with the orientation derived from the moment tensor, though the large $|\varepsilon|$-value indicates striking differences to the simple plane shear model. If the large $|\varepsilon|$-values are no effect of the procedure, for example due to lateral-inhomogenities in the source region, a multiple rupture process on one or more focal planes with stable orientation may cause this effect.

Although the inversion of moment tensors is a very powerful and objective tool in the determination of source parameters, it cannot replace the fault-plane solution completely. In the case of a complicated and multiple rupture process, fault-plane solution and, in addition, master event techniques and forward modelling of waveforms (Bruestle, 1985) have to be applied for a detailed analysis of the source mechanism.

The distance parameter D proved to be a good measure

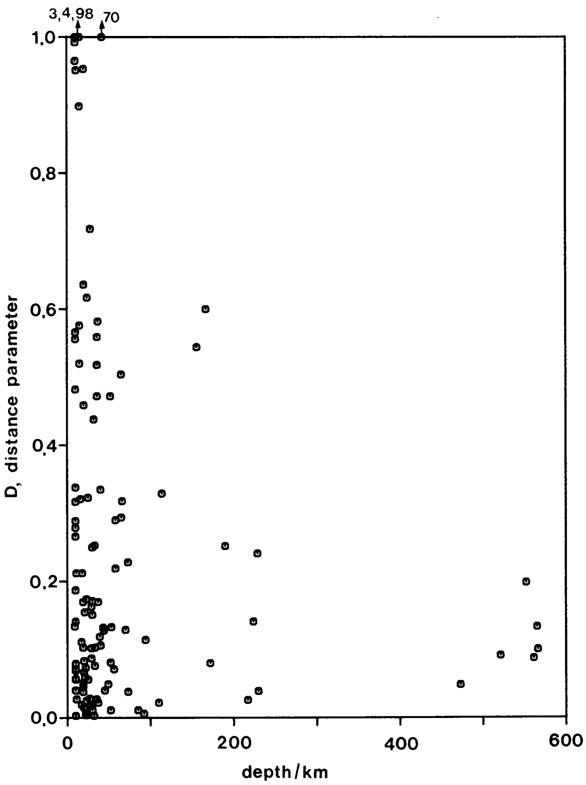

Fig. 3. The distance parameters between fault-plane solutions and the best double couple of Centroid Moment Tensors are shown as a function of source depth. The depth is that of the centroid. The notation is the same as in Fig. 1

for a comparison of source orientations of earthquakes obtained by different methods. In this study results of two methods applied to one earthquake have been examined. The distance parameter may also be used for other purposes. For example, applied to a cluster analysis it can help to discriminate between earthquake mechanisms of different types and to test whether an event belongs to a certain group of source mechanisms or not.

Acknowledgements. The basic work for this study was carried out during my time at the Institut für Geophysik of the Ruhr-Universität Bochum. I am grateful to R.-G. Ferber and H.P. Harjes with whom I had helpful discussions over the course of this research. I thank two reviewers for their comments and H.-U. Worm for carefully reading the manuscript.

References

Aki, K., Patton, H.: Determination of seismic moment tensor using surface waves. Tectonophys. **49**, 213–222, 1978

Aki, K., Richards, P.G.: Quantitative seismology, Vol. 1, 557 pp. San Francisco: Freeman 1980

Anderson, R.N. Forsyth, D.W., Molnar, P., Mammerickx, J.: Fault plane solutions of earthquakes on the Nazca plate boundaries and the Easter plate. Earth Planet. Sci. Lett. **24**, 188–202, 1974

Banghar, A.R., Sykes, L.R.: Focal mechanisms in the Indian Ocean and adjacent regions, J. Geophy. Res. **74**, 632–649, 1969

Barker, J.S., Langston, C.A.: A teleseismic body-wave analysis of the May 1980 Mammoth Lakes, California, earthquakes Bull. Seism. Soc. Am. **73**, 419–434, 1983

Bruestle, W.: Der Bruchvorgang im Erdbebenherd – Untersuchung ausgewählter Erdbeben mit beobachteten und synthetischen Seismogrammen. Ber. d. Inst. f. Met. u. Geoph. Univ. Frankfurt, Nr. 63, 1985

Choy, G.L., Boatwright, J., Dewey, J.W., Sipkin, S.A.: A teleseismic analysis of the New Brunswick earthquake of January 9, 1982. J. Geophys. Res. **88**, 2199–2212, 1983

Dziewonski, A.M., Chou, T.-A., Woodhouse, J.H.: Determination of earthquake source parameters from waveform data for studies of global and regional seismicity. J. Geophys. Res. **86**, 2825–2852, 1981

Dziewonski, A.M., Friedman, A., Giardini, D., Woodhouse, J.H.: Global seismicity of 1982: Centroid-Moment Tensor Solutions for 308 earthquakes. Phys. Earth Planet. Inter. **33**, 76–90, 1983a

Dziewonski, A.M., Friedman, A., Woodhouse, J.H.: Centroid-Moment Tensor Solutions for January-March, 1983. Phys. Earth Planet. Inter. **33**, 71–75, 1983b

Dziewonski, A.M., Woodhouse, J.H.: An experiment in systematic study of global seismicity: Centroid-Moment Tensor Solutions for 201 moderate and large earthquakes of 1981. J. Geophys. Res. **88**, 3247–3271, 1983

Forsyth, D.W.: Mechanisms of earthquakes and plate motions in the East Pacific. Earth Planet. Sci. Lett. **17**, 189–193, 1972

Giardini, D.: Systematic analysis of deep seismicity: 200 Centroid-Moment Tensor solutions for earthquakes between 1977 and 1980. Geophys. J. R. Astron. Soc. **77**, 883–914, 1983

Giardini, D., Woodhouse, J.H.: Deep seismicity and modes of deformation in the Tonga subduction zone. Nature **307**, 505–509, 1984

Gilbert, F.: Exicitation of normal modes of the earth by earthquake sources. Geophys. J. R. Astron. Soc. **22**, 223–226, 1970

Gilbert, F., Dziewonski, A.M.: An application of normal mode theory to the retrieval of structural parameters and source mechanisms from seismic spectra. Phil. Trans. Roy. London. Ser. A, **278**, 187–269, 1975

Ichikawa, M.: Reanalysis of mechanism of earthquakes which occurred in and near Japan, and statistical studies of the nodal plane solutions obtained, 1926–1968. Geophys. Mag. JMA, **35**, 207–274, 1971

Isacks, B., Cardwell, K.R., Chatelain, J.-L., Barazangi, M., Martelot, J.-M., Chinn, D., Louat, R.: Seismicity and tectonics of the central New Hebrides island arc. In: Earthquake Prediction, D.W. Simpson and P.G. Richards, eds. Washington: Am. Geophys. Union 1981

Isacks, B., Sykes, L.R., Oliver, J.: Focal mechanisms of deep and shallow earthquakes in the Tonga-Kermadeo Region and tectonics of island arcs. Bull. Geol. Soc. Am. **80**, 1443–1470, 1969

Johnson, T., Molnar, P.: Focal mechanisms of southwest Pacific. J. Geophys. Res. **77**, 5000–5032, 1972

Kanamori, H., Given, J.W.: Use of long-period surface waves for fast determination of earthquake source parameters. Phys. Earth Planet Inter. **27**, 8–31, 1981

Katsumata, M., Sykes, L.R.: Seismicity and tectonics of the western Pacific: Izu-Mariana-Caroline and Ryukyu-Taiwan Regions. Bull. Geol. Soc. Am. **74**, 5923–5948, 1969

Knopoff, L., Randall, M.J.: The compensated linear vector dipole: a possible mechanism for earthquakes. J. Geophys. Res. **75**, 4957–4963, 1970

Langston, C.A.: Source inversion of seismic waveforms: the Koyna, India earthquake of 13 September 1967. Bull. Seism. Soc. Am. **71**, 1–24, 1981

McCowman, D.W.: Moment tensor representation of surface waves. Geophys. J. R. Astron. Soc. **44**, 595–599, 1976

Mendiguren, J.: Inversion of surface wave data in source mechanism studies. J. Geophys. Res. **82**, 889–894, 1976

Molnar, P.: Fault plane solutions of earthquakes and directions of motion in the Gulf of California Ribera fracture zone. Geol. Soc. Amer. Bull. **84**, 1651–1658, 1973

Molnar, P., Sykes, L.R.: Tectonics of the Caribbean and Middle American Regions from focal mechanism and seismicity studies. Bull. Geol. Soc Am. **88**, 1639–1684, 1969

Ritsema, A.R.: Some reliable fault plane solutions. Pure Appl. Geophys. **59**, 58–74, 1964

Ritsema, A.R.: The mechanisms of some deep and intermediate earthquakes in the region of Japan. Bull. Tokyo Univ. Earthq. Res. Inst. **43**, 39–52, 1965

Ritsema, A.R.: The fault plane solutions of earthquakes of Athe Hindu Kush centre. Tectonophys. **3**, 147–163, 1966

Sipkin, S.A.: Estimation of earthquake source parameters by inversion of waveform data: synthetic waveforms. Phys. Earth Planet. Inter. **30**, 242–259, 1982

Stauder, W.: Mechanism of the Rat Island earthquake sequence of February 4, 1965 with relation to island arcs and seafloor spreading. J. Geophys. Res. **73**, 3847–3858, 1968

Stauder, W.: Subduction of the Nazca plate under Peru as evidenced by focal mechanisms and by seismicity. J. Geophys. Res. **80**, 1053–1064, 1975

Stauder, W., Bollinger, G.A.: The focal mechanism of the Alaska earthquake of March 28., 1964 and its aftershock sequence. J. Geophys. Res. **71**, 5283–529, 1966

Strelitz, R.A.: The fate of the downgoing stab: study of the moment tensor from body waves of complex deep-focus earthquakes. Phys. Earth Planet. Inter. **21**, 83–96, 1980

Sykes, L.R.: Mechanism of earthquakes and nature of faulting on the mid-oceanic ridges. J. Geophys. Res. **72**, 2131 ff, 1967

Ward, S.N.: Body wave calculations using moment tensor sources in spherically symmetric, inhomogenious media. Geophys. J. R. Astron. Soc. **60**, 53–66, 1980

Received July 11, 1985; revised version December 16, 1985
Accepted December 18, 1985

J Geophys (1986) 59:119–128

Journal of Geophysics

A teleseismic study of the Upper Rhinegraben area: array mislocation diagram and 3-D velocity inversion

M. Granet

Institut de Physique du Globe de Strasbourg, 5, Rue René Descartes, F-67084 Strasbourg Cédex, France

Abstract. *P* arrival times of 119 teleseismic events recorded on 14 local short-period stations are used to investigate the Upper Rhinegraben structure. An analysis of an array mislocation diagram is first performed. It reveals a slow direction for waves coming from N340E and it shows the major influence of the stations located on the graben on the azimuth anomaly pattern. A 3-D velocity inversion is then performed by using the ACH method (Aki et al., 1977). This inversion reveals that the northwestern part of the investigated area is slow, with increasing velocities to the south. This could be the cause for the observed mislocation pattern. The 3-D structure also presents a well-resolved velocity contrast between the graben and its adjacent areas, the main graben effect being limited to within the crust.

Key words: Upper Rhinegraben – Mislocation diagram – 3-D velocity inversion – Azimuthal anomaly – Upper mantle – Crust

Introduction

The crustal structures of the Upper Rhinegraben area and its vicinity have been studied for a long time using refraction and reflection profiles. While detailed characteristics of the crust are available (Streicher, 1974; Edel, 1975; Peterschmitt, 1979), the upper mantle has not yet been well investigated using teleseismic body waves, except in very large-scale 3-D velocity inversions (Romanowicz, 1980; Babuška et al., 1984). Recently, Raikes and Bonjer (1983) used the variation of *P*-wave travel-time residuals to compute a velocity model for the Rhenish Massif, located north of the region investigated here.

The Rhinegraben formation was formed in mid-Eocene to early Miocene times. It is likely that it took place in a region of pre-existing Hercynian zones of weakness (Illies, 1965). This is a good example of continental graben structure. Various authors agree to expect a deep cause for this geological structure: Kahle and Werner (1980), for example, suggest a deep-seated thermal anomaly underneath the Rhinegraben from gravity anomalies. In the present paper, classical seismological techniques such as slowness-azimuth calculations and 3-D velocity inversion are used in order to improve our knowledge of the Upper Rhinegraben structure.

Data

We initially selected 119 teleseismic events recorded at 14 short-period stations of the Upper Rhinegraben area (Fig. 1). The selected events are well distributed in azimuth, thus allowing a proper study of azimuthal dependence of anomalies. The epicentral distance range has been chosen between 22–95 degrees in order to eliminate the upper mantle arrivals. The aperture of the array is approximately 150 km from west to east and 200 km from south to north. We read the *P* arrival times directly from the seismograms for stations GWF, STR, WLS, ECH, BAF and ROF, and either from seismograms or bulletins for stations BUH, FEL and CDF. Only bulletin data are used for stations KRL, BFO, HBG and BSF. In order to get high-quality *P* arrival times, one fair method is to correlate the waveforms as proposed by King et al. (1973). Unfortunate-

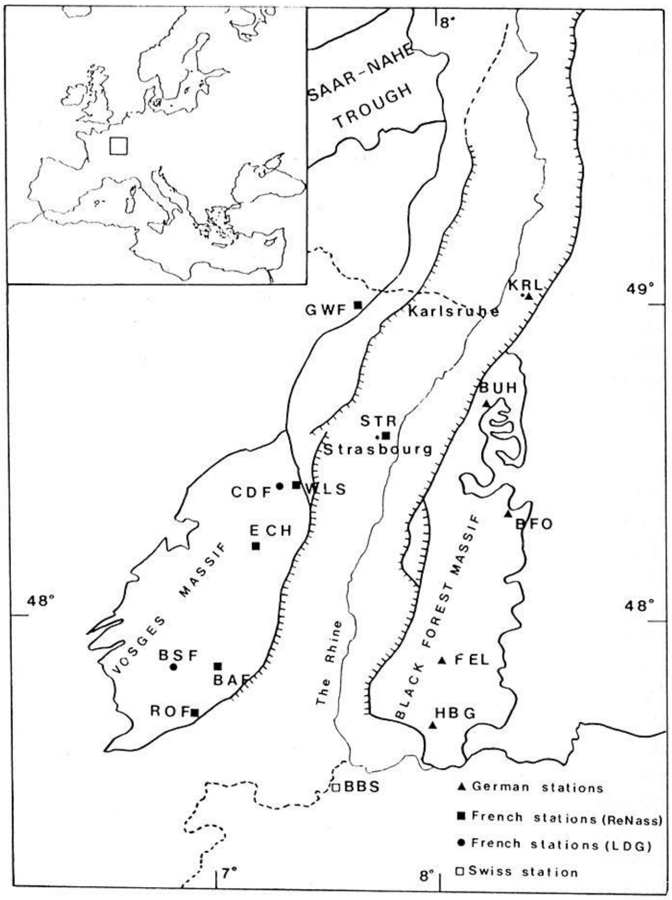

Fig. 1. A schematic map of the Rhinegraben area. The stations used in this paper are indicated

ly, because part of the data comes from bulletins in the present study, it was not possible to apply such a method. However, an "eye correlation method" was used for the data read from seismograms. The residuals were computed from the hypocentral parameters given by ISC and by using the Jeffreys-Bullen velocity model (hereafter quoted as J.B.). They were corrected for station elevation, sediment thickness and the Earth's ellipticity.

The slowness-azimuth calculation

Two classical methods permit the calculation of the slowness and azimuth parameters: a plane wavefront method and a curved wavefront method. In the case of the plane wavefront method, the observed azimuth and ray parameter are determined by fitting a plane wave to the observed *P* arrival times (Otsuka, 1966a; Herrmann, 1982). For large aperture networks, it is necessary to take into account the curvature of the Earth's surface and the curvature of the wavefront. Walck and Minster (1982) have developed an elegant method which fits a plane to the J.B. residuals of an event, thus including first-order curvature correction in the calculated $dT/d\Delta$ and azimuth values.

The plane and curved wavefront methods were compared on a subset of data. For this test, we kept only those events for which at least two *P* arrival times are available for the Vosges massif and the Black Forest massif. We also eliminated data with *P* residuals greater than 2 s. From the former 119 selected events, 69 were used for this test.

The mislocation diagram

Slowness-azimuth calculations are presented in the form of an "array mislocation diagram" (Burdick and Powell, 1980; Briden et al., 1982). Such a diagram is a polar plot of $dT/d\Delta$ versus azimuth; usually, each event is represented by a vector whose tail gives the azimuth and slowness observed on the array and the head gives the azimuth and slowness predicted from the ISC location and J.B. tables.

Figure 2 shows the array mislocation diagram in the case of the Walck and Minster method. The thick vector plotted in the centre of the diagram is the mean mislocation vector oriented in the N333E direction. Its amplitude is 0.45 s/degree.

The same pattern of the mislocation diagram was observed in the case of a plane wavefront from the test described above. The absence of significant discrepancies between the two methods is due to the small aperture of the array with regard to the large epicentral distances. Although the curved wavefront method does not yield significantly different results, we have used it in the later parts of this paper.

Array mislocation diagrams are generally interpreted in terms of receiver structure having a dipping interface with constant velocity contrast or by lateral velocity contrast: arrows point in the downdip direction of the interface or in the direction of slower velocity (Briden et al., 1982; Walck and Minster, 1982). No such effect is clearly observed in Fig. 2, even if there is some coherent direction marked by the thick mean vector. In order to get more detailed information from this array mislocation diagram, the slowness anomaly and the azimuth anomaly are studied below.

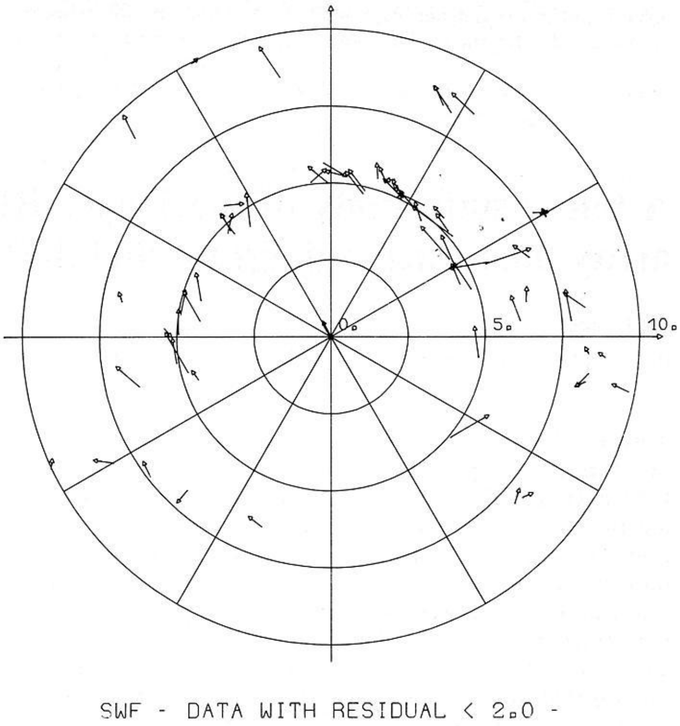

Fig. 2. The array mislocation diagram deduced from the Walck and Minster method. *Circles* are drawn for $dT/d\Delta = 2.5$, 5, 7.5 and 10 s/degree. The *thick vector* plotted on the centre is the mean mislocation vector. Each event is represented by a vector whose tail gives the azimuth and slowness observed on the array, and the head gives the azimuth and slowness predicted from the ISC location and J.B. tables

The slowness anomaly

Following Otsuka (1966a), the slowness anomaly is defined as the difference between the $dT/d\Delta$ observed on the array and the $dT/d\Delta$ estimated from the ISC location and J.B. tables (Fig. 3a). A large scatter is apparent and no significant slowness anomaly pattern can be derived from these data. Note the rather large standard errors obtained from the covariance matrix. Furthermore, due to this scatter, no coherent azimuthal variation of the slowness anomaly function can be obtained.

The azimuth anomaly

The azimuth anomaly is the difference between the observed azimuth deduced from the array and the azimuth estimated from the ISC location and J.B. tables (Fig. 3b). One feature is the cyclic pattern shown by the smoothed anomaly function. The maxima occur for waves propagating close to the N65E and N275E directions. From similar observations, Otsuka (1966b) and Niazi (1966) suggest that a dipping interface may constitute a plausible reason for such a trend. Furthermore, Otsuka (1966b) demonstrates that directions for which the azimuth anomaly is null correspond to the dip discontinuity with an ambiguity of 180 degrees. Changes of sign of the smoothed function at approximately N190E and N340E may be clearly noticed (Fig. 3b).

Taking the Moho discontinuity as the dipping interface, one can easily compute the theoretical azimuth anomalies from both a N190E and a N340E dipping interface (Niazi,

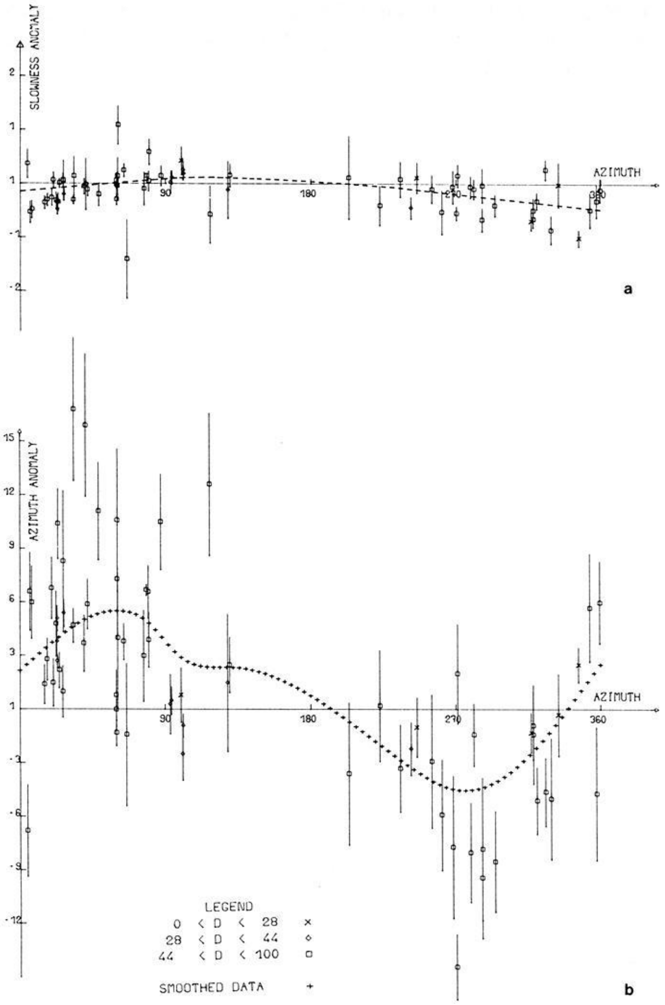

Fig. 3. a Slowness anomaly and its standard errors plotted versus great circle azimuth. The smoothed function (symbol −) is obtained from a square spline function. **b** Azimuth anomaly and its standard errors plotted versus great circle azimuth. No major influence of the epicentral distance is observed on the azimuth anomaly pattern. The smoothed function (symbol +) is obtained from a square spline function

1966). However, in order to explain the large amplitudes observed (up to +15 degrees and down to −15 degrees), one has to expect a dip value as high as 10 degrees. This seems too large with respect to the aperture of the array: a 10-degree dip value leads to an increase in the Moho depth of about 20 km beneath the array. This is too much if we consider the previously published contour map of the crust/mantle boundary in the Rhinegraben area (Fig. 4). An interesting question is to know if a multiple dipping layer zone could explain the large amplitudes observed with a smaller overall slope. Following Otsuka (1966b), we have computed the theoretical azimuth anomalies due to a set of parallel dipping layers having a plausible dip angle of 2.5 degrees instead of 10 degrees, with velocities varying from 6.1 to 8.1 km/s. The maximum azimuth anomaly thus obtained is 2.4 degrees, which is far too small to explain the observed azimuth anomaly.

In order to look for another explanation of the observed azimuth anomaly, we tested the reliability of its cyclic pattern. To do that, the two graben stations STR and KRL, which could present an anomalous behaviour, were eliminated from the data set (Fig. 5). As in the case shown in Fig. 3b, the computation was performed only if at least two *P* onsets were available for the Vosges massif and the Black Forest massif. This leads to a subset of 68 events. The cyclic trend in Fig. 3b is no longer observed. Because azimuth and slowness are obtained by a method which fits

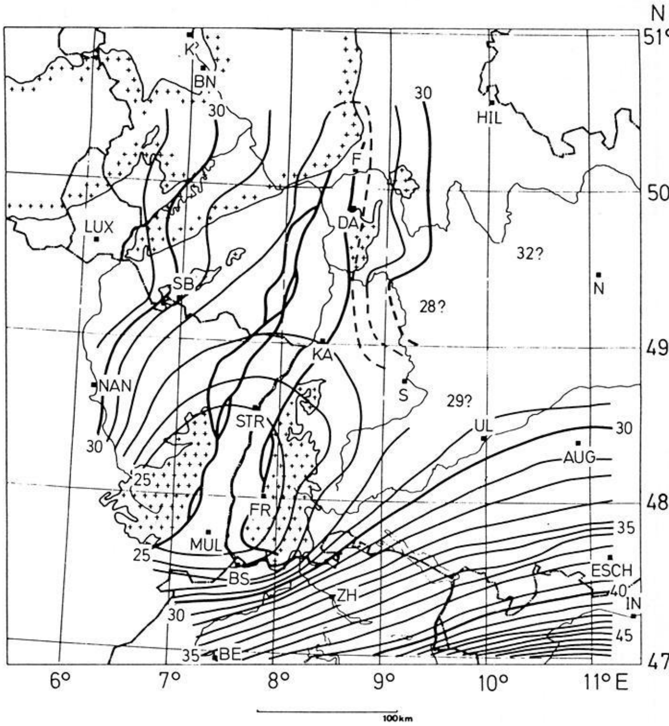

Fig. 4. Contour map of the crust/mantle boundary in the Rhinegraben area. Depths are in km (Kahle and Werner, 1980)

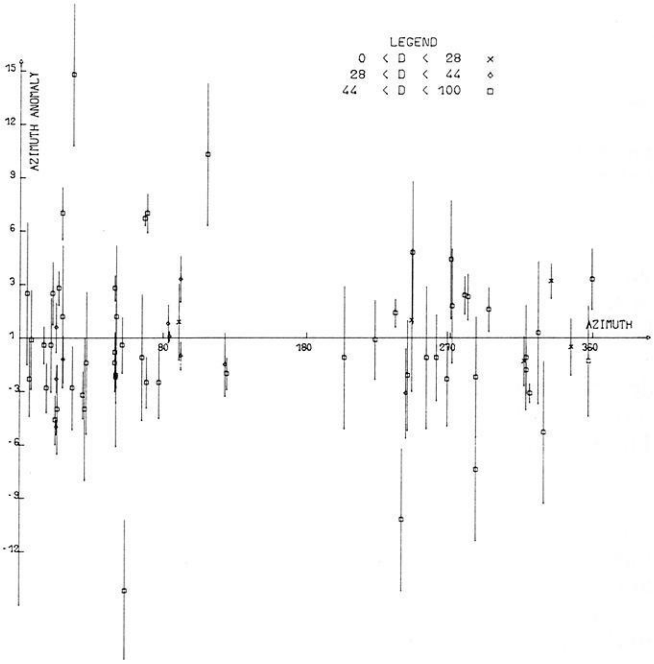

Fig. 5. Azimuth anomaly and its standard errors computed after eliminating the *P* arrival times of the two graben stations STR and KRL from the data

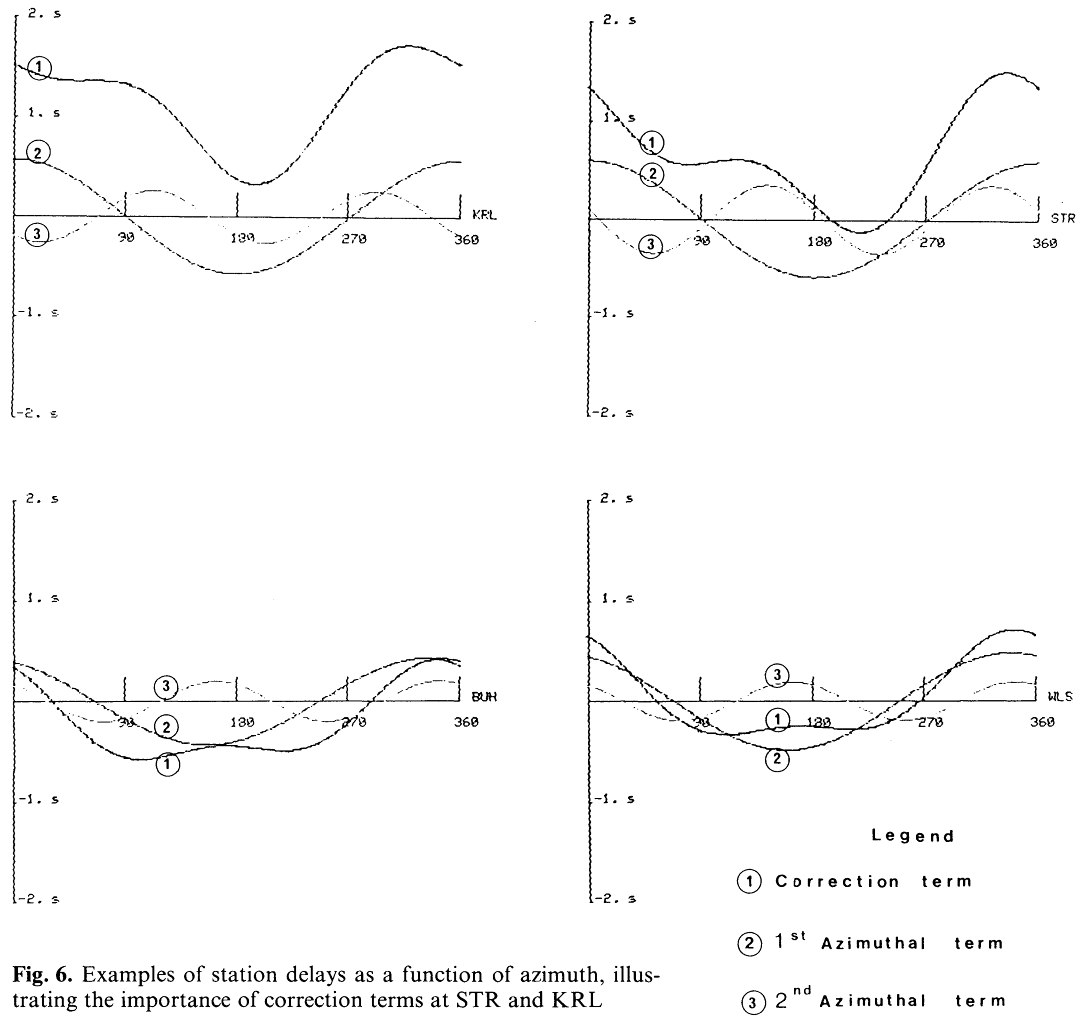

Fig. 6. Examples of station delays as a function of azimuth, illustrating the importance of correction terms at STR and KRL

the residuals, one can expect that large azimuthal variations of the static delays at these stations might be responsible for such a behaviour.

In order to check this point, let us look at the static delays computed with a large set of data for some of the stations used here by Dziewonski and Anderson (1983). These authors gave a correction term of the form:

$$\delta t = A_0 + A_1 \cos(\xi - E_1) + A_2 \cos 2(\xi - E_2)$$

where ξ is the azimuth of the P-wave arrival, A_n are constant coefficients and E_1, E_2 correspond to the slow directions.

The correction term is shown in Fig. 6 for stations KRL, BUH, STR and WLS. The most striking feature of this figure is the apparent similarity of shape for KRL and STR on the one hand and for stations outside the graben, BUH and WLS, on the other: in this latter case, the δt functions exhibit no internal differences. Furthermore, the general pattern of the correction terms is mostly dependent on the first azimuthal term $A_1 \cos(\xi - E_1)$ when considering the whole set of stations. This is confirmed by the ratio A_1/A_2 which clearly demonstrates the major role of the first term (Table 1).

Following Dziewonski and Anderson (1983), one can thus expect a major slow direction in the studied area as inferred from the coherent values of E_1. This direction is oriented to the north inside the graben and near N340E outside the graben area.

Table 1. The correction term parameters of the Rhinegraben area stations analysed by Dziewonski and Anderson (1983). The correction term has the form:
$\delta t = A_0 + A_1 \cos(\xi - E_1) + A_2 \cos 2(\xi - E_2)$
where ξ is the azimuth of the P-wave arrival

	A_0 (s)	A_1 (s)	E_1 (deg)	A_2 (s)	E_2 (deg)	A_1/A_2
KRL	1.12	0.57	1	0.26	113	2.19
STR	0.65	0.59	1	0.35	143	1.69
BUH	−0.22	0.43	337	0.20	164	2.15
CDF	−0.03	0.32	342	0.14	15	2.29
BAF	−0.25	0.42	322	0.17	162	2.47
BSF	−0.11	0.22	338	0.14	2	1.57
WLS	0.04	0.48	340	0.19	164	2.53

One can notice the difference in the correction term between the stations in the massifs and those located in the graben (Fig. 6). The peak-to-peak amplitude is larger for KRL and STR (1.4 and 1.6 s respectively) than for BUH and WLS (0.95 and 1.05 s). Such differences clearly explain the major influence of the graben stations on the azimuthal anomaly pattern. Indeed, according to the geometry of the array, a large residuals anomaly varying with azimuth for the two graben stations can explain the azimuthal pattern observed (Fig. 3b). Note that these differences are partly caused by the combined effect of the two azimuthal terms near N180E for STR and KRL, while this is not the case for the stations located in the massifs. We suggest that this shift of the second azimuthal term could be due to different structural preferential orientation beneath the graben (a Rhenish orientation) and beneath the massifs (a Variscan orientation).

This example shows that it is very difficult to get clear information from the pattern of mislocation diagrams. In order to better understand the cause of the observed anomaly and to get some constraints on the Upper Rhinegraben structure, we have performed a 3-D velocity inversion of the *P* residual data.

The 3-D velocity inversion

The residual analysis of propagation travel-time is a classical method to study the velocity distribution in the crust and the upper mantle. Numerous studies have already been performed, in particular in Europe, on such a topic. Poupinet (1977), Romanowicz (1980) and Babuška et al. (1984) analysed the *P* residuals with respect to the Jeffreys-Bullen (1948) or Herrin (1968) *P*-wave velocity models. However, such studies were conducted on a very large scale and no detailed information was obtained concerning the Upper Rhinegraben area. Velocity models might be deduced from the slowness anomaly but, due to large scatter in these vectors, we have preferred to apply a 3-D inversion technique directly to the residuals. In order to perform a successful recovery of the laterally varying structure from the data, we used the azimuthally well-distributed set of 119 teleseismic events selected in the first part. The *P* arrival times at station HAU were added to the data used in the previous section (Fig. 7). We used 991 *P*-wave readings, corresponding to 119 events, to perform the 3-D velocity inversion.

Description of the method

We used a program based on the original technique developed by Aki et al. (1977) in the damped least-squares formulation, referred to below as the ACH method. The structure beneath the array is modelled by a set of plane layers divided into blocks characterized by a constant velocity. The Earth outside this region is considered to have a known velocity structure.

Different sources of error have to be considered in the ACH method:

1) the plane wave approximation
2) the simplified block sampling (the ray path is assigned to the block in which it spends its maximum time)
3) the fact that the lateral refraction at the vertical and horizontal block boundaries caused by the linearisation is omitted

The first approximation causes no difficulties in our case due to the small aperture of the array and the limited depth investigated (220 km). Approximations (2) and (3) have to be examined more closely: high contrast of lateral velocity anomalies can be underestimated due to these approximations (Koch, 1985). Using a newly developed 3-D ray tracing program in block geometry Koch (1985) showed, however, that approximation (2) does not cause a significant degradation of the solution. Moreover, one can expect in such an approximation that we smooth out the artificial vertical boundaries of blocks in the case of

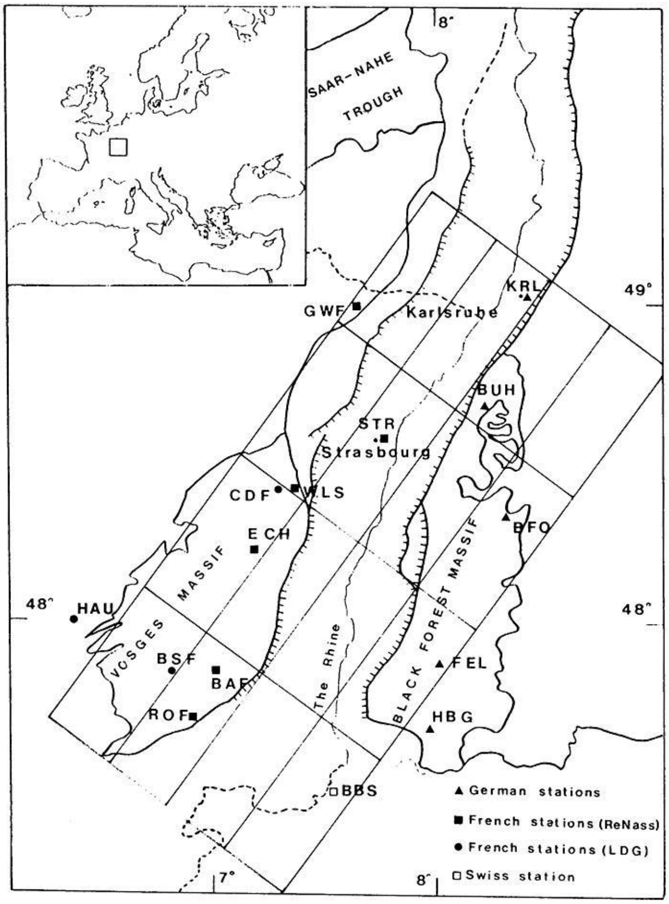

Fig. 7. The block configuration used for the 3-D velocity inversion. The blocks are numbered from left to right in each row, from north to south in each layer and from the top layer to the bottom layer. Model centre: latitude 48.25 N, longitude 7.65 E. Rotation angle: −35.0°

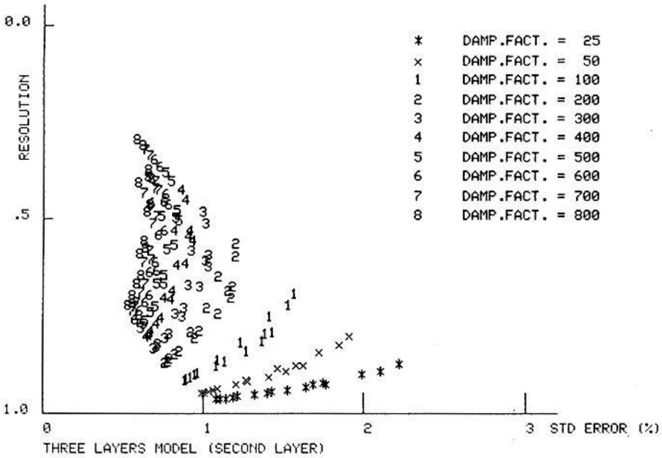

Fig. 8. The "trade-off" between resolution and standard errors computed for the second layer of the three-plane-layer model. Similar diagrams were obtained in the case of the four-plane-layer model

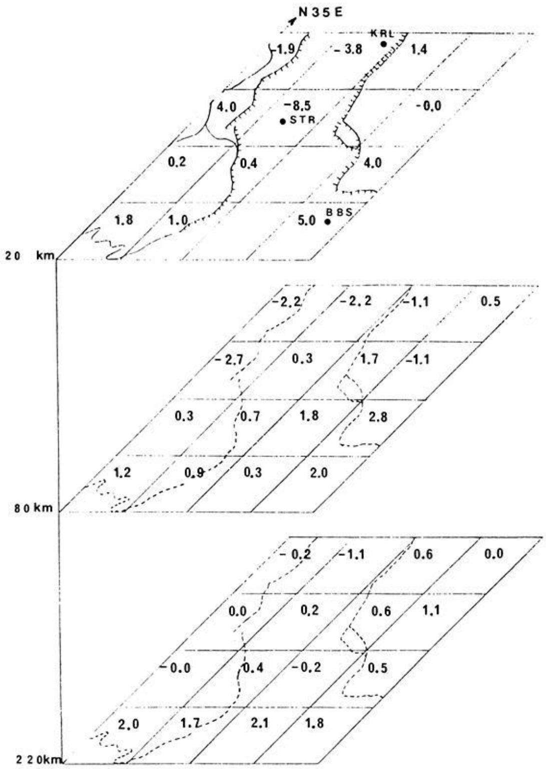

Fig. 9. Three-layer model obtained by 3-D inversion of teleseismic *P* residuals. The velocity perturbations are expressed in percent with respect to the initial model: a positive change indicates higher velocity and a negative change lower velocity

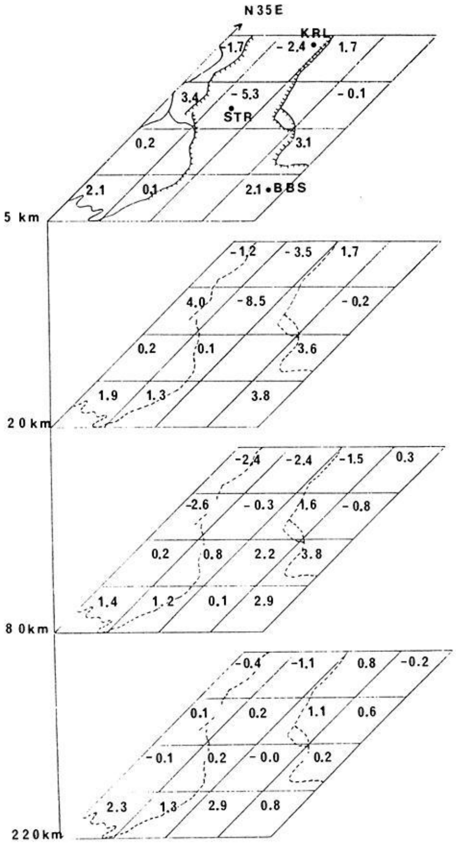

Fig. 10. Same as Fig. 9, but for the case of the four-layer model

Table 2. Observational matrix, diagonal term of the resolution matrix and standard errors in the layer block format for the case of three plane layers. The observational matrix gives the number of intersecting rays in each block. The standard errors are expressed in percent

Initial model

Layer	*P*-Velocity (km/s)	Thickness (km)	Block size (km × km)
1	6.1	20	55 × 25
2	8.1	60	55 × 25
3	7.9	140	55 × 25

Observational matrix

36	20	112	0
143	96	3	23
227	30	0	54
113	79	0	22
41	81	100	45
149	162	63	42
193	124	76	60
151	165	37	26
87	58	65	83
142	91	76	78
100	86	77	69
56	14	16	15

Diagonal term of the resolution matrix

0.299	0.311	0.552	
0.561	0.600		0.360
0.597	0.212		0.424
0.581	0.661		0.349
0.680	0.763	0.754	0.617
0.840	0.817	0.632	0.493
0.845	0.807	0.683	0.590
0.832	0.741	0.602	0.522
0.919	0.895	0.875	0.882
0.947	0.941	0.883	0.901
0.948	0.946	0.897	0.880
0.795	0.754	0.648	0.566

Standard errors

0.85	0.97	0.86	
0.95	0.91		0.94
0.95	0.83		0.92
0.96	0.85		0.94
0.88	0.84	0.79	0.98
0.68	0.73	1.00	0.96
0.66	0.75	0.94	0.89
0.69	0.85	1.00	0.98
0.57	0.64	0.68	0.67
0.46	0.49	0.67	0.61
0.46	0.46	0.64	0.66
0.84	0.91	0.99	1.04

Table 3. Same as Table 2, but for the case of four plane layers

Initial model

Layer	*P*-Velocity (km/s)	Thickness (km)	Block size (km × km)
1	4.0	5	55 × 25
2	6.1	15	55 × 25
3	8.1	60	55 × 25
4	7.9	140	55 × 25

Observational matrix

36	16	109	0
98	74	0	23
209	0	0	53
113	157	0	22
35	20	112	0
140	91	2	23
169	30	0	54
90	178	0	22
40	83	108	44
151	163	63	43
193	120	76	59
150	171	37	27
86	59	65	79
142	94	77	79
98	89	77	70
60	16	17	15

Diagonal term of the resolution matrix

0.097	0.057	0.117	
0.225	0.115		0.062
0.283			0.151
0.215	0.191		0.062
0.162	0.187	0.354	
0.412	0.420		0.213
0.378	0.137		0.218
0.337	0.439		0.202
0.695	0.755	0.769	0.611
0.846	0.818	0.630	0.478
0.854	0.811	0.680	0.621
0.840	0.758	0.582	0.556
0.921	0.898	0.883	0.877
0.948	0.943	0.865	0.902
0.951	0.949	0.898	0.876
0.796	0.762	0.652	0.568

Standard errors

0.56	0.45	0.45	
0.80	0.50		0.41
0.79			0.65
0.71	0.63		0.42
0.65	0.80	0.77	
0.89	0.85		0.77
0.88	0.70		0.71
0.83	0.81		0.76
0.89	0.86	0.78	1.00
0.66	0.73	1.01	0.98
0.64	0.76	0.96	0.89
0.67	0.82	1.01	0.99
0.57	0.64	0.66	0.68
0.46	0.49	0.71	0.61
0.45	0.46	0.64	0.68
0.85	0.91	1.00	1.05

a good azimuthal distribution of events (Ellsworth and Koyanagi, 1977; Romanowicz, 1979). As for approximation (3), Koch (1985) demonstrates that it is necessary to perform a nonlinear inversion, especially if high-quality arrival-time data are available. In this paper, the ACH method is strictly applied and approximation (3) was made.

The choice of the size of the blocks is also important in such a method: large block dimensions can link, in the same block, stations with different mean travel-time residuals reflecting, for example, major differences in the crust. After several trials, we selected a 4 × 4 block configuration, oriented N35E (Fig. 7), with a north extension of 220 km and an east extension of 100 km. Using this block configuration, the possible influence of the graben can be put in evidence. The Rhinegraben is represented by a model made of three–four layers with boundaries at depths of 20, 80 and 220 km (or 5, 20, 80 and 220 km). Their respective average velocities are 6.1, 8.1 and 7.9 km/s (or 4.0, 6.1, 8.1 and 7.9 km/s). The region is divided into rectangular blocks of 55 km × 25 km.

The damping parameter Θ has to be selected carefully when running the inversion. Ellsworth and Koyanagi (1977) suggest a Θ value:

$$\Theta = \frac{\sigma_d^2}{\sigma_m^2}$$

where σ_d is the standard error of the data and σ_m the root mean square velocity fluctuation of the actual model. Note that in this damped least-squares formulation, the contribution of eigenvectors with eigenvalues smaller than Θ is smoothed out. The difficulty is to find a compromise between the velocity perturbation, the resolution and the standard error. If the damping parameter is too large, the resolution becomes poor. On the other hand, if the damping parameter is too small, the solution becomes unstable with large velocity fluctuations and unacceptable standard errors due to the small eigenvalues.

We performed a set of calculations to test the smoothing effect in the stochastic inversion, with a damping factor varying from 25 to 800. Figure 8 shows the "trade-off" diagram obtained in the case of the three-layer model for the second layer. On such a diagram, we plot the diagonal term of the resolution matrix versus the standard errors. Similar diagrams were obtained for other layers or individual parameters. This diagram clearly illustrates the difficulty of how to select a Θ value. A damping factor of 300 has been chosen. It gives acceptable standard errors less than 1% with a rather good resolution (greater than 0.5).

Results and discussion

In the ACH method, only relative velocity fluctuations were obtained in each block. Results obtained for the models made of three and four plane layers, are shown in Figs. 9 and 10, respectively. Only blocks with a minimum number of ten intersecting rays are taken into account when running the inversion. The observational matrices are listed in Tables 2 and 3.

Because the station configuration is not the same for all the events, the mean travel-time residual for a given event can be influenced by the presence or the absence of anomalous stations. In order to test a possible scattering in the model due to such an influence, we performed another 3-D inversion where, for each event, the delays at a reference station were subtracted from the delays at the other stations. Following Raikes and Bonjer (1983), station BUH was selected. Doing that, we used 921 *P*-wave readings corresponding to 109 events. Because the same pattern of the velocity perturbations was obtained for our block configuration, the normal mean residual normalisation of the ACH method was finally used.

Let us now consider the results in the case of three plane layers (Fig. 9). The data variance reduction is 28%. One important result is the good discrimination between higher and lower velocity zones in the first layer. This is particularly true for blocks 1, 2 and 6 with negative velocity fluctuations of -1.9%, -3.8% and -8.5% and blocks 5, 12 and 16 with positive velocity fluctuations of 4.0%, 4.0% and 5.0%. The diagonal term of the resolution matrix is always greater than 0.5 in the bottom layers, greater than 0.5 in the first layer for blocks 3, 5, 6, 9, 13, 14 and less than 0.5 for the others (Table 2). Note that the standard errors are less than 1%.

In order to check the reliability of these high perturbations and the possible coupling between blocks, let us consider the resolution curves obtained for the blocks of the first layer (Fig. 11). The resolution curves, which are the rows of the resolution matrix, provide a measure of non-uniqueness. One can see that there is no major coupling between the parameters except a large one between vertical layers for blocks 1 and 17. We also present in Fig. 11 typical resolution curves for blocks situated in layers 2 and 3. Inspection of these curves computed for the other blocks situated in layers 2 and 3 also shows that the resolution is of high quality in these two layers.

On the other hand, one can speculate that the great amplitudes observed beneath stations KRL (block 2) and STR (block 6) could be produced by sedimentary layers. This is very unlikely because sediment corrections obtained from the crust model proposed by Streicher (1974) and Edel (1975) from seismic profiles with a mean sediment velocity of 3.6 km/s were applied to the data. Without these sediment thickness corrections, the velocity perturbations reached -7.4% (KRL) and -15.2% (STR) in the first layer.

Our results underline the presence of the graben in the northern part of the investigated area whose influence seems limited to the upper 20-km-thick layer with slow velocities, while adjacent zones corresponding to the Vosges and the Black Forest massifs exhibit higher velocities. This is consistent with the model proposed by Raikes and Bonjer (1983) which shows high velocities beneath the Vosges and the Black Forest massifs. No such influence is evident in the southern part, due to the lack of stations located in the graben in this region. However, block 16 situated beneath station BBS at the boundaries is rather fast. This could indicate an increasing velocity from north to south. Note that most of the velocity fluctuations are limited to the crust. The second and third layers exhibit smaller velocity perturbations. One can notice, too, that the blocks located beneath the Black Forest massif exhibit higher velocities than those located beneath the Vosges massif. We can conclude that no major influence of the graben is observed on the velocity structure of the upper mantle at the horizontal scale investigated here.

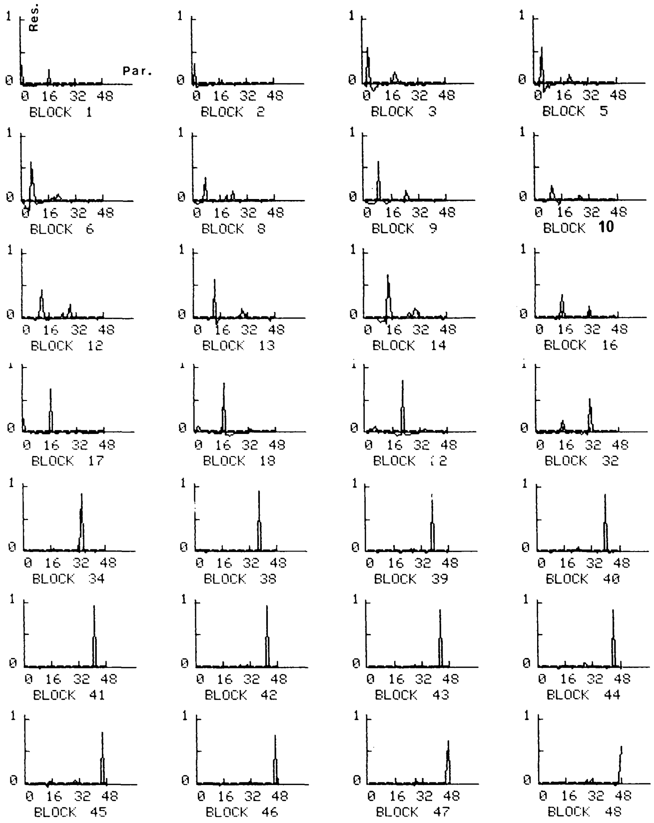

Fig. 11. The resolution curves computed in the case of the three-plane-layer model with a damping parameter $\Theta = 300$. All the curves obtained for the blocks situated in the first layer are shown. We give, in addition, some typical curves of the second and third layers. Blocks 18 and 34 are situated beneath KRL, blocks 22 and 38 beneath STR, blocks 32 and 48 beneath BBS

Figure 10 gives the results obtained in the same block configuration and a four-layer model. The data variance reduction increases to 32%. However, the teleseismic rays cannot resolve well the two upper layers. This is shown in Fig. 12 where the resolution curves computed for layers 1 and 2 are plotted. In deeper layers, the same features appear in the three- and four-layer models. In particular, one can notice a persistent and stable rather large positive velocity perturbation in the 20- to 80-km depth range beneath the southern part of the Black Forest. As already mentioned, the upper mantle structure deduced from this 3-D velocity inversion is more homogenous than the crustal structure

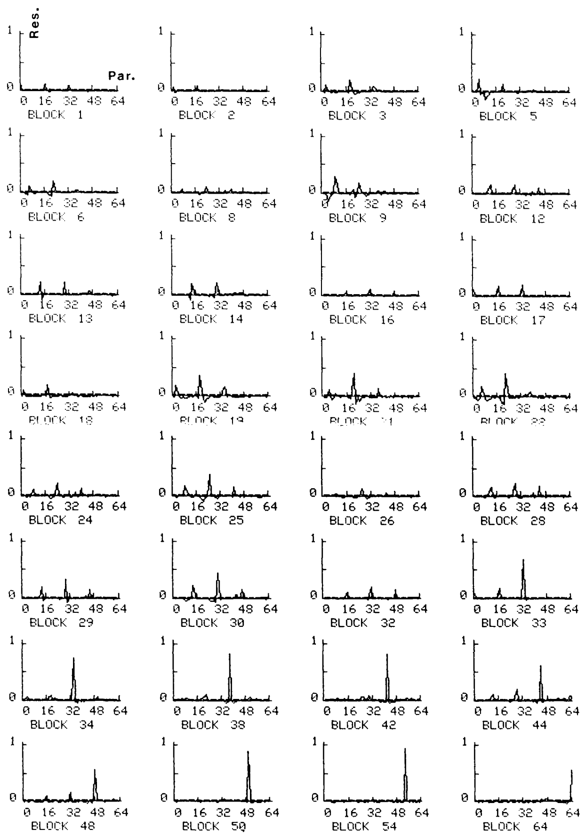

Fig. 12. Same as Fig. 11, but for the case of the four-plane-layer model. All the resolution curves of the blocks situated in the first and second layers are shown. Blocks 2, 18, 34 and 50 are situated beneath KRL, blocks 6, 22, 38 and 54 beneath STR, blocks 16, 32, 48 and 64 beneath BBS

and is not correlated with the graben geometry. Note also that the general pattern of the upper mantle velocity model inferred from the 3-D inversion is consistent with the inferences we have made in the first section: a slow direction toward the north for *P* arrivals. The blocks located in the north have rather negative velocity perturbations, while the blocks located in the south have rather positive ones.

Conclusion

The Rhinegraben area has been studied from the double point of view of mislocation diagram and 3-D velocity inversion. The mislocation vectors are dispersed and no clear and coherent direction appears at first sight in their pattern. The azimuth anomaly deduced from this array mislocation diagram exhibits, however, clear indication of a sign change near N190E and N340E directions. This can be interpreted by large azimuthal effects at stations KRL and STR located in the graben and by a significant slow direction oriented N340E, affecting the whole area.

The inversion reveals the differences between the graben and its adjacent zones in the upper 20-km layer and the northern part of the investigated area. Relatively small velocity fluctuations are observed below the Moho and are not correlated to the graben geometry. This could indicate that there is no major influence of the graben on the upper part of the mantle. The 3-D velocity inversion pattern is also in good agreement with the slow direction inferred from the azimuth anomaly and from the correction terms of the stations. More homogenous and precise *P*-wave readings from a larger set of well-distributed stations in the Rhinegraben area must be used for a more detailed investigation of the structure.

Acknowledgements. I thank M. Cara and P. Hoang Trong for their helpful comments. Discussion with H. Haessler and J.B. Edel has been very useful in developing some of the ideas contained in this paper. I am indebted to K.P. Bonjer and U. Achauer for providing the list of *P*-wave readings at stations HBG, BFO, BUH and FEL. I also thank two anonymous reviewers for their comments and criticisms which were helpful in improving the paper substantially.

References

Aki, K., Christoffersson, A., Husebye, E.S.: Determination of the three-dimensional seismic structure of the lithosphere. J. Geophys. Res. **82**, 277–296, 1977

Babuška, V., Plomerová, J., Šilený, J.: Spatial variations of *P* residuals and deep structure of the European lithosphere. Geophys. J. R. Astron. Soc. **79**, 363–383, 1984

Briden, J.C., Mereu, R.F., Whitcombe, D.N.: A teleseismic study of the West African margin in Senegal: *P*-wave slowness and azimuth anomalies. Geophys. J. R. Astron. Soc. **71**, 793–808, 1982

Burdick, L.J., Powell, C.: Apparent velocity measurements for the lower mantle from a wide aperture array. J. Geophys. Res. **85**, 3845–3856, 1980

Dziewonski, A.M., Anderson, D.L.: Travel times and station corrections for *P* waves at teleseismic distances. J. Geophys. Res. **88**, 3295–3314, 1983

Edel, J.B.: Structure de la croûte terrestre sous le fossé Rhénan et ses bordures. Thèse de Doctorat d'Ingénieur, Université Louis Pasteur, Strasbourg, 1975

Ellsworth, W.L., Koyanagi, R.Y.: Three-dimensional crust and mantle structure of Kilauea Volcano, Hawaii. J. Geophys. Res. **82**, 5379–5394, 1977

Herrin, E.: 1968 Seismological Tables for *P*-waves. Bull. Seismol. Soc. Am. **58**, 1193–1241, 1968

Herrmann, R.B.: Digital processing of regional network data. Bull. Seismol. Soc. Am. **72**, S261–S276, 1982

Illies, H.: Bauplan und Baugeschichte des Oberrheingrabens. Oberrh. Geol. Abh. **14**, 1–54, 1965

Jeffreys, H., Bullen, K.E.: Seismological Tables. British Association for the Advancement of Science, London, 1948

Kahle, H.G., Werner, D.: A geophysical study of the Rhinegraben-II. Gravity anomalies and geothermal implications. Geophys. J. R. Astron. Soc. **62**, 631–647, 1980

King, D.W., Mereu, R.F., Muirhead, K.J.: The measurement of apparent velocity and azimuth using adaptive processing techniques on data from the Warramunga seismic array. Geophys. J. R. Astron. Soc. **35**, 137–167, 1973

Koch, M.: A numerical study on the determination of the 3-D structure of the lithosphere by linear and non-linear inversion of teleseismic travel times. Geophys. J. R. Astron. Soc. **80**, 73–93, 1985

Niazi, M.: Corrections to apparent azimuths and travel time gradients for a dipping Mohorovicic discontinuity. Bull. Seismol. Soc. Am. **56**, 491–509, 1966

Otsuka, M.: Azimuth and slowness anomalies of seismic waves measured on the central California seismographic array. Part I. Observations. Bull. Seismol. Soc. Am. **56**, 223–239, 1966a

Otsuka, M.: Azimuth and slowness anomalies of seismic waves measured on the central California seismographic array. Part II. Interpretation. Bull. Seismol. Soc. Am. **56**, 655–675, 1966b

Peterschmitt, E.: Modèles de structure de l'écorce terrestre en Europe occidentale d'après les résultats des sondages sismiques profonds et les données des séismes naturels. Thèse de Doctorat d'Etat, Université Louis Pasteur, Strasbourg, 1979

Poupinet, G.: Hétérogénéités du manteau terrestre déduites de la propagation des ondes de volume – implications géodynamiques. Thèse de Doctorat d'Etat, Université de Grenoble, 1977

Raikes, S., Bonjer, K.P.: Large-scale mantle heterogeneity beneath the Rhenish Massif and its vicinity from teleseismic *P*-residuals measurements. In: Plateau Uplift – The Rhenish Massif, a case history, Fuchs, K., von Gehlen, K., Malzer, H., Murawski, H., Semmel, A. eds., pp. 315–331. Berlin, Heidelberg, New York: Springer 1983

Romanowicz, B.: Ondes de volume et structure tridimensionnelle du manteau supérieur: le cas des Etats-Unis d'Amérique. Thèse de Doctorat d'Etat, Université de Paris VI, Paris, 1979

Romanowicz, B.: A study of large-scale lateral variations of *P* velocity in the upper mantle beneath Western Europe. Geophys. J. R. Astron. Soc. **63**, 217–232, 1980

Streicher, P.: L'influence du remplissage sédimentaire sur la propagation des ondes sismiques dans le fossé Rhénan. Diplôme d'Ingénieur Géophysicien, Université Louis Pasteur, Strasbourg, 1974

Walck, M.C., Minster, J.B.: Relative array analysis of upper mantle lateral velocity fluctuations in Southern California. J. Geophys. Res. **87**, 1757–1772, 1982

Received July 2, 1985; revised version February 4, 1986
Accepted February 5, 1986

J Geophys (1986) 59:129–139

Journal of Geophysics

Interactive high-resolution polarization analysis of broad-band seismograms

A. Plešinger [1], M. Hellweg [2] and D. Seidl [3]

[1] Geophysical Institute, Czechoslovakian Academy of Sciences, 14131 Praha 4, Czechoslovakia
[2] Institut für Meteorologie und Geophysik, Feldbergstr. 47, D-6000 Frankfurt/M., Federal Republic of Germany
[3] Seismologisches Zentralobservatorium Gräfenberg, Krankenhausstr. 1, D-8520 Erlangen, Federal Republic of Germany

Abstract. In the laterally heterogeneous and anisotropic earth the particle motions of seismic waves are three-dimensionally polarized. This paper presents a method for determining a local wave coordinate system using the zeros of some component operators in rotated systems. It is applicable to broad-band composite waveforms and offers higher precision and resolution for the determination of azimuth and incidence angle than the usual least-squares techniques. The algorithms have been implemented in an interactive program for preprocessing three-component digital recordings. In addition, the program allows the use of particle motion diagrams and component products for the determination of wave types, onset times and pulse durations. Its performance is demonstrated on regional and teleseismic events recorded at the European broad-band stations GRF (Gräfenberg, West Germany), KHC (Kăsperské Hory, Czechoslovakia) and KSP (Ksiaz, Poland).

Key words: Broad-band seismology – Polarization analysis – Azimuth and incidence angle – Particle motion – Component products

Introduction

The seismic wave field is a superposition of many overlapping wave groups: direct, reflected, refracted, converted and scattered body and surface waves. At any point in the earth each wave group has its own shape, velocity and direction. Broad-band stations record the complex local wave field with "high fidelity" as a pronounced multi-pulse seismogram, as compared to the smooth seismograms recorded at narrow-band stations. For further analysis and interpretation, it is essential to separate and identify the various wave groups. This can best be accomplished by a transformation of the seismograms from the coordinate system of the recording seismometers to the apparent local wave coordinate systems of the different wave groups.

At any point on a seismic ray, an intrinsic coordinate system, the Frenet frame, is defined by the basis vectors $\{\mathbf{t}, \mathbf{n}, \mathbf{b}\}$ parallel to the tangent, normal and binormal, respectively (for example, see Aki and Richards, 1980). For a spherically symmetric and isotropic model earth, the tangent $\mathbf{t}$ and the normal $\mathbf{n}$ would be in the plane determined by the source, station and centre of the earth. P waves and S waves would be polarized in the $\mathbf{t}$ direction and in the $\mathbf{n}-\mathbf{b}$ plane, respectively. The Frenet frame could then be determined at a three-component point station using only the polarizations of P and S waves.

In the laterally heterogeneous and anisotropic earth, however, the particle motion of seismic waves is three-dimensionally polarized. Additional criteria are necessary to define a local wave coordinate system, which is no longer directly correlated to the Frenet frame. For narrow-band, quasi-harmonic wave groups an ellipsoidal least-squares fit can be used to determine the local wave coordinate system (for example, see Matsumura, 1981). For broad-band waveforms with arbitrary polarization, an average system can be derived for each wave group from the zeros of some component products and sums in rotated analysis systems. The orientation of the wave system for each wave group in a composite seismogram, described by its azimuth and incidence angle, is important information for the investigation of heterogeneous and anisotropic structures. Furthermore, seismograms, particle motion diagrams and component products calculated in the wave coordinate systems can be used for discrimination of wave type, and for the determination of onset time and estimation of pulse duration.

An interactive procedure for such analysis is demonstrated on regional and teleseismic events recorded at the European broad-band stations GRF (Gräfenberg, West Germany), KHC (Kašperské Hory, Czechoslovakia) and KSP (Ksiaz, Poland).

Apparent local wave coordinate system

Given the seismograms $s_Z(t)$, $s_E(t)$, $s_N(t)$ of a three-component station recording in the right-handed vertical-east-north system with the basis vectors $\{\mathbf{e}_Z, \mathbf{e}_E, \mathbf{e}_N\}$, the orientation of a local wave system with the basis vectors $\{\mathbf{e}_L, \mathbf{e}_Q, \mathbf{e}_T\}$ can be defined by two angles: a and i.

The longitudinal unit vector $\mathbf{e}_L$ (P direction) is given in the recording system by

$$\mathbf{e}_L = (\cos i, \ -\sin i \sin a, \ -\sin i \cos a). \tag{1}$$

Offprint requests to: D. Seidl

a ($0° \leqq a \leqq 360°$) is the back-azimuth (to the epicentre) of the projection of $\mathbf{e}_L$ into the horizontal plane against north and i ($0° \leqq i \leqq 90°$ for a station on the earth's surface) is the incidence angle between $\mathbf{e}_L$ and $\mathbf{e}_Z$.

The transverse unit vector $\mathbf{e}_T$ (SH direction) is given by the vector product $\mathbf{e}_L \times \mathbf{e}_Z / |\mathbf{e}_L \times \mathbf{e}_Z|$:

$$\mathbf{e}_T = (0, -\cos a, \sin a). \tag{2}$$

The transverse unit vector $\mathbf{e}_Q$ (SV direction) is determined by the vector product $\mathbf{e}_T \times \mathbf{e}_L$ so that the basis vectors $\{\mathbf{e}_L, \mathbf{e}_Q, \mathbf{e}_T\}$ form a right-handed system. Thus $\mathbf{e}_Q$ becomes

$$\mathbf{e}_Q = (\sin i, \cos i \sin a, \cos i \cos a). \tag{3}$$

The transformation relationship between the seismogram vector $\mathbf{s} = \{s_Z, s_E, s_N\}$ in the recording system and $\mathbf{u} = \{u_L, u_Q, u_T\}$ in the local ray system can be written in matrix notation as

$$\begin{pmatrix} u_L \\ u_Q \\ u_T \end{pmatrix} = \mathbf{M} \begin{pmatrix} s_Z \\ s_E \\ s_N \end{pmatrix} = \begin{pmatrix} \cos i & -\sin i \sin a & -\sin i \cos a \\ \sin i & \cos i \sin a & \cos i \cos a \\ 0 & -\cos a & \sin a \end{pmatrix} \begin{pmatrix} s_Z \\ s_E \\ s_N \end{pmatrix}. \tag{4}$$

The elements in the first, second and third line of the transformation matrix $\mathbf{M}$ are the components of the basis vectors $\{\mathbf{e}_L, \mathbf{e}_Q, \mathbf{e}_T\}$ in the recording system $\{\mathbf{e}_Z, \mathbf{e}_E, \mathbf{e}_N\}$ given in Eqs. (1) through (3).

The inverse relationship to Eq. (4) is given by

$$\begin{pmatrix} s_Z \\ s_E \\ s_N \end{pmatrix} = \mathbf{M}^T \begin{pmatrix} u_L \\ u_Q \\ u_T \end{pmatrix} = \begin{pmatrix} \cos i & \sin i & 0 \\ -\sin i \sin a & \cos i \sin a & -\cos a \\ -\sin i \cos a & \cos i \cos a & \sin a \end{pmatrix} \begin{pmatrix} u_L \\ u_Q \\ u_T \end{pmatrix} \tag{5}$$

where $\mathbf{M}^T$ is the transpose of $\mathbf{M}$.

Determination of azimuth and apparent incidence angle

For azimuth determination the seismogram vector $\mathbf{s}$ is transformed to a vector $\mathbf{v}$ in a rotated analysis system, using Eq. (4) for $i = 90°$ and variable a:

$$\begin{pmatrix} v_R \\ v_Z \\ v_T \end{pmatrix} = \begin{pmatrix} 0 & -\sin a & -\cos a \\ 1 & 0 & 0 \\ 0 & -\cos a & \sin a \end{pmatrix} \begin{pmatrix} s_Z \\ s_E \\ s_N \end{pmatrix} = \begin{pmatrix} -s_E \sin a - s_N \cos a \\ s_Z \\ -s_E \cos a + s_N \sin a \end{pmatrix}. \tag{6}$$

v_R and v_T are the radial and transverse components in the horizontal plane and v_Z is the vertical component of the seismogram vector $\mathbf{v}$ in the rotated analysis system, a is the back-azimuth of the v_R axis.

If a linearly polarized P wave $u_L(t)\,\mathbf{e}_L$ with $i = i_0$ and $a = a_0$ arrives at a seismic station, the seismogram vector $\mathbf{s}$ can be derived from Eq. (5):

$$\begin{pmatrix} s_Z \\ s_E \\ s_N \end{pmatrix} = \mathbf{M}^T \begin{pmatrix} u_L \\ 0 \\ 0 \end{pmatrix} = \begin{pmatrix} \cos i_0 \\ -\sin i_0 \sin a_0 \\ -\sin i_0 \cos a_0 \end{pmatrix} u_L. \tag{7}$$

The vector $\mathbf{v}$ calculated in Eq. (6) will then be:

$$\begin{pmatrix} v_R \\ v_Z \\ v_T \end{pmatrix} = \begin{pmatrix} \cos(a_0 - a) \sin i_0 \\ \cos i_0 \\ \sin(a_0 - a) \sin i_0 \end{pmatrix} u_L. \tag{8}$$

The component products $v_T v_Z$ and $v_R v_Z$ are then:

$$v_T v_Z = u_L^2(t) \sin(a_0 - a) \sin i_0 \cos i_0 \tag{9}$$

$$v_R v_Z = u_L^2(t) \cos(a_0 - a) \sin i_0 \cos i_0. \tag{10}$$

A SV wave $u_Q(t)\,\mathbf{e}_Q$ with $i = i_0$ and $a = a_0$ can be described using Eq. (5):

$$\begin{pmatrix} s_Z \\ s_E \\ s_N \end{pmatrix} = \mathbf{M}^T \begin{pmatrix} 0 \\ u_Q \\ 0 \end{pmatrix} = \begin{pmatrix} \sin i_0 \\ \cos i_0 \sin a_0 \\ \cos i_0 \cos a_0 \end{pmatrix} u_Q. \tag{11}$$

Inserting Eq. (11) into Eq. (6) the vector $\mathbf{v}$ will be:

$$\begin{pmatrix} v_R \\ v_Z \\ v_T \end{pmatrix} = \begin{pmatrix} -\cos(a_0 - a) \cos i_0 \\ \sin i_0 \\ -\sin(a_0 - a) \cos i_0 \end{pmatrix} u_Q. \tag{12}$$

The component products $v_T v_Z$ and $v_R v_Z$ are then given by

$$v_T v_Z = -u_Q^2(t) \sin(a_0 - a) \cos i_0 \sin i_0, \tag{13}$$

$$v_R v_Z = -u_Q^2(t) \cos(a_0 - a) \cos i_0 \sin i_0. \tag{14}$$

The product $v_T v_Z$ has a zero with regard to a at a_0 for both linearly polarized P waves and SV waves and can therefore be used as an operator for the determination of the azimuth a_0.

For a SH wave, $u_T(t)\,\mathbf{e}_T$ with $i = i_0$ and $a = a_0$, Eq. (5) gives:

$$\begin{pmatrix} s_Z \\ s_E \\ s_N \end{pmatrix} = \mathbf{M}^T \begin{pmatrix} 0 \\ 0 \\ u_T \end{pmatrix} = \begin{pmatrix} 0 \\ -\cos a_0 \\ \sin a_0 \end{pmatrix} u_T. \tag{15}$$

Inserting Eq. (15) into Eq. (6) it follows for the vector $\mathbf{v}$:

$$\begin{pmatrix} v_R \\ v_Z \\ v_T \end{pmatrix} = \begin{pmatrix} -\sin(a_0 - a) \\ 0 \\ \cos(a_0 - a) \end{pmatrix} u_T. \tag{16}$$

The component products $v_T v_Z$ and $v_R v_Z$ are given by

$$v_T v_Z = 0, \tag{17}$$

$$v_R v_Z = 0. \tag{18}$$

For a sinusoidal Rayleigh-wave $(\varepsilon_0 \cos\omega t,\ \varepsilon_0 \sin\omega t, 0)$ with surface ellipticity ε_0 (ratio of horizontal to vertical amplitudes) and back-azimuth a_0, Eq. (5) gives, with $i_0 = 90°$:

$$\begin{pmatrix} s_Z \\ s_E \\ s_N \end{pmatrix} = \mathbf{M}^T \begin{pmatrix} u_L \\ u_Q \\ 0 \end{pmatrix} = \begin{pmatrix} \sin\omega t \\ -\varepsilon_0 \sin a_0 \cos\omega t \\ -\varepsilon_0 \cos a_0 \cos\omega t \end{pmatrix}. \tag{19}$$

Inserting Eq. (19) into Eq. (6) it follows:

$$\begin{pmatrix} v_R \\ v_Z \\ v_T \end{pmatrix} = \begin{pmatrix} \varepsilon_0 \cos(a_0 - a) \cos\omega t \\ \sin\omega t \\ \varepsilon_0 \sin(a_0 - a) \cos\omega t \end{pmatrix}. \tag{20}$$

The component product $v_R v_Z$ is given by

$$v_R v_Z = 0.5\, \varepsilon_0 \cos(a_0 - a) \sin 2\omega t. \tag{21}$$

For Love-waves $(0, 0, u_T)$, the component product $v_R v_Z$ is given by Eq. (18).

As a function of time, the component product $v_R v_Z$ is therefore always positive for P waves [Eq. (10)], negative for SV waves [Eq. (14)] and zero for SH and Love waves [Eq. (18)]. For Rayleigh waves, $v_R v_Z$ oscillates between positive and negative values with frequency 2ω for sinusoidal Rayleigh waves of frequency ω [Eq. (21)]. $v_R v_Z$ can therefore be used as an operator for wave type discrimination. (REMODE-Filter; for example, see Kanasewich, 1981).

The ground motion generated by an incident body wave at the free surface is a superposition of three waves: the incident P or S wave, the reflected P or S wave and the converted S or P wave. The displacement recorded by a three-component station thus differs from that of the incident wave. For linearly polarized incident P waves the particle motion remains linear in the plane of incidence for any angle of incidence. For linearly polarized S waves with an under-critical angle of incidence, all three components are in phase and the resultant particle motion remains linear. In the over-critical case the components are out of phase and the resultant motion becomes three-dimensional. The relationships between the apparent and true angle are expressed by conversion formulas published, for example, by Nuttli and Whitmore (1961). A practical application of the conversion formulas is epicentre location with a single three-component station. For the inversion of seismograms and particle motion diagrams with synthetics, the conversion at the earth's surface is incorporated in the numerical algorithm.

To determine the apparent angle of incidence, the seismogram vector $\mathbf{s}$ is transformed to a vector $\mathbf{v}'$ in a rotated analysis system, using $a = a_0$ and $i' = i + 45°$ in Eq. (4):

$$\begin{pmatrix} v'_L \\ v'_Q \\ v'_T \end{pmatrix} = \begin{pmatrix} s_Z \cos i' + v_R \sin i' \\ s_Z \sin i' - v_R \cos i' \\ -s_E \cos a_0 + s_N \sin a_0 \end{pmatrix} \tag{22}$$

where v_R is calculated from Eq. (6) for $a = a_0$. Inserting Eq. (7) for a linearly polarized P wave into Eq. (22) and using Eq. (6) for v_R and $a = a_0$, the component difference $v'_L - v'_Q$ is given by

$$v'_L - v'_Q = \sqrt{2}\, u_L \sin(i_0 - i). \tag{23}$$

Using Eq. (11) for a SV wave, it then follows in the same way for the component sum $v'_L + v'_Q$:

$$v'_L + v'_Q = \sqrt{2}\, u_Q \sin(i_0 - i). \tag{24}$$

In terms of the rotation angle i, the component difference $v'_L - v'_Q$ and the component sum $v'_L + v'_Q$ have zeros at $i = i_0$ for linearly polarized P waves and SV waves, respectively, and can therefore be used as operators for the determination of the apparent incidence angle i_0.

Interactive analysis

An efficient application of the algorithm is provided by an interactive program using a graphics terminal. Analysis takes place in two steps. First, the azimuth and apparent angle of incidence are determined for each wave group using component operators. Then the seismograms are calculated in the wave coordinate systems and plotted along with particle motion diagrams and the component products.

The component operators yielding the best resolution for the determination of azimuth, incidence angle and onset time are summarized in Table 1. Corresponding to Eqs. (9) and (13), the component product $v_T v_Z$, calculated for linearly polarized P waves and pure SV waves using Eq. (6), changes sign if the azimuth of the rotated system passes the wave azimuth a_0. If the P or SV wave is non-linearly polarized, the change of first-motion sign of $v_T v_Z$ determines the first-motion azimuth. The average azimuth is defined by the condition $\int v_T(a)\, v_Z\, dt = 0$, where the integration interval can be obtained from the pulse duration of the component product $v_R(a)\, v_Z$. In the same way, the first-motion and average incidence angles for P and SV waves can be determined using $v'_L - v'_Q$ [Eq. (23)] and $v'_L + v'_Q$ [Eq. (24)], respectively.

After the determination of azimuth and apparent incidence angle, seismograms and component products are calculated in the $L-Q-T$ wave system using Eq. (4). They can be displayed along with particle motion diagrams on a graphics terminal. It is also possible to identify and mark phases and to measure onset-times on seismogram traces as well as particle motion diagrams and component products. Marked times can be indicated in the other representations.

Table 1. Component operators for polarization analysis

Determination of	Wave type	Component operator
Azimuth a_0	P, SV	$v_T(a) \cdot v_Z$
Apparent	P	$v'_L(a_0, i) - v'_Q(a_0, i)$
Incidence angle i_0	SV	$v'_L(a_0, i) + v'_Q(a_0, i)$
Onset time	P	$v_R(a_0) \cdot v_Z$
Pulse duration	SV	
Wave type	SH	$v_T(a_0)$

Examples

The polarization analysis is demonstrated on digital broad-band recordings of events from Hokkaido, Afghanistan, the Aegean Sea and the Swabian Jura. The hypocentral and station parameters are summarized in Table 2. The digital recordings of stations KHC (Kašperské Hory) and KSP (Ksiaz) are proportional to displacement in the period range from T_L to T_U given in Table 2. They were obtained from the original analog (FM) broad-band velocity-proportional magnetic tape recordings by analog filtering (Plěsinger and Horálek, 1976) and computer-aided A/D conversion (Plěsinger, 1981). The displacement seismograms of stations GRFA1 and GRFB1 of the Gräfenberg array (Harjes and Seidl, 1978; Seidl and Stammler, 1984) are calculated from the original broad-band velocity-proportional recordings by digital restoration filtering (Seidl, 1980) for the period band T_L to T_U.

Figures 1–3 present the analysis of the multi-pulse *P* wave group of the Hokkaido event, recorded at station KHC.

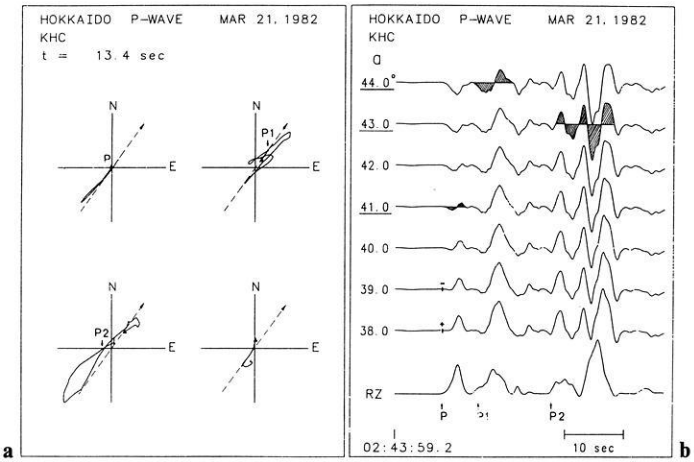

Fig. 1. **a** Horizontal particle motion diagrams in consecutive 13.4-s intervals for the composite *P* wave group of the Hokkaido event in Table 2. The *triangles* mark the beginning of the intervals. The *dashed line* is the great circle direction towards the epicentre. The *arrows* indicate the onsets of the pulses marked on the *RZ* trace in **b**. **b** $v_T(a)\,v_Z$ traces for the determination of the average azimuths *a* of the pulses indicated using the condition $\int v_T(a)\,v_Z\,dt = 0$. The integration intervals, indicated by the *hatched areas*, are obtained from the product *RZ* plotted for the azimuth $a = 41°$. The first-motion azimuth, indicated by the change of sign, is in the interval [38°, 39°]

Figure 1a shows the horizontal particle motion diagrams for successive 13.4-s time intervals. The first diagram begins with a nearly linearly polarized pulse, followed by signals with highly irregular two-dimensional polarization patterns. In Fig. 1b the component product $v_T(a)\,v_Z$ is plotted for various values of the azimuth *a*. The onset of $v_T v_Z$ changes its sign for an azimuth in the interval [38°, 39°]. This value is the first-motion azimuth, corresponding to the slope of the tangent on the particle motion diagram at the onset time. The average azimuths of the two-dimensionally polarized wave groups *P*, *P1* and *P2* are determined by the condition $\int v_T(a)\,v_Z\,dt = 0$, where the integration intervals are obtained from the component product *RZ*.

Table 2. Hypocentral and station parameters for the events analysed

Hypocentral data							Station data				
Location	Date	Origin time	Latitude (N)	Longitude (E)	Depth (km)	$\frac{m_b}{M_S}$	Station ((T_L, T_U))	Epicentral distance (degrees)	Azimuth (degrees N)	Incidence angle[a] (degrees)	
										P	*S*
Swabian Jura	Sep 03 1978	05:08:30.7	48.34	9.14	6	$\frac{4.9}{5.3}$	GRFA1 (1, 25)	1.9	226.2	(50)	(50)
							GRFB1 (1, 25)	2.0	238.6	(50)	(50)
							KHC (0.25, 60)	3.0	256.6	(50)	(50)
Afghanistan –	May 02 1981	16:04:54.6	36.40	71.15	223	5.9	GRFA1 (1, 60)	44.6	83.8	25	26
USSR Border Region						–	KHC (0.5, 150)	43.1	84.8	26	26
Aegean Sea	Dec 19 1981	14:10:51.1	39.22	25.25	16	$\frac{6.0}{7.2}$	KSP (0.3, 280)	13.2	148.1	(50)	(50)
Hokkaido	Mar 21 1982	02:32:05.9	42.23	142.46	36	$\frac{6.3}{6.9}$	KHC (0.3, 280)	78.5	36.2	17	19

[a] The theoretical incidence angles are taken from Pho and Behe (1972) and Chandra (1972). The values in parentheses are estimations for a single layer crustal model

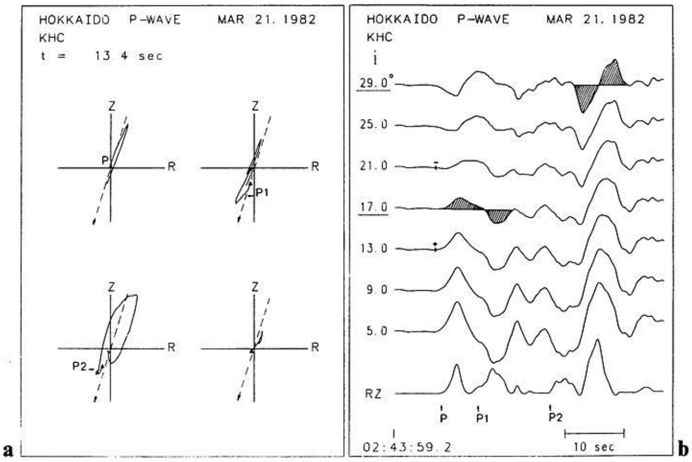

Fig. 2. **a** Particle motion diagrams in the $R-Z$ (radial-vertical) plane for $a=41^\circ$. The *dashed line* indicates the theoretical incidence angle, $i_0=17^\circ$. **b** $v'_L-v'_Q$ traces for the determination of the average apparent incidence angle i for the P wave group shown in Fig. 1 using the condition $\int [v'_L(a,i)-v'_Q(a,i)]\,dt=0$. Integration intervals and labels as in Fig. 1b. The first-motion and average apparent incidence angles are in the same interval, [15°, 19°]

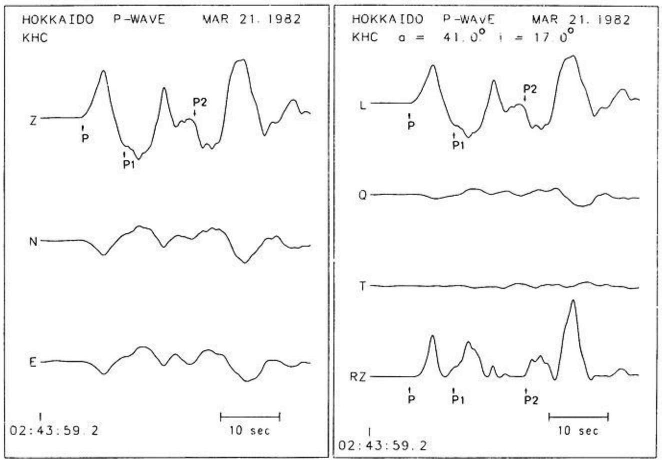

Fig. 3. Displacement recordings for the P wave group of the Hokkaido event and the seismograms transformed into the $L-Q-T$ system for $a=41^\circ$ and $i=17^\circ$ together with the RZ product

The value of the integral changes its sign in the interval [40.5°, 41.5°] for the P pulse. For the pulses $P1$ and $P2$, the intervals are [43°, 45°] and [42°, 44°], respectively. The great circle azimuth is 36°.

Figure 2a shows the corresponding particle motion diagrams in the vertical-radial plane for azimuth $a=41^\circ$ of the first P pulse. Again, the polarization of the first pulse is nearly linear, followed by signals with two-dimensional polarization patterns. Figure 2b shows the component differences $v'_L-v'_Q$ for various incidence angles i. The average incidence angle for P and $P1$ is in the interval [15°, 19°], and for $P2$ in the interval [28°, 30°]. The true angle of incidence, taken from the tables from Pho and Behe (1972), is 17°.

Figure 3 shows the original recordings as well as the seismograms transformed into the $L-Q-T$ coordinate system for azimuth $a=41^\circ$ and incidence angle $i=17^\circ$ together with the RZ product. The polarization is mainly linear in the L direction with slight contamination visible on the Q and T components. This is due to the non-linearity of the polarization and the variations in the azimuth and incidence angle for the incoming wavefront as a function of time. Thus, the P wave group consists of at least three different pulses. The onset times for $P1$ and $P2$ are best measured using the RZ trace.

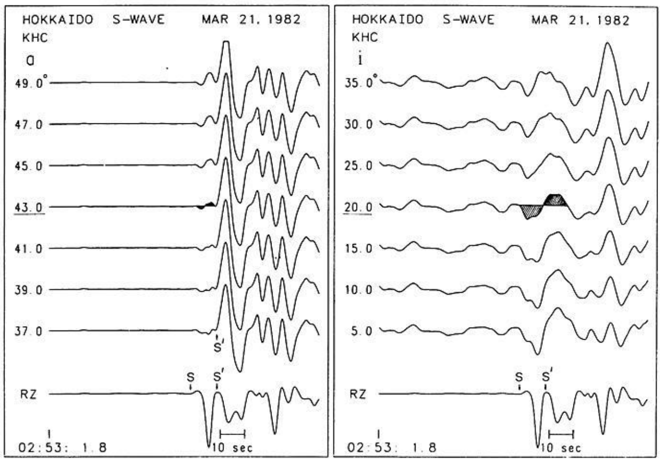

Fig. 4. $v_T(a)\,v_Z$ and $v'_L(a,i)+v'_Q(a,i)$ traces for the determination of average azimuth a and average apparent incidence angle i for the S wave group of the Hokkaido event using the conditions $\int v_T v_Z\,dt=0$ and $\int (v'_L+v'_Q)\,dt=0$. The *arrow* labelled S on the RZ trace indicates the Jeffreys-Bullen arrival time. The tiny positive initial pulse results from using the average wave-group azimuth to compute v_R rather than the azimuth determined by the first onset

The analysis of the S wave group of the Hokkaido event is presented in Figs. 4 and 5. The $v_T v_Z$ traces in Fig. 4 indicate a multiple wave group with an average azimuth in the interval [42°, 44°] for the first pulse. The diagrams of the component sum $v'_L+v'_Q$ have no clear multiple waveform. The average incidence angle is in the interval [18°, 22°] for the first pulse. The $L-Q-T$ seismograms, component products and particle motion diagrams in Fig. 5 exhibit clear S-wave splitting, which cannot be resolved in the original three-component recordings. The wave group begins with a SV-polarized pulse S, followed by a wave group S' with SV and SH components 7.8 s later. The pulses with SV components can be recognized using the RZ component product. The arrows indicate the JB arrival times of phases S, SKS and ScS. The transition from SV- to SH-polarization can be seen exceptionally clearly in the $Q-T$ particle motion diagram. An additional clear onset labelled SKS can be recognized in the $Q-L$ and $L-T$ diagrams. Generally, first-motion onset times can best be measured using the $L-Q-T$ seismograms. For later phases, the products TZ and RZ used in conjunction with the $L-Q-T$ diagrams produce higher accuracy and resolution for arrival time readings.

Figure 6 presents the analysis of the composite P wave group of the event in the Aegean Sea region, recorded at station KSP. The average azimuth for the complete wave group is in the interval [149.5°, 150.5°].

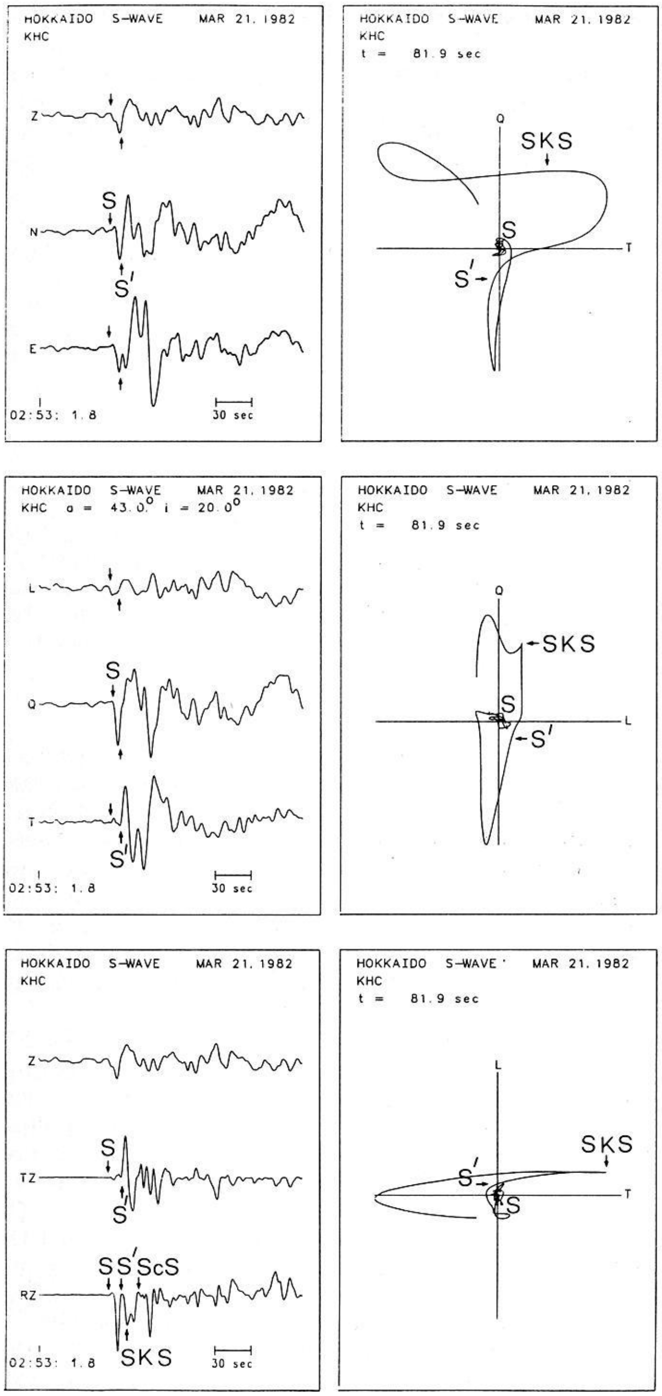

Fig. 5. Displacement recordings and component products as well as seismograms and particle motion diagrams in the $L-Q-T$ system for the S wave group of the Hokkaido event. The most interesting feature is the resolution of wave splitting in the first S pulse, labelled S and S'. The *arrows* on the RZ trace indicate the Jeffreys-Bullen arrival times of S, SKS and ScS

Within the time window of the first RZ pulse, $v'_L - v'_Q$ changes sign in the interval [44°, 48°] for the apparent incidence angle. The values for the great circle azimuth and the true angle of incidence are 148° and about 50° for a standard earth model. The seismograms and particle motion diagrams in the corresponding $L-Q-T$ system reveal pronounced P-wave splitting. The L trace begins with a linearly polarized P pulse, followed by a signal P' with SV-polarization on the Q trace. The delay in the onset times is 4.8 s. The SH contaminations on the T trace are very small during the time interval analysed. This splitting can also be seen in the polarization diagrams for the $Q-L$ and $L-T$ planes, plotted for the first 54.4-s time segment. The P pulse duration is 12.3 s, measured on the RZ trace. The P pulse is followed by a PL mode with regular dispersion in the period interval from about 60 to 30 s. Superimposed on this mode is a high-frequency P wave group $P1$, interpreted by Rademacher et al. (1983) as the $P-P$ reflection from the 400-km discontinuity.

Figures 7 and 8 show the seismograms and particle motion diagrams of the Love-Rayleigh wave segment of the earthquake in the Aegean Sea region. The ground motion consists of a regularly dispersed Love wave on the T trace with three superimposed Rayleigh wave groups. The onset of the first wave group R is indicated by the RZ product. The onsets of the multi-pathing wave groups R' and R'' can be determined best from the particle motion diagrams.

Figures 9 and 10 present the analysis of the P wave group of an intermediate-depth earthquake in the Afghanistan region, recorded at stations KHC and GRFA1. The first sections of the particle motion diagrams are nearly linearly polarized, followed by coda waves with irregular two-dimensional polarization patterns. The intervals for the azimuth and the apparent incidence angle are [88.75°, 89.25°] and [25°, 27°] for KHC, [89.25°, 89.75°] and [29°, 31°] for GRFA1. The values for the great circle azimuth and the true incidence angle are given in Table 2. The seismograms and component products are summarized in Fig. 10. The low-frequency part of the seismograms is linearly polarized with little contamination in the Q and T components. The superimposed high-frequency wave groups show enhanced amplitudes in the GRFA recordings with irregular polarization pattern, indicated by the contamination in the Q and T components and by the component products QT, LT and LQ. The onset times of the various overlapping pulses can best be measured using the RZ trace. The theoretical arrival times are labelled for some phases.

As an example for a near event, Figs. 11–13 show the analysis of the Pn wave group of the Swabian Jura earthquake on September 3, 1978, recorded at stations GRFA1, GRFB1 and KHC. The displacement seismograms have a double-pulse waveform. The second pulse was identified by Kind (1979) as being sPn. At station GRFA1, the azimuth for the Pn and sPn pulses are in the intervals [231°, 233°] and [225°, 227°], respectively. The interval for the apparent incidence angle is [53°, 57°] for both phases. The most astonishing feature apparent in the particle motion diagrams is the nearly circular polarization in the radial-vertical plane for both Pn and sPn. The seismograms in the $L-Q-T$ system reveal that this polarization patterns is caused by a pulse on the Q component with a signal form approaching the time derivative of the L-component seismogram. This effect is also visible but less pronounced on the GRFB1 recordings shown in Fig. 12. Possible explanations include wave propagation through anisotropic layers and near-field terms. At

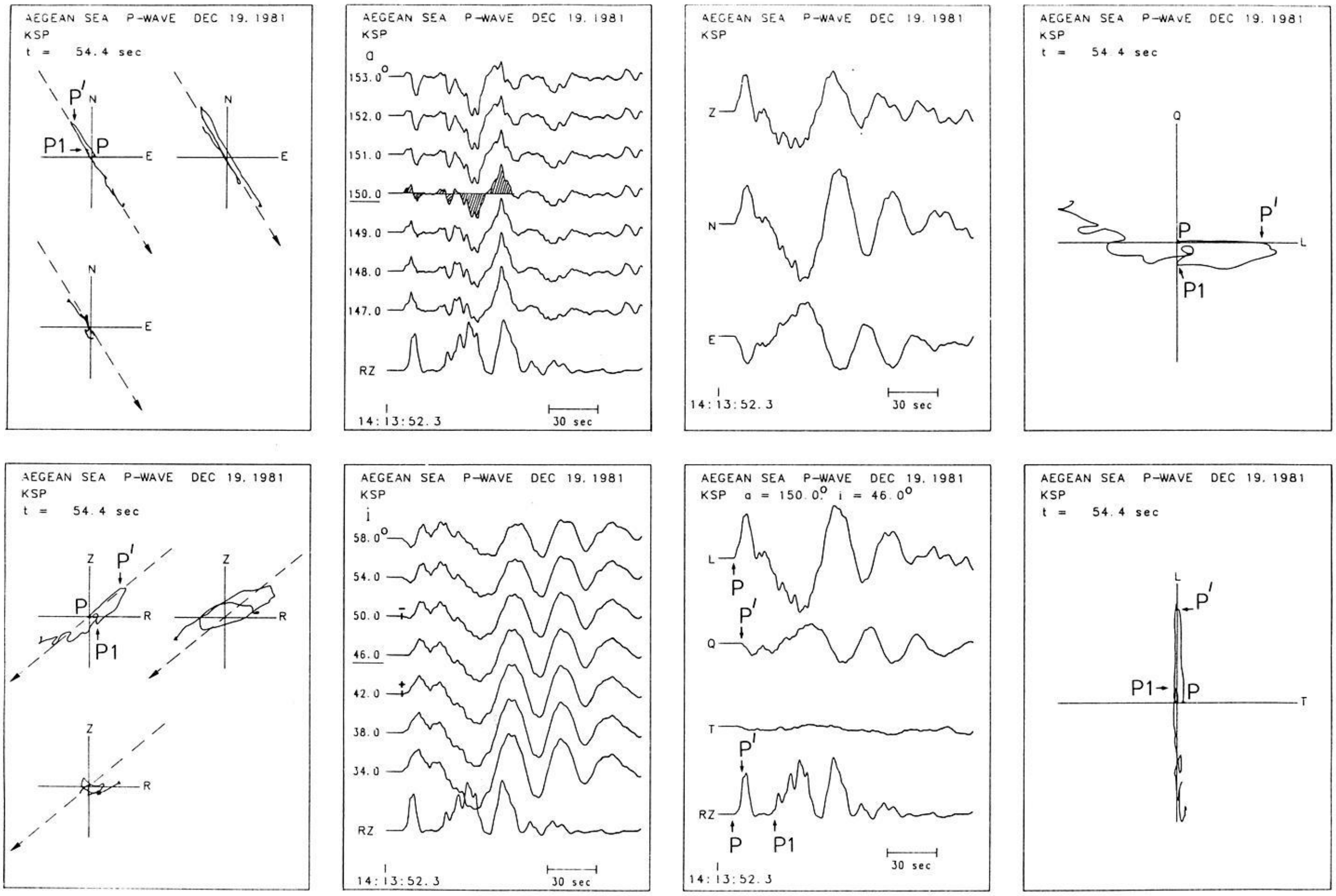

Fig. 6. Analysis of the composite P wave group for the Aegean Sea event in Table 2. The determination of azimuth and apparent incidence angle is analogous to Fig. 1. The seismograms and particle motion diagrams in the $L-Q-T$ system reveal wave splitting in the first P pulse, labelled P and P'. The high-frequency phase $P1$, superimposed on the long-period PL mode, was interpreted by Rademacher et al. (1983) as the $P-P$ reflection from the 400-km discontinuity

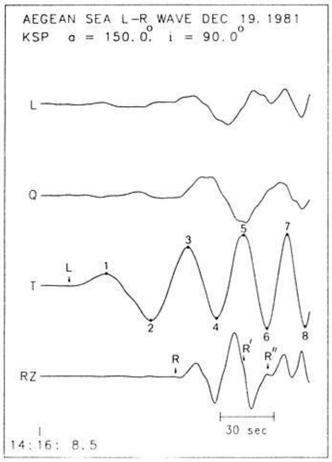

Fig. 7. Seismograms in the $L-Q-T$ system and RZ component product for the Love-Rayleigh wave segment of the Aegean Sea event with labelled onsets of the Love wave and the three Rayleigh wave groups R, R' and R''

KHC (Fig. 13) the Q component has no "derivative" signal form. Both the *Pn* and *sPn* pulses are non-linearly polarized in the horizontal plane, and the polarization anomaly in the radial-vertical $(R-Z)$ plane is considerably less pronounced.

Conclusions

Broad-band recordings of seismic waves are composite waveforms, generated by multiple events, multi-path propagation, conversion and wave splitting in the laterally heterogeneous and anisotropic earth. A procedure for the time-domain analysis of digital three-component broad-band recordings using seismograms, particle motion diagrams and component products in rotated coordinate systems has been described. The orientations for these systems are determined using the zeros of wave-type-dependent component operators. In comparison to standard methods, such as ellipsoidal least-squares fits of narrow-band particle motion diagrams (for example, see Matsumara, 1981), the method

(1) is applicable to composite waveforms with arbitrary three-dimensional polarization,

(2) offers higher precision and resolution for the determination of azimuth, incidence angle, onset time and pulse duration, and

(3) gives azimuth and incidence angle as intervals instead of mean values with standard errors.

The procedure has been demonstrated using broad-band displacement seismograms of regional and teleseismic events. The results, although presented phenomenologically without interpretation, illustrate the useful-

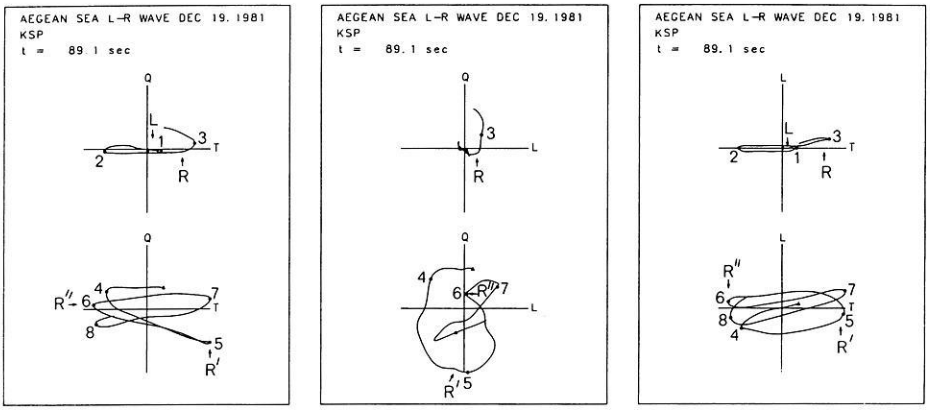

Fig. 8. Particle motion diagrams in the $L-Q-T$ system for the Love-Rayleigh wave segment in Fig. 7. The *numbers* indicate the times of the maxima and minima of the T trace in Fig. 7

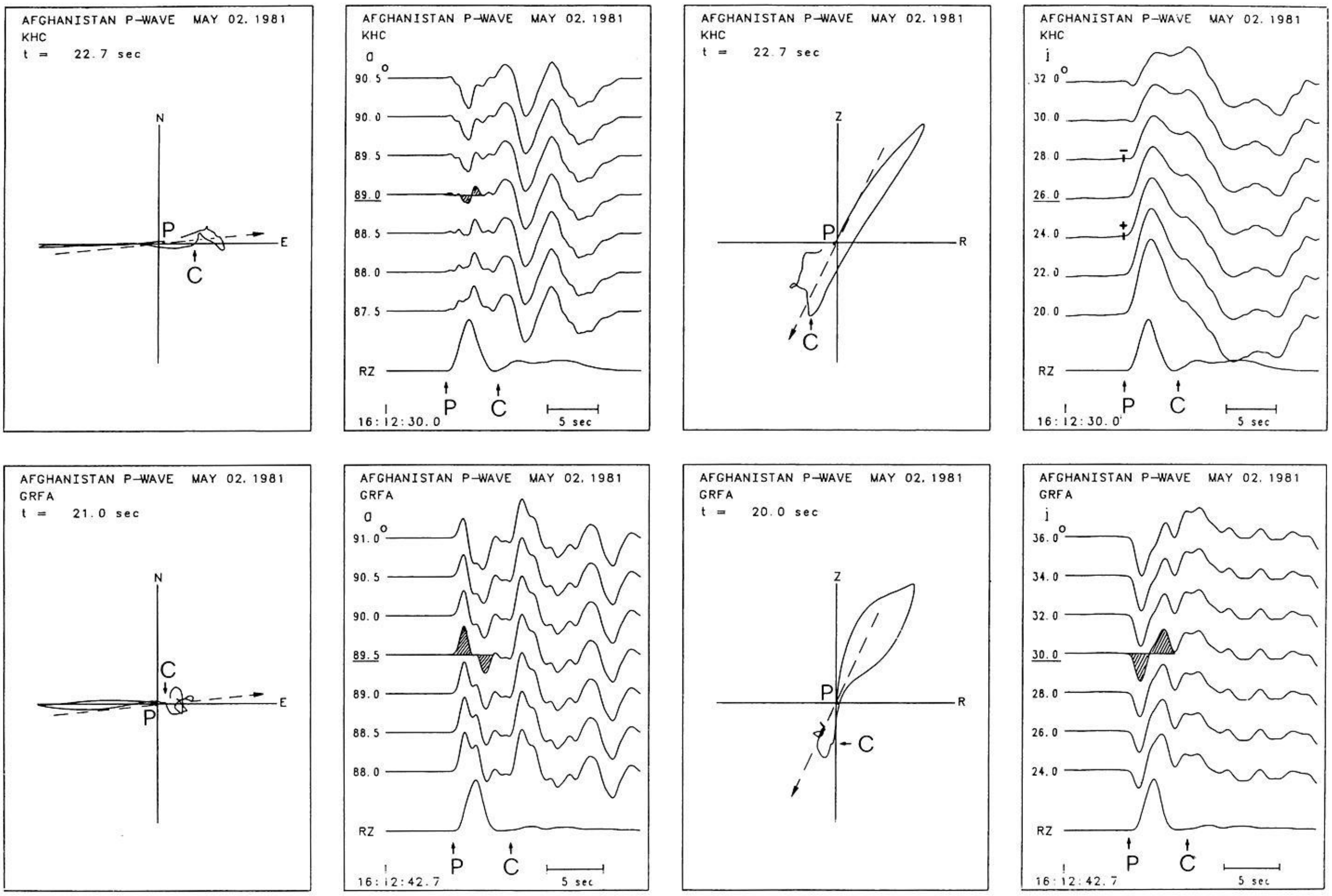

Fig. 9. Determination of azimuth and apparent incidence angle for the P wave group of an intermediate-depth-focus earthquake in the Afghanistan region, recorded at stations KHC and GRFA1. The hypocentre and station parameters are given in Table 2

Fig. 10. Displacement recordings as well as seismograms and component products in the $L-Q-T$ system for the Afghanistan earthquake. The *arrows* on the RZ trace indicate the theoretical arrival times for the labelled phases

Fig. 11. Determination of azimuth and apparent incidence angle as well as displacement recordings and $L-Q-T$ seismograms for the $Pn-sPn$ phases of the Swabian Jura earthquake in Table 2, recorded at station GRFA1. The most interesting feature is the nearly circular polarization of both phases in the vertical-radial plane. Note the sharp onset of sPn on the RZ trace

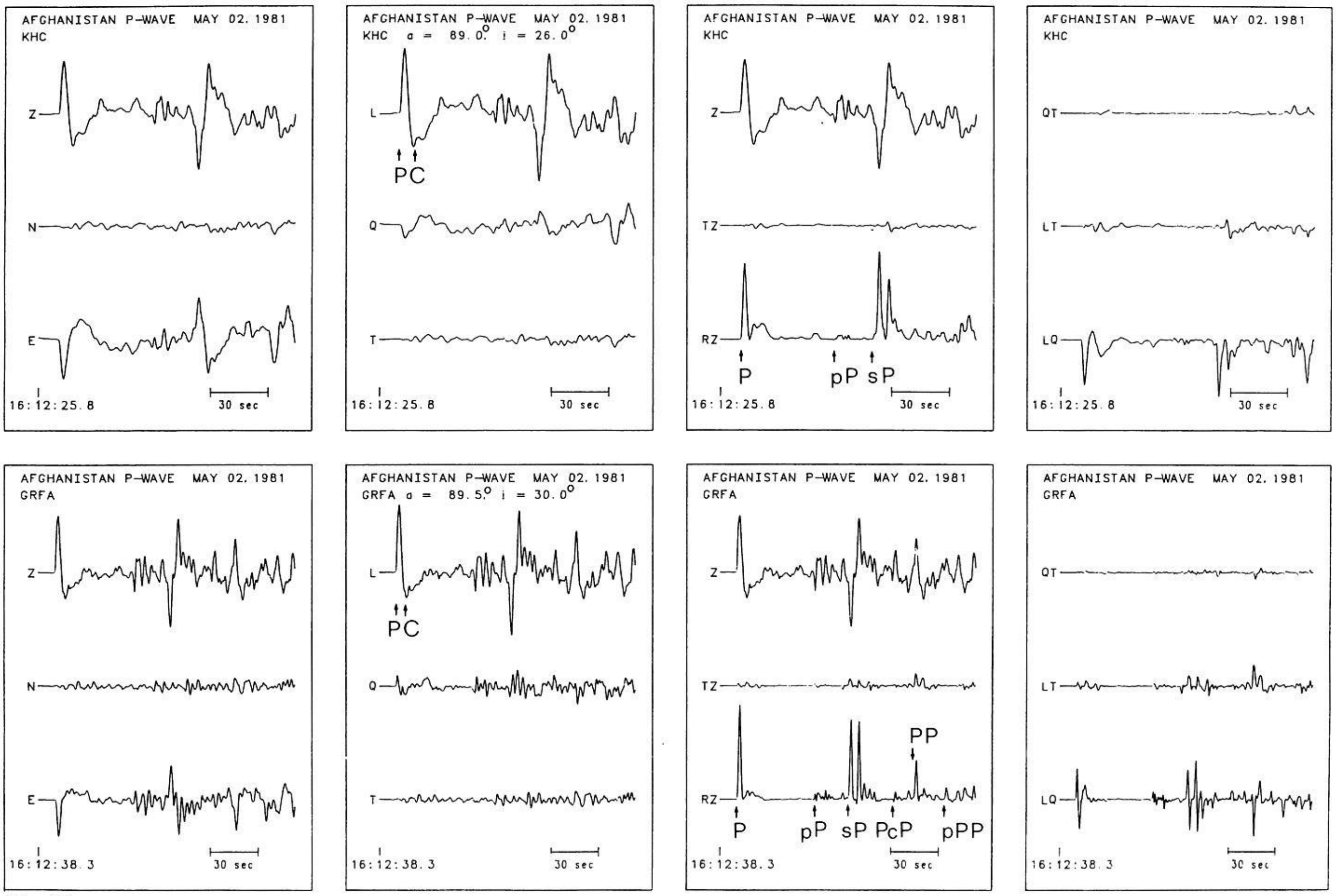
AFGHANISTAN P-WAVE MAY 02, 1981
KHC
KHC a = 89.0° i = 26.0°
Z
N
E
L
Q
T
TZ
RZ
QT
LT
LQ
P C
P
pP
sP
16:12:25.8
30 sec
GRFA
GRFA a = 89.5° i = 30.0°
PP
pP
sP
PcP
pPP
16:12:38.3

Fig. 10

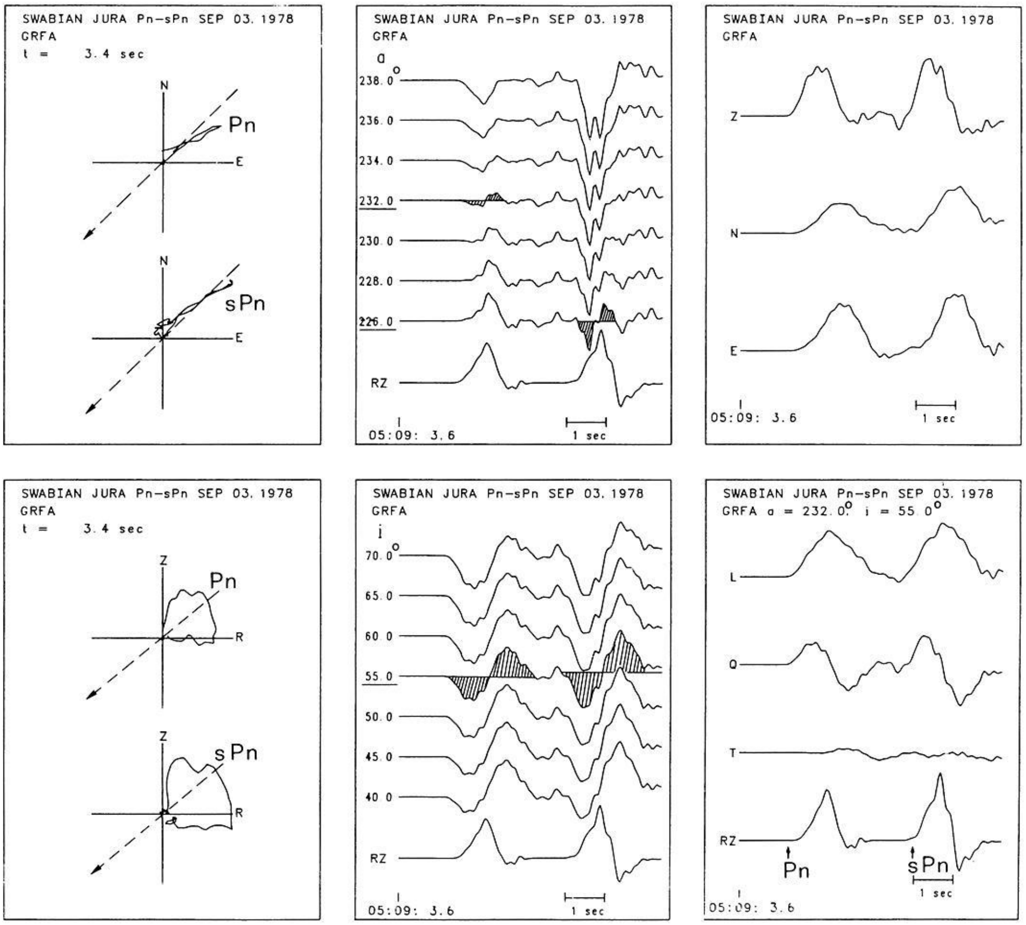
SWABIAN JURA Pn-sPn SEP 03, 1978
GRFA
t = 3.4 sec
N
E
Pn
sPn
Z
R
a°
238.0
236.0
234.0
232.0
230.0
228.0
226.0
RZ
05:09: 3.6
1 sec
i°
70.0
65.0
60.0
55.0
50.0
45.0
40.0
GRFA a = 232.0° i = 55.0°
L
Q
T

Fig. 11

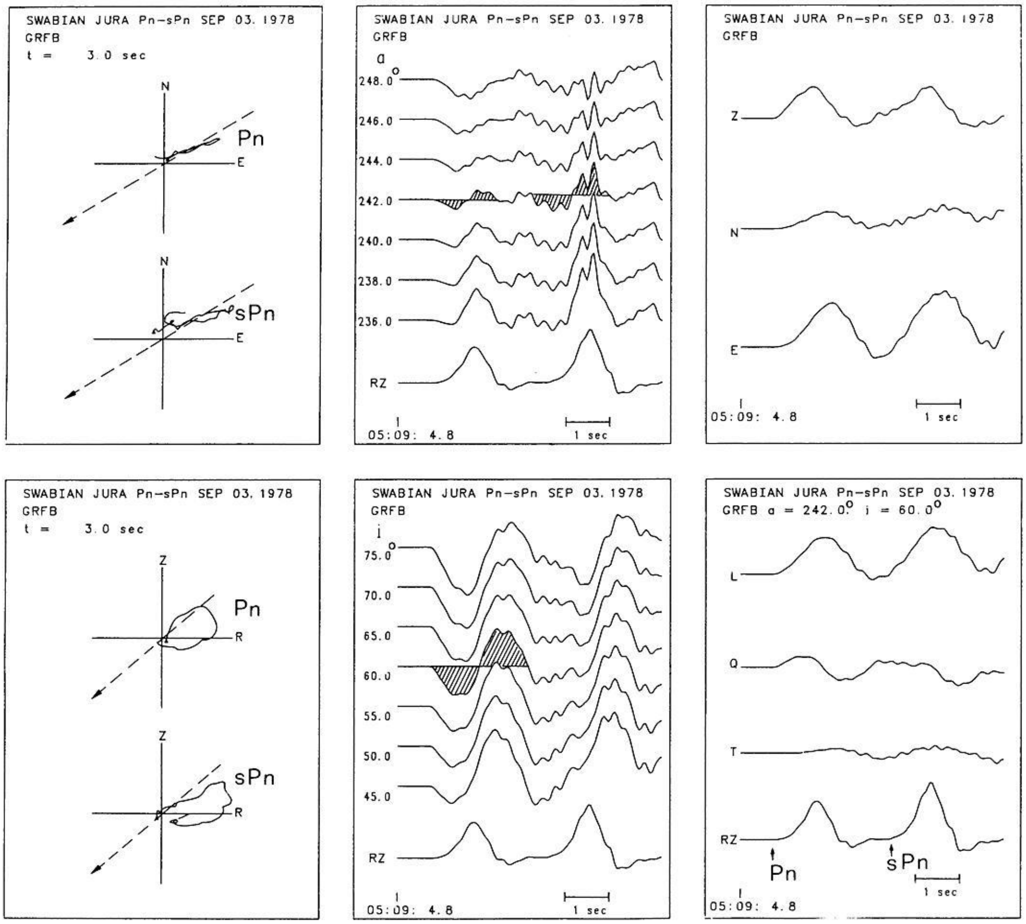

Fig. 12. Analysis of the *Pn – sPn* wave group of the Swabian Jura earthquake recorded at station GRFB1

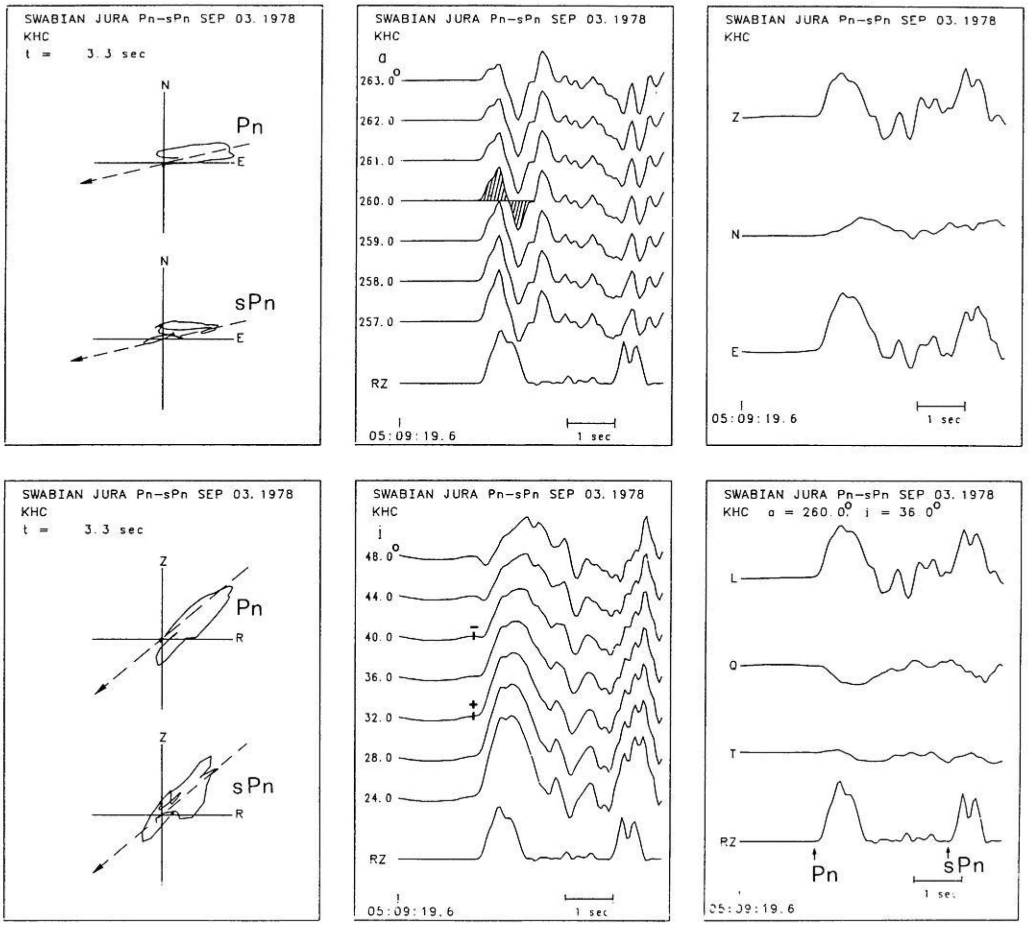

Fig. 13. Analysis of the *Pn – sPn* wave group of the Swabian Jura earthquake recorded at station KHC

ness of polarization analysis for source studies and structural investigations. From the variety of applications the following should be mentioned:

As has been demonstrated by Brüstle (1985), modelling of complex, multiple sources from broadband recordings is performed best in the time domain. Seismogram pre-processing by polarization analysis provides criteria for the decomposition of composite waveforms into single pulses and for the determination of wave parameters such as pulse duration and displacement time integrals.

For the modelling of laterally heterogeneous structures, the input data are anomalies of onset times, azimuths and incidence angles with regard to a three-dimensional model earth. These data can be measured for the different pulses of a composite waveform using seismograms, particle motion diagrams and component products in properly rotated coordinate systems. As a special result, it has been found that the azimuth anomalies with respect to a spherically homogeneous earth are usually small compared to the anomalies for the incidence angle. This result has been confirmed for *S* waves by numerical experiments performed by Cormier (1984).

The most important application of polarization analysis of three-component broad-band seismograms is likely to be the investigation of anisotropic structures, especially when combined with digital band-pass frequency filtering (Bamford, 1977; Crampin et al., 1984). In anisotropic media, both body and surface waves are three-dimensionally polarized (Crampin, 1977; Keith and Crampin, 1977a, b, c). Rotated seismograms, particle motion diagrams and component products enable the resolution of wave splitting, and aid in the investigation of the fine structure of "quasi-P" and "quasi-*S*" waves as well as different types of "inclined", "tilted" and "sloping" Rayleigh waves.

Acknowledgements. The authors are greatly indebted to Dr. Ivan Pšenčik for stimulating discussions. One of the authors (A.P.) thanks the German Research Council and the University of Stuttgart for enabling him to carry out the present study during his stay at the Geophysical Institute, and the Federal Institute for Geosciences and Natural Resources in Hannover for providing the necessary facilities at the Central Seismological Observatory Gräfenberg in Erlangen. The study is also part of a research project of the Institute for Geophysics and Meterology of the University of Frankfurt supported by the German Research Council.

References

Aki, K., Richards, P.G.: Quantitative seismology, pp. 103–104. San Francisco: Freeman 1980

Bamford, D.: Seismic anisotropy – the state of the art. Geophys. J. **49**, 1–8, 1977

Brüstle, W.: Der Bruchvorgang im Erdbebenherd – Untersuchung ausgewählter Erdbeben mit beobachteten und synthetischen Seismogrammen. Berichte des Instituts für Meteorologie und Geophysik der Universität. Frankfurt/M., Nr. 63, 1985

Chandra, U.: Angles of incidence of S waves. Bull. Seismol. Soc. Am. **62**, 903–915, 1972

Cormier, V.F.: The polarization of S waves in a heterogeneous isotropic earth model. J. Geophys. **56**, 20–23, 1984

Crampin, S.H.: A review of the effects of anisotropic layering on the propagation of seismic waves. Geophys. J. **49**, 9–27, 1977

Crampin, S., Chesnokov, E.M., Hipkin, R.G.: Seismic anisotropy – the state of the art: II. Geophys. J. **76**, 1–16, 1984

Harjes, H.-P., Seidl, D.: Digital recording and analysis of broad-band seismic data at the Graefenberg (GRF)-array. J. Geophys. **44**, 511–523, 1978

Kanasewich, E.R.: Time sequence analysis in geophysics, 3rd ed. Alberta: The University of Alberta Press 1981

Keith, C.M., Crampin, S.: Seismic body waves in anisotropic media: reflection and refraction at a plane interface. Geophys. J. **49**, 181–208, 1977a

Keith, C.M., Crampin, S.: Seismic body waves in anisotropic media: propagation through a layer. Geophys. J. **49**, 209–223, 1977b

Keith, C.M., Crampin, S.: Seismic body waves in anisotropic media: synthetic seismograms. Geophys. J. **49**, 225–243, 1977c

Kind, R.: Observations of sPn from Swabian Alb earthquakes at the GRF array. J. Geophys. **45**, 337–340, 1979

Matsumura, S.: Three-dimensional expression of seismic particle motions by the trajectory ellipsoid and its application to the seismic data observed in the Kanto district, Japan. J. Phys. Earth **29**, 221–239, 1981

Nuttli, O., Whitmore, J.D.: An observational determination of the variation of the angle of incidence of *P* waves with the epicentral distance. Bull. Seismol. Soc. Am. **51**, 269–276, 1961

Pho, H.-T., Behe, L.: Extended distances and angles of incidence of *P* waves. Bull. Seismol. Soc. Am. **62**, 885–902, 1972

Plešinger, A., Horálek, J.: The seismic broadband recording and data processing system FBV/DPS and its seismological applications. J. Geophys. **42**, 201–217, 1976

Plešinger, A.: Acquisition, processing and interpretation of broadband seismic data. In: Geophysical syntheses in Czechoslovakia, pp. 58–78. Bratislava: VEDA 1981

Rademacher, H., Odom, R.I., Kind, R.: The upper mantle structure under south-east Europe derived from broadband records of Greek earthquakes. J. Geophys. **52**, 7–13, 1983

Seidl, D.: The simulation problem for broad-band seismograms. J. Geophys. **48**, 84–93, 1980

Seidl, D., Stammler, W.: Restoration of broad-band seismograms (Part I). J. Geophys. **54**, 114–122, 1984

Received October 13, 1985; revised version December 9, 1985
Accepted December 10, 1985

J Geophys (1986) 59:140–141

Journal of Geophysics

The relationship between the polarization of whistlers and their dispersion

S. Shimakura[1], **T. Okada**[2], **M. Hayakawa**[2], **and Y. Tanaka**[2]

[1] Department of Electrical Engineering, Chiba University, Chiba, 260, Japan
[2] Research Institute of Atmospherics, Nagoya University, Toyokawa, Aichi, 442, Japan

Abstract. It is found, based on the whistler data obtained at Moshiri, that there exists a definite relationship between the phase difference (Φ) of wave magnetic fields of daytime whistlers on two crossed loop aerials and the dispersion (D); Φ (deg) $= -3.34 \times D(\mathrm{s}^{1/2}) + 82.2$. This relation in conjunction with our previous empirical formula relating the dispersion with path latitude will suggest a diagnostic tool of inferring the path latitude of VLF emissions only by using the simple polarization measurement for those waves.

Key words: Magnetosphere – Whistlers – Dispersion – Phase difference measurement – Polarization

1. Introduction

The ground-based measurement of polarization of VLF waves; the measurement of amplitude ratio and phase difference of VLF signals on crossed loop aerials, provides useful information on the ionospheric transmission mechanism of VLF waves after having propagated through the magnetosphere (Tanaka et al., 1976; Okada et al., 1977, 1981; Machida and Tsuruda, 1984). The present paper deals with the polarization characteristics of whistlers as a function of dispersion value, and points out that the phase difference of whistler wave fields on the crossed loops can be extensively used to infer the latitude where whistlers emerge from the ionosphere.

2. Polarization characteristics as a function of dispersion

The present study is based on the whistler data obtained at a middle latitude station of Moshiri, Japan (geomagnetic latitude $= 34.5°$ N; $L = 1.59$). The measurement of polarization is made as follows. The wideband (0–10 kHz) VLF signals, together with calibration signals, recorded on analogue magnetic tapes are digitized by means of an A/D converter, and those digitized data are analyzed by a computer to deduce the amplitude ratio and phase difference of the signals on crossed loop aerials over the full frequency range of whistler spectrum (see Okada et al., 1983, for the detailed procedure). The polarization is defined as $p(= -H_{NS}/H_{EW}$, where H_{NS} and H_{EW} are the wave magnetic field components in the geomagnetic NS and EW directions) $= re^{i\Phi}$. In the following, we use the information of phase differences in a narrow frequency band from 3.0–4.0 kHz where the whistler energy is maximized in the spectrum.

Figure 1 illustrates the final result in the form of the relationship between the phase difference and dispersion value. This figure is concerned with daytime whistlers as termed by Hayakawa and Tanaka (1978) which occurred during the local time interval of 17 h through 20 h and is based on the data obtained from three daytime occurrence peaks at 14:00–14:05 on 14th January 1983, 17:25–17:30 on 24th January 1984 and 19:55–20:00 on 13th February 1985. Only strongest whistlers are used to deduce reliable polarization data. Each dot represents the mean value of the occurrence distribution of phase differences for the frequency range from 3.0 to 4.0 kHz for a specific whistler. Open dots refer to the whistlers on 14th January 1983, black dots those on 24th January 1984, and triangles those on 13th February 1985. A horizontal arrow indicates the average value of phase differences for each dispersion value. As seen from the figure, we understand that there exists a clear and definite relationship between the phase differences Φ and dispersion value D. The following regression line is obtained with an extremely high correlation coefficient of -0.93 and is shown in the figure in full line.

$$\Phi(\mathrm{deg}) = -3.34 \times D(\mathrm{s}^{1/2}) + 82.2.$$

The previous direction finding study (Hayakawa et al., 1981) has found that the ionospheric exit points of whistlers with dispersion for which we have the highest occurrence number, are very close to the observing station. So, we have examined the distribution of dispersion value measured in every 5 $\mathrm{s}^{1/2}$ in the local time intervals from 17:00 to 20:00 for two Januaries in 1983 and 1984 and for February 1985, and the result is that the most probable dispersion is close to, but slightly larger than 40 $\mathrm{s}^{1/2}$. The use of this most probable dispersion ($D = 41 - 42\ \mathrm{s}^{1/2}$) in our previous experimental formula, $D(\mathrm{s}^{1/2}) = 1.22\ (\Lambda - 0.72)$ (Λ: geomagnetic latitude) (Hayakawa and Tanaka, 1978) has yielded $\Lambda = 34.3 - 35.1°$, which is in good agreement with the actual latitude of the station of Moshiri. Hence, the use of Hayakawa and Tanaka (1978)'s empirical formula enables us to infer the path latitude of the whistlers, and so at the top of Fig. 1, the corresponding path latitude is also indicated. For example, $D = 75\ \mathrm{s}^{1/2}$ in the figure corresponds to the path latitude of $\Lambda = 58.1°$, about 2,460 km away from the station of Moshiri in the magnetic meridian plane. For larger dispersion such as 57.5 and 75 $\mathrm{s}^{1/2}$, the

---

Offprint requests to: M. Hayakawa

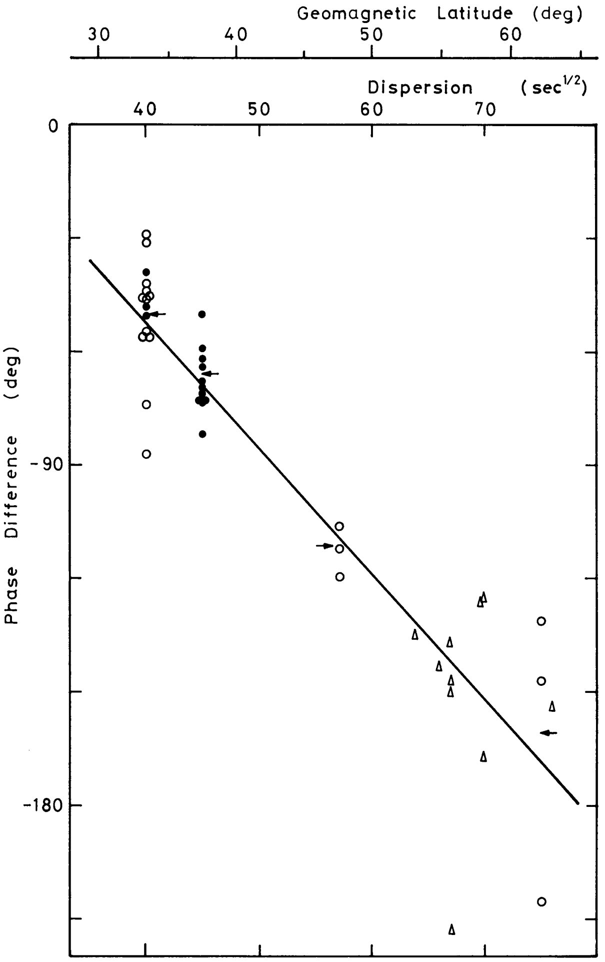

Fig. 1. The relationship between the phase difference and the dispersion value. The regression line is indicated in *full line*

azimuth of arrival is considered to be close to the magnetic meridian plane, because the propagation distance becomes larger for off-meridional whistlers, suggesting more absorption in the Earth-ionosphere waveguide propagation. Actually, we have tried to deduce the azimuths of whistlers with dispersions of 57.5 and 75 $s^{1/2}$, by using a rough estimation of $\Theta(\text{azimuth}) = \tan^{-1} r$ on the assumption of linearly polarization, and we find that all of those whistlers have propagated from a small range of azimuth (less than 30°) around the magnetic meridian plane. For whistlers with larger D's having propagated over great distances in the Earth-ionosphere waveguide, the waves will be more linearly and vertically polarized so that $\phi \sim -180°$, which is roughly consistent with Fig. 1. On the contrary, one would expect ϕ closer to $-90°$ for $D \sim 40\ s^{1/2}$ because circularly polarized whistler-mode waves are incident nearly from the vertical directions and also the scatter in ϕ may indicate the reception of off-meridional whistlers.

3. Conclusion and future application

A clear tendency as found in Fig. 1 will be useful for the future study of whistlers based on the polarization measurement. Furthermore, we can propose a useful diagnostic for magnetospheric VLF/ELF emissions such that when we apply the relationship as obtained in the present paper, to VLF emissions such as hiss and chorus whose path latitudes are difficult to determine, we may be able to infer the approximate path latitude of those emissions on the assumption of meridional propagation only by using the simple polarization measurement.

Acknowledgement. Useful discussion with Dr. K. Ohta of Chubu University is greatly appreciated. This work is partly supported by Takeda Science Foundation, to which we are grateful.

References

Hayakawa, M., and Y. Tanaka, On the propagation of low-latitude whistlers, Rev. Geophys. Space Phys. **16**, 111, 1978

Hayakawa, M., T. Okada and A. Iwai, Direction finding of medium-latitude whistlers and their propagation characteristics, J. Geophy. Res. **86**, 6939, 1981

Machida, S., and K. Tsuruda, Intensity and polarization characteristics of whistlers deduced from multi-station observations, J. Geophys. Res. **89**, 1675, 1984

Okada, T., A. Iwai, and M. Hayakawa, The measurement of incident and azimuthal angles and the polarization of whistlers at low latitudes, Planet. Space Sci. **25**, 233, 1977

Okada, T., Y. Tanaka, M. Hayakawa, A. Iwai, and S. Shimakura, Experimental study of the relationship between the propagation distance and the polarization characteristics of whistlers, Trans. Inst. Electr. Comm. Engrs. Japan, 66-B, 1355, 1983 (in Japanese)

Tanaka, Y., M. Hayakawa and M. Nishino, Study of auroral VLF hiss observed at Syowa Station, Antarctica, Mem. Nat'l Inst. Polar Res., Ser. A, No. 13, 58p., 1976

Received November 27, 1985; revised version February 4, 1986
Accepted February 12, 1986

J Geophys (1986) 59:142–145

Journal of Geophysics

Short communication

A simple statistical model on the degree of interconnection in partially molten rocks

H. Schmeling*
Institut für Meteorologie und Geophysik, Feldbergstr. 47, D-6000 Frankfurt/M., Federal Republic of Germany

Abstract. The connectiveness of the melt phase strongly influences physical properties of partially molten rock such as seismic absorption due to melt squirt or electrical conductivity. The interrelation between the connectiveness, the geometry and the fraction of melt is studied theoretically for the idealistic case of melt occurring in ellipsoidal (spheroidal or penny-shaped) inclusions. A critical melt fraction leading to complete grain-boundary wetting is found ranging between 2α and 5α, where α is the aspect ratio of the melt films. The probability of overlapping of randomly distributed inclusions is estimated by a statistical approach. This probability depends on the melt fraction β and the aspect ratio α and is used to define (a) the degree of interconnection and (b) the mean number n of connections to neighbouring inclusions. (a) may be important for seismic absorption due to melt squirt, while (b) controls the electrical conductivity. The function $n(\alpha, \beta)$ is given approximately by $n \simeq (5.65 + 1.72/\alpha)\beta$. It is concluded that in mantle regions of moderate seismic-velocity decrease a reduced degree of interconnection might be important if melt occurs either in films or pockets.

Key words: Partial melt – Degree of interconnection – Melt films

Introduction

Physical properties of partially molten rocks such as seismic velocity, absorption and electrical conductivity are strongly dependent on the melt fraction and the geometrical distribution of the melt phase. A lot of work has been spent on modelling of the physical properties for different melt geometries such as penny-shaped melt inclusions, melt films, tubes or pockets (Walsh, 1969; O'Connell and Budiansky, 1977; Mavko, 1980; Waff, 1974; Honkura, 1975; Chelidze, 1978; Shankland et al., 1981; Schmeling, 1983, 1985, 1986). Although few workers considered a variable degree of interconnection in their conductivity models (Waff, 1974; Shankland and Waff, 1974; Hermance, 1979), the interrelation between the melt fraction, the melt geometry and the degree of interconnection remained unexplored. Some indications can be obtained from laboratory work. While some experiments show that the degree of interconnection is high regardless of how small the fraction of melt in intergranular tubes is (Waff and Bulau, 1979), others find a decreasing degree of interconnection for small melt fractions in films (Arzi, 1978; Van der Molen and Paterson, 1979; Berckhemer et al., 1982).

The aim of the present paper is to develop a statistical model describing the degree of interconnection as a function of the melt fraction and melt geometry for the idealized case of ellipsoidal melt films or pockets. Such a model can be included in theories on the physical properties of partial molten rock as has been done by Schmeling (1983, 1985, 1986). The connectiveness of intergranular melt tubes will not be considered here.

Critical melt fractions for complete interconnection

In this section the critical melt fraction β_c for films leading to complete grain-boundary wetting will be estimated. Assume the rock to be composed of grains with plane surfaces. If a melt film occurs at the j-th face of the i-th grain, its aspect ratio can be defined by

$$\alpha_{ij} = c_{ij}/a_{ij} \tag{1}$$

where c_{ij} is the half thickness, a_{ij} the equivalent radius $(=\sqrt{F_{ij}/\pi})$ and F_{ij} the area of the film. The critical melt fraction is then given by

$$\beta_c = \frac{1}{\sqrt{\pi}} \frac{\sum_{i=1}^{M} \sum_{j=1}^{m_i} F_{ij}^{3/2} \alpha_{ij}}{\sum_{i=1}^{M} V_i} \tag{2}$$

where m_i is the number of faces of the i-th grain, M the total number of grains and V_i the volume of the i-th grain. Assuming no correlation between the aspect ratios and the film surface areas and between the shape and the volume of the grains, the arithmetic mean of the aspect ratios can be drawn in front of the summations and the sums can be evaluated giving

---

* *Present address:* University of Uppsala, Institute of Geology, Department of Mineralogy and Petrology, Box 555, S-75122 Uppsala, Sweden

$$\beta_c = \pi^{-1/2} \bar{\alpha} \bar{A} \tag{3}$$

where

$$A_i = \left(\sum_{j=1}^{m_i} F_{ij}^{3/2} \right) \Big/ V_i.$$

The bars indicate the arithmetic mean to be taken over all films or grains, respectively. A_i describes the shape of the grains ranging around 3.5 for compact polyhedrons like a truncated octahedron. A increases approximately to 5, 6 or 10 for octahedrons, cubes or tetrahedrons, respectively. With these values we can find bounds for β_c

$$2\alpha < \beta_c < 5\alpha. \tag{4}$$

The critical melt fraction as constructed above would lead to a loss of the shear strength of the composite material. O'Connell and Budiansky (1974, 1977) determined the shear modulus for a material containing fluid-filled cracks. The unrelaxed modulus (defined by assuming isolated inclusions) dropped to 0 at $\beta/\alpha = 5.9$, while the relaxed modulus (defined by assuming the same fluid pressure in all inclusions) vanished at $\beta/\alpha = 2.4$. This agrees well with (4) and strongly supports O'Connell and Budiansky's (1974, 1977) elastical analysis down to vanishing modulus, a point which was questioned by Bruner (1976).

Variable degree of interconnection

In this section a variable degree of interconnection is determined for statistically distributed and oriented melt films and spheroidal melt inclusions. Seismic absorption due to melt squirt requires fluid flow between neighbouring inclusions of different orientations (Mavko and Nur, 1975). On the other hand, electrical conductivity depends strongly on the existence of continuous liquid paths through the material. For the first problem, the degree of interconnection ζ will be defined by the probability of an average inclusion being connected or overlapping with at least one neighbouring inclusion. For the second problem, theory on random resistor networks shows that the mean number n of direct connections to neighbouring inclusions is the important quantity (Waff, 1974; Kirkpatrick, 1973; Schopper, 1966).

The quantities ζ and n are determined as follows. For simplicity only inclusions of same spheroidal shape and size are assumed. In the mathematical model statistically distributed and oriented inclusions are assumed. A possible configuration of two such inclusions with the half axes a and c (defining the aspect ratio $\alpha = c/a$) is illustrated in Fig. 1. If the total volume of the material is V_t and the total number of inclusions is N, the probability of finding i centres of neighbouring inclusions within the volume V around one inclusion denoted by the number 0 is given by

$$P = \left(\frac{V_t - V}{V_t} \right)^{N-i} \cdot \left(\frac{V}{V_t} \right)^i \cdot \binom{N}{i}. \tag{5}$$

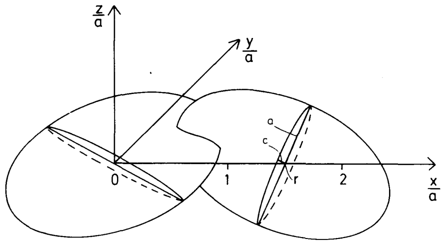

Fig. 1. Illustration of an example of two overlapping spheroidal inclusions used in the mathematical model. They have a distance r and an aspect ratio $\alpha = c/a$

For large N, P approaches the Poisson distribution

$$P = \exp(-V/v) \frac{V^i}{v^i} \frac{1}{i!} \tag{6}$$

where $v = V_i/\beta$ (V_i = inclusion volume) is the mean solid volume surrounding the inclusion 0. The probability of finding the centre of the $(i+1)$-th neighbouring inclusion in the additional volume dV is given by

$$\tilde{P} = \exp(-V/v) \frac{V^i}{v^i} \frac{1}{i!} \frac{dV}{v}. \tag{7}$$

Replacing v by $4\pi a^3 \alpha/3\beta$ and V by $4\pi(r \cdot a)^3/3$, where r is the distance from the centre of the inclusion 0, normalized by the half axis a, the probability density $P_i dr$ of finding the centre of the i-th neighbouring inclusion in the interval $[r, r+dr]$ is given by

$$P_i dr = \exp\left(-\frac{r^3 \beta}{\alpha} \right) \frac{1}{r} \left(\frac{r^3 \beta}{\alpha} \right)^i \frac{3}{(i-1)!} dr. \tag{8}$$

In addition to the distances between neighbouring inclusions, the inclusion shapes will influence the probability of connection or overlapping. Assuming two inclusions with a distance r between their centre points (see Fig. 1), this probability P_r is calculated numerically for different aspect ratios for the range $0 < r < 2$ by integrating a function f (which equals 1 for the case of overlapping, else being 0) over all possible orientations of the two inclusions. The probability that the inclusion 0 overlaps with *any* of its neighbours (i.e. the degree of interconnection ζ) is finally given by

$$\zeta = 1 - \prod_{i=1}^{k} [1 - P_i'(\beta)] \tag{9}$$

where

$$P_i'(\beta) = \int_0^2 P_r(r) P_i(r, \beta) dr. \tag{10}$$

The product in Eq. (9) has to be extended over all k inclusions whose distance is smaller than 2.

The results for ζ as a function of melt fraction and aspect ratio are shown qualitatively in Fig. 2a and quantitatively in Fig. 2b. The curve for $\zeta = 99.5\%$ corresponds to melt fractions and aspect ratios leading to a vanishing shear modulus according to the film model of O'Connell and Budiansky (1977). For films, the melt fraction and aspect ratio can be combined by one pa-

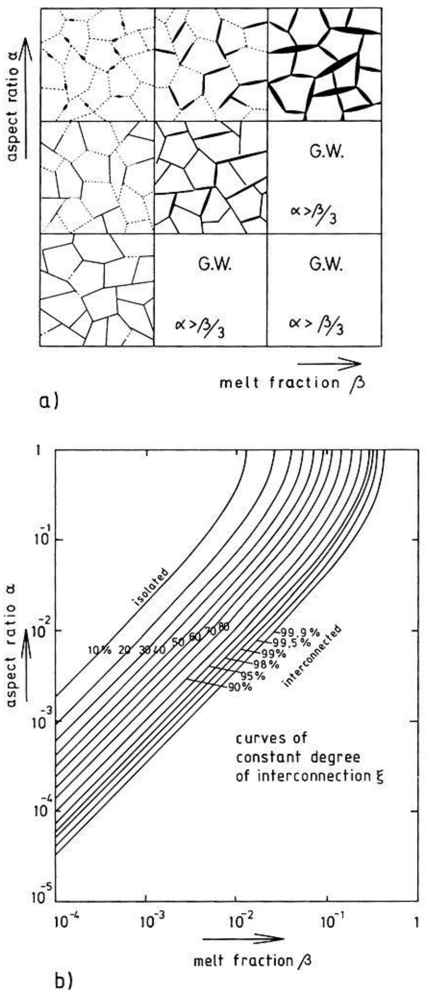

Fig. 2. a Illustration of the variable degree of interconnection for spheroidal inclusions as a function of melt fraction β and aspect ratio α. The fields *G.W.* correspond to melt fractions greater than β_c [see relation (4)] representing complete grain boundary wetting. **b** Curves of constant degree of interconnection ζ for statistically distributed geometrically similar spheroidal inclusions. The numbers beside the curves give ζ, the total probability of overlapping with neighbouring inclusions

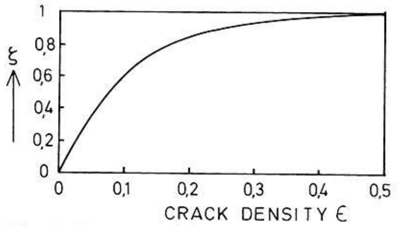

Fig. 3. Degree of interconnection ζ as a function of the crack density ε for films

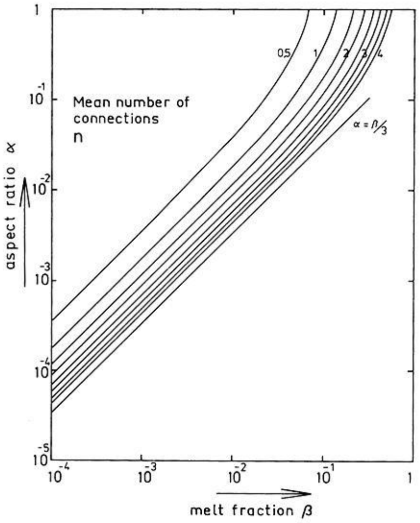

Fig. 4. Curves of constant n, the average number of connections (i.e. overlaps) with neighbouring inclusions for statistically distributed geometrically similar inclusions

rameter, the crack density ε (O'Connell and Budiansky, 1974)

$$\varepsilon = \frac{3}{4\pi}\frac{\beta}{\alpha}. \tag{11}$$

The degree of interconnection as a function of this crack density is shown in Fig. 3.

To determine the mean number of neighbouring inclusions with a direct connection to the considered inclusion, the probabilities P_i' [Eq. (10)] have to be summed over the k inclusions having the potential of overlapping at all or certain orientations

$$n(\beta) = \sum_{i=1}^{k} P_i'(\beta). \tag{12}$$

Figure (4) shows n as a function of α and β. As a comparison, the line $\alpha = \beta/3$ shows a possible critical melt fraction according to the relation (4), above which the loss of the shear strength has to be expected. The function $n(\alpha, \beta)$ can be approximated by a simple semi-empirical formula showing a standard deviation of about 2%:

$$n(\alpha, \beta) \simeq (c_1 - c_2/\alpha)\beta \tag{13}$$

with $c_1 = 5.65$ and $c_2 = 1.72$.

Discussion and conclusion

As a main result it was found that the transition from isolated ($\zeta < 10\%$) to interconnected ($\zeta > 90\%$) inclusions covers more than a decade of the melt fraction (Fig. 2b) or a range from 0.01 to 0.25 in the crack density (Fig. 3). Such crack densities correspond to a decrease of the unrelaxed (relaxed) shear modulus of a few percent to about 25% (40%) (O'Connell and Budiansky, 1977). Thus, in regions of a moderate decrease of seismic velocities an incomplete degree of interconnection might be important if melt occurs in films or pockets. As was shown by Schmeling (1985, 1986), the seismic absorption due to melt squirt and the electrical conductivity would be lower than those determined e.g. by O'Connell and Budiansky (1977) and Shankland et al. (1981) who assumed complete interconnection.

The function $n(\alpha, \beta)$ (Fig. 4) has another important implication for the threshold probability of a least one continuously connected liquid path through the material. Using percolation theory (Vyssotsky et al., 1961), Schmeling (1986) estimated this critical n-value to range between 0.75 and 1.5. This corresponds to a crack density between 0.1 and 0.2, implying that for smaller crack densities conduction is mainly controlled by the solid phase.

It should be emphasized that the model presented here is highly idealistic. It assumes ellipsoidal melt inclusions or films. Superpositions of different melt geometries were not considered. In nature, however, melt films are expected to develop by migration of melt from grain corners or edges into the grain faces. Furthermore, the system of grain faces in a polycrystalline material is principally different from a purely statistical distribution of surfaces. Nevertheless, by keeping these deficiencies of the model in mind the main principle conclusions should still be applicable to partially molten systems in which the melt occurs either in films or in melt pockets.

Acknowledgements. Financial support from the Deutsche Forschungsgemeinschaft under grant number Be 299/59 is gratefully acknowledged.

References

Arzi, A.A.: Fusion kinetics, water pressure, water diffusion and electrical conductivity in melting rock, interrelated. J. Petrol. **19**, 153–169, 1978

Berckhemer, H., Kampfmann, W., Aulbach, E., Schmeling, H.: Shear modulus and Q of forsterite and dunite near partial melting from forced oscillation experiments. Phys. Earth Planet. Inter. **29**, 30–41, 1982

Bruner, W.M.: Comment on "Seismic velocities in dry and saturated cracked solids" by R.J. O'Connell and B. Budiansky. J. Geophys. Res. **81**, 2573–2576, 1976

Chelidze, T.L.: Structure-sensitive physical properties of partially melted rocks. Phys. Earth Planet. Inter. **17**, P41–P46, 1978

Hermance, J.F.: The electrical conductivity of materials containing partial melts: a simple model from Archie's Law. Geophys. Res. Lett. **6**, 613–616, 1979

Honkura, Y.: Partial melting and electrical conductivity anomalies beneath the Japan and Philippine Seas. Phys. Earth Planet. Inter. **10**, 128–134, 1975

Kirkpatrick, S.: Percolation and conduction. Rev. Mod. Phys. **45**, 574–588, 1973

Mavko, G.M.: Velocity and attenuation in partially molten rocks. J. Geophys. Res. **85**, 5173–5189, 1980

Mavko, G.M., Nur, A.: Melt squirt in the asthenosphere. J. Geophys. Res. **80**, 1444–1448, 1975

O'Connell, R.J., Budiansky, B.: Seismic velocities in dry and saturated cracked solids. J. Geophys. Res. **79**, 5412–5426, 1974

O'Connell, R.J., Budiansky, B.: Viscoelastic properties of fluid-saturated cracked solids. J. Geophys. Res. **82**, 5719–5735, 1977

Schmeling, H.: Numerische Modelle über den Einfluß partieller Schmelze auf elastische, anelastische und elektrische Eigenschaften von Gesteinen mit Anwendung auf Labordaten und die Asthenosphäre. Dissertation, 268 S., Inst. für Meteorologie und Geophysik, Frankfurt/M., 1983

Schmeling, H.: Numerical models on the influence of partial melt on elastic, anelastic, and electric properties of rocks. Part I: Elasticity and anelasticity. Phys. Earth Planet. Inter. **41**, 34-57, 1985

Schmeling, H.: Numerical models on the influence of partial melt on elastic, anelastic, and electric properties of rocks. Part II: Electrical conductivity. Phys. Earth Planet. Inter., 1986 (in press)

Schopper, J.R.: A theoretical investigation on the formation factor/permeability/porosity relationship using a network model. Geophys. Prosp. **14**, 301–341, 1966

Shankland, T.J., Waff, H.S.: Conductivity in fluid-bearing rocks. J. Geophys. Res. **79**, 4863–4868, 1974

Shankland, T.J., O'Connell, R.J., Waff, H.S.: Geophysical constraints on partial melt in the upper mantle. Rev. Geophys. Space Phys. **19**, 394–406, 1981

Van der Molen, I., Paterson, M.S.: Experimental deformation of partially-melted granite. Contrib. Mineral. Petrol. **70**, 299–318, 1979

Vyssotsky, V.A., Gordon, S.B., Frisch, H.L., Hammersley, J.M.: Critical percolation probabilities (bond problem). Phys. Rev. **123**, 1566–1567, 1961

Waff, H.S.: Theoretical considerations of electrical conductivity in a partially molten mantle and implications for geothermometry. J. Geophys. Res. **79**, 4003–4010, 1974

Waff, H.S., Bulau, J.R.: Equilibrium fluid distribution in an ultramafic partial melt under hydrostatic stress conditions. J. Geophys. Res. **84**, 6109–6114, 1979

Walsh, J.B.: New analysis of attenuation in partially melted rock. J. Geophys. Res. **74**, 4333–4337, 1969

Received September 16, 1985
Accepted January 6, 1986

J Geophys (1986) 59:146–147

Journal of Geophysics

Book reviews

Hurtig E., Stiller H. (Hrsg.): Erdbeben und Erdbebengefährdung. Akademie-Verlag, Berlin, 328 S., 158 Abb., 25 Tab., 1984 (deutsch)

Das vorliegende Buch gibt einen umfassenden Überblick über das Phänomen Erdbeben, sowie über Probleme der Erdbebengefährdung. Dabei stehen überwiegend seismologische Aspekte im Vordergrund. Das Buch ist das Werk eines Teams von zwölf Autoren des Zentralinstituts für Physik der Erde der Akademie der Wissenschaften der DDR. E. Hurtig und H. Stiller haben als Verfasser und Herausgeber durch ihre Überarbeitung eine weitgehende Homogenisierung in der Darstellung des Stoffes erreicht, ohne daß die spezielle Kenntnis und Neigung des Einzelautors zu kurz kommt. Insofern unterscheidet sich dieses Buch wohltuend von einer bloßen Sammlung von Fachartikeln. Die einzelnen Kapitel können jedoch trotz dieser Integration unabhängig voneinander gelesen werden.

Kapitel 2 bis 7 behandeln die Entwicklung der Seismologie, seismische Wellen, Seismographen, Auswertung von Seismogrammen, Seismizität und Tektonik, sowie Herdmechanismen und Herdparameter. Der Schwerpunkt liegt meiner Ansicht nach jedoch eher im zweiten Teil: Seismische Gefährdung (Kapitel 8), induzierte Seismizität (Kapitel 9) und Erdbebenvorhersage (Kapitel 10).

Das Buch kann dem Fachmann und einem fortgeschrittenen Studenten mit entsprechendem Interesse als Nachschlage- und Arbeitsbuch für Erdbeben-Seismologie, sowie als Einstieg in die Spezialliteratur dienen. Im Detail kann es jedoch weder ein Lehrbuch noch die Originalliteratur ersetzen. Auch als populärwissenschaftliche Einführung für den Laien ist es nicht zu empfehlen, wohingegen der naturwissenschaftlich vorgebildete und an Detailfragen interessierte Nicht-Fachmann durchaus angesprochen wird.

Die Autoren verzichten zwar generell auf theoretische Ableitungen in Lehrbuchcharakter und beschränken sich im Formelwerk auf das Wesentlichste, betonen aber durchweg den mathematischen und den quantitativen Aspekt des Stoffes. Bemerkenswert sind häufige tabellarische Aufzählungen und die große Zahl instruktiver Abbildungen. In der Darstellung klassischer Methoden und Erkenntnisse wurde eine weitgehende Vollständigkeit erreicht. Diese Themen werden auch etwas ausführlicher behandelt, wohingegen die neuere und neueste Thematik eher skizziert ist. Die Fallstudien und Erdbebenbeispiele aus dem Gebiet der DDR sind trotz der relativ geringen Seismizität der DDR instruktiv und dem Gesamtcharakter des Buches angemessen. Besonders hervorheben möchte ich die extensive Sichtung der Originalliteratur.

Dagegen halte ich die folgenden Punkte für verbesserungsfähig: Ohne den generellen Übersichtscharakter zu verlieren, könnte man da, wo auf einzelne Themen näher eingegangen wird, durchaus konsequent, präzieser sein. Dies betrifft etwa Formeln, Berechnungsvorschriften und zum Teil auch die Abbildungen. Eine noch stärkere Betonung des quantitativen Aspekts würde somit im Einzelfall ein direkte Anwendung ermöglichen und den Wert des Buches als Arbeitsbuch für Seismologen wesentlich erhöhen. Um das Gesamtthema weiter abzurunden, könnte ein Kapitel über vulkanische Erdbeben aufgenommen werden. Bei einer Überarbeitung sollte auch das Stichwortverzeichnis erweitert, sowie die bedauerlicherweise noch enthaltenen Druckfehler verbessert werden.

Insgesamt ist diesem Buch dann eine weite Verbreitung zu wünschen.

W. Bruestle

Arnett, W.D., Truran, J.W. (eds.): Nucleosynthesis: challenges and developments. Proceedings of a Conference on Nucleosynthesis held at Yerkes Observatory in 1983. University of Chicago Press, Chicago, pp. 308, 1985

This volume, which was dedicated to William A. Fowler in honor of his sharing the 1984 Nobel Prize in Physics, is an excellent summary of our present understanding of where and how elements are synthesized in astronomical environments. However, as with most proceedings, the presentation and content are for the near-specialist and not the casual reader. For those with some background in the material I recommend first the article by Steigman on "primordial" element production in the Big Bang. It looks as if nucleosynthesis of deuterium, helium-3 and -4, and lithium-7 from an original hot bath of hydrogen is well understood and fits the observations of abundances of those elements as seen today. Of special interest to the geophysicist might be the paper by Schramm which discusses the problem of isotopic "anomalies" in meteoritic inclusions, cosmic rays, or in the tenuous gas comprising the medium between the stars. Anomalies here means deviations from a baseline defined by the composition of carbonaceous chondrites which, presumably, have seen the least chemical processing of any material in the solar system. The question that arises quite naturally, and is the one discussed by Schramm, is whether solar system material is really representative of material in our Galaxy, or is the solar system itself anomalous in some respects.

Most of the other papers in this volume discuss either the nuclear physics needed to compute thermonuclear reaction rates in stars or the Big Bang, or the processes of quiet or explosive stellar evolution which induce nucleosynthesis. Again, the reader should have some background before attempting to read these. All articles are by respected authorities in the field.

The layout and price of the book are acceptable, although an index is not included.

C.J. Hansen

Saltzman, B. (ed.): Advances in geophysics. Academic Press, Orlando, Florida, Vol. 26, 349 p., $ 62.–, 1984

This volume consists of four review articles:

1. Structure of the core and lower mantle (D.E. Loper)
2. Pre-Pleistocene Paleoclimates: The geological and paleontological evidence; modeling strategies, boundary conditions, and some preliminary results (C.R. Lloyd)
3. Climate model simulations of CO_2-induced climate Change (M.E. Schlesinger)

4. Retrieval of worldwide precipitation and allied parameters from satellite microwave observations (M.S.V. Rao).

The recent progress in the construction of different models of the earth's deep interior is described in the first contribution, particularly for the inner and outer core and the lower mantle. The author discusses the question of the best explanation for the energy source for the geodynamo and the implications for the structure and thermal evolution of the earth.

After these general considerations on the thermal history of the earth, in the second contribution the reader's interest is focused on the Pre-Pleistocene paleoclimates. The author reviews the geological and paleontological evidences for the climatic history of the last 100 m.y. Findings from plate tectonics and their effects on the shape of the oceans are used for the interpretation of the changes of climate, e.g. the formation of the Antarctic ice sheets. The effects of changes of the dynamic properties of the earth like earth rotation, and the chemical contents of the atmosphere are discussed, too.

The third contribution contains the climate model simulation of CO_2-induced climatic changes. The current issues are formulated with concern to the study of possible changes by the physical method, that is, by the use of mathematical climate models. The changes in temperature, precipitation rate, and soil moisture induced by double and quadrupled CO_2 concentrations are simulated by atmospheric general circulation models (CGM) coupled to two different models of the ocean.

The last article reviews two of the major parameters in atmospheric and hydrospheric investigation, rainfall and sea ice. Satellite-born microwave radiometers provide a unique method of estimating these variables on a global scale. The significance of the data and the limitations, as well as the vast capabilities for future observations are discussed.

Although the four articles are independent of each other, they complement one another. Thus, considerations for the thermal history of the earth, the findings for the climatic development of the last 100 m.y., the mathematical modeling of recent climatic changes, as well as newest developments in instrumentation are put together to form a very interesting volume. Many references and carfully drawn pictures are of special value. Therefore one can recommend this volume to the specialist as well as to a general audience.

G. Jentzsch

J Geophys (1986) 59:149-156

Journal of Geophysics

Original investigations

Complete seismogram synthesis for transversely isotropic media

B. Mandal and B.J. Mitchell

Department of Earth and Atmospheric Sciences, Saint Louis University, P.O. 8099, Laclede Station,
Saint Louis, MO 63156, USA

Abstract. The response at the surface of a layered transversely isotropic medium due to a buried dislocation source can be expressed by using propagator matrices and discrete wavenumber summation. These operations produce complete seismograms for earth-quake or explosion sources which include all body- and surface-wave phases for this specialized anisotropic structure. In order to test the numerical procedures, synthetic seismograms at near distances for an isotropic model are compared with those generated by other methods. The agreement is found to be satisfactory in all cases. Comparisons of synthetic seismograms for anisotropic models having a small degree of anisotropy with similar but isotropic models, show that significant differences in travel times, amplitudes and wave forms can be caused by the anisotropy.

Key words: Anisotropy – Transverse isotropy – Propagator matrices – Wavenumber summation – Synthetic seismogram

Introduction

In recent years, increasing numbers of observational studies have required interpretations in terms of anisotropic elastic properties. These have included regional studies (e.g. Schlue and Knopoff, 1977; Yu and Mitchell, 1979; Cara et al., 1980) and global studies (e.g. Anderson and Dziewonski, 1982; Tanimoto and Anderson, 1984) of seismic surface waves, observations of azimuthal variations of body-wave velocities (e.g. Bamford and Crampin, 1977; Kogan, 1984) and observations of shear-wave splitting (e.g. Bezgodkov and Yegorkina, 1984). These and other studies have provided strong support for the existence of wide-spread anisotropy with consistent orientation in at least some regions of the earth as first proposed by Hess (1964). Such anisotropy may be caused by a variety of mechanisms including preferred crystal orientation, aligned cracks and rheological alignments.

The theoretical formulation required for computing surface-wave velocities in stratified anisotropic media which is transversely isotropic with a vertical axis of symmetry was developed by Anderson (1961) and Harkrider and Anderson (1962), and in general anisotropic media by Crampin (1970) and Crampin and Taylor (1971). It has also been possible to compute synthetic seismograms for body waves in general anisotropic media (Keith and Crampin, 1977). Synthesis schemes have also been developed for general anisotropy in stratified media (Booth and Crampin, 1983; Fryer and Frazer, 1984) by using Kennett's (1974) reflectivity approach.

This study presents a method for computing complete seismograms, which include all phases which traverse an anisotropic medium which is transversely isotropic with a vertical axis of symmetry. This type of anisotropy has been observed in some sediments (Robertson and Corigan, 1983) and may be expected to occur in planar igneous bodies or floating ice-sheets. It has also been proposed that this type of anisotropy occurs in the asthenosphere (Schlue and Knopoff, 1977) where molten inclusions have been modeled as flat, penny-shaped cracks.

We begin by using expressions from Takeuchi and Saito (1972) for surface-wave displacements and stresses in cylindrical coordinates. Those equations are based on an earlier formulation by Alterman et al. (1959). In the present paper we assume that the earth is composed of transversely isotropic layers overlying a half-space which may also be transversely isotropic. We compute the response of the medium to a point dislocation source using propagator matrices (Gilbert and Backus, 1966) and discrete wavenumber integration (Bouchon, 1981). We verify our computations of ground motion time history by comparing results for an isotropic model with results obtained using existing methods.

Theory

We define our model as $N-1$ homogeneous, anisotropic (transversely isotropic with vertical axis of symmetry) or isotropic layers overlying a half-space. With this symmetry, each anisotropic layer is characterized by five elastic constants A, C, L, N, F as defined by Love (1927, p. 160) and density ρ. A and C are related to dilatational wave velocity and L and N to shear wave velocity. Three kinds of plane waves corresponding to P, SV, and SH waves in isotropic media can be transmitted independently (Matuzawa, 1943). The velocities of such waves are as follows, for horizontal trans-

---

Offprint requests to: B.J. Mitchell

mission:

$$\begin{aligned} &\frac{A}{\rho}=\alpha_H^2 \quad \text{for } P \text{ waves} \\ &\frac{L}{\rho}=\beta_V^2 \quad \text{for } SV \text{ waves} \\ &\frac{N}{\rho}=\beta_H^2 \quad \text{for } SH \text{ waves} \end{aligned} \tag{1}$$

and for vertical transmission:

$$\begin{aligned} &\frac{C}{\rho}=\alpha_V^2 \quad \text{for } P \text{ waves} \\ &\frac{L}{\rho}=\beta_V^2 \quad \text{for } S \text{ waves.} \end{aligned} \tag{2}$$

For the isotropic case, $A=C=\lambda+2\mu$, $L=N=\mu$ and $F=\lambda$ (Love, 1927) where λ and μ are Lamé's constants. A cylindrical coordinate system (r, φ, z) is chosen with the origin on the free surface just above the source, with the z-axis taken positive downward.

We have rearranged Takeuchi and Saito's (1972) Eqs. 46 and 62, for SH and $P-SV$ cases, respectively, to obtain

$$\begin{aligned} \frac{df_1}{dz}&=-kf_2+\frac{1}{L}f_4 \\ \frac{df_2}{dz}&=\frac{kF}{C}f_1+\frac{1}{C}f_3 \\ \frac{df_3}{dz}&=-\omega^2\rho f_2+kf_4 \\ \frac{df_4}{dz}&=\left[k^2\left(A-\frac{F^2}{C}\right)-\omega^2\rho\right]f_1-\frac{kF}{C}f_3 \\ \frac{df_5}{dz}&=\frac{1}{L}f_6 \\ \frac{df_6}{dz}&=(k^2N-\omega^2\rho)f_5 \end{aligned} \tag{3}$$

where f_1, f_2 and f_5 are variables proportional to radial, vertical and transverse components of displacement and f_3, f_4 and f_6 are proportional to vertical, radial and tangential components of stress, respectively. k and ω represent horizontal wavenumber and angular frequency, respectively.

Equation (3) in matrix form

$$\frac{df}{dz}=\mathbf{Q}(\mathbf{z})f(z) \tag{4}$$

is a system of n linear homogeneous ordinary differential equations for the functions $f_i(z)$, $i=1, 2, \ldots, n$. Here $\mathbf{Q}(\mathbf{z})$ is a matrix representing material properties. An essential requirement of the propagator matrix method is that these properties are uniform within each layer (Gilbert and Backus, 1966). The solution of Eq. (4) is, using Sylvester's theorem,

$$\begin{aligned} f(z)&=e^{(z-z_0)\mathbf{Q}(\mathbf{z})}f(z_0) \\ &=af(z_0) \end{aligned} \tag{5}$$

where z_0 is a reference depth. The function $e^{(z-z_0)\mathbf{Q}(\mathbf{z})}=a$ is called the matricant, matrizant or layer matrix for a homogeneous medium. Using the familiar $\mathbf{E}$ matrix (Haskell 1953, Harkrider 1964), the most general solution of Eq. (4) is

$$f=\mathbf{E}\Lambda\mathbf{K} \tag{6}$$

and

$$a=\mathbf{E}\Lambda\mathbf{E}^{-1} \tag{7}$$

where $\mathbf{E}$ is the eigenvector matrix of $\mathbf{Q}(\mathbf{z})$ (Appendix A), Λ is a diagonal matrix which explains the phase variation along the depth direction and consists of eigenvalues of $\mathbf{Q}(\mathbf{z})$, and $\mathbf{K}$ is a constant vector which consists of coefficients of both up-going and down-going waves. Expressions for these quantities are

$$\Lambda=\operatorname{diag}\left[e^{v_1z}, e^{v_2z}, e^{-v_1z}, e^{-v_2z}, e^{v_3z}, e^{-v_3z}\right] \tag{8}$$

where v_1, v_2 and v_3 are eigenvalues of $\mathbf{Q}(\mathbf{z})$, and

$$\mathbf{K}=[\mathbf{A}'', \mathbf{B}'', \mathbf{A}', \mathbf{B}', \mathbf{C}'', \mathbf{C}']^{\mathbf{T}}. \tag{9}$$

In this expression $''$ refers to up-going waves and $'$ refers to down-going waves. v_1 and v_2 are roots of the equation

$$v^4-\left[\frac{k^2A-\omega^2\rho}{L}+\frac{k^2L-\omega^2\rho}{C}-\frac{k^2(F+L)^2}{CL}\right]v^2 +\frac{(k^2L-\omega^2\rho)(k^2A-\omega^2\rho)}{CL}=0 \tag{10}$$

and v_3 is obtained from

$$v_3^2=\frac{Nk^2-\omega^2\rho}{L}. \tag{11}$$

For the isotropic case, there are only two eigenvalues

$$\begin{aligned} v_\alpha^2&=k^2-\frac{\omega^2}{\alpha^2} \\ v_\beta^2&=k^2-\frac{\omega^2}{\beta^2} \end{aligned} \tag{12}$$

where α, β are P-, S-wave velocities respectively.

The derivation of the relation between surface displacements and wave coefficients in the half-space, in terms of $\mathbf{K}_N$ (N stands for half-space) is given for an isotropic medium by Wang and Herrmann (1980) and Wang (1981) as

$$\mathbf{K}_N=XS+R(f)_1 \tag{13}$$

where

$$\begin{aligned} X&=E_N^{-1}\alpha_{N-1}\ldots\alpha_m(d_m-h_m) \\ Z&=\alpha_m(h_m)\ldots\alpha_1 \\ R&=XZ=E_N^{-1}\alpha_{N-1}\ldots\alpha_1. \end{aligned} \tag{14}$$

S is the source vector for a double-couple or explosion source (Appendix B) and $(f)_1$ is the surface value of f. d_m is the thickness of the m-th layer containing the source with depth h_m beneath the $m-1$ interface. At the free surface, stresses will vanish, yielding

$$(f)_1 = [f_1, f_2, 0, 0, f_5, 0]^{\mathrm{T}}. \tag{15}$$

In the half-space, there are no up-going waves, so

$$\mathbf{K}_N = [0, 0, \mathbf{A}'_N, \mathbf{B}'_N, 0, \mathbf{C}'_N]^{\mathrm{T}}. \tag{16}$$

The function f on the free surface becomes

$$\begin{pmatrix} f_1 \\ f_2 \end{pmatrix}_1 = \frac{(-1)}{R|_{12}^{12}} \begin{bmatrix} R_{22} & -R_{12} \\ -R_{21} & R_{11} \end{bmatrix} \cdot \begin{bmatrix} X_{1i} & S_i \\ X_{2i} & S_i \end{bmatrix} \qquad i=1, \ldots, 4 \tag{17}$$

$$(f_5)_1 = (-1)\frac{X_{5i}S_i}{R_{55}} \qquad i=5, 6. \tag{18}$$

For numerical accuracy in computation, relation (17) can be written as a compound matrix ($R|_{kl}^{ij} = R_{ik}R_{jl} - R_{il}R_{jk}$),

$$\begin{pmatrix} f_1 \\ f_2 \end{pmatrix}_1 = \frac{1}{R|_{12}^{12}} \begin{pmatrix} -S_i & X|_{ij}^{12} & Z_{j2} \\ S_i & X|_{ij}^{12} & Z_{j1} \end{pmatrix} \tag{19}$$

where from (14) and Dunkin (1965),

$$\begin{aligned} X|_{ij}^{12} &= E_N^{-1}|_{mn}^{12}\, a_{N-1}|_{op}^{mn} \ldots a_{m+1}|_{st}^{qr}\, a_m|_{ij}^{st} \\ R|_{12}^{12} &= E_N^{-1}|_{mn}^{12}\, a_{N-1}|_{op}^{mn} \ldots a_2|_{st}^{qr}\, a_1|_{12}^{st}. \end{aligned} \tag{20}$$

These matrices are listed in Appendix A. The advantages of using compound matrices have been discussed in several previous publications (Knopoff, 1964; Dunkin, 1965; Gilbert and Backus, 1966). We have found that the use of analytical expressions for compound matrices is more stable than element multiplication for computations.

Integral solution and times histories

For a point source, the free surface displacements are:

$$u_z(r, \varphi, 0, \omega) = \frac{1}{2\pi} \sum_{m=-\infty}^{\infty} \int_0^{\infty} Y_k^m(r, \varphi) f_2(\omega, k)\, k\, dk, \tag{19a}$$

$$u_r(r, \varphi, 0, \omega) = \frac{1}{2\pi} \sum_{m=-\infty}^{\infty} \int_0^{\infty} \left[\frac{\partial Y_k^m}{\partial r} f_1(\omega, k) + \frac{1}{r}\frac{\partial Y_k^m}{\partial \varphi} f_5(\omega, k)\right] dk, \tag{19b}$$

$$u_\varphi(r, \varphi, 0, \omega) = \frac{1}{2\pi} \sum_{m=-\infty}^{\infty} \int_0^{\infty} \left[\frac{1}{r}\frac{\partial Y_k^m}{\partial \varphi} f_1(\omega, k) - \frac{\partial Y_k^m}{\partial r} f_5(\omega, k)\right] dk \tag{19c}$$

where $Y_k^m(r, \varphi) = J_m(kr)\, e^{im\varphi}$ $m = 0, \pm 1, \pm 2, \ldots$ (Takeuchi and Saito, 1972).

For a buried double-couple source without moment, with unit vector $\mathbf{n} = (n_1, n_2, n_3)$ normal to the fault and $v = (v_1, v_2, v_3)$ in the direction of the force (Haskell, 1963; Saito, 1967; Takeuchi and Saito, 1972), the Fourier transformed displacements at the free surface at a distance r from the origin (Wang and Herrmann, 1980; Herrmann and Wang, 1985) are

$$\begin{aligned} &u_z(r, 0, \omega) \\ &= ZSS[(v_1 n_1 - v_2 n_2)\cos 2\varphi + (v_1 n_2 + v_2 n_1)\sin 2\varphi] \\ &\quad + ZDS[(v_1 n_3 + v_3 n_1)\cos\varphi + (v_2 n_3 + v_3 n_2)\sin\varphi] \\ &\quad + ZDD[v_3 n_3], \end{aligned} \tag{20a}$$

$$\begin{aligned} &u_r(r, 0, \omega) \\ &= RSS[(v_1 n_1 - v_2 n_2)\cos 2\varphi + (v_1 n_2 + v_2 n_1)\sin 2\varphi] \\ &\quad + RDS[(v_1 n_3 + v_3 n_1)\cos\varphi + (v_2 n_3 + v_3 n_2)\sin\varphi] \\ &\quad + RDD[v_3 n_3], \end{aligned} \tag{20b}$$

$$\begin{aligned} &u_\varphi(r, 0, \omega) \\ &= TSS[(v_1 n_1 - v_2 n_2)\sin 2\varphi - (v_1 n_2 + v_2 n_1)\cos 2\varphi] \\ &\quad + TDS[(v_1 n_3 + v_3 n_1)\sin\varphi - (v_2 n_3 + v_3 n_2)\cos\varphi]. \end{aligned} \tag{20c}$$

In the notations *ZDD*, *ZDS*, *ZSS*, *RDD*, *RDS*, *RSS*, *TDS* and *TSS*, the first letter refers to component (*Z* - vertical, *R* - radial and *T* - tangential) and the last two letters refer to one of the three fundamental shear dislocations of Harkrider (1976). *DD* refers to 45° dip-slip, *DS* to 90° dip-slip and *SS* to pure strike-slip motion.

Integral representations of the displacement in the frequency domain in Eqs. 19 and 20 are summarized in general form as

$$I_m = \int_0^{\infty} F(k, \omega)\, J_m(kr)\, dk \qquad m = 0, 1, 2 \tag{21}$$

where the kernel $F(k, \omega)$ (Appendix B) is a function of wavenumber, frequency, source depth and layer parameters. The wavenumber integration (21) can be evaluated by a discrete wavenumber summation described by Bouchon (1981). Yao and Harkrider (1983) discussed details of this technique. The wavenumber sample interval (dk) and total number of samples depend on the distance, frequency, the depth of the source and the layer parameters. To obtain a complete seismogram, the wavenumber summation method requires very dense wavenumber sampling. This requires extensive computation time and large amounts of computer memory. In order to efficiently use time and space, sampling may be optimized with the distance of computation, frequency, layer parameters and depth of the source. Some criteria for deciding on the wavenumber sampling interval (dk) had been discussed by Bouchon (1981).

To avoid the influence of singularities of the kernel $F(k, \omega)$, two techniques can be used (Bouchon, 1981). Frequency can be made complex or attenuation can be introduced into the computations to make the velocities complex. In the present study, we have chosen the first technique. We later remove the imaginary part of the frequency (damping factor) from the time-domain solution.

The time-domain response, in general is

$$u(t) = \int_{-\infty}^{\infty} S(\omega)\, u(\omega)\, e^{i\omega t}\, d\omega \tag{22}$$

where $S(\omega)$ is the frequency-domain response of the source-time function. In our test cases we have used a

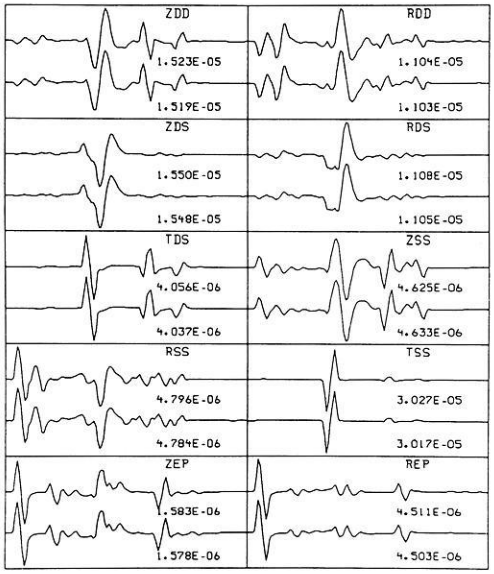

1

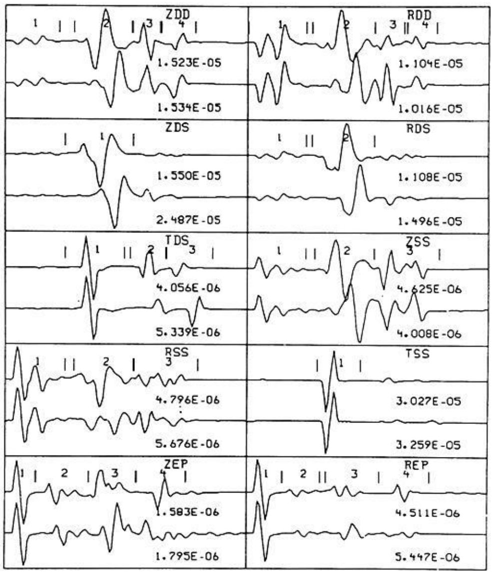

2

Fig. 1. Synthetic seismograms at a distance of 75 km, for a source at a depth of 10 km, using present computations (*upper trace*) and results of Herrmann and Wang (1985) (*lower trace*). Ground velocity is computed over a time interval between 11.30 and 43.05 s. The numerical value adjacent to each trace is the peak ground velocity in units of cm/s. EP refers to an explosion source. Both seismograms are computed for the isotropic model given in Table 1

Fig. 2. Synthetic seismograms at a distance of 75 km, for a source at a depth of 10 km, using methods of this study for an isotropic model (*upper trace*) and an anisotropic model (*lower trace*). Ground velocity is computed over a time interval between 11.30 and 43.05 s

Table 1. Layer parameters for the test models

d (km)	α_H (km/s)	α_V (km/s)	β_V (km/s)	β_H (km/s)	η (km/s)	ρ (gm/cm^3)
Isotropic simple crustal models						
40	6.15	6.15	3.55	3.55	3.552	2.8
	8.09	8.09	4.67	4.67	4.6723	3.3
Anisotropic simple crustal model						
40	6.15	5.8425	3.195	3.55	3.525	2.8
	8.09	8.09	4.67	4.67	4.6723	3.3

where $\eta=\sqrt{\frac{F}{\rho}}$.

parabolic pulse (Herrmann, 1979) as a source-time function.

We used the simple crustal model in Table 1 for testing the program with an isotropic model. This model was used by Herrmann and Wang (1985) and allows us to compare our computational results with those of other methods. The velocity response at a distance of 75 km for a source depth of 10 km and sampling interval of 0.25 s, using present computations (upper trace), are compared with results of Hermann and Wang (1985) (lower trace) in Fig. 1. This comparison shows that our new algorithm provides results which are consistent with other methods for a model with isotropic elastic parameters ($A=C=\lambda+2\mu$, $L=N=\mu$ and $F=\lambda$).

Numerical examples for anisotropic medium

We alter the isotropic crustal model in Table 1 to obtain an anisotropic model on which to perform numerical tests. For the anisotropic model, the velocity of the vertically traveling P wave is decreased by 5% and that of the vertically traveling S wave is decreased by 10% compared to the velocities in the isotropic model. The synthetics obtained for this model are compared to

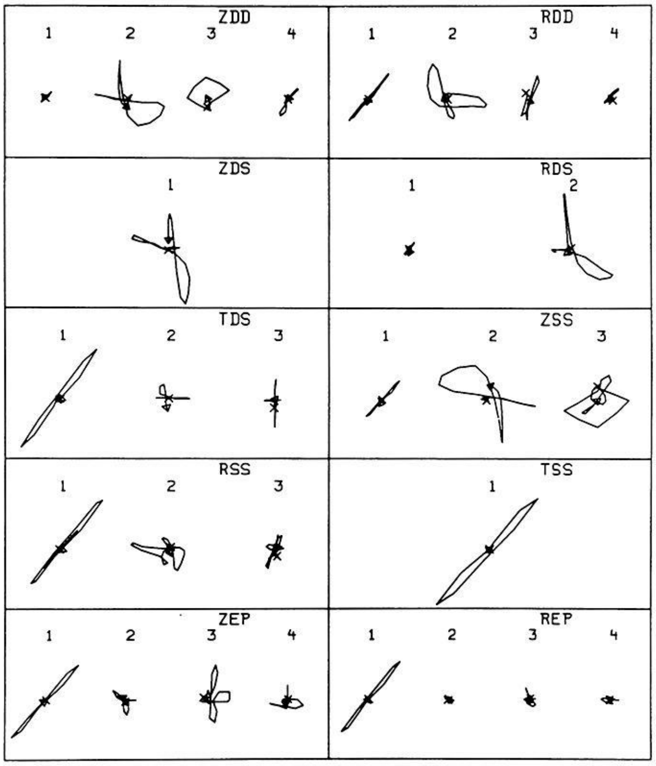

Fig. 3. Particle motion diagrams for different time windows of seismograms in Fig. 2

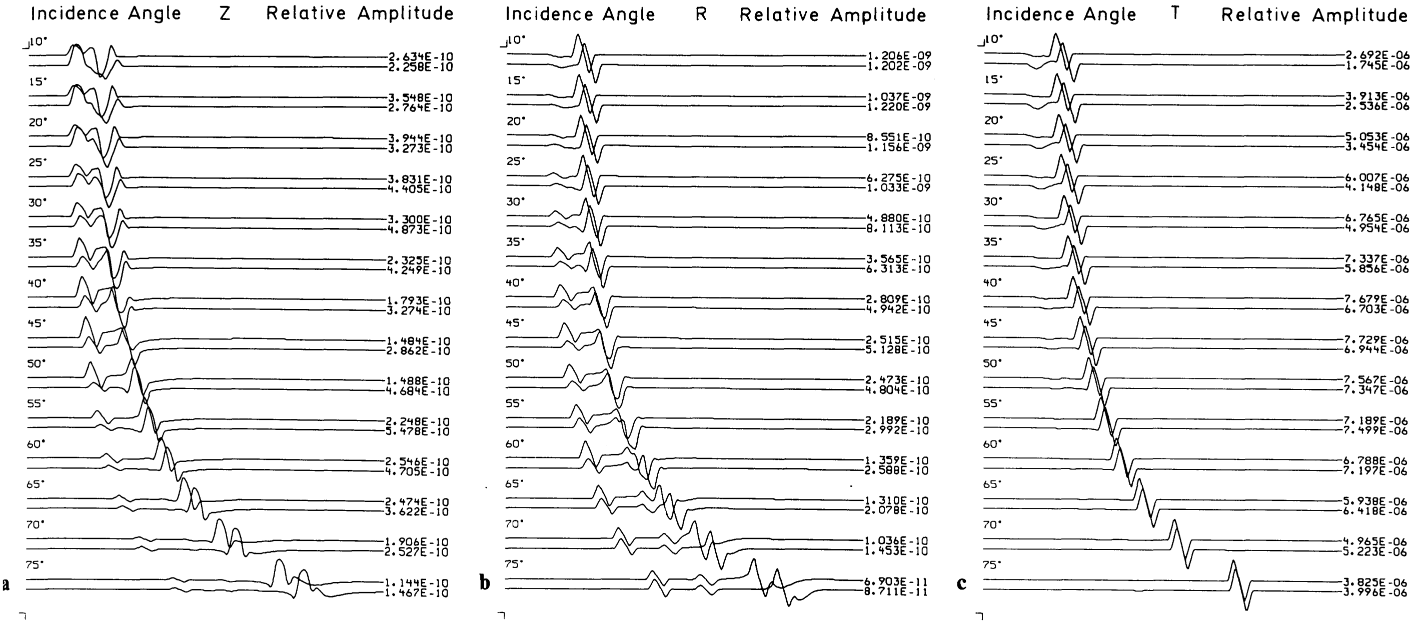

Fig. 4. **a** Vertical-component seismograms at different incidence angles for an isotropic half-space (*upper trace*) and an anisotropic half-space (*lower trace*) from a source buried at a depth of 40 km. A pure vertical strike-slip focal mechanism is used. The duration of each seismogram is 64 s with sampling interval of 0.25 s. The seismograms were recorded at an azimuth of 0° from the strike direction of the source. **b** Radial-component seismograms for the same model and source as those described in Fig. 4a. **c** Transverse-component seismograms for the same model and source as those described in Fig. 4a

those for the isotropic case in Fig. 2. As in Fig. 1, they pertain to a distance of 75 km, a source depth of 10 km and a sampling interval of 0.25 s. The seismograms are plotted adjacent to one another for easy comparison, the upper trace pertaining to the isotropic case and lower trace to the anisotropic case. Notable differences occur in the amplitudes and phases between each pair of seismograms. In the transverse components (*TDS* and *TSS*), the primary *S* phases arrive at the same time because the wave at this distance is traveling nearly horizontally, so the *S*-wave velocity is nearly identical for both the isotropic and anisotropic case. Later phases arrive at different times because of splitting of the shear waves. Interesting phases are observed on the vertical (*ZDD*, *ZDS*, *ZSS*, *ZEP*) and radial (*RDD*, *RDS*, *RSS*, *REP*) components. At this distance the *S* wave arrives later for the anisotropic model and the shape of the seismogram differs from that for the isotropic model.

Figure 3 shows the particle motion for the different time windows in Fig. 2. The horizontal axis represents motion for the isotropic model and the vertical axis for the anisotropic model. From the particle motion plot, we see that the motion for the *P* phases is almost the same even though the velocity variation is 5 %. For the vertical and radial components, the *S* and Rayleigh wave portions of the seismograms (window 2 for *ZDD*, *RDD*, *RDS*, *ZSS* and window 1 for *ZDS* in Figs. 2 and 3) for the isotropic case lead those for the anisotropic case by more than 90°. Notable difference also occur in the amplitudes and times of the later arrivals.

In a general anisotropic medium, the energy traveling in the group-velocity direction does not necessary coincide with the phase-velocity direction (Crampin, 1981). This deviation depends on the type of symmetry in the medium, the type of wave and the propagation direction of the wave. Polarization angles of the various waves give some idea of the nature of the anisotropy, provided that the source or other effects do not cause anomalous particle motion in the observed seismograms.

In a transversely isotropic medium, fundamental-mode waves travel along their phase-velocity direction, but compressional waves are not, in general, parallel to, nor are the shear waves perpendicular to, the phase-velocity direction. For a vertical axis of symmetry, the phase velocity varies with incidence angle. To illustrate the different phenomena in transversely isotropic media, we have computed individual synthetic seismograms at different incidence angles for a pure strike-slip dislocation source in both an isotropic medium and an anisotropic medium. Both models consist of a semi-infinite half-space with the parameters of the upper layer of the model in Table 1. The incidence angle is measured from the downward normal to the surface. Seismograms were computed at 14 different distances with an interval in incidence angle of 5°. All computations were for an azimuth of 0° from a source with a depth of 40 km. With this configuration, both vertically and horizontally polarized shear waves will be present. The seismograms are shown in Fig. 4a–c for vertical, radial and transverse components, respectively. In these figures, the upper trace pertains to the isotropic model and the lower trace to the anisotropic model. For the vertical and radial components, the shear wave is an *SV* wave and for the transverse component it is an *SH* wave. From the figures, *SV* waves in the anisotropic medium appear later than those in the isotropic medium when the wave propagates vertically and horizontally. For the transverse component, the *SH* wave in the anisotropic model arrives substantially later than that in the isotropic model at short distances but comes closer and closer to it as the waves travel more horizontally at larger distances. This phenomenon was observed in near surface shale by Robertson and Corrigan (1983) and has been explained by Crampin (1981) and Peacock and Crampin (1985).

Conclusions

We have developed a method to compute complete synthetic seismograms, including all body and surface waves, generated in a transversely isotropic medium by a dislocation or explosion source. These seismograms can include very high frequencies, thus making it possible to study regional phases in various frequency bands. To obtain a complete seismogram, the wavenumber summation method requires very dense wavenumber sampling. This requires extensive computation time and large amounts of computer memory. In order to efficiently use time and space, sampling may be optimized with the distance of computation, frequency, layer parameters and depth of the source. We have performed these computations using propagator matrices and the discrete wavenumber summation method and have verified the algorithm by comparing results for a simple crustal model with results observed using other isotropic methods. A comparison of time histories of the wave motion for a transversely isotropic model with that predicted for an isotropic model shows that amplitudes and wave forms of both body and surface waves, as well as travel times, can be markedly altered by the presence of anisotropy.

Appendix A: Layer matrices for transversely isotropic media

Notation

ρ = density; ω = frequency; k = wavenumber; v_i, $i=1,2,3$ are eigenvalues as defined in the main text.

$$\gamma_i=\frac{k v_i(F+L)}{\omega^2\rho-k^2L+v_i^2C},$$

$$X_i=Cv_i\gamma_i-kF,$$

$$Y_i=L(v_i+k\gamma_i),$$

$i=1,2$ for P-SV case.

$$\mathbf{a}=\frac{1}{X_2-X_1},$$

$$\mathbf{b}=\frac{1}{Y_1\gamma_2-Y_2\gamma_1},$$

$$P=v_1z;\quad Q=v_2z,$$

$$CP=\cosh P;\quad CQ=\cosh Q,$$

$$SP=\sinh P;\quad SQ=\sinh Q.$$

E matrix:

$$\mathbf{E}=\begin{bmatrix}1&1&1&1&0&0\\ \gamma_1&\gamma_2&-\gamma_1&-\gamma_2&0&0\\ X_1&X_2&X_1&X_2&0&0\\ Y_1&Y_2&-Y_1&-Y_2&0&0\\ 0&0&0&0&1&1\\ 0&0&0&0&Lv_3&-Lv_3\end{bmatrix}$$

$\mathbf{E}^{-1}$ matrix:

$$\mathbf{E}^{-1}=\frac{\mathbf{1}}{\mathbf{2}}\begin{bmatrix}\mathbf{a}X_2&-\mathbf{b}Y_2&-\mathbf{a}&\mathbf{b}\gamma_2&0&0\\ -\mathbf{a}X_1&\mathbf{b}Y_1&\mathbf{a}&-\mathbf{b}\gamma_1&0&0\\ \mathbf{a}X_2&\mathbf{b}Y_2&-\mathbf{a}&-\mathbf{b}\gamma_2&0&0\\ -\mathbf{a}X_1&-\mathbf{b}Y_1&\mathbf{a}&\mathbf{b}\gamma_1&0&0\\ 0&0&0&0&1&\dfrac{1}{Lv_3}\\ 0&0&0&0&1&-\dfrac{1}{Lv_3}\end{bmatrix}$$

a matrix: $\mathbf{E}\Lambda\mathbf{E}^{-1}$

$$a_{11}=\mathbf{a}(X_2CP-X_1CQ)$$
$$a_{12}=\mathbf{b}(Y_1SQ-Y_2SP)$$
$$a_{13}=\mathbf{a}(CQ-CP)$$
$$a_{14}=\mathbf{b}(\gamma_2SP-\gamma_1SQ)$$
$$a_{21}=\mathbf{a}(X_2\gamma_1SP-X_1\gamma_2SQ)$$
$$a_{22}=\mathbf{b}(Y_1\gamma_2CQ-Y_2\gamma_1CP)$$
$$a_{23}=\mathbf{a}(\gamma_2SQ-\gamma_1SP)$$
$$a_{24}=\mathbf{b}\gamma_1\gamma_2(CP-CQ)$$
$$a_{31}=\mathbf{a}X_1X_2(CP-CQ)$$
$$a_{32}=\mathbf{b}(X_2Y_1SQ-X_1Y_2SP)$$
$$a_{33}=\mathbf{a}(X_2CQ-X_1CP)$$
$$a_{34}=\mathbf{b}(X_1\gamma_2SP-X_2\gamma_1SQ)$$
$$a_{41}=\mathbf{a}(X_2Y_1SP-X_1Y_2SQ)$$
$$a_{42}=\mathbf{b}Y_1Y_2(CQ-CP)$$
$$a_{43}=\mathbf{a}(Y_2SQ-Y_1SP)$$
$$a_{44}=\mathbf{b}(Y_1\gamma_2CP-Y_2\gamma_1CQ)$$
$$a_{55}=\cosh v_3z$$
$$a_{56}=\frac{1}{Lv_3}\sinh v_3z$$
$$a_{65}=Lv_3\sinh v_3z$$
$$a_{66}=\cosh v_3z$$

Compound layer matrix:

$$a|^{12}_{12}=a|^{34}_{34}=\mathbf{a}\mathbf{b}[(X_1Y_2\gamma_1+X_2Y_1\gamma_2)CPCQ\\ -(X_1Y_1\gamma_2+X_2Y_2\gamma_1)\\ -(X_1Y_2\gamma_2+X_2Y_1\gamma_1)SPSQ]$$
$$a|^{12}_{13}=a|^{24}_{34}=\mathbf{a}[\gamma_2CPSQ-\gamma_1CQSP]$$
$$a|^{12}_{14}=a|^{23}_{34}=\mathbf{a}\mathbf{b}[\gamma_1\gamma_2(X_2+X_1)(1-CPCQ)\\ +(X_2\gamma_1^2+X_1\gamma_2^2)SPSQ]$$
$$a|^{12}_{23}=a|^{14}_{34}=\mathbf{a}\mathbf{b}[(Y_1\gamma_2+Y_2\gamma_1)(CPCQ-1)\\ -(Y_1\gamma_1+Y_2\gamma_2)SPSQ]$$
$$a|^{12}_{24}=a|^{13}_{34}=\mathbf{b}[\gamma_1CPSQ-\gamma_2CQSP]$$
$$a|^{12}_{34}=\mathbf{a}\mathbf{b}[2\gamma_1\gamma_2(CPCQ-1)-(\gamma_1^2+\gamma_2^2)SPSQ]$$
$$a|^{13}_{12}=a|^{34}_{24}=\mathbf{b}[X_2Y_1CPSQ-X_1Y_2CQSP]$$
$$a|^{13}_{13}=a|^{24}_{24}=CPCQ$$
$$a|^{13}_{14}=a|^{23}_{24}=\mathbf{b}[X_1\gamma_2CQSP-X_2\gamma_1CPSQ]$$
$$a|^{13}_{23}=a|^{14}_{24}=\mathbf{b}[Y_1CPSQ-Y_2CQSP]$$
$$a|^{13}_{24}=-\frac{\mathbf{b}}{\mathbf{a}}SPSQ$$

$$a|_{12}^{14}=a|_{23}^{34}=\mathbf{a}\,\mathbf{b}[Y_1Y_2(X_1+X_2)(CPCQ-1)$$
$$-(X_1Y_2^2+X_2Y_1^2)SPSQ]$$

$$a|_{13}^{14}=a|_{23}^{24}=\mathbf{a}[Y_2\,CPSQ-Y_1\,CQSP]$$

$$a|_{14}^{14}=a|_{23}^{23}=\mathbf{a}\,\mathbf{b}[(X_2Y_1\gamma_2+X_1Y_2\gamma_1)$$
$$-(X_1Y_1\gamma_2+X_2Y_2\gamma_1)\,CPCQ$$
$$+(X_1Y_2\gamma_2+X_2Y_1\gamma_1)SPSQ]$$

$$a|_{23}^{14}=\mathbf{a}\,\mathbf{b}[2Y_1Y_2(CPCQ-1)-(Y_1^2+Y_2^2)SPSQ]$$

$$a|_{12}^{23}=a|_{14}^{34}=\mathbf{a}\,\mathbf{b}[X_1X_2(Y_1\gamma_2+Y_2\gamma_1)(1-CPCQ)$$
$$+(X_2^2Y_1\gamma_1+X_1^2Y_2\gamma_2)SPSQ]$$

$$a|_{13}^{23}=a|_{14}^{24}=\mathbf{a}[X_2\gamma_1\,CQSP-X_1\gamma_2\,CPSQ]$$

$$a|_{14}^{23}=\mathbf{a}\,\mathbf{b}[2X_1X_2\gamma_1\gamma_2(CPCQ-1)-(X_1^2\gamma_2^2+X_2^2\gamma_1^2)SPSQ]$$

$$a|_{12}^{24}=a|_{13}^{34}=\mathbf{a}[X_1Y_2\,CPSQ-X_2Y_1\,CQSP]$$

$$a|_{13}^{24}=-\frac{\mathbf{a}}{\mathbf{b}}\,SPSQ$$

$$a|_{12}^{34}=\mathbf{a}\,\mathbf{b}[2X_1X_2Y_1Y_2(CPCQ-1)-(X_1^2Y_1^2+Y_1^2Y_2^2)SPSQ]$$

$\mathbf{E}^{-1}|_{ij}^{12}$ matrix

$$E^{-1}|_{12}^{12}=\frac{1}{4}\mathbf{a}\,\mathbf{b}(X_2Y_1-X_1Y_2)$$

$$E^{-1}|_{13}^{12}=\frac{\mathbf{a}}{4}$$

$$E^{-1}|_{14}^{12}=\frac{\mathbf{a}\,\mathbf{b}}{4}(X_1\gamma_2-X_2\gamma_1)$$

$$E^{-1}|_{23}^{12}=\frac{\mathbf{a}\,\mathbf{b}}{4}(Y_1-Y_2)$$

$$E^{-1}|_{24}^{12}=-\frac{\mathbf{b}}{4}$$

$$E^{-1}|_{34}^{12}=\frac{\mathbf{a}\,\mathbf{b}}{4}(\gamma_1-\gamma_2)$$

Appendix B

Integrals: I

$$ZDD=\int_0^\infty F_1(k,\omega)J_0(kr)\,k\,dk$$

$$RDD=-\int_0^\infty F_2(k,\omega)J_1(kr)\,k\,dk$$

$$ZDS=\int_0^\infty F_3(k,\omega)J_1(kr)\,k\,dk$$

$$RDS=\int_0^\infty F_4(k,\omega)J_0(kr)\,k\,dk$$
$$-\frac{1}{r}\int_0^\infty [F_4(k,\omega)+F_9(k,\omega)]\,J_1(kr)\,dk$$

$$TDS=\int_0^\infty F_9(k,\omega)J_0(kr)\,k\,dk$$
$$-\frac{1}{r}\int_0^\infty [F_4(k,\omega)+F_9(k,\omega)]\,J_1(kr)\,dk$$

$$ZSS=\int_0^\infty F_5(k,\omega)J_2(kr)\,k\,dk$$

$$RSS=\int_0^\infty F_6(k,\omega)J_1(kr)\,k\,dk$$
$$-\frac{2}{r}\int_0^\infty [F_6(k,\omega)+F_{10}(k,\omega)]\,J_2(kr)\,dk$$

$$TSS=\int_0^\infty F_{10}(k,\omega)J_1(kr)\,k\,dk$$
$$-\frac{2}{r}\int_0^\infty [F_6(k,\omega)+F_{10}(k,\omega)]\,J_2(kr)\,dk$$

$$ZEP=\int_0^\infty F_7(k,\omega)J_0(kr)\,k\,dk$$

$$REP=-\int_0^\infty F_8(k,\omega)J_1(kr)\,k\,dk$$

Kernels: $F_i(k,\omega)$

$$F_1(k,\omega)=\frac{1}{R|_{12}^{12}}[S_2^0(-X|_{12}^{12}Z_{11}+X|_{23}^{12}Z_{31}+X|_{24}^{12}Z_{41})$$
$$+S_4^0(X|_{14}^{12}Z_{11}+X|_{24}^{12}Z_{21}+X|_{34}^{12}Z_{31})]$$

$$F_2(k,\omega)=\frac{1}{R|_{12}^{12}}[S_2^0(-X|_{12}^{12}Z_{12}+X|_{23}^{12}Z_{32}+X|_{24}^{12}Z_{42})$$
$$+S_4^0(X|_{14}^{12}Z_{12}+X|_{24}^{12}Z_{22}+X|_{34}^{12}Z_{32})]$$

$$F_3(k,\omega)=\frac{S_1^1}{R|_{12}^{12}}[X|_{12}^{12}Z_{21}+X|_{13}^{12}Z_{31}+X|_{14}^{12}Z_{41}]$$

$$F_4(k,\omega)=-\frac{S_1^1}{R|_{12}^{12}}[X|_{12}^{12}Z_{22}+X|_{13}^{12}Z_{32}+X|_{14}^{12}Z_{42}]$$

$$F_5(k,\omega)=-\frac{S_4^2}{R|_{12}^{12}}[X|_{14}^{12}Z_{11}+X|_{24}^{12}Z_{21}+X|_{34}^{12}Z_{31}]$$

$$F_6(k,\omega)=\frac{S_4^2}{R|_{12}^{12}}[X|_{14}^{12}Z_{12}+X|_{24}^{12}Z_{22}+X|_{34}^{12}Z_{32}]$$

$$F_7(k,\omega)=\frac{1}{R|_{12}^{12}}[S_2^E(-X|_{12}^{12}Z_{11}+X|_{23}^{12}Z_{31}+X|_{24}^{12}Z_{41})$$
$$+S_4^E(X|_{14}^{12}Z_{11}+X|_{24}^{12}Z_{21}+X|_{34}^{12}Z_{31})]$$

$$F_8(k,\omega)=\frac{1}{R|_{12}^{12}}[S_2^E(-X|_{12}^{12}Z_{12}+X|_{23}^{12}Z_{32}+X|_{24}^{12}Z_{42})$$
$$+S_4^E(X|_{14}^{12}Z_{12}+X|_{24}^{12}Z_{22}+X|_{34}^{12}Z_{32})]$$

$$F_9(k,\omega)=-\frac{S_5^1X_{55}}{R_{55}}$$

$$F_{10}(k,\omega)=-\frac{S_6^1X_{56}}{R_{55}}$$

Source matrices: S^m, $m=0,1,2$

Dislocation source

$$S^0=M_0(\omega)\begin{bmatrix}0\\ \frac{1}{C}\\ 0\\ -\frac{k}{2}\left(1+\frac{2F}{C}\right)\\ 0\\ 0\end{bmatrix}\quad\text{for 45° dip-slip.}$$

$$S^1=M_0(\omega)\begin{bmatrix}\frac{i}{2L}\\ 0\\ 0\\ 0\\ \frac{1}{2L}\\ 0\end{bmatrix}\quad\text{for vertical dip-slip.}$$

$$S^2 = M_0(\omega)\begin{bmatrix} 0 \\ 0 \\ 0 \\ \frac{ik}{2} \\ 0 \\ \frac{k}{2} \end{bmatrix} \quad \text{for vertical strike-slip.}$$

Here $M_0(\omega)$ is the seismic moment.

Explosion source

$$S^E = M_0(\omega)\begin{bmatrix} 0 \\ \frac{1}{C} \\ 0 \\ k\left(1-\frac{F}{C}\right) \end{bmatrix}$$

Acknowledgements. The authors wish to thank Dr. Robert B. Herrmann for discussion of numerical problems during these computations. We would also like to thank Drs. C.Y. Wang and C.K. Saikia for helpful discussions. This research was supported by the Advanced Research Projects Agency of the Department of Defense and was monitored by the Air Force Geophysics Laboratory under Contract F19628-85-k-0021.

References

Alterman, Z., Jarosch, H., Pekeris, C.L.: Oscillations of the earth. Proc. Roy. Soc. Ser. A **252**, 80-95, 1959

Anderson, D.L.: Elastic wave propagation in layered anisotropic media. J. Geophys. Res. **66**, 2953-2963, 1961

Anderson, D.L., Dziewonski, A.M.: Upper mantle anisotropy: evidence from free oscillations. Geophys. J. R. Astron. Soc. **69**, 383-404, 1982

Bamford, D., Crampin, S.: Seismic anisotropy – the state of the art. Geophys. J. R. Astron. Soc. **49**, 1-8, 1977

Bezgodkov, V.A., Yegorkina, G.V.: Experimental study of the anisotropy of longitudinal and transverse waves from local earthquake records. Geophys. J. R. Astron. Soc. **76**, 179-189, 1984

Booth, D.C., Crampin, S.: The anisotropic reflectivity technique theory. Geophys. J. R. Astron. Soc. **72**, 755-766, 1983

Bouchon, M.: A simple method to calculate Green's functions for elastic layered media. Bull. Seismol. Soc. Amer. **73**, 959-971, 1981

Cara, M., Nercessian, A., Nolet, G.: New inferences from higher mode data in western Europe and northern Eurasia. Geophys. J. R. Astron. Soc. **61**, 459-478, 1980

Crampin, S.: The dispersion of surface waves in multilayered anisotropic media. Geophys. J. R. Astron. Soc. **21**, 387-402, 1970

Crampin, S.: A review of wave motion in anisotropic and cracked elastic-media. Wave Motion **3**, North-Holland Publishing Company, 343-391, 1981

Crampin, S., Taylor, D.B.: The propagation of surface waves in anisotropic media. Geophys. J. R. Astron. Soc. **25**, 71-87, 1971

Dunkin, J.W.: Computation of modal solutions in layered, elastic media at high frequencies. Bull. Seismol. Soc. Amer. **55**, 335-358, 1965

Fryer, G.J., Frazer, L.N.: Seismic waves in stratified anisotropic media, elastic media at high frequencies. Geophys. J. R. Astron. Soc. **78**, 691-710, 1984

Gilbert, F., Backus, G.E.: Propagator matrices in elastic wave and vibration problems. Geophysics **31**, 326-332, 1966

Harkrider, D.G.: Surface waves in multi-layered elastic media I: Rayleigh and Love waves from buried sources in a multilayered half space. Bull. Seismol. Soc. Amer. **54**, 627-679, 1964

Harkrider, D.G.: Potentials and displacements for two theoretical seismic sources. Geophys. J. R. Astron. Soc. **47**, 97-133, 1976

Harkrider, D.G., Anderson, D.L.: Computation of surface wave dispersion for multilayered anisotropic media. Bull. Seismol. Soc. Amer. **52**, 321-332, 1962

Haskell, N.A.: The dispersion of surface wave on multilayered media. Bull. Seismol. Soc. Amer. **43**, 17-34, 1953

Haskell, N.A.: Radiation pattern of Rayleigh waves from a fault of arbitrary dip and direction of motion in a homogeneous medium. Bull. Seismol. Soc. Amer. **53**, 619-642, 1963

Herrmann, R.B.: *SH*-wave generation by dislocation sources-*A* numerical study. Bull. Seismol. Soc. Amer. **69**, 1-15, 1979

Herrmann, R.B., Wang, C.Y.: A comparison of synthetic seismograms. Bull. Seismol. Soc. Amer. **75**, 41-56, 1985

Hess, H.H.: Seismic anisotropy of the uppermost mantle under oceans. Nature **203**, 629-631, 1964

Keith, C.M., Crampin, S.: Seismic body waves in anisotropic media: synthetic seismograms. Geophys. J. R. Astron. Soc. **49**, 225-243, 1977

Kennett, B.L.N.: Reflections, ray, and reverberations. Bull. Seismol. Soc. Amer. **64**, 1685-1696, 1974

Knopoff, L.: A matrix method for elastic wave problems. Bull. Seismol. Soc. Amer. **54**, 431-438, 1964

Kogan, S.D.: The azimuthal variation of teleseismic *P*-wave travel times. Geophys. J. R. Astron. Soc. **76**, 201-207, 1984

Love, A.E.H.: The mathematical theory of elasticity. London and New York: Cambridge Univ. Press 1927

Matuzawa, T.: Elastische Wellen in einem anisotropen Medium. Bull. Earthq. Res. Inst. Tokyo **21**, 231-234, 1943

Peacock, S., Crampin, S.: Shear-wave vibrator signals in transversely isotropic shale. Geophysics **52**, 1285-1293, 1985

Robertson, J.D., Corrigan, D.: Radiation patterns of a shear-wave vibrator in near-surface shale. Geophysics **48**, 19-26, 1983

Saito, M.: Excitation of free oscillations and surface waves by a point source in a vertically heterogeneous earth. J. Geophys. Res. **72**, 3689-3699, 1967

Schule, J.W., Knopoff, L.: Shear-wave polarization anisotropy in the Pacific Basin. Geophys. J. R. Astron. Soc. **49**, 145-165, 1977

Takeuchi, H., Saito, M.: Seismic surface waves. Methods in computational physics. Academic Press, New York, **11**, 217-295, 1972

Tanimoto, T., Anderson, D.L.: Mapping convection in the mantle. Geophys. Res. Lett. **11**, 287-290, 1984

Wang, C.Y.: Wave theory for seismogram synthesis. Ph. D. Dissertation, Saint Louis University, St. Louis, Missouri, 1981

Wang, C.Y., Herrmann, R.B.: A numerical study of *P*-, *SV*-, and *SH*-wave generation in a plane layered medium. Bull. Seismol. Soc. Amer. **70**, 1015-1036, 1980

Yao, Z.X., Harkrider, D.G.: A generalized reflection-transmission coefficient matrix and discrete wavenumber method for synthetic seismograms. Bull. Seismol. Soc. Amer. **73**, 1685-1699, 1983

Yu, G.K., Mitchell, B.J.: Regionalized shear velocity models of the Pacific upper mantle from observed Love and Rayleigh wave dispersion. Geophys. J.R. Astron. Soc. **57**, 311-341, 1979

Received December 6, 1985; revised version April 11, 1986
Accepted April 14, 1986

J Geophys (1986) 59:157–163

Journal of Geophysics

The influence of a dilatant region in the Earth's crust on the Earth tide tilt and strain*

R. Kirsch and J. Zschau

Institut für Geophysik der Universität, Olshausenstr. 40–60, D-2300 Kiel, Federal Republic of Germany

Abstract. A model is presented to account for the influence of a buried dilatant 3-*D* ellipsoidal inclusion on the Earth tide tilt and strain. The additional Earth tide effects due to the inclusion thus obtained are here referred to as dilatant zone tidal effects (DZE). Magnitude and phase shift of these effects are determined by the geometrical properties of the inclusion and the contrast between the elastic parameters in the inclusion and in the surrounding material. As an application, tidal effects of dilatant earthquake preparation zones are calculated using observed travel-time delays of seismic waves. So the dilatant zone of the $M=2.6$ Blue Mountain Lake earthquake leads to a DZE tidal tilt of more than 300% of the undisturbed tidal tilt. This suggests that tidal observations are a viable tool for earthquake prediction, especially for shallow earthquakes with focal depths of less than 10 km.

Key words: Earth tides – Dilatancy – Earthquake prediction

Introduction

Beaumont and Berger (1974), in their pioneering work using finite element methods, showed that an amplification of the Earth tide tilts and strains of up to 60% could be expected by a buried dilatant inclusion in the Earth's crust (Fig. 1). Similar results were obtained by Molodensky (1983) who found an analytical solution of this problem. This led to the expectation that measurements of Earth tide tilts could be a very useful tool in earthquake prediction (Zschau, 1979). But all these calculations were made by two-dimensional models and, therefore, the coupling effect of the third component of the tidal strain had to be neglected. Hence, no phase shift between the regular Earth tide field and the induced tidal field due to the ellipsoidal inclusion was obtained. In order to avoid this disadvantage of two-dimensional models an attempt is made to construct a three-dimensional model, in order to calculate the tidal field induced by dilatant zones. This model is based on Eshelby's (1957) solution of the problem of calculating the strain field in the vicinity of an ellipsoidal inclusion in a homogeneous body.

Construction of the model

Consider an ellipsoidal inclusion with semi-axes a, b, c and located at depth z (all dimensions are in km, Fig. 2) of the Earth's crust, having elastic properties different from those of the surrounding material. What will be the influence of this body on Earth tide tilt and strain observed at a point (x, y) on the surface in the vicinity of the inclusion? To answer this question we calculate the amplitude of the additional tilt and strain at the point (x, y) produced by the inclusion under the influence of the Earth tide strain field. The additional tidal effects will be referred to here as the dilatant zone tidal effects (DZE). The actual tidal field measured at (x, y) is obtained by vector addition of the regular and the DEZ tidal field.

The semidiurnal tidal potential as presented by Laplace is given (Melchior, 1978) by

$$W=\frac{3}{4} G \cdot M \cdot \frac{r^2}{d^3} \cos^2\theta \cos 2\vartheta, \tag{1}$$

G = gravity constant,
M = mass of the tide-generating celestial body (in the equatorial plane),
r = radius of the Earth,
d = distance between the centres of mass of the Earth and the celestial body,
θ = latitude of the observation point,
ϑ = hour angle of celestial body with respect to the Greenwich meridian.

Assuming the conditions of a free surface (this assumption is valid to great depths due to the long wavelength of the semidiurnal tides), the tidal strain is given by

$$\begin{aligned}
\varepsilon_{11}&=\varepsilon_{\theta\theta}=\frac{l}{g \cdot r} \cdot \frac{\delta^2 W}{\delta \theta^2}+\frac{h}{g \cdot r} W, \\
\varepsilon_{22}&=\varepsilon_{\vartheta\vartheta}=\frac{l}{g \cdot r \cdot \sin^2\theta} \frac{\delta^2 W}{\delta \vartheta^2} \\
&\quad+\frac{l \cdot \cos\theta}{g \cdot r \cdot \sin\theta} \frac{\delta W}{\delta \theta}+\frac{l}{g \cdot r} W, \\
\varepsilon_{33}&=\varepsilon_{rr}=-\frac{v}{1-v}(\varepsilon_{11}+\varepsilon_{22}) \qquad \varepsilon_{13}=\varepsilon_{23}=0, \\
\varepsilon_{12}&=\varepsilon_{\theta\vartheta}=\frac{2l}{g \cdot r \cdot \sin\theta} \cdot \frac{\delta^2 W}{\delta\theta\,\delta\vartheta}-\frac{2l\cos\theta}{g \cdot r \cdot \sin^2\theta} \frac{\delta W}{\delta \vartheta},
\end{aligned} \tag{2}$$

---

* Contribution No. 301, Institut für Geophysik der Universität Kiel

Offprint requests to: J. Zschau

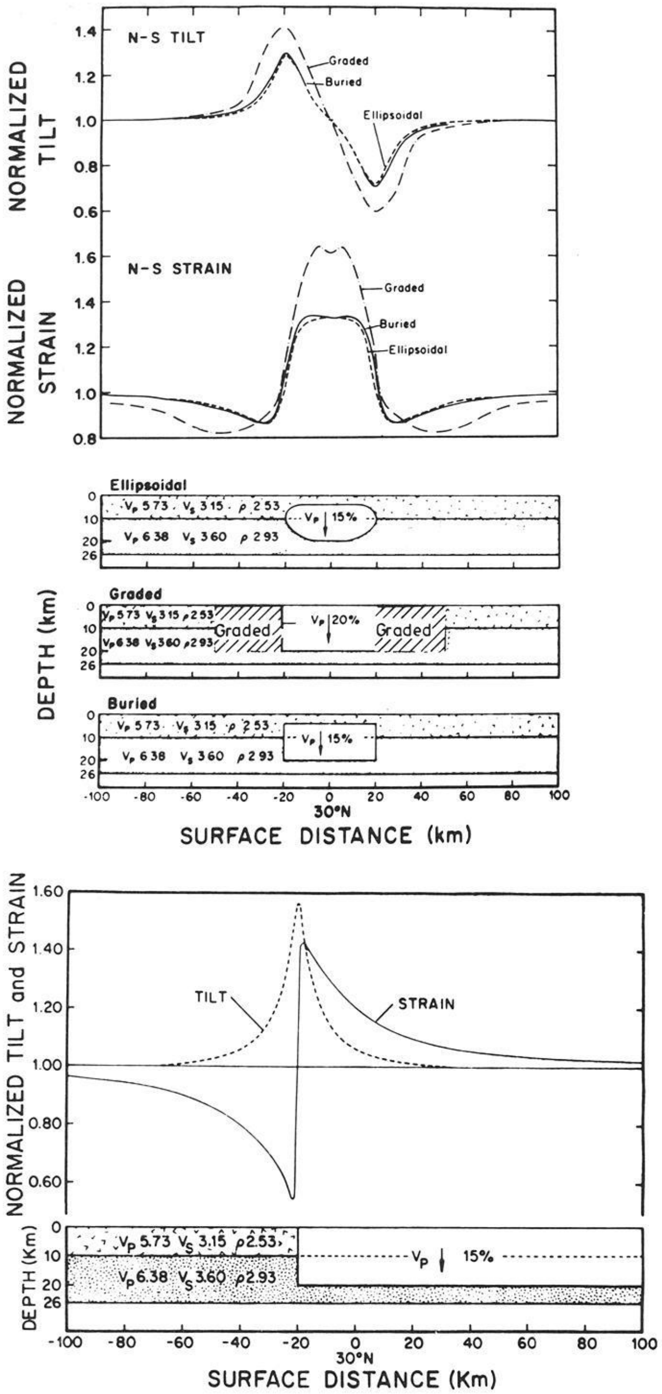

Fig. 1. Finite-element results for tidal modifications due to dilatant regions (after Beaumont and Berger, 1974)

where ν = Poisson's ratio for the Earth's crust, h, k, l = Love's numbers (Melchior, 1978) and g = gravity acceleration.

Eshelby (1957) gives the relationship connecting an external strain field ε^A [here the tidal strain field given by Eq. (2)] to the strain field caused by an ellipsoidal inclusion embedded in an otherwise homogeneous, isotropic and unlimited matrix

$$\varepsilon_{ij}^c(\text{out}) = Q_{ijmn}\,\varepsilon_{mn}^A \tag{3}$$

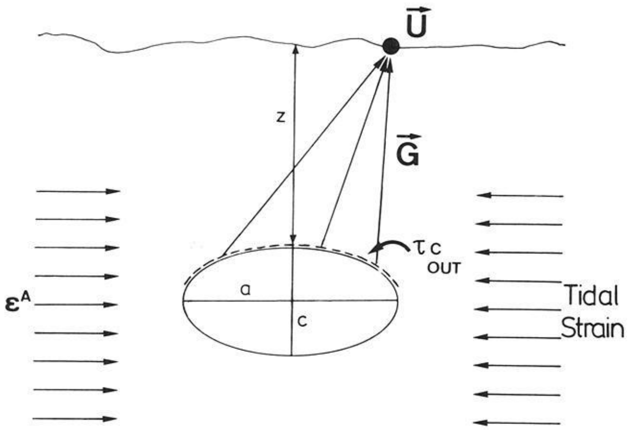

Fig. 2. The ellipsoidal dilatant inclusion: basics for the calculation of tidal modifications

[Eq. 6 of Beavan (1978), who gives a very good explanation of Eshelby's method].

Due to the restrictions of Eshelby's method to the unlimited matrix, one cannot obtain the DZE tidal strain on the Earth's surface by Eq. (3). We use formula (3) merely to calculate the strain field just outside the inclusion and the corresponding stress field is given by Hooke's law.

$$\tau_{ij}^c(\text{out}) = \lambda\,\varepsilon_{ij}^c(\text{out}) + 2\mu\,\varepsilon_{ij}^c(\text{out}). \tag{4}$$

These stresses can be regarded as being caused by a layer of forces surrounding the inclusion.

To transfer these forces to the Earth's surface we make use of Galerkin vectors given by Mindlin and Cheng (1950). By means of these vectors the displacement field at the free surface of a body due to double forces with and without moment acting inside can be calculated by their partial derivatives as shown in Eq. 7. The layer of forces surrounding the inclusion is taken as a layer of double forces without moment for the normal components of τ_{ij}^c(out) or of double forces with moment for its shear components.

So the Galerkin vector $\mathbf{g}(x, y)$ for the observation point at the Earth's surface corresponding to the forces at a point (x', y') on the surface of the inclusion is given by the multiplication between the Galerkin vectors for double forces with and without moment and the corresponding components of the stress tensor τ_{ij}^c(out) for the point (x', y')

$$\mathbf{g}(x, y) = \sum_{i=1}^{3}\sum_{j=1}^{3} \mathbf{g}_{ij}(x, y, x', y') \cdot \tau_{ij}^c(\text{out})(x', y'). \tag{5}$$

So the total Galerkin vector $\mathbf{G}(x, y)$ for the observation point is given by the integral over the surface of the inclusion:

$$\mathbf{G}(x, y) = \int_S \mathbf{g}(x, y)\, ds. \tag{6}$$

The displacement vector of the observation point is obtained from the components of the Galerkin vector using

$$\begin{aligned} u(x,y) &= \frac{1}{2\mu}\left[2(1-\nu)\Delta G_x - \frac{\delta}{\delta x}\operatorname{div}\mathbf{G}(x,y)\right] \\ v(x,y) &= \frac{1}{2\mu}\left[2(1-\nu)\Delta G_y - \frac{\delta}{\delta y}\operatorname{div}\mathbf{G}(x,y)\right] \\ w(x,y) &= \frac{1}{2\mu}\left[2(1-\nu)\Delta G_z - \frac{\delta}{\delta z}\operatorname{div}\mathbf{G}(x,y)\right] \end{aligned} \tag{7}$$

where G_x, G_y, G_z are the components of $\mathbf{G}(x, y)$ (Mindlin and Cheng, 1950).

This leads to strain and tilt given by

$$\begin{aligned} \mathrm{STRAIN}_{\mathrm{NS}}(x,y) &= \frac{\delta U(x,y)}{\delta x}, \\ \mathrm{STRAIN}_{\mathrm{EW}}(x,y) &= \frac{\delta V(x,y)}{\delta y}, \\ \mathrm{TILT}_{\mathrm{NS}}(x,y) &= \frac{\delta W(x,y)}{\delta x}, \\ \mathrm{TILT}_{\mathrm{EW}}(x,y) &= \frac{\delta W(x,y)}{\delta y}. \end{aligned} \tag{8}$$

In the following, the DZE tidal effects are normalized by the regular tidal tilt and strain for a radially symmetric Earth without inclusion. This is done using Eq. (2) for the tidal strain.

The tidal tilt is calculated (Melchior, 1978) by

$$\begin{aligned} \mathrm{TILT}_{\mathrm{NS}}(\mathrm{regular}) &= (1+k-h)\frac{1}{r\cdot g}\frac{\delta W}{\delta\theta}, \\ \mathrm{TILT}_{\mathrm{EW}}(\mathrm{regular}) &= (1+k-h)\frac{1}{r\cdot g\cdot\sin\theta}\frac{\delta W}{\delta\vartheta}. \end{aligned} \tag{9}$$

In summary, the calculation of the DZE tidal effects is done in three steps (Fig. 2):

- the stress field τ^c_{out} just outside an ellipsoidal inclusion is calculated using the formalism given by Eshelby (1957)
- the Galerkin vector $\mathbf{G}(x, y)$ belonging to this stress field is calculated for an observation point at the Earth's surface using the formulas of Mindlin and Cheng (1950)
- the displacement vector $\mathbf{u}$ and the resulting tilts and strains are obtained by partial derivatives of the Galerkin vector $\mathbf{G}$.

The relationship between the external strain field ε^A and the strain field $\varepsilon^c_{\mathrm{out}}$ due to the inclusion is given by the matrix $\mathbf{Q}$, Eq. (3). It can be seen that each component of $\varepsilon^c_{\mathrm{out}}$ is obtained by a linear combination of all components of ε^A. The normal components of ε^A are proportional to the cosine of the doubled hour angle ϑ, while the shear components are proportional to the sine of this angle. So the DZE tidal effect is a combination of a sine part and a cosine part, while all regular N-S and E-W tidal effects are proportional to the cosine of the doubled hour angle. Consequently, the phase shift between an arbitrary DZE tidal effect and its corresponding undisturbed tidal effect is given by the arctangent of the ratio of its sine and cosine parts.

The calculated normalized DZE tidal effects are shown along a traverse crossing the buried ellipsoidal inclusion (Fig. 3). For comparison, the geometric and elastic properties of matrix and inclusion, as well as the geographical latitude of the inclusion, are the same as those chosen by Beaumont and Berger (1974) for their model (Fig. 1) with the exception of a thinner overburden (2 km instead of 4 km), a reduced shear modulus inside the inclusion (to obtain a phase shift as explained later) and a semi-axis in the y-direction equal to that in the x-direction.

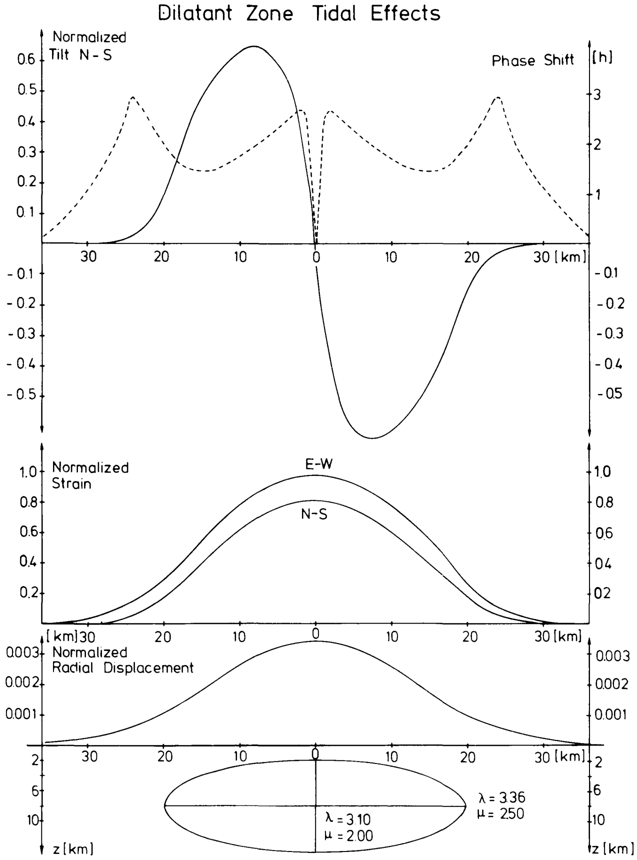

Fig. 3. DZE tidal effect along a N-S profile at 30° N crossing a buried ellipsoidal inclusion

The amplitude of the DZE effects thus obtained are in accordance with those obtained by Beaumont and Berger (1974). The radial displacement along the traverse shows that an additional uplift occurs due to the inclusion, leading to the calculated DZE tilts and strains. Both components of the DZE strain field reach the maximum amplitude just above the centre of the inclusion, the amplitudes being similar to the amplitudes of the regular tidal strain. The maximum DZE N-S tilt is reached at about one-third of the distance from the centre of the inclusion to its edge and the amplitude is about 60% of the regular tilt amplitude. The maximum phase shift is reached over the edge of the inclusion. The phase shift over the centre of the inclusion is not defined because of zero values for both sine and cosine parts. As these effects are shown along a traverse above the large semi-axis of the inclusion, the DZE E-W tilt along this path is zero. The influences of elastic and geometric parameters of the inclusion on the DZE tidal effects are shown in Figs. 4 and 5. Figure 4 shows the DZE tidal effects caused by a

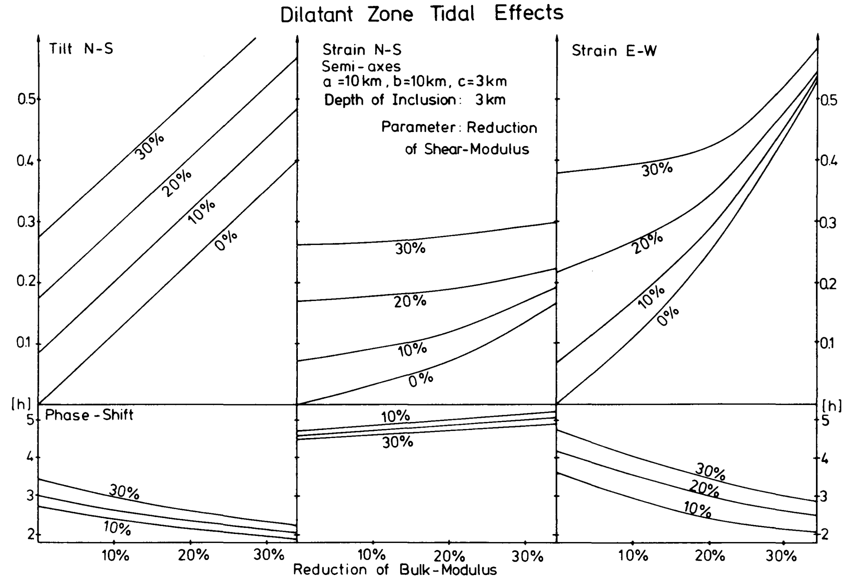

Fig. 4. DZE tidal effects as a function of the reduction of elastic moduli inside the inclusion. Calculations are made for surface points where maximum DZE tidal effects are reached, different for tilt and strain. For N-S tilt this is near the edge of the inclusion, while for both strain components it is above the centre of the inclusion

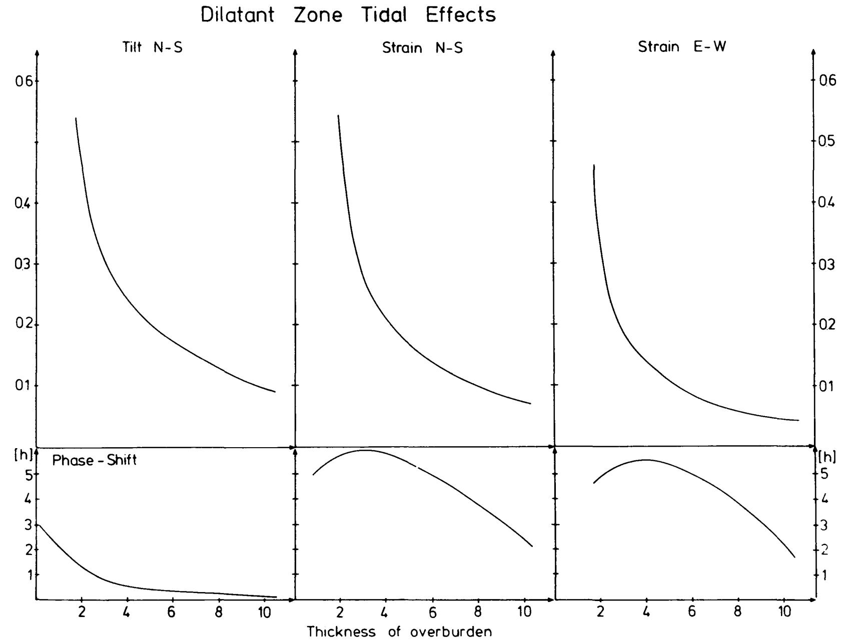

Fig. 5. DZE tidal effects as a function of the thickness of the overburden

reduction of bulk modulus and shear modulus of up to 30% inside the inclusion. Both tilt and strain amplitudes increase with increasing difference of bulk and shear modulus between inside and outside the inclusion.

The phase shifts of N-S tilt and E-W strain reach maximum values when the shear modulus inside the inclusion is reduced while the bulk modulus remains constant, which means that the Poisson's ratio inside the inclusion is higher than outside. The phase behaviour of the N-S strain is contrary to the phase behaviour of the E-W strain and the N-S tilt, which means the phase shift is increasing with a reducing Poisson's ratio inside the inclusion. Since the amplitude of the sine component of all DZE tidal effects is governed by the difference of the shear moduli of matrix and inclusion (as a consequence of Eshelby's matrix Q), no phase delay is obtained for vanishing shear moduli difference.

Among the geometrical parameters, the most crucial one is the thickness of the overburden (i.e. depth of the inclusion) as shown in Fig. 5. All components of the DZE tidal effects show a sharp increase of amplitude for decreasing depth of the inclusion. The limiting case of zero depth can not be calculated because of the restrictions in the formalism given by Eshelby (1957).

Application to earthquake prediction

Prior to an earthquake the physical properties of the crustal material in a certain region near to the future focal area undergo characteristic changes (Scholz et al., 1973). The most striking effect is the decrease in the

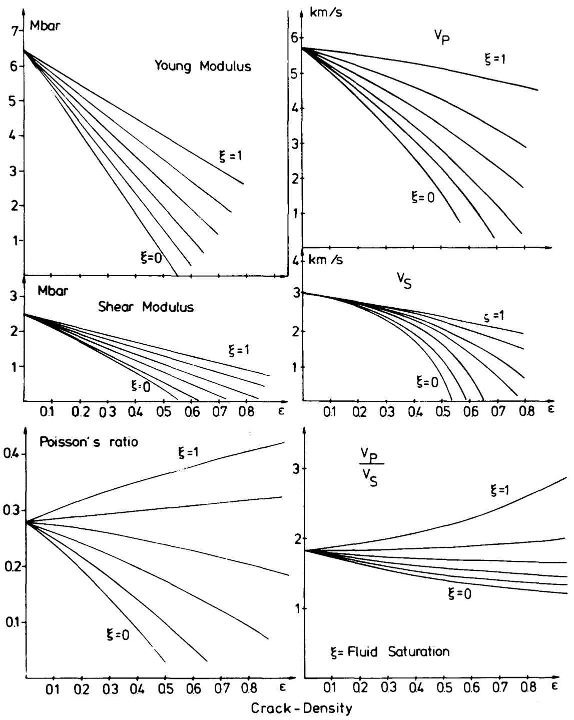

Fig. 6. Elastic moduli and seismic velocities for cracked solids as a function of crack density and pore-fluid saturation (after O'Connell and Budiansky, 1974

v_p/v_s ratio of about 10 % followed by a return to normal just prior to the earthquake. An explanation for this behaviour is given by the dilatancy-diffusion theory (Nur, 1972). During the stress-accumulation phase, prior to the earthquake, microcracks in the rock open in a direction parallel to the major compression axis. As a result of this crack-volume increase the pore space becomes undersaturated; this reduces the velocity ratio v_p/v_s and increases the frictional strength of the rock. After a time depending on the extent of the newly created dilatant region, water diffuses into the opened cracks and the velocity ratio recovers. The increased pore pressure decreases the frictional strength of the rock and failure occurs (Gowd and Rummel, 1977).

The change in seismic velocities prior to an earthquake reflects a change in the elastic properties of the crustal material in the vicinity of the future focal region. The influence of cracks and pore-water saturation on the elastic parameters of rocks can be estimated by formulas of O'Connell and Budiansky (1974). Its general behaviour is shown in Fig. 6. Elastic constants are decreasing with increasing crack density ε, a parameter combining the number of cracks per unit volume and the average length of the cracks. This decrease is steeper for dry cracks than for saturated cracks. In the case when more than 70 % of cracks are saturated with pore-fluid, Poisson's ratio and the v_p/v_s velocity ratio increases with increasing crack density.

Anderson and Whitcomb (1975) have proposed that the radius L of the dilatant area is connected to the magnitude of the subsequent earthquake by the empirical relation

$$\log L = 0.26M + 0.46.$$

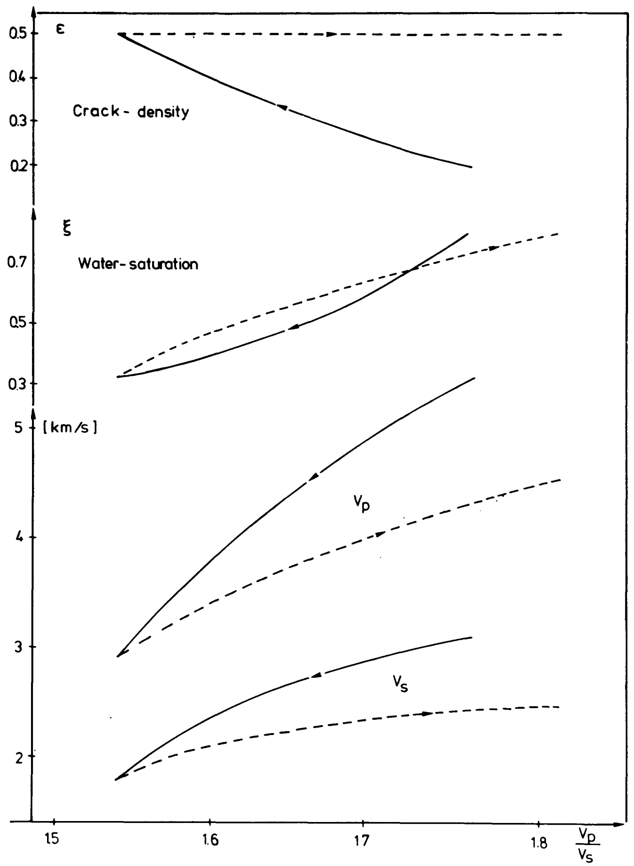

Fig. 7. Dilatancy-diffusion diagram and resulting seismic velocities (after O'Connell and Budiansky, 1974. The *continuous line* indicates the crack-opening phase, while the *dashed line* refers to the water-saturation phase

This suggests that the dilatant region may be much more extended than the aftershock zone. In connection with the reduced elastic parameters within the dilatant zone this leads to the expectation that such a dilatant region can produce DZE tidal effects as described in the previous section. To demonstrate this idea further, consider a dilatancy-diffusion cycle (Fig. 7) containing decreasing pore-space saturation due to the increase in crack density and the subsequent recovery of saturation while crack density remains constant. The model might be an oversimplification of the mechanism but it enables us to estimate the magnitude of the DZE effects to be expected. The resulting seismic velocities inside the dilatant region, obtained from the method given by O'Connell and Budiansky (1974), are shown in Fig. 7. They are used to determine the elastic parameters inside an inclusion having the same geometrical properties as the one used in Fig. 4. The resulting DEZ tidal effects are shown in Fig. 8. The maximum amplitudes for DZE tilt and strain are obtained at the lowest v_p/v_s ratio, while the maximum phase delay occurs during the phase of velocity recovery. Both DZE tilt and strains are in the order of magnitude of the undisturbed body tide effects.

The next step is the calculation of the DZE tidal effects for an actual earthquake. The 1973 $M = 2.6$ Blue Mountain Lake earthquake was chosen for this test because exact estimations of velocity anomalies as well as dimensions of the dilatant region have been pub-

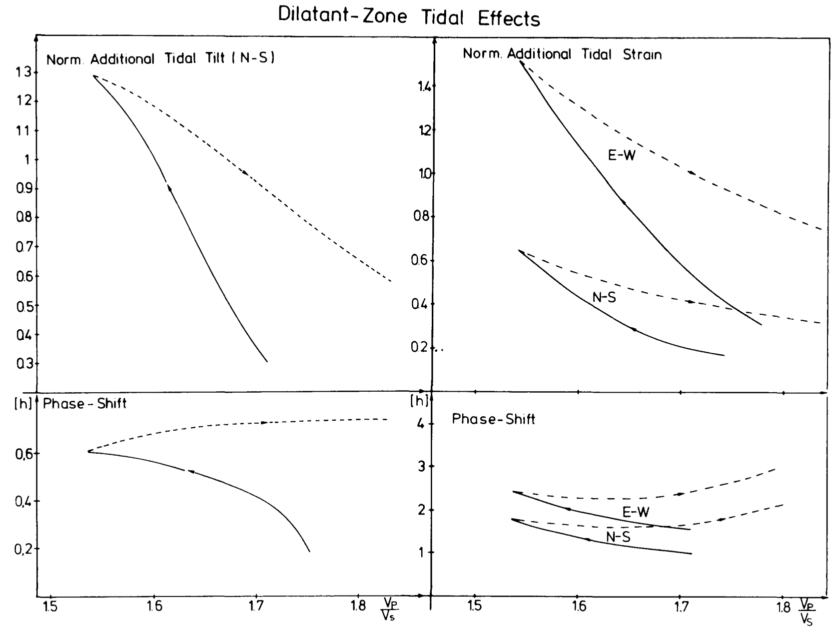

Fig. 8. DZE tidal effects resulting from a dilatancy-diffusion cycle

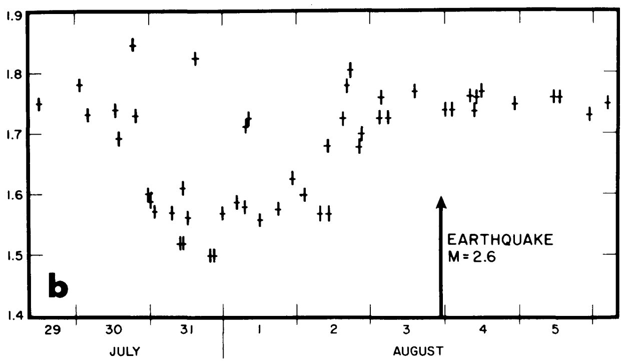

Fig. 9. Observed v_p/v_s ratios prior to the $M = 2.6$ Blue Mountain Lake Earthquake (after Aggarwal et al., 1975)

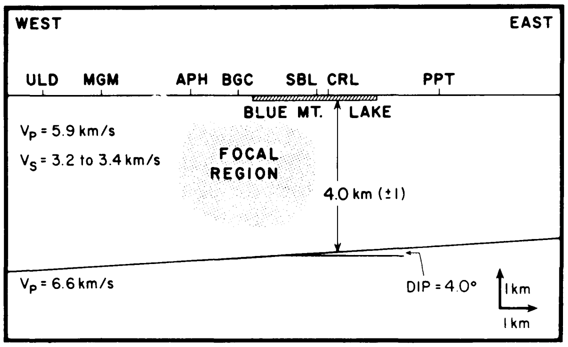

Fig. 10. Dimensions of the dilatant region of the $M = 2.6$ Blue Mountain Lake Earthquake (after Aggarwal et al., 1975

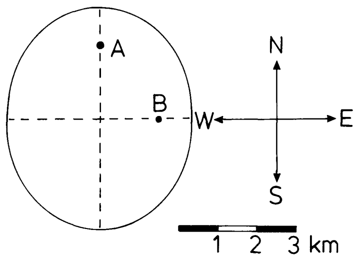

Fig. 11. Position sketch of the imaginary tidal observation points *A* and *B* above the semi-axes of the ellipsoid approximating the dilatant zone of the Blue Mountain Lake earthquake

lished (Aggarwal et al., 1975). The decrease of the v_p/v_s ratio (Fig. 9) and its subsequent increase are evaluated in terms of crack density and saturation degree to obtain the elastic parameters inside the dilatant region. The dilatant region (Fig. 10) is approximated by an ellipsoidal inclusion with semi-axes of 2 km (horizontal E-W), 2.5 km (horizontal N-S) and 1.3 km (vertical); the thickness of the overburden is 1 km. In order to calculate both E-W and N-S components of DZE tidal tilt, two imaginary observation points are chosen situated above the horizontal semi-axes of the inclusion (Fig. 11). The results are shown in Fig. 12; the ordinate refers to the time scale in Fig. 9, i.e. day no. 1 refers to July 30.

The amplitude of all DZE tidal effects is high because of the thin overburden of the dilatant region. The amplitude reaches its maximum while the v_p/v_s ratio is at a minimum; for all DZE tidal effects, the phase delay is increasing up to 3–4 h just prior to the earthquake.

Conclusions

A model is presented to account for the influence of a buried dilatant inclusion on Earth tide tilts and strains. This model is based on Eshelby's solution of the strain field due to an ellipsoidal inclusion and, because of its 3-dimensional character, not only the magnitude but also the phase of the induced tilt and strain can be calculated. For the limiting case of a very elongated ellipsoid (corresponding to the 2-dimensional case) results on the magnitude similar to those of Beaumont and Berger (1974) and Molodensky (1983) were obtained.

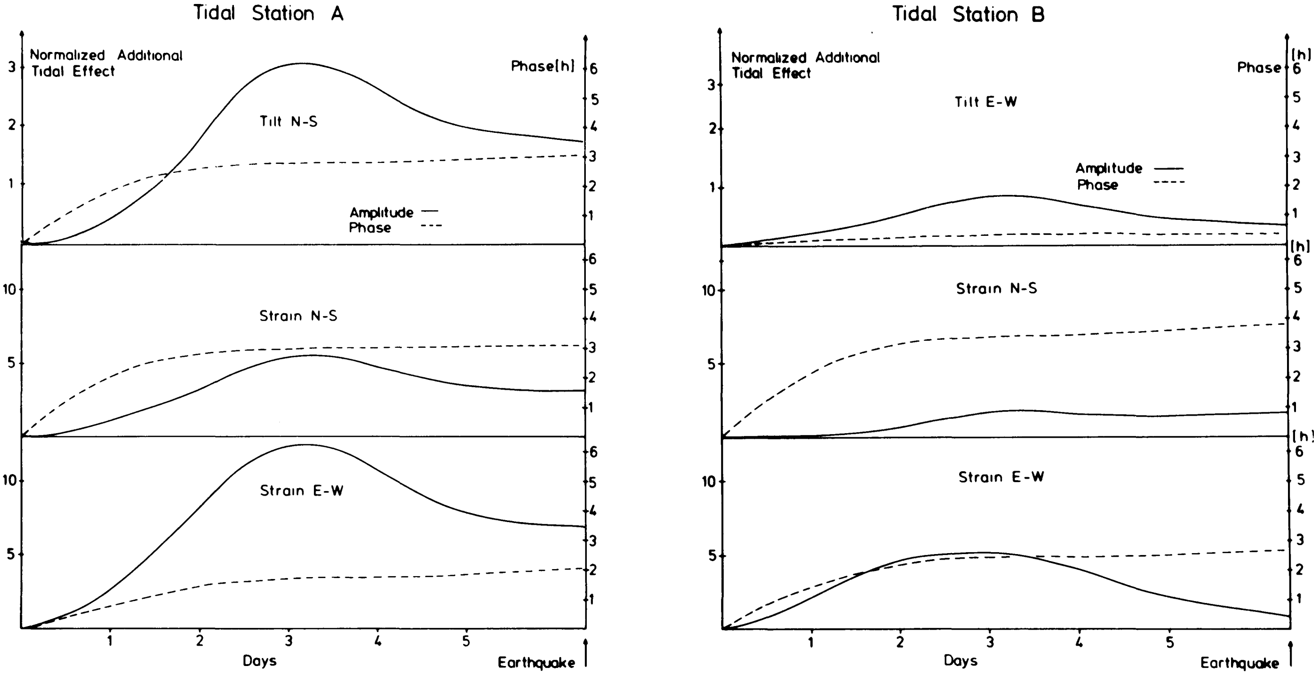

Fig. 12 A, B. DZE tidal effects prior to the Blue Mountain Lake earthquake using the v_p/v_s ratio shown in Fig. 9

The magnitude is determined by the geometrical properties of the inclusion and the contrast between the elastic parameters in the inclusion and in the surrounding material. A very crucial parameter is the thickness of the overburden. No significant tidal effect due to the inclusion can be expected for a thickness of overburden of more than 10 km. Two restrictions of the presented model must be taken into account. First, the dilatant zone must be of ellipsoidal shape, so no statement about the influence of irregularities in the shape of the inclusion can be made. Also, the effect of a gradual transition from the dilatant region to the surrounding crustal material, instead of a sharp boundary, cannot be modelled. Beaumont and Berger (1974) showed that this would slightly reduce the DZE tilt and strain.

Second, the rheological parameters of the dilatant region were obtained by the observed reduction of seismic velocities which were interpreted as changes only in the linear elastic parameters λ and μ. However, the most striking effect of dilatancy is the nonlinear inelastic increase in rock volume prior to failure. These influences, including possible anisotropy of elasticity, could not be modelled. Due to this objection, the model presented here should be taken as an order of magnitude estimation of the amplitude and phase of tidal effects due to a buried dilatant inclusion in the Earth's crust. The pre-seismic tidal modifications calculated under the above-stated assumptions are, nevertheless, extremely high (up to several hundred percent in amplitude and several hours in phase), and they consequently suggest that tidal observations are a viable tool for the prediction of shallow earthquakes.

Acknowledgements. We thank D. Bower for critical remarks on the manuscript and B. Borth-Hoffmann, L. Bittner, H. Wiederhold, K. Helbig and A. Gabeler for their help in preparing the manuscript.

References

Aggarwal, Y.P., Sykes, L.R., Simpson, D.W., Richards, P.G.: Spatial and temporal variations in *ts/tp* and *P*-wave residuals at Blue Mountain Lake. New York: application to earthquake prediction. J. Geophys. Res. **80**, 718-732, 1975

Anderson, D.L., Whitcomb, J.H.: Time depending seismology. J. Geophys. Res. **80**, 1497-1503, 1975

Beaumont, C., Berger, J.: Earthquake prediction: modification of the Earth tide tilts and strains by dilatancy. Geophys. J.R. Astron. Soc. **39**, 111-121, 1974

Beavan, R.J.: A note on the strains at a distance from an ellipsoidal inhomogeneity. Geophys. J.R. Astron. Soc. **54**, 713-719, 1978

Eshelby, J.D.: The determination of the elastic field of an ellipsoidal inclusion and related problem. Proc. Roy. Soc., Ser. A, **241**, 376-396, 1957

Gowd, T.N., Rummel, F.: Effect of fluid injection on the fracture behaviour of porous rock. Int. J. Rock. Mech. Min. Sci. & Geomech. Abstr. **14**, 203-208, 1977

Melchior, P.: The tides of the planet Earth. Oxford, New York, Toronto, Sydney, Paris, Frankfurt, 1978

Mindlin, R.D., Cheng, D.H.: Nuclei of strain in the semi-infinite Solid. Journal of Applied Physics, 926-930, 1950

Molodensky, S.M.: Local anomalies in amplitude and phase of tidal tilts and deformations. Izvestiya, Earth Physics, **19**, No. 7, 501-505, 1983

Nur, A.: Dilatancy, pore fluids and premonitory variations of *ts/tp* travel times. BSSA, **62**, 1217-1222, 1972

O'Connell, R.J., Budiansky, B.: Seismic velocities in dry and saturated cracked solids. J. Geophys. Res. **79**, 5412-5426, 1974

Scholz, C.H., Sykes, L.R., Aggarwal, J.P.: Earthquake prediction: a physical basis. Science **181**, 803-810, 1973

Zschau, J.: Earthquake prediction using tiltmeters. Proc. ESA Council of Europe Seminar on Earthquake Prediction, ESA-SP-149, 41-45, 1979

Received July 30, 1985; revised version April 1, 1986
Accepted April 1, 1986

J Geophys (1986) 59:164-170

Journal of Geophysics

The influence of atmospheric loading on VLBI-experiments

W. Rabbel[1] **and H. Schuh**[2]

[1] Institut für Geophysik, Christian Albrechts Universität, Olshausenstr. 40-60, D-2300 Kiel, Federal Republic of Germany
[2] Geodätisches Institut der Universität Bonn, Nussallee 17, D-5300 Bonn, Federal Republic of Germany

Abstract. Air pressure lows and highs with periods of some days and seasonal variations of mean air pressure can be regarded as loading functions on the Earth's surface. They result in quasi-periodic surface deformations. The influence of such displacements on the results and the accuracy of VLBI experiments (Very Long Baseline Interferometry) is investigated by simulation calculations for the transatlantic Effelsberg-Haystack baseline. Different models for the time dependence of air-pressure-induced station displacements are considered. It is shown that today's standard VLBI data analysis, including model parameters for clock- and atmospheric-refraction effects, is not able to correct the measurements for atmospheric loading effects. It leads to erroneous baseline vectors. Hence, for every geodetic VLBI experiment, the amount by which (1) the local air pressure at the station and (2) the mean air pressure in a surrounding area of 2,000 km radius has changed during the experiment should be tested. These two values give an estimate of the resulting vertical displacements by the use of a regression formula. The corresponding delay-time corrections have to be applied to the VLBI data. Most of the radiotelescopes participating in geodetic VLBI experiments are situated in regions with small seasonal variations of the station position. However, an increasing VLBI accuracy and an expanded and denser VLBI network will also require the consideration of seasonal displacements.

Key words: Geodynamics – Atmospheric loading – Global deformation – Global positioning – VLBI

Introduction

The improvement of geodetic space methods with regard to instrumentation and processing has reached centimetre precision for the determination of changes of global baselines (Lundquist, 1984). This enables us to investigate geodynamical processes which are associated with point displacements on the Earth's surface. For example, the determination of continental drift rates of some centimetres per year may become possible in the near future via Very Long Baseline Interferometry (VLBI), Lunar or Satellite Laser Ranging (LLR, SLR) or even by the differential application of the Global Positioning System (GPS). Deformations of the Earth's surface, however, are not only of endogenic, i.e. tectonic, origin. The Earth's surface is affected by a lot of exogenic deformation effects of partly periodic, partly quasi- and non-periodic character. The most prominent example of the former are the body tides and ocean loading tides. An example of not strictly periodic deformations are those effects which are caused by the atmosphere: by air pressure lows and highs (deviations from the 1,013-mbar atmospheric mean), snow coverage during winter or anomalous sea-level changes caused by storms.

Since geodetic methods have come close to the accuracy which is necessary for large-scale tectonic investigations, the question of data correction corresponding to exogenic displacements has become more important.

This paper deals with errors of VLBI data analysis which are introduced by air-pressure-induced, large-scale surface deformations. Their magnitude can exceed the approached VLBI accuracy. The next section gives a short summary of theoretical estimations of air-pressure-induced station displacements, followed by a section which deals with the corresponding correction of the VLBI observables. In the subsequest section, the influence of air-pressure-induced station displacements is simulated for the transatlantic Effelsberg-Haystack baseline. Different models for the time dependence of the displacements are assumed. The final section contains a proposal for the treatment of such station displacements for the interpretation of VLBI measurements.

Air-Pressure-Induced Displacements at the Earth's surface

Air pressure lows and highs (cyclones and anticyclones) can be regarded as time-dependent loading on the Earth's surface. According to their geometry they generate large-scale deformation fields with some hundred up to some thousand kilometres wavelength. Due to the velocity of the passing (anti-)cyclones, the periods of the loading function are between a few days and some weeks. Such air pressure anomalies can cause vertical displacements in the centimetre range and horizontal displacements in the millimetre range (Trubytsin and

---

Offprint requests to: W. Rabbel

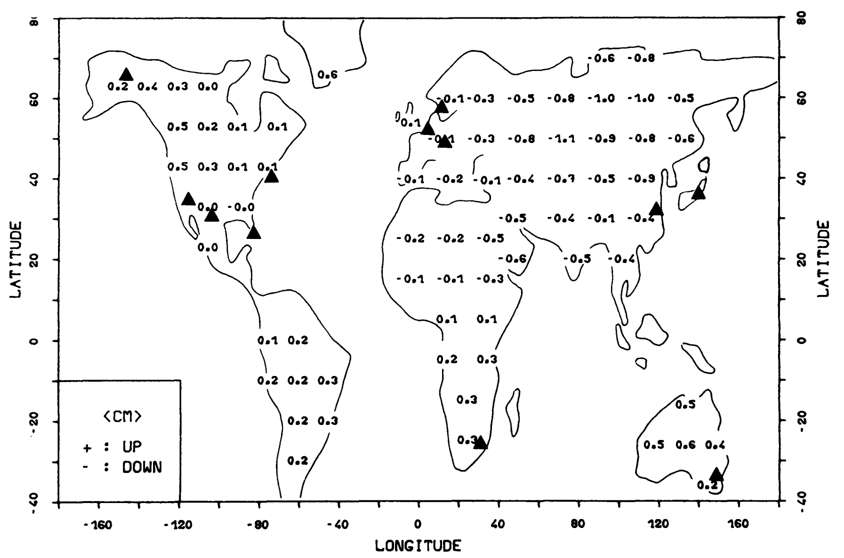

Fig. 1. Vertical displacements due to seasonal changes in the global air pressure distribution: mean deviation "January minus July" (from Rabbel and Zschau, 1985). Positions of radiotelescopes participating in geodetic VLBI experiments are indicated by *triangles*

Makalkin, 1976; Rabbel and Zschau, 1985). The isobars of many (anti-)cyclones are close to being circular and can be roughly approximated by bell-shaped pressure distributions. Such an (anti-)cyclone, of typically 2,000-km diameter and extreme maximum pressure of ±60 mbar (see e.g. Faust, 1968) in its centre (deviation from atmospheric mean), yields ∓25 mm vertical and ±2.5 mm horizontal displacements as a maximum estimation.

Discontinuities of the pressure distribution, e.g. which can be generated at coastlines due to the static response of the sea (inverted barometer effect), will modify these values but do not change their order of magnitude. Seasonal air pressure variations with a quasi-period of 1 year can be estimated from the mean values in January and July. They are about 10 mm double amplitude for the vertical displacements (Fig. 1) and 1 mm double amplitude for the horizontal displacements. Extreme values are to be found in Siberia, Greenland and the Antarctic (Stolz and Larden, 1979; Rabbel and Zschau, 1985).

The standard method for the estimation of loading effects is the method of Green's functions: the (visco-) elastic equation of motion is integrated numerically for a radially symmetric Earth model with a surface point load as exciting function. The resulting deformation response, expressed in terms of loading Love numbers and Legendre polynomials, are the so-called Green's functions. They are convolved with the desired arbitrary surface load distribution in order to obtain the total deformation (e.g. see Longman, 1962; Farrell, 1972; Zschau, 1979).

Vertical displacements are not only determined by the local pressure but also by the long-wavelength terms of the load distribution. Therefore, the somewhat laborious method of the Green's functions cannot be replaced by a simple regression between local air pressure and vertical displacement. However, under static conditions it is possible to estimate the vertical displacement by a regression approximation introducing two regression coefficients, namely for the short- and the long-wave-length loading (Rabbel and Zschau, 1985):

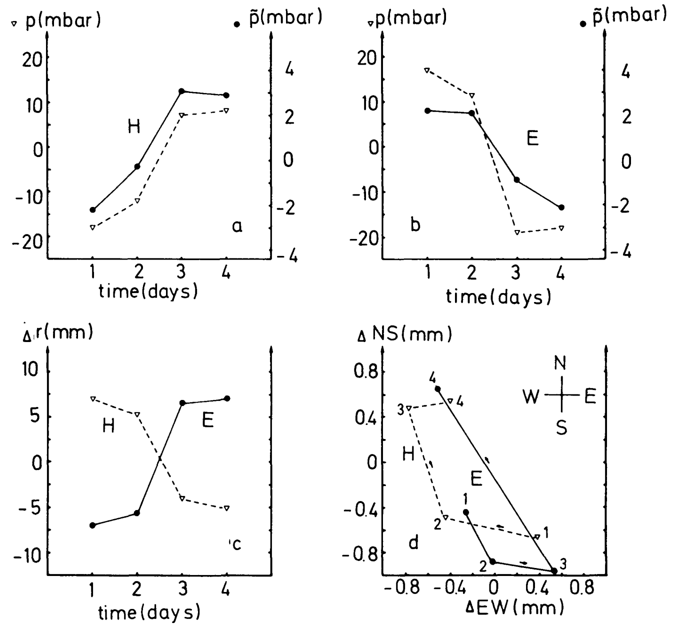

Fig. 2a–d. Air pressure situation and displacements of Haystack (H) and Effelsberg (E) between 4th and 7th February 1983: **a** local air pressure anomaly p and mean regional air pressure anomaly $\tilde{p}$ [see Eq. (1)] for Haystack; **b** local air pressure anomaly p and mean regional air pressure anomaly $\tilde{p}$ for Effelsberg; **c** vertical displacement; **d** horizontal displacements (parameter "time" in days)

$$\Delta r = -0.90\tilde{p} - 0.35(p - \tilde{p}). \tag{1}$$

Here Δr(mm) is the vertical displacement, p(mbar) is the local air pressure anomaly at the station position and $\tilde{p}$(mbar) is the mean value of the pressure anomaly within a circular region of 2,000-km radius. $\tilde{p}$ denotes the long-wavelength component of the pressure variation. For ocean areas the pressure contribution to $\tilde{p}$ has to be set to zero due to the static response of the water masses. Equation (1) allows to estimate seasonal displacements with an error of less than 1 mm. Figure 2 gives an example of the variation of site positions within four succeeding days. The local and mean regional air pressure anomaly p, $\tilde{p}$ and the resulting vertical and horizontal displacements Δr, ΔNS, ΔEW are shown for the VLBI stations Effelsberg (W. Germany) and Haystack (Mass., USA) between 4th and 7th February 1983. In this time interval the variation of the vertical displacement exceeded the 1-cm limit and the maximum horizontal movements were about 1 mm. The given displacement values correspond to the Gutenberg-Bullen *A* earth model as tabulated in Alterman et al. (1961).

Correction of VLBI observables for atmospheric loading

The basic VLBI equation for the geometric delay τ is

$$\tau = \frac{-\vec{\mathbf{b}}\cdot\vec{\mathbf{k}}}{c} \tag{2}$$

τ consists of the scalar product of the baseline vector $\vec{\mathbf{b}}$ and the unit vector in radio source direction $\vec{\mathbf{k}}$, divided by the velocity of light c. Equation (2) can be used to compute the delay corrections τ_{ld} due to displacements $\Delta\vec{\mathbf{r}}^i_{\mathrm{ld}} (i=1,2)$ of two VLBI stations which may be caused by atmospheric loading. Referring to Fig. 3, we define

$$\vec{\mathbf{b}}_0(t) = \vec{\mathbf{r}}^2(t) - \vec{\mathbf{r}}^1(t) \tag{3a}$$

and

$$\vec{\mathbf{b}}_{\mathrm{ld}}(t) = [\vec{\mathbf{r}}^2(t) + \Delta\vec{\mathbf{r}}^2_{\mathrm{ld}}(t)] - [\mathbf{r}^1(t) + \Delta\mathbf{r}^1_{\mathrm{ld}}(t)] \tag{3b}$$

and

$$\Delta\vec{\mathbf{b}}_{\mathrm{ld}}(t) = \vec{\mathbf{b}}_{\mathrm{ld}}(t) - \vec{\mathbf{b}}_0(t). \tag{3c}$$

$\vec{\mathbf{b}}_0(t)$ is the baseline vector at time t under reference conditions (e.g. for a constant global air pressure), $\vec{\mathbf{b}}_{\mathrm{ld}}(t)$ is the baseline vector after consideration of the load-induced displacements $\Delta\vec{\mathbf{r}}^i_{\mathrm{ld}}$ of the VLBI stations. The displacement vectors $\Delta\vec{\mathbf{r}}^i_{\mathrm{ld}}$ of the two stations may be expressed in vertical and horizontal components. Inserting the difference vector $\Delta\vec{\mathbf{b}}_{\mathrm{ld}}(t)$ into Eq. (2), one obtains the delay correction $\tau_{\mathrm{ld}}(t)$ which has to be subtracted from the observed delay:

$$\tau_{\mathrm{ld}}(t) = \frac{1}{c}[\Delta\vec{\mathbf{r}}^1_{\mathrm{ld}}(t) - \Delta\vec{\mathbf{r}}^2_{\mathrm{ld}}(t)]\cdot\vec{\mathbf{k}}. \tag{4}$$

τ_{ld} depends on the difference of the two displacement vectors $\Delta\vec{\mathbf{r}}^i_{\mathrm{ld}}$ at time t and, therefore, on the length and the direction of the vectors $\Delta\vec{\mathbf{r}}^i_{\mathrm{ld}}$ (see Fig. 3). In addition, τ_{ld} is proportional to the cosine of angle θ between the difference vector and the direction of the source vector $\vec{\mathbf{k}}$. During an experiment the corrections τ_{ld} vary according to the variation of the displacement vectors $\Delta\vec{\mathbf{r}}^i_{\mathrm{ld}}$ with time as well as according to the specific direction of the observed radio source. Of course, τ_{ld} corresponds to the error contribution of the observed delays, if the atmospheric loading effect is disregarded.

Simulation of the effect of atmospheric loading on VLBI experiments

Air pressure changes by (anti-)cyclones

The effects of atmospheric loading on VLBI observations and on the parameters obtained in a baseline solution are investigated by studying the time dependence of station displacements for different models.

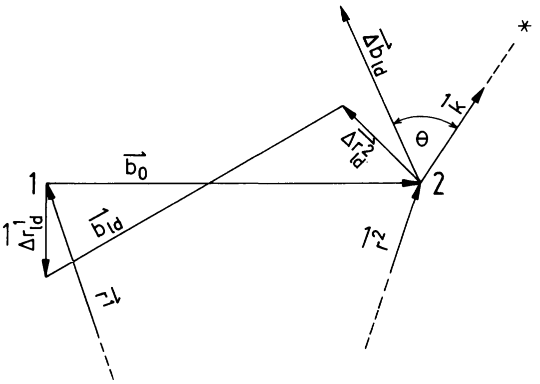

Fig. 3. Baseline-radiosource geometry of VLBI observations
$\vec{\mathbf{r}}^i$ - position vectors of VLBI stations $i=1,2$
$\vec{\mathbf{b}}_0$ - baseline vector under reference conditions
$\vec{\mathbf{b}}_{\mathrm{ld}}$ - baseline vector after consideration of the load-induced displacements $\Delta\vec{\mathbf{r}}^i_{\mathrm{ld}}$ of the VLBI stations $(i=1,2)$
$\Delta\vec{\mathbf{b}}_{\mathrm{ld}}$ - load-induced baseline difference $\vec{\mathbf{b}}_{\mathrm{ld}} - \vec{\mathbf{b}}_0$
$\vec{\mathbf{k}}$ - unit vector in source direction
θ - angle between $\Delta\vec{\mathbf{b}}_{\mathrm{ld}}$ and $\vec{\mathbf{k}}$

In order to use a realistic dataset for the simulations, real VLBI observations were taken from the MkIII experiment of 5/6 May 1983 of the transatlantic baseline between Effelsberg ($\varphi = 50°31'$, $\lambda = 6°53'$) and Haystack ($\varphi = 42°37'$, $\lambda = 288°30'$). The length of this baseline is approximately 6,000 km. A least-squares baseline solution of the 24-h dataset yields a delay rms σ_τ of 0.11 ns.

To separate the effect of the simulated air-pressure-induced displacements on the data analysis from other error sources, the original dataset has to be "optimized": the residuals of first analysis are added to the data in such a way that a repetition of the same process would yield error-free results. After this the air-pressure-induced delay corrections $\tau_{\mathrm{ld}}(t)$ are added and the "new" data set is analysed again to investigate the artificially introduced errors. Simulations of this kind have been carried out for the following types of station movements (see Fig. 4).

Model 1: linear change of vertical displacements $\Delta\mathbf{r}$ of both stations by 2 cm/24 h (acting in the same direction); no horizontal displacements (Fig. 4, top, left).

Model 2: linear change of vertical displacements $\Delta\mathbf{r}$ of station Effelsberg by +2 cm/24 h, of station Haystack by −2 cm/24 h; no horizontal displacements (Fig. 4, middle, left).

Model 3: sinusoidal change of vertical displacements of station Haystack with daily period and an amplitude of 1 cm; no displacement of Effelsberg; no horizontal displacements (Fig. 4, bottom, left).

Model 4: "mixed model"; non-linear changes of vertical and horizontal displacements of both stations (Fig. 4, right).

Extreme air pressure conditions will generate larger displacements than those supposed here. In this case the resulting delay corrections increase proportionally. In order to separate short periodic and seasonal air pressure effects, the vertical and horizontal displacements

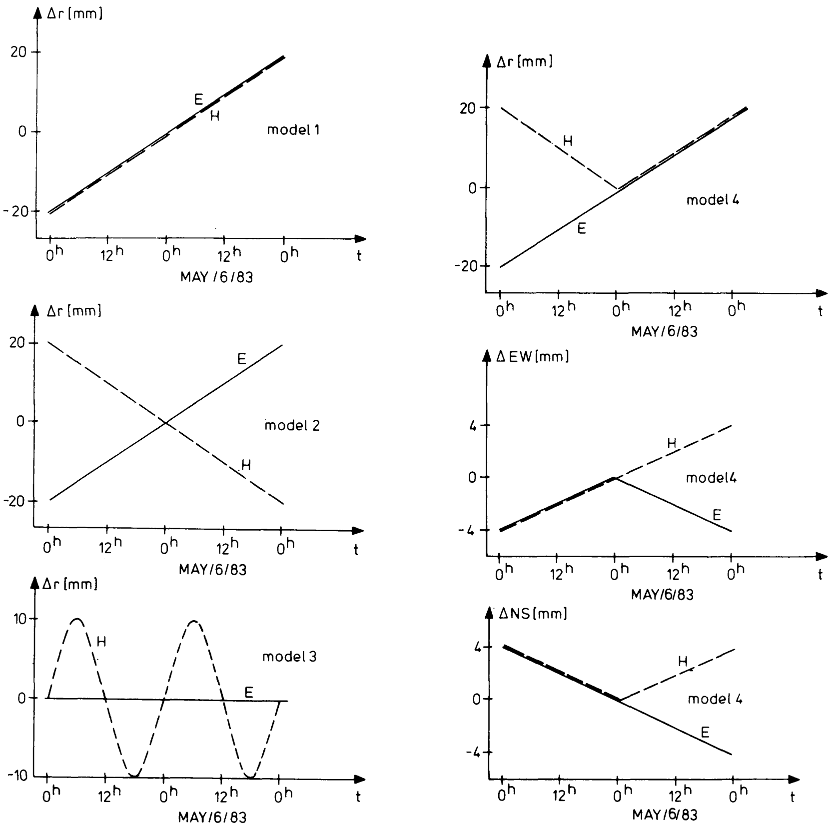

Fig. 4. Models of load-induced displacements used for simulations: E-Effelsberg, H-Haystack; Models 1–3, only vertical displacements; Model 4, vertical and horizontal displacements

are regarded as deviations from a mean station position due to a mean surface air pressure of 1,013 mbar.

For the simulations, the VLBI program package BVSS (Bonn VLBI Software System; Schuh, 1985) developed at the Geodetic Institute of the University of Bonn was used. In the standard solution of a single VLBI experiment the components of the baseline vector $\vec{b}$, the parameters of the clock model (i.e. the behaviour of the station clocks referred to a reference clock) and the parameters of a model of the tropospheric zenith delay ("atmospheric parameters") (Lundquist, 1984) are estimated. For the "optimal" dataset (see above), different combinations of the parameter groups of the VLBI model (baseline components, atmospheric parameters, clock parameters) were analysed. Thus, the influence of atmospheric loading on the various groups of unknowns can be separated. The influence on radio source positions and earth rotation parameters (pole coordinates and UT1 variations) was not examined. Whereas the positions of those radio sources which are normally observed in geodetic experiments are known with high precision and are usually fixed in single-experiment solutions, the earth rotation parameters in a single-baseline solution are directly connected with the baseline orientation and are therefore influenced equally.

The choice of the parameters to be solved was based on the following questions:

1. Does atmospheric loading decrease the precision of VLBI observations?

2. Are the baseline components, and above all the baseline length, affected?

3. Are the loading effects due to air pressure variations covered by those parameters of the VLBI model which are used for the description of tropospheric zenith delay?

4. Can the clock parameters of the VLBI model be used to remove air-pressure-induced errors? (With these parameters most of the systematic effects besides the clock behaviour can be removed.)

The results of the simulations are summarized in Table 1. As an example of the resulting delay corrections τ_{ld}, those of Model 2 are plotted in Fig. 5. It can clearly be seen that the opposite vertical displacements lead to a linear trend of the corrections, which can mainly be removed by a simple clock model with three parameters (reduction of the delay rms from 0.025 ns to 0.004 ns). The source specific differences mentioned previously, i.e. the dependence of the corrections on the direction of the source vector, can also be seen in Fig. 5.

Figure 6 shows the corrections which result from Model 4. Table 1 indicates that those more "accidental" contributions of atmospheric loading cannot be described completely: neither by the baseline components (decrease of σ_τ from 0.024 ns to 0.013 ns), nor by the clock parameters (decrease of σ_τ to 0.014 ns).

From the results in Table 1, further conclusions can be derived:

The effects of short-period atmospheric loads on VLBI stations can cause errors in the delay observations which, even in the worst cases, are below the actual VLBI precision of ±3 cm (=0.10 ns). However,

Table 1. Delay rms σ_τ(ns) and change in baseline length Δb(mm) from simulations of the influence of different models of station displacements (Models 1-4) on the "error-free" dataset of the MkIII VLBI experiment from May 5-6, 1983, Effelsberg-Haystack baseline

Model	Error contribution from atmospheric loading (ns)	Delay rms σ_τ(ns) and change in baseline length Δb after solving for:			
		Only baseline components	Baseline components + atmospheric parameters	Only clock parameters (2^{nd} order polynomial)	Baseline components + atmos. parameters + clock parameters
1	0.008	0.007 $\Delta b = -3$ mm	0.007 $\Delta b = -2$ mm	0.008	0.007 $\Delta b = -2$ mm
2	0.025 (Fig. 5)	0.024 $\Delta b = 1$ mm	0.024 $\Delta b = 7$ mm	0.004	0.004 $\Delta b = 0$ mm
3	0.017	0.016 $\Delta b = -2$ mm	0.016 $\Delta b = -5$ mm	0.009 with sine: 0.005	0.009 $\Delta b = -3$ mm 0.005 $\Delta b = -2$ mm
4	0.024 (Fig. 6)	0.013 $\Delta b = -6$ mm	0.013 $\Delta b = -8$ mm	0.014	0.008 $\Delta b = -6$ mm

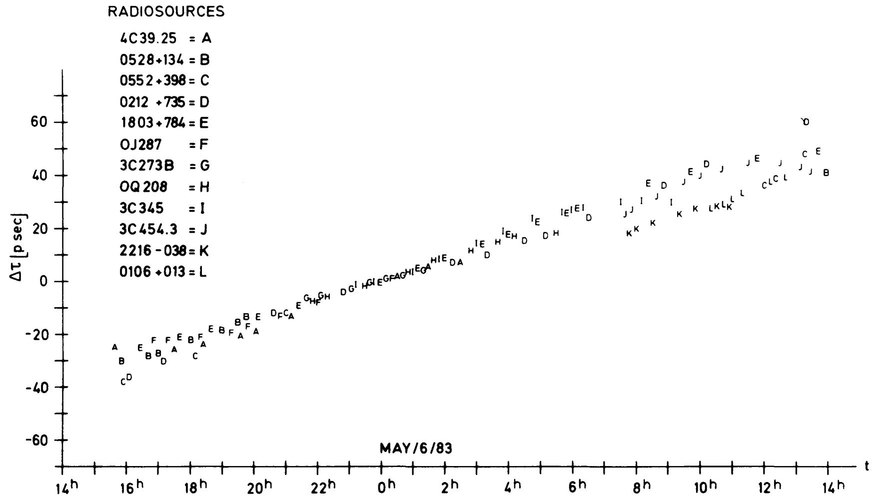

Fig. 5. Delay corrections τ_{ld} caused by the station displacements simulated in Model 2 (see Fig. 4, top, left)

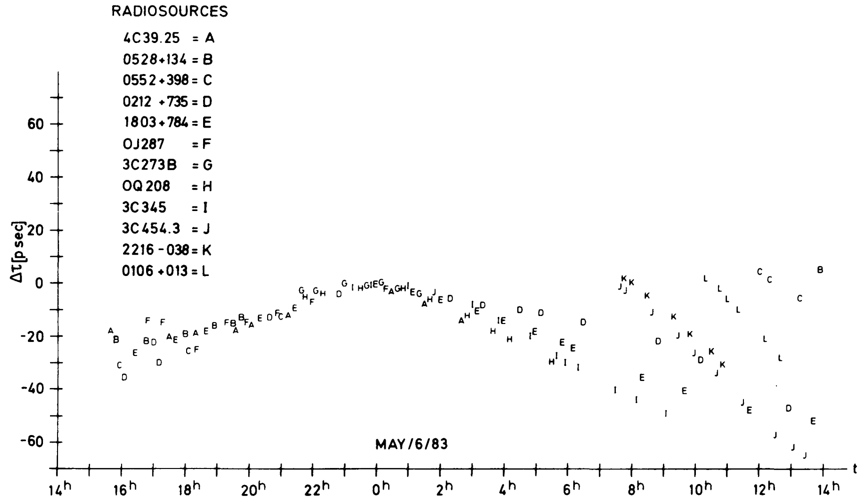

Fig. 6. Delay corrections τ_{ld} caused by the station displacements simulated in Model 4 (see Fig. 4, right)

to reach the general scope of the so-called "1-cm accuracy" they have to be considered.

The delay errors τ_{ld} can influence the baseline components derived in a geodetic solution, and, therefore, they can also falsify the baseline length. The change in the baseline length for the considered displacement models is within some millimetres. It will easily exceed 1 cm under more extreme conditions.

Except for special cases, the delay errors cannot be described by the general clock parameters of the VLBI

Table 2. Delay rms σ_τ(ns) and change in baseline length Δb(mm) from simulations of the influence of constant station displacements (Models 5 and 6) on the "error-free" dataset of the MkIII VLBI experiment from May 5-6, 1983, Effelsberg-Haystack baseline

Model	Error contribution from atmospheric loading (ns)	Delay rms σ_τ(ns) and change in baseline length Δb after solving for:			
		Only baseline components	Baseline components + atmospheric parameters	Only clock parameters (2^{nd} order polynomial)	Baseline components + atmos. parameters + clock parameters
5	0.022	0.000 $\Delta b = -1$ mm	0.000 $\Delta b = 0$ mm	0.004	0.000 $\Delta b = 0$ mm
6	0.007	0.000 $\Delta b = -5$ mm	0.000 $\Delta b = -5$ mm	0.007	0.000 $\Delta b = -5$ mm

model (Models 2, 3). Anyway, a careful choice of the clock parameters is necessary: for example, in Model 2 using a polynomial the delay rms decreases only from 0.017 ns to 0.009 ns, whereas introducing a sine it is reduced to 0.005 ns.

Although the station displacements are caused by variations of surface air pressure, the resulting delay errors seem to be almost completely independent of the so-called atmospheric parameters. As can be seen from comparison of columns 3 and 4 of Table 1, the rms does not decrease when atmospheric parameters are included. Only the baseline lengths (as well as the baseline components) change. This can be traced back to the well-known high correlations between the station heights and the atmospheric parameters (Campbell et al., 1984).

Seasonal air pressure variations

The influence of global seasonal air pressure variations on VLBI observations has also been analysed using the test dataset. As can be seen from Eq. (4) and Fig. 3, constant station displacements do not lead to constant corrections τ_{1d}, because these depend on the specific radio source (by the angle θ).

In order to investigate the effect of long periodic changes on VLBI observables, the following constant vertical shifts of the stations were simulated:

Model 5: vertical displacement of Effelsberg +5 mm, of Haystack −5 mm

Model 6: vertical displacement of Effelsberg +5 mm, of Haystack +5 mm.

The corrections for Model 5 are shifted by a constant offset (+0.022 ns) and differ between 0.014 and 0.030 ns. The various solutions mentioned above were also computed for these models of constant displacements. The results are summarized in Table 2. Constant displacements, of course, are completely absorbed by the estimated baseline components. Depending on the configuration between baseline vector and station displacement vectors, not only the components but also the length of the baseline itself can change by several millimetres. Thus, for the 6,000-km Effelsberg-Haystack baseline a constant vertical displacement of +5 mm for both stations (Model 6) leads to a 5-mm change in the baseline length, as confirmed by the results of the least-squares solution ($\Delta b = 5$ mm in Table 2).

Conclusions

Concerning the interpretation of geodetic VLBI experiments, the following conclusions can be drawn:

1) Large-scale atmospheric loading causes errors in baseline length and station coordinates which are of the same order of magnitude as the VLBI precision. They are not corrected by today's standard VLBI data analysis methods (so-called clock- and atmosphere parameters). Therefore, magnitude and time-dependence of air-pressure-induced displacements should be evaluated by forward modelling.

2) Since the exact calculation of surface displacements by the method of Green's functions is rather laborious, it will not become a routine procedure for all worldwide VLBI experiments in the near future. On the other hand, the amplitudes of local and mean regional air pressure variations can easily be obtained from station logs and weather charts for the duration of the VLBI experiments. Equation (1) can then be used to calculate approximate correction values for the vertical displacements. If higher accuracy is required, the method of Green's functions has to be applied. For the present, however, this will be necessary only for a few VLBI experiments.

3) At the moment, all radiotelescopes used for geodetic experiments are situated in areas with less than ±2 mm seasonal variation in the vertical displacement. Increasing VLBI accuracy and an expanding VLBI network will also require the consideration of seasonal displacements which can exceed the 1-cm limit. Seasonal variations of station position can easily be included in every VLBI data analysis program.

This paper has only treated the atmospheric loading effect on VLBI stations. The procedure that has been applied can be used to treat all deformation effects of similar character. The envisaged 1-cm accuracy for geodynamic investigations (e.g. NASA's Crustal Dynamics Project, see NASA, 1984) requires, in addition, the consideration or investigation of other exogenic surface deformations as caused by body tides, ocean loading tides, long-term variations of the sea level, local groundwater level or snow loading (e.g. see Varga, 1981; Scherneck, 1983).

Acknowledgements. We are grateful to P. Varga (Budapest), J. Kümpel (Kiel) and J. Zschau (Kiel) for fruitful discussions and critical comments on this paper. One of the authors

(H. Schuh) gratefully acknowledges the financial support provided by the Deutsche Forschungsgemeinschaft (DFG/ SFB 78). We thank K. Helbig for typing the manuscript.

References

Alterman, Z., Jorosch, H., Pekeris, C.L.: Propagation of Rayleigh waves in the earth. Geophys. J.R. Astron. Soc. **4**, 219-241, 1961

Campbell, J., Cloppenburg, H., Lohmar, F.J.: Estimating the ionospheric refraction effect on interferometric GPS-measurements. Proceedings of the International Symposium on Space Techniques for Geodynamics **2**, 196-206, Soppon, 1984

Farrell, W.E.: Deformation of the earth by surface loads. Rev. Geophys. Space Physics **10**, 761-797, 1972

Faust, H.: Der Aufbau der Erdatmosphäre. Braunschweig: Verlag Vieweg und Sohn 1968

Longman, J.M.: A Green's function for determining the deformation of the Earth under surface mass loads. J. Geophys. Res. **67**, 845-850, 1962

Lundquist, G.L.: Radio interferometry as a probe of tectonic plate motion. Chalmers University of Technology, Technical Report No. 250, 1984

NASA: NASA Technical Memorandum 87359. NASA Geodynamics Program: Fifth Annual Report. Houston, 1984

Rabbel, W., Zschau, J.: Static deformation and gravity changes at the earth's surface due to atmospheric loading. J. Geophys. **56**, 81-99, 1985

Scherneck, H.-G.: Crustal loading affecting VLBI sites. University of Uppsala, Institute of Geophysics, Department of Geodesy, Report No. 20, Uppsala, 1983

Schuh, H.: Auswertemodelle der astronomisch/geodätisch genutzten VLBI. Mitteilungen der Geodätischen Institute der Rheinischen Friedrich-Wilhelm-Univ. Bonn, No. 70, 17-28, 1985

Stolz, A., Larden, D.R.: Seasonal displacement and deformation of the earth by the atmosphere. J. Geophys. Res. **84**, 6185-6194, 1979

Trubytsin, A.P., Makalkin, A.V.S.: Deformation of the earth's crust due to atmospherical cyclones. Izv. Acad. Sci. USSR, Phys. Solid Earth **12**, 343-344, 1976

Varga, P.: Displacements of the Earth surface caused by external forces. 4th Intern. Symp. Geodesy and Physics of the Earth, G.D.R. Karl-Marx-Stadt, 1980, proc. part III, Veröffentlichungen des Zentralinstituts für Physik der Erde Nr. 63, Teil III, 793-807, 1981

Zschau, J.: Auflastgezeiten. Habilitation-thesis, University of Kiel, 1979

Received February 14, 1986; revised version May 1, 1986
Accepted May 1, 1986

J Geophys (1986) 59:171-176

Journal of Geophysics

Discrete frequency inequalities for magnetotelluric impedances of one-dimensional conductors

P. Weidelt

Institut für Geophysik und Meteorologie, Technische Universität, Mendelssohnstr. 3, D-3300 Braunschweig,
Federal Republic of Germany

Abstract. For the one-dimensional magnetotelluric inverse problem the ties between the impedances at neighbouring frequencies, reflecting the analytical properties of the transfer function, are expressed in terms of inequalities between the data. After the derivation of some elementary necessary constraints for data sets with two or three frequencies, a set of necessary and sufficient conditions warranting the existence of a one-dimensional conductivity model in the general M-frequency case is given. This set of constraints characterizes a 1-D data set by the signs of $2M$ determinants derived from the data.

Key words: Magnetotellurics – Inverse problem

Introduction

The transfer functions of electromagnetic induction are analytical functions of frequency which, in principle, are completely defined for all frequencies by prescribing them only on an arbitrarily small interval. This introduces strong ties between the values of the transfer functions at neighbouring frequencies. Measured data in general do not show these strong interrelations, they are inconsistent and can be interpreted only in the least squares sense. The nature of the frequency constraints depends on the allowed class of models, being defined by the conductivity distribution and the source field. Of interest is the problem of finding both necessary and sufficient criteria which identify a given data set as belonging to a specified class of models. Necessary conditions are diagnostic if at least one of them is violated; on the other hand, sufficient conditions are diagnostic if all of them are satisfied. If the set of necessary and sufficient conditions is identical, they will provide a complete characterization of the admitted data sets.

In the present paper a complete characterization of data is given for the simple class of one-dimensional conductivity models with a quasi-uniform inducing field, which is the classical magnetotelluric case (Cagniard, 1953). The solution in terms of inequalities to be satisfied within the data set is presented in the third section. In the preceding section, some elementary necessary inequalities for two and three data sets are derived.

All inequalities also hold for the slightly extended class of spatially harmonic source fields, provided that the data belong to the same modulus of the horizontal wavenumber vector. The inequalities also apply to a spherically layered earth with a single spherical harmonic of fixed degree as source field (Weidelt, 1972).

Necessary conditions for data sets with two and three frequencies

Assuming a time factor $e^{i\omega t}$ and SI units, Schmucker's transfer function $c(\omega)$ is defined as

$$c(\omega)=\frac{E_x(\omega)}{i\omega\mu_0 H_y(\omega)}=g(\omega)-ih(\omega)=|c(\omega)|\,e^{-i\psi(\omega)}, \tag{1}$$

where E_x and H_y are two orthogonal horizontal components of the electric and magnetic field at the surface, and μ_0 is the magnetic permeability of free space. The relation between c and the commonly used impedance Z, apparent resistivity ρ_a, and phase φ is

$$Z=i\omega\mu_0 c, \qquad \rho_a=\omega\mu_0|c|^2, \qquad \varphi=90^\circ-\psi. \tag{2}$$

For a 1-D conductivity structure the theoretical data allow the spectral expansion (Weidelt, 1972; Parker, 1980)

$$c(\omega)=a_0+\int_0^\infty \frac{a(\lambda)\,d\lambda}{\lambda+i\omega} \tag{3}$$

with $a_0 \geqq 0$, $a(\lambda)\geqq 0$, where $a(\lambda)$ is a generalized function to include both the discrete and continuous part of the spectrum. For sake of convenience the following discussion is confined to a fully discrete version of Eq. (3)

$$c(\omega)=a_0+\sum_{n=1}^{N}\frac{a_n}{b_n+i\omega} \tag{4}$$

with $a_0\geqq 0$, $a_n>0$, $b_n\geqq 0$. The set b_n is assumed to be distinct. The extension of all results to the more general case (3) is straightforward.

The discrete frequency inequalities given in this section are generalizations of a set of smoothness constraints given by Weidelt [1972, Eqs. (2.33a, b) and (2.34a, b)], which read

$$|c'|\leqq h/\omega, \qquad |(\omega c)'|\leqq g, \tag{5a, b}$$

$$|c'+\omega c''|\leqq h/\omega, \qquad |(\omega c)'+\omega(\omega c)''|\leqq g, \tag{6a, b}$$

where $c' := dc/d\omega$, $c'' := d^2c/d\omega^2$. These inequalities are necessary conditions for real data to be consistent with a 1-D conductivity model. Since the required differentiations are difficult to perform with real data, discrete frequency analogues are more appropriate. In the following, the abbreviations $c_j := c(\omega_j)$, etc. are used.

a) Let ω_1 and ω_2 be two distinct frequencies. Then the analogues of (5a, b) are

$$\left|\frac{c_2-c_1}{\omega_2-\omega_1}\right|^2 \leqq \frac{h_1 h_2}{\omega_1\omega_2}, \qquad \left|\frac{\omega_2 c_2-\omega_1 c_1}{\omega_2-\omega_1}\right|^2 \leqq g_1 g_2. \tag{7a, b}$$

b) Let ω_1, ω_2 and ω_3 be three equidistant frequencies with $\omega_1=\omega_2-\Delta$, $\omega_3=\omega_2+\Delta$, $\Delta \neq 0$ (e.g. three successive harmonics). Then the counterparts of (6a, b) are

$$\left|\frac{c_3-c_1}{2\Delta}+\omega_2\frac{c_3-2c_2+c_1}{\Delta^2}\right|^2 \leqq \frac{h_1 h_3}{\omega_1\omega_3}, \tag{8a}$$

$$\left|\frac{\omega_3 c_3-\omega_1 c_1}{2\Delta}+\omega_2\frac{\omega_3 c_3-2\omega_2 c_2+\omega_1 c_1}{\Delta^2}\right|^2 \leqq g_1 g_3. \tag{8b}$$

The proofs follow almost immediately by inserting Eq. (4). Consider as an example the most involved inequality (8b). With the abbreviation

$$A := \frac{\omega_3 c_3-\omega_1 c_1}{2\Delta}+\omega_2\frac{\omega_3 c_3-2\omega_2 c_2+\omega_1 c_1}{\Delta^2}$$

one finds

$$A = a_0+\sum_{n=1}^{N}\frac{a_n b_n(b_n-i\omega_2)}{(b_n+i\omega_1)(b_n+i\omega_2)(b_n+i\omega_3)},$$

$$|A| \leqq a_0+\sum_{n=1}^{N}\frac{a_n b_n}{(b_n^2+\omega_1^2)^{1/2}(b_n^2+\omega_3^2)^{1/2}}.$$

The Cauchy-Schwarz inequality

$$\left(\sum_{n=0}^{N} p_n q_n\right)^2 \leqq \sum_{n=0}^{N} p_n^2 \sum_{m=0}^{N} q_m^2$$

with $p_0=q_0 := \sqrt{a_0}$ and

$$p_n := \left(\frac{a_n b_n}{b_n^2+\omega_1^2}\right)^{1/2}, \qquad q_n := \left(\frac{a_n b_n}{b_n^2+\omega_3^2}\right)^{1/2}, \qquad n \geqq 1$$

then yields $|A|^2 \leqq g_1 g_3$.

Equality holds in Eqs. (7a) and (8a) only for $N=0$ or $N=1$, equality in Eqs. (7b) and (8b) requires either $N=0$, $a_0>0$ or $N=1$, $a_0=0$. In the special case $\omega_1=0$, $\omega_2=\omega$, Eq. (7b) reduces to $|c(\omega)|^2 \leqq g(0)g(\omega)$, implied already in Eq. (5.6) of Parker (1972). The formulation of the above constraints in terms of apparent resistivity and phase does not lead to simple results.

Existence conditions for the general *M*-frequency case

The M complex data $c_j=g_j-ih_j$, $j=1,\ldots,M$ are given for M distinct frequencies ω_j. The necessary and sufficient conditions, under which the data can be interpreted by a 1-D model are, investigated. This problem of existence has previously been discussed by Parker (1980), who states as necessary and sufficient conditions for the consistency with a 1-D model that the data have to allow a representation of type (4). The actual consistency check then requires the solution of a quadratic programming problem with positivity constraints. In the present approach the answer to the existence problem is given in terms of $2M$ inequality constraints to be satisfied within the data set.

The complete formulation of the constraints requires the distinction between a regular and a degenerate case. In the *regular* case there exists a representation of the data as an expansion (4) involving *at least* $2M$ positive constants. In theory this requirement is met for all physical conductors (i.e. not infinitely thin conductors), which lead to a representation with an infinite number of positive constants. The regular case also results from a conductivity structure with more than M thin sheets. For the given frequency set ω_j, $j=1,\ldots,M$, any theoretical response $c(\omega)$ of the regular case can be interpolated by two different representations requiring exactly $2M$ positive constants

$$1)\ c_j=\sum_{m=1}^{M}\frac{A_m}{B_m+i\omega_j}, \tag{9}$$

$$2)\ c_j=\bar{A}_0+\sum_{m=1}^{M-1}\frac{\bar{A}_m}{\bar{B}_m+i\omega_j}+\frac{\bar{A}_M}{i\omega_j}, \tag{10}$$

$j=1,\ldots,M$ (Weidelt, 1985). These representations allow a physical interpretation as an equivalent stack of thin sheets. The $2M$ positive constants in Eqs. (9) or (10) will induce a set of $2M$ positivity constraints as consistency conditions within the data set.

In the *degenerate* case the data are represented by Eq. (4) with *less than* $2M$ positive constants. The existence conditions will now also involve a number of equality constraints corresponding to the number of deficient constants. Therefore, the more complicated degenerate case is of no relevance for consistency checks with real data and will be discussed in the Appendix for completeness only.

Before stating the consistency conditions, some further definitions are required. By linear combination with the weights

$$\alpha_{jk} := (-\omega_j^2)^k \Big/ \prod_{\substack{l=1\\ l\neq j}}^{M}(\omega_l^2-\omega_j^2) \tag{11}$$

$k=0,\ldots,M-1$, $j=1,\ldots,M$ and $\alpha_{10}=1$ for $M=1$, a set of new data β_m is defined as

$$\beta_{2k} := \sum_{j=1}^{M}(h_j/\omega_j)\alpha_{jk}, \tag{12a}$$

$$\beta_{2k+1} := \sum_{j=1}^{M} g_j\alpha_{jk}, \tag{12b}$$

$k=0,\ldots,M-1$. With these data we form the symmetrical $(j+1)$-order determinants

$$\Delta^{(i)}_{j+1}=\begin{vmatrix}\beta_i & \beta_{i+1} & \cdots & \beta_{i+j}\\ \beta_{i+1} & \beta_{i+2} & \cdots & \beta_{i+j+1}\\ \vdots & \vdots & & \vdots\\ \beta_{i+j} & \beta_{i+j+1} & \cdots & \beta_{i+2j}\end{vmatrix}=\det\{\beta_{i+m+n}\} \tag{13}$$

$m,n=0,\ldots,j$. The argument i indicates that β_i is the upper-left corner element. The matrices associated with $\Delta_{j+1}(i)$ are Hankel matrices, i.e. the entries depend only on the sum of the indices of the rows and the columns. Since β_m is defined only up to $m=2M-1$, Eq. (13) is subject to the constraint $0\leqq i+2j\leqq 2M-1$. With the above definitions the characterization theorem for the regular case reads:

The necessary and sufficient conditions, in order that the data $c_j=g_j-ih_j$ for the frequencies ω_j, $j=1,\ldots,M$ can be interpreted by a regular one-dimensional conductivity model, are the $2M$ positivity constraints

$$\Delta_k(i)>0, \quad i=0,1 \quad \text{and} \quad k=1,\ldots,M. \tag{14}$$

Necessity

It has to be shown that the response function representation of type (4) with at least $2M$ positive constants implies the inequalities (14). Using the partial fraction expansion

$$x^{2k}\Big/\prod_{j=1}^{M}(x^2+\omega_j^2)=\sum_{j=1}^{M}\frac{\alpha_{jk}}{x^2+\omega_j^2}, \quad k=0,\ldots,M-1 \tag{15}$$

with α_{jk} defined in Eq. (11) and

$$g_j=a_0+\sum_{n=1}^{N}\frac{a_n b_n}{b_n^2+\omega_j^2}, \tag{16a}$$

$$h_j/\omega_j=\sum_{n=1}^{N}\frac{a_n}{b_n^2+\omega_j^2}, \tag{16b}$$

$$\sum_{j=1}^{M}\alpha_{jk}=\delta_{k,M-1}, \quad 0\leqq k\leqq M-1,$$

where δ_{km} is the Kronecker symbol, Eqs. (4) and (12a, b) yield

$$\beta_m=a_0\delta_{m,2M-1}+\sum_{n=1}^{N}\gamma_n b_n^m, \quad m=0,\ldots,2M-1 \tag{17}$$

with

$$\gamma_n:=a_n\Big/\prod_{j=1}^{M}(b_n^2+\omega_j^2)>0. \tag{18}$$

The determinants $\Delta_k(i)$ defined in Eq. (13) are according to the Cauchy-Binet theorem (e.g. Smirnov, 1964, p. 28) for $i+2k<2M+1$ given by

$$\Delta_k(i)=\sum\left\{\prod_{m=1}^{k}\gamma_{n_m}b^i_{n_m}\right\}\cdot\begin{vmatrix}1 & b_{n_1} & \cdots & b_{n_1}^{k-1}\\ \vdots & \vdots & & \vdots\\ 1 & b_{n_k} & \cdots & b_{n_k}^{k-1}\end{vmatrix}^2. \tag{19}$$

For $i+2k=2M+1$, the term $a_0\delta_{m,2M-1}$ in Eq. (17) gives rise to the additional term $a_0\Delta_{k-1}(i)$ on the right-hand side. The summation in Eq. (19) extends over all k-tuples n_m, $m=1,\ldots,k$ with $1\leqq n_1<n_2<\ldots<n_k\leqq N$. This summation can equivalently be represented by

$$\frac{1}{k!}\sum_{n_1=1}^{N}\cdots\sum_{n_k=1}^{N}$$

(e.g. Smirnov, 1964, p. 23), which is immediately generalized to a k-fold integral in the case of the integral representation (3). The determinants $\Delta_k(i)$ are positive for $k<N$, so that Eq. (14) is certainly satisfied for $M<N$. Since it is assumed that Eq. (4) involves at least $2M$ positive constants, it is excluded that a_0 and $\min\{b_n\}$ vanish simultaneously in the case $M=N$. The determinant $\Delta_M(1)$ involves the additional term $a_0\Delta_{M-1}(1)$ and, therefore, is positive even if $\min\{b_n\}=0$.

Sufficiency

It has to be shown that the data constraints (14) are sufficient to ensure the existence of *any* regular 1-D response function. This may be of type (4) with $N\geqq M$ or even of the simpler type (9) or (10). For ease of presentation, attention is confined to Eq. (9); identical sufficient conditions, however, are obtained when starting from Eq. (10), which is of course a necessary requirement (cf. the remark at the end of the Appendix).

Using the same procedure, which has led to Eq. (17), we infer from Eq. (9)

$$\sum_{n=1}^{M}G_n B_n^m=\beta_m, \quad m=0,\ldots,2M-1 \tag{20}$$

with

$$G_n:=A_n\Big/\prod_{j=1}^{M}(B_n^2+\omega_j^2). \tag{21}$$

The conditions on the data β_m, under which the nonlinear system (20) has $2M$ positive solutions G_k (or A_k) and B_k, $k=1,\ldots,M$, has to be investigated. This is just the finite moment problem, for which the existence conditions are well-known (e.g. Gantmacher, 1959, Chap. 15, §16). The main arguments are briefly repeated here in a slightly modified way. Taking the generic pair G_p, B_p, $p\in[1,M]$, a set of M variables $x_k=x_k(p)$ is defined by the expansion

$$\prod_{m=1}^{M}{}'\,\frac{\lambda-B_m}{B_p-B_m}=\sum_{k=0}^{M-1}x_k\lambda^k, \tag{22}$$

where the prime denotes the omission of the factor $m=p$. Then Eqs. (20) and (22) yield

$$\sum_{k=0}^{M-1}\beta_{i+j+k}x_k=G_pB_p^{i+j}, \quad i+j=0,\ldots,M,$$

from which the final result

$$\sum_{k=0}^{M-1}\sum_{j=0}^{M-1}\beta_{i+j+k}x_jx_k=G_pB_p^i, \quad i=0,1 \tag{23}$$

is obtained by appealing again to Eq. (22). The left-hand side of Eq. (23) presents the M-dimensional *quadratic form*

$$Q(i)=\sum_{j=0}^{M-1}\sum_{k=0}^{M-1}q_{jk}(i)x_jx_k, \quad i=0,1 \tag{24}$$

with $q_{jk}=q_{kj}=\beta_{i+j+k}$.

At this point it is necessary to recall some properties of quadratic forms (e.g. Smirnov, 1964, pp. 125–130). A quadratic form Q is called *positive definite* if it assigns a positive value to any real M-tuple $x_0, \ldots, x_{M-1}$ with $\sum x_m^2 > 0$. Criteria for the positive definite character of Q can be formulated in terms of the signs of certain determinants derived from the elements q_{jk}. A *principal minor* of order k of the M-dimensional quadratic form Q is the determinant of the remainder of the quadratic array q_{jk} after deleting *any* $(M-k)$ rows and columns intersecting at the main diagonal. A subset of these principal minors are the *corner minors* Δ_k obtained by deleting the *last* $(M-k)$ rows and columns. Then Q is positive definite if (and only if) $\Delta_k > 0$, $k = 1, \ldots, M$. This result is proved by Jacobi's theorem (Smirnov, 1964, p. 130), which reduces Q to a sum of squares on using a triangular transformation

$$\xi_k = x_k + \sum_{l=k+1}^{M-1} a_{kl} x_l, \qquad k = 0, \ldots, M-1, \tag{25}$$

and leads under the conditions $\Delta_k > 0$ to

$$Q = \sum_{k=0}^{M-1} (\Delta_{k+1}/\Delta_k)\xi_k^2, \qquad \Delta_0 = 1. \tag{26}$$

Since the determinant of the transformation (25) is nonzero, all ξ_k vanish only if all x_k vanish. Therefore, the conditions $\Delta_k > 0$ are sufficient to ensure that Eq. (26) assigns a positive value to any set x_k with $\sum x_k^2 > 0$, i.e. that Q is positive definite.

The positive definite character of Q does not change by renumbering the variables x_k. However, the corner minors will change and a set of different but equivalent conditions is obtained. By a suitable renumbering each principal minor can serve as corner minor. Hence, all principal minors of a positive definite quadratic form are positive.

The conditions (14) ensure, in view of Eq. (26), that $Q(0)$ and $Q(1)$ are positive definite. From $Q(0)$ it then follows, via Eq. (23), that G_p is positive. This result, in conjunction with $Q(1) > 0$, shows also that B_p is positive and completes the proof for the regular case. From the principal minors of $Q(0)$ and $Q(1)$ one may obtain $2(2^M - 1)$ inequalities from which, however, only $2M$ are independent.

The evaluation of the conditions (14) yields

a) for $M = 1$:

$$\beta_0 > 0, \quad \beta_1 > 0 \quad \text{or} \quad h_1 > 0, \quad g_1 > 0,$$

b) for $M = 2$:

$$\beta_0 > 0, \quad \beta_1 > 0,$$

$$\beta_0\beta_2 - \beta_1^2 > 0, \quad \beta_1\beta_3 - \beta_2^2 > 0$$

or

$$\frac{h_2/\omega_2 - h_1/\omega_1}{\omega_2 - \omega_1} < 0, \qquad \frac{g_2 - g_1}{\omega_2 - \omega_1} < 0, \tag{27a, b}$$

$$\left|\frac{c_2 - c_1}{\omega_2 - \omega_1}\right|^2 < \frac{h_1 h_2}{\omega_1 \omega_2}, \qquad \left|\frac{\omega_2 c_2 - \omega_1 c_1}{\omega_2 - \omega_1}\right|^2 < g_1 g_2. \tag{27c, d}$$

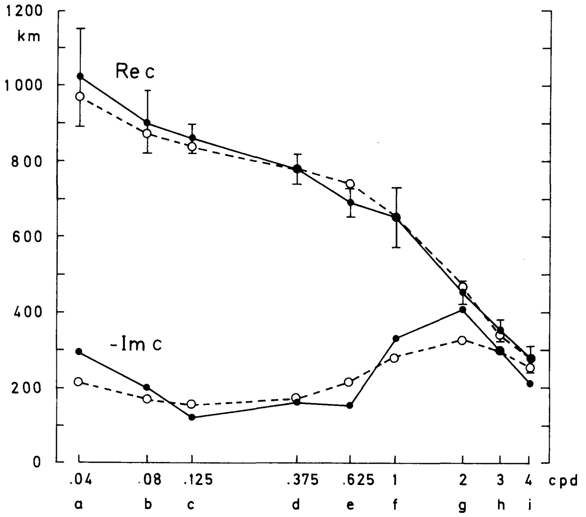

	a	b	c	d	e	f	g	h
b	+							
c	–	–						
d	+	+	+					
e	+	+	+	–				
f	+	+	+	–	–			
g	+	+	+	–	–	–		
h	+	+	+	+	–	+	–	
i	+	+	+	+	–	+	–	–

Fig. 1. Pairwise existence checks for a real data set *(full lines)*. A "+" (or "–") in the *table at the bottom* indicates that the particular frequency pair can (or cannot) be interpreted by a 1-D conductivity model. The best 1-D fit is shown by *dashed lines*

There exist equivalent constraint sets in which $\beta_0 > 0$ and/or $\beta_1 > 0$ are replaced by $\beta_2 > 0$ and/or $\beta_3 > 0$, i.e.

$$\frac{h_2\omega_2 - h_1\omega_1}{\omega_2 - \omega_1} > 0 \quad \text{and/or} \quad \frac{g_2\omega_2^2 - g_1\omega_1^2}{\omega_2 - \omega_1} > 0.$$

Explicit expressions of the constraints (14) for $M > 2$ are lengthy and not particularly illuminating. The inequalities (27c, d) agree with (7a, b). Therefore, one might expect that in the equidistant three-frequency case the conditions $\Delta_2(i) > 0$, $i = 0, 1$ would reproduce (8a, b). However, $\Delta_2(i) > 0$ yields the different inequalities

$$\left|\frac{F_3 - F_1}{2\Delta} - \omega_2 \frac{F_3 - 2F_2 + F_1}{\Delta^2}\right|^2 < f_1 f_3 - \omega_2 f_2 \frac{f_3 - f_1}{\Delta}$$
$$+ 2\omega_2^2 \frac{f_1 f_2 - 2 f_1 f_3 + f_2 f_3}{\Delta^2} = f_1 f_3 - \omega_2 f_2 \frac{f_3 - f_1}{\Delta}$$
$$+ 2\omega_2^2 \left[2 \frac{f_2 - f_1}{\Delta} \cdot \frac{f_3 - f_2}{\Delta} - f_2 \frac{f_3 - 2f_2 + f_1}{\Delta^2}\right]$$

with $F_j = c_j$, $f_j = h_j/\omega_j$ for $i = 0$ and $F_j = \omega_j c_j$, $f_j = g_j$ for $i = 1$.

For moderate M the signs of the determinants (14) can be obtained by counting the negative signs in the nontrivial diagonal after an LU-decomposition of the associated matrix, allowing for the possible interchange of rows by pivotting. Since consistency depends only on the relative amplitudes of data and frequencies, these quantities can be scaled to avoid large or small numbers.

Figure 1 shows an application of Eq. (27a–d) to a set of real data, consisting of nine low-frequency response estimates for Europe (U. Schmucker, personal communication). The data (connected by full lines) are of good quality, as is seen by comparing them with the best-fitting 1-D model (dashed lines). This best fit to a representation (4) is obtained by quadratic programming, using a least-squares norm with the inverse variances as weights (Parker, 1980). The residuals generally lie within one standard deviation (given in Fig. 1 only for $g = \mathrm{Re}\ c$; the same error estimate, however, applies also to $h = -\mathrm{Re}\, c$). The table at the bottom shows the results of consistency checks for all pairs of frequencies. The diagonal indicates that, despite the good data quality, the response estimates for successive frequencies are generally inconsistent. On the other hand, the ties between data with a wide frequency separation are weak and no consistency problems arise.

Conclusion

The present study establishes necessary and sufficient data constraints for the existence of a 1-D conductivity model. It complements a previous result of Parker (1980), who characterizes the data by a representation (4). Although the results are mostly of theoretical interest, quick pairwise existence checks can be performed by (27a–d).

The approach does not shed any light on the extremely difficult problem of how to characterize the data when two- or even three-dimensional conductivity models are allowed. It is generally assumed that the necessary requirements for the lower dimensional counterpart of the transfer function are relaxed when the class of conductivity models is widened. However, in two and three dimensions the response function is tensorial and the relaxation of constraints for the frequency dependence of individual tensor elements will be counteracted by additional constraints between the elements, which might be even more severe. Nevertheless, it would be useful to study the relaxation of necessary constraints in an extended class of models because it could be concluded from a violated relaxed constraint that, even in the extended class, no satisfactory model exists.

Appendix

Existence conditions for the degenerate case

In the degenerate case the data are represented by an expansion of type (4) with less than $2M$ (positive) constants, i.e.

$$c(\omega_j) = a_0 + \sum_{n=1}^{r} \frac{a_n}{b_n + i\omega_j} + \frac{a_{r+1}}{i\omega_j}, \quad j = 1, \dots, M \tag{28}$$

with $0 \leqq r \leqq M-1$, $a_n > 0$, $b_n > 0$ for $n = 1, \dots, r$, $a_0 \geqq 0$, $a_{r+1} \geqq 0$. In addition, for $r = 0$ the sum in Eq. (28) is omitted and for $r = M-1$ there is the extra condition $a_0 \cdot a_M = 0$ (in order to have less than $2M$ positive constants). The response function of the degenerate case can be interpreted by only one conductivity profile, and this lies in the class of thin sheets (Parker, 1980; Weidelt, 1985). The structure of Eq. (28) will also be reflected in the existence conditions. There will be $2r$ positivity constraints, 2 non-negativity constraints and $2(M-r-1)$ equality constraints. The latter refer to the $2(M-r-1)$ deficient constants.

A degenerate data set is characterized as follows:

There exists an integer r with $0 \leqq r \leqq M-1$ such that

$$\Delta_k(i) > 0, \quad i = 0, 1 \quad \text{and} \quad k = 1, \dots, r, \tag{29}$$

but

$$\Delta_{r+1}(0) \cdot \Delta_{r+1}(1) = 0. \tag{30}$$

For this number r holds

$$\Delta_{r+1}(0) \geqq 0, \quad \Delta_{r+1}(2M-2r-1) \geqq 0. \tag{31}$$

For $r < M-1$ there are the $2(M-r-1)$ equality constraints

$$\Delta_{r+1}(i) = 0, \quad i = 1, \dots, 2(M-r-1). \tag{32}$$

The *necessity* of the above conditions is easily inferred from the explicit expression of $\Delta_k(i)$ in Eq. (19). Considering the *sufficient* conditions on the data β_m to ensure a representation (28), we first find as analogues of Eq. (20) [or Eq. (17), since the data set does not permit an alternative representation]

$$\sum_{n=1}^{r} \gamma_n b_n^m = \bar{\beta}_m, \quad m = 0, \dots, 2M-1 \tag{33}$$

with

$$\begin{aligned} &\bar{\beta}_0 = \beta_0 - \gamma_{r+1}, \quad \bar{\beta}_{2M-1} = \beta_{2M-1} - a_0, \\ &\bar{\beta}_m = \beta_m, \quad m = 1, \dots, 2M-2, \end{aligned} \tag{34}$$

and β_m and γ_n defined in Eqs. (12a, b) and (18), respectively. Absorbing for the moment the constants a_0 and γ_{r+1} in the data $\bar{\beta}_m$, Eq. (33) is a system of $2M$ equations for the $2r$ unknowns b_n and γ_n. The existence of a solution requires $2M-2r$ consistency conditions between the $\bar{\beta}_m$. Defining a set of r variables y_k by the expansion

$$\prod_{m=1}^{r} (\lambda - b_m) = \sum_{k=0}^{r} y_k \lambda^k, \quad y_r = 1, \tag{35}$$

a linear combination of the equations (33) yields

$$\sum_{k=0}^{r} \bar{\beta}_{j+k} y_k = 0, \quad j = 0, \dots, 2M-r-1. \tag{36}$$

In order that a solution of these $2M-r$ linear equations for r unknowns exists, any $r+1$ equations have to be linearly dependent. Taking the equations from $j = i$ to $j = i+r$, $i = 0, \dots, 2M-2r-1$, the $2M-2r$ consistency conditions are $\bar{\Delta}_{r+1}(i) = 0$, where $\bar{\Delta}$ is built as Δ in Eq. (13) with β_m replaced by $\bar{\beta}_m$. For the original data this implies

$$\Delta_{r+1}(0) = \gamma_{r+1} \Delta_r(2), \tag{37a}$$

$$\Delta_{r+1}(i) = 0, \quad i = 1, \dots, 2(M-r-1), \tag{37b}$$

$$\Delta_{r+1}(q) = a_0 \Delta_r(q) = a_0 \Delta_r(1) \prod_{n=1}^{r} b_n^{q-1} \tag{37c}$$

with $q:=2M-2r-1$. In Eq. (37c) use was made of the recurrence relation following from Eq. (19)

$$\Delta_r(l+1)=\Delta_r(l)\cdot\prod_{n=1}^{r} b_n,\qquad l\geqq 1.$$

Before evaluating Eq. (37a–c), the conditions warranting the positivity of a_p and b_p, $p\in[1,r]$ are derived by defining another set of variables, z_k, by

$$\prod_{m=1}^{r}{}' \frac{\lambda-b_m}{b_p-b_m}=\sum_{k=0}^{r-1} z_k\lambda^k,$$

where the prime again denotes the omission of the factor $m=p$. Then Eq. (33) yields (cf. the regular case)

$$\sum_{j=0}^{r-1}\sum_{k=0}^{r-1}\beta_{i+j+k}z_jz_k=\gamma_p b_p^i,\qquad i=1,2, \tag{38}$$

where it has been noted that in the required range of subscripts $\beta_m=\bar{\beta}_m$. With a new appeal to quadratic forms, sufficient conditions for $a_p>0$ and $b_p>0$ are

$$\Delta_k(i)>0,\qquad i=1,2\quad\text{and}\quad k=1,\ldots,r. \tag{39}$$

Now we are in a position to identify Eqs. (29) to (32) as sufficient conditions for the degenerate case. The inequalities (39) almost agree with (29), except that they involve $\Delta_k(2)$ rather than $\Delta_k(0)$. The conditions (29), $\Delta_k(0)>0$, $k=1,\ldots,r$ imply that the r-dimensional quadratic form $Q_r(0)$ is positive definite. Hence, also the principal minors $\Delta_k(2)$, $k=1,\ldots,r-1$ of the associated determinant are positive. To prove the positivity of $\Delta_r(2)$, the cases $\Delta_{r+1}(0)>0$ and $\Delta_{r+1}(0)=0$ have to be distinguished. In the former case also $Q_{r+1}(0)$ is positive and therefore the same holds for the principal minor $\Delta_r(2)$ of the associated determinant. However, if $\Delta_{r+1}(0)=0$ then it follows from Eq. (37a) that $\gamma_{r+1}=0$, because

$$\Delta_r(2)=\Delta_r(1)\prod_{i=1}^{r} b_i$$

[from Eq. (19)] is non-zero since $\gamma_p b_p>0$ as a consequence of $\Delta_k(1)>0$, $k=1,\ldots,r$. For $\gamma_{r+1}=0$, Eq. (19) shows that

$$\Delta_r(2)=\Delta_r(0)\prod_{i=1}^{r} b_i^2>0.$$

The conditions (31) ensure, according to (37a) and (37c) that a_{r+1} and a_0 are non-negative. Finally, in the case $r<M-1$ the conditions (32) grant, according to (37b), the existence of a solution. The condition (30) in conjunction with (29) defines the integer r.

The regular representation (10) can be considered as a special case of Eq. (28) with $r=M-1$ and $a_i=\bar{A}_i$, $b_i=\bar{B}_i$, $\bar{A}_0\cdot\bar{A}_M>0$. Then the remaining conditions (29) and (31) lead to the regular conditions (14).

Acknowledgements. I am grateful to Prof. Dr. U. Schmucker for providing the data treated in Fig. 1.

References

Cagniard, L.: Basic theory of the magneto-telluric method. Geophysics **18**, 605–635, 1953

Gantmacher, F.R.: The theory of matrices, Vol. II. New York: Chelsea 1959

Parker, R.L.: Inverse theory with grossly inadequate data. Geophys. J.R. Astron. Soc. **29**, 123–138, 1972

Parker, R.L.: The inverse problem of electromagnetic induction: existence and construction of solutions based on incomplete data. J. Geophys. Res. **85**, 4421–4428, 1980

Smirnov, V.I.: A course of higher mathematics. Vol. III/1. Oxford: Pergamon Press 1964

Weidelt, P.: The inverse problem of geomagnetic induction. Z. f. Geophys. **38**, 257–289, 1972

Weidelt, P.: Construction of conductance bounds from magnetotelluric impedances. J. Geophys. **57**, 191–206, 1985

Received October 25, 1985 / Revised February 24, 1986
Accepted February 26, 1986

J Geophys (1986) 59:177–182

Journal of Geophysics

Thermally stimulated currents in rocks

E. Dologlou-Revelioti[1] **and P. Varotsos**[2]

[1] University of Athens, Department of Geology, Geophysics-Geothermy Division, Athens, Greece
[2] University of Athens, Department of Physics, Athens, Greece

Abstract. Thermally stimulated currents (T.S.C) have been observed in seven rock samples, selected intentionally to represent the mean crustal structure in Greece. All these rock samples exhibit a transient thermally stimulated current. These currents are observed when the rock samples are heated at a certain rate, *with* and *without* the application of any external electric field. The main properties of these thermally stimulated currents are:

1. All the rock samples showed the maximum value of the T.S.C within a narrow temperature range, i.e. between 6° C and 23° C.
2. The T.S.C spectrum is complex, presumably due to different kinds of impurities in the rocks and different dipole mechanisms.
3. The relaxation times of the dipoles, as obtained from the T.S.C, are of the order of 1 min at temperatures ~20° C.
4. The values of the migration enthalpy are of the order of some eV.

Key words: Rocks – Stimulated currents – Relaxation parameters

Introduction

Since 1981 the electric field of the earth has been continuously monitored at various sites in Greece. Before each sizeable earthquake a transient variation of the electrotelluric field was observed with a time-lag between 6 h and 1 week. An extensive description of the physical properties of this precursor was published by Varotsos and Alexopoulos (1984a, b, 1986).

The above field observations were motivated from the following tentative physical model: rocks usually contain piezoelectric material (e.g. quartz) in a non-perfect directional distribution. Before an earthquake, and in the region close to the focus, the stress gradually increases so that an electric field is generated. Furthermore, this stress-variation may decrease the relaxation time of the dipoles existing in the rocks (whenever the migration volume is negative, see below). It can then be shown (Varotsos et al. 1982) that when the stress reaches a certain value, i.e. the so-called critical stress σ_{cr}, a transient current is emitted (we assume, of course, that $\sigma_{cr} < \sigma_{fr}$, where σ_{fr} denotes the stress at which the rocks fracture). Details of this model have been published by Varotsos and Alexopoulos (1986).

If the basic assumptions of the above scheme are correct (i.e. existence of dipoles due to the aliovalent impurities and creation of the electric field due to the piezoelectric inclusions) then the rocks should also emit transient currents upon a gradual increase of temperature, which results in a decrease of the relaxation time of dipoles. It is the object of this paper to report on the existence of such thermally stimulated currents in natural rocks.

Theory

Relaxation of dipoles

When an aliovalent impurity ion, e.g. M^{+2}, is introduced into an ionic crystal of the form $A^+ B^-$, a number of cation vacancies are formed for reasons of charge compensation (Varotsos and Miliotis, 1974). A portion of these vacancies is attracted by aliovalent impurities and forms "complex dipoles" which can change their orientation when subjected to an external electric field. The relaxation time τ, needed for them to change orientation, depends on temperature T and pressure P according to the formula (Varotsos and Alexopoulos, 1981; Varotsos et al., 1980)

$$\tau(T,P) = \tau_0 \exp(h_m/kT) \tag{1}$$

where τ_0 is the pre-exponential factor, h_m is the enthalpy of the orientation process and k Boltzmann's constant. The relaxation time τ always decreases, because τ_0 and h_m are positive, with increasing temperature as obvious from Eq. (1). On the other hand, its variation with increasing pressure depends on the algebraic sign of the quantity

$$U_m = \frac{\vartheta g_m}{\vartheta P} \,|T \tag{2}$$

(index "m" = "migration") where g_m is the Gibbs energy of the re-orientation process and U_m the so-called migration volume (Varotsos and Alexopoulos, 1980). Whenever U_m is positive, Eqs. (1) and (2) indicate that the relaxation time τ increases when hydrostatic pressure P also increases; on the other hand, if $U_m < 0$ the relaxation time τ decreases with increasing pressure (Varotsos et al., 1982).

Thermally stimulated currents

Depending on the procedure followed for the application of the external electric field, thermally stimulated currents

---

Offprint requests to: P. Varotsos, Knossou Str. 36, Ano Glyfada, Athens 165 61, Greece

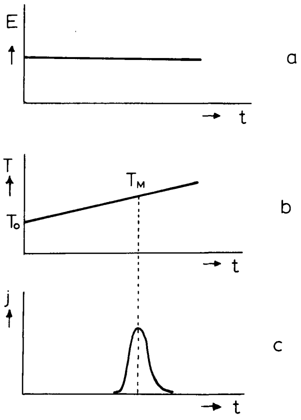

1

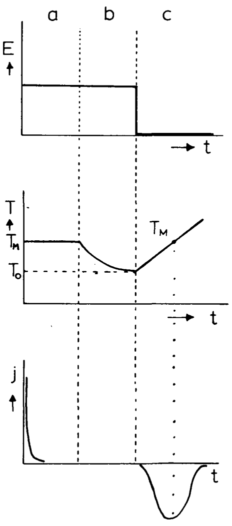

2

Fig. 1a–c. Schematic representation of the thermally stimulated polarization current techniques

Fig. 2a–c. Schematic representation of the thermally stimulated depolarization current techniques

can be detected due to either "polarization" or "depolarization" of dipoles.

The experimental procedure for a thermally stimulated *polarization* current (Mckeever and Hughes, 1975) consists of the following steps (Fig. 1).

Assume an unpolarized solid at a relatively low temperature T_0, so that the relaxation time $\tau(T_0)$ is appreciably high (e.g. several hours). At this temperature an external electric d.c. field E (Fig. 1a) is applied for a time $t \ll \tau(T_0)$. The dipoles – due to their large relaxation time – remain randomly orientated. The temperature T is now increased (Fig. 1b) at a constant rate and, hence, the relaxation time decreases. As the temperature reaches the "stimulation temperature" T_M (Mckeever and Hughes 1975), the relaxation time of dipoles becomes sufficiently short; then, under the influence of the applied external electric field, the dipoles tend to align with the field direction and, hence, produce a polarization π. This polarization is equivalent to the emission of charges from the outer surface, with a current density $j=\frac{d\pi}{dt}$ (Fig. 1c). This current is termed the "thermally stimulated polarization current" (T.S.P.C) and is a transient phenomenon because it almost vanishes when all dipoles have been aligned with the external electric field as far as the thermal motion allows it.

A thermally stimulated depolarization current (T.S.D.C) can be detected according to the following procedure, consisting of three steps (Bucci et al., 1966):

A) In the first step (Fig. 2, stage a), a constant electric field E is applied at a high temperature T and for a time t appreciably larger than the relaxation time $\tau(T)$ of the dipoles. All dipoles can then freely rotate and align with the external field E. A current appears due to this alignment of the dipoles.

B) Now the solid is cooled to an appreciably low temperature T_0, so that the relaxation time $\tau(T_0)$ reaches values of the order of several hours. Although switching off the external electric field E, the dipoles remain aligned with this field (Fig. 2, stage b).

C) Now we increase the temperature T at a constant rate (Fig. 2, stage c). The relaxation time $\tau(T)$ decreases gradually and thus the dipoles become free to rotate into random directions, so that a thermally stimulated depolarization current is emitted. It has a maximum (Bucci et al., 1966) at a certain temperature T_M.

In summarizing, we can say that solids containing dipoles will emit transient polarization or depolarization currents when they are heated. This, however, assumes that an external electric field has been used for the (re)orientation of these dipoles. So far, such currents *have not been detected in the absence of any external field.* In the case of rocks, however, piezoelectric or pyroelectric inclusions (Parkhomenko, 1971) give rise to an internal electric field which may substitute the above-mentioned external electric field. In order to examine this possibility, experiments without any application of an external electric field have been carried out on a large variety of rocks.

Table 1. Chemical analysis of rock samples (%)

Chemical compounds	Rock type						
	Sample 1	Sample 2	Sample 3	Sample 4	Sample 5	Sample 6	Sample 7
	Granite	Mica-schist	Sipoline	Crystalline limestone	Marble	Gneiss	Limestone
SiO_2	71.80	65.0	17.30	2.70	0.60	72.00	1.30
CaO	1.64	2.0	40.50	49.00	54.50	0.35	54.00
Al_2O_3	15.50	16.00	3.60	0.85	0.11	13.50	0.32
Fe_2O_3	0.14	1.50	2.15	1.16	0.26	2.50	0.21
FeO	0.50	7.00	–	–	–	0.15	–
MnO	0.03	0.07	0.13	0.01	0.006	0.03	0.01
MgO	0.17	3.00	1.38	3.31	0.83	1.05	0.56
Na_2O	4.56	0.50	0.27	0.02	0.02	2.70	0.09
K_2O	4.12	2.00	1.20	0.02	0.02	5.70	0.10
Cr_2O_3	–	–	–	–	–	–	–
TiO_2	0.12	1.00	–	–	–	0.20	–
H_2O	0.60	4.00	–	–	–	–	–
Heat loss	–	–	3.2	42.7	43.4	1.5	43.0

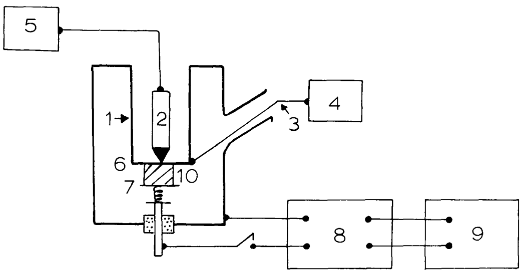

Fig. 3. Experimental set up. *1* Cryostate; *2* heating element; *3* Fe-Const thermocouple; *4* digital millivoltmeter; *5* A.C. power supply (0–250 V); *6–7* Pt electrodes; *8* vibrating reed electrometer Cary 401; *9* pen chart-recorder; *10* sample

The experiment

Due to the fact that all rocks contain aliovalent impurities it is natural to expect that they contain complex dipoles of the form "aliovalent impurity + vacancy" or "aliovalent impurity + interstitial". Thus, by applying the thermally stimulated current technique to them, one should expect, in principle, the detection of a thermally stimulated current.

Seven samples of various rock types representing the mean crustal structure of Greece (Papanikolaou 1980, 1984) have been studied in this way. Their chemical composition is given in Table 1. A brief description of the instrumentation used for the experiments is given below (see also Triantis, 1983).

The apparatus (Fig. 3) consists of two chambers made of stainless steel. The inner chamber (cryostate in Fig. 3) is filled with air. A heating element and nitrogen liquid were used to heat and cool the samples, respectively. The samples had typical dimensions of 1 cm × 1 cm × 0.5 cm and were placed between two Pt electrodes. The temperature was measured by a Fe-Const thermocouple and the measuring junction was positioned as close to the sample as practicable. When using a heating rate $b = 4$ K/min, the temperature difference between the upper and lower part of the sample does not exceed 1–2 K (this fact has been verified by experiments with two thermocouples positioned at the upper and lower part of the sample, respectively). In any case, this temperature gradient can not be the origin of the observed T.S.C current for reasons discussed below.

Therefore, when using heating rate $b = 4$ K/min, the systematic uncertainties in temperature must be 2 K at most. Electrical connection with the electrodes was provided through Teflon insulated connectors in the outer chamber. Thermally stimulated currents were measured with a Cary 401 electrometer and displayed on a YEW-3057 pen chart-recorder.

It should be emphasized that test noise measurements were carried out by heating at a constant rate, from $-80°$ C to $+100°$ C, without putting any sample between the electrodes. In these cases, no current was observed with an intensity three orders of magnitude smaller than the maximum current described below. Therefore, the noise level can be considered as 10^{-14} A at most.

The Teflon insulation, is continously kept at room temperature in order to avoid thermocurrents from Teflon (Kostopoulos et al., 1980, 1981). It should also be mentioned that T.S.C currents for Teflon measured by ourselves, and by Bucci (Bucci et al., 1966), are three orders of magnitude smaller than the observed T.S.C for our rock samples.

The following type of experiments were carried out on each rock sample. *Without* the application of any external electric field, the rock sample was cooled down from room temperature to $T = -80°$ C and then heated at a constant temperature rate of 4 K/min up to $T = 100°$ C.

Results

The measured thermally stimulated current spectrum for each rock sample is depicted in Figs. 4–10. The spectra are complicated, probably due to the various migration mechanisms and/or types of complex dipoles contained in the rocks. For a single mechanism, however, and at any temperature, the value of the relaxation time τ can be calculated

4

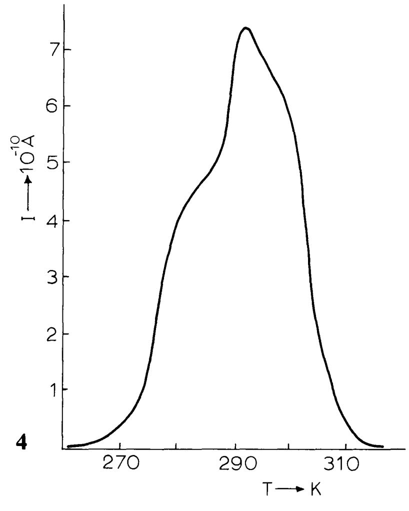

5

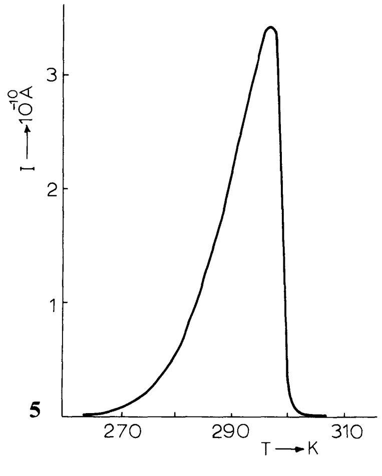

6

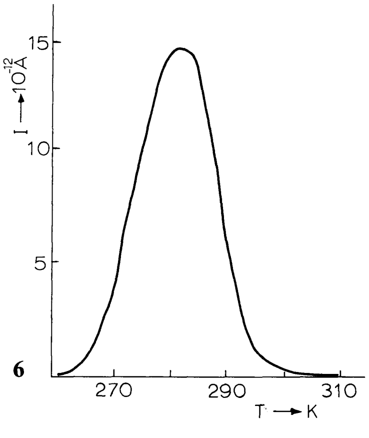

Fig. 4. Spectrum of the current emitted from granite for gradual temperature increase ($b = 4$ K/min)

Fig. 5. Spectrum of the current emitted from mica-schist for gradual temperature increase ($b = 4$ K/min)

Fig. 6. Spectrum of the current emitted from sipoline for gradual temperature increase ($b = 4$ K/min)

7

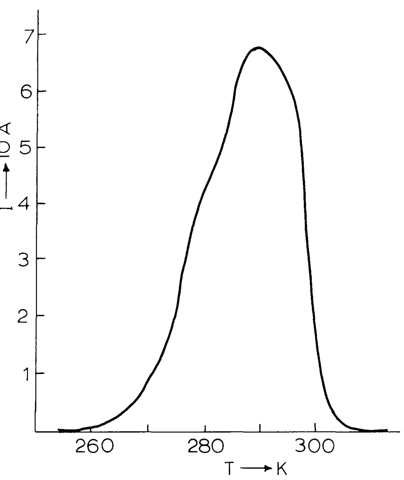

8

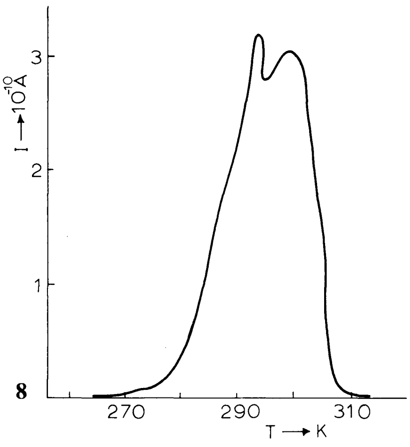

9

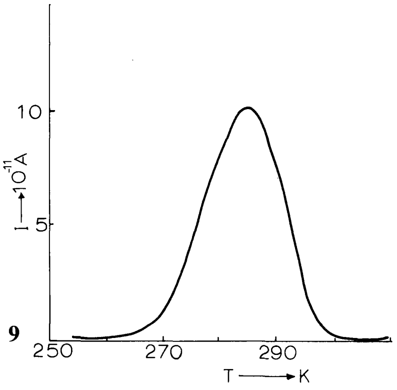

Fig. 7. Spectrum of the current emitted from crystalline limestone for gradual temperature increase ($b = 4$ K/min)

Fig. 8. Spectrum of the current emitted from marble for gradual temperature increase ($b = 4$ K/min)

Fig. 9. Spectrum of the current emitted from gneiss for gradual temperature increase ($b = 4$ K/min)

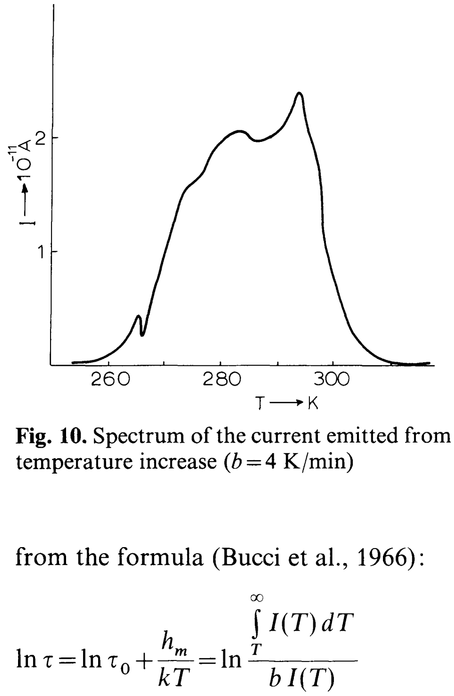

Fig. 10. Spectrum of the current emitted from limestone for gradual temperature increase ($b = 4$ K/min)

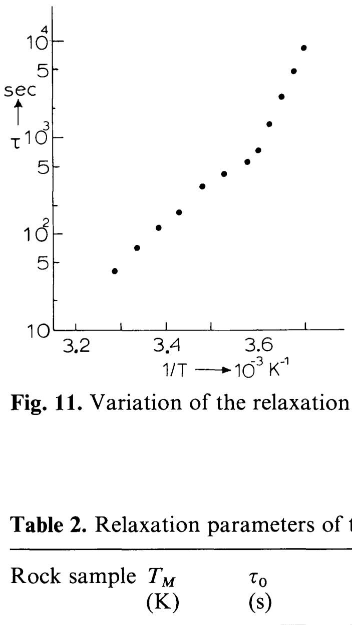

Fig. 11. Variation of the relaxation time τ versus $1/T$ for granite

from the formula (Bucci et al., 1966):

$$\ln \tau = \ln \tau_0 + \frac{h_m}{kT} = \ln \frac{\int_T^{\infty} I(T)\, dT}{b\, I(T)} \tag{3}$$

where $b = \frac{dT}{dt}$. The integral of the right-hand side can be obtained graphically. Due to the lack of knowledge of the various mechanisms involved, we apply Eq. (3) for the lower-temperature tail of our experimental curve. It should be clarified that, although T_M and the shape of the I spectrum depend on b, the relaxation times calculated from Eq. (3) do not depend on the heating rate. The resulting τ values for the case of granite, are depicted in Fig. 11 in the form of a $\ln\tau$ vs $1/T$ plot. An inspection of this plot shows that the low-temperature part can be described approximately by a straight line which – according to Eq. (3) – indicates the existence of a single overwhelming mechanism (or type) of dipole for the low part. A least-squares fit to the straight line leads to the values of τ_0 and h_m corresponding to that mechanism.

Table 2. Relaxation parameters of the various rock samples

Rock sample	T_M (K)	τ_0 (s)	h_m (eV)	$\tau(T_M)$ (s)
Granite	292 ± 2	$(1^{+3}_{-0.5}) \times 10^{-33}$	2.0 ± 0.2	165 ± 50
Mica-schist	296 ± 1	$(1^{+3}_{-0.5}) \times 10^{-21}$	1.3 ± 0.1	40 ± 10
Sipoline	281 ± 2	$(2^{+4}_{-0.6}) \times 10^{-34}$	2.0 ± 0.1	90 ± 20
Crystalline limestone	289 ± 2	$(0.2^{+12}_{-0.8}) \times 10^{-23}$	1.4 ± 0.1	140 ± 30
Marble	293 ± 1	$(1.7^{+4}_{-0.3}) \times 10^{-30}$	1.8 ± 0.1	165 ± 30
Gneiss	285 ± 1	$(4^{+4}_{-0.3}) \times 10^{-28}$	1.6 ± 0.1	108 ± 10
Limestone	294 ± 2	$(8^{+80}_{-1.2}) \times 10^{-27}$	1.5 ± 0.2	76 ± 10

This procedure was applied to all samples and resulting values of τ_0 and h_m are given in Table 2. In the same Table we have inserted the corresponding T_M values along with the "apparent" relaxation time $\tau(T_M)$ resulting from Eq. (3) by applying it at $T = T_M$. Due to the complexity of the spectrum, it is obvious that the latter values of $\tau(T_M)$ do not have a direct physical meaning but only give the order of magnitude of the relaxation time belonging to the predominant mechanism at $T=T_M$.

A striking result obtained from Table 2 is that, in a large variety of rocks, the T_M values vary only within a narrow range, i.e. from 6° C to 23° C. A large number of T.S.C spectra were obtained after testing samples of the same material or repeating the experiment with the same sample under the same conditions. In both cases, no significant differences were observed in the T.S.C spectra, concerning T_M and the relaxation parameters τ_0 and h_m.

In addition, experiments with a different orientation of the mica-schist sample were carried out, but the influence of the structural anisotropy of the mica-schist on the T.S.C spectrum was dubious.

Discussion

The following, very tentative, physical model is proposed in order to explain the above transient electrical current in the absence of any external electric field.

From the chemical analysis (Table 1) and from the mineral composition of the samples, it is easily observed that all rock samples contain a number of ionic crystals (e.g. Na_2O) which are carriers of "complex dipoles". Also, all samples contain either a piezoelectrical material (e.g. quartz SiO_2) or a pyroelectric one. As rock has a complex structure consisting of various minerals with different thermal expansion coefficients, internal stresses will arise when cooling or heating the sample. They stimulate the piezoelectric inclusions to produce a piezoelectric field E. Furthermore, a change in the temperature creates a pyroelectric field (Zheludev, 1971). We must point out that although one could expect – due to the random distribution of quartz grains in the rock – the sample as a whole not to show any piezoelectric effect, Parkhomenko (1971) established the existence of piezoelectric effects in a number of rock types (e.g. gneiss, granite, etc.) and also measured the piezoelectric moduli of these rocks.

Thus, a piezoelectric or pyroelectric field is generated due to piezoelectric and/or pyroelectric effects by simply cooling and heating the sample. During the whole experiment, this field acts as an external electric polarizing field applied to the dipoles within the rock sample. Briefly, we have the following situation. When gradually heating from low temperature, an internal electric field is generated (due to piezoelectric-pyroelectric effects). When increasing the temperature T, the dipoles – already existing in the sample – will become more and more mobile and will be able to align with this internal field, giving rise to a thermally stimulated polarization current.

The above model is further strengthened by the following experimental fact. Measurements have been carried out *with* application of an external d.c. electric field (a few kV/cm), as illustrated in Fig. 2a. This external field was applied at room temperature T_p, for a time t_p ($\sim$10 min) long enough compared to the relaxation time $\tau(T_p)$ of the dipoles at room temperature. Following the procedure depicted in Fig. 2a, a T.S.C current was observed with maxima at temperatures T_M which *are the same* as in the case of the experiments without the external field. A series of such current spectra (i.e. *with* an external electric field) has been described by Dologlou (1984).

In order to preclude any possibility that the observed current is an artifact or a result of the asymmetrical heating of the sample, the study of various samples of the same block or repeated measurements by turning a given sample upside down led to the following results:

A) Samples from the same block do not show the same current polarity and the same current intensity. This proves that the current is not due to a temperature gradient.

B) Repeated measurements on the same sample, in the same orientation, give the same current polarity.

C) Reversing the sample, the current polarity changes; thus indicating that the polarity is a property of the sample and simultaneously excluding an artifact due to the experimental set up.

Repeating the experiment with different heating rates from 1 K/min to 6 K/min, the temperature T_M of the maximum current was shifted as expected.

Conclusions

Summarizing the present experimental results, we point out the following. During gradual variation of temperature and in the absence of any external electric field, all rock samples give rise to a transient electric current (10^{-9} to 10^{-11} A) which is a maximum at roughly one and the same temperature T_M ($\sim$room temperature). The relaxation time at $T=T_M$ is of the order of 1 min. A very tentative physical model is suggested which explains the observed results qualitatively.

Acknowledgements. We are thankful to Prof. K. Alexopoulos for his useful comments, to Prof. I. Mariolakos for the chemical analysis of the samples, to Dr. D. Papanikolaou for the suggestion of appropriate samples and to Dr. D. Triantis for his assistance during measurements.

References

Bucci, C., Fieschi, R., Guidi, G.: Ionic thermocurrents in dielectrics. Phys. Rev. **148**, 816–823, 1966

Dologlou, E.: Thermocurrents in Greek rocks. PhD Thesis, University of Athens, 1984

Kostopoulos, D., Varotsos, P., Mourikis, S.: Measurements of ionic thermocurrents in sodium-iodide. J. Phys. C: Solid State Phys. **13**, 3003–3009, 1980

Kostopoulos, D., Mourikis, S., Varotsos, P.: Ionic thermocurrent in KCl doped with SO_4^{-2}. J. Physique **42**, 1481–1483, 1981

Mckeever, S., Hughes, D.: Thermally stimulated currents in dielectrics. J. Phys. D: Applied Phys. **8**, 1520–1529, 1975

Papanikolaou, D.: Geotraverse S. Rhodope-Crete (preliminary results). In: UNESCO/IGCP N. 5, Newsletter 2, F.P. Sassi (ed.), pp. 41–48, Padova, 1980

Papanikolaou, D.: The three metamorphic belts of the Hellenides. A review and kinematic interpretation. Geol. Soc. London, Spec. Public. **17**, 551–561, 1984

Parkhomenko, E.: Electrification Phenomena in Rocks. New York-London: Plenum Press 1971

Triantis, D.: Ionic thermocurrents at temperatures lower than the Debye temperature. PhD thesis, University of Athens, 1983

Varotsos, P., Miliotis, D.: New aspects on dielectric properties of alkali halides doped with divalent cations. J. Phys. Chem. Sol. **35**, 927–930, 1974

Varotsos, P., Kostopoulos, D., Mourikis, S.: ITC measurements on sodium fluoride doped with calcium. Phys. Status Solidi. **57**, 331–335, 1980

Varotsos, P., Alexopoulos, K.: On the question of the calculation of migration volumes in ionic crystals. Phil. Magazine **42**, 13–18, 1980

Varotsos, P., Alexopoulos, K.: Migration parameters for the bound fluorine motion in alkaline earth fluorides II. J. Phys. Chem. Sol. **42**, 409–410, 1981

Varotsos, P., Alexopoulos, K., Nomicos, K.: Comments on the pressure variation of the Gibbs energy for bound and unbound defects. Phys. Status Solidi (b) **111**, 581–590, 1982

Varotsos, P., Alexopoulos, K.: Physical properties of the variations of the electric field of the earth preceding earthquakes, I. Tectonophysics **110**, 73–98, 1984a

Varotsos, P., Alexopoulos, K.: Physical properties of the variations of the electric field of the earth preceding earthquakes, II. Determination of epicenter and magnitude. Tectonophysics **110**, 99–125, 1984b

Varotsos, P., Alexopoulos, K.: Thermodynamics of point defects and their relation with bulk properties, S. Amelinckx, R. Gevers, J. Nihoul (eds.), pp. 130–142, 403–406, 410–412, 417–420. Amsterdam: North Holland 1986

Zheludev, I.: Physics of crystalline dielectrics, Vol. 1, pp. 206–211. New York-London: Plenum Press 1971

Received March 11, 1985; revised version February 10, 1986
Accepted February 13, 1986

J Geophys (1986) 59:183–194

Journal of Geophysics

Magnetostratigraphy of Neogene equatorial Pacific pelagic sediments

Norbert Weinreich[1, 3] **and Fritz Theyer**[2]

[1] Institut für Geophysik, Ruhr-Universität Bochum, Postfach 102148, 4630 Bochum 1, Federal Republic of Germany
[2] Department of Geological Science, University of Southern California, University Park, Los Angeles, CA 90089, USA

Abstract. The magnetostratigraphic record of lower Miocene to Quaternary sediments cored in the central equatorial Pacific is presented in this study. The VLHPC (variable length hydraulic piston corer) recovered Neogene deposits at the DSDP (Deep Sea Drilling Project) Leg 85 sites 573, 574 and 575, which are relatively uniform siliceous-calcareous oozes. The basis for all paleomagnetic analyses are the progressive alternating demagnetization experiments of each sample. The results constitute the first opportunity to elaborate a magnetostratigraphic record down to the lower Miocene in this area. In various sections biostratigraphic age control was applied to calibrate the measured paleomagnetic polarity patterns to the geomagnetic timescale. The systematic increase of accumulation/time downhole at each site, as well as the systematic decrease of deposition on the profile from south (site 573) to north (site 575), reflects the northward motion of the Pacific plate underneath the equatorial Pacific stationary zone of high biogenic mass-production. The generally constant morphology of its northern flank for the last 20 million years is documented by the paleomagnetic results.

Key words: Paleomagnetism – Magnetol – biostratigraphy – Equatorial Pacific – Sedimentation rates

Introduction

Repeatedly, the central Pacific was the destination of cruises of the DSDP (Deep Sea Drilling Project) Legs 5, 8, 9 and 16, recovering several hundreds of metres of sediment with the conventional 'rotary' technique (McManus et al., 1970; Tracey et al., 1971; Hays et al., 1972; van Andel et al., 1973). The focal point of all investigations was to obtain almost complete biostratigraphies and to study the geologic evolution and paleo-oceanography of this region during the Cenozoic (Berger, 1973; Winterer, 1973; van Andel et al., 1975).

The prominent geological structure in this area is a tight equator-parallel zone of extremely high accumulation of predominantly calcareous microfossils which extend from about 4°S to 5°N and is believed to be about constant at least for the Neogene (van Andel et al., 1975). With increasing latitude the composition of sediments changes gradually and then more rapidly from a dominant calcareous to a more siliceous one. In principle, the lateral Pacific plate motion relative to this belt of high bio-productivity provides, together with the abnormal deep-reaching calcium compensation depth, CCD (Berger, 1970), the characteristic lithostratigraphic composition of the central equatorial Pacific deposits.

Despite the relatively frequent work on conventional piston cores (Hays et al., 1969; Opdyke et al., 1974; Theyer and Hammond, 1974; Theyer et al., 1978), most were located more to the west, the central equatorial Pacific having yielded rather meagre paleomagnetic results in the past. This was generally due to the limitation given by the maximum length of traditional piston cores and to the very weak intensities of the natural remanent magnetization, NRM, of the highly calcareous sediments. Therefore, the use of the VLHPC technique provides the first opportunity of establishing more extensive magnetostratigraphic reference profiles in this region for much of the Neogene.

At sites 573 to 575, which form a south-north transect parallel to 134° of western longitude across the northern flank of the equatorial sediment bulk (Fig. 1), the paleomagnetic studies cover the Quaternary and Pliocene and parts of the Miocene. Measurable NRM intensities were observed only throughout sections with predominant siliceous composition. The more calcareous deposits, in general, provided no interpretable results.

The down-hole patterns of the magnetic reversals are correlated to the geomagnetic polarity time-scale of Berggren et al., (1986) in this study. For some of the Miocene sections biostratigraphic criteria had to be employed in places to calibrate the identified polarity transitions which are separated from the younger continuous sequences either by the lack of sampling or by prominent hiatuses found in the sedimentary column (Baron et al., 1985). The magnetostratigraphic data are then used to calculate apparent rates of sedimentation. Their systematic variations with age and latitude, in turn, are interpreted as the response of Pacific plate motion and constant biogenic mass-production during the Neogene.

Materials and methods

The sampling broadly followed age versus depth relations based on the biostratigraphic record. The intervals typically represent a resolution in time on the order of 10^4 years.

---

[3] *Present address:* De-Vries-Hof 9, D-3000 Hannover 61, Federal Republic of Germany

Offprint requests to: N. Weinreich

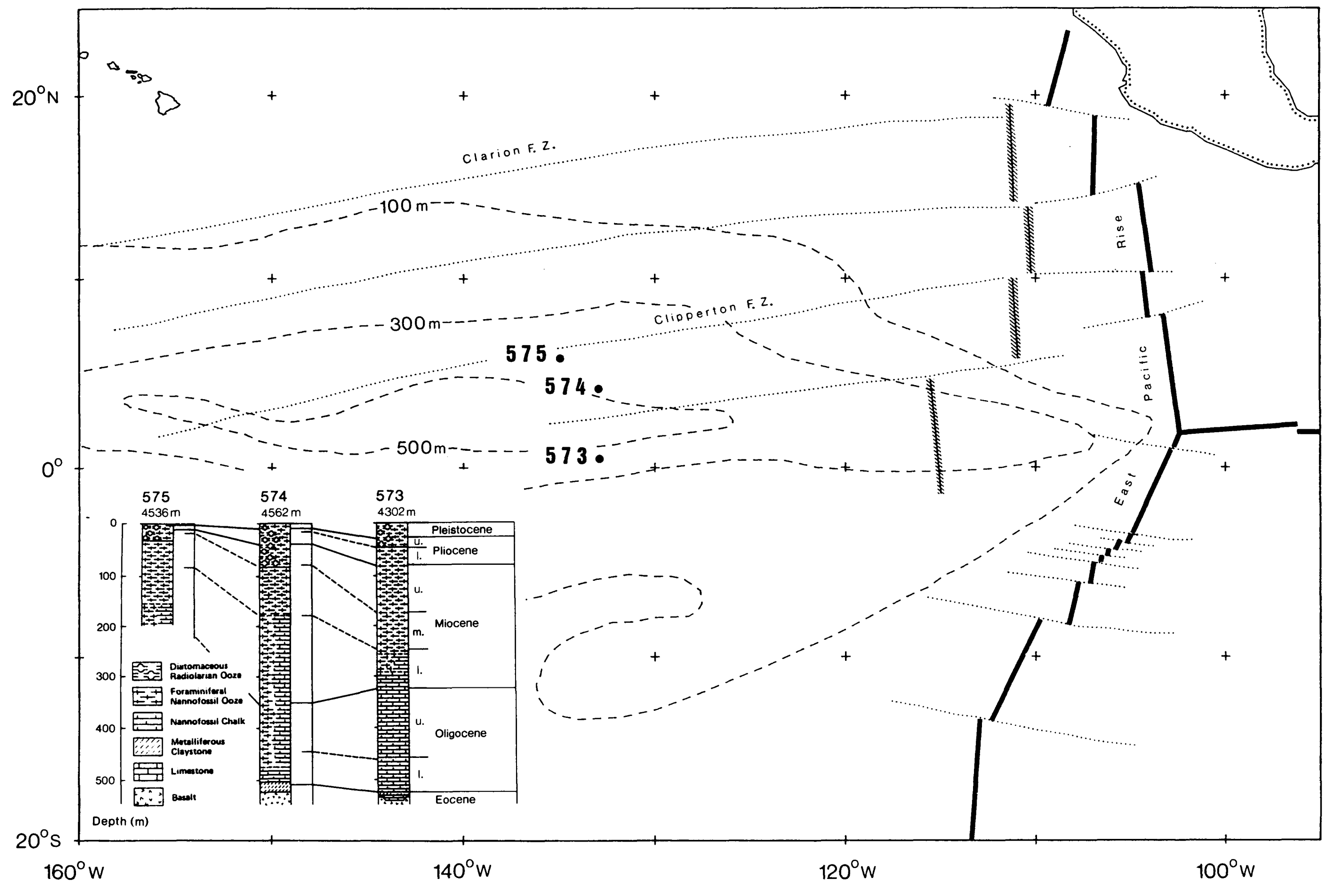

Fig. 1. Location map of DSDP Leg 85 sites 573, 574 and 575 in the central equatorial Pacific. Isochrons of the sediment thickness are marked by *dashed lines*. *Dotted lines* indicate fracture zones (F.Z.), *heavy black lines* the East-Pacific-Rise and the Galapagos Rise, *hatches* the fossil 'Mathematicians-Ridge'. The *insert* shows the lithostratigraphy, the biostratigraphic ages and the depth below sea-level

For the present study, all measurements were made on triaxial cryogenic magnetometers.

In addition to the NRM measurements, systematic stepwise alternating-field, AF, demagnetization series were applied to each sample using a Schonstedt GSD-1 single-axis demagnetizer. These series were taken mostly to the 50 mT level in steps of either 2.5 mT or 5 mT. Then the direction of the stable remanence was determined for each sample individually by analyses of different graphic representations of the demagnetization data. For this purpose the NRM-normalized intensity of magnetization versus the applied demagnetization field, vetor diagrams (Zijderveld, 1967) and stereographic projections of the total vectors and difference vectors (Hoffman and Day, 1978) were analysed. After this, a stable remanence direction for each sample was defined by the mean of measured directions during at least three consecutive demagnetization steps which showed the least directional scatter.

Because of the low, near-equatorial latitudes of the Leg 85 sites, the measured inclination data show mostly scatter of a few degrees about zero. Therefore, 180° changes in the stable declination data were used to define polarity transitions of the Earth's magnetic paleofield, which makes the determination of true polarity of the samples difficult in the absence of an absolute azimuthal orientation. Coring related variations in the declination data, in addition, give a complex polarity signal (Weinreich and Theyer, 1985). The declinations used for the magnetostratigraphic analyses are corrected by means of their respective stable core-mean values to, on average, 0° or 180° for either normal or reverse paleofield polarity (Weinreich and Theyer, 1985). For the Neogene, the series of the Earth's magnetic polarity patterns are specified to the traditional nomenclature of McDougall (1977), using the numerical ages of Berggren et al. (1986).

Results

Before discussing the results there will be a brief review of typical examples of the paleomagnetic response of different sediments to successive AF demagnetization. At the same time, this will allow a general outline of their magnetization characteristics and illustrate the paleomagnetic methods used in this study. The examples of demagnetization response discussed below are typical for the recovered siliceous-calcareous biogenic oozes essentially deposited during the Neogene in the central equatorial Pacific.

Figure 2 shows a typical Type I demagnization behaviour (Tauxe et al., 1984; Bleil, 1986). As illustrated here, most of all Type I samples show a monotonous decrease in remanent magnetization upon progressive AF demagnetization (Fig. 2a). The vector diagrams (Fig. 2b), whose orthogonal components decrease continuously towards the origin of the coordinate system in both the horizontal and vertical plane, prove the above interpretation. The total vectors of remanence as well as the difference vectors form

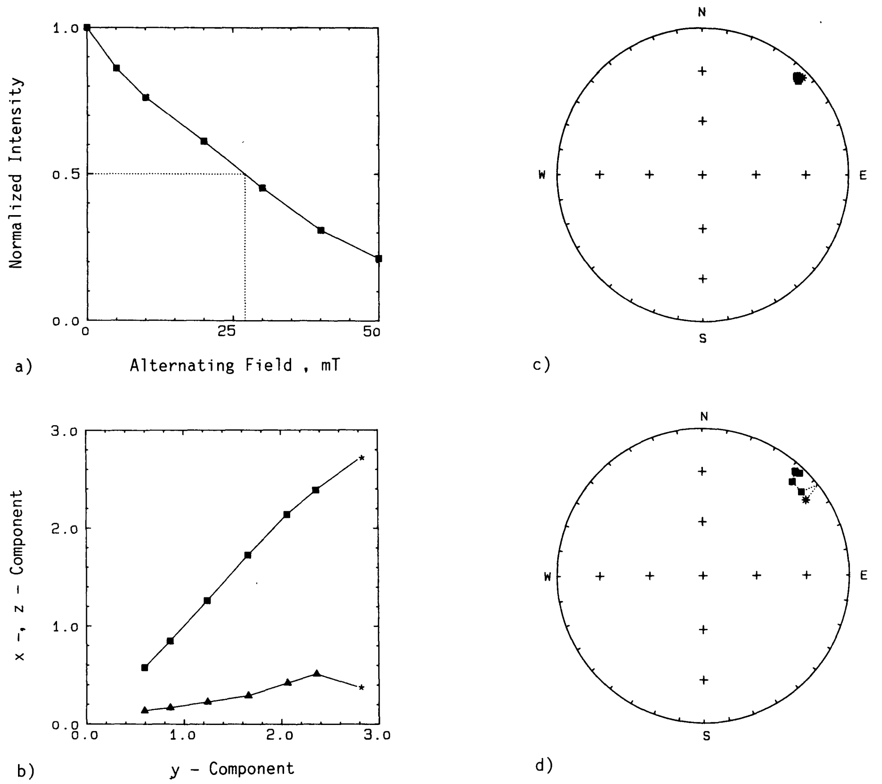

Fig. 2a–d. Type I demagnetization characteristics of the remanence.
a Demagnetization curve: variation of the NRM-normalized remanent intensity of the magnetization as a function of the maximum alternating-field amplitude. The *dotted line* indicates the mean destructive field.
b Vector diagrams: variation of the orthogonal components of the remanence (in 10^{-3} A/m) in the *x,y* plane (*squares*) and the *y,z* plane (*triangles*). The *asterisks* indicate the NRM values. The sequence of demagnetization steps follow those in **a**.
c Stereographic projection of the total vectors of the remanence. The *asterisk* indicates the NRM direction.
d Stereographic projection of the difference vectors of the remanence. The *asterisk* indicates the first demagnetization interval. On the stereographic projections *closed symbols* mark positive, *open symbols* negative inclinations. Subsequent demagnetization steps are connected by great circles

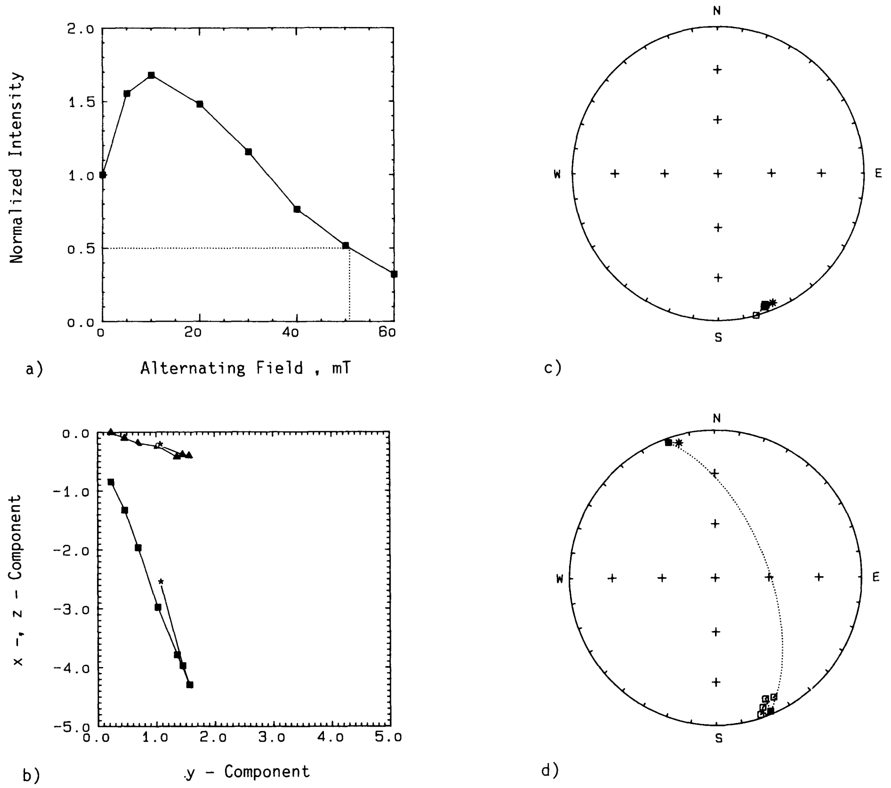

Fig. 3a–d. Type II demagnetization characteristics of the remanence (see Fig. 2)

a very close cluster in the stereographic projections round the same directional mean (Fig. 2c and d). This confirms an essential single-component stable remanence.

In clear contrast, Fig. 3 illustrates a Type II demagnetization response of a multi-component system with almost antiparallel directions of remanence. This is demonstrated by the increase of the NRM-normalized magnetization upon progressive demagnetization followed by a continuous decrease (Fig. 3a). After the destruction of a predominant less stable component, causing the observed increase of the remanent total intensity by the vectorial superposition of two antiparallel-directed components, the stable one

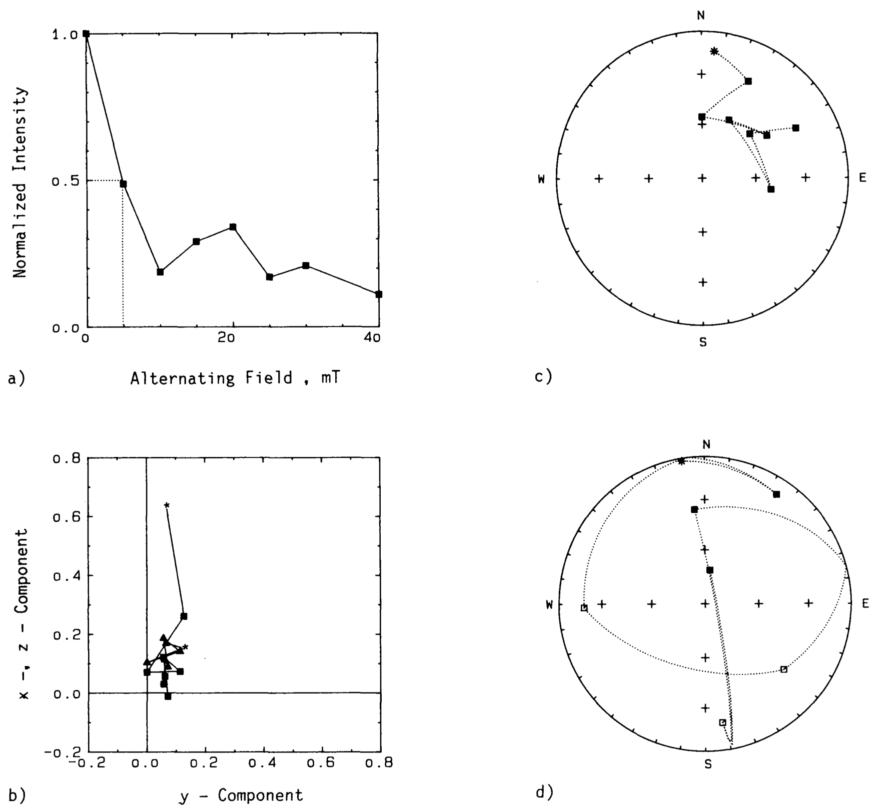

Fig. 4a–d. Type III demagnetization characteristics of the remanence (see Fig. 2)

dominates exclusively. This interpretation is supported by the increase of the orthogonal components in the vector diagrams which turns to a decrease towards the origin (Fig. 3b). Even though the stereographic projection of the total vector of magnetization (Fig. 3c) shows only one direction, the difference-vector diagram (Fig. 3d) allows a qualitative and quantitative definition of two roughly antiparallel directions. Here the magnetically less stable fraction of remanence is interpreted as a viscous magnetic overprint during the present normal geomagnetic Brunhes Epoch.

Finally, Fig. 4 gives an example of the demagnetization response labelled as Type III. Although apparently stable in direction, as one might infer from the stereographic projection of the total vectors (Fig. 4c), the other diagrams point to the erratic behaviour upon AF treatment (Fig. 4). These features have been observed as dominant throughout the highly calcareous sediments which, in turn, have very low NRM intensities.

In the graphic representations of the demagnetization behaviour discussed, the declination data have already been corrected as previously described. The very detailed AF demagnetization and interpretation of the demagnetization features of each sample is of essential advantage at low latitudes. It became obvious that the directional information of a Type I magnetization can be correlated to a normal polarity and a Type II one to a reverse polarity of the magnetic paleofield configuration, respectively. Independent of the lithofacies of the sediment sequences recovered, the remanence carried by the magnetic grain fraction deposited during the Neogene in the central equatorial Pacific is, in general, highly accepted as opposed to viscous overprinting during the normal magnetic paleofield configuration of the Brunhes Epoch. This causes the Type II characteristics of those samples deposited during reverse paleomagnetic field configurations. Therefore, with the classification of the demagnetization behaviour of remanent magnetism used in this study, an additional relevant criterion is available to unequivocally define the exact magnetic polarity of the magnetization so analysed.

Magnetostratigraphies

The declination/inclination logs (Figs. 5, 6 and 9) elaborated from the analyses discussed above provide the basis for the magnetostratigraphic interpretation that follows. The individual polarity sequence at each bore-hole is in general correlated to the geomagnetic time-scale assuming that the topmost continuous polarity indicates the Brunhes normal Epoch and the first 180° shift of the stable declination defines the Brunhes/Matuyama boundary at 0.73 my. The magnetic data from subsequent cores were stratigraphically compiled assuming that 180° changes between cores were not indicative of polarity transitions but, rather, results of rotations of the cores themselves. In any case, this method was guided by the demagnetization classification and by the inclination where possible and, in addition, aided by biostratigraphic criteria.

Site 573

Site 573 is the southernmost of the three-site SN transect along about 134°W, which cuts across the northern flank of the equatorial Pacific high-productivity belt (Fig. 1). A drastic decrease in the NRM intensity at about 45 m downhole, exceeding one order of magnitude, defines the limit of the paleomagnetically interpretable data. This gradient coincides with the lithologic change from cyclic siliceous-calcareous oozes to entirely calcareous oozes, documented by a significant colour change (Mayer and Theyer et al., 1985). The NRM intensities throughout this lithologic unit

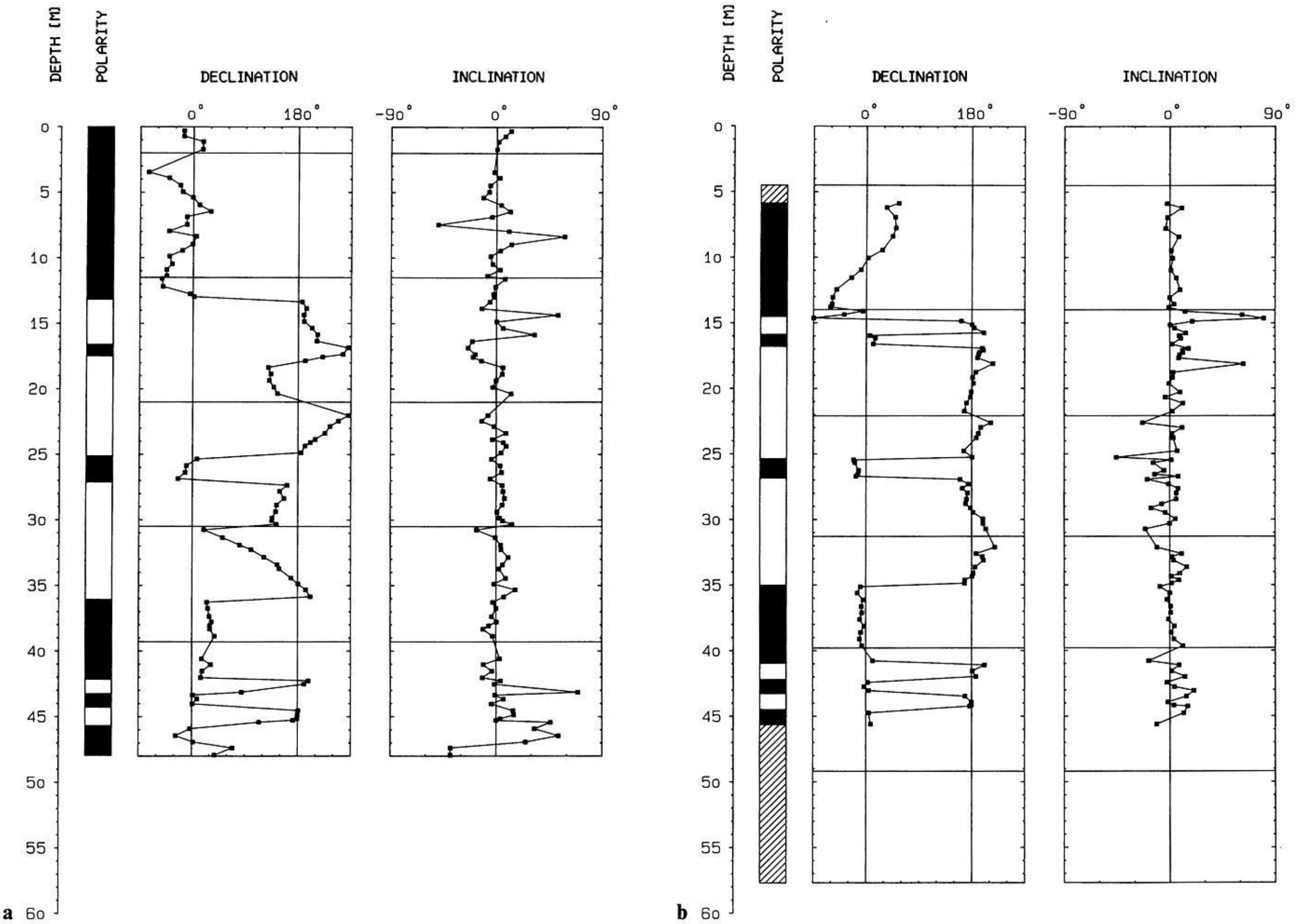

Fig. 5a, b. Paleomagnetic polarity for (**a**) hole 573 and (**b**) hole 573A. The columns show the down-hole variation of stable inclination and corrected declination (see text) and paleomagnetic polarity. *Black* indicates intervals of normal polarity; *white*, intervals of reversed polarity; and *striping*, intervals that could not be interpreted

vary about a mean of (1.41 ± 0.82 × 10^{-3} A/m, similar to other Neogene siliceous-calcareous marine sediments (Kent and Spariosu, 1983; Tauxe et al., 1984; Bleil, 1986).

The down-hole polarity pattern derived from the stable declination data (Fig. 5) and their magnetostratigraphic correlation is shown in Fig. 11. At this site all polarity changes were found within cores and the interpretation of either normal or reverse polarity is proved by the variation between Type I and Type II magnetization characteristics.

As the topmost sediments represent the radiolarian *Buccinosphaera invaginata* zone (Riedel and Sanfilippo, 1978) defined by the First Appearance Datum, FAD, of this species, they can be dated younger than 0.23 my (Johnson and Knoll, 1975; Nigrini, 1985). This result agrees well with the nannofossil CN15 zone (Bukry, 1975; Pujos, 1985), therefore, defining the uppermost sequence of uniform declination clearly as of Brunhes age. The directional change further down in the two holes (Fig. 5) are interpreted as the Brunhes/Matuyama boundary at 0.73 my. In the cored sections below, the down-hole pattern in the declinations yield an unequivocal reversal stratigraphy for the last 3.3 my. A more or less constant rate of sedimentation was calculated, from the age versus depth relation of Fig. 11, to be 14.2 ± 0.2 m/my throughout the Plio-/Pleistocene with a small amount of variation down-hole at both parallel holes. This calculation is based on the linear interpolation between magnetostratigraphic fixpoints.

Site 574

At site 574, located near the northern edge of the equatorial Pacific high-productivity belt, throughout the upper Miocene to Quaternary sections of cyclic siliceous-calcareous oozes, a mean NRM intensity of (1.8 ± 1.2) × 10^{-3} A/m was measured. Due to the limitations imposed by these sediments, polarity sequences could be derived from the stable declinations down-hole only for the upper 50 m sub-bottom and a short interval between 76 m and 84 m sub-bottom (Fig. 6).

The uppermost core at hole 574 shows one uniform polarity sequence which can be interpreted as being of Brunhes age, proved by the positive stable inclination data (Fig. 6). Biostratigraphically, these sediments are dated to late Pleistocene as indicated by the distinguished nannofossil CN14/CN15 zones (Bukry, 1975; Pujos, 1985). The coincidence with the nannofossil FAD of *Gephyrocapsa caribbeanica* in the topmost deposits of core 574-2 dates its top older than the geomagnetic Jaramillo Event within the reversed Matuyama Epoch (Barron et al., 1985). Below, the next interval of normal polarity, as defined by the stable inclinations and Type I characteristics of remanence, indicates the Olduvai Event; the Brunhes/Matuyama boundary and the Jaramillo Event are missing in this hole. This gap is probably caused by lost sediments during coring. Because of mechanic deformations within core 574-3, the polarity

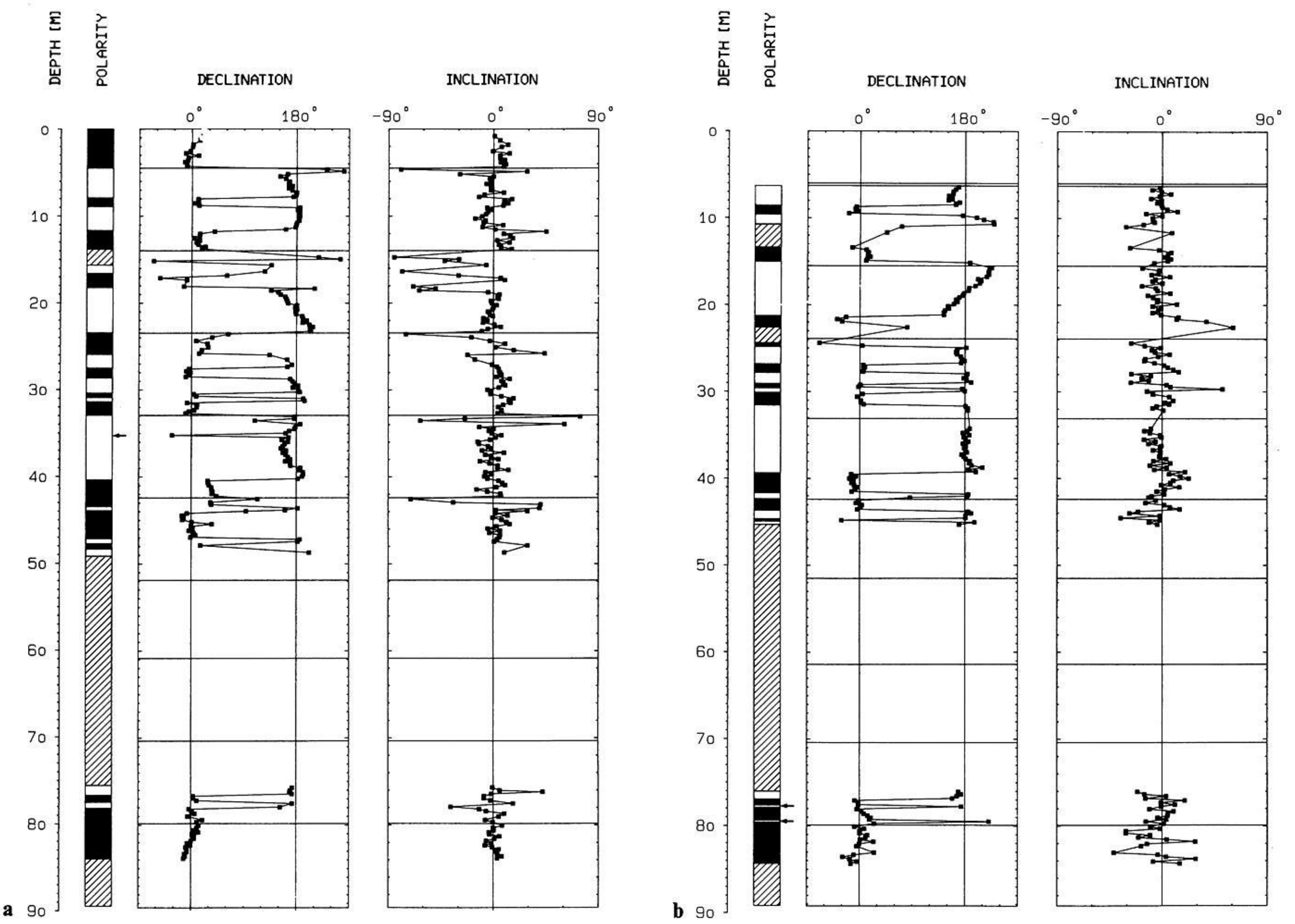

Fig. 6a, b. Paleomagnetic polarity for (**a**) hole 574 and (**b**) hole 574A (see Fig. 5)

pattern of the geomagnetic Gauss Epoch can only partially be identified. The four normal events within the reversed Gilbert Epoch can easily be identified (Fig. 11). The transitions in core 574-5/6 define the geomagnetic Epoch 5. Furher below, a brief normal event occurs which had not been known in any magnetostratigraphy (Opdyke et al., 1974; Theyer and Hammond, 1974; Theyer et al., 1978) or in the geomagnetic time-scales based on marine magnetic anomalies (Berggren et al., 1986).

In hole 574A, a similar situation to the one in hole 574 occurs (Figs. 6 and 11). Core 574A-2 correlates with the reversed Matuyama Epoch based on the stable inclinations and the Type II demagnetization characteristics. Then the first interval of normal polarity was interpreted as the Olduvai Event, biostratigraphically proved by the nannofossil LAD *Coccolithus pelagicus* (Pujos, 1985). The following polarity sequence, in parts, is incomplete throughout this hole because of disturbed sediments (Fig. 6). The complete polarity pattern of the geomagnetic Gilbert Epoch and Epoch 5 can be distinguished at hole 574A, as well as the short interval of normal polarity below Epoch 5. It is identified at the same stratigraphic level as in hole 574. Therefore, this interval can be assumed to be real.

The apparent rates of sedimentation vary about a factor of two throughout the last 6 my. They increase from 5.3 ± 0.2 during the geomagnetic Brunhes to Gauss Epochs to 11.1 ± 0.1 m/my during the Gilbert Epoch and Epoch 5.

In the two parallel holes 574 and 574A between 76 m and 84 m sub-bottom, paleomagnetic unequivocally interpretable data could be obtained (Fig. 6). Intervals of normal and reverse polarity were derived from the change between Type I and Type II demagnetization characteristics of remanence. The magnetostratigraphic interpretation of this interval is based on the results of biostratigraphy. Figure 7 shows the zonations of the four dominant groups of planctonic microfossils throughout the sedimentary column. In the tropical Pacific, the foraminifera zones N14 and N16 as well as the nannofossil zones CN7 and CN6 are characteristic of the geomagnetic Epoch 11 (Berggren and Van Couvering, 1974). The radiolarian species *Diartus petterssoni* is also usually correlated to Epoch 11 (Theyer and Hammond, 1974; Theyer et al., 1978). The transition of diatom species *Actinocyclus moronensis*/*Coscinodiscus yabei* is dated to 11.3 my (Burckle, 1978) and, therefore, falls within this geomagnetic epoch. For this sub-bottom interval, the biostratigraphically derived rate of sedimentation was calculated to be about 24 m/my (Barron et al., 1985). Referring to this relation, the paleomagnetically studied sequence of 8.3 m length should cover about 0.35 my (Fig. 11). Considering that geomagnetic Epoch 11 consists of two intervals of normal paleofield configurations (Berggren et al., 1986), the derived polarity pattern has to be correlated to one of these intervals. Two biostratigraphic data can be identified within this sediment sequence: the transition of nannofossil zones CN6/CN7, dated to 12 my (Bukry, 1975; Pujos, 1985), and the above-mentioned dia-

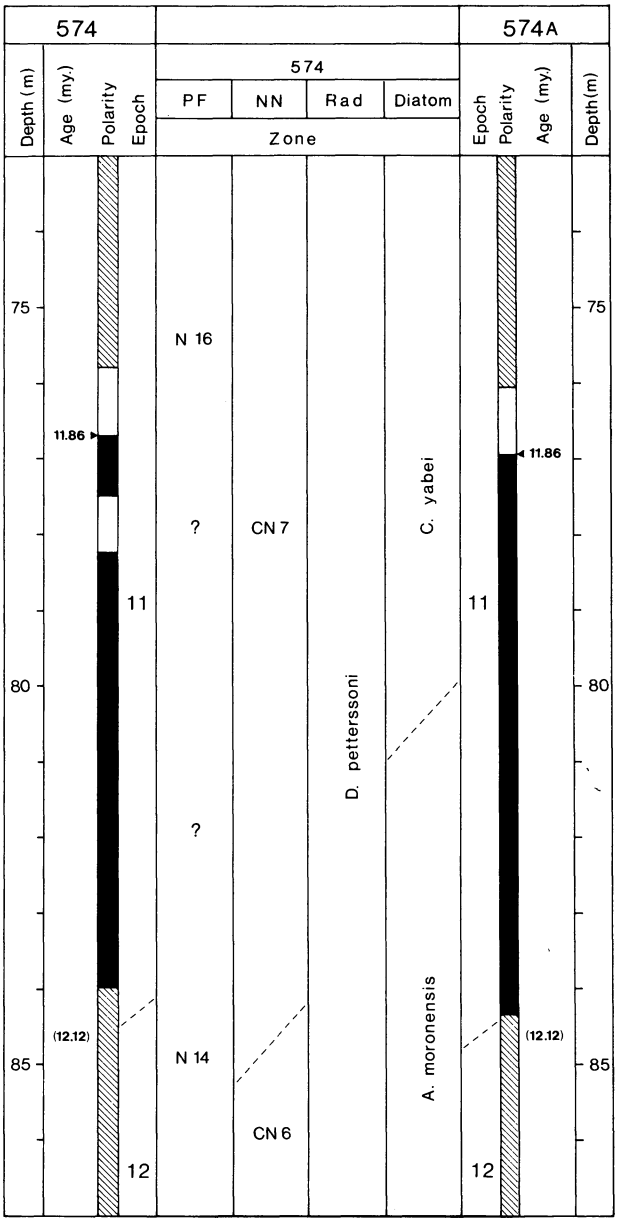

Fig. 7. Magneto- and biostratigraphy throughout the upper Miocene sediments at hole 574 and 574A. The foraminifera zones (*PF*) follow those given by Berggren (1969), nannofossil zones (*NN*) from Bukry (1975), radiolarian zones (Rad) from Riedel and Sanfilippo (1978) and diatom zones from Burckle (1972). *Black intervals* indicate normal, *white intervals* reversed polarity of the Earth's magnetic paleofield. Throughout the *hatched intervals* no data are available or the paleomagnetic measurements do not provide unequivocally interpretable results. The numbers are ages in my

tom transition *A. moronensis*/*C. yabei*. In addition, the entire interval belongs to the radiolarian zone *D. petterssoni* (Nigrini, 1985) which is usually dated from 12.6 and 11.1 my. According to the biostratigraphic data, it is obvious to correlate this specific interval of normal polarity to the oldest sequence of normal paleofield configuration within Epoch 11 (Fig. 11).

Site 575

Site 575 constitutes the endpoint of the SN transect across the equatorial Pacific high-productivity zone (Fig. 1). At this site Miocene to Quaternary sediments were recovered. The NRM intensities throughout the cyclic siliceous-calcareous oozes, which gradually change to pale brown oozes, are similar to those previously discussed. A mean of $(2.1 \times 1.2) \times 10^{-3}$ A/m was measured.

A magnetostratigraphy from Quaternary into the lower Miocene was established (Fig. 11), unfortunately with some upper and middle Miocene gaps due to prominent hiatuses (Barron et al., 1985). The radiolarian zone *B. invaginata* and the nannofossil zone CN16 prove that the topmost sediments in the two parallel holes 575 and 575C were deposited during the Brunhes Epoch (Pujos, 1985; LaBracherie, 1985). Below, in the sequence, follow the Matuyama and Gauss Epochs as documented by the declination data (Fig. 8) and the demagnetization characteristics. The latter defines the actual paleofield polarity easily (Fig. 11). The Gauss/Gilbert boundary at 3.4 my is immediately followed by the Gilbert/Epoch 5 boundary at 5.35 my. This is in agreement with the biostratigraphy (Barron et al., 1985), substantiating the fact that the entire sequence of the Gilbert normal events is missing due to a late Miocene hiatus (Barron et al., 1985). Hole 575C bottoms with its second core at about 6.4 my defined by the magnetostratigraphy (Fig. 11).

The paleomagnetic sequence throughout hole 575, in parts, provides a poor magnetic record masking the magnetostratigraphic information of Epochs 6 to 8 (Fig. 8). The simultaneous FAD of the two diatom species *Thalassiosira burckliana* and *C. yabei* at the same stratigraphic level (Barron, 1985) is caused by a prominent hiatus covering the entire geomagnetic Epoch 9. This interpretation is proved by other planctonic microfossils (Fig. 9). Within a short interval the two radiolarian data FAD *Didymocyrtis antepenultimus* and FAD *D. petterssoni*, both dated to about 9.5 my (Theyer and Hammond, 1974), and the radiolarian FAD *Diartus hughesi*, dated to 11.5 my (Theyer et al., 1978; Nigrini, 1985), are observed in the tropical Pacific. According to this biostratigraphic record throughout cores 575-3/4 (Fig. 9), the magnetostratigraphic interpretation of the polarity record derived from the declination log and the demagnetization behaviour of remanence covers geomagnetic Epochs 11 to 14 (Fig. 11). The magnetostratigraphic age of bottom of core 575-4, the deepest one studied at this hole, is about 13.5 my which agrees well with the biostratigraphy. Differences between both datings may result from deformed sediments as well as from the solution affecting the calcareous microfossils (Pujos, 1985). Due to the disturbed sediments at hole 575B, cored parallel to holes 575 and 575C, the magnetostratigraphic results are poor and not discussed in detail here. Nevertheless, they are shown on the appropriate Figs. 8 and 11. The apparent rates of sedimentation which are calculated from the magnetostratigraphy at holes 575 and 575C are listed in Table 1.

In Fig. 8 the hole 575A inclination/declination logs are shown and the elaborated polarity pattern opposed against the biostratigraphic results in Fig. 10. The coincidence of the nannofossil zone CN2 and the foraminifera zone N6 with the geomagnetic Epoch 17 verify the results of previously published analyses (Ryan et al., 1974; Berggren and Van Couvering, 1974). Hence, the radiolarian datum FAD *Stichocorys wolffii* dated to 17.6 my (Nigrini, 1985) appears to be too young according to the magnetostratigraphy. The poorly defined transition between the diatom species *Triceratum pileus* and *Denticulopsis nicobarica* is usually observed

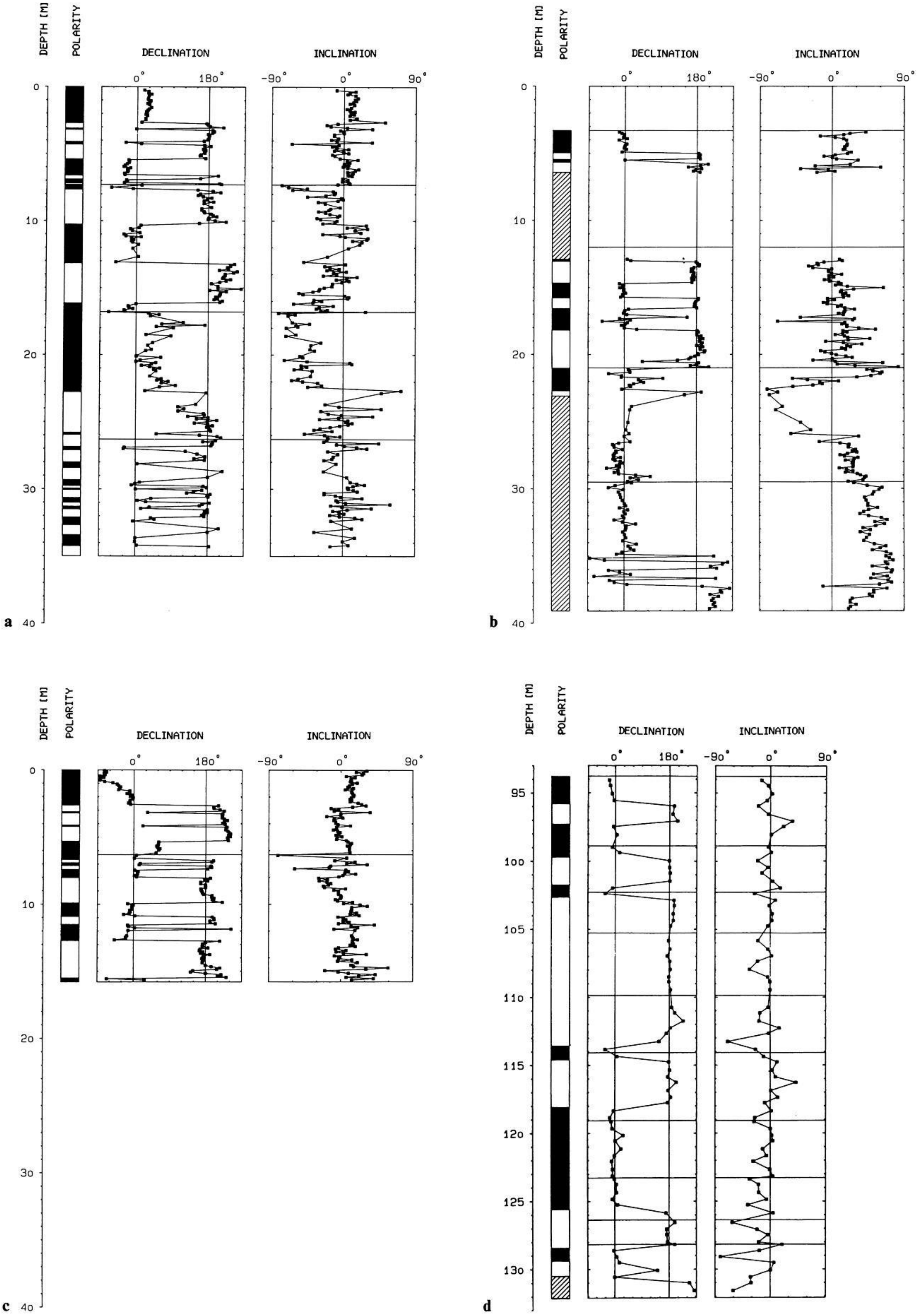

Fig. 8 a–d. Paleomagnetic polarity for (**a**) hole 575, (**b**) hole 575B, (**c**) hole 575C and (**d**) hole 575a (see Fig. 5)

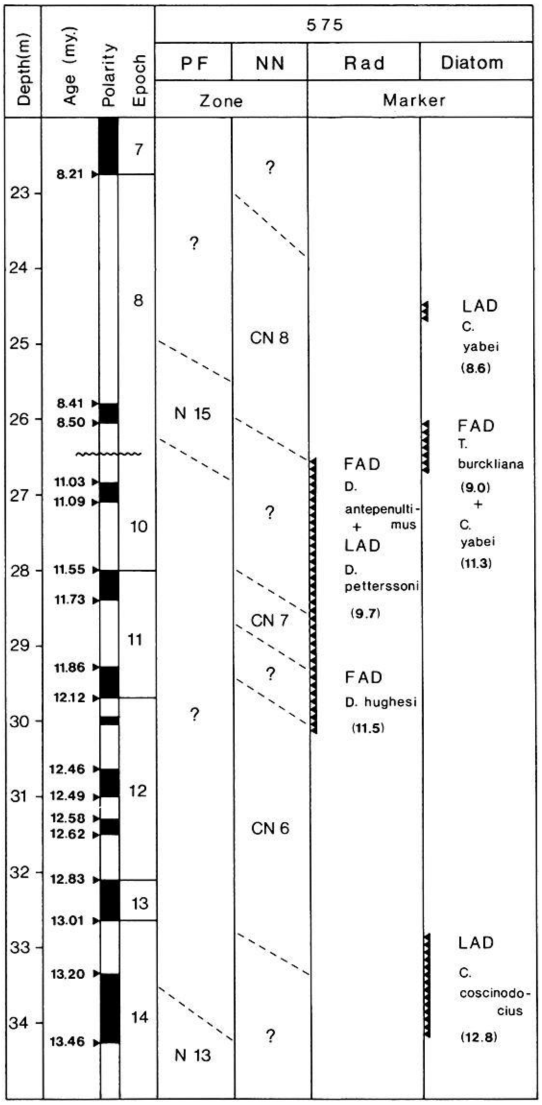

Fig. 9. Magneto- and biostratigraphy throughout the upper Miocene sediments at hole 575 (see Fig. 7)

in the younger sequence of Epoch 17 (Burckle, 1978; Barron, 1985). The geomagnetic Epoch 17/16 boundary mostly coincides with the radiolarian FADs *Dorcadospyris dentata* and *Calocyletta costata*, dated to 17.3–17.1 my (Theyer and Hammond, 1974; Nigrini, 1985). The geomagnetic Epoch 16 is characterised by the following bio-horizons: nannofossil zone CN3, foraminifera zone N7, radiolarian zone *C. costata* and diatom zone *D. nicobarica* (Berggren, 1969; Bukry, 1975; Barron, 1985). The transition of diatom zones *D. nicobarica*/*Cescinodiscus peplum* can be distinguished together with the youngest interval of normal polarity within geomagnetic Epoch 16, as demonstrated in Fig. 10 (Burckle, 1978; Barron, 1985). This gives sufficient agreement of Miocene magneto- and biostratigraphies throughout the sedimentary column at hole 575A and in comparison to the literature.

From the magnetostratigraphically derived age versus depth relation at hole 575A, an apparent rate of deposition of about 21.1 m/my can be calculated. In comparison to the younger rates, a systematic increase of sediment accumulation can be observed with increasing depth at this site.

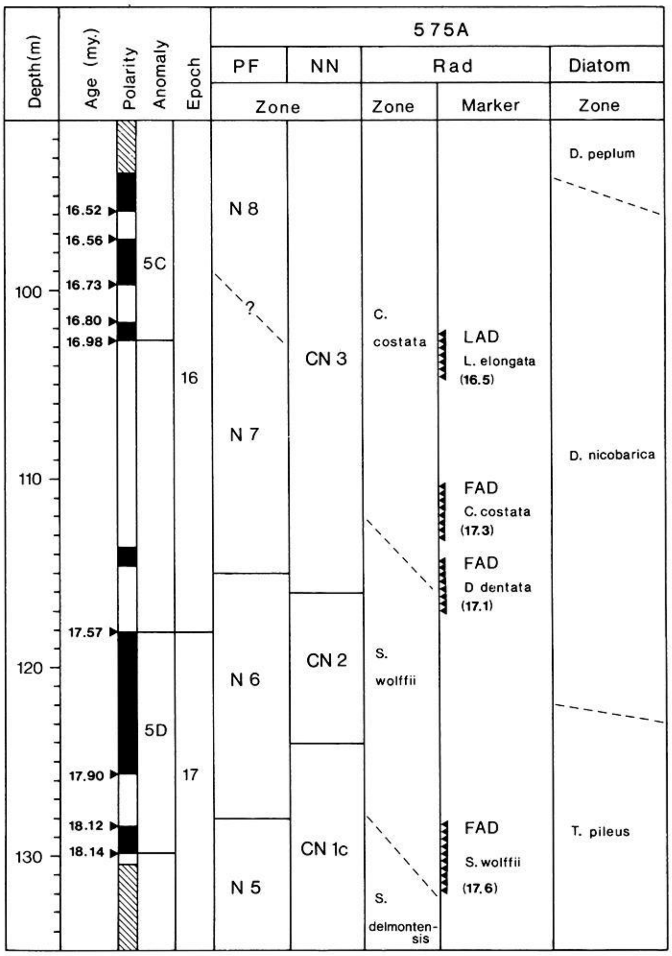

Fig. 10. Magneto- and biostratigraphy throughout the lower Miocene sediments at hole 575A. The marine magnetic anomalies are numbered after LaBrecque et al. (1977) (see Fig. 7)

Table 1. Variation of apparent rates of sedimentation at sites 573, 574 and 575 with age and plate-tectonically reconstructed paleogeographic latitudes

Site No.	Age range (my)	Latitude range	Apparent rate of sedimentation (m/my)
573	0 – 3.3	*0.5°N*–0.4°S	14.2±0.2
574	0 – 3.4	*4.2°N*–3.2°N	5.3±0.2
	3.4– 6.0	3.2°N–2.4°N	11.1±0.1
	11.8–12.1	0.7°N–0.5°N	24
575	0 – 3.5	*5.9°N*–4.8°N	2.3±0.1
	5.1– 8.8	4.3°N–3.2°N	5.6±0.2
	10.5–13.5	2.7°N–1.8°N	3.1
	16.5–18.1	0.9°N–0.5°N	21.1

The present-day geographic site-latitude is underlined

This behaviour is very unusual for marine sediments, due to the continuously increasing compaction with depth. At 114 m sub-bottom an additional interval of normal polarity occurs within geomagnetic Epoch 16, which is not known in the literature and, therefore, can not be correlated to the geomagnetic time-scale. Assuming a constant rate of deposition, this event lasts about 50 ky.

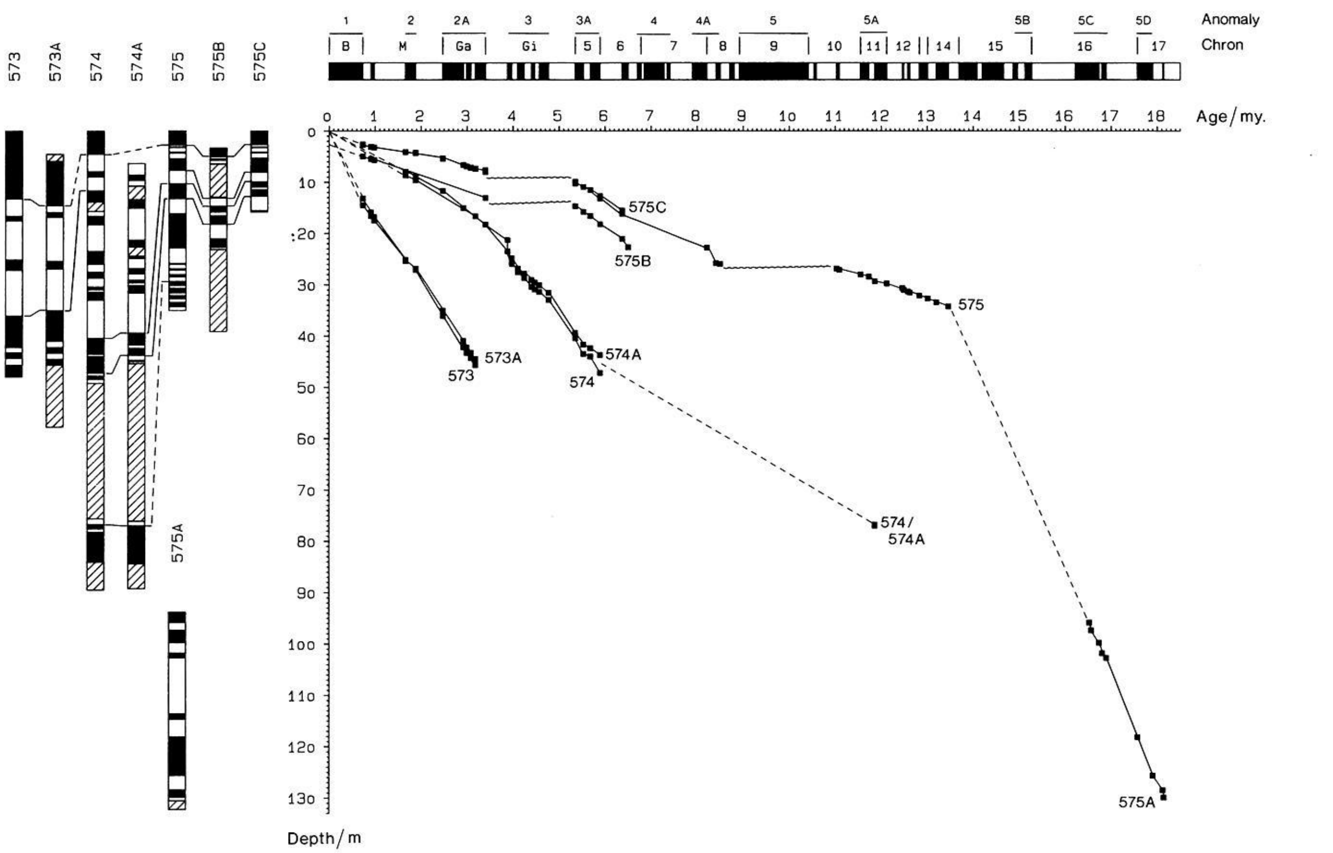

Fig. 11. Summary of the magnetostratigraphies at site 573, 574 and 575. The paleomagnetically derived polarity patterns are correlated to the geomagnetic polarity time-scale of Berggren et al. (1986). *Black intervals* indicate normal, *white intervals* reversed polarity of the Earth's magnetic paleofield. Throughout the *hatched intervals* no data are available or the paleomagnetic measurements do not provide unequivocally interpretable results. *Arrows* indicate polarity intervals identified by one datapoint and in one hole only. *Wavy lines* mark hiatuses

Regional magnetostratigraphic synthesis

Figure 11 summarizes the magnetostratigraphies of all discussed sediment sequences at sites 573 to 575 (Fig. 1). The age versus depth relations show an obvious increase with age and a systematic decrease with progressive northward distance from the equator. These results are quantified in Table 1. For various time intervals the range of paleolatitude, where the deposition took place, and the corresponding rates are listed. The separation is based on significant changes in the rate of sedimentation and/or is oriented due to gaps of information. The latitudinal range derived by the paleo-tectonical reconstructions is calculated from a northward drift of the Pacific plate during the Neogene of about 0.3°/my (Epp, 1978; 1984; Weinreich, 1985).

It becomes obvious that, independent of the appropriate age, the sediments are deposited at comparable paleolatitudes at about the same rates. The sedimentation rate of 21.1 m/my of lower Miocene deposits at site 575 accumulated at 0.4°N–0.9°N correlates according to size with 24 m/my for the upper Miocene at site 574 accumulated at 0.5°N–0.7°N. Almost identical rates can be observed for the upper Miocene at site 575 and the Plio-Pleistocene sediments at site 574, both deposited at identical paleolatitudes (Table 1). In Fig. 12 the apparent rates of sedimentation are plotted as a function of the plate-tectonically reconstructed paleogeographic latitudes. From south to north, first, an increase can be observed, followed by a continous decrease of sedimentation. The interval between 13.5–10.5 my at site 575 (Table 1) disagrees with this unequivocal trend. Here, an extremely high solution of the biogenic carbonate (Pujos, 1985) causes the obvious difference between the calculated *apparent rate of sedimentation and their actual* accumulation. In this context it has to be considered that almost similar paleolatitudes do not correspond to the same age. Therefore, time-dependent variations in the paleogeographic regime, e.g. changes in depth of the CCD, influence carbonate solution.

The variation of accumulation rates, derived from magnetostratigraphies (Fig. 11) depending on different geological ages and paleogeographic latitudes, is the result of two superposed effects: the northward motion of the Pacific plate and the paleogeographically fixed position of the equatorial high-productivity belt of biogenic deposits. After van Andel et al. (1975), the NS extension of this structure and the general behaviour of deposition can be assumed to be constant at least during the Neogene. Therefore, the increase of accumulation with depth at sites 574 and 575 cannot be interpreted as the time-dependent variation of sedimentation at the present-day drillsite location. Rather, they reflect the northward drift of the paleo-sedimentation floor underneath the zone of extreme, but constant, gradients of sediment accumulation. This interpretation explains the distinguished differences of sedimentation rates and, therefore, describes the geographic structure of the equatorial sediment bulk since the Miocene (Fig. 12). The

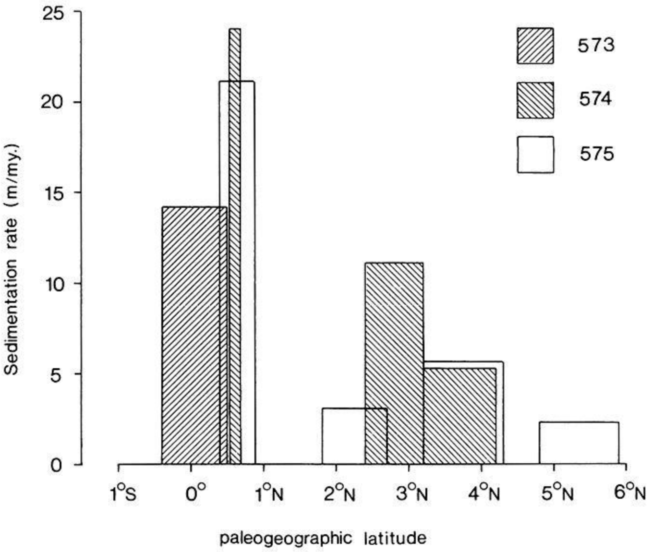

Fig. 12. Variation of the apparent rates of sedimentation as a function of the plate-tectonically reconstructed paleomagnetic latitude

latitudinal range represented by the oldest sediments at sites 574 and 575 define the maximum of sedimentation of microfossil skeletons a little north of the equator. The Plio-/Pleistocene deposits at site 573 were accumulated at latitudes south of this maximum (Fig. 12). To the north, the sedimentation decreases to less than 25% of its maximum. The low rate of 2.3 m/my observed for the Plio-/Pleistocene sediments at site 575 represent the northern edge of the equatorial sediment bulk (Fig. 1). Figure 12 can be interpreted as an image of the equatorial sediment bulk paleotopography during the last 20 my, which implies that any changes in the paleoceanographic regime or prominent geological events like the closing of the central American Isthmus did not affect its sedimentary conditions.

This discussed model of the paleogeographic structure of the equatorial Pacific extreme biogenic mass-production, based on the magnetostratigraphic record of deep-sea cores, corroborates and quantifies the results of previous studies in this area. Those results locate the maximum of deposition at about 1° north of the equator with an extension to about 5°N. Now, this statement could first be conspicuously verified by magnetostratigraphic investigations. Finally, the results prove the assumed northward drift of the Pacific plate of 0.3°/my during the Neogene.

Acknowledgements. We would like to thank all our ship-board colleagues of DSDP Leg 85 for their friendly co-operation. Special thanks are due to Prof. Bleil and V. Spieß for their discussion and valuable comments. J. Barron and C. Nigrini kindly assisted with their stratigraphic data.

The financial support of N.W.'s research by the Deutsche Forschungsgemeinschaft is gratefully acknowledged. F.T.'s research was in part supported under National Science Foundation grants OCE78-000 and OCE82-00000.

References

Barron, J.A.: Late Eocene to Holocene biostratigraphy of the equatorial Pacific Ocean, DSDP Leg 85. In: Initial reports of the Deep Sea Drilling Project **85,** Mayer, L., Theyer, F., et al., pp. 413–456. Washington: U.S. Government Printing Office 1985

Barron, J.A., Nigrini, C.A., Pujos, A., Saito, T., Theyer, F., Thomas, E., Weinreich, N.: Synthesis of central equatorial Pacific DSDP Leg 85 biostratigraphy: refinement of Oligocene to Quaternary biochronology. In: Initial reports of the Deep Sea Drilling Project, vol. **85**, Mayer, L., Theyer, F., et al., pp. 905–934. Washington: U.S. Government Printing Office 1985

Berger, W.H.: Planctonic foraminifera: selective solution and the lysocline. Marine Geology **8**, 111–138, 1970

Berger, W.H.: Cenozoic sedimentation in the eastern tropical Pacific. Geol. Soc. Am. Bull. **84,** 1941–1954, 1973

Berggren, W.A.: Paleogene biostratigraphy and planctonic foraminifera of northern Europe. In: Leiden, Proc. First Internat. Conf. Planctonic Microfossils, Bronnimann, P., Renz, H.H., eds. 121–160, 1969

Berggren, W.A., Van Couvering, J.A.: The late Neogene: biostratigraphy, geochronology, and paleoclimatology of the last 15 million years in marine and continental sediments. Palaeogeography, Palaeoclimatology, Palaeoecology **16,** 1–126, 1974

Berggren, W.A., Kent, D.V., Flynn, J.J.: Paleogene geochronology and chronostratigraphy. In: Geochronology and the geological record, Snelling, N.J., ed.: London, Geol. Soc. London, Spec. paper, 1986 (in press)

Bleil, U.: The magnetostratigraphy of NW Pacific sediments, DSDP Leg 86, In: Initial reports of the Deep Sea Drilling Project **86,** Heath, G.R., Burckle, L.H., et. al.: Washington: U.S. Government Printing Office 1986 (in press)

Bukry, D.: Coccolith and silicoflagellate stratigraphy, north-western Pacific. In: Initial reports of the Deep Sea Drilling Project vol. 32, Larson, R.L., Moberly, R., et al., pp. 677–701. Washington: US Government Printing Office 1975

Burckle, L.H.: Late Cenozoic planctonic diatom zones from the eastern equatorial Pacific. Nova Hedwigia **39,** 217–246, 1972

Burckle, L.H.: Early Miocene to Pliocene diatom levels for the equatorial Pacific. Geol. Res. Devel. Cent. Indonesia, Spec. Publ. **1,** 25–44, 1978

Epp, D.: Age and relationships among volcanic chains on the Pacific plate. Ph.D. thesis, University of Hawaii, 1978

Epp, D.: Possible perturbations to hotspot traces and implications for the origin and structure of the Line Islands. J. Geophys. Res. **89,** 273–287, 1984

Hays, J.D., Saito, T., Opdyke, N.D., Burckle, L.H.: Pliocene-Pleistocene sediments of the eastern equatorial Pacific: their paleomagnetic, biostratigraphic, and climatic record. Geol. Soc. Am. Bull. **80,** 1481–1514, 1969

Hays, J.D., et al.: Initial reports of the Deep Sea Drilling Project, vol. **9**. Washington: US Government Printing Office 1972

Hoffman, K.A., Day, R.: Separation of multi-component NRM: a general method. Earth Planet. Sci. Lett. **40:** 422–438, 1978

Johnson, D.A., Knoll, A.H.: Absolute ages of Quaternary radiolarian datum levels in the equatorial Pacific. Quaternary Res. **5,** 99–110, 1975

Kent, D.V., Spariosu, D.J.: High-resolution magnetostratigraphy of Caribbean Plio-Pleistocene deep-sea sediments. Palaeogeography, Palaeoclimatology, Palaeoecology **42,** 46–64, 1983

LaBracherie, M.: Quaternary radiolarians from the equatorial Pacific, DSDP Leg 85. In: Initial reports of the Deep Sea Drilling Project vol. **85,** Mayer, L., Theyer, F., et al., pp. 499–510. Washington: US Government Printing Office 1985

LaBrecque, J.L., Kent, D.V., Cande, S.C.: Revised magnetic polarity time scale for the late Cretaceous and Cenozoic time. Geology **5,** 330–335, 1977

Mayer, L., Theyer, F., et al.: Initial reports of the Deep Sea Drilling Project **85**. Washington: U.S. Government Printing Office 1985

McDougall, I.: The present status of the geomagnetic polarity time scale. Research School of Earth Sciences, A.N.U., Publ. No. 1288, 1977

McManus, D.A., et al.: Initial reports of the Deep Sea Drilling Project, vol. **5**. Washington: US Government Printing Office 1970

Nigrini, C.A.: Radiolarian biostratigraphy in the central equatorial

Pacific. In: Initial reports of the Deep Sea Drilling Project, vol. **85**, Mayer, L., Theyer, F., et al., pp. 511–552. Washington: US Government Printing Office 1985

Opdyke, N.D., Burckle, L.H., Todd, A.: The extension of the magnetic time scale in sediments of the central Pacific ocean. Earth Planet. Sci. Lett. **22,** 300–306, 1974

Pujos, A.: Cenozoic nannofossils, central equatorial Pacific, DSDP Leg 85. In: Initial reports of the Deep Sea Drilling Project, vol. **85**, Mayer, L., Theyer, F., et al., pp. 581–608. Washington: U.S. Government Printing Office 1985

Riedel, W.R., Sanfilippo, A.: Stratigraphy and evolution of tropical Cenozoic radiolarians. Micropaleontology **24,** 61–96, 1978

Ryan, W.B.F., Cita, M.B., Dreyfus-Rauson, M., Burckle, L.H., Saito, T.: A paleomagnetic assignment of Neogene stage boundaries and the development of isochronous datum planes between Mediterranean, the Pacific, and Indian Ocean in order to investigate the response of the world ocean to the Mediterranean "Salinity crisis". Riv. Ital. Paleont. Strat. **80,** 631–688, 1974

Tauxe, L., Tucker, P., Petersen, N.P., LaBrecque, J.L.: Magnetostratigraphy of Leg 73 sediments. In: Initial reports of the Deep Sea Drilling Project, vol. **73**. Hsü, K.J., LaBrecque, J.L., et al., pp. 609–622. Washington: US Government Printing Office 1984

Theyer, F., Hammond, S.R.: Paleomagnetic polarity sequence and radiolarian zones, Brunhes to polarity Epoch 20. Earth Planet. Sci. Lett. **22,** 307–319, 1974

Theyer, F., Mato, C.Y., Hammond, S.R.: Paleomagnetic and geochronologic calibration of latest Oligocene to Pliocene radiolarian events, equatorial Pacific. Marine Micropaleontology **3,** 377–395, 1978

Tracey, J.I., et al.: Initial reports of the Deep Sea Drilling Project **8.** Washington: U.S. Government Printing Office 1971

van Andel, T.H., et al.: Initial reports of the Deep Sea Drilling Project **16.** Washington: U.S. Government Printing Office 1973

van Andel, T.H., Heath, G.R., Moore, T.C.: Cenozoic history and paleo-oceanography of the central equatorial Pacific ocean. Geol. Soc. Am. Mem. **143,** 1–134, 1975

Weinreich, N.: Magnetische Untersuchungen neogener pelagischer Sedimente des zentralen Äquatorialpazifik. Ph.D. thesis, Ruhr-Universität Bochum, 1985

Weinreich, N., Theyer, F.: Paleomagnetism of the Leg 85 sediments: Neogene magnetostratigraphy and tectonic history of the Central Equatorial Pacific. In: Initial reports of the Deep Sea Drilling Project vol. **85**, Mayer, L., Theyer, F., et al., pp. 849–901. Washington: US Government Printing Office 1985

Winterer, E.L.: Sedimentary facies and plate tectonics of the equatorial Pacific. Am. Assoc. Petrol. Geol. Bull. **57,** 265–282, 1973

Zijderveld, J.D.A.: A.C. demagnetization of rocks: analysis of results. In: Methods in palaeomagnetism, Collinson, D.W., Creer, K.M., Runcorn, S.K., (eds.), Amsterdam: Elsevier 1967

Received April 2, 1985 / revised August 22, 1985,
and March 10, 1986
Accepted April 2, 1986

J Geophys (1986) 59:195–201

Journal of Geophysics

Deconvolution as a method for the separation of Pi2 pulsations from background field variations

Jörg Behrens[1] and Karl-Heinz Glaßmeier[2]

Institut für Geophysik, Universität Münster, Corrensstr. 24, D-4400 Münster, Federal Republic of Germany

Abstract. In high-latitude magnetograms Pi2 pulsations are usually accompanied by pronounced background magnetic field variations due to substorm activity. A detailed analysis of Pi2 characteristics therefore requires a separation of the Pi2 signal from these background variations. The standard procedure to perform this separation is high-pass filtering. However, this is an insufficient way of separation as is discussed by means of artificial time series. An alternative procedure of separation is thus suggested which is based on the transient response theory of Pi2 pulsations. According to this theory a substorm magnetogram is regarded as the convolution of a driving function and a transfer function, where the latter is identified as the Pi2 pulsation. Subsequently, a model for the driving function is derived and a deconvolution filter designed. Application of this deconvolution filter to a large number of real substorm magnetograms shows that this filter may well be approximated by a second derivative filter. We suggest this filter is more useful in detrending high-latitude Pi2 records than using a simple high-pass filter.

Key words: Pi2 pulsations – Substorm onset – Transient response mechanism – Deconvolution

Introduction

Pi2 pulsations are transient magnetohydrodynamic waves associated with auroral brightenings or substorm onsets in the Earth's magnetosphere. Studying the properties of these transient waves not only helps in an understanding of hydromagnetic wave propagation in planetary magnetospheres, but also serves to elucidate in more detail the processes associated with X-type neutral line formation in the geomagnetic tail.

However, studying Pi2 signals is not an easy task as both Pi2 and substorm magnetic field variations are recorded simultaneously. At least, they are entities of one and the same physical process occurring in the Earth's magnetotail. It is therefore questionable whether the traditional treatment of high-latitude magnetograms as the addition of Pi2 pulsations and substorm magnetic field variations is justified at all, regarding a physical point of view. However, if one accepts that magnetic variations observed near substorm onset regions in high-latitudes are the sum of Pi2 pulsations, i.e. magnetic disturbances due to MHD waves, and substorm magnetic field variations due to the sudden enhancement of the westward polar electrojet, the following problem arises. As the rise time of the substorm onset magnetic signature, henceforth called background field variation, is typically about 2 min (e.g. Samson et al., 1985) and typical Pi2 periods are of the same order, simple high-pass filtering of magnetic field variations in the Pi2 period range results in a contamination of the Pi2 spectrum by parts of the background field spectrum (see also Stuart, 1972; Pashin et al., 1982).

To illustrate this problem Fig. 1 shows records of the *D* component of geomagnetic field variations observed at the three stations MAT, RIJ and NAM of the Scandinavian Magnetometer Array (SMA; see Küppers et al., 1979) on January 12, 1978, 2105–2130 UT, when a moderate substorm occurred in the geomagnetic tail. Data from the three stations NAM ($L \sim 4.5$), RIJ ($L \sim 5.5$) and MAT ($L \sim 6.5$) are chosen to represent records from mid-, subauroral- and high-latitude regions. In all three records the Pi2 pulsation, starting at about 2115 UT, is clearly identifiable. However, at MAT and RIJ the Pi2 magnetic signature appears together with pronounced background field variations, while at the mid-latitude station NAM hardly any trend in the record is visible.

Power spectra of the records shown are displayed in the bottom part of Fig. 1. For NAM a clear spectral peak at a frequency of 11 mHz appears, representing the Pi2 pulsation. Some indication of such a peak is still visible in the RIJ spectrum, but hardly detectable in the MAT record. It is this missing separation of the Pi2 spectrum and the background field spectrum which causes high-pass filtering to be an insufficient tool with which to study Pi2 pulsations, especially at high-latitudes.

To further demonstrate the shortcomings of a simple high-pass filtering procedure, artificial time series as shown in the upper part of Fig. 2 are regarded as *H* and *D* components of an observed geomagnetic varia-

---

[1] *New address:* Dornier System GmbH, D-7990 Friedrichshafen, Federal Republic of Germany

[2] *New address:* Institut für Geophysik und Meteorologie, Universität zu Köln, Albertus-Magnus-Platz, D-5000 Köln 41, Federal Republic of Germany

Offprint requests to: K.H. Glaßmeier

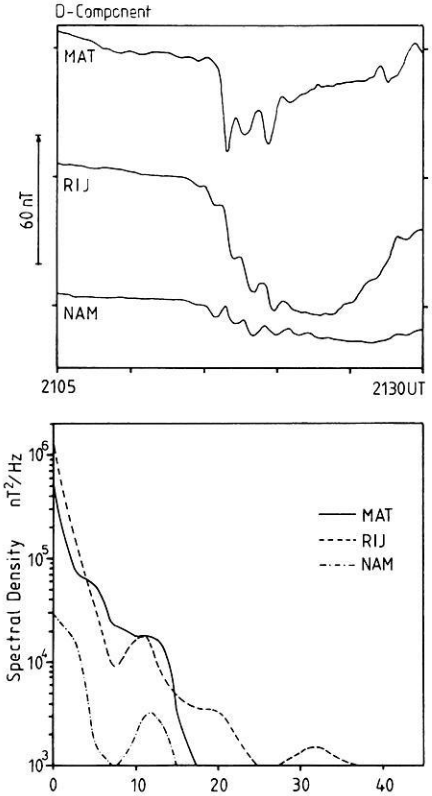

Fig. 1. *Upper panel:* substorm onset magnetograms recorded at three stations of the Scandinavian Magnetometer Array at different L values. *Lower panel:* power spectral density estimations of the corresponding time series

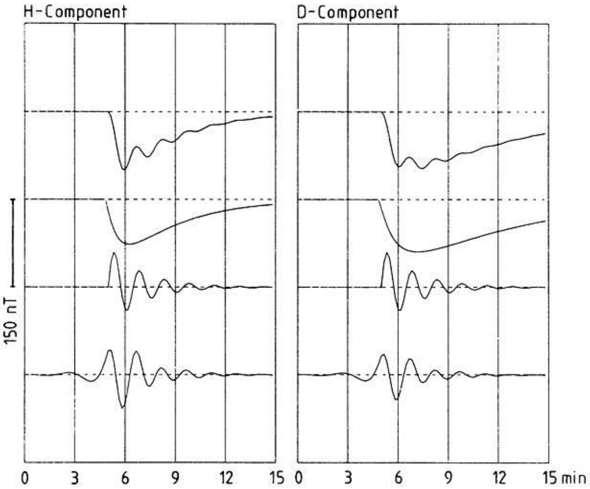

Fig. 2. Artificial magnetograms of horizontal H and D components *(upper traces)*. The following two panels show the used driving and transfer functions, respectively (see text). The corresponding high-pass filtered signals for each component are displayed in the lowest two panels

tion. Both artificial series result from a time convolution of the two functions $x(t)$ and $h(t)$ (the reason for using a convolution rather than the sum of $h(t)$ and $x(t)$ will be given later), where $x(t)$ is given by

$$x(t)=x_0 \exp(-\alpha t) \tan^{-1}(\beta t)$$

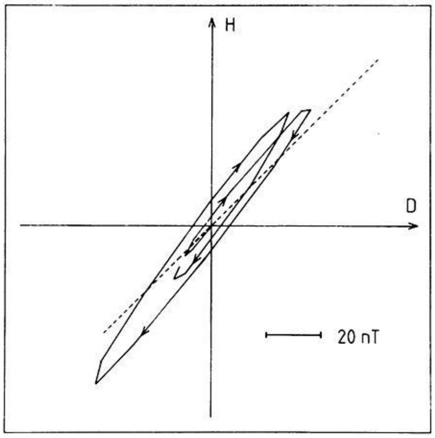

Fig. 3. Hodograms of the horizontal disturbance vectors of the Pi2 input *(dashed line)* and the high-pass filtered time series *(solid line)*, plotted for the first 450 s of the time series. For the latter hodogram, the sense of rotation is indicated by *arrows*

and regarded as the background field variation. $h(t)$ is regarded as an Pi2 signal and is given by

$$h(t)=h_0 \exp(-\gamma t) \sin(\delta t).$$

For the $H(D)$ component parameters $\alpha=5\times10^{-3}\,\mathrm{s}^{-1}$ $(2.5\times10^{-3}\,\mathrm{s}^{-1})$ and $\beta=2\times10^{-2}\,\mathrm{s}^{-1}$ $(1.5\times10^{-2}\,\mathrm{s}^{-1})$ have been chosen, while $x_0=-100$, $h_0=75$, $\gamma=8.3\times10^{-3}\,\mathrm{s}^{-1}$ and $\delta=7\times10^{-2}\,\mathrm{s}^{-1}$ are the same for both components. The background field variations, $x(t)$, and artificial Pi2 signals, $h(t)$, are displayed in the middle two traces of Fig. 2. Comparison of Figs. 1 and 2 also shows that the above parameter set results in sufficient similarity between observed magnetic variations during a substorm onset and the simulated ones.

Application of a standard high-pass filter (a Butterworth filter of order 8 is used) to the artificial H and D components results in the filtered signals shown in the bottom part of Fig. 2. Obvious differences between $h(t)$, the assumed Pi2 signal, and the filtered signals are given in the amplitude behaviour, where a distortion of the originally e-folding sinusoid oscillation may be seen. The sharp onset with the maximum amplitude at one quarter period of the input Pi2 is not reconstructed by the applied high-pass filter, with the consequence, that we now see the beginning of the oscillation shifted to earlier times.

It is not only the amplitude which is affected by the high-pass filter technique, but also the polarization of the two signals H and D. As can be seen from the above parameter set, H and D as constructed from $h(t)$ represent a linearly polarized signal, while after high-pass filtering of the simulated substorm magnetograms a clearly elliptically polarized Pi2 signal results as the hodogram in Fig. 3 shows.

As analysis of Pi2 polarization properties recently gave further important information on Pi2 generation mechanisms (e.g. Pashin et al., 1982, Samson and Harrold, 1983; Lester et al., 1984; Southwood and Hughes, 1985), our above comments demonstrate that a more refined method to separate the Pi2 signal from background field variation is necessary to reduce bias in amplitude and polarization studies of these pulsations.

Derivation of a deconvolution filter

In deriving the artificial H and D components displayed in Fig. 2 the time convolution between $x(t)$ and $h(t)$ rather than their sum has been used to construct an artificial substorm magnetogram. This is justified as current theories (e.g. Nishida, 1979; Kan et al., 1982; Baumjohann and Glaßmeier, 1984) regard Pi2 pulsations as the transient response of the magnetosphere-ionosphere system to sudden changes in the night-time magnetosphere.

Any change of, for example, the field-aligned current distribution in the magnetotail must be communicated to other parts of the magnetosphere by Alfvén waves. These Alfvén waves may bounce back and forth between conjugate ionospheres or other boundaries in the magnetosphere until a new current equilibrium is set up. For simple magnetospheric models, detailed expressions for the temporal and spatial variations of the magnetic and electric fields associated with such a transient Alfvén wave been given, e.g. by Lysak and Dum (1983) or Hughes (1983). In general, the temporal behaviour of such transients can be described as the convolution $y(t)$ of an impulse response $h(t)$ and a driving function $x(t)$

$$y(t)=\int_{-\infty}^{+\infty} h(\tau)\,x(t-\tau)\,d\tau=h(t)*x(t). \tag{1}$$

This approach is also in accord with early work by Boström (1972) who modelled the magnetosphere-ionosphere system by an equivalent current loop with lumped impedances, where Pi2 pulsations are excited by a 'switch-on' process of this current circuit.

Identifying $y(t)$ with measured magnetic variations, e.g. during a substorm event, it is natural to try to deconvolve the signal to get either information about the impulse response or the driving function. As both $x(t)$ and $h(t)$ are unknown, the deconvolution of $y(t)$ is a nonunique problem unless a sophisticated physical model for one of the functions is available. Because we regard Pi2 pulsations as transient responses of the magnetosphere-ionosphere system it seems natural to model the driving function and to reach the impulse response by a deconvolution of the measured signal. It is this impulse response function we regard as the desired Pi2 signal.

The driving function we like to identify as what we loosely call background field variation. A uniform definition of what is meant by background variation can not be given. However, it is a common feature of substorm magnetic signatures observed near the substorm onset region in high-latitudes that there is a sudden decrease of the magnetic field followed by a longer-lasting recovery phase. And it is this temporal trend which we regard as the driving function. As an empirical model for this temporal behaviour we assume an analytic function of the form

$$x(t)=\begin{cases}0 & t<0\\ c[\exp(-a\cdot t)-\exp(-b\cdot t)] & t>0\end{cases} \tag{2}$$

which closely resembles the characteristics of substorm-associated background field variations as displayed in Fig. 1. A large variability of the possible waveforms of the driving function is guaranteed by the three parameters a, b and c. For parameter values $a=1\times10^{-2}\,\mathrm{s}^{-1}$, $b=2.5\times10^{-3}\,\mathrm{s}^{-1}$ and an arbitrary value of c, the function $x(t)$ is displayed in Fig. 4. It is easily recognized that the chosen functional form $x(t)$ well reproduces typical features of the temporal behaviour of substorm magnetograms (as shown in Fig. 1), namely sudden decrease and longer-lasting recovery of the magnetic field.

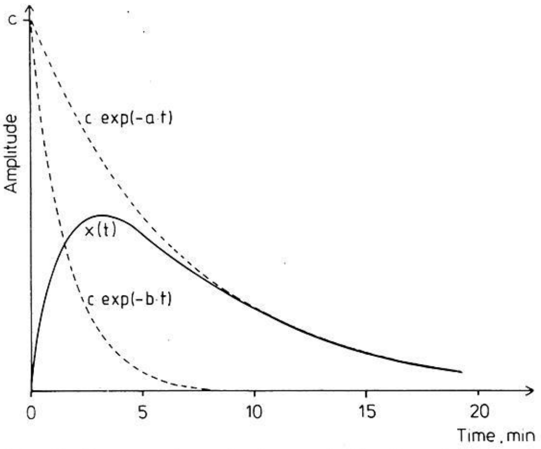

Fig. 4. Temporal variations of the functions $\exp(-at)$ and $\exp(-bt)$ as well as their compositions (see text)

It may well be argued that the choice of a functional form for $x(t)$ will seriously influence the measured $h(t)$. We are well aware of this problem, but a better choise requires a much more detailed understanding of the physical processes occurring in the Earth's magnetotail than presently available. Thus, our approach should be regarded as a first-order solution to a very complex problem.

A choice of a functional form $x(t)$ as given by Eq. (2) is also suitable for the following mathematical treatment as the deconvolution is best performed in the frequency domain. The z-transform of Eq. (2) is easily performed and for equidistant digital data with a sampling period Δt given by

$$X(z)=\frac{c(e^{-a\cdot\Delta t}-e^{-b\cdot\Delta t})\,z^{-1}}{(1-z^{-1}e^{-a\cdot\Delta t})(1-z^{-1}e^{-b\cdot\Delta t})} \tag{3}$$

from which the inverse operator

$$X^{-1}(z)=\frac{p}{z^{-1}}(1-gz^{-1}+fz^{-2}) \tag{4}$$

can be derived by taking the reciprocal, collecting terms and using the set of independent filter coefficients (p,f,g) instead of the set of independent parameters (c,a,b) with $g=e^{-a\cdot\Delta t}+e^{-b\cdot\Delta t}$, $f=e^{(-a-b)\cdot\Delta t}$, $p^{-1}=c(e^{-a\cdot\Delta t}-e^{b\cdot\Delta t})$, and $z=\exp(i\omega\Delta t)$. Note that due to our choice of $x(t)$ as given by Eq. (2), $X^{-1}(z)$ is a simple three-term and non-recursive phase-shift filter.

To find optimum coefficients p, f and g, a linear least-squares fit of the function $x(t)$ to the actually observed signal $y(t)$ is performed. The resulting parameter set a, b and c then gives the filter coefficients. As an example, Fig. 5 shows actually observed substorm magnetograms at stations EVE and MIK of the Scan-

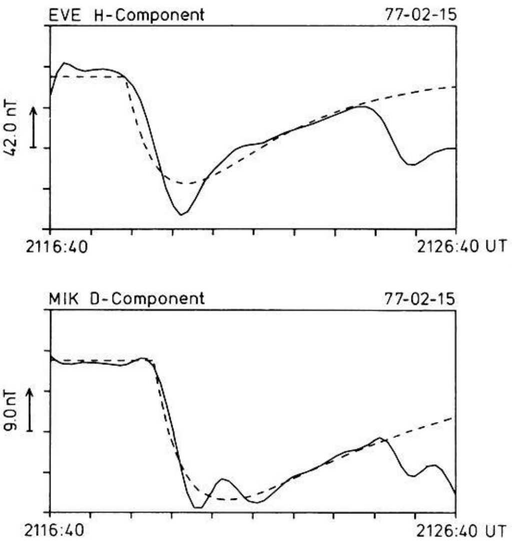

Fig. 5. Magnetograms of the *H* component recorded at station EVE and of the *D* component recorded at station MIK of the Scandinavian Magnetometer Array during the 77-02-15, 2118 UT substorm together with a linear least-squares fit *(dashed line)* of the function given by Eq. (2)

dinavian Magnetometer Array together with the fitted function $x(t)$. It can be seen that $x(t)$ describes the trend in the observed signals reasonably well.

However, working with magnetic field observations from an extended magnetometer array like the SMA (Küppers et al., 1979) the above-mentioned way to find the filter coefficients is inappropriate as the resulting coefficients for the different components at different locations are independently determined. Subsequent deconvolution of measured magnetic variations thus may violate physical constraints imposed on ground magnetic variations. Such a constraint, for example, is the irrotational character of the horizontal ground magnetic field (e.g. Fukushima, 1976; Glaßmeier, 1984). To conserve this property the filter coefficients can no longer be selected independently, but must fulfil certain conditions. However, to avoid an inter-component and inter-location dependent determination of the filter coefficients and to keep things as simple as possible, one may seek a uniform set of coefficients such that every signal is deconvolved by the same filter operator. Though this implies that each signal is no longer deconvolved in its optimum sense, the choice of a uniform set of filter coefficients guarantees to conserve, for example, the irrotational character of the ground magnetic field.

To determine such a uniform set of filter coefficients we analysed SMA data from two typical substorm events on February 15, 1977 (cf. Pashin et al., 1982) and January 12, 1978. For altogether 136 different horizontal and vertical components from 36 different stations the coefficients a, b and c have been determined by the linear least-squares procedure described above. With $\Delta t = 10\,\mathrm{s}$ for the SMA data, the filter coefficients f and g (cf. Eq. 4) have been calculated and histograms of which are displayed in Fig. 6 together with the values of a and b. They show distributions with pronounced peaks at $a=3\times10^{-3}\,\mathrm{s}^{-1}$, $b=1.1\times10^{-2}\,\mathrm{s}^{-1}$, $f=0.87$ and $g=1.86$. Due to the small variance of the parameter distributions in Fig. 6 it is tempting to use the peak values of f and g as a uniform set of filter coefficients in our search for a filter operator (we keep the scaling factor p undetermined here for reasons to be discussed later):

$$X^{-1}(z)=\frac{p}{z^{-1}}(1-1.86z^{-1}+0.87z^{-2}). \tag{5}$$

However, to justify the use of the above operator as a uniform filter it is advisable to study the properties of the filter operator as defined by Eq. (4) a little further. For this one can try to reduce the number of inde-

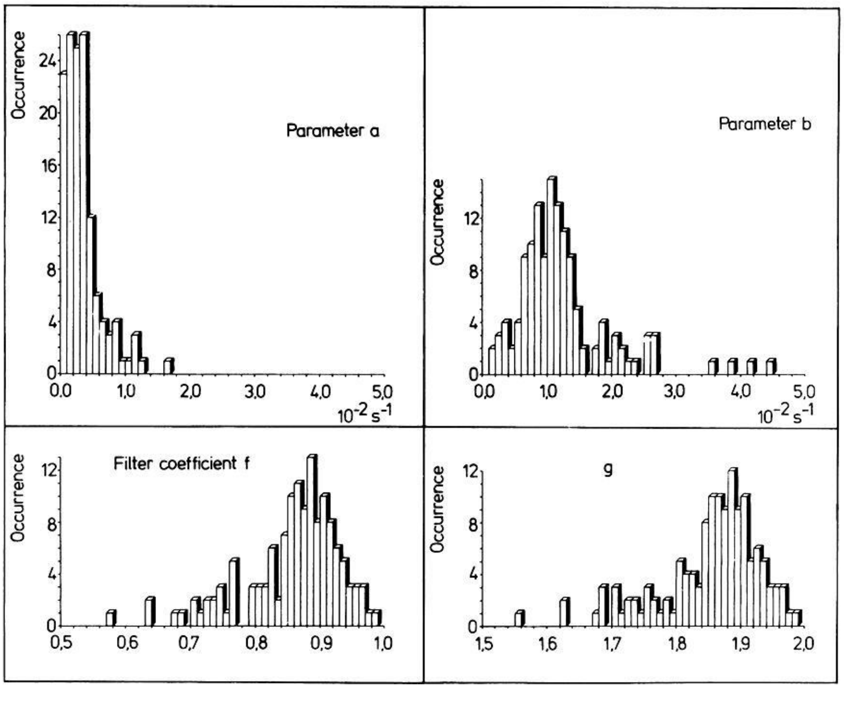

Fig. 6. Histograms of the parameters a and b as well as the corresponding filter coefficients f and g determined by fitting the analytic function $x(t)$ to real data by a linear least-squares fit (see text)

pendent variables in Eq. (4) and study the properties of the operator (4) as a function of one filter coefficient, either f or g. A relation between both is given by, for example,

$$g = e^{a \cdot \Delta t} f + e^{-a \cdot \Delta t} \tag{6}$$

which follows directly from their definition in Eq. (4). It should be noted that insertion of Eq. (6) in Eq. (4) does not reduce the number of independent variables in our filter operator. This is only accomplished after specifying a value for a.

With the peak value found for the parameter a, $3 \times 10^{-3}\,\mathrm{s}^{-1}$, and $\Delta t = 10$ s, Eq. (6) reduces to

$$g = 1.03 \cdot f + 0.97. \tag{7}$$

Insertion of this relation in Eq. (4) now leads to a filter operator which only depends on one parameter, f

$$X^{-1}(z) = \frac{p}{z^{-1}}\left[1 - (1.03f + 0.97)\, z^{-1} + f z^{-2}\right]. \tag{8}$$

The gain and phase responses of this filter are plotted in Fig. 7 for different values of the coefficient f in the interval $0 < f < 1$. It is obvious that changes of f do not affect the amplitude spectrum for larger values of f, i.e. the gain is relatively insensitive to variations of the parameter f. This holds especially for the values of f found from the analysis of the two substorm events (cf. Fig. 6), where f is always found to be larger than 0.6. From this it follows that our choice of the peak values of the f- and g-parameter distributions in Fig. 6 as a uniform set of filter coefficients still provides us with an optimum filter given by Eq. (5) as far as the gain response is concerned.

This does not apply to the phase response as Fig. 7 shows that small changes of f result in larger variations of the phase function. Thus a choice of the peak values of f and g as filter coefficients may no longer give us an optimum filter for a large class of signals as far as the phase response is concerned.

To tackle this dilemma we suggest using a zero-phase-shift filter. This certainly is a drawback from the idea of deconvolving substorm variations to yield the Pi2 waveform. However, one should keep in mind that both $x(t)$ and $h(t)$ in our deconvolution problem [cf. Eq. (1)] are undetermined, and that one has to look for a suitable model of $x(t)$. From the above discussion of the results displayed in Fig. 7 it is clear that the choice of a slightly incorrect model of $x(t)$ mainly affects the phase response rather than the gain. It is thus advisable to leave the phase spectrum of the signal to be analysed unchanged. In doing so one has to realize that one only yields an improvement of the amplitude - but not of the phase characteristics - of the Pi2 signal as compared with an ordinary high-pass filter. This still implies a contamination of the polarisation parameters of the Pi2 by phase information of the associated background field variations.

Using a filter operator like Eq. (8) a zero-phase-shift filter is realized by the choice $f = 1$ and $p < 0$, and the filter operator now reads

$$X^{-1}(z) = p(z^{+1} - 2 + z^{-1}). \tag{9}$$

The gain response of this filter is shown in Fig. 7 as a dashed line.

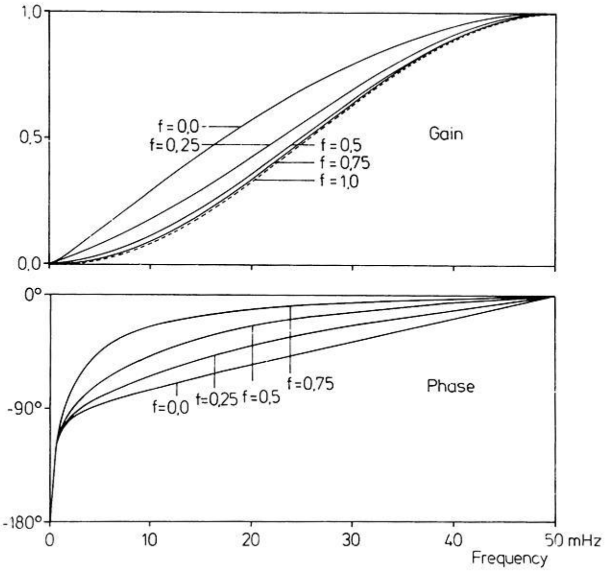

Fig. 7. Gain *(upper panel)* and phase *(lower panel)* characteristics of the deconvolution filter $X^{-1}(z)$ for different values of f

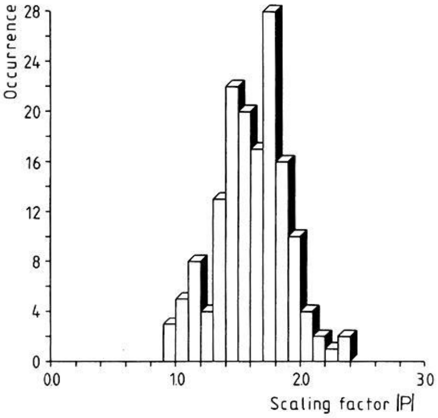

Fig. 8. Histogram of the modulus of the scale factor p determined by fitting the analytic function $x(t)$ to real data (see text)

As a multiplication by a factor z^{-1} means physically nothing but a delay of the time series by one sampling period, one may finally get the Pi2 time series $h(t)$ by

$$h_n = p(y_{n+1} - 2y_n + y_{n-1}) \tag{10}$$

where y_n denotes the n-th digital sample point of the input time series and h_n the corresponding one of the output series. Besides the scale factor p, $h(t)$ is nothing but the second derivative of the input time series.

Finally, the determination of the scale factor p remains. In principle one could follow a similar approach as for the filter coefficients f and g. A histogram for $|p|$ is given in Fig. 8. The distribution is as narrow as found before in the case of f and g (cf. Fig. 6). The peak value is $|p| = 1.7$. However, as this value represents the strength of an observed substorm event and is at least unpredictable, we suggest determining the scale factor p by normalizing the gain of $X^{-1}(z)$ to 1 at the supposed Pi2 frequency of a certain event rather than using some mean value of p.

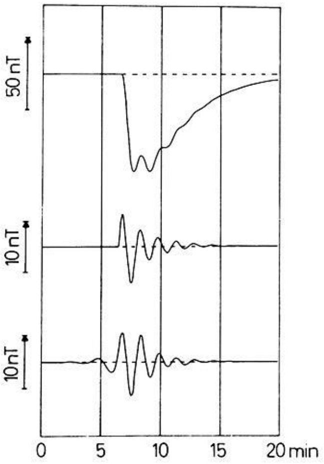

Fig. 9. Artificial substorm magnetogram *(upper trace)* and the corresponding deconvolution filtered time series *(middle trace)* as well as the high-pass filtered signal *(lower trace)*

Application aspects

To illustrate the efficiency, but also the weak points, of our approach to detrend Pi2 signals, in the following we want to discuss the analysis of artificial substorm magnetograms where the background field variations are not explicitly derivable from the analytical expression for $x(t)$ as used in Eq. (2) as well as a real magnetogram.

As a first example, Fig. 9 shows an artificial substorm onset magnetogram (upper time series) computed as the convolution between the driving function $x(t>0) = -100\tan^{-1}(9\times10^{-3}t)\exp(-5\times10^{-3}t)$ and the already used transfer function $h(t)$ (cf. Fig. 2). Use of the traditional high-pass filter (in our case a Butterworth filter of order 8 has been used) to separate Pi2 and substorm variations results in the time series shown as the bottom trace in Fig. 9. It has the already discussed defects, namely overshootings and oscillations before the true onset due to the Gibb's phenomenon. The deconvolution filter method suggested above, however, provides us with the time series displayed as the middle trace in Fig. 9. It suppresses the Gibb's phenomenon in an optimal way, provides us with a signal showing a very sharp onset and recovers, in a much better way than the high-pass filter, the highly damped waveform of the Pi2 pulsation which has initially been chosen as an *e*-fold damped sinusoid.

The improvement in recovering the Pi2 signal by using the deconvolution filter approach is also demonstrated by Fig. 10 where power spectra of the transfer function used in Fig. 9 (thick full line), the corresponding substorm magnetogram (thin full line), the standard filter magnetogram (dashed-dotted line) and the deconvolved time series (dotted line) are shown. The standard filtered magnetogram provides a spectrum which approximates that of the input Pi2 (thick full line) only roughly around its peak value at 11 mHz and at higher frequencies. However, the low-frequency part of the original spectrum is reproduced absolutely wrongly.

The deconvolution filtered magnetogram, on the other hand, provides a spectrum which approximates major portions of the original spectrum. Only the very-low-frequency part is less well reconstructed. Thus the deconvolution filter indeed represents a much better way to separate Pi2 and background magnetic variations.

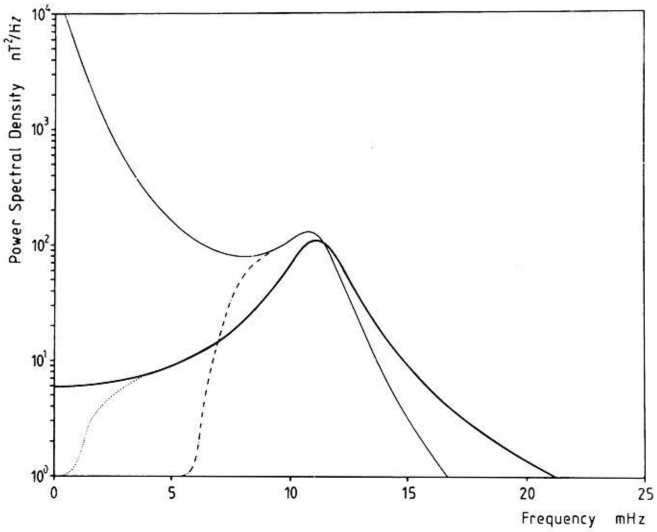

Fig. 10. Power spectral density estimates of the artificial substorm magnetogram *(thin full line)*, the high-pass *(dashed-dotted line)* and deconvolution filtered time series *(dotted line)* together with that of the original Pi2 signal *(thick full line)*

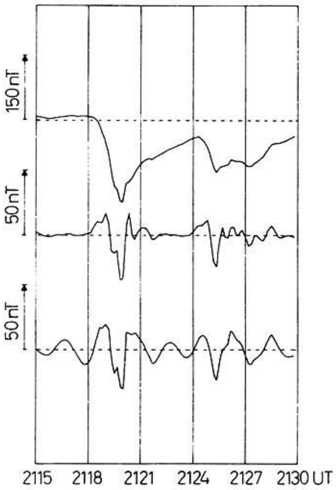

Fig. 11. High-latitude magnetogram *(upper trace)* with two successive substorm intensifications at 2118 and 2124 UT. The deconvolved time series *(middle trace)* shows the beginning of Pi2 pulsations with a clear separation of the two signals, whereas the standard high-pass filtered one *(lower trace)* is strongly superimposed by the oscillations of the filter response

An additional advantage of the deconvolution filter may be seen in Fig. 11 where a high-latitude substorm magnetogram showing two successive substorm onsets or intensifications is given. Using the standard high-pass magnetogram (lower panel) it is impossible to determine accurately either the first or the second onset time and therefore to separate both onsets and associated Pi2 trains. The deconvolution filter suggested, however, provides one with two clearly separated Pi2 signals (middle trace in Fig. 11). This may be useful to detect and distinguish in certain cases between several successive substorm intensifications, even when they are separated from each other only by a short time interval.

Summary and conclusion

In the present paper we have discussed the shortcomings of using an ordinary high-pass filter to separate Pi2 pulsations from background field variations. It has been demonstrated that the Pi2 amplitude - as well as phase - characteristics are contaminated by background field variations in such a way that the interpretation of actually measured data may lead to wrong results.

In order to optimize the separation of the Pi2 signal from the background variations we propose a matched filter operator which is based on the 'transient response model' for Pi2 pulsations (cf. the review by Baumjohann and Glaßmeier, 1984). In this model a substorm magnetogram is regarded as resulting from a convolution of two time series, a driving function and a transfer function, where we interpret the latter as the Pi2 signal. As both driving and transfer functions are unknown for the Pi2 problem, we estimate the driving function to deconvolve substorm magnetograms. The deconvolution filter thus derived could be approximated by a three-term and zero-phase-shift filter.

The suggested filter operator may also be interpreted as a second-order difference filter and it is interesting to note that two-dimensional wavenumber second-derivative filters are commonly used to determine the trend or regional field and residual maps in gravity or magnetic data (e.g. Kulhánek, 1976, p. 148 and references therein). Thus our starting point, the transient response model for Pi2 pulsations (e.g. Nishida, 1979, Kan et al., 1982; Baumjohann and Glaßmeier, 1984), leads us to the same type of filter as also used to detrend data in other fields of geophysics.

Application of this filter to artificial magnetograms shows major advantages in recovering the Pi2 signals compared to an ordinary high-pass filter. The amplitude spectra of the filtered signals nearly coincide with the input Pi2 except at very low frequencies. An improvement of the phase spectrum, however, was not achieved due to our choice of a zero-phase-shift filter.

The performance of the deconvolution filter was also tested on a real high-latitude magnetogram, and it was demonstrated that the deconvolution filtered Pi2 signal has a much sharper onset than the usually filtered one. This property of the suggested filter might be of interest in further studies of Pi2 delay times across magnetometer arrays as recently done by Samson et al. (1985).

Concluding, we may say that at present an absolutely exact recovery of Pi2 signals, comprising the amplitude and the phase spectra, is impossible due to the lack of a sophisticated physical model of the driving function. However, under the given situation we were able to design a filter by using an empirical model, which requires a minimum number of parameters and which provides obviously better results as compared with those of standard high-pass filtering. We regard our new method in filtering Pi2s as a basis for constructing a more realistic filter for detrending these pulsations. Nevertheless, future work should be invested in a more detailed comparison between the polarization filter, introduced by Samson and Olson (1981), and the deconvolution filter, where perhaps a combination of these two different types of filters may provide improved Pi2 signals.

Acknowledgements. We would especially like to thank J. Untiedt for constant support and encouragement and W. Baumjohann, F. Glangeaud, G.K. Hartmann, R.L. McPherron and J.C. Samson for helpful discussions and constructive criticisms. Our work was financially supported by the Deutsche Forschungsgemeinschaft.

References

Baumjohann, W., Glaßmeier, K.H.: The transient response mechanism and Pi2 pulsations at substorm onset. Planet. Space Sci. **32**, 1361-1370, 1984

Boström, R.: Magnetospheric-ionospheric coupling. In: Critical problems of magnetospheric physics, E.R. Dyer, ed.: pp. 139-156. IUCSTP Secretariat, National Academy of Sciences, Washington D.C., 1972

Fukushima, N.: Generalized theorem of no ground magnetic effect of vertical current connected with Pedersen currents in the uniform conductivity ionosphere. Rep. Ionos. Space Res. Jpn. **30**, 35-40, 1976

Glaßmeier, K.H.: On the influence of ionospheres with non-uniform conductivity distribution on hydromagnetic waves. J. Geophys. **54**, 125-137, 1984

Hughes, W.J.: Hydromagnetic waves in the magnetosphere. In: Solar terrestrial physics, Carovillano, R.L., Forbes, J.M., eds. Dordrecht: D. Reidel Pub. Co., 1983

Kan, J.R., Longenecker, D.U., Olson, J.V.: A transient response model of Pi2 pulsations. J. Geophys. Res. **87**, 7483-7488, 1982

Kulhánek, O.: Introduction to digital filtering in geophysics. New York: Elsevier Scientific Publishing Company, 1976

Küppers, F., Untiedt, J., Baumjohann, W., Lange, K., Jones, A.G.: A two-dimensional magnetometer array for ground based observations of auroral zone electric currents during the International Magnetospheric Study (IMS). J. Geophys. **46**, 429-450, 1979

Lester, M., Hughes, W.J., Singer, H.J.: Longitudinal structure in Pi2 pulsations and the substorm current wedge. J. Geophys. Res. **89**, 5489-5494, 1984

Lysak, R.L., Dum, C.T.: Dynamics of magnetosphere-ionosphere coupling including turbulent transport. J. Geophys. Res. **88**, 365-380, 1983

Nishida, A.: Possible origin of transient dusk-to-dawn electric fields in the nightside magnetosphere. J. Geophys. Res. **84**, 3409-3412, 1979

Pashin, A.B., Glaßmeier, K.H., Baumjohann, W., Raspopov, O.M., Yahnin, A.G., Opgenoorth, H.J., Pellinen, R.J.: Pi2 magnetic pulsations, auroral break-ups, and the substorm current wedge: A case study. J. Geophys. **51**, 223-233, 1982

Samson, J.C., Olson, J.V.: Data adaptive polarization filters for multichannel geophysical data. Geophysics **46**, 1423-1431, 1981

Samson, J.C., Harrold, B.G.: Maps of the polarisation of high-latitude Pi2's. J. Geophys. Res. **88**, 5736-5744, 1983

Samson, J.C., Harrold, B.G., Yeung, K.L.: Characteristic time constants and velocities of mid-latitude Pi2's. J. Geophys. Res. **90**, 3448-3456, 1985

Southwood, D.J., Hughes, W.J.: Concerning the structure of Pi2 pulsations. J. Geophys. Res. **90**, 386-392, 1985

Stuart, W.F.: A special feature of impulsive pulsations (Pi2). J. Atmos. Terr. Phys. **34**, 829-836, 1972

Received September 16, 1985; revised version February 3, 1986
Accepted March 19, 1986

J Geophys (1986) 59:202–203

Journal of Geophysics

Laudatio

Presentation of the Emil Wiechert Medal to Don L. Anderson, Pasadena

April 8, 1986, Karlsruhe

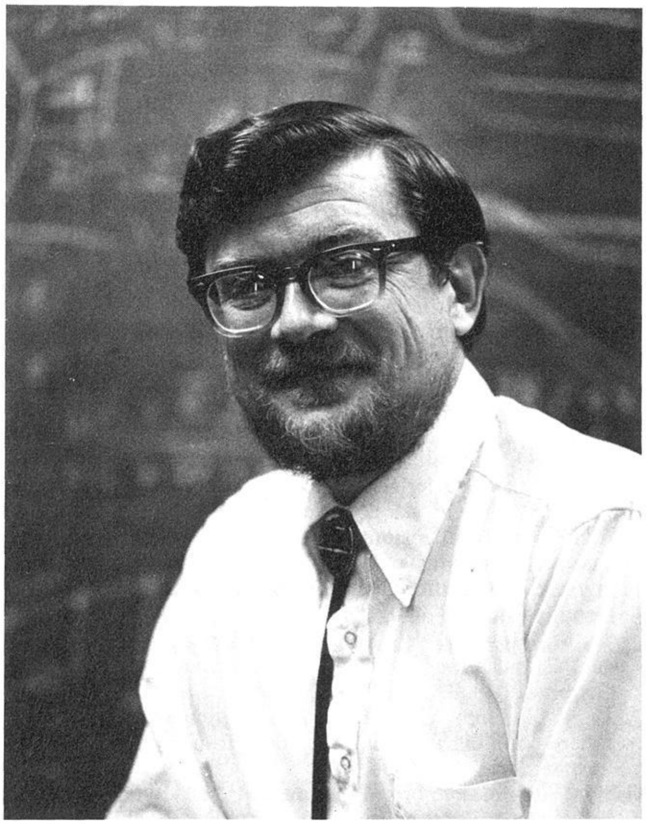

The Executive Committee of the Deutsche Geophysikalische Gesellschaft has decided to bestow its highest award, the Emil Wiechert Medal, on Don L. Anderson. The medal bears the name of the first president of the Deutsche Geophysikalische Gesellschaft following its foundation in 1924. Since first being awarded to Julius Bartels, the Emil Wiechert Medal has been conferred on Beno Gutenberg, Albert Defant, Inge Lehmann, Sydney Chapman, Ludwig Biermann, Leon Knopoff and Ulrich Schmucker. This year, during its 46th Annual Meeting at Karlsruhe, the Deutsche Geophysikalische Gesellschaft awards the Emil Wiechert Medal to a scientist who, in his own pioneering research, unifies many of the rapidly expanding branches of geophysics and of the earth sciences.

Physics and chemistry of the earth's interior and planetology are his prime interests. However, seismology is still the base of his exploration of the solid earth and other planets. He provided the earliest comprehensive dispersion tables of surface waves for oceanic and continental paths. Propagation of surface waves in heterogeneous anisotropic media was among his earliest interest in seismology. This subject can be followed through his entire career to the new frontier of three-dimensional seismic mapping of convection in the mantle, similar to medical tomography, and of delineating the direction of convection from the orientation of anisotropy. Together with A. Dziewonski, he established the preliminary earth model PREM which comprises our present knowledge of radially symmetric earth properties.

It is the strength of seismology to provide not only structure, but also physical properties of the earth's interior. There was always a certain fascination for seismologists to reach beyond their own realm of research. Early seismologists, like Wiechert, Gutenberg, Adams and Williamson, were tempted to explore the implications of their seismological findings for the physics and chemistry of the earth's interior. Don Anderson shares this fascination. Finite-strain theory led him to a seismic equation of state, relating the two seismic wave velocities directly to density. He studied the effect of partial melting on the seismic wave velocities and devoloped a model for the frequency-dependent attenuation and viscosity of the earth, comprising the range from seismic to tidal frequencies.

Geophysical tests of petrological hypotheses have always been a challenge to Don Anderson. Noteworthy are his investigations of the mantle-transition zone Bullen C and its relation to a change in composition. From the sharpness of the 650-km discontinuity, he postulated the lower mantle to be chemically different from the rest of the mantle.

Looking at the earth from an extraterrestrial perspective, Don Anderson explained the thin crust of the earth in comparison to that of the moon by the difference in thermal parameters of the two bodies. He concluded that most of the terrestrial "crust" is buried as an eclogite layer on top of the transition zone.

Recently he developed a hypothesis for cyclic continental aggregation and disaggregation. He related the breakup of Pangea as a supercontinent to the shape of the geoid, global heat flow, the insulating effect of the continental lithosphere and true polar wandering. Thus he explained the peculiarity of synchronous global tectonics and magmatic activity, rapid breakup and dispersal of continents, following long periods of static pole positions separated by periods of rapid polar wandering. He even linked tectonic and magnetic field variations.

Don Anderson is Professor of Geophysics and the present Director of the Seismological Laboratory at the California Institute of Technology in Pasadena. In this position he succeeded Beno Gutenberg and Frank Press. He is President-Elect of the American Geophysical Union. As a member of the National Academy of Sciences, as a fellow of the American Academy of Arts and Sciences and Foreign Honorary Fellow of the European Union of Geosciences, his merits have been previously recognized.

It is my duty and honour to award the medal. It bears the inscription:

„Die Deutsche Geophysikalische Gesellschaft e.V. verleiht die Emil Wiechert-Medaille an Don L. Anderson, Pasadena, für seinen grundlegenden Beitrag zur Erforschung der Struktur und Zusammensetzung der Erde".

Heinrich Soffel
Vorsitzender
der Deutschen Geophysikalischen Gesellschaft

J Geophys (1986) 59:204–205

Journal of Geophysics

Correction

J Geophys (1986) 59:56–61

A comparison of upper mantle subcontinental electrical conductivity for North America, Europe and Asia

W.H. Campbell and E.R. Schiffmacher

In the analysis of the regional geomagnetic field components we discovered a small programming error that affected the modelling of the southern hemisphere D and Z components used to compute the spherical harmonic coefficients for each continental sector. Revised Fig. 2 below illustrates the corrected internal currents. Note the particular changes required at low and equatorial latitudes.

Because the spherical harmonic coefficients determine the conductivity profiles reported in this paper, Figs. 3 and 4 and Table 1 also need revision. Paired values of the equivalent substitute layer conductivities and depths for sets of odd (n − m), separated for m (i.e., separated by wavelength) were smoothed using a regionally weighted regression technique on each set. A regionally weighted regression representation of all smoothed set values is presented in the revised Fig. 3, below. The best fitting exponentials representing the data are shown in Fig. 4 and Table 1. Old Fig. 5 may be omitted.

Table 1

Region	Approx. depth d (km)	Conductivity σ (s/m)
North America	32– 42	0.07
	279–336	0.00089 exp (0.014 d)
	341–487	0.035 exp (0.0027 d)
Europe	3–126	0.0078 exp (0.018 d)
	187–274	0.010 exp (0.0036 d)
	357–501	0.0027 exp (0.0073 d)
Central Asia	90–186	0.0062 exp (0.0128 d)
	270–370	0.0067 exp (0.0081 d)
	440–653	0.032 exp (0.0039 d)
East Asia	69–119	0.010 exp (0.0013 d)
	189–288	0.0089 exp (0.0063 d)
	294–430	0.017 exp (0.0035 d)
	466–587	0.024 exp (0.0031 d)

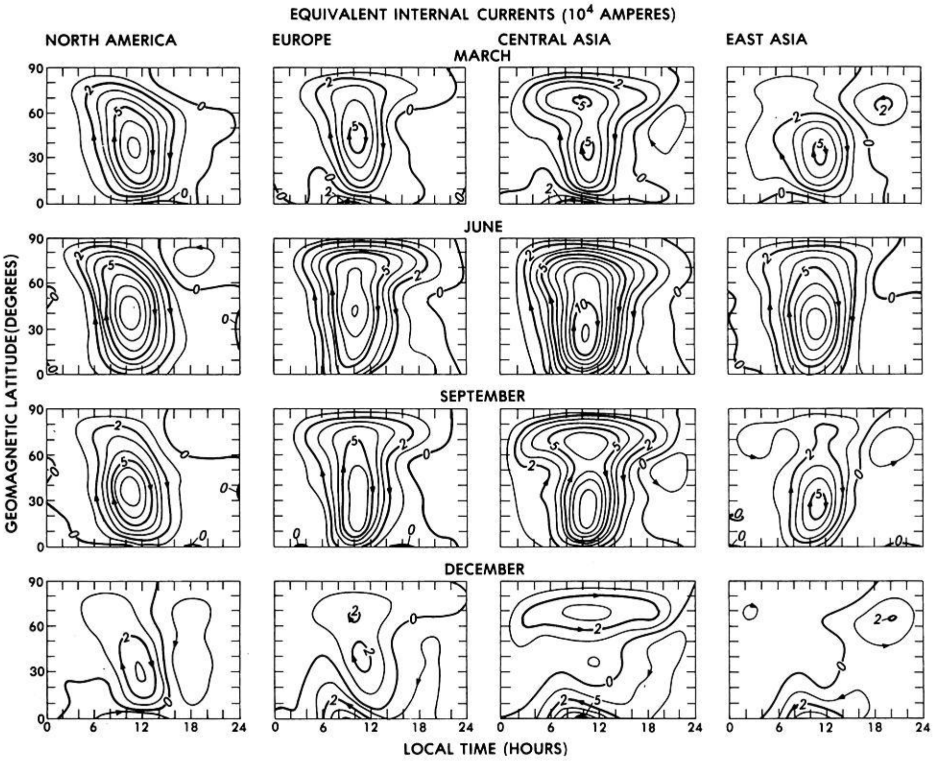

Fig. 2. Equivalent internal induced current for Sq daily variations of field in continental regions of North America (*first column*), Europe (*second column*), Central Asia (*third column*) and East Asia (*fourth column*). Examples for the four selected months of March, June, September and December are given in the top to bottom rows respectively. Each pattern in local-time versus latitude coordinates shows the equivalent current contours in 10^4-A steps with *arrows* for the required flow direction. A midnight zero current level was assumed

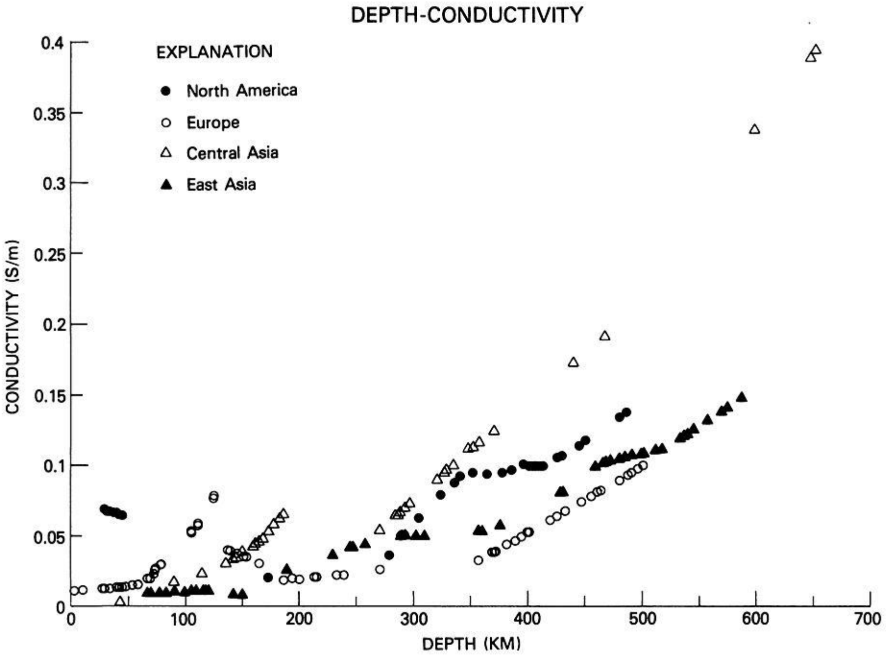

Fig. 3. Depth-conductivity values from Eqs. (10) and (11) obtained by application of the spherical harmonic analysis coefficients to Eqs. (7) and (8). The evaluations are separated for the North American, European, Central Asian and East Asian regions

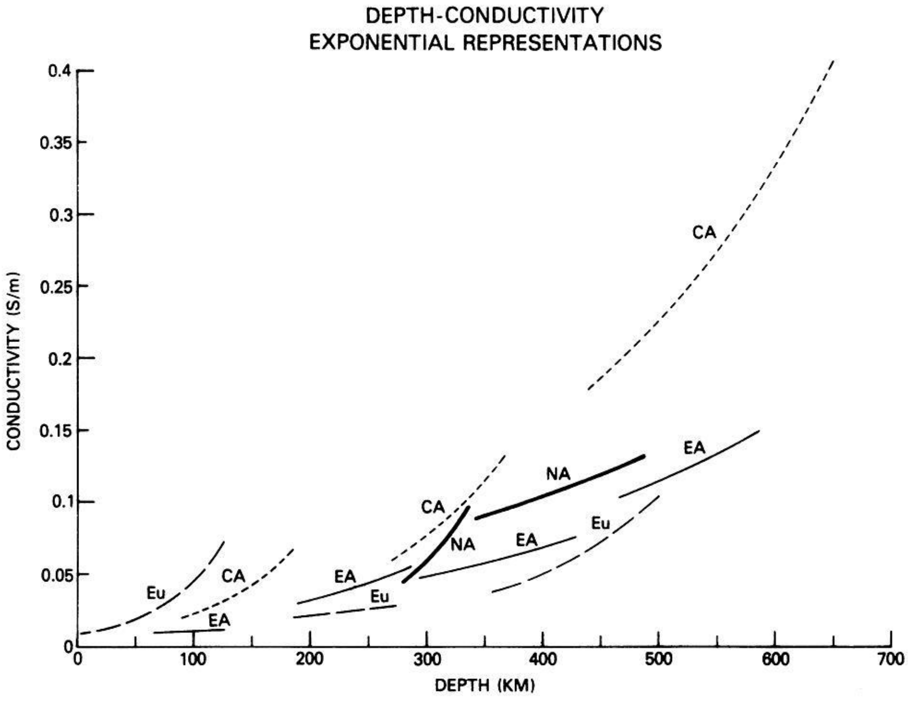

Fig. 4. Best exponential representations of depth-conductivity data given in Fig. 3. Separate curves are shown for North America, Europe, Central Asia and East Asia. The functions are listed in Table 1

J Geophys (1986) 59:206–207

Journal of Geophysics

Book reviews

Landolt-Börnstein: Zahlenwerte und Funktionen aus Naturwissenschaft und Technik. Neue Serie, Gruppe V, Bd. 2 Geophysik der festen Erde, des Mondes und der Planeten (Teilband b) 468 S. Fuchs, K. und Soffel, H. (Hrsg.) Springer-Verlag, Berlin, Heidelberg, New York, Tokyo 1985.

Die Beiträge des Teilbandes 2b befassen sich mit den Gebieten Thermodynamik, Magnetfeld und Massentransport im Erdinnern. Die Aufteilung des Bandes 2 auf die Teilbände a und b erfolgte nicht nach einer thematischen Einteilung, sondern nach den Daten der Fertigstellung der Manuskripte. Gesamt-Inhaltsverzeichnis und Übersichten auf den vorderen Buchdeckeln sollen dem Leser helfen, die Ordnung wieder herzustellen. Wie im Vorwort zu Band 2a erläutert, mußten die Text-Teile (Definitionen, Erläuterungen der Meßmethoden usw.) im Verhältnis zu den Datenteilen bei den Geophysik-Bänden länger sein, als bei den anderen Bänden des Landolt-Börnstein. Das entspricht dem Stand unseres Wissens. Als Beispiel dafür, wie schwierig es sei, unkommentierte geophysikalische Daten anzugeben, wurde im Vorwort zu 2a die Temperaturverteilung im Erdinnern genannt.

Man ist deshalb darauf gespannt, wie sie in 2b behandelt wird: Frau Lubimova schreibt im Text-Teil von 2.2.3, die Temperaturverteilung sei über die geothermische, geoelektrische und seismische Methode, sowie mit Hilfe der experimentellen Petrologie zu ermitteln. In Tabellen gibt sie für die Kern-Mantelgrenze 3790 K nach Stacey und 3131 K nach Andersen an. In dem Artikel 2.2.4 von Stacey über Wärmetransport im Erdinnern findet man wieder 3790 K. Im Abschnitt 2.3 über die elektrischen Eigenschaften des Erdinnern sucht man vergeblich nach einem Schluß auf die Temperatur. Dagegen benutzt Busse für die Theorie des Erdmagnetfeldes (4.2.4) eine Temperatur von 3157 K. So unsicher sind solche Werte noch trotz der angegebenen Dezimalen.

Die meisten der im Teilband 2b gebrachten Daten sind aber viel zuverlässiger. Vergleicht man den gegenwärtigen mit dem Landolt-Börnstein von 1952, so handelt es sich gelegentlich um eine Erweiterung und Fortschreibung, so im Kaptiel 4.2.3 von Voppel über erdmagnetisches Hauptfeld und Säkularvariation. Da erscheint der Abstand von 33 Jahren zwischen den Erscheinungsdaten als nicht zu lange. Anderes ist aber in den 3 Jahrzehnten völlig neu entstanden, so die Lehre vom Paläomagnetismus, die schon über eine detaillierte und sicher nützliche Datenbasis verfügt (Soffel 4.3, paläomagnetische Daten aber auch unter 4.2.1.6).

Einen Schwerpunkt im vorliegenden Teilband bilden die Kapitel von Schmucker über erdmagnetische Variationen im Außenraum und im Erdinnern (induzierter Anteil) inhaltlich, und in der Nomenklatur zusammenhängend, doch über den Band verstreut (4.1, 4.2.2, 2.3). Inhaltlich gehören auch die Leitfähigkeitsanomalien (Haak 2.3.2) zu diesem Komplex. Neu ist auch der ganze Abschnitt 5 von Hagedorn und Gierloff-Emden über das Relief der Erde und von Jacoby über Theorien und Hypothesen der globalen Tektonik, letzterer mehr eine Sammlung von Definitionen als von Daten.

Der Teilband 2b ist alles andere als eine langweilige Tabellensammlung. Vielleicht ist die Darstellung wegen ihrer Kürze so faszinierend. Dazu kommt der ästhetische Genuß der vom Springer-Verlag gelieferten Abbildungen und Tabellen. Schade, daß die Abschnitte so durcheinander gewürfelt sind – ich habe keine Regel dafür gefunden, nach der der Abschnitt 2.3 auf die letzten Seiten verbannt wurde. Gut, daß es ein Sachregister gibt für alle bisherigen Teilbände der Gruppe V. Es bleibt für Leser und Herausgeber zu hoffen, der Landolt-Börnstein werde von allen Bibliotheken angeschafft, so daß keiner der Benutzer ernsthaft die Frage stellt, ob er sein Geld wert ist.

W. Kertz

Wilfried Schröder (ed): Historical events and people in geosciences Selected papers from the symposia of the Interdivisional Commission on History of IAGA during the IUGG General Assembly, held in Hamburg, 1983. European University Studies, Series XXXIX, Interdepartmental Congress Reports, Vol. 2, 220 pages – Peter Lang, Frankfurt am Main Bern New York, 1985

During the IUGG General Assembly, held in Hamburg, 1983, two sessions on the history of geomagnetism and aeronomy took place. One session was devoted to historical events and the people involved in them. This book is a collection of many of the papers presented in this session, with the addition of those presented in the other session that are appropriate to the theme of historical events.

The lengths of the 20 contributions (one in French) are rather different, three of them being only abstracts to which, however, numerous references are added. The authors are from various countries: Austria, Canada, China, France, Federal Republic of Germany, Italy, Japan, Norway and the United Kingdom. Thus, the national endeavours as well as international cooperations in geomagnetism and aeronomy become obvious. Figures, photographs and portraits enlarge the presentations. However, the reproductions are of rather poor quality. The representatives of IAGA should have devoted a more respectable publication to the sources and the history of their association.

The broad scope of the book can only be outlined here by pointing out various themes: Halley's (1656–1742) Atlantic magnetic surveys between 1698 and 1701; the Göttinger Magnetische Verein and the Antarctic expedition of James Clark Ross (1839–1843); K.F. Gauss (1777–1852) et l'Astronomie géodésique ou le succès différé de la méthode des hauteurs égales; the promoters of international polar research; commencement of hourly geomagnetic observation in Japan (15 March 1883) during the First International Polar Year; the Haldde Observatory (1899) – the cradle of modern auroral research; the Ben Nevis Observatory (1883); the earliest observations of noctilucent clouds; an eyewitness account of the eruption of Krakatoa found in the papers of Charles Lapworth; radio communication and solar-terrestrial physics; Erich Regener (1881–1955): a pioneer of geophysical research; Balfour Currie (1902–1981) and the Second International Polar Year; on the history of the solar wind concept.

This book may be recommended to more than just IAGA people, in order that scientists realize that today they are standing and working on a platform set up by engaged pioneers of science over the course of centuries.

H. Schwentek

Keary, P., Brooks M.: An Introduction to Geophysical Exploration. Blackwell Scientific Publications, Inc., Oxford, 296 p., 210 illustrations, US $ 21.00, 1984

Reading this book has given me considerable pleasure. I have enjoyed its style and presentation of methodology and theory, although naturally the latter is short in an introductory text. I also enjoy the way the subject of geophysical exploration is organized, clarifying both general principles and special aspects and methods.

"By working at different scales, geophysical methods may be applied to a wide range of investigations from studies of the entire earth ... to exploration of a localized region of the upper crust" (p. 1). I have always thought that "Applied Geophysics" or "Geophysical Exploration" is more than the search of resources and I welcome this view being expressed in the book.

There is an introductory chapter *1* on "The principles and limitations of geophysical exploration methods" and a closing chapter *10* on "Major fields of application of geophysical exploration" discussing a number of case histories and giving a general impression of the broad field of geophysical studies. Such a chapter at the end is a particularly good idea, I think. Another good idea is another general chapter *2* on "geophysical data processing". Appropriate to the practical importance of seismology, there are then three chapters; *3* on "elements of seismic surveying, *4* on reflection and *5* on refraction surveying. The other geophysical methods cover about the same volume in the book (as seismology does); *6* on gravity, *7* on magnetics, *8* on electrical surveying and *9* on electromagnetic surveying.

To me, having taught Applied Geophysics for many years to students of geophysics and to students of geology, the theoretical treatment appears clear, concise and very accurately formulated. Maybe it is so short that the beginner for whom the book has been written will hardly grasp the ideas. In connection with a course this problem is, of course, not so serious since questions may be asked and exercises will be done. A list of problems for exercise is not included, in contrast to most other texts.

The book is well illustrated and didactically well written. Of course, it is not always that a clear presentation makes the reader think hardest. On the other hand, an obscure presentation will generally confuse the reader instead of making him ask the right questions. The present text, I think, has the advantage of being clear *and* leaving questions open, thus challenging students and lecturers to amplify on the subjects.

In conclusion, I recommend this text to teachers and also to students for their self study. I personally shall probably take the text as the basis for an introductory course in Applied Geophysics, which I am presently developing for students of geology.

W.R. Jacoby